IDENTIFICATION OF NEW MOLECULAR MECHANISMS OF BONE DISEASE

EDITED BY: Andrea Del Fattore, Roberto Baldelli and Amélie E. Coudert
PUBLISHED IN: Frontiers in Cell and Developmental Biology

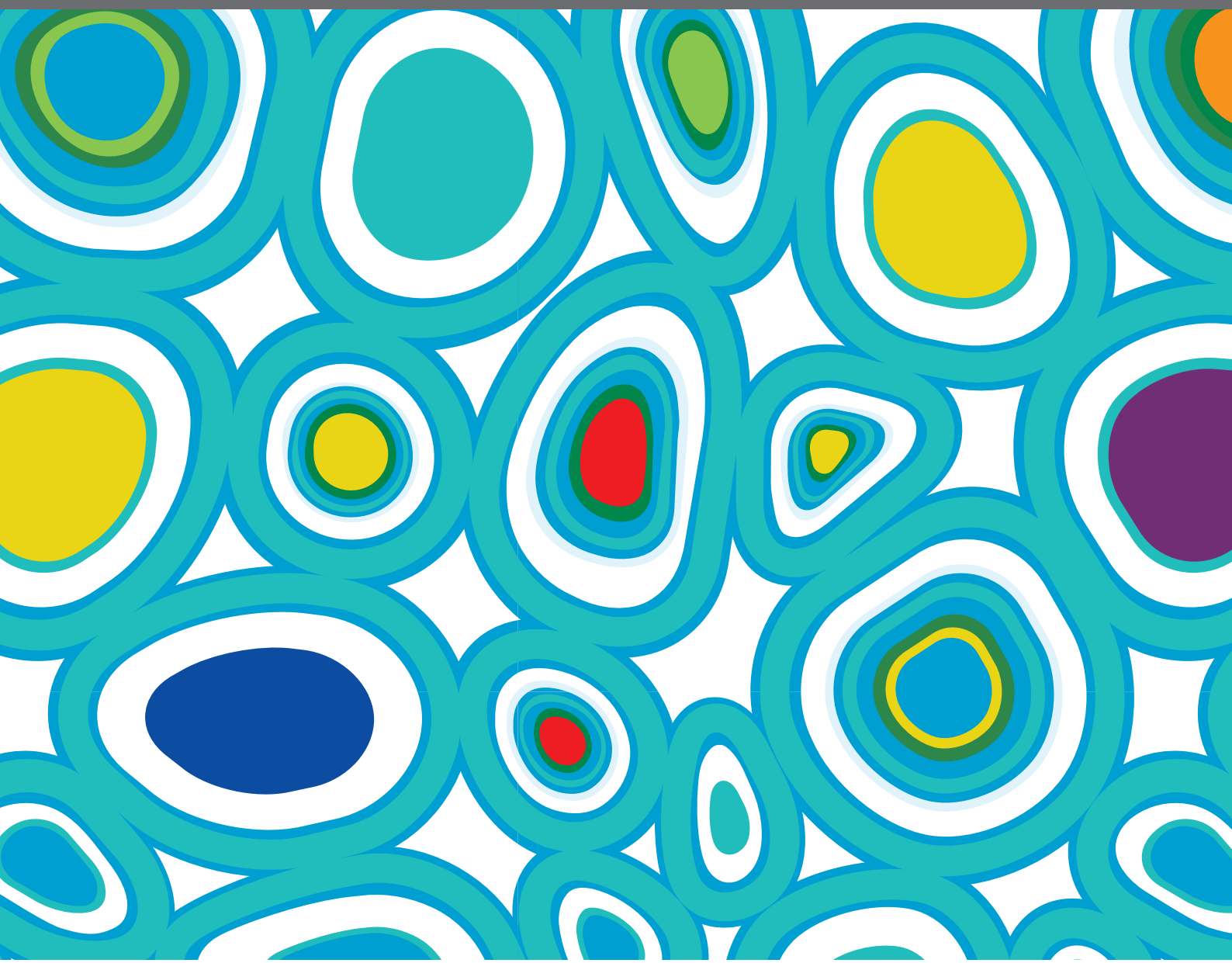

frontiers Research Topics

frontiers

ISSN 1664-8714
ISBN 978-2-88976-848-6
DOI 10.3389/978-2-88976-848-6

About Frontiers

Frontiers is more than just an open-access publisher of scholarly articles: it is a pioneering approach to the world of academia, radically improving the way scholarly research is managed. The grand vision of Frontiers is a world where all people have an equal opportunity to seek, share and generate knowledge. Frontiers provides immediate and permanent online open access to all its publications, but this alone is not enough to realize our grand goals.

Frontiers Journal Series

The Frontiers Journal Series is a multi-tier and interdisciplinary set of open-access, online journals, promising a paradigm shift from the current review, selection and dissemination processes in academic publishing. All Frontiers journals are driven by researchers for researchers; therefore, they constitute a service to the scholarly community. At the same time, the Frontiers Journal Series operates on a revolutionary invention, the tiered publishing system, initially addressing specific communities of scholars, and gradually climbing up to broader public understanding, thus serving the interests of the lay society, too.

Dedication to Quality

Each Frontiers article is a landmark of the highest quality, thanks to genuinely collaborative interactions between authors and review editors, who include some of the world's best academicians. Research must be certified by peers before entering a stream of knowledge that may eventually reach the public - and shape society; therefore, Frontiers only applies the most rigorous and unbiased reviews.
Frontiers revolutionizes research publishing by freely delivering the most outstanding research, evaluated with no bias from both the academic and social point of view. By applying the most advanced information technologies, Frontiers is catapulting scholarly publishing into a new generation.

What are Frontiers Research Topics?

Frontiers Research Topics are very popular trademarks of the Frontiers Journals Series: they are collections of at least ten articles, all centered on a particular subject. With their unique mix of varied contributions from Original Research to Review Articles, Frontiers Research Topics unify the most influential researchers, the latest key findings and historical advances in a hot research area! Find out more on how to host your own Frontiers Research Topic or contribute to one as an author by contacting the Frontiers Editorial Office: frontiersin.org/about/contact

IDENTIFICATION OF NEW MOLECULAR MECHANISMS OF BONE DISEASE

Topic Editors:
Andrea Del Fattore, Bambino Gesù Children's Hospital (IRCCS), Italy
Roberto Baldelli, San Camillo-Forlanini Hospital, Italy
Amélie E. Coudert, Université Paris Cité, France

Citation: Del Fattore, A., Baldelli, R., Coudert, A. E., eds. (2022). Identification of New Molecular Mechanisms of Bone Disease. Lausanne: Frontiers Media SA. doi: 10.3389/978-2-88976-848-6

Table of Contents

05 ***Classification of Osteosarcoma Based on Immunogenomic Profiling***
Xinwen Wang, Liangming Wang, Weifeng Xu, Xinwu Wang, Dianshan Ke, Jinluan Lin, Wanzun Lin and Xiaochun Bai

17 ***ELMO1 Regulates RANKL-Stimulated Differentiation and Bone Resorption of Osteoclasts***
Xinyue Liang, Yafei Hou, Lijuan Han, Shuxiang Yu, Yunyun Zhang, Xiumei Cao and Jianshe Yan

28 ***The Potential Role of RP105 in Regulation of Inflammation and Osteoclastogenesis During Inflammatory Diseases***
Zhou Fan, Janak L. Pathak and Linhu Ge

49 ***Autophagy-Related Genes and Long Noncoding RNAs Signatures as Predictive Biomarkers for Osteosarcoma Survival***
Jian Zhang, Rui Ding, Tianlong Wu, Jingyu Jia and Xigao Cheng

65 ***Stimulation of Treg Cells to Inhibit Osteoclastogenesis in Gorham-Stout Disease***
Michela Rossi, Ippolita Rana, Paola Sabrina Buonuomo, Giulia Battafarano, Viviana De Martino, Matteo D'Agostini, Ottavia Porzio, Cristiana Cipriani, Salvatore Minisola, Rita De Vito, Davide Vecchio, Michaela Veronika Gonfiantini, Alessandro Jenkner, Andrea Bartuli and Andrea Del Fattore

76 ***A Dominant Heterozygous Mutation in* COG4 *Causes Saul–Wilson Syndrome, a Primordial Dwarfism, and Disrupts Zebrafish Development via Wnt Signaling***
Zhi-Jie Xia, Xin-Xin I. Zeng, Mitali Tambe, Bobby G. Ng, P. Duc S. Dong and Hudson H. Freeze

90 ***Sestrin2-Mediated Autophagy Contributes to Drug Resistance* via *Endoplasmic Reticulum Stress in Human Osteosarcoma***
Zhen Tang, Xinghui Wei, Tian Li, Wei Wang, Hao Wu, Hui Dong, Yichao Liu, Feilong Wei, Lei Shi, Xiaokang Li, Zheng Guo and Xin Xiao

104 ***Corrigendum: Sestrin2-Mediated Autophagy Contributes to Drug Resistance* via *Endoplasmic Reticulum Stress in Human Osteosarcoma***
Zhen Tang, Xinghui Wei, Tian Li, Wei Wang, Hao Wu, Hui Dong, Yichao Liu, Feilong Wei, Lei Shi, Xiaokang Li, Zheng Guo and Xin Xiao

109 ***PPARβ/δ Agonist Alleviates Diabetic Osteoporosis* via *Regulating M1/M2 Macrophage Polarization***
Miao Chen, Weimin Lin, Rui Ye, Jianru Yi and Zhihe Zhao

121 ***YAP/TAZ in Bone and Cartilage Biology***
Mylène Zarka, Eric Haÿ and Martine Cohen-Solal

134 ***GLIS Family Zinc Finger 1 was First Linked With Preaxial Polydactyly I in Humans by Stepwise Genetic Analysis***
Jie-Yuan Jin, Pan-Feng Wu, Fang-Mei Luo, Bing-Bing Guo, Lei Zeng, Liang-Liang Fan, Ju-Yu Tang and Rong Xiang

144 *Whole-Exome Sequencing Identifies a Novel* CPT2 *Mutation in a Pedigree With Gout*
Yong Guo, Jing Jin, Zhenni Zhou, Yihui Chen, Li Sun, Chunwu Zhang and Xiaoru Xia

152 *Corrigendum: Whole-Exome Sequencing Identifies a Novel CPT2 Mutation in a Pedigree With Gout*
Yong Guo, Jing Jin, Zhenni Zhou, Yihui Chen, Li Sun, Chunwu Zhang and Xiaoru Xia

153 *Self-Assembling Imageable Silk Hydrogels for the Focal Treatment of Osteosarcoma*
Zhibin Peng, Ming Li, Yuan Wang, Hongbo Yang, Wei Wei, Min Liang, Jianhui Shi, Ruixuan Liu, Rui Li, Yubo Zhang, Jingsong Liu, Xu Shi, Ran Wan, Yao Fu, Rui Xie and Yansong Wang

frontiers in Cell and Developmental Biology

ORIGINAL RESEARCH
published: 16 July 2021
doi: 10.3389/fcell.2021.696878

Classification of Osteosarcoma Based on Immunogenomic Profiling

Xinwen Wang[1,2†], Liangming Wang[3†], Weifeng Xu[4†], Xinwu Wang[5], Dianshan Ke[6], Jinluan Lin[7], Wanzun Lin[8] and Xiaochun Bai[1,2*]*

[1] The Third Affiliated Hospital of Southern Medical University, Guangzhou, China, [2] Guangdong Provincial Key Laboratory of Bone and Joint Degeneration Diseases, Guangzhou, China, [3] Department of Orthopedics, The Second Affiliated Hospital of Fujian Medical University, Quanzhou, China, [4] Department of Medical Oncology, The Affiliated Cancer Hospital of Zhengzhou University, Zhengzhou, China, [5] Department of Orthopedics, The First Hospital of Putian City, Putian, China, [6] Department of Orthopedics, Jiangmen People's Hospital, Jiangmen, China, [7] Department of Orthopedics, The First Affiliated Hospital of Fujian Medical University, Fuzhou, China, [8] Department of Radiation Oncology, Shanghai Proton and Heavy Ion Center, Fudan University Cancer Hospital, Shanghai, China

OPEN ACCESS

Edited by:
Andrea Del Fattore, Bambino Gesù Children Hospital (IRCCS), Italy

Reviewed by:
Zhan Wang, Zhejiang University, China
Yongbiao Huang, Huazhong University of Science and Technology, China

***Correspondence:**
Wanzun Lin
68729499@qq.com
Xiaochun Bai
baixc15@smu.edu.cn

[†] These authors have contributed equally to this work

Specialty section:
This article was submitted to Molecular Medicine, a section of the journal Frontiers in Cell and Developmental Biology

Received: *18 April 2021*
Accepted: *14 June 2021*
Published: *16 July 2021*

Citation:
Wang X, Wang L, Xu W, Wang X, Ke D, Lin J, Lin W and Bai X (2021) Classification of Osteosarcoma Based on Immunogenomic Profiling. Front. Cell Dev. Biol. 9:696878. doi: 10.3389/fcell.2021.696878

Accumulating evidence has supported that osteosarcoma is heterogeneous, and several subtypes have been identified based on genomic profiling. Immunotherapy is revolutionizing cancer treatment and is a promising therapeutic strategy. In contrast, few studies have identified osteosarcoma classification based on immune biosignatures, which offer the optimal stratification of individuals befitting immunotherapy. Here, we classified osteosarcoma into two clusters: immunity high and immunity low using the single-sample gene-set enrichment analysis and unsupervised hierarchical clustering. Immunity_H subtype was associated with high immune cells infiltration, a favorable prognosis, benefit to immunotherapy, high human leukocyte antigen gene expression, and activated immune signal pathway indicating an immune-hot phenotype. On the contrary, the Immunity_L subtype was correlated with low immune cell infiltration, poor prognosis, and cancer-related pathway, indicating an immune-cold phenotype. We also identified TYROBP as a key immunoregulatory gene associated with $CD8^+$ T cell infiltration by multiplex immunohistochemistry. Finally, we established an immune-related prognostic model that predicted the survival time of osteosarcoma. In conclusion, we established a new classification system of osteosarcoma based on immune signatures and identified TYROBP as a key immunoregulatory gene. This stratification had significant clinical outcomes for estimating prognosis, as well as the immunotherapy of osteosarcoma patients.

Keywords: osteosarcoma, immune subtype, immune checkpoint inhibitors, TYROBP, prognosis

INTRODUCTION

Osteosarcoma, originating from mesenchymal stem cells, is the most common primary malignancy of bone (ElKordy et al., 2018). With the advancement of surgical resection, radiotherapy, and neoadjuvant chemotherapy, the survival rate of osteosarcoma patients has increased up to 60–70% (Kansara et al., 2014; Simpson and Brown, 2018). However, the prognosis of patients with

recurrent, metastatic, or unresectable osteosarcomas is extremely poor. The long-term survival rate for patients with primary osteosarcoma is approximately 65%, whereas it is less than 20% for patients with metastatic osteosarcomas (Durfee et al., 2016; Whelan and Davis, 2018). Hence, a novel therapeutic strategy for advanced sarcomas should be developed to improve the outcome of osteosarcomas. Recently, cancer immunotherapy has received tremendous attention for the treatment of numerous refractory malignancies (Baxevanis et al., 2009; Yang, 2015; Emens et al., 2017; O'Donnell et al., 2019; Lin et al., 2020). Hence, it is worth considering immunotherapy for osteosarcoma, as the treatment options for this disease are still limited.

Accumulating evidence has suggested that osteosarcoma tends to be susceptible to immunotherapy (Chen et al., 2021). Osteosarcoma tumors have a high proportion of $CD8^+$ invading lymphocytes relative to other sarcoma subtypes, and the number of infiltrating immune cells associates positively with overall survival (OS) (Wang et al., 2016). Besides, some osteosarcomas have an elevated programmed cell death protein-1 ligand (PD-L1) expression, with a high level of genomic instability, indicating prospective sensitivity to programmed cell death protein-1 (PD-1)/PD-L1 cascade suppressors (Shen et al., 2014). Although some patients benefit from different immunotherapeutic interventions, the majority fail to experience benefit. Thus, considering the low response rate, novel and accurate classification methods should be developed to identify patients befitting immunotherapy.

Here, we performed the single-sample gene-set enrichment analysis (ssGSEA) of the transcriptome data of 29 immune gene sets and established a novel classification of osteosarcoma. We also tried to characterize the subtype-distinct molecular features, including immune signaling cascades, and key genes and to construct and validate the immune-associated prognostic biosignature.

MATERIALS AND METHODS

Datasets

The RNA-seq transcriptome data, as well as the clinicopathological information of osteosarcoma patients, were obtained from TARGET as a training set. Similarly, patients from Gene Expression Omnibus (GSE21257) were abstracted as a validation set.

Single-Sample Gene-Set Enrichment Analysis

For each osteosarcoma dataset, the levels of enrichment of the 29 immune biosignatures were quantified in each osteosarcoma sample using ssGSEA (Barbie et al., 2009). The ssGSEA enrichment score was obtained by "GSVA" and "GSEABase" packages in R software (version 4.0.0). Gene signatures for each immune cell type and immune pathway were obtained from previously published data, representing the overall immune activity of the tumor microenvironment (He et al., 2018).

Clustering of Osteosarcoma Samples

Then, we carried out a hierarchical grouping of osteosarcoma based on the 29 immune biosignature enrichment levels (ssGSEA scores). ESTIMATE was carried out to explore the immune score, as well as the tumor purity for each osteosarcoma sample.

Principal Component Analysis

Principal component analysis (PCA) was performed to compare the transcriptional profiles between the different immune subtypes. The gene names with corresponding expression value and sample information were loaded, and the analysis was conducted by "limma" package using princomp function and visualized by "ggplot2" package in R software (version 4.0.0).

Identification of Differentially Expressed Immune-Related Genes

The differential expression of immune-related genes was identified using the "limma" R package. Adj. $p < 0.05$, and $|\text{fold change}| > 2$ were defined as the threshold values. The differentially expressed immune-related genes were visualized by the "ggplot2" package in R software (version 4.0.0).

Multiplex Immunohistochemistry

Tissue microarray of osteosarcoma specimens (L714901) was obtained from Biotech Company (Xian, China) and used to explore further the association of TYROBP expression with $CD8^+$ T cell in the osteosarcoma tumor microenvironment.

Multiplex immunohistochemistry was conducted using the sequential staining cycles as follows. In brief, formalin-fixed, paraffin-embedded osteosarcoma tissue sections were deparaffinized and then underwent microwave treatment in citrate for antigen retrieval. Then, they were blocked with 10% normal goat serum and incubated overnight with primary antibodies: mouse anti-CD8 antibody (1:100, ab17147, Abcam) and rabbit anti-TYROBP antibody (1:200, ab124834, Abcam). Next, sections were incubated with the corresponding horseradish peroxidase-conjugated second antibodies (Abcam, CN) for 30 min at room temperature. The antigenic binding sites were visualized using the tyramide signal amplification dye. Fluorescein isothiocyanate-tyramide (1:1,000, G1235, Servicebio) and Cy3-tyramide (1:1,000, G1235, Servicebio) were applied to each antibody.

Constitution of a Risk Model

Critical immune-related genes (IRGs) that presented protein–protein interaction (PPI) network were utilized in Lasso Cox regression to calculate the coefficients; the risk-score formula was formulated as:

$$\text{Risk score} = \sum_{i=1}^{N} \left(Exp_i \times Coe_i\right)$$

where $N = 2$, Expi was the expression value of every five hypoxia genes, whereas the Coei denoted the corresponding multivariable Cox regression coefficient.

Survival Analyses

Kaplan–Meier curves were used to visualize and compare the OS of osteosarcoma patients in different immunogenomic subtypes *via* survival and survminer R package. A receiver operating characteristic curve was constructed to verify our risk model accuracy *via* the survivalROC R package.

Visualization of Protein–Protein Interaction Network

We constricted the PPI network using the STRING database Cytoscape software. Cytoscape[1] constitutes a publicly accessible software web source used in visualizing complex networks, as well as for integrating these with any kind of attribute data. The Cytoscape web portal was used to build a protein cross talk association network and investigated the interaction association of the core IRGs.

RESULTS

Immunogenomic Profiling Identifies Two Osteosarcoma Subtypes

We assessed 29 immune-linked gene sets that represented multiple immune cell types, cascades, and functions. The enrichment levels or the activity of immune cells and signaling cascades were quantified in the osteosarcoma samples using ssGSEA analysis. Totally, we hierarchically categorized osteosarcoma in two cohorts (TARGET and GSE21257). Noteworthy, all cohorts presented similar clustering findings, with two clusters clearly being identified. We termed the classes as immunity high (Immunity_H) and immunity low (Immunity_L). Overall, the Immunity_H subtype was correlated with high immune cell infiltration and activated immune pathways indicating an immune-hot phenotype, whereas the Immunity_L subtype was associated with low immune cell infiltration indicating an immune-cold phenotype (**Figures 1A,B**). Moreover, the immune scores were remarkably elevated in Immunity_H than that in Immunity_L in TARGET and GSE21257 datasets (**Figure 1C**). Besides, opposite trends were reported with regards to tumor purity between the two subtypes, with tumor purity escalating from Immunity_L to Immunity_H (**Figure 1D**).

Altogether, these data indicate that Immunity_H has the greatest number of immune cells, which may benefit from immune checkpoint blockade therapy.

Immunity_H Subtype Is Associated With Immune-Related Signaling Pathways, a Favorable Prognosis and a Potential Benefit to Immunotherapy

Principal component analysis was then performed to compare the transcriptional profiles between the Immunity_H and Immunity_L subtypes, which displayed a clear distinction. In detail, PCA showed that the samples from the two clusters were well separated from each other (**Figure 2A**). To further identify relevant signaling cascades activated in the Immunity_H and the Immunity_L groups, we performed a GSEA analysis. Gene sets were differentially enriched in the Immunity_H groups of the TARGET web portal, as they were associated with processes that trigger immunity, such as dendritic cell antigen processing and presentation, interleukin-10 secretion, interleukin-12 secretion, and natural killer cell chemotaxis (**Figure 2B**). On the contrary, the cancer-linked signaling cascades were hyperactivated in the Immunity_L group, including the positive modulation of G1/S transition of the mitotic cell cycle and vascular endothelial cell proliferation. A similar trend was observed in the GES21257 dataset (**Figure 2C**). This finding verified the increased immune activity in Immunity_H.

Previous studies showed that osteosarcoma with elevated immune activity and high immune cell infiltration was associated with more favorable clinical outcomes. In line with these pieces of evidence, survival analyses showed that these immune subtypes had distinct clinical outcomes. The Immunity_H subtype had a better survival prognosis than the Immunity_L subtypes (**Figure 2D**).

We then used TIDE (a computational framework developed to evaluate the potential of tumor immune escape from the gene expression profiles of cancer samples: [2]) to evaluate the potential clinical efficacy of immunotherapy in these immune subtypes. In our results, the Immunity_H subtype had a higher response rate than the Immunity_L subgroup, implying that Immunity_H patients could benefit more from immune checkpoint inhibitor (ICI) therapy (**Figure 2E**). Besides, chemosensitivity of these subtypes was assessed by the Genomics of Drug Sensitivity in Cancer database, and the results showed that half-maximal inhibitory concentration scores of gemcitabine and mitomycin C in immunity_H were significantly lower than immunity_L subtype, indicating sensitivity to chemotherapy (**Figure 2F**).

Differences in Human Leukocyte Antigen Genes and Immune Checkpoint Expression Related to Immune Phenotypes

Tumor-related antigen presentation *via* MHC class I complexes is a prerequisite for immune surveillance and is instrumental for the clinical response of immunotherapies targeting immune checkpoints. Hence, we assessed transcript levels of 24 human leukocyte antigen (HLA) genes in TARGET and GSE21257 validation cohorts. Most immune HLA genes exhibited markedly lower expression levels in Immunity_L, indicating impaired antigen presentation on tumor cells as an escape mechanism from immune surveillance (**Figures 3A,B**). Expression of immune checkpoints has been exploited as predictive biomarkers for checkpoint inhibitor-based immunotherapy; we further compared the differences in immune checkpoints (PD-L1, PD-1, CTLA4, TIM3, LAG3, and TIGIT) related to immunity high and immunity low subtypes. Interestingly,

[1] https://cytoscape.org/

[2] http://tide.dfci.harvard.edu/

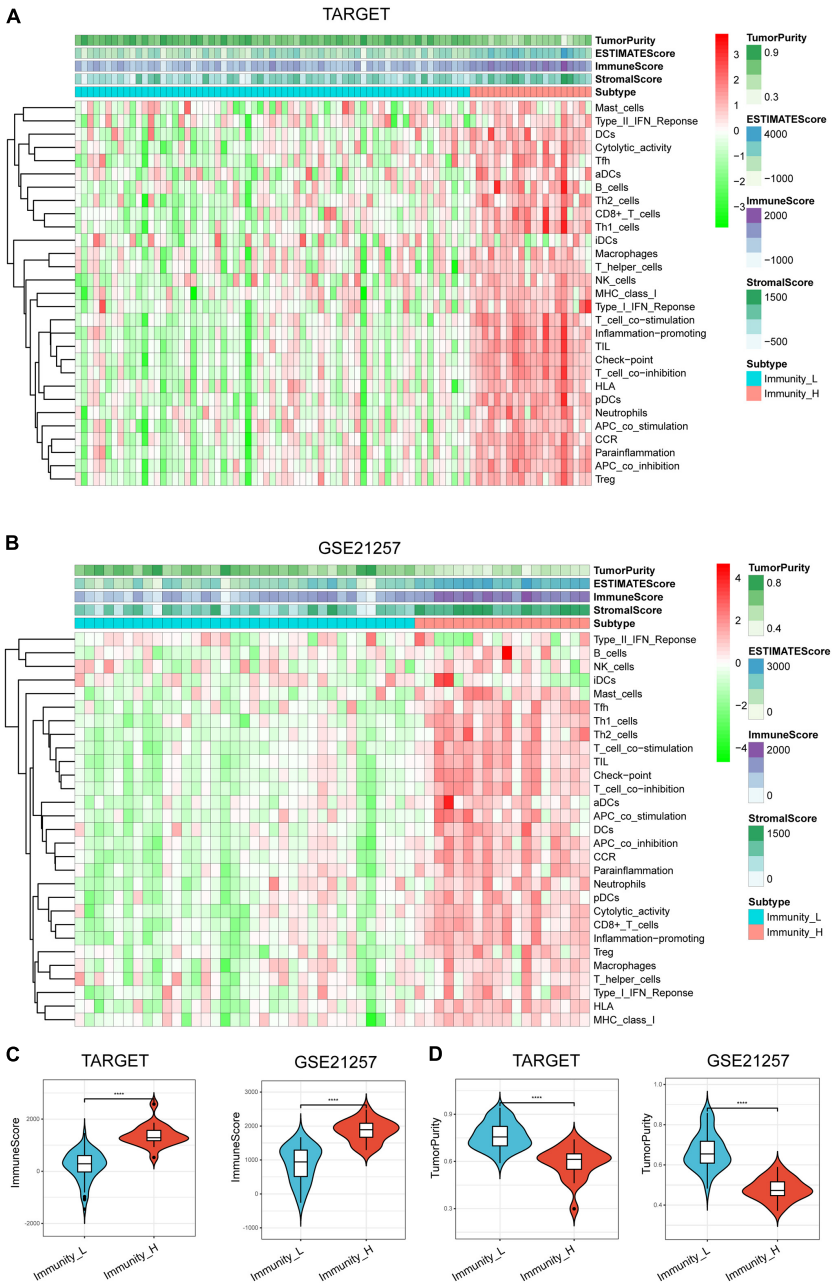

FIGURE 1 | Hierarchical clustering of osteosarcoma identified two immune subtypes in TARGET **(A)** and GSE21257 datasets **(B)**. Correlation between immunogenomic subtypes and immune cell invasion level in immune score **(C)** and tumor purity **(D)**. Violin plots particularly indicated differences in two subtypes. ****$p < 0.0001$.

high immune checkpoint expression was observed in the Immunity_H subtype, indicating a potential benefit from checkpoint inhibitor-based immunotherapy (**Figures 3C,D**).

Identification of Key Genes Between Immunity_H and Immunity_L Subtypes

We further identified the differentially expressed genes (DEGs) between Immunity_H and Immunity_L groups and revealed the critical immune-linked genes. A total of 303 DEGs in the TARGET cohort and 173 genes in the GES21257 cohort were identified with an intersection of 83 genes in the two datasets, and most of the genes were upregulated in the Immunity_H group (**Figures 4A,B**). PPI network was then performed to reveal the key genes associated with the immune subtypes. The top 10 immune-related genes with the highest degrees of interaction were determined, including TYROBP, ITGB2, LCP2, C1QB, C1QC, CD74, HLA-DRA, CXCL10, CCL5, and

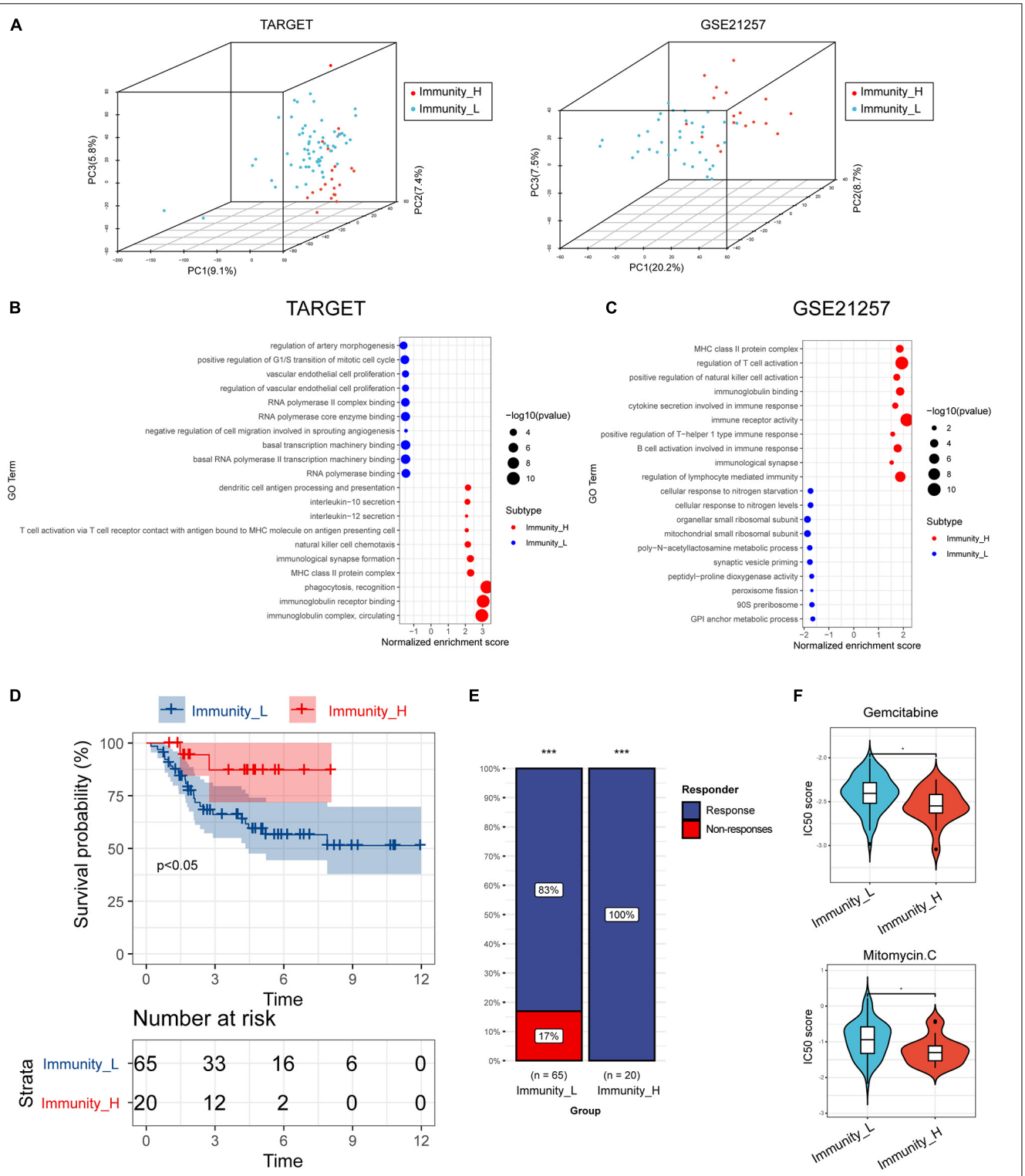

FIGURE 2 | (A) Principal component analysis plots. Red dots represent Immunity_H samples, and blue dots represent Immunity_L samples; **(B,C)** GSEA identified differential immune-related signaling cascades enriched in Immunity_H, as well as Immunity_L subtypes in TAGRT and GSE21257 datasets. Size of dots represented -log10 (p-value); **(D)** Kaplan–Meier curves of OS in Immunity_H and Immunity_L subtypes; **(E)** response rate to immunotherapy predicted by TIDE (a computational framework developed to evaluate potential of tumor immune escape from gene expression profiles of cancer samples: http://tide.dfci.harvard.edu/); **(F)** half-maximal inhibitory concentration scores of gemcitabine and mitomycin C in immunity_H and immunity_L subtypes. *$p < 0.05$, ***$p < 0.001$, and ****$p < 0.0001$.

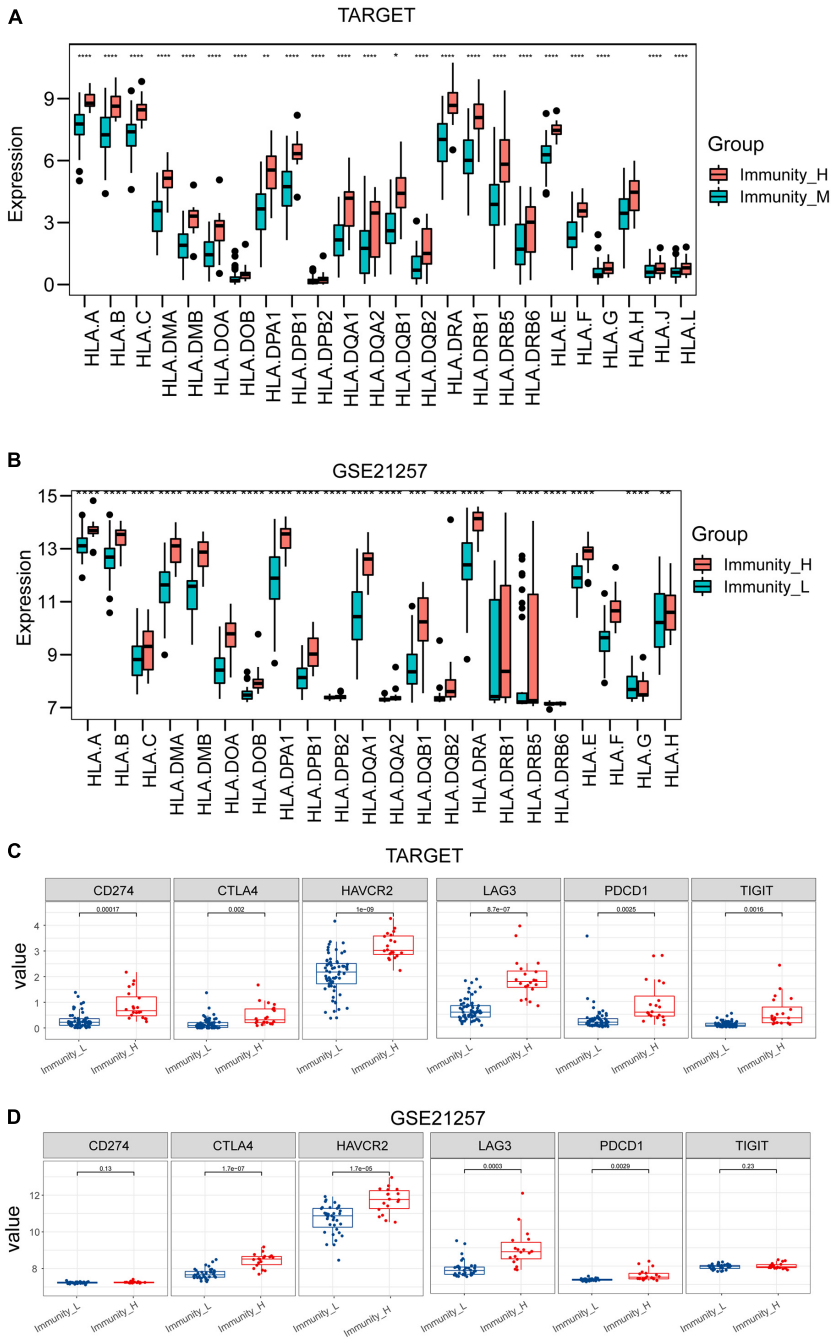

FIGURE 3 | Box plots presented differential expression of HLA genes **(A,B)** and multiple immune checkpoints **(C,D)** between Immune_H and Immune_L subtypes. $^{**}p < 0.01$, $^{***}p < 0.001$, and $^{****}p < 0.0001$.

CXCL9, suggesting their pivotal role in modulating tumor immunity (**Figure 4C**).

TYROBP Expression Is Associated With CD8$^+$ T Cell Infiltration

According to PPI analysis, TYROBP showed the highest degrees of interaction with other DEGs, suggesting its important role in driving the immunophenotype. We further investigated the association of TYROBP expression with immune cells in the osteosarcoma tumor microenvironment. Using the CIBERSORT method in combination with the LM22 signature matrix, we calculated differences in the immune infiltration of 22 immune cell types between low- and high-TYROBP groups. **Figure 5A** summarized the 22 immune cell landscapes among osteosarcoma patients in the TARGET dataset. The results showed that

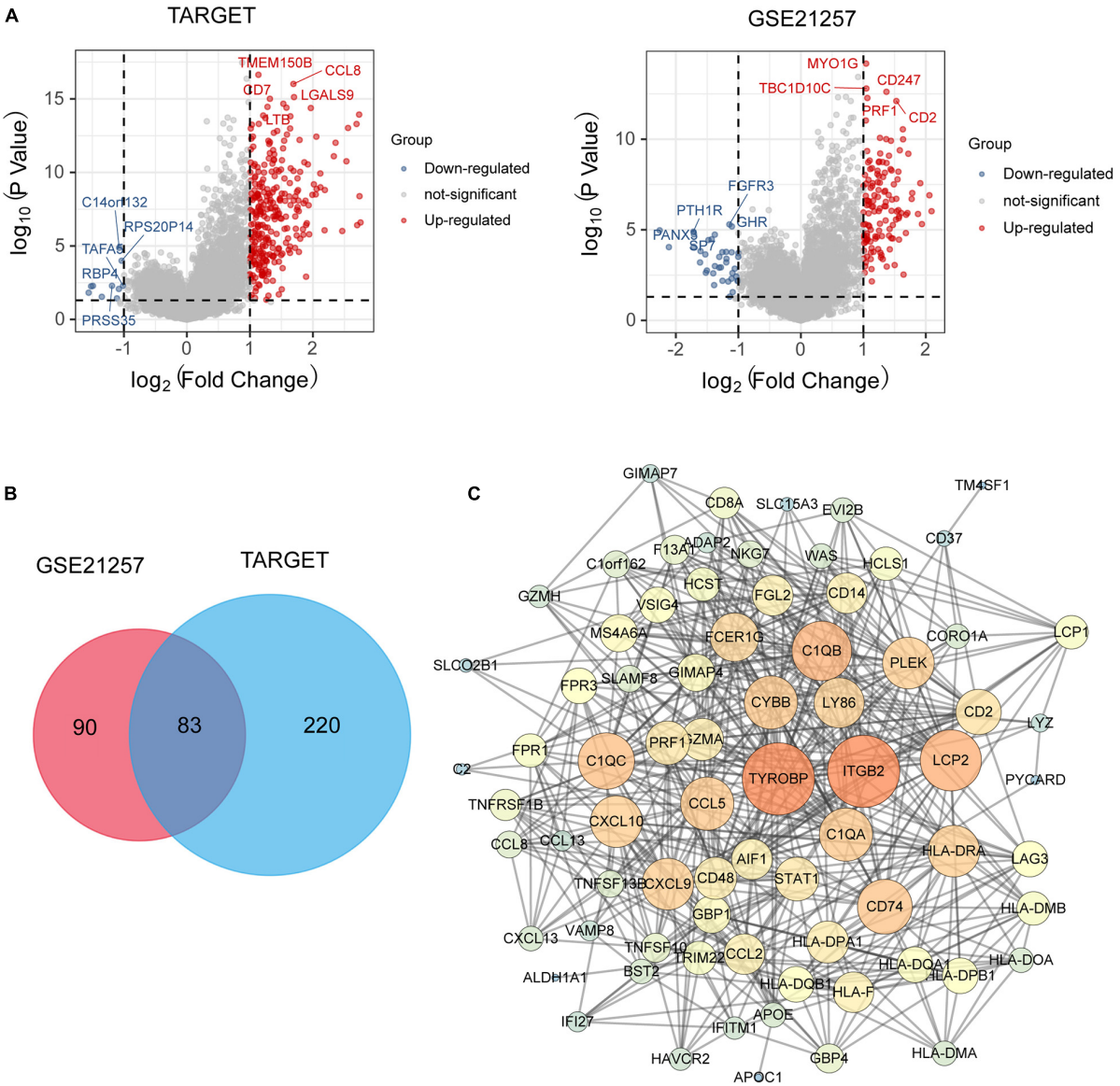

FIGURE 4 | (A) Volcano plot presented distribution of differentially expressed genes (DEGs) quantified among Immune_H and Immune_L subtypes with threshold of | log2 Fold change| > 1 and $P < 0.05$ in TARGET and GSE21257 cohort; **(B)** Venn plot showed intersection of differentially expressed genes among Immune_H and Immune_L subtypes; **(C)** PPI network analysis showed interactions among 83 DEGs.

patients with high TYROBP expression had significantly higher proportions of immune cells (e.g., CD8 T cell, CD4 naive T cell, CD4 memory activated T cell, macrophages M0, macrophages M1, and macrophages M2) (**Figure 5B**). Among the immune cells, $CD8^+$ T cells, also known as cytotoxic T cells, play a vital role in antitumor immunity by killing cancer cells. Our results demonstrated that TYROBP expression showed a positive correlation with $CD8^+$ cell infiltration (**Figure 5C**), and a high TYROBP expression group was infiltrated with a high $CD8^+$ T cell level (**Figure 5D**). To further validate the association between TYROBP and $CD8^+$ T cells in osteosarcoma, we performed multiplex immunohistochemistry. In line with results from bioinformatics analysis, multiplexed immunohistochemistry showed that high TYROBP expression was associated with high $CD8^+$ T cell levels in the tumor microenvironment (**Figure 5E**).

Construction and Confirmation of the Immune-Related Prognostic Biosignature

To improve the accuracy and reliability of the predictive model, we treated TARGET as the training set and the GES21257 as validation sets. Lasso Cox regression analysis was subsequently carried out to construct an immune-associated predictive model using 34 critical IRGs presented in the PPI network

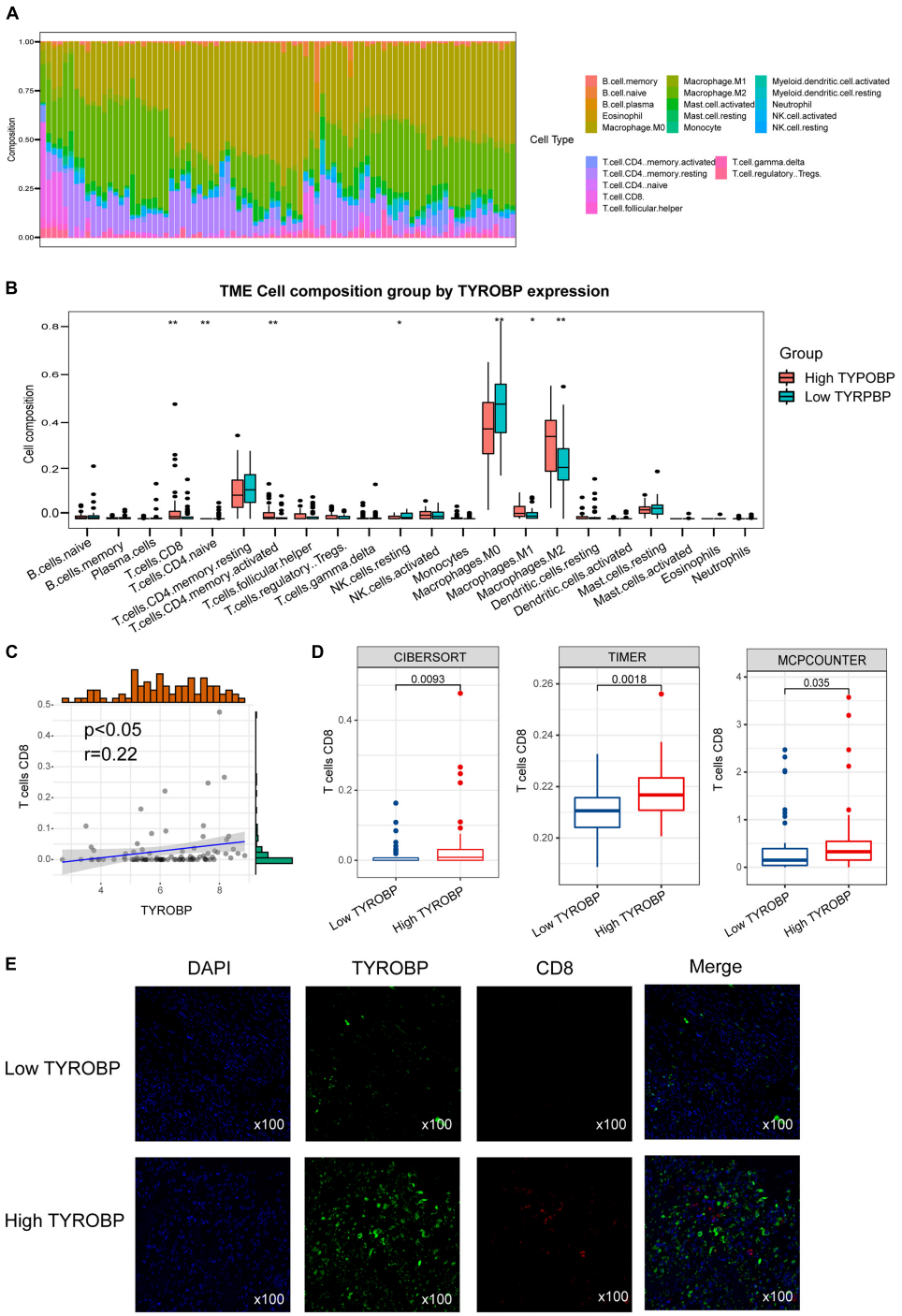

FIGURE 5 | (A) Relative proportion of immune infiltration in Immune_H and Immune_L groups; **(B)** box plots visualizing significantly different immune cells between Immune_H and Immune_L groups; **(C)** correlation of TYROBP and CD8$^+$ T cell infiltration; **(D)** box plot showed CD8$^+$ T cell infiltration level in TYROBP high and low groups; **(E)** multiplex immunohistochemistry validated differentially infiltrated CD8$^+$ T cell in TYROBP high and low groups. $^{**}p < 0.01$, $^{***}p < 0.001$, and $^{****}p < 0.0001$.

(**Figures 6A,B**). A risk-score formula was established as follows: risk score = −0.267 × FPR1–0.001 × FCER1G. As shown in **Figures 6A,B**, the heatmap showed that the expression level of FPR1 and FCER1G was decreased, accompanied by the higher risk scores. Additionally, we examined the correlation between risk score and survival status (**Figure 6C**). Our data showed that the number of alive statuses in the low-risk group was markedly higher relative to the high-risk group (**Figure 6D**).

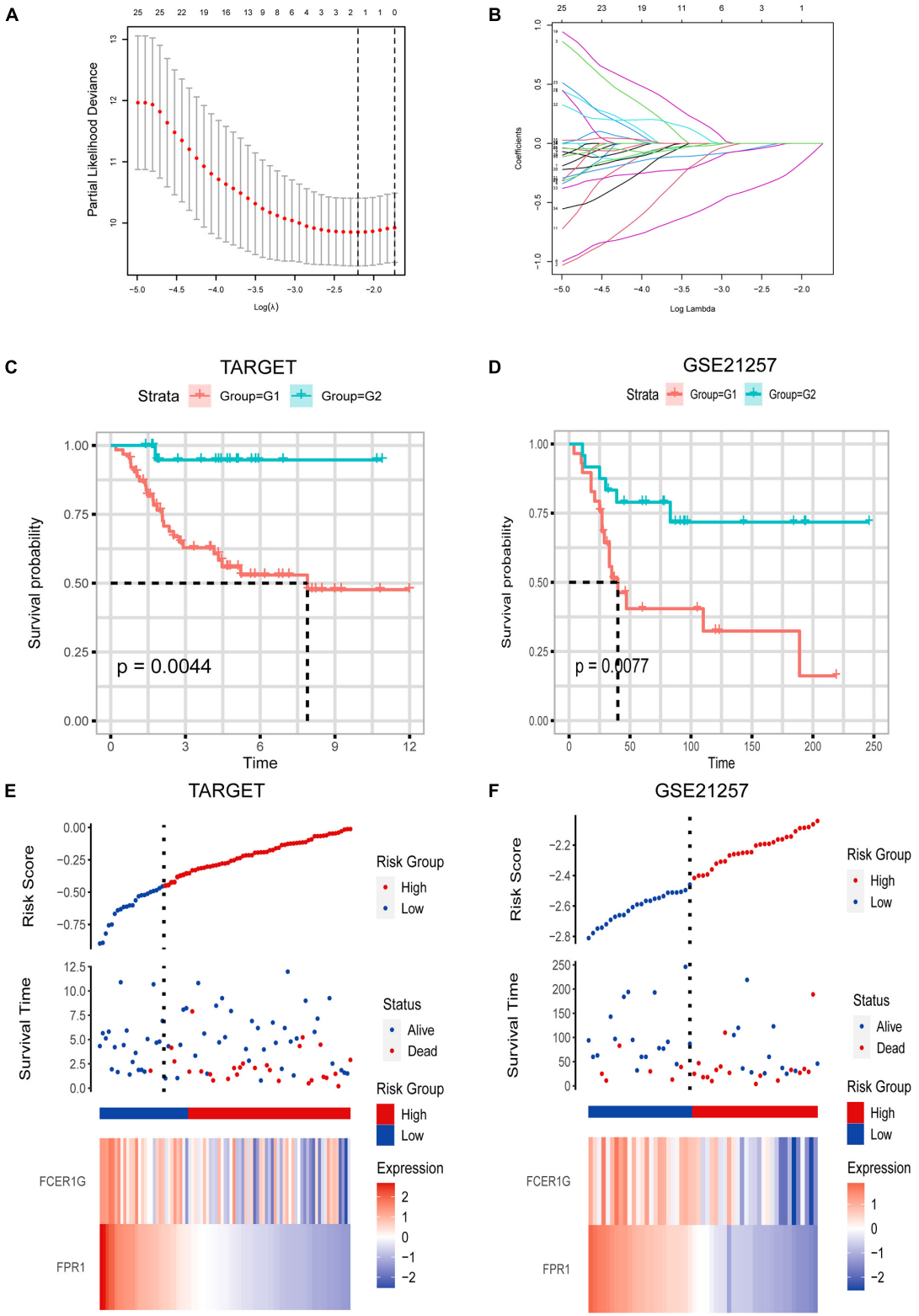

FIGURE 6 | (A,B) Lasso Cox analysis uncovered two genes most associated with OS in TARGET dataset. **(C,D)** Kaplan–Meier curves of OS for LGG patients based on IPS in TARGET cohort and GSE21257 cohort. **(E,F)** Risk scores distribution, survival status of each patient, and heatmaps of prognostic four-gene biosignature in TARGET and GSE21257 datasets.

To explore the prognostic significance of the risk model in osteosarcoma, we performed a Kaplan–Meier analysis. As indicated in **Figure 6**, the high-risk score was correlated with dismal OS in the TARGET dataset (cutoff values = −0.44), which was further confirmed by the GSE21257 dataset (cutoff values = −2.4) (**Figure 6E**).

DISCUSSION

In this study, we focused on uncovering immune-associated osteosarcoma subtypes through immunogenomic profiling. Our study demonstrates that osteosarcoma could be categorized into immunity low and immunity high subtypes. We established that this categorization was reproducible, as well as predictable. The immunity high osteosarcoma subtype was enriched with high immune cell infiltration and immunoactive signaling pathway indicating an immune hot phenotype, whereas immunity low was associated with low immune cell infiltration and immunosuppressive signaling pathway indicating an immune cold phenotype. Moreover, we developed and validated an immune-related prognostic signature.

Immunity_H had a higher level of immune cell invasion, as well as antitumor immune activities, such as high levels of immunoactivated cell infiltration, and activated immune signaling pathway. This analysis validated the increased antitumor immune activity in the Immunity_H subtype. Indeed, accumulating evidence has documented that the density and level of tumor-infiltrating lymphocytes are positively correlated with survival prognosis in multiple cancers (Hendry et al., 2017; Jiang et al., 2017; Wang et al., 2020; Yao et al., 2017).

The HLA genes code for MHC I, as well as MHC II molecules, which deliver pathogen-originated short peptides to T cells and trigger an adaptive immune response (Apanius et al., 2017; Danchin et al., 2004). Previous researches have reported that the expression of HLA may regulate ICI response in metastatic melanoma (Chowell et al., 2018; Garrido et al., 2016; O'Donnell et al., 2019). The study demonstrated that elevated tumor-distinct expression of MHC-I was pivotal for the response to therapy with anti-CTLA-4. In the meantime, tumor-specific MHC-II expression was critical for the response to the therapy with anti-PD-1 (Johnson et al., 2016). Additionally, recent studies have identified predictive biomarkers (e.g., PD-L1, PD-1, and CTLA-4) that can be exploited to predict response to ICI therapy (Gibney et al., 2016; Lin et al., 2021). In our study, in the Immunity_H subtype, the HLA genes and immune checkpoint expression levels were also the highest compared with the Immunity_L subtype. In contrast, we revealed that Immunity_High exhibited strong immune activity given the high immune invasion level, percentage of distinct tumor-infiltrating lymphocytes, HLA richness, and level of expression and exhibited relatively improved clinical outcomes.

We also identified several key genes with the highest interaction degrees between Immune_H and Immunity_L subtypes, including TYROBP, ITGB2, LCP2, C1QB, C1QC, CD74, HLA-DRA, CXCL10, CCL5, and CXCL9. Previous studies have demonstrated that TYROBP, also known as DAP12, is overexpressed in various cancers. Functionally, TYROBP encodes a transmembrane signaling polypeptide on the surface of a variety of immune cells that contains an immunoreceptor tyrosine-based activation motif in its cytoplasmic domain and mediates signaling transductions (Dietrich et al., 2000; Shabo et al., 2013; Töpfer et al., 2015). It has been reported that TYROBP expression is associated with CD8 T cell infiltration in gastric cancer and clear cell renal cell carcinoma (Jiang et al., 2020; Wu et al., 2020). In line with these pieces of evidence, our result showed that TYROBP expression is positively correlated with CD8 T cell infiltration in the osteosarcoma tumor microenvironment. CD74 plays an important function in the processing of MHC class II antigens through the stabilization of peptide-free class II alpha/beta heterodimers in a complex shortly following their synthesis and directs the transportation of the complex to the endosomal/lysosomal system from the endoplasmic reticulum (Badve et al., 2002; Denzin et al., 1996). High CD74 expression in Immune_H indicated a high antigen presentation and is important for the clinical response of immunotherapies. Pro-inflammatory cytokine participates in a wide variety of processes such as differentiation, chemotaxis, activation of peripheral immune cells, and regulation of immune cell growth (Morrell et al., 2014). CXCL10 is an important pro-inflammatory cytokine and has been reported to mediate the mobilization of tumor-inhibitory $CXCR3^{+}$ T cells, as well as natural killer cells, into solid cancers (Tokunaga et al., 2018). Respectively, a high CXCL10 concentration is correlated with a higher immune cell infiltration and better survival in several malignancies (Bronger et al., 2016).

In our research, we established a novel classification of osteosarcoma based on immunogenomic profiling. We also construct and validate the immune-associated prognostic signature. This classification of osteosarcoma based on immunogenomic profiling may provide valuable information for immunotherapy strategies in osteosarcoma patients. Besides, we also identified TYROBP as a key immunoregulatory gene. Nevertheless, it should be noted that our findings require further validation *in vitro* or *in vivo* and a larger sample cohort. Our findings should be interpreted with this limitation in mind.

In conclusion, we established a novel osteosarcoma classification based on the differences in the transcriptome of 29 immune biosignatures in tumor samples. This classification had significant clinical outcomes for estimating the prognosis, as well as the responsiveness of immunotherapy.

DATA AVAILABILITY STATEMENT

The datasets presented in this study can be found in online repositories. The names of the repository/repositories and accession number(s) can be found in the article/supplementary material.

ETHICS STATEMENT

The studies involving human participants were reviewed and approved by Ethics Review Committee of the Third

Affiliated Hospital of Southern Medical University. Written informed consent for participation was not required for this study in accordance with the national legislation and the institutional requirements.

AUTHOR CONTRIBUTIONS

XeW, LW, and WX: conceptualization, methodology, and writing. XuW: software. DK: validation. JL: data curation. WL and XB: project administration and funding acquisition. All authors have read and agreed to the published version of the manuscript.

FUNDING

This work was supported by Jiangmen Medical and Health Technology Plan Project (Project No.2019B003).

REFERENCES

Apanius, V., Penn, D., Slev, P. R., Ruff, L. R., and Potts, W. K. (2017). The nature of selection on the major histocompatibility complex. *Crit. Rev. Immunol.* 37, 75–120. doi: 10.1615/CritRevImmunol.v37.i2-6.10

Badve, S., Deshpande, C., Hua, Z., and Lögdberg, L. (2002). Expression of invariant chain (CD 74) and major histocompatibility complex (MHC) class II antigens in the human fetus. *J. Histochem. Cytochem.* 50, 473–482. doi: 10.1177/002215540205000404

Barbie, D. A., Tamayo, P., Boehm, J. S., Kim, S. Y., Moody, S. E., Dunn, I. F., et al. (2009). Systematic RNA interference reveals that oncogenic KRAS-driven cancers require TBK1. *Nature* 462, 108–112. doi: 10.1038/nature08460

Baxevanis, C. N., Perez, S. A., and Papamichail, M. (2009). Cancer immunotherapy. *Crit. Rev. Clin. Lab. Sci.* 46, 167–189. doi: 10.1080/10408360902937809

Bronger, H., Singer, J., Windmüller, C., Reuning, U., Zech, D., Delbridge, C., et al. (2016). CXCL9 and CXCL10 predict survival and are regulated by cyclooxygenase inhibition in advanced serous ovarian cancer. *Br. J. Cancer* 115, 553–563. doi: 10.1038/bjc.2016.172

Chen, C., Xie, L., Ren, T., Huang, Y., Xu, J., and Guo, W. (2021). Immunotherapy for osteosarcoma: fundamental mechanism, rationale, and recent breakthroughs. *Cancer Lett.* 500, 1–10. doi: 10.1016/j.canlet.2020.12.024

Chowell, D., Morris, L. G. T., Grigg, C. M., Weber, J. K., Samstein, R. M., Makarov, V., et al. (2018). Patient HLA class I genotype influences cancer response to checkpoint blockade immunotherapy. *Science* 359, 582–587. doi: 10.1126/science.aao4572

Danchin, E., Vitiello, V., Vienne, A., Richard, O., Gouret, P., McDermott, M. F., et al. (2004). The major histocompatibility complex origin. *Immunol. Rev.* 198, 216–232. doi: 10.1111/j.0105-2896.2004.00132.x

Denzin, L. K., Hammond, C., and Cresswell, P. (1996). HLA-DM interactions with intermediates in HLA-DR maturation and a role for HLA-DM in stabilizing empty HLA-DR molecules. *J. Exp. Med.* 184, 2153–2165. doi: 10.1084/jem.184.6.2153

Dietrich, J., Cella, M., Seiffert, M., Bühring, H. J., and Colonna, M. (2000). Cutting edge: signal-regulatory protein beta 1 is a DAP12-associated activating receptor expressed in myeloid cells. *J. Immunol.* 164, 9–12. doi: 10.4049/jimmunol.164.1.9

Durfee, R. A., Mohammed, M., and Luu, H. H. (2016). Review of osteosarcoma and current management. *Rheumatol. Ther.* 3, 221–243. doi: 10.1007/s40744-016-0046-y

ElKordy, M. A., ElBaradie, T. S., ElSebai, H. I., KhairAlla, S. M., and Amin, A. A. E. (2018). Osteosarcoma of the jaw: challenges in the diagnosis and treatment. *J. Egypt Natl. Canc. Inst.* 30, 7–11. doi: 10.1016/j.jnci.2018.02.001

Emens, L. A., Ascierto, P. A., Darcy, P. K., Demaria, S., Eggermont, A. M. M., Redmond, W. L., et al. (2017). Cancer immunotherapy: opportunities and challenges in the rapidly evolving clinical landscape. *Eur. J. Cancer* 81, 116–129. doi: 10.1016/j.ejca.2017.01.035

Garrido, F., Aptsiauri, N., Doorduijn, E. M., Garcia Lora, A. M., and van Hall, T. (2016). The urgent need to recover MHC class I in cancers for effective immunotherapy. *Curr. Opin. Immunol.* 39, 44–51. doi: 10.1016/j.coi.2015.12.007

Gibney, G. T., Weiner, L. M., and Atkins, M. B. (2016). Predictive biomarkers for checkpoint inhibitor-based immunotherapy. *Lancet Oncol.* 17, e542–e551. doi: 10.1016/s1470-2045(16)30406-5

He, Y., Jiang, Z., Chen, C., and Wang, X. (2018). Classification of triple-negative breast cancers based on immunogenomic profiling. *J. Exp. Clin. Cancer Res.* 37:327. doi: 10.1186/s13046-018-1002-1

Hendry, S., Salgado, R., Gevaert, T., Russell, P. A., John, T., Thapa, B., et al. (2017). Assessing tumor-infiltrating lymphocytes in solid tumors: a practical review for pathologists and proposal for a standardized method from the international immuno-oncology biomarkers working group: part 2: TILs in melanoma, gastrointestinal tract carcinomas, non-small cell lung carcinoma and mesothelioma, endometrial and ovarian carcinomas, squamous cell carcinoma of the head and neck, genitourinary carcinomas, and primary brain tumors. *Adv. Anat. Pathol.* 24, 311–335. doi: 10.1097/pap.0000000000000161

Jiang, D., Liu, Y., Wang, H., Wang, H., Song, Q., Sujie, A., et al. (2017). Tumour infiltrating lymphocytes correlate with improved survival in patients with esophageal squamous cell carcinoma. *Sci. Rep.* 7:44823. doi: 10.1038/srep44823

Jiang, J., Ding, Y., Wu, M., Lyu, X., Wang, H., Chen, Y., et al. (2020). Identification of TYROBP and C1QB as two novel key genes with prognostic value in gastric cancer by network analysis. *Front. Oncol.* 10:1765. doi: 10.3389/fonc.2020.01765

Johnson, D. B., Estrada, M. V., Salgado, R., Sanchez, V., Doxie, D. B., Opalenik, S. R., et al. (2016). Melanoma-specific MHC-II expression represents a tumour-autonomous phenotype and predicts response to anti-PD-1/PD-L1 therapy. *Nat. Commun.* 7:10582. doi: 10.1038/ncomms10582

Kansara, M., Teng, M. W., Smyth, M. J., and Thomas, D. M. (2014). Translational biology of osteosarcoma. *Nat. Rev. Cancer* 14, 722–735. doi: 10.1038/nrc3838

Lin, W., Qiu, X., Sun, P., Ye, Y., Huang, Q., Kong, L., et al. (2021). Association of IDH mutation and 1p19q co-deletion with tumor immune microenvironment in lower-grade glioma. *Mol. Ther. Oncolytics* 21, 288–302. doi: 10.1016/j.omto.2021.04.010

Lin, W., Xu, Y., Chen, X., Liu, J., Weng, Y., Zhuang, Q., et al. (2020). Radiation-induced small extracellular vesicles as "carriages" promote tumor antigen release and trigger antitumor immunity. *Theranostics* 10, 4871–4884. doi: 10.7150/thno.43539

Morrell, C. N., Aggrey, A. A., Chapman, L. M., and Modjeski, K. L. (2014). Emerging roles for platelets as immune and inflammatory cells. *Blood* 123, 2759–2767. doi: 10.1182/blood-2013-11-462432

O'Donnell, J. S., Teng, M. W. L., and Smyth, M. J. (2019). Cancer immunoediting and resistance to T cell-based immunotherapy. *Nat. Rev. Clin. Oncol.* 16, 151–167. doi: 10.1038/s41571-018-0142-8

Shabo, I., Olsson, H., Stål, O., and Svanvik, J. (2013). Breast cancer expression of DAP12 is associated with skeletal and liver metastases and poor survival. *Clin. Breast Cancer* 13, 371–377. doi: 10.1016/j.clbc.2013.05.003

Shen, J. K., Cote, G. M., Choy, E., Yang, P., Harmon, D., Schwab, J., et al. (2014). Programmed cell death ligand 1 expression in osteosarcoma. *Cancer Immunol. Res.* 2, 690–698. doi: 10.1158/2326-6066.Cir-13-0224

Simpson, E., and Brown, H. L. (2018). Understanding osteosarcomas. *JAAPA* 31, 15–19. doi: 10.1097/01.JAA.0000541477.24116.8d

Tokunaga, R., Zhang, W., Naseem, M., Puccini, A., Berger, M. D., Soni, S., et al. (2018). CXCL9, CXCL10, CXCL11/CXCR3 axis for immune activation–a target for novel cancer therapy. *Cancer Treat. Rev.* 63, 40–47. doi: 10.1016/j.ctrv.2017.11.007

Töpfer, K., Cartellieri, M., Michen, S., Wiedemuth, R., Müller, N., Lindemann, D., et al. (2015). DAP12-based activating chimeric antigen receptor for NK cell

tumor immunotherapy. *J. Immunol.* 194, 3201–3212. doi: 10.4049/jimmunol.1400330

Wang, J., Tian, S., Sun, J., Zhang, J., Lin, L., and Hu, C. (2020). The presence of tumour-infiltrating lymphocytes (TILs) and the ratios between different subsets serve as prognostic factors in advanced hypopharyngeal squamous cell carcinoma. *BMC Cancer* 20:731. doi: 10.1186/s12885-020-07234-0

Wang, Z., Li, B., Ren, Y., and Ye, Z. (2016). T-cell-based immunotherapy for osteosarcoma: challenges and opportunities. *Front. Immunol.* 7:353. doi: 10.3389/fimmu.2016.00353

Whelan, J. S., and Davis, L. E. (2018). Osteosarcoma, chondrosarcoma, and chordoma. *J. Clin. Oncol.* 36, 188–193. doi: 10.1200/jco.2017.75.1743

Wu, P., Xiang, T., Wang, J., Lv, R., and Wu, G. (2020). TYROBP is a potential prognostic biomarker of clear cell renal cell carcinoma. *FEBS Open Bio.* 10, 2588–2604. doi: 10.1002/2211-5463.12993

Yang, Y. (2015). Cancer immunotherapy: harnessing the immune system to battle cancer. *J. Clin. Invest.* 125, 3335–3337. doi: 10.1172/jci83871

Yao, W., He, J. C., Yang, Y., Wang, J. M., Qian, Y. W., Yang, T., et al. (2017). The prognostic value of tumor-infiltrating lymphocytes in hepatocellular carcinoma: a systematic review and meta-analysis. *Sci. Rep.* 7:7525. doi: 10.1038/s41598-017-08128-1

Conflict of Interest: The authors declare that the research was conducted in the absence of any commercial or financial relationships that could be construed as a potential conflict of interest.

frontiers in Cell and Developmental Biology

BRIEF RESEARCH REPORT
published: 26 July 2021
doi: 10.3389/fcell.2021.702916

ELMO1 Regulates RANKL-Stimulated Differentiation and Bone Resorption of Osteoclasts

Xinyue Liang[1†], Yafei Hou[2†], Lijuan Han[1], Shuxiang Yu[1], Yunyun Zhang[1], Xiumei Cao[2] and Jianshe Yan[1,2*]*

[1] School of Life Sciences, Shanghai University, Shanghai, China, [2] Department of Immunology and Microbiology, Shanghai Institute of Immunology, Shanghai Jiao Tong University School of Medicine, Shanghai, China

Bone homeostasis is a metabolic balance between the new bone formation by osteoblasts and old bone resorption by osteoclasts. Excessive osteoclastic bone resorption results in low bone mass, which is the major cause of bone diseases such as rheumatoid arthritis. Small GTPases Rac1 is a key regulator of osteoclast differentiation, but its exact mechanism is not fully understood. ELMO and DOCK proteins form complexes that function as guanine nucleotide exchange factors for Rac activation. Here, we report that ELMO1 plays an important role in differentiation and bone resorption of osteoclasts. Osteoclast precursors derived from bone marrow monocytes (BMMs) of Elmo1$^{-/-}$ mice display defective adhesion and migration during differentiation. The cells also have a reduced activation of Rac1, p38, JNK, and AKT in response to RANKL stimulation. Importantly, we show that bone erosion is alleviated in Elmo1$^{-/-}$ mice in a rheumatoid arthritis mouse model. Taken together, our results suggest that ELMO1, as a regulator of Rac1, regulates osteoclast differentiation and bone resorption both *in vitro* and *in vivo*.

Keywords: ELMO1, osteoclast differentiation, bone resorption, adhesion, migration

OPEN ACCESS

Edited by:
Mitsugu Fujita,
Kindai University, Japan

Reviewed by:
Jiake Xu,
University of Western Australia, Australia
Orest William Blaschuk,
McGill University, Canada

***Correspondence:**
Xiumei Cao
caoxm@yahoo.com
Jianshe Yan
jiansheyan@shu.edu.cn

[†] These authors have contributed equally to this work

Specialty section:
This article was submitted to Cell Adhesion and Migration, a section of the journal Frontiers in Cell and Developmental Biology

Received: *30 April 2021*
Accepted: *30 June 2021*
Published: *26 July 2021*

Citation:
Liang X, Hou Y, Han L, Yu S, Zhang Y, Cao X and Yan J (2021) ELMO1 Regulates RANKL-Stimulated Differentiation and Bone Resorption of Osteoclasts. Front. Cell Dev. Biol. 9:702916. doi: 10.3389/fcell.2021.702916

INTRODUCTION

Bone homeostasis is a metabolic balance between the formation and resorption of the bone in which osteoblasts and osteoclasts play crucial roles, respectively. When bone resorption goes beyond formation, the homeostasis is disrupted with the consequence of low bone mass and causing bone diseases such as rheumatoid arthritis (RA), which is characterized by the presence of inflammatory synovitis accompanied by bone destruction mainly caused by osteoclasts. Derived from BMM lineage cells, osteoclast precursors differentiate into osteoclasts under the regulation of two cytokines, namely, macrophage colony-stimulating factor (M-CSF) and Receptor activator of NF-kB ligand (RANKL). Binding of M-CSF to its receptor c-Fms leads to the activation of downstream signal pathways such as AKT and mitogen-activated protein kinases (MAPKs) including extracellular signal-regulated kinase (ERK), c-Jun N-terminal kinase (JNK), and p38 and resulting in the proliferation and survival of osteoclast precursors. Association of RANKL with its receptor RANK triggers the signal transduction pathways to induce the differentiation of osteoclast precursors to giant multinucleated osteoclasts, which play a major role in the degradation and resorption of the bone matrix (Lee and States, 2000; Lee et al., 2018).

As an essential osteoclastogenic factor, RANKL governs the signal pathways to induce the differentiation of osteoclast precursors into osteoclasts (Park et al., 2017; **Supplementary Figure 1**). Activation of RANK by binding to RANKL prompts the cytoplasmic recruitment of the TNF receptor-associated factor (TRAF) proteins, in which TRAF6 is found to play a major role in regulating osteoclast differentiation (Lomaga et al., 1999; Naito et al., 1999; Lamothe et al., 2007). By forming a complex with Src, TRAF6 activates downstream signal transduction pathway PI3K (Wong et al., 1999), resulting in the generation of phosphatidylinositol-(3,4,5)-trisphosphate (PIP3). This phospholipid leads to the membrane translocation of proteins containing pleckstrin homology domains, such as Cytosolic Regulator of Adenylyl Cyclase and Protein Kinase B (Akt/PKB) (Parent and Devreotes, 1999; Sasaki et al., 2004). Akt is reported to be involved in osteoclast differentiation (Lee et al., 2002). The phosphatase PTEN functions as an antagonist of PI3K by dephosphorylating PIP3 to generate PIP2 and suppresses RANKL-mediated osteoclast differentiation (Funamoto et al., 2002; Iijima and Devreotes, 2002; Sugatani et al., 2003). By forming a complex with transforming growth factor–β (TGF-β)–activated kinase 1 (TAK1) and TAK1-binding protein2 (TAB2), TRAF6 transduce the RANK signaling to activate downstream MAPKs such as p38, JNK and ERK to play vital roles in the differentiation of osteoclast precursors (David et al., 2002; Li et al., 2002; Mizukami et al., 2002; He et al., 2011). RANKL-TRAF6 signaling also activates IκB kinase (IKK), which, in turn, phosphorylates IκB for degradation that ultimately releases NF-κB from its inactive state. IKKβ is found to play a critical role for RANKL-stimulated degradation of IκB and is required for osteoclastogenesis *in vitro* and *in vivo* (Ruocco et al., 2005). Released NF-κB and activation of MAPKs eventually induce the master osteoclast transcription factor, the nuclear factor of activated T cells cytoplasmic 1 (NFATc1) (Asagiri et al., 2005), and promote the expression of related genes such as cathepsin K, osteoclast-associated receptor (OSCAR), and tartrate-resistant acid phosphatase (TRAP) during terminal differentiation of osteoclasts (Reddy et al., 1995; Matsumoto et al., 2004; Kim et al., 2005).

Rho GTPases have been found to play important roles in osteoclast differentiation and function (Gao et al., 2020). By regulating the cytoskeleton rearrangement, Rho GTPases control migration of mononuclear osteoclast precursors to form multinucleated osteoclasts, and to form the actin ring, the specific organization for bone resorption (Touaitahuata et al., 2014). Much work have demonstrated that Rac GTPase plays a pivotal role in activation of MAPKs signaling pathways (Lopez-Bergami et al., 2005; Guo et al., 2013). It has been reported that Rac1 is involved in the RANKL-dependent activation of p38 MAPK in osteoclast precursors (Lin et al., 2015), and that Dock5, p130Cas, and CrkII play essential roles in function of osteoclasts through activation of Rac1 (Vives et al., 2011; Nagai et al., 2013; Kim et al., 2016). Importantly, a recent study demonstrated that Rac1 and Cdc42 exchange factor Triple functional domain (Trio) is critical for bone resorption, and mice bearing the conditional knockout of Trio showed increased bone mass due to the impaired bone resorption (Gu et al., 2020). Amongst other pathways, Dock180 family members function in conjunction with the ELMO (Engulfment and cell motility) family proteins as a guanine nucleotide exchange factor (GEF) to activate Rac GTPase (Reddien and Horvitz, 2004). In previous studies, we have demonstrated that chemoattractant-stimulation of G-protein-coupled receptors (GPCRs) trigger downstream heterotrimeric G-proteins, such as Gα and Gβγ subunits, to form complexes with ELMO family proteins, which in turn activate Rac GTPase to regulate F-actin dynamics during migration of *D. discoideum* and cancer cells (Yan et al., 2012; Li et al., 2013; Wang et al., 2016). Recently it was reported that ELMO1, as a cytoplasmic regulator in neutrophils, is involved in inflammatory arthritis (Arandjelovic et al., 2019).

Despite much progress, our understanding on the role and regulation of signaling networks controlling osteoclast differentiation and function remains incomplete. In this study, we report the roles of ELMO1 in RANKL-induced osteoclast differentiation. Our data indicate that ELMO1 regulates the adhesion and migration of osteoclast precursors, and participates in osteoclast differentiation through Rac1, AKT, p38, and JNK signal pathways. In addition, we show that activity of bone resorption is compromised in osteoclasts lacking ELMO1, and Elmo1 knockout mice exhibit alleviated bone erosion in a serum transfer induced rheumatoid arthritis model, suggesting that ELMO/DOCK/RAC axis regulates RANKL-stimulated osteoclast differentiation and bone resorption activity, both *in vitro* and *in vivo*.

RESULTS

ELMO1 Plays a Role in Bone Resorption by Affecting Osteoclast Differentiation

To investigate the impact of Elmo1 in osteoclasts, we isolated BMMs from Elmo1$^{+/+}$ (wild-type) and Elmo1$^{-/-}$ (knockout) mice that came from heterozygote mating (**Supplementary Figure 2**), and treated them with RANKL in the presence of M-CSF on inorganic crystalline calcium phosphate plates. Elmo1$^{-/-}$ osteoclasts displayed a significant decreased bone resorption activity compared to Elmo1$^{+/+}$ osteoclasts (**Figures 1A,B**). To examine whether ELMO1 is involved in osteoclast differentiation, osteoclast precursors were cultured with M-CSF and RANKL and then stained for TRAP, a marker of mature osteoclasts. We found that the formation of TRAP-positive multinucleated cells containing more than three nuclei was remarkably higher in wild-type cells compared to that in Elmo1$^{-/-}$ cells (**Figures 1C,D**). One representative image of multinucleated cells with a higher magnification is shown in **Supplementary Figure 3**. Moreover, the mRNA level of TRAP, NFATc1, and DC-STAMP, which are essential factors for osteoclast differentiation, were much higher in wild-type cells relative to those in Elmo1$^{-/-}$ cells (**Figures 1E–G**). Considering the fact that RANKL may induce cell apoptosis (Bharti et al., 2004), we next examined whether the defect of osteoclast differentiation in Elmo1$^{-/-}$ cells was a consequence of reduced cell number caused by the treatment of RANKL. To rule out this possibility, we detected the cell apoptosis by Annexin V assay. It

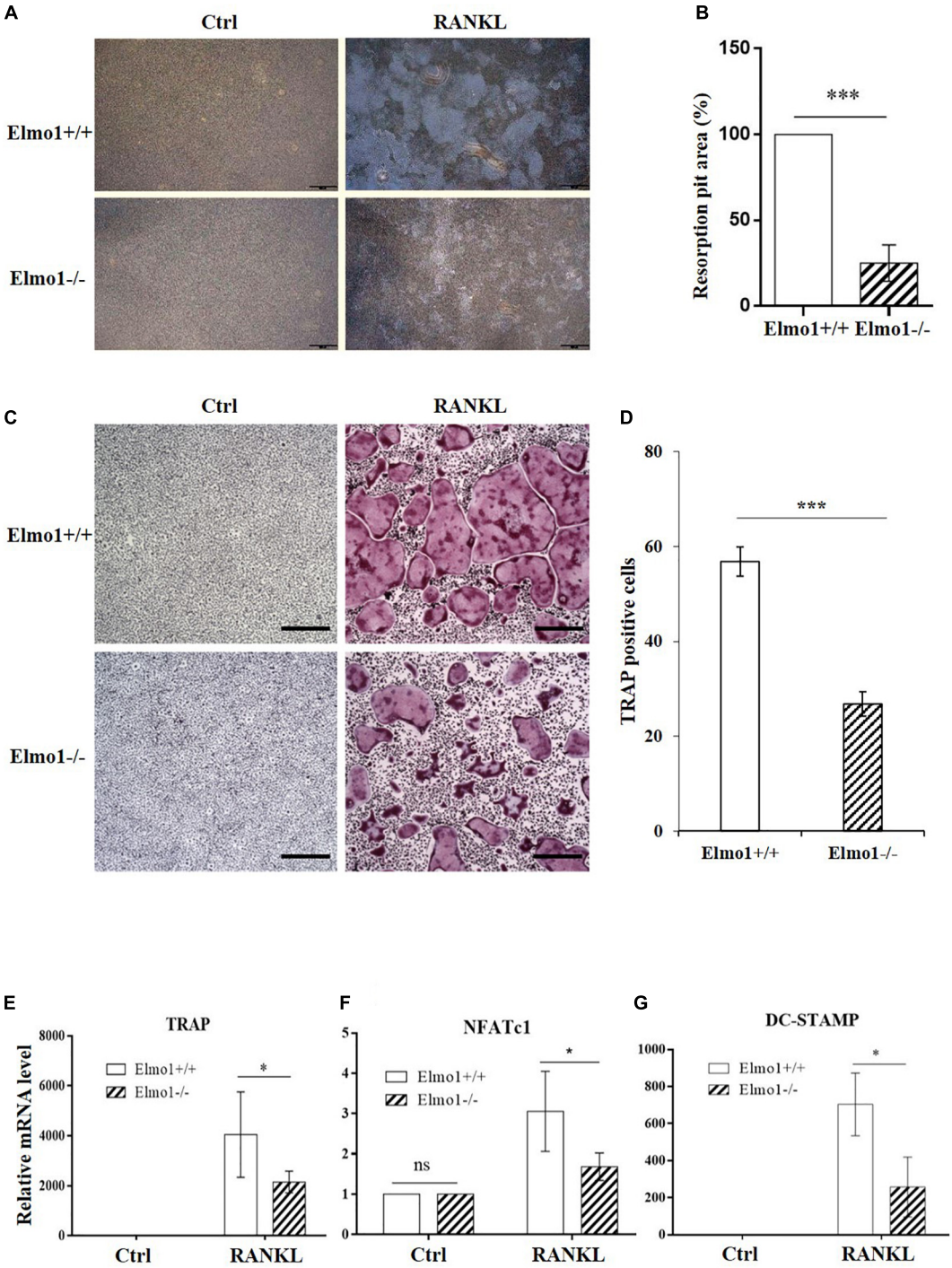

FIGURE 1 | Elmo1-deficient osteoclasts show impaired bone resorption activity and differentiation. **(A)** Pit formation assay. BMMs were cultured with M-CSF alone or M-CSF and RANKL on inorganic crystalline calcium phosphate plates. Attached cells were removed and resorption lacunae were visualized by bright-field microscopy. One representative photograph is shown. Scale bar, 500 μm. **(B)** Pit areas were quantified using ImageJ and graphed. Data are indicated as means ± SEM (n = 3). **(C)** RANKL-induced osteoclast differentiation of BMMs. Mouse BMMs were cultured in the presence of M-CSF and RANKL for 4 days. The cells were fixed and stained for TRAP staining. One representative picture is shown. Scale bar, 100 μm. **(D)** The numbers of TRAP-positive cells were counted and graphed. Data are indicated as means ± SEM (n = 13). **(E–G)** Relative mRNA level of TRAP, NFATc1, and DC-STAMP. Osteoclast precursors were treated with M-CSF and RANKL for 4 days, then relative mRNA level of TRAP (n = 6), NFATc1 (n = 4), and DC-STAMP (n = 3) were determined by qRT-PCR. Data are indicated as means ± SEM. Statistical significance was assessed by t-test, $^{*}P < 0.05$ and $^{***}P < 0.001$.

turned out that although RANKL treatment indeed triggered cell apoptosis, there was no significant difference between Elmo1$^{+/+}$ and Elmo1$^{-/-}$ cells (**Figures 2A,B**). Taken together, our data suggest that ELMO1 plays a role in bone resorption by affecting osteoclast differentiation.

Elmo1 Deficiency Suppresses the Adhesion and Migration of Osteoclast Precursors

Adherence and migration to the bone surface play essential roles during early stage of osteoclast differentiation (Kim et al., 2015). Thus, we assessed the effect of ELMO1 on adhesion and migration in osteoclast precursors. We found that osteoclast precursors derived from Elmo1$^{-/-}$ mice showed significant reduced adhesion capacity compared to the cells from wild-type mice (**Figure 2C**). Consistently, the expression of integrin β3, which is required for cell adhesion (Jung et al., 2012), was remarkably downregulated in the Elmo1$^{-/-}$ osteoclast precursors (**Figure 2D**). In addition, we assessed the expression of other adhesion molecules such as cadherin-2 and cadherin-11. Surprisingly, the mRNA levels of them in KO cells were much higher than that in WT cells (**Supplementary Figure 4**). We also detect integrin β3 and cadherins by immunofluorescence assay. However, there was no significant difference in the distribution and fluorescence intensity of these molecules between the WT and KO cells (**Supplementary Figures 5–7**). These results suggested that ELMO1 may play diverse roles in regulating the expression of adhesion molecules. Future work is needed to reveal the detailed mechanism of this phenomenon. We then examined the migration of osteoclast precursors stimulated by M-CSF. Elmo1$^{-/-}$ osteoclast precursors exhibited significant decreased chemotactic migration rate in a transwell assay (**Figure 2E**) compared to wild-type cells. These findings indicate that Elmo1 deficiency suppresses the capacities of adhesion and migration of osteoclast precursors, which are critical processes for mature osteoclasts formation.

ELMO1 Upregulates RANKL-Induced Activation of Rac1, MAPKs, and AKT

Because Rac1 was found to play an important role in the differentiation of BMMs into osteoclasts through p38 activation (Lin et al., 2015), we tested whether ELMO1 regulates this process through activation of Rac1 and MAPKs. As expected, Rac1 activation was considerably impaired in Elmo1$^{-/-}$ cells (**Figures 3A,B**) upon RANKL stimulation. Since ELMO1 is involved in Rac1 signaling that modulates actin reorganization, we visualized the cytoskeleton by staining F-actin with Alexa Fluor 633-phalloidin. As expected, we found that phalloidin was enriched at the actin-ring of giant multinucleated osteoclasts, particularly in WT cells, suggesting that ELMO1 may be involved in the actin-ring formation through activation of Rac1 (**Supplementary Figure 8**). We next examined whether ELMO1 regulates the activation of MAPKs with stimulation of RANKL. Relative to wild-type cells, Elmo1$^{-/-}$ cells exhibited a significant reduction in the level of phosphorylation of p38 and JNK (**Figures 3C–E**). Phosphorylation of ERK in Elmo1$^{-/-}$ cells was decreased to a certain degree as well although it was not significant (**Figure 3F**). In addition, we found that phosphorylation of AKT got reduced in Elmo1$^{-/-}$ cells (**Figure 3G**). Our data suggest that ELMO1 plays a role in activation of Rac1, MAPKs, and AKT under the stimulation of RANKL in the differentiation of osteoclasts.

Bone Erosion in Elmo1$^{-/-}$ Mice Is Alleviated in a Rheumatoid Arthritis Model

To further investigate the importance of ELMO1 on osteoclast bone resorption function *in vivo*, we compared the focal bone erosion in mice by generating RA model which displays many of the characteristic features including bone destruction (Pettit et al., 2001). To accomplish this, Elmo1$^{-/-}$ mice and their littermates of Elmo1$^{+/+}$ were injected with serum from K/BxN arthritic mice, and the progression of arthritis was monitored by recording clinical index and ankle thickness over time. As expected, both Elmo1$^{+/+}$ and Elmo1$^{-/-}$ mice injected with K/BxN serum developed severe arthritis compared to the PBS-injected controls, manifesting the onset of clinical signs (**Figure 4A**) and increase of ankle thickness (**Figure 4B**) within 6 days. However, the ankle thickness in Elmo1$^{-/-}$ mice was significantly lower than it in Elmo1$^{+/+}$ mice after 12 days of serum transfer (**Figure 4B**), suggesting that Elmo1 deficiency ameliorates the progression of arthritis.

Moreover, micro-CT of ankle joints and histological analyses of corresponding sections were used to assess the degree of bone erosion in the mice. As shown in **Figure 4C**, Elmo1$^{-/-}$ mice exhibited a marked reduction of bone erosion compared to Elmo1$^{+/+}$ mice. We further found that the ratio of bone volume to total volume (BV/TV) and the bone mineral density (BMD) of cortical bone of the ankle joints in Elmo1$^{+/+}$ mice was significantly lower than in Elmo1$^{-/-}$ mice, while the ratio of bone surface to bone volume (BS/BV) in Elmo1$^{+/+}$ mice was significantly higher than it in Elmo1$^{-/-}$ mice (**Figure 4D** and **Supplementary Figures 9A,B**). Consistent with this data, lower degree of bone destruction was found in Elmo1$^{-/-}$ mice in the matched H&E-stained sections (**Figure 4E**). The substantial reduction in bone erosion could be a consequence of decreased number of mature TRAP-stained osteoclasts in Elmo1$^{-/-}$ mice, as shown in and **Supplementary Figure 10**. Taken together, our data indicated that Elmo1 deficiency reduces bone resorption in Elmo1$^{-/-}$ mice.

DISCUSSION

The evidence presented here reveals the biological functions of ELMO1 in osteoclast for differentiation and bone resorption. We showed that ELMO1 modulates the differentiation of osteoclast via regulating the adhesion and migration of osteoclast precursors. We found that ELMO1 participates in RANKL-induced osteoclast differentiation through Rac1, p38, JNK, and AKT signal pathways. Furthermore, we discovered that bone erosion is alleviated in Elmo1 knockout mice in rheumatoid arthritis model. Taken together, our data suggest that ELMO1

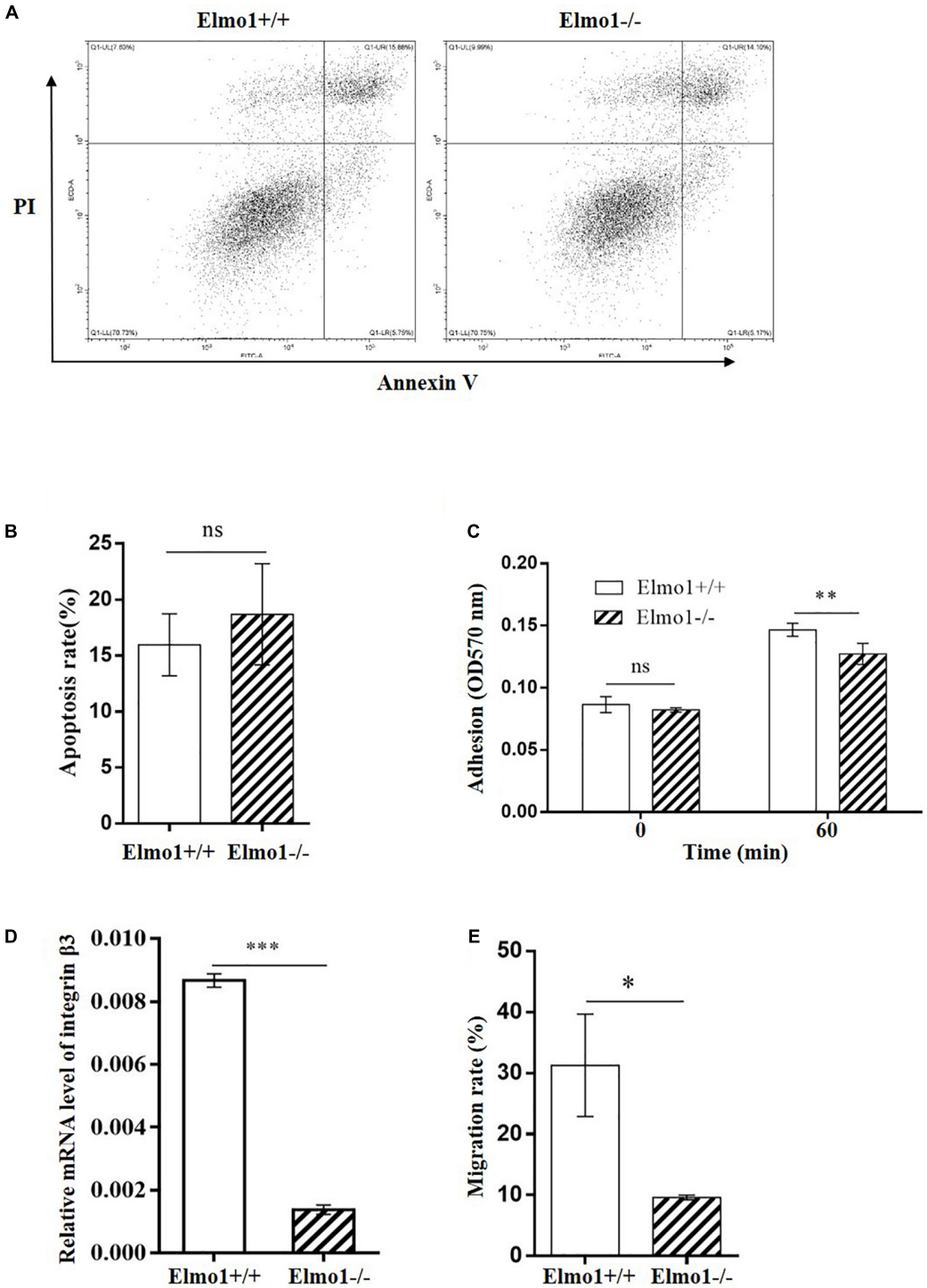

FIGURE 2 | Effect of Elmo1 deficiency on apoptosis, adhesion and migration of osteoclast precursors. **(A)** Apoptosis of osteoclast precursors. RANKL-induced osteoclasts were stained with Annexin V-FITC and PI to detect the apoptosis by flow cytometry. One representative result is shown. **(B)** The percentage of Annexin V-FITC positive cells were quantified with FlowJo software and the data was indicated as means ± SEM (n = 4). **(C)** Osteoclast precursors adhesion assay. Cells were incubated at 37°C for 0 or 60 min, and stained with crystal violet followed by DMSO dissolving for measuring absorbance at 570 nm. The data was indicated as means ± SEM (n = 4). **(D)** Relative mRNA level of integrin β3 in osteoclast precursors. Cells were treated with RANKL for 4 days in the presence of M-CSF, then relative mRNA level of integrin β3 was determined by qRT-PCR. The data was indicated as means ± SEM (n = 3). **(E)** Osteoclast precursors migration assay. Cells were allowed to migrate under stimulation of M-CSF for 24 h. Migrated cell numbers in the bottom chamber were counted. The data was indicated as means ± SEM (n = 3). Statistical significance was assessed by t-test, $^{*}P < 0.05$, $^{**}P < 0.01$, $^{***}P < 0.001$, and $^{ns}P > 0.05$.

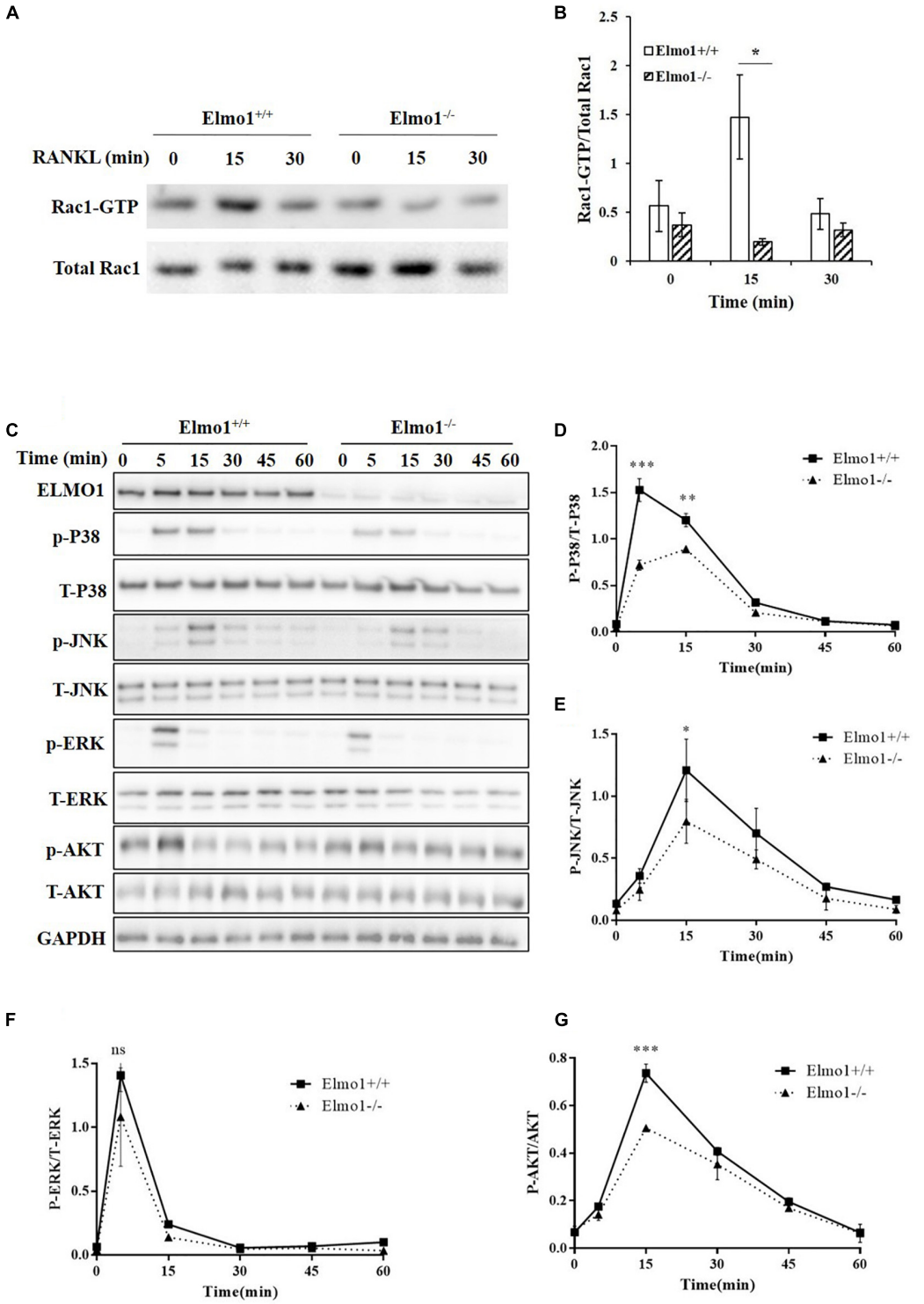

FIGURE 3 | Elmo1 upregulates RANKL-induced activation of Rac1, MAPKs, and AKT. **(A)** RANKL-induced Rac1 activation assay. Osteoclast precursors were lysed after RANKL stimulation for 15 and 30 min. The lysates were incubated with PAK-PBD beads, and proteins complexed to the beads were subjected to SDS-PAGE and analyzed by immunoblotting using anti-Rac1. **(B)** The ratio of Rac1-GTP to total Rac1 was quantified and graphed. Data are indicated as means ± SEM (n = 3). **(C)** Osteoclast precursors were stimulated by RANKL for the indicated time. Cell lysates were subjected to SDS-PAGE and analyzed by immunoblotting for detecting phosphorylation form and total p38, JNK, ERK, and AKT. **(D–G)** The intensity of phosphorylated p38 (n = 3), JNK (n = 4), ERK (n = 3), and AKT (n = 3) was quantified by densitometry using ImageJ software and expressed as the ratio of phosphorylated form to total protein. Data are indicated as means ± SEM. Statistical significance was assessed by t-test, $^{*}P < 0.05$, $^{**}P < 0.01$, $^{***}P < 0.001$, and $^{ns}P > 0.05$.

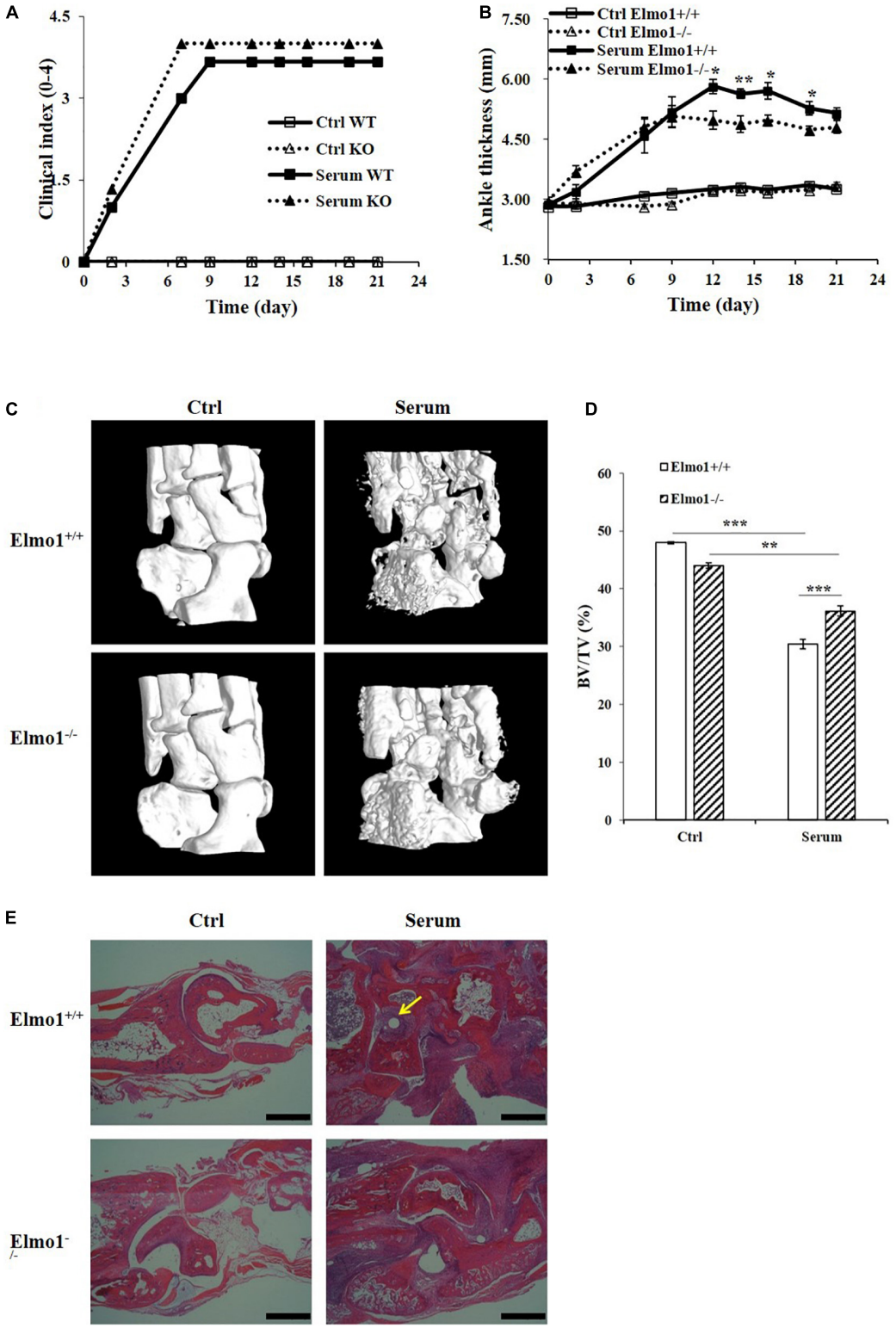

FIGURE 4 | Bone erosion of Elmo1$^{-/-}$ mice is alleviated in rheumatoid arthritis. Generation of serum transfer mouse model of arthritis was performed as mentioned in the materials and methods. **(A)** Arthritis was monitored by clinical index. Data are indicated as means ± SEM (n = 6). **(B)** Measurement of ankle thickness over time. Data are indicated as means ± SEM (n = 6). **(C)** Representative micro-CT images of ankle joints are shown. **(D)** Bone volume as a fraction of total bone volume (BV/TV) of ankle joints cortical bone. Data are indicated as means ± SEM (n = 6). **(E)** H&E-stained corresponding histological joint sections. Yellow arrow indicates site of bone erosion. Scale bar, 200 μm. Statistical significance was assessed by t-test, $^{*}P < 0.05$, $^{**}P < 0.01$, and $^{***}P < 0.001$.

serves as a regulator for the RANKL-induced osteoclast differentiation and bone resorption.

Previous studies in *C. elegans, D. discoideum,* cancer cells, and neutrophils have established that ELMO family proteins play a crucial role in cell migration (Reddien and Horvitz, 2004; Côté and Vuori, 2007; Yan et al., 2012; Li et al., 2013; Wang et al., 2016; Arandjelovic et al., 2019). In this study, we showed that deletion of Elmo1 caused defective migration in osteoclast precursors as well (**Figure 2E**). Our data supports the notion that ELMO/DOCK complex functions as an evolutionarily conserved GEF to regulate Rac activation in cell migration. We found that osteoclasts lacking ELMO1 had a lower bone-resorbing activity *in vitro* (**Figures 1A,B**), which was associated with abnormal phenotypes characterized by the less multinucleated cells formed when BMMs were developed with the treatment of RANKL (**Figures 1C,D**). In line with our findings, Lin and colleagues reported that RANKL-stimulated osteoclast formation in Rac1-overexpressing cells is significantly enhanced (Lin et al., 2015). In addition, it was found that osteoclasts lacking Dock5, the Rac1 exchange factor, have impaired adhesion (Vives et al., 2011). We therefore propose that ELMO1 and Rac1 function in regulating RANKL-induced osteoclast differentiation during bone resorption.

It has been well established that RANK recruits TRAF6 to form a TRAF6-TAB2-TAK1 complex, which in turn activates downstream MAPKs to regulate the development and function of osteoclasts (Mizukami et al., 2002; Lee et al., 2016). Rac1 is known to activate numerous signal pathways such as JNK and p38 (Van Aelst and D'Souza-Schorey, 1997; Etienne-Manneville and Hall, 2002). We therefore, examined whether ELMO1, as the upstream regulator for Rac1, was involved in these RANKL-stimulated signal pathways. Our results showed that RANKL-triggered phosphorylation of p38 and JNK occurred but with a significantly lower level in $Elmo1^{-/-}$ osteoclast precursors compared to $Elmo1^{+/+}$ cells, indicating that ELMO1 functions in RANKL-mediated activation of p38 and JNK (**Figures 3C–E**). A recent study revealed a novel role for ELMO1 which functions as a cytoplasmic regulator downstream of neutrophil receptors for C5a and LTB4 and thereby promotes inflammatory arthritis (Arandjelovic et al., 2019). Interestingly, we also demonstrated in this study that bone erosion in $Elmo1^{-/-}$ mice is alleviated in a K/BxN serum transfer induced rheumatoid arthritis model, indicating that ELMO1 also affects bone resorption by osteoclasts. Moreover, our data is consistent with *in vivo* studies on Rac GTPases in osteoclasts (Croke et al., 2011; Vives et al., 2011; Zhu et al., 2016), suggesting that ELMO1/DOCK/Rac1 signaling nexus may play a crucial role in bone resorption by regulating the differentiation and function of osteoclasts.

The findings reported herein show that ELMO1 functions in the differentiation of osteoclasts and regulates their bone resorption activity *in vitro* and *in vivo*. It should be noted, however, that our results do not exclude the possible involvement of additional mechanisms of ELMO1 involving, for examples, osteoblasts and fibroblast-like synoviocytes that play vital roles in balance of bone metabolism. Further studies would shed light on the functions and mechanisms of ELMO1 in regulating bone resorption, which may lead to new therapeutic strategies for the treatment of diseases related to metabolic bone disorders.

METHODS

Mice

ELMO1 deficient mice ($Elmo1^{-/-}$) were purchased from European Mouse Mutant Archive. Mice were housed and bred under specific pathogen-free conditions in individual ventilated cages. Age- matched pairs of mice with normal physical characteristics were used in experiments (**Supplementary Figure 2**). All animal experiments were performed in accordance with the guidelines and regulations of School of Life Sciences, Shanghai University. Experimental protocols or methods were reviewed and approved by Ethics Committee of Shanghai University.

Preparation of Bone Marrow-Derived Osteoclast Precursors

Bone marrow monocytes were prepared as osteoclast precursors for osteoclastogenesis assay *in vitro*. Under sterile conditions, the bone marrow cells from the tibias and femurs of 6– 8-week-old mice were flushed from the bone marrow cavity with Dulbecco's modified Eagle's medium (DMEM) (Hyclone) containing 10% fetal bovine serum (FBS) (Biological Industries), 100 U/ml penicillin and 100 μg/ml streptomycin. The cells were harvested by centrifugation at 500 g at room temperature for 5 min, then resuspended in 1 ml red blood cell lysis buffer and incubated for 1 min to remove the red blood cells. The clarified cells were cultured in DMEM containing 10% FBS, 1% penicillin and streptomycin in the presence of 50 ng/ml M-CSF (PeproTech).

In vitro Osteoclast Differentiation and TRAP Staining

Osteoclast precursors obtained from BMMs were loaded into a 24-well plate at a density of 5×10^4 cells/well and treated with 30 ng/ml RANKL (R&D Systems) in DMEM supplemented with 10% FBS, 1% penicillin and streptomycin and 50 ng/ml M-CSF for 4 days. The culture medium was replaced every 2 days. After osteoclast differentiation, the cells were fixed with 4% paraformaldehyde for 10 min and then stained for TRAP according to the manufacturer's instructions of Acid Phosphatase Kit (Sigma-Aldrich). The TRAP- positive cells containing three or more nuclei were recorded.

Immunofluorescence and Phalloidin Staining Assay

Osteoclast precursors were cultured in fibrinogen–coated glass-bottom dishes (NEST) at a density of 2×10^5 cells per dish in the presence of RANKL (30 ng/ml). After 4 days, the cells were fixed with 4% PFA for 10 min and permeabilized with 0.1% TritonX-100, washed with phosphate buffer, and incubated with antibodies Rabbit anti-integrin β3 (Proteintech), anti-cadherins (ABclonal) for 2 h at 37°C with 100-fold dilution. Cells were then washed and incubated with secondary antibody Alexa Fluor 488

donkey anti-Rabbit H&G (Abcam) with 500-fold dilution. For phalloidin staining, the cells were incubated with Alexa Fluor 633-phalloidin (Life technologies) for 30 min followed by 4, 6-diamidino-2-phenylindole (DAPI) (Life technologies) staining for 2 min. The cells were imaged using a Zeiss 710 LSM confocal microscope (Zeiss, Germany).

Quantitative Real-Time PCR (qRT-PCR)

Total RNA from osteoclasts that differentiated from BMMs was isolated with TRIzol reagent (Life technologies) according to the manufacturer's instructions. Reverse transcription was performed with 2 μg of total RNA using FastQuant RT Kit (TIANGEN) and the resulting cDNAs were analyzed by real-time PCR for TRAP, NFATc1, DC-STAMP, integrin β3, cadherin-2, cadherin-11, and 18s RNA with the Power SYBR Green PCR Master Mix (Life technologies). 18s RNA was used as the invariant control. The relative mRNA level of target gene was expressed as $2^{-\triangle Ct}$, in which △Ct are defined as the mean threshold cycle differences after normalization to endogenous control of 18s RNA. The primers used for qRT-PCR were as follows.

TRAP sense: 5′-CGACCATTGTTAGCCACATACG-3′;
TRAP antisense: 5′-TCGTCCTGAAGATACTGCAGG TT-3′;
NFATc1 sense: 5′- CCTGGAGATCCCGTTGC-3′;
NFATc1 antisense: 5′-GGTGTTCTTCCTCCCGATGT-3′;
DC-STAMP sense: 5′-AAAACCCTTGGGCTGTTCTT-3′;
DC-STAMP antisense: 5′-CTTCGCATGCAGGTA TTCAA-3′;
Integrin β3 sense: 5′-GCCTTCGTGGACAAGCCTGT-3′;
Integrin β3 antisense: 5′-GGACAATGCCTGCCAGTCTT-3′;
Cadherin-2 sense: 5′-AAGAGCGCCAAGCCAAGCAG-3′;
Cadherin-2 antisense: 5′-GGTACTGTGGCTCAGCA TG-3′;
Cadherin-11 sense: 5′-CTGGGTCTGGAACCAAT TCTTT-3′;
Cadherin-11 antisense: 5′-GCCTGAGCCATCAG TGTGTA-3′;
18s RNA sense: 5′-AGGCCCTGTAATTGGAATGA GTC-3′;
18s RNA antisense: 5′-GCTCCCAAGATCCAAC TACGAG-3′;

Transwell Migration Assay

Osteoclast precursors migration assay was performed in a 24-well cell culture insert companion plate with 8-μm pore-sized Transwell filter (BD Falcon). 5×10^4 cells suspended in 200 μl DMEM were added in triplicate to the upper chamber of the inserts, of which the membranes were pre-coated with 25 μg/ml fibronectin (Sigma-Aldrich). Then, 600 μl DMEM containing 50 ng/ml M-CSF, was added to the lower chamber for cell migration. After 24 h incubation, 200 μl 0.25% trypsin was added to the lower chamber to digest the cells for 5 min. Then the cells in lower chamber were collected and counted by flow cytometry. The migration rate was defined as the ratio of (experimental group-control group)/control group.

Adhesion Assay

Osteoclast precursors adhesion assay was conducted in a 96-well plate. Cells suspended in 100 μl cell culture medium were seeded triplicate at a density of 1×10^5 cells per well and incubated at 37°C for 60 min. Cells were washed with PBS and fixed with 4% PFA for 10 min after the non-adherent cells were aspirated out. The fixed cells were stained with crystal violet for 10 min and dissolved by DMSO for measuring absorbance at 570 nm using a microplate spectrophotometer.

Analysis of RANKL-Induced Apoptosis

Osteoclast precursors were plated in 6-well plates and cultured in the presence of M-CSF and RANKL for 4 days. At the end, cells were collected and washed twice with PBS for analysis of RANKL-induced apoptosis using Annexin V/PI double staining kit (BD Pharmingen) following the manufacturer's instructions. The apoptosis rate was determined by flow cytometry with Beckman CytoFLEX.

Rac Activity Assay

Activation of Rac1 in response to RANKL was examined using Rac1 activation assay kit (Cytoskeleton). In brief, osteoclast precursors seeded on 6-well plates were stimulated with 30 ng/ml RANKL for the indicated time after starvation of serum for 2 h, then lysed in 200 μl ice-cold lysis buffer containing protease inhibitor cocktail. Cell lysates were clarified by centrifugation at 12,000 g for 1 min and 15 μl of these lysates was saved to detect the total level of Rac1, while the residual lysates were incubated with 10 μg of PAK-PBD beads at 4℃ for 1 h. The beads were pelleted by centrifugation at 5,000 g at 4°C for 3 min, washed with wash buffer, and suspended with Laemmli sample buffer. The samples were subjected to SDS-PAGE and western blot analysis with an anti-Rac1 antibody.

Activation of MAPKs and AKT

Osteoclast precursors were seeded into 6-well plates, stimulated with RANKL (30 ng/ml) for the indicated time and terminated directly by adding Laemmli sample buffer. Protein samples were separated by 10% SDS-polyacrylamide gel electrophoresis after being boiled for 10 min and then transferred to a polyvinylidene difluoride (PVDF) membrane. The PVDF membrane was blocked with 5% skim milk and probed with antibodies against p-JNK, p-p38, p-ERK, p-AKT, JNK, p38, ERK, and AKT (Cell Signaling Technology), Elmo1 (Abcam), and GAPDH (Tianjin Sungene Biotech) for indicated proteins.

Generation of Rheumatoid Arthritis Mouse Model

RA mouse model was generated by serum transfer obtained from K/BxN mice according to the protocol as described (Pettit et al., 2001). In brief, arthritis of recipient mice was induced by caudal vein injection (10 μl serum/g weight of mouse) with K/BxN serum at days 0, 2, 7, and 12, and monitored throughout

the next 21 days, whereas PBS was administered to control animals. Clinical index and ankle thickness were determined and measured at the indicated days.

Microcomputed Tomography (Micro-CT) and Histology

Inflamed ankle joints were assessed by micro-CT and histology. For micro-CT imaging, ankle joints were analyzed using SkyScan1176 (Bruker). For each sample, about 200 slices with thickness of 18 μm were acquired to cover the entire width of the ankle. Images were reconstructed with the software of NRecon (Version: 1.6.9.8, Bruker) in 1,612 × 1,070 pixel matrices to provide a nominal resolution of 18 μm. 2-D slices from the 3-D stack of micro-CT images were evaluated for bone erosion. For histological analysis, ankle joints were wiped off skin and outer muscle, decalcified with 14% EDTA for 3 weeks, and then followed by paraffin embedding. Sections with thickness of 4 μm were cut for H&E and TRAP staining. The stained sections were observed under a Zeiss Axio Vert A1 microscope and the TRAP-positive cells were counted. Histopathological scoring was executed as described (Pettit et al., 2001).

Pit Formation Assay

Osteoclast precursors from BMMs were cultured on Osteo assay plates (Corning) in the presence of M-CSF (50 ng/ml) and RANKL (30 ng/ml) for 4 days. Attached cells were removed and resorption lacunae were visualized by a Zeiss Axio Vert A1 microscope and quantified using ImageJ.

Statistical Analysis

Statistical significance was evaluated with GraphPad Prism 6 using unpaired Student's two-tailed *t*-test analysis of variance. $P < 0.05$ was considered significant.

DATA AVAILABILITY STATEMENT

The original contributions presented in the study are included in the article/**Supplementary Material**, further inquiries can be directed to the corresponding author/s.

ETHICS STATEMENT

The animal study was reviewed and approved by the Minghong Wu, Ethics Committee of Shanghai University.

AUTHOR CONTRIBUTIONS

XC and JY contributed to conception and design of the study and wrote the manuscript. XL, YH, SY, YZ, and LH performed the experiments. XL and YH performed the statistical analysis. All authors contributed to manuscript revision, read, and approved the submitted version.

FUNDING

This work was supported by grants of the National Nature Science Foundation of China (31972901, 31571430, and 31671234), the National Basic Research Program of China (2014CB541804), the Innovation Program of Shanghai Municipal Education Commission (15ZZ053), the Science and Technology Commission of Shanghai Municipality (15ZR1436300), the Health and Family Planning Commission Foundation of Shanghai (201440300 and 20164Y0149).

ACKNOWLEDGMENTS

We thank F. Li at SJTUSM for providing serum of K/BxN.

SUPPLEMENTARY MATERIAL

The Supplementary Material for this article can be found online at: https://www.frontiersin.org/articles/10.3389/fcell.2021.702916/full#supplementary-material

REFERENCES

Arandjelovic, S., Perry, J. S. A., Lucas, C. D., Penberthy, K. K., Kim, T. H., Zhou, M., et al. (2019). A noncanonical role for the engulfment gene ELMO1 in neutrophils that promotes inflammatory arthritis. *Nat. Immunol.* 20, 141–151. doi: 10.1038/s41590-018-0293-x

Asagiri, M., Sato, K., Usami, T., Ochi, S., Nishina, H., Yoshida, H., et al. (2005). Autoamplification of NFATc1 expression determines its essential role in bone homeostasis. *J. Exp. Med.* 202, 1261–1269. doi: 10.1084/jem.20051150

Bharti, A. C., Takada, Y., Shishodia, S., and Aggarwal, B. B. (2004). Evidence that receptor activator of nuclear factor (NF)-kappaB ligand can suppress cell proliferation and induce apoptosis through activation of a NF-kappaB-independent and TRAF6-dependent mechanism. *J. Biol. Chem.* 279, 6065–6076. doi: 10.1074/jbc.m308062200

Côté, J.-F., and Vuori, K. (2007). GEF what? Dock180 and related proteins help Rac to polarize cells in new ways. *Trends Cell Biol.* 17, 383–393. doi: 10.1016/j.tcb.2007.05.001

Croke, M., Ross, F. P., Korhonen, M., Williams, D. A., Zou, W., and Teitelbaum, S. L. (2011). Rac deletion in osteoclasts causes severe osteopetrosis. *J. Cell Sci.* 124, 3811–3821. doi: 10.1242/jcs.086280

David, J. P., Sabapathy, K., Hoffmann, O., Idarraga, M. H., and Wagner, E. F. (2002). JNK1 modulates osteoclastogenesis through both c-Jun phosphorylation-dependent and -independent mechanisms. *J. Cell Sci.* 115, 4317–4325. doi: 10.1242/jcs.00082

Etienne-Manneville, S., and Hall, A. (2002). Rho GTPases in cell biology. *Nature* 420, 629–635.

Funamoto, S., Meili, R., Lee, S., Parry, L., and Firtel, R. A. (2002). Spatial and temporal regulation of 3-phosphoinositides by PI 3-kinase and PTEN mediates chemotaxis. *Cell* 109, 611–623. doi: 10.1016/s0092-8674(02)00755-9

Gao, L., Kong, L., and Zhao, Y. (2020). The regulatory role of Rho GTPases and their substrates in osteoclastogenesis. *Curr. Drug Targets* 22, 1064–1070. doi: 10.2174/1389450121666200925150446

Gu, J., Yang, Z., Yuan, L., Guo, S., Wang, D., Zhao, N., et al. (2020). Rho-GEF trio regulates osteoclast differentiation and function by Rac1/Cdc42. *Exp. Cell Res.* 396:112265. doi: 10.1016/j.yexcr.2020.112265

Guo, Y., Wang, W., Wang, J., Feng, J., Wang, Q., Jin, J., et al. (2013). Receptor for activated C kinase 1 promotes hepatocellular carcinoma growth by enhancing mitogen-activated protein kinase kinase 7 activity. *Hepatology* 57, 140–151. doi: 10.1002/hep.25978

He, Y., Staser, K., Rhodes, S. D., Liu, Y., Wu, X., Park, S. J., et al. (2011). Erk1 positively regulates osteoclast differentiation and bone resorptive activity. *PLoS One* 6:e24780. doi: 10.1371/journal.pone.0024780

Iijima, M., and Devreotes, P. (2002). Tumor suppressor PTEN mediates sensing of chemoattractant gradients. *Cell* 109, 599–610. doi: 10.1016/s0092-8674(02)00745-6

Jung, Y. K., Han, S. W., Kim, G. W., Jeong, J. H., Kim, H. J., and Choi, J. Y. (2012). DICAM inhibits osteoclast differentiation through attenuation of the integrin alphaVbeta3 pathway. *J. Bone Miner. Res.* 27, 2024–2034. doi: 10.1002/jbmr.1632

Kim, J. H., Kim, K., Kim, I., Seong, S., Nam, K. I., Lee, S. H., et al. (2016). Role of CrkII signaling in RANKL-induced osteoclast differentiation and function. *J. Immunol.* 196, 1123–1131. doi: 10.4049/jimmunol.1501998

Kim, K., Kim, J. H., Lee, J., Jin, H. M., Lee, S. H., Fisher, D. E., et al. (2005). Nuclear factor of activated T cells c1 induces osteoclast-associated receptor gene expression during tumor necrosis factor-related activation-induced cytokine-mediated osteoclastogenesis. *J. Biol. Chem.* 280, 35209–35216. doi: 10.1074/jbc.m505815200

Kim, M. J., Kim, H., Lee, S. H., Gu, D. R., Lee, S. Y., Lee, K., et al. (2015). ADP-Ribosylation factor 1 regulates proliferation, migration, and fusion in early stage of osteoclast differentiation. *Int. J. Mol. Sci.* 16, 29305–29314. doi: 10.3390/ijms161226168

Lamothe, B., Webster, W. K., Gopinathan, A., Besse, A., Campos, A. D., and Darnay, B. G. (2007). TRAF6 ubiquitin ligase is essential for RANKL signaling and osteoclast differentiation. *Biochem. Biophys. Res. Commun.* 359, 1044–1049. doi: 10.1016/j.bbrc.2007.06.017

Lee, A. W., and States, D. J. (2000). Both src-dependent and -independent mechanisms mediate phosphatidylinositol 3-kinase regulation of colony-stimulating factor 1-activated mitogen-activated protein kinases in myeloid progenitors. *Mol. Cell. Biol.* 20, 6779–6798. doi: 10.1128/mcb.20.18.6779-6798.2000

Lee, K., Chung, Y. H., Ahn, H., Kim, H., Rho, J., and Jeong, D. (2016). Selective regulation of MAPK signaling mediates RANKL-dependent osteoclast differentiation. *Int. J. Biol. Sci.* 12, 235–245. doi: 10.7150/ijbs.13814

Lee, K., Seo, I., Choi, M., and Jeong, D. (2018). Roles of mitogen-activated protein kinases in osteoclast biology. *Int. J. Mol. Sci.* 19:3004. doi: 10.3390/ijms19103004

Lee, S. E., Woo, K. M., Kim, S. Y., Kim, H. M., Kwack, K., Lee, Z. H., et al. (2002). The phosphatidylinositol 3-kinase, p38, and extracellular signal-regulated kinase pathways are involved in osteoclast differentiation. *Bone* 30, 71–77. doi: 10.1016/s8756-3282(01)00657-3

Li, H., Yang, L., Fu, H., Yan, J., Wang, Y., Guo, H., et al. (2013). Association between Galphai2 and ELMO1/Dock180 connects chemokine signalling with Rac activation and metastasis. *Nat. Commun.* 4:1706.

Li, X., Udagawa, N., Itoh, K., Suda, K., Murase, Y., Nishihara, T., et al. (2002). p38 MAPK-mediated signals are required for inducing osteoclast differentiation but not for osteoclast function. *Endocrinology* 143, 3105–3113. doi: 10.1210/endo.143.8.8954

Lin, J., Lee, D., Choi, Y., and Lee, S. Y. (2015). The scaffold protein RACK1 mediates the RANKL-dependent activation of p38 MAPK in osteoclast precursors. *Sci. Signal.* 8:ra54. doi: 10.1126/scisignal.2005867

Lomaga, M. A., Yeh, W. C., Sarosi, I., Duncan, G. S., Furlonger, C., Ho, A., et al. (1999). TRAF6 deficiency results in osteopetrosis and defective interleukin-1, CD40, and LPS signaling. *Genes Dev.* 13, 1015–1024. doi: 10.1101/gad.13.8.1015

Lopez-Bergami, P., Habelhah, H., Bhoumik, A., Zhang, W., Wang, L. H., and Ronai, Z. (2005). RACK1 mediates activation of JNK by protein kinase C [corrected]. *Mol. Cell* 19, 309–320. doi: 10.1016/j.molcel.2005.06.025

Matsumoto, M., Kogawa, M., Wada, S., Takayanagi, H., Tsujimoto, M., Katayama, S., et al. (2004). Essential role of p38 mitogen-activated protein kinase in cathepsin K gene expression during osteoclastogenesis through association of NFATc1 and PU.1. *J Biol Chem.* 279, 45969–45979. doi: 10.1074/jbc.m408795200

Mizukami, J., Takaesu, G., Akatsuka, H., Sakurai, H., Ninomiya-Tsuji, J., Matsumoto, K., et al. (2002). Receptor activator of NF-kappaB ligand (RANKL) activates TAK1 mitogen-activated protein kinase kinase kinase through a signaling complex containing RANK, TAB2, and TRAF6. *Mol. Cell. Biol.* 22, 992–1000. doi: 10.1128/mcb.22.4.992-1000.2002

Nagai, Y., Osawa, K., Fukushima, H., Tamura, Y., Aoki, K., Ohya, K., et al. (2013). p130Cas, Crk-associated substrate, plays important roles in osteoclastic bone resorption. *J. Bone Miner. Res.* 28, 2449–2462. doi: 10.1002/jbmr.1936

Naito, A., Azuma, S., Tanaka, S., Miyazaki, T., Takaki, S., Takatsu, K., et al. (1999). Severe osteopetrosis, defective interleukin-1 signalling and lymph node organogenesis in TRAF6-deficient mice. *Genes Cells* 4, 353–362. doi: 10.1046/j.1365-2443.1999.00265.x

Parent, C. A., and Devreotes, P. N. (1999). A cell's sense of direction. *Science* 284, 765–770.

Park, J. H., Lee, N. K., and Lee, S. Y. (2017). Current understanding of RANK signaling in osteoclast differentiation and maturation. *Mol. Cells* 40, 706–713.

Pettit, A. R., Ji, H., von Stechow, D., Müller, R., Goldring, S. R., Choi, Y., et al. (2001). TRANCE/RANKL knockout mice are protected from bone erosion in a serum transfer model of arthritis. *Am. J. Pathol.* 159, 1689–1699. doi: 10.1016/s0002-9440(10)63016-7

Reddien, P. W., and Horvitz, H. R. (2004). The engulfment process of programmed cell death in caenorhabditis elegans. *Annu. Rev. Cell Dev. Biol.* 20, 193–221. doi: 10.1146/annurev.cellbio.20.022003.114619

Reddy, S. V., Hundley, J. E., Windle, J. J., Alcantara, O., Linn, R., Leach, R. J., et al. (1995). Characterization of the mouse tartrate-resistant acid phosphatase (TRAP) gene promoter. *J. Bone Miner. Res.* 10, 601–606. doi: 10.1002/jbmr.5650100413

Ruocco, M. G., Maeda, S., Park, J. M., Lawrence, T., Hsu, L. C., Cao, Y., et al. (2005). I{kappa}B kinase (IKK){beta}, but not IKK{alpha}, is a critical mediator of osteoclast survival and is required for inflammation-induced bone loss. *J. Exp. Med.* 201, 1677–1687. doi: 10.1084/jem.20042081

Sasaki, A. T., Chun, C., Takeda, K., and Firtel, R. A. (2004). Localized Ras signaling at the leading edge regulates PI3K, cell polarity, and directional cell movement. *J. Cell Biol.* 167, 505–518. doi: 10.1083/jcb.200406177

Sugatani, T., Alvarez, U., and Hruska, K. A. (2003). PTEN regulates RANKL- and osteopontin-stimulated signal transduction during osteoclast differentiation and cell motility. *J. Biol. Chem.* 278, 5001–5008. doi: 10.1074/jbc.m209299200

Touaitahuata, H., Blangy, A., and Vives, V. (2014). Modulation of osteoclast differentiation and bone resorption by Rho GTPases. *Small GTPases* 5:e28119. doi: 10.4161/sgtp.28119

Van Aelst, L., and D'Souza-Schorey, C. (1997). Rho GTPases and signaling networks. *Genes Dev.* 11, 2295–2322. doi: 10.1101/gad.11.18.2295

Vives, V., Laurin, M., Cres, G., Larrousse, P., Morichaud, Z., Noel, D., et al. (2011). The Rac1 exchange factor Dock5 is essential for bone resorption by osteoclasts. *J. Bone Miner. Res.* 26, 1099–1110. doi: 10.1002/jbmr.282

Wang, Y., Xu, X., Pan, M., and Jin, T. (2016). ELMO1 directly interacts with Gbetagamma subunit to transduce GPCR signaling to Rac1 activation in chemotaxis. *J. Cancer* 7, 973–983. doi: 10.7150/jca.15118

Wong, B. R., Besser, D., Kim, N., Arron, J. R., Vologodskaia, M., Hanafusa, H., et al. (1999). TRANCE, a TNF family member, activates Akt/PKB through a signaling complex involving TRAF6 and c-Src. *Mol. Cell* 4, 1041–1049. doi: 10.1016/s1097-2765(00)80232-4

Yan, J., Mihaylov, V., Xu, X., Brzostowski, J. A., Li, H., Liu, L., et al. (2012). A Gbetagamma effector, ElmoE, transduces GPCR signaling to the actin network during chemotaxis. *Dev. Cell* 22, 92–103. doi: 10.1016/j.devcel.2011.11.007

Zhu, M., Sun, B.-h, Saar, K., Simpson, C., Troiano, N., Dallas, S. L., et al. (2016). Deletion of rac in mature osteoclasts causes osteopetrosis, an age-dependent change in osteoclast number, and a reduced number of osteoblasts In Vivo. *J. Bone Miner. Res.* 31, 864–873. doi: 10.1002/jbmr.2733

Conflict of Interest: The authors declare that the research was conducted in the absence of any commercial or financial relationships that could be construed as a potential conflict of interest.

Publisher's Note: All claims expressed in this article are solely those of the authors and do not necessarily represent those of their affiliated organizations, or those of the publisher, the editors and the reviewers. Any product that may be evaluated in this article, or claim that may be made by its manufacturer, is not guaranteed or endorsed by the publisher.

frontiers in Cell and Developmental Biology

REVIEW
published: 03 August 2021
doi: 10.3389/fcell.2021.713254

The Potential Role of RP105 in Regulation of Inflammation and Osteoclastogenesis During Inflammatory Diseases

Zhou Fan[1], Janak L. Pathak[1] and Linhu Ge[1,2]**

[1] Guangzhou Key Laboratory of Basic and Applied Research of Oral Regenerative Medicine, Affiliated Stomatology Hospital of Guangzhou Medical University, Guangzhou, China, [2] Institute of Oral Disease, Guangzhou Medical University, Guangzhou, China

Inflammatory diseases have a negative impact on bone homeostasis via exacerbated local and systemic inflammation. Bone resorbing osteoclasts are mainly derived from hematopoietic precursors and bone marrow monocytes. Induced osteoclastogenesis during inflammation, autoimmunity, metabolic diseases, and cancers is associated with bone loss and osteoporosis. Proinflammatory cytokines, pathogen-associated molecular patterns, or endogenous pathogenic factors induce osteoclastogenic differentiation by binding to the Toll-like receptor (TLR) family expressed on surface of osteoclast precursors. As a non-canonical member of the TLRs, radioprotective 105 kDa (RP105 or CD180) and its ligand, myeloid differentiation protein 1 (MD1), are involved in several bone metabolic disorders. Reports from literature had demonstrated RP105 as an important activator of B cells, bone marrow monocytes, and macrophages, which regulates inflammatory cytokines release from immune cells. Reports from literature had shown the association between RP105 and other TLRs, and the downstream signaling mechanisms of RP105 with different "signaling-competent" partners in immune cells during different disease conditions. This review is focused to summarize: (1) the role of RP105 on immune cells' function and inflammation regulation (2) the potential regulatory roles of RP105 in different disease-mediated osteoclast activation and the underlying mechanisms, and (3) the different "signaling-competent" partners of RP105 that regulates osteoclastogenesis.

Keywords: osteoclasts, Toll-like receptors, liposaccharides, radioprotective 105kDa protein, osteoporosis

OPEN ACCESS

Edited by:
Andrea Del Fattore, Bambino Gesù Children Hospital (IRCCS), Italy

Reviewed by:
Imranul Alam, Indiana University, United States
Giacomina Brunetti, University of Bari Aldo Moro, Italy

****Correspondence:***
Janak L. Pathak
j.pathak@gzhmu.edu.cn
Linhu Ge
gelinhu@yeah.net

Specialty section:
This article was submitted to Molecular and Cellular Pathology, a section of the journal Frontiers in Cell and Developmental Biology

Received: *22 May 2021*
Accepted: *09 July 2021*
Published: *03 August 2021*

Citation:
Fan Z, Pathak JL and Ge L (2021) The Potential Role of RP105 in Regulation of Inflammation and Osteoclastogenesis During Inflammatory Diseases. Front. Cell Dev. Biol. 9:713254. doi: 10.3389/fcell.2021.713254

Abbreviations: AP1, activator protein-1; BLNK, B cell linker protein; BMMs, Bone marrow macrophages; CEACAM1, carcinoembryonic antigen-related cell adhesion molecule-1; DC, dendritic cell; ERK, extracellular-signal-regulated kinase; g-MDSCs, granulocytic MDSCs; IFN, interferon; Ikaros, identified IKZF1; ITAM, immunoglobulin-like receptor/immunoreceptor tyrosine-based activation motif; LPS, lipopolysaccharides; LRR, leucine-rich repeat; M-CSF, macrophage colony-stimulating factor; MD1, myeloid differentiation protein 1; MDSC, myeloid-derived suppressor cell; NFATc1, nuclear factor of activated T-cells cytoplasmic 1; OPG, osteoprotegerin; OS, osteosarcoma; PAMP, pathogen-associated molecular pattern; PI3K, phosphatidylinositol-3-kinase; Pim-1, proviral integration site for Moloney murine leukemia virus 1; Pim-1L, long isoform of Pim-1; Pim-1S, short isoform of Pim-1; PRR, pattern recognition receptor; RANKL, receptor activator of NF-kB ligand; RP105/CD180, radioprotective 105 kDa; SLE, systemic lupus erythematosus; STAT, signal transducer and activator of transcription; TIR, intracellular interleukin-1 receptor; TLR, Toll-like receptor; TNF, tumor necrosis factor; TNFR, TNF-α receptor.

BACKGROUND

Osteoclasts, multinucleated bone-resorbing cells, are required for bone remodeling. Osteoclasts originate from embryonic erythromyeloid progenitors, bone marrow hematopoietic stem cells, and mononuclear precursors, which are usually present in peripheral circulation and bone marrow (Takayanagi, 2007; McGrath et al., 2015). Studies suggest that osteoclasts are generated via the fusion of hematopoietic stem-cell-derived monocytic precursors in the presence of conducive growth factors macrophage colony-stimulating factor (MCSF/CSF-1) and receptor activator of nuclear factor- kappa B ligand (RANKL) (Udagawa et al., 1990). Excessive osteoclast activity contributes to bone loss, whereas reduced osteoclast function is associated with the development of osteopetrosis (Jacome-Galarza et al., 2019). Bacterial inflammatory diseases such as periodontitis (Blasco-Baque et al., 2017; Gu and Han, 2020) and osteomyelitis (Taubman et al., 2005), multiple myeloma (Westhrin et al., 2020), and metabolic diseases like diabetes mellitus (Watanabe et al., 2013) result in hyperactive osteoclastogenesis and progress into severe osteolytic bone diseases. Some autoimmune diseases such as systemic lupus erythematosus (SLE) (Qiao et al., 2020) and osteosarcoma (Endo-Munoz et al., 2010) induce the development of hyperostosis or arthritis as bone destruction is hampered in such cases. Recently, numerous studies have demonstrated that radioprotective 105 kDa (RP105 or CD180) and its ligand, myeloid differentiation protein 1 (MD1) are involved in inflammatory disease-induced osteoclastogenesis and bone loss.

Toll-like receptors (TLRs) play an important role in the pathophysiology of infectious diseases and inflammatory disorders (Akira et al., 2001). A total of 10 TLRs, i.e., TLR1-10 have been reported in humans. Although RP105 is a non-canonical member of the TLR family, RP105 is the most frequently encountered TLR on cells, including different kinds of bone marrow cells like bone marrow monocytes (Kikuchi et al., 2018) and immune cells including B cells (Miura et al., 1998; Ogata et al., 2000; Nagai et al., 2002; Yazawa et al., 2003), dendritic cells (DCs) (Divanovic et al., 2005) and macrophages (Liu B. et al., 2013). Multiple myeloma cells express RP105 suggesting its role in the pathophysiology of MM (Bohnhorst et al., 2006). Lipopolysaccharides (LPS) or other TLR ligands stimulate the release of proinflammatory cytokines and chemokines in immune cells such as B cells and T cells (Liu et al., 2010). Proinflammatory cytokines such as tumor necrosis factor (TNF)-α, interleukin (IL)-1, and IL-6 promote osteoclastogenesis (Ru and Wang, 2020). Osteoclast differentiation in pathological conditions is different than in physiological conditions. RP105 and MD1 are considered to be the negative regulators of TLRs, particularly TLR4 and TLR2 (Schultz and Blumenthal, 2017), and TLR-related proinflammatory cytokine production (Miura et al., 1998; Chaplin et al., 2011; Liu B. et al., 2013; Bastiaansen et al., 2014). This negative regulation might act as a compensatory mechanism to mitigate exacerbated inflammation. The binding of RP105 to MD-1 results in the activation of B cells, DCs, monocytes, and macrophages, and these RP105/MD-1-mediated phenomena enhance upon LPS stimulation (Schultz and Blumenthal, 2017). This phenomenon could be responsible for excessive osteoclastogenesis and bone loss in inflammatory diseases. Further research on the RP105/MD-1-associated signaling during osteoclastogenic differentiation of precursor cells are needed to provide insights on the development of novel strategies to mitigate inflammation and bone loss during inflammatory diseases.

PHYSIOLOGICAL OSTEOCLASTOGENESIS

In normal physiological conditions, osteoclastogenesis depends on RANKL and MCSF, which are produced by osteoblast lineage cells (Ueki et al., 2007). MCSF regulates mononuclear precursor survival and proliferation, whereas RANKL regulates precursor cell fusion and maturation (Park et al., 2017). RANKL binds to the RANK receptor expressed on the surface of mononuclear cells, forms a tripolymer, and recruits TNF receptor-associated factor 6 (TRAF6) via its cytoplasmic C-terminal domain to trigger downstream signaling cascades (Takayanagi et al., 2000). TRAF6 are two important adapter proteins involved in the NF-κB and MAPK pathways (Moresco et al., 2011) (**Figure 1**). Expression of TRAF6 results in the production of the receptor for activated C kinase 1 (Rac1) (Kim et al., 2009) and NADPH oxidase 1 (Nox1) (Lee et al., 2005). Rac1 and Nox1 produce reactive oxygen species (ROS) and induce the phosphorylation of p38, extracellular signal-regulated kinase (ERK), and c-Jun N-terminal kinase (JNK), ultimately resulting in MAPK pathway activation and activator protein-1 (AP1) expression (Mao et al., 2006). TRAF6 activates NF-κB by inducing the nuclear localization of NF-κB via the phosphorylation of IkB kinases (IKKs) (Okamoto K. et al., 2017). As important downstream targets of the RANKL signaling pathway in the early stage of osteoclastogenesis, AP1 and NF-κB activate nuclear phosphoprotein AP-1 transcription factor comprising Fos (c-Fos) (Grigoriadis et al., 1994; Takayanagi et al., 2002). In the late stage of RANKL signaling, c-Fos cooperates with nuclear factor of activated T-cells cytoplasmic 1 (NFATc1), as well as other transcription factors, like interferon regulatory factor 4 (PU.1) and microphthalmia-associated transcription factor (MITF) to induce dendritic-cell-specific transmembrane protein (DC-STAMP), vacuolar proton pump subunit Atp6v0d2, and c-Src substrate Tks5, and regulate osteoclast fusion (Park et al., 2017).

Immunoglobulin-like receptor/immunoreceptor tyrosine-based activation motif (ITAM) signalings such as TREM-2/DAP12 and OSCAR/FcRγ activate Ca^{2+} signaling, recruit tyrosine-protein kinase SYK (Syk), and lead to the rapid activation of NFATc1 (Shinohara et al., 2008; Negishi-Koga and Takayanagi, 2009) (**Figure 1**). The RANKL/RANK complex also induces NFATc1 expression and nuclear localization by reducing the phosphorylation of glycogen synthase kinase-3β via the production of protein kinase C β type (PKCβ) (Shin et al., 2014) and activation of the phosphatidylinositol-3-kinase (PI3K)-Akt pathway (Moon et al., 2012) (**Figure 1**). As a key initiation factor of osteoclastogenesis, NFATc1 regulates the expression of integrin β3 (Crotti et al., 2006), DC-STAMP (Yagi et al., 2005), osteoclast stimulatory transmembrane protein (OC-STAMP)

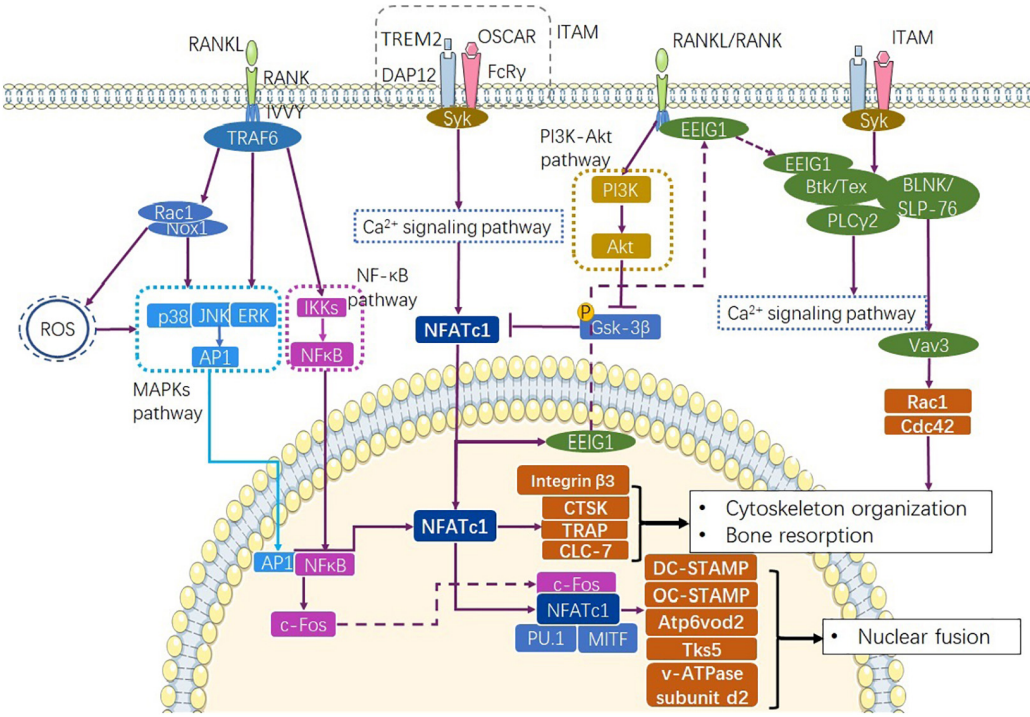

FIGURE 1 | Pathways involve in physiological osteoclastogenesis. RANKL/RANK complex recruits TRAF6 to express AP1 through MAPKs and NF-κB through NF-κB signaling pathway (Gyori and Mocsai, 2020). At the same time, Ca^{2+} signaling pathway mediated by ITAM signaling promotes transcription of NFATc1 as well as the production osteoclastogenic factors CTSK, TRAP, and CLC-7. RANKL/RANK and ITAM signaling together complete the differentiation progress though the Ca^{2+} signaling pathway (Park et al., 2017). RANKL/RANK also enhance NFATc1 via inhibiting GSK-3β (Shin et al., 2014). ITAM, immunoreceptor tyrosine-based activation motif.

(Miyamoto et al., 2012), and V-type proton ATPase (v-ATPase) subunit d2 (Lee et al., 2006) via the Ca^{2+} signaling pathway. Furthermore, NFATc1 cooperates with c-Fos and Jun to induce the transactivation of tartrate-resistant acid phosphatase (TRAP) (Matsumoto et al., 2004; Matsuo et al., 2004), and promotes the transactivation of the osteoclast-associated immunoglobulin-like receptor (OSCAR) upon interacting with PU.1 and MITF (Kim K. et al., 2005; Kim Y. et al., 2005) (**Figure 1**). NFATc1 exhibits the phenomenon of autoregulation (Negishi-Koga and Takayanagi, 2009). At the same time, NFATc1 induces the expression of early estrogen-induced gene 1 (EEIG1), which triggers crosstalk between RANKL/RANK and the Ca^{2+} signaling pathway by regulating Btk/Tec (Choi et al., 2013). Btk/Tec interacts with B cell linker protein (BLNK)/SLP-76 and PLCγ2 to induce Ca^{2+} oscillation and calmodulin and calcineurin activation. Moreover, ITAM signaling activates Rac1 and Cdc42 production to modulate cytoskeleton organization through the Syk/SLP-76/Vav3 signaling axis (Kim et al., 2009) (**Figure 1**). These transcription factors are specific to osteoclasts and directly activate cell fusion and osteoclastic bone resorption.

In physiological osteoclastogenesis, osteoprotegerin (OPG) negatively regulates the RANKL-RANK signaling pathway and works as a decoy receptor for RANKL (Leite et al., 2015) (**Figure 2**). Several factors, such as IRF-8 (Zhao et al., 2009), Bcl6 (Miyauchi et al., 2010), Stat5 (Hirose et al., 2014), and RBP-J (Zhao et al., 2012; Li et al., 2014) are known to negatively regulate osteoclastogenesis by preventing the expression of NFTAc1. In addition, the adaptor protein SH3BP2 and microRNA such as miR-34a are reported to inhibit osteoclastogenesis (Ueki et al., 2007; Levaot et al., 2011). SH3BP3 regulates the phosphorylation of Syk and Vav whereas miR-34a influences the transforming growth factor-induced factors (Tgif2) to regulate the JNK protein phosphorylation (Krzeszinski et al., 2014). Interferon (IFN)-γ and IL-4 expressed by activated T cells, Th1 and Th2 cells, CTLA-4, TGF-β and IL-10 expressed by Treg cells inhibit osteoclast differentiation, whereas IL-17 expressed by Th17 cells upregulates RANKL expression in mesenchymal cells (Sato et al., 2006).

OSTEOCLASTOGENESIS UNDER PATHOLOGICAL CONDITIONS

Systemic diseases such as diabetes mellitus (Blasco-Baque et al., 2017), hyperthyroidism (Baliram et al., 2012), SLE (Lim et al., 2011, 2012), rheumatoid arthritis (Murata et al., 2017; Rauber et al., 2017), and neoplastic diseases like multiple myeloma are associated with excessive osteoclastogenesis and osteoporosis (Westhrin et al., 2020). Similarly, inflammatory diseases caused by bacterial infections such as periodontitis (AlQranei and Chellaiah, 2020; Gu and Han, 2020), peri-implantitis (Yu et al., 2018), and osteomyelitis (Kavanagh et al., 2018) are associated with enhanced osteoclastogenesis leading to bone resorption.

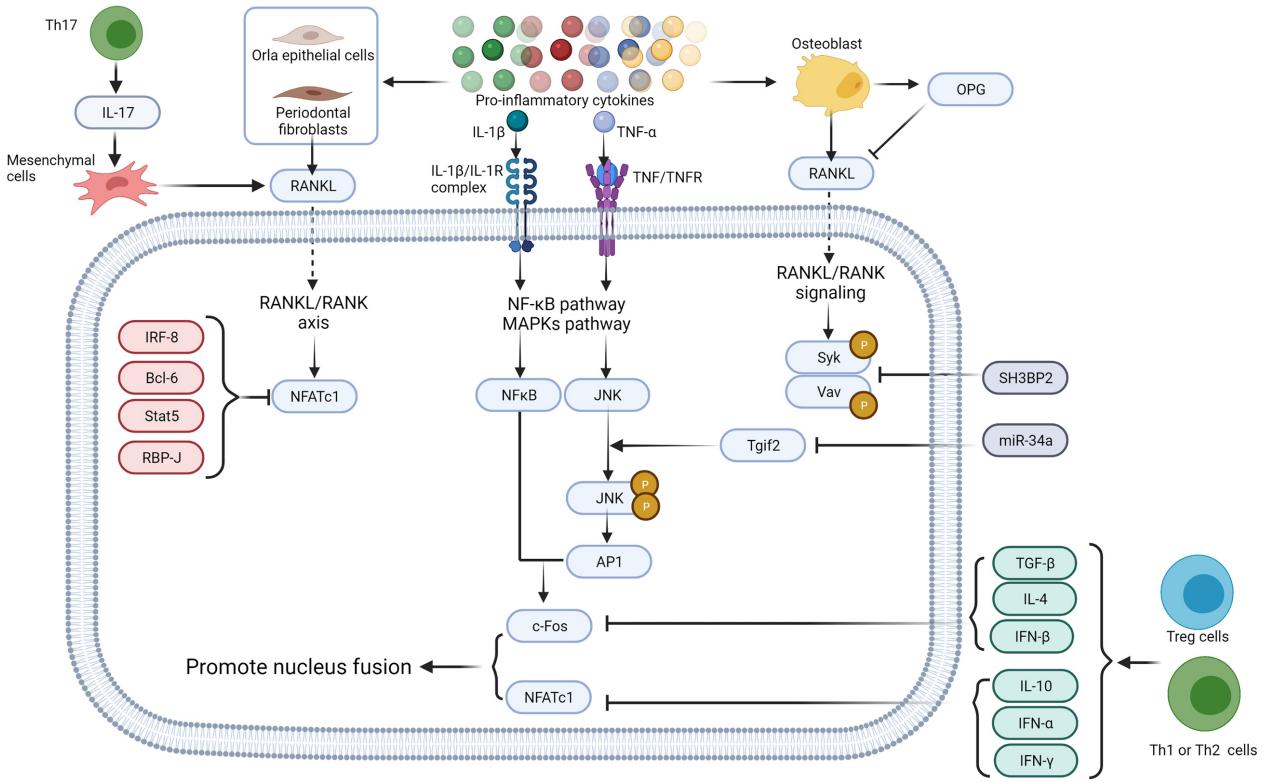

FIGURE 2 | Proinflammatory cytokines regulate osteoclastogenesis via direct interaction with their receptors. Proinflammatory cytokines such as IL-1β, IL-6, IL-17, and TNF-α secreted by different immune cells induce RANKL production in endothelial cells (Batool et al., 2020), fibroblasts (Nagasawa et al., 2007; Hienz et al., 2015), and osteoblast lineage cells (Algate et al., 2016). OPG, secreted by osteoblast, works as a decoy receptor of RANKL to negatively regulate osteoclastogenesis (Lam et al., 2000). Intracellular IRF-8, Bcl6, Stat5, and RBP-J also negatively regulate osteoclastogenesis by inhibiting the expression of NFTAc1 (Ru and Wang, 2020). SH3BP2 (Ueki et al., 2007; Levaot et al., 2011) and miR-34a (Krzeszinski et al., 2014) negatively regulates Syk, Vav, and JNK protein phosphorylation. TGF-β, IFN-α, IFN-β, IFN-γ, IL-4, and IL-10 secreted by immune cells inhibit c-Fos thereby restrain osteoclastogenesis (Gao et al., 2007; Fujii et al., 2012; Xiong et al., 2016; Amarasekara et al., 2018), whereas IL-17 expressed by Th17 cells up-regulates RANKL expression in mesenchymal cells (Sato et al., 2006). Figure was created using BioRender.com.

Although the pathogeneses of these conditions are different, there is consensus that the inflammatory cytokines produced in these diseases play an important role in osteoclastogenesis and bone destruction (Takayanagi, 2007).

As typical pathogen-associated molecular patterns (PAMPs), LPS and other lipoproteins stimulate TLR4 and TLR2 (Taubman et al., 2005) to enhance complete RANKL-dependent osteoclastogenesis (AlQranei and Chellaiah, 2020). In RANKL-dependent osteoclastogenesis, LPS binds to TLR4/MD-2 complex. LPS/TLR4/MD-2 directs the recruitment of myeloid differentiation primary response protein (MyD88) via the C-terminal Toll/IL-1 receptor domain (TIR domain). TIR domain is homologous to the intracellular domain of interleukin-1 receptor of TLR4. TRAF6, recruited by MyD88, activates the NF-κB and MAPK pathways, resulting in the nuclear localization of NFκB and AP1 (Kobayashi et al., 2001; Sun et al., 2019) (**Figure 3**). Further, in the presence of RANKL, proinflammatory cytokines such as TNF-α and IL-1 enhance the osteoclastic phenotype of monocytes and macrophages (Liu et al., 2009) in an autocrine/paracrine manner, independent of RANKL (Nason et al., 2009) (**Figure 2**). TNF-α induces osteoclast formation via both the RANKL and TNF-α/TNFR axis dependent. In the presence of TNF-α, RANKL primes macrophages to differentiate into osteoclasts, and this phenomenon is completely abrogated by OPG, a decoy receptor of RANKL (Lam et al., 2000). RANKL commits the cells to the osteoclastic lineage and TNF-α ensures the induction of differentiation through TNF-α receptor (TNFR) signaling, suggesting a synergistic relationship between RANKL and TNF-α (Fuller et al., 2002). In contrast, LPS/TLR4 signaling initiates RANKL-dependent osteoclastogenesis partially by promoting RANKL production in osteoblasts (Algate et al., 2016), gingival fibroblasts (Nagasawa et al., 2007; Hienz et al., 2015), oral epithelial cells (Batool et al., 2020), and DCs (Alnaeeli et al., 2007). Inhibition of TLR4 and TLR2 in osteoblasts results in decreased RANKL expression even after exposure to LPS (Tang et al., 2011). Proinflammatory cytokines such as IL-6 and TNF-α also enhance osteoclastogenesis by promoting RANKL production in osteoblasts (Taubman et al., 2005).

Notably, LPS structure varies among microbial species (Wang et al., 2015) that may induce different signaling pathways downstream of TLRs. For example, *Porphyromonas endodontalis* LPS had been reported to enhance RANKL

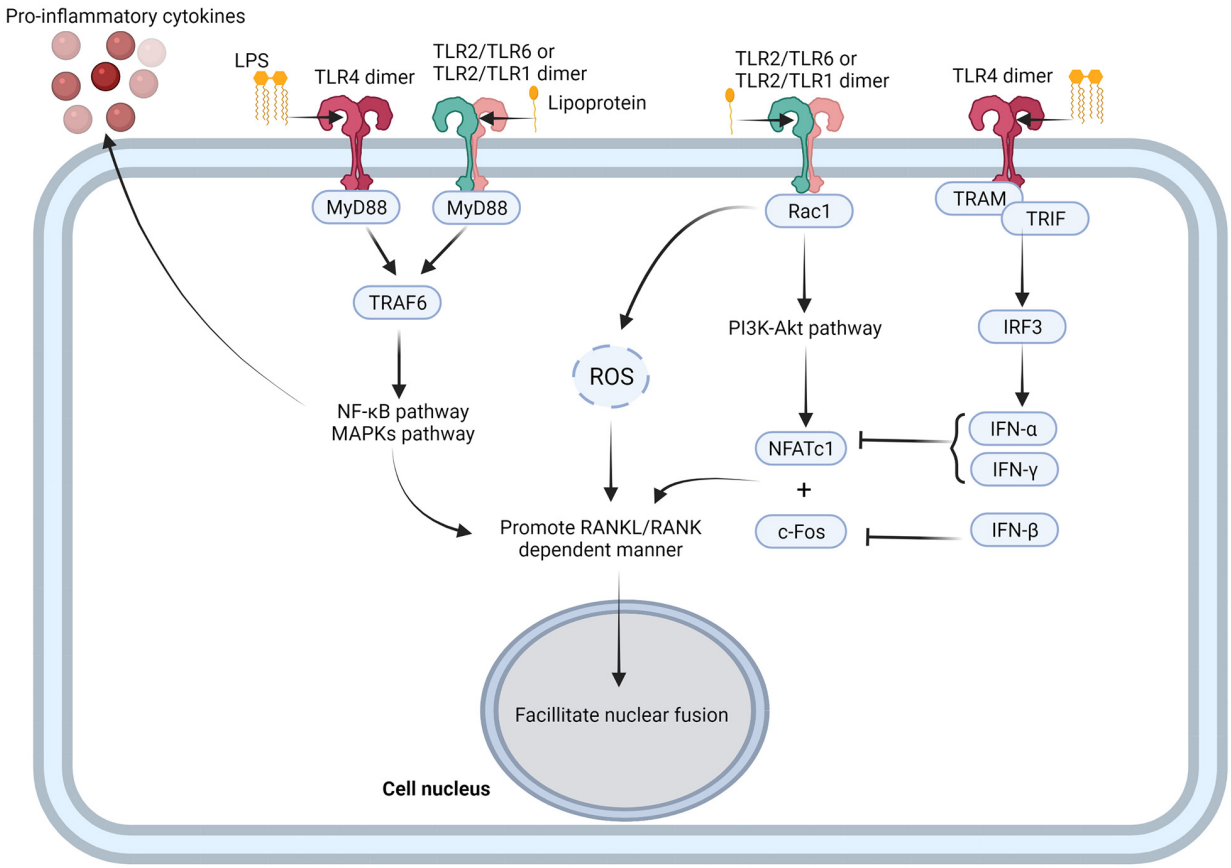

FIGURE 3 | TLRs-mediated activation of osteoclastogenesis. TLR4 and TLR2 combine with PAMPs, such as LPS and lipoprotein, to form TLR4 dimer, TLR2/TLR1, and TLR2/TLR6 dimer. TLRs recruit TRAF6 with MyD88, and activate NF-κB and MAPK pathway (Souza and Lerner, 2019). NF-κB and MAPK pathways not only promote inflammatory cytokine production from osteoclast precursor cells, but also promote RNAKL/RANK dependent manner and facilitate nuclear fusion of osteoclast precursor cells (Souza and Lerner, 2019). TLR2/TLR1 dimer and TLR2/TLR6 dimer also activate PI3K-Akt pathway through recruitment of Rac1 and facilitate expression of NFATc1 (Shen et al., 2010; Kanzaki et al., 2016), while TLR4 dimer promotes expression of IFN-α and IFN-β though TRAM/TRIF/IRF3 signaling axis to negative regulate NFATc1 (Liu et al., 2016; Kwon et al., 2019). Figure was created using BioRender.com.

expression in osteoblasts via the JNK pathway (Tang et al., 2011). *Porphyromonas gingivalis* LPS enhances RANKL expression in osteoblasts via activating JNK and AP1 transcription (Burns et al., 2006). Whereas *Escherichia coli* LPS stimulates RANKL expression via ERK or PI3K signaling, without the involvement of NF-κB (Tang et al., 2011). In contrast to *E. coli* LPS, *Porphyromonas gingivalis* LPS activates TLR2 (Burns et al., 2006) and stimulates RANKL-dependent periodontal bone resorption via TLR2 signaling (Lin et al., 2014).

TLRs DURING INFLAMMATORY BONE RESORPTION

In general, TLRs positively regulate osteoclastogenesis as they interact with pathogenic factors or endogenous therapeutic factors and activate the inflammatory NF-κB and MAPK pathways with or without MyD88 to induce cytokine production (Moresco et al., 2011). TLR2 could form a complex with TLR1 or TLR6 to recruit Rac1 to promote production of ROS and activate PI3K-Akt signaling pathway (Shen et al., 2010; Kanzaki et al., 2016). Moreover, TLR4 activate the non-canonical MyD88-independent TRIF pathway (Souza and Lerner, 2019). Activation of the MyD88-dependent pathway mainly leads to the production of proinflammatory cytokines, whereas the TRIF pathway triggers interferon production (Souza and Lerner, 2019). Most proinflammatory cytokines like TNF-α, IL-1β, and IL-17 function as promoters of osteoclastogenesis, whereas interferons, including IFN-α, IFN-β, and IFN-γ stimulated with TLRs, like TLR4, act as inhibitors of osteoclastogenesis (**Figure 2**) (Amarasekara et al., 2018). Upon ligand stimulation, TLRs, especially TLR4, TLR2, TLR1, and TLR6 suppress the osteoclastogenic ability of the precursor cells via a MyD88-denpendent manner (Takami et al., 2002) (**Figure 3**). Several studies have reported that the addition of TLR agonist along with RANKL at the early stages of osteoclast differentiation inhibits osteoclast formation (Zhang et al., 2011; Chen et al., 2015; Kassem et al., 2015, 2016). Bone marrow macrophages (BMMs) isolated from long bones of mice and pre-treated with LPS fail to differentiate into osteoclasts with or without RANKL

(Liu et al., 2009). This is possibly due to the activation of TLR4 with *E. coli* LPS, which downregulates RANKL-induced activation of NFATc1 (Liu et al., 2009). Activation of TLR2 with *Porphyromonas gingivalis* LPS also inhibits the expression of NFATc1 (Zhang et al., 2011) and c-Fos (Okamoto K. et al., 2017). This suggests the presence of various downstream signaling pathways between RANK and TLR2. Similar results had been reported in human peripheral blood monocyte cells (Takami et al., 2002) and human $CD14^+$ monocyte cultures (Ji et al., 2009). Recently, LPS was also found to promote TLR4 mRNA and protein expression in MC3T3-E1 cells and to inhibit osteoblast differentiation by downregulating matrix mineralization and alkaline phosphatase activity, which play key roles in skeletal mineralization (Liu et al., 2016). Amcheslavsky et al. found that CpG-ODN, a ligand of TLR9, stimulates sustained and transient phosphorylation of ERK with or without RANKL (Amcheslavsky and Bar-Shavit, 2007). Although the duration of ERK phosphorylation directly influences the induction of c-Fos, CpG-ODN degrades c-Fos mRNA and protein to inhibit its' induction by RANKL (Amcheslavsky and Bar-Shavit, 2007).

IFN-β induced by TLR4 signaling is an important negative regulator of RANKL-related osteoclastogenesis. IFN-β combines with the IFNAR receptor to recruit JAK1/TYK2, activate the JAK-STAT signaling pathway, and inhibit c-Fos production (Takayanagi et al., 2002). It has been reported that haptoglobin decreases osteoclast formation via activation of TLR4 and induction of IFN-β (Kwon et al., 2019). In mouse BMMs, haptoglobin also decreases osteoclast formation via TLR4 and increases mRNA and protein expression of IFN-β. Treatment of mice with haptoglobin results in a decrease in osteoclasts, even after co-stimulation by RANKL injections (Kwon et al., 2019).

RP105: AN UNCONVENTIONAL MEMBERS OF THE TLR FAMILY

Unique Structure of RP105 and Its' Ligand MD-1

TLRs harbor "horseshoe"-like N-terminal leucine-rich repeat (LRR) domains as the ligand binding sites (Moresco et al., 2011). This LRR domain contains 20–30 amino acids and a high proportion of hydrophobic leucine residues (Yoon et al., 2011). The TIR domain of TLRs facilitates the recruitment of adaptor molecules and activation of conserved signaling cascades (Moresco et al., 2011). TLRs recruit MyD88 via their TIR domains, thereby leading to the activation of NF-κB, IFN regulatory factors, and transcription factors downstream of MAPKs (Moresco et al., 2011). At the protein level, the transmembrane domain and the N-terminal LRR domain of RP105 share 30% sequence homology with the TLR4 (Yoon et al., 2011; Schultz and Blumenthal, 2017). LPS, a typical PAMP widely present on the membranes of gram-negative bacteria, functions as an agonist of RP105. LPS has three functional groups, i.e., O-antigen, core oligosaccharide, and lipid A (Maldonado et al., 2016). O-antigen, also known as O polysaccharide, comprises repeating oligosaccharide units and is in direct contact with the external milieu. The O-antigen is structurally diverse and is therefore responsible for the immunological-specificity (Raetz and Whitfield, 2002). Core oligosaccharide, a structurally conservative region, links O-antigen to lipid A and maintains the integrity of the bacterial outer membrane (Maldonado et al., 2016). Lipid A is a hydrophobic moiety that anchors LPS to the outer leaflet of the outer membrane and also serves as the functional group for binding to the TLRs (especially TLR4) and activating the downstream NF-κB and MAPKs signaling pathways (Maldonado et al., 2016). In LPS-induced bone loss, lipid A regulates the expression of osteoclast differentiation factor (ODF) in primary osteoblasts and enhances the differentiation of osteoclast precursors (Kikuchi et al., 2001). In murine osteoblasts, lipid A also enhances RANKL expression and ERK activation (Kikuchi et al., 2003). The most common lipid A is the Kdo2-lipid A type which contains 4–6 acyl chains (Raetz et al., 2007). Previous studies suggest that the acylate structure directly influences LPS-induced inflammation (Herath et al., 2013). Expression of TLR4 and TLR2 differs in human gingival fibroblasts upon their stimulation with Tetra- and Penta-acylated LPS (LPS_{1690} and $LPS_{1435/1449}$) isolated from a major periodontal pathogen *Porphyromonas gingivalis* (Herath et al., 2013). $LPS_{1435/1449}$ fails to activate the NF-κB and p38 MAPK pathways. $LPS_{1435/1449}$ has weaker stimulatory potential in the production of inflammatory cytokines GM-CSF, CXCL10, G-CSF, IL-6, IL-8, and CCL2 than that of LPS_{1690} (Herath et al., 2013). The binding of Hexa-acylated lipid A to MD-2 (the ligand of TLR4) induces a conformational change in the F126 loop of MD-2. Consequently, structural deformation is induced in TLR4, and the contact area of C-terminal TIR domains, and signal acquisition efficiency is enhanced (Scott et al., 2017). Moreover, the Penta-acylated LPS of *E. coli* is recognized as being a clinically applicable vaccine in inflammatory reactions (Ledov et al., 2019) and cancer immunotherapy (Jeong et al., 2020). Nemoto et al. compared the regulation of cementoblast function by LPS_{1690} and $LPS_{1435/1449}$ in 6 h and found that RANKL production in the murine cementoblast cell line treated with LPS_{1690} is three times higher than $LPS_{1435/1449}$ (Nemoto et al., 2006).

MD-1 is the ligand of RP105 and a member of the group I lipid-recognition family. MD1 shares approximately 20% sequence identity with MD-2 at the protein level (Yoon et al., 2010). MD-1 harbors a hydrophobic cavity to accommodate the lipid A moiety of LPS, which then binds to RP105 and activates downstream signaling (Nagai et al., 2002). This cavity is highly flexible and can be precisely adjusted to match its volume based on the lipid ligand acylation structure (Yoon et al., 2010). Yoon et al. suggested that large endotoxin molecules like Hexa-acylated lipids act as a "plug" to stabilize the flexible folding of MD-1 (Yoon et al., 2011). Three-dimensional simulation analysis of the molecular structure of MD-1 revealed that this cavity could expand up to seven times its original volume when bound to Hexa-acylated lipid A (Ortiz-Suarez and Bond, 2016). A recent *in vitro* study revealed that *Porphyromonas gingivalis* LPS_{1690} significantly upregulates the expression of RP105 transcripts compared to $LPS_{1435/1449}$ (Ding et al., 2017). As a receptor expressed on macrophages, RP105 also mediates mycobacterial-lipoprotein-induced macrophage

activation (Blumenthal et al., 2009). *Mycobacterium tuberculosis* is the key causative agent of human tuberculosis. Mycobacterial LPS lacks the teichoic acid residue present in the LPS of gram-positive and gram-negative bacteria. A recent report suggested that in lipoproteins such as the 19-kDa lipoprotein of *Mycobacterium tuberculosis*, the position of non-polar alanine residues but not the lipid moiety determines RP105 dependency (Schultz et al., 2018). This expands our understanding of the ligands of RP105 and also indicates that this receptor recognizes lipid PAMPs via numerous mechanisms. Greater attention should be paid to the relationship between RP105 and bacteria that cannot be defined by gram staining.

Mediators in RP105-Dependent Signaling

After binding to ligands, two TLRs usually form a face-to-face "M" shaped dipolymer that brings the extracellular C-domains close to each other (Moresco et al., 2011). This conformational change allows two TIRs to form a dimer and ensures cytokine recruitment (Yoon et al., 2011). The activation of MyD88 and TRIF is TIR dimer dependent (Moresco et al., 2011). Instead of the TIR region, RP105 has a short C-domain cytoplasmic chain with 11 tyrosine residues, which does not allow RP105 to directly recruit MyD88 nor to activate MyD88-dependent downstream signaling (Kimoto et al., 2003; Ohto et al., 2011). Hence, researchers have speculated that RP105 cannot directly activate conventional TIR domain-mediated TLR signaling, and therefore, it requires "signaling-competent" partners to activate cellular responses (Kimoto et al., 2003; Schultz and Blumenthal, 2017). Based on this hypothesis, several "signaling-competent" partners of RP105 have been recognized, including CD19, Gp96, CD150, and Pim-1L.

CD19 regulates innate immunity via RP105 signaling in B lymphocytes (Miura et al., 1998; Zarember and Godowski, 2002; Yazawa et al., 2003; Nagai et al., 2013) (**Table 1**). Although CD19 deficiency does not affect RP105 expression, the anti-RP105 antibody induces CD19 phosphorylation in B cells. The splenic B cells from $CD19^{-/-}$ mice express less RP105 antibody compared to B cells from wildtype mice (Yazawa et al., 2003). Anti-RP105 ligation induces normal proliferation of B cells in MyD88-deficient mice and anti-RP105 antibody and LPS significantly reduced B cell proliferation in $CD19^{-/-}$ mice (Yazawa et al., 2003). Both anti-RP105 antibody and LPS simulates CD19 phosphorylation in splenic B cells, suggesting a central role for the RP105/CD19 signaling in B cell activation (Singh et al., 2014). Besides, anti-RP105 antibody treatment not only enhances IgG and IgM production in memory B cells, but also promotes the production of other serum antibodies (except IgGb and IgA) in mature B cells independent of memory B cells, T cells, and TLR adaptor proteins (Chaplin et al., 2011).

Gp96, an endoplasmic reticulum chaperone, plays an important role in the B cell secretory pathway. Absence of Gp96 decreases cell surface expression of RP105 and MD-1, suggesting the requirement of Gp96 for the assembly of the RP105/MD-1 complex (Weekes et al., 2012). This complex is different from TLR4/MD-2, as the absence of Gp96 does not influence TLR4 and MD-2 expression (Staron et al., 2010). Recently, the interaction between CD150 and RP105 has been shown to regulate Akt and MAPK signaling in chronic lymphocytic leukemia B cells *in vitro* and *in vivo* (Gordiienko et al., 2017). CD150 and RP105 cross-linking in chronic lymphocytic leukemia B cells leads to the activation of Akt and MAPK networks. More importantly, the co-ligation between these two receptors reduces the phosphorylation of Akt, ERK1/2, and c-Jun, and completely blocks p38-MAPK phosphorylation (Gordiienko et al., 2017). Serine/threonine kinase proviral integration site for Moloney murine leukemia virus 1 (Pim-1) has a long (Pim-1L) and short (Pim-1S) isoforms (Tursynbay et al., 2016). Egli et al. found that Pim-1L colocalizes and physically associates with RP105 via its N-terminal extension. This complex has autonomous signaling capabilities in transporting inflammatory signals into B cell survival programs (Egli et al., 2015). RP105/Pim-1L triggers the upregulation of anti-apoptotic BAD protein phosphorylation in a Pim-1 kinase-dependent manner in mature B cells (Egli et al., 2015). Moreover, in human primary B cells, monoclonal antibody-stimulated cross-linking of RP105 present a new pathway for cell survival, proliferation, and activity of B cells (Egli et al., 2015).

RP105 AND PRO-INFLAMMATORY CYTOKINES

TLR4

Although the RP105 signaling pathway depends on TLR4, TLR2, and TLR9, the RP105 is being increasingly considered as a negative regulator of downstream signaling pathways of these receptors, including NF-κB, MAPKs, and Akt-PI3K in monocytes and immune cells (Park et al., 2017). RP105 acts as a physiological and endogenous inhibitor of TLR4 in macrophages (Yu et al., 2015; Carreras-Gonzalez et al., 2018), DCs (Gorczynski et al., 2006; Tada et al., 2008; Okamoto N. et al., 2017), and monocytes (Honda et al., 2007; Wezel et al., 2015; Zhang et al., 2019). RP105 negatively regulates TLR4-mediated IFN-β expression (Okamoto N. et al., 2017), signaling elements such as p38MAPK (Kikuchi et al., 2018), kinase phosphorylation levels of c-Jun/AP1 (Dong et al., 2019) and Akt (Yu et al., 2015), and production of proinflammatory cytokines such as IL-6 (Wezel et al., 2016), IL-1β (Chen et al., 2019), and TNF-α (Louwe et al., 2014; Carreras-Gonzalez et al., 2018). Targeted inhibition of MD-1 stimulates the TLR4/MyD88/NF-κB signaling axis in colitis-induced mice (Chen et al., 2019), which also proves the role of RP105 as a TLR4 inhibitor.

Ohto et al. analyzed the structure of the RP105/MD-1 complex combined with the TLR4 dimer and generated a hypothetical docking model of the hetero-oligomer consisting of TLR4/MD-2 and RP105/MD-1 (Ohto et al., 2011). In this model, the RP105/MD-1 dimer inserts itself into the TLR4/MD-2 dimer, with the C-termini of RP105 extending outward. This docking model confirmed that RP105 interacts with the TLR4/MD-2 complex and is accessible to the C-termini of TLR4. This model also revealed the mechanism of RP105/MD-1-mediated inhibition of TLR4 signaling. RP105/MD-1 blocks the association of the cytoplasmic TIR domains between two TLR4 monomers and inserts into the homodimerization interface of

TABLE 1 | Potential "signaling-competent" partners of RP105/MD-1 during osteoclastogenesis.

Cell type	Signaling-competent	Associated pathways	References
Monocytes	CD14	Ca^{2+} pathway, PI3K-Akt pathway, and crosstalk with NF-κB pathway	Zhang et al. (2019)
Bone marrow macrophages	TLR2	Akt-PI3K and NF-κB pathway	Yu et al. (2015)
	Pim-1L	JAK/STAT and PI3K-Akt pathway	Hu et al. (2009); Kim et al. (2010)
	TLR7, TLR9	Ca^{2+} pathway	Zhang et al. (2019)
CD19 + B lymphocytes	CD19	Ca^{2+} pathway; Akt-PI3K pathway; MAPKs pathway (MyD88-independent signaling); NF-κB pathway (MyD88-independent signaling)	Yazawa et al. (2003); Hebeis et al. (2005); Shinohara et al. (2008); Yoon et al. (2009); You et al. (2017); Gavali et al. (2019)

the TLR4/MD-2/LPS complex to inhibit LPS-induced TLR4/MD-2 oligomerization. RP105/MD-1 and TLR4 accommodate lipid molecules in proximity to the lipopeptide-binding site of TLR4, suggesting that RP105/MD-1 facilitates downstream signaling by transferring the ligand to TLR4. Yoon et al. (2011) also propose two hypothetical models, with the first one being similar to the model suggested by Ohto et al. (2011). The second model proposes a cross binding structure located on the descending side of the N-terminal domain in RP105. This model explains why the RP105/MD-1 complex usually forms a unique 2:2 stoichiometry rather than a 1:1 organization observed in the TLR4/MD-2 inhibition complex, i.e., RP105/MD-1 inserts into the homodimerization interface of TLR4/MD-2/LPS to close the entrance sites of LPS on the MD-2 cavity. Yoon et al. supported the credibility of the first model. Ortiz-Suarez et al. compared the structures of the bovine MD-1 monomer protein and the bovine and human RP105/MD-1 complexes (Ortiz-Suarez and Bond, 2016). Their findings confirmed the malleability and stability of MD-1. With these characteristics, MD-1 binds to bulky endotoxins like LPS and forms an expansive structure. Therefore, the RP105/MD-1/LPS complex can competitively block the TLR4/MD-2 oligomerization interface. Their results support the hypothesis that RP105 acts as a "decoy receptor" and "sink" to sequester LPS from TLR4 under certain conditions.

TLR2

TLR2 activation does not depend on the extracellular segment helper proteins. X-ray crystallography confirmed that TLR2 forms heterodimers with TLR1 (Jin et al., 2007) or TLR6 (Kang et al., 2009) to receive ligands like lipoproteins and lipopeptides. Nagai et al. reported that $RP105^{-/-}$ B cells exhibit low sensitivity to lipid A and lipopeptides Pam3CSK4 and MALP-2 (Nagai et al., 2005). Furthermore, $RP105^{-/-}$ mice displayed impaired polyclonal antibody production, especially IgG2b, IgG3, and IgM, upon stimulation with LPS and Pam3CSK4 (Nagai et al., 2005). Liu et al. emphasized that RP105-dependent reduction of polyclonal antibody production in B cells and deficiency of RP105 in BMMs does not impair lipid A or lipopeptides-induced TNF-α production (Liu B. et al., 2013). Moreover, the response to synthetic TLR2 agonists such as Pam3CSK4 and MALP-2 in $RP105^{-/-}$ macrophages and DCs is similar to that of wildtype cells (Murofushi et al., 2015). This cell-specific difference suggests different roles of RP105 in mediating activation of different immune cells.

RP105 also regulates the NF-κB pathway via TLR2 and TLR4 in HEK cells stimulated with *Lactobacillus plantarum* N14, neutral, and acidic exopolysaccharides (Murofushi et al., 2015). Furthermore, in epithelial cells, RP105/MD-1 is involved in the recognition of phosphopolysaccharides produced by lactic acid bacteria. RP105/MD-1 interacts with phosphopolysaccharides to activate the NF-κB and PI3K pathways and produces proinflammatory cytokines in intestinal epithelial cells (Laiño et al., 2016).

TLR7 and TLR9

The ligands of TLR7 and TLR9 are endogenous RNA and DNA, respectively, which are implicated in autoimmune diseases such as SLE (Yang et al., 2018a). The ligands of TLR7 and TLR9 restrain RP105 expression in human peripheral blood monocytes and immune cells including macrophages and DCs (You et al., 2017). Knocking out RP105 in these cells downregulates the expression of TLR7 and TLR9. An *in vivo* study showed that the proportion of RP105-negative B cells and DCs is significantly increased in patients with SLE and MRL/lpr mice (mutant mice susceptible to lupus) (Yang et al., 2018a). This degenerative feedback is based on the Lyn-SHP-1/2 axis (Yang et al., 2018a). Lyn inhibits B cell activation in SLE via inhibiting the TLR-MyD88 axis (Liossis et al., 2001; Flores-Borja et al., 2005; Ban et al., 2016). These reports suggest a negative feedback mechanism of TLR pathway activation, i.e., RP105 negatively regulates the activation of TLR7 and TLR9-mediated pathways, and TLR7 and TLR9-mediated pathways also act as negative regulators of RP105 activation.

RP105 INVOLVED IN BONE METABOLISM DURING INFLAMMATORY DISEASES

Multiple Myeloma

Multiple myeloma is a heterogeneous bone marrow cancer characterized by increased osteoclast formation and activity. More than 90% of multiple myeloma patients have extensive lytic bone destruction (Coleman et al., 2020). Kikuchi et al. reported that in almost all skeletal-related events, the RP105/MD-1 complex is expressed on multiple myeloma cells but not on normal counterparts, and the complex abundance is markedly up-regulated under adherent and hypoxic conditions (Kikuchi et al., 2018). They also found that LPS and anti-RP105 antibodies,

but not other TLR ligands, enhances the growth of multiple myeloma cells via activation of MAP kinases ERK and JNK (Kikuchi et al., 2018). Additionally, directly inoculated multiple myeloma cells attach to bone marrow stromal cells in a murine xenograft model. LPS stimulation significantly increased the number of RP105/CD138 double-positive cells (Kikuchi et al., 2018). Knockdown of RP105 canceled the LPS response of multiple myeloma cells *in vitro* and *in vivo* (Kikuchi et al., 2018). Via promoter analysis, Furukawa et al. identified IKZF1 (Ikaros) as a pivotal transcriptional activator of the RP105 gene. The transcription of RP105 on multiple myeloma cells is also activated by increasing Ikaros expression and its binding to the promoter region (Furukawa et al., 2018). Furukawa et al. performed pharmacological targeting of Ikaros with lenalidomide to improve the response of multiple myeloma cells to LPS in an RP105-dependent manner *in vitro* and *in vivo* (Furukawa et al., 2018). Recently, Kikuchi et al. found that the administration of lenalidomide prevented the LPS-triggered activation of multiple myeloma cells by targeting RP105 (Kikuchi and Furukawa, 2020). These studies suggest that the RP105/MD-1 pathway may represent a novel mechanism of growth regulation of multiple myeloma cells in a bone marrow milieu.

Osteosarcoma

Compared to normal bone, the expression of osteoclastogenesis markers and antigen presentation is reduced in osteosarcoma (Endo-Munoz et al., 2010). Chen et al. compared the RNA-seq data of 82 osteosarcoma samples as well as their clinical information and constructed a prognostic model (Chen et al., 2020). They identified five predictors, including RP105, MYC, PROSER2, DNA11, and FATE1 are the optimal multivariable Cox regression model. In accordance with the Cox regression analyses, RP105 was downregulated and the other four genes were upregulated in the high-risk group. Among the five prognostic genes, only RP105 leads NF-κB activation and negatively correlates with osteosarcoma survival. Chen et al. proposed that a high expression of RP105 might indicate a high anticancer activity of lymphocytes and suppress the growth of osteosarcoma tumor (Chen et al., 2020).

Diabetes Mellitus

Diabetes-induced osteoporosis is commonly encountered in clinics. In the insulin resistance state, macrophages are activated by the recognition of free fatty acids from hypertrophied adipocytes or LPS through the TLR4/MD-2 complex to induce TNF-α production (Watanabe et al., 2012, 2013). Paracrine and/or autocrine TNF-α combines with TNFR on preosteoclasts. In continuous exposure to TNF-α, preosteoclasts differentiate into fully mature osteoclasts and this event is independent of RANKL (Blasco-Baque et al., 2017; Coleman et al., 2020).

Yasuharu et al. reported that RP105 mRNA is highly expressed in most adipose tissue macrophages (Watanabe et al., 2012). A high-fat diet (HFD) remarkably increases RP105/MD-1 complex expression on the M1 subset of adipose tissue macrophages. Both RP105 and TLR4 are involved in HFD-induced NF-κB activation in the epididymal white adipose tissue of mice. RP105 KO and MD-1 KO mice had lesser HFD-induced adipose tissue inflammation and insulin resistance compared to TLR4 KO and wildtype mice (Watanabe et al., 2012). RP105/MD-1 complexes contribute to HFD-induced obesity, adipose tissue inflammation, and insulin resistance independent TLR4 signaling (Nagai et al., 2013). Liang et al. isolated monocytes from human peripheral blood mononuclear cells and found that exposed lipid infusion *in vivo* enhances the LPS-stimulated IL-1β secretion in monocytes (Liang et al., 2018). IL-1β increases the level of TLR4 protein as well as phosphorylation of JNK and p38/MAPK in monocytes, which directly correlates with reduced peripheral insulin sensitivity (Liang et al., 2018). Additionally, increased lipid levels are linked to RP105, as well as multiple genes associated with osteoclastogenesis such as MAP3K7 and CXCL10 (Liang et al., 2018).

SLE

SLE is a chronic autoimmune inflammatory disease. Bone erosions and inflammatory bone loss are common features in autoimmune arthritis such as in rheumatoid arthritis (RA) (Lim et al., 2011). However, bone erosions and inflammatory bone loss are usually absent in patients with SLE and are observed in $< 5\%$ of cases (Lim et al., 2012). Qiao et al. found that the deposition of IgG, monocytes/macrophages, and TNF-α is required for the development of RA in SLE (Qiao et al., 2020). However, lupus serum or IgG inhibits RANKL-induced differentiation of monocytes into osteoclasts in a dose-dependent manner, as lupus IgG competes for FcγRI binding with RANKL (Qiao et al., 2020).

The number of RP105-negative B cells is significantly increased in peripheral blood mononuclear cells from patients with SLE and is positively associated with disease severity (Koarada et al., 1999; Koarada and Tada, 2012). Only RP105-negative B cells obtained from patients with SLE spontaneously produced IgG and IgM *in vitro* (Kikuchi et al., 2002). These studies suggest that RP105-negative B cells may be responsible for the production of autoantibodies. Moreover, the binding of RP105 by anti-RP105 antibodies could inhibit the IFN-α-induced interferon stimulated gene (ISG) expression in B cells both *in vitro* and *in vivo* (You et al., 2017). IFN-α inhibits the fusion of osteoclast precursor cells by downregulating c-Fos expression in a dose-dependent manner (Xiong et al., 2016; Amarasekara et al., 2018). Mechanistically, RP105 down-regulates the tyrosine phosphorylation of signal transducer and activator of transcription 2 (STAT2) induced by IFN-α via a Lyn-dependent pathway (You et al., 2017). Moreover, SLE is characterized by the formation of a variety of autoantibodies by hyper-reactive B cells. B-cell antigen receptors recognize endogenous DNA and RNA-associated auto-antigens and deliver to endosomal TLR9 and TLR7, respectively (Yang et al., 2018a). In this way, overactivation of B cells leads to the excess production of autoantibodies, contributing to the inflammatory amplification loop characteristic of SLE. Although TLR7 and TLR9 signaling could downregulate RP105 expression and attenuate the inhibitory effect of anti-RP105 on the activation of IFN-α signaling in B cells (You et al., 2017), the critical role of RP105 in regulating TLR7 and TLR9-mediated activation of macrophages and DCs suggests that RP105 could be a potential therapeutic target for the treatment of SLE (Yang et al., 2018a).

Rheumatoid Arthritis

Rheumatoid arthritis is an inflammatory joint disease, which is characterized by chronic inflammations that irreversibly affect the surrounding bone tissue (Gyõri and Mócsai, 2016). As a chronic autoimmune disease, the inflammatory condition in rheumatoid arthritis not only enhances bone degradation by raising the crosstalk between osteoclastogenesis and the immune system, but also stimulates TLR2 on osteoblasts and increases the production of RANKL (Kassem et al., 2015). Moreover, TLR7 induces RANKL expression and increases osteoclasts derived from peripheral blood CD14 + monocytes in rheumatoid arthritis (Kim et al., 2019). Because of the ability of RP105 in blocking TLR2 and TLR7, it can be speculated that RP105 could regulate osteoclastogenesis in rheumatoid arthritis via a TLR2/TLR7. Although there is no evidence directly proving the influence of RP105 on osteoclastogenesis in rheumatoid arthritis, an intersection of positional and functional candidate information analysis provided some evidence of novel rheumatoid arthritis loci near the PI3KR1/RP105 gene (Kim et al., 2019). Another study demonstrated an antibody against mouse CD79b, which blocks B cell proliferation, is induced via RP105 but not via TLR4 and TLR. Anti-CD79 reduces inflammation and improves synovial hyperplasia as well as bone and cartilage destruction (Kim et al., 2019). These results suggest that RP105 could be a biomarker in predicting the occurrence and development of rheumatoid arthritis. Furthermore, blocking RP105 may be a promising treatment for preventing bone resorption in rheumatoid arthritis.

RP105 AND OSTEOCLASTOGENESIS

In the following sections, we describe RP105 as a regulator in activating monocytes, macrophages, and B cells, as well as summarize osteoclastogenesis regulating signaling pathways that are activated by RP105 in different osteoclast precursor cell types.

Monocyte-Derived Osteoclasts

The mononuclear precursors located in peripheral blood and the bone marrow are the key source of osteoclast precursors (Vaananen, 2005). Monocytes derived from the spleen and thymus also differentiate into osteoclasts under a suitable microenvironment (Udagawa et al., 1990). In hind limb ischemia (HLI) mouse model, before HLI development, the predominant resident monocyte subtype was $LY6C^{low}$, accounting for 30% of the total $CD11b^{+}$ cells in the gastrocnemius and adductor muscles of both WT and $RP105^{-/-}$ mice (Bastiaansen et al., 2014). After the development of HLI, RP105 knockout leads to increased activation of $Ly6C^{high}$ monocytes, implying that RP105 deficiency inhibits the regenerative response of mice following ischemia (Bastiaansen et al., 2014). RP105 also directly influences the migratory capacity of monocytes. Wezel et al. compared the monocytes influx and neutrophil influx to the peritoneum of low-density lipoprotein receptor (LDLr) deficient ($LDLr^{-/-}$) mice and LDLr/RP105 double knockout ($LDLr^{-/-}/RP105^{-/-}$) mice fed with Western-type diet (Wezel et al., 2015). They found although the neutrophil influx was unaltered between the two kinds of mutant mice, the monocytes influx was almost 3-fold lower in $LDLr^{-/-}/RP105^{-/-}$ mice than $LDLr^{-/-}$ mice (Wezel et al., 2015). More important, the results of *in vitro* experiment showed a down-regulation of CCR2 in the two kinks of receptor knockout monocytes when stimulated with LPS, which is more pronounced in $LDLr^{-/-}/RP105^{-/-}$ monocytes than $LDLr^{-/-}$ monocytes (Wezel et al., 2015). CCR2 is an important chemokine receptor of classical monocytes. Deficiency or low expression of CCR2 severely inhibited the osteoclastogenesis potential of monocytes (Puchner et al., 2018).

RP105, MD-1, and CD14 form a complex on murine bone monocytes in response to the early phase expression of IL-6 in LPS-treated mice (Zhang et al., 2019). Upon *Listeria monocytogenes* infection in mice, IL-6 production is also influenced by carcinoembryonic antigen-related cell adhesion molecule-1 (CEACAM1) via the G-CSFR-STAT3 pathway (Pan and Shively, 2010). CEACAM1 regulates IL-1β in LPS-treated neutrophils via the TLR4-Syk pathway (Lu et al., 2012). In these two events, CEACAM1 is recruited by an activated receptor such as G-CSFR or TLR4 phosphorylated by Src. CEACAM1 recruits and dephosphorylates SHP-1 to activate the insulin receptor in the liver (Poy et al., 2002), and recruits epidermal growth factor receptor in the epithelial cells (Abou-Rjaily et al., 2004) or B cell receptors (Lobo et al., 2009; Chen et al., 2011). However, neither TLR4 mRNA nor protein was detected in murine monocytes, which means that the murine bone marrow monocytes do not express TLR4 (Ketloy et al., 2008). Instead, RP105/MD-1/CD14/Src/PI3K signaling occurs in response to LPS stimulation, which also crosstalks with NF-κB to regulate the production of IL-6 (Zhang et al., 2019) (**Figure 4** and **Table 1**). At the same time, with the presence of CEACAM1, the activation of RP105 also leads to recruitment of SHP-1 and prevents PI3K activation, inhibit the tyrosine phosphorylation of Vav1, and sequestrate pVav and β-actin from the RP105 complex (Zhang et al., 2019).

Macrophage-Derived Osteoclasts

Macrophage and osteoclast share a common monocyte precursor (Nason et al., 2009). BMMs and monocyte macrophages are the key sources of osteoclast precursors (Boyle et al., 2003). Mature macrophages and osteoclasts two competing differentiation outcomes from myeloid progenitors share many common antigens (AlQranei and Chellaiah, 2020). Because of the differential role of macrophages and osteoclasts in bone remodeling, the balance between these two types of cells is especially important for bone metabolism. Broadly, activated macrophages are divided into two major types, M1 and M2 macrophages. M1 macrophages are proinflammatory and are classically activated by LPS or T helper 1 (Th1) cell-related cytokines such as IFN-γ (Chang et al., 2008; Sinder et al., 2015). M2 macrophages are identified as anti-inflammatory macrophages activated by Th2 cell-related cytokines such as IL-4 and IL-13 (Chang et al., 2008; Sinder et al., 2015). M1 macrophage-related cytokines TNF-α, IL-6, and IL-1β induce osteoclastogenesis. While the M2 macrophage-related cytokines IL-4 and IL-10 inhibit osteoclastogenesis through the inhibition of NFATc1 (Varol et al., 2015). Thus, the polarization of

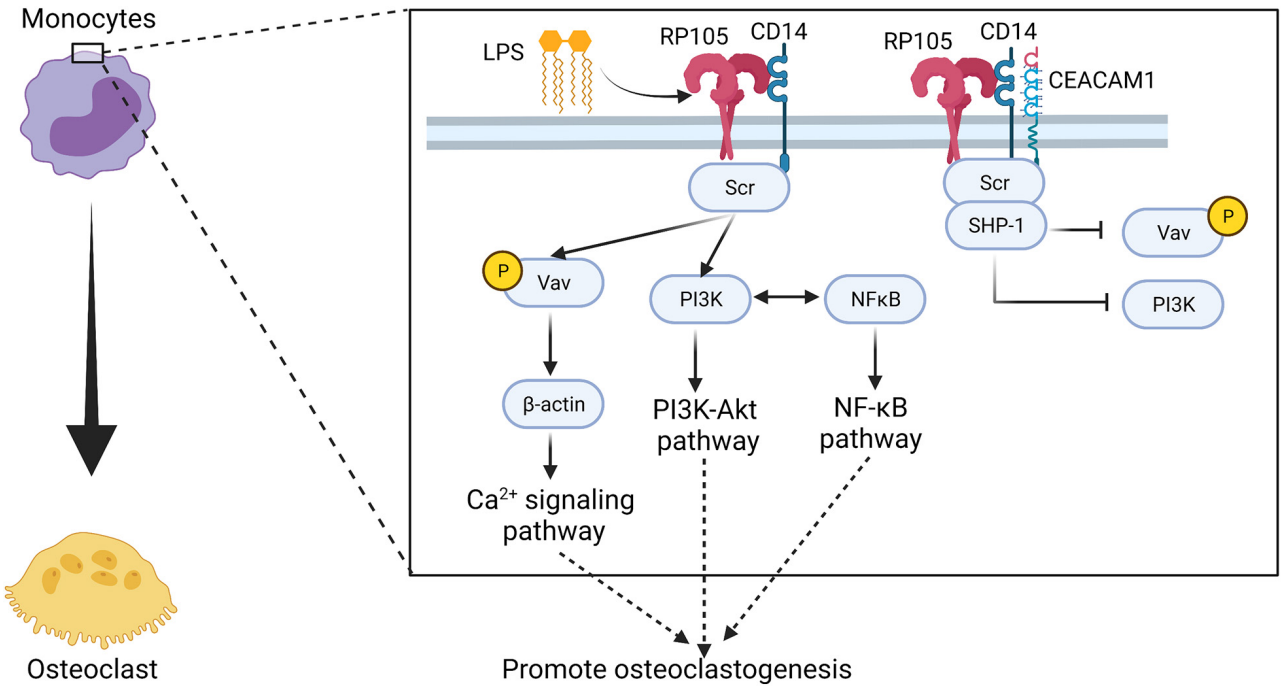

FIGURE 4 | Potential regulatory manner of RP105 in driving osteoclastogenesis of monocytes. RP105 may promote the differentiation of monocytes into osteoclasts via a RP105/MD-1/CD14/Src/Vav1/β-actin axis (Zhang et al., 2019). At the same time, with the stimulation of LPS, RP105/MD-1/CD14/Scr also activates the PI3K-Akt pathway and induces crosstalk with the NF-κB signaling pathway (Zhang et al., 2019). But, in presence of CEACAM1, SHP-1 recruitment blocks the tyrosine phosphorylation of Vav1, and sequestrates pVav and β-actin from the downstream signaling axis of RP105 (Zhang et al., 2019). Figure was created using BioRender.com.

macrophages (M1/M2) is important for the determination of osteoclastogenesis (Yang and Wan, 2019).

Under inflammatory conditions, the recruitment and proliferation rate of monocytes (Wezel et al., 2015, 2016) and macrophages (Wezel et al., 2016) in RP105$^{-/-}$ mice is higher than in WT mice. Several studies support the concept that RP105 also initiates the polarization of macrophages into M1 types (Nagai et al., 2013). The mRNA expression and protein levels of RP105 and MD-1 in macrophages are up-regulated when in contact with tumor cells (Watanabe et al., 2012). Czimmerer et al. analyzed that IL-4 as well as IFN-γ + IFN-α stimulate human monocyte-derived macrophages and identified RP105 as well as MS4A4A, SLA, and ENPP2 as novel IL-4 regulated alternative activation markers (Czimmerer et al., 2012). *Mycobacterium tuberculosis* lipopeptide ligands stimulate RP105 on macrophages and induce RP105-dependent TNF-α and IL-6 production by macrophages. Moreover, di- and tripalmitoylated variants of this lipopeptide can elicit an equivalent RP105-dependent response, indicating that the lipid moiety is required for macrophage activation but this event is RP105-independent (Schultz et al., 2018). RP105 is a key determinant of macrophage activation in *Mycobacterium tuberculosis* infection. Myeloid-derived suppressor cells (MDSCs) play an immunosuppressive role in the pathogenesis of inflammatory diseases. Compared with non-treated controls, the expression of RP105 of MDSCs, especially granulocytic MDSCs (G-MDSCs), from mice challenged with LPS was significantly increased (Dong et al., 2019). *In vitro*, binding of RP105 with an anti-RP105 antibody not only inhibits the expansion of MDSCs by preventing the phosphorylation of signal transducer and activator of transcription 3 (STAT3) but also reduces the immunosuppressive activity of MDSCs on M1 macrophage polarization through the inhibition of Arg-1 expression (Dong et al., 2019). The injection of anti-RP105 antibody significantly aggravates pathological lesions in mice stimulated with LPS (Dong et al., 2019). Furthermore, the injection of anti-RP105 antibody inhibits the accumulation of G-MDSCs in LPS-challenged mice and reduced the immunosuppressive activity of G-MDSCs on M1 macrophage polarization (Dong et al., 2019).

Carreras-González et al. reported increase in CD14 protein and gene expression but decrease in RP105 expression in *Borrelia burgdorferi* stimulated BMMs (Carreras-Gonzalez et al., 2018). *In vitro* differentiated human macrophages also show reduced expression of RP105. However, in this study, human blood monocytes show downregulation of CD14 and upregulation of RP105. Carreras-González et al. also observed that silencing of RP105 significantly reduces TNF-α and IL6 production in mouse mononuclear macrophage cell line RAW264.7 (Carreras-Gonzalez et al., 2018). PI3K is a classical multifunctional signaling protein, which influences several cellular metabolic processes such as autophagy and differentiation (Werner et al., 2010). PI3K consists of one regulatory subunit and one of four p110 catalytic subunits, including class 1A: α, β, δ, and class 1Bγ (Vanhaesebroeck et al., 2005). The p110δ subunit of PI3K

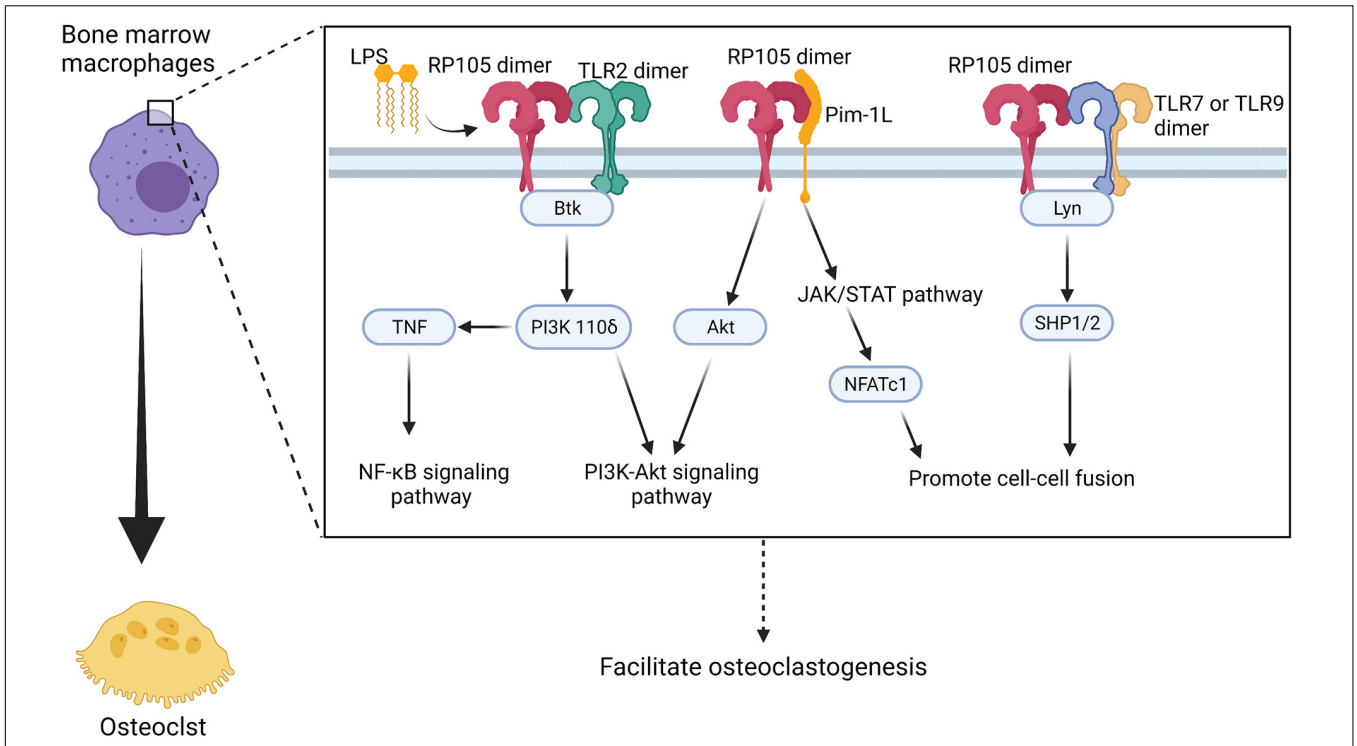

FIGURE 5 | Potential regulatory manner of RP105 in activating osteoclastogenesis of bone marrow macrophages. RP105 promotes the differentiation of bone marrow macrophages into osteoclasts with different "signaling-competent" partners. As a result, there're three potentially regulate manner of RP105 in the differentiation process: (1) TLR2 works as a "signaling-competent" of RP105 (Carreras-Gonzalez et al., 2018) and forms RP105/TLR2/Btk axis to up-regulate PI3K p110δ to activate the PI3K-Akt as well as promotes production of TNF and activation of NF-κB pathways (Blumenthal et al., 2009; Yu et al., 2015); (2) Pim-1L works another "signaling-competent" of RP105 (Egli et al., 2015) and stimulate expression of NFATc1 through JAK/STAT pathway (Kim et al., 2010) and activate Akt to promote PI3K-Akt signaling pathway (Hu et al., 2009); (3) RP105 also could inhibit TLR7 and TLR9 signaling and the downstream Lyn/SHP-1/2 manner, which activate Ca^{2+} signaling pathway and promote cell-cell fusion (Yang et al., 2018a). Figure was created using BioRender.com.

is the central regulator in inducing inflammatory responses in immune cells (Kim et al., 2007; Werner et al., 2010). In macrophages, PI3K p110δ is required for the fission of TNF-α containing vesicles and their transport to the cell surface upon stimulation of LPS (Low et al., 2010). In mycobacteria-infected macrophages, RP105 and Btk are required for PI3K p110δ activation (Blumenthal et al., 2009; Yu et al., 2015) (**Figure 5** and **Table 1**). Moreover, PI3K signaling in macrophages induced by bacterial infection contribute to the production of cytokines TNF, IL-6, G-CSF, and CCL5 that contribute to macrophage recruitment and polarization (Andrade et al., 2009). In myocardial ischemia and reperfusion injury, RP105 activates the PI3K-Akt signaling pathway, which protects patients from ischemia/reperfusion-induced cardiac injury and myocardial pyroptosis (Guo et al., 2021).

Notably, PI3K recruitment is dependent on the YXXM motifs (Wang et al., 2002; Troutman et al., 2012). CD19 has two YXXM motifs in the cytoplasmic region, which means that CD19 recruits the p85α sites of PI3K (Wang et al., 2002). However, instead of the TIR domain, RP105 contains at least one tyrosine residue in the cytoplasmic tail, which cannot be embedded into a classical YXXM motif. As a result, RP105 can either directly stimulate PI3K signaling or activate this pathway with a competent partner (Schultz and Blumenthal, 2017) such as CD19 (Aiba et al., 2008). However, CD19 is usually detected on lymphocytes circulating in peripheral blood (Wang et al., 2002), and B cells in the spleen (Wang et al., 2002), bone marrow (Engel et al., 1995), thymus, and lymph nodes (Ishiura et al., 2010). To date, there are no reports of the presence of CD19 on macrophages. Therefore, the YXXM-containing partner of RP105 remains to be elucidated in macrophages. There is a possibility that the tyrosine tail of RP105 phosphorylates in response to an activating interaction, thereby provides a recruitment platform for Btk or PI3K regulatory subunits in macrophages (Yu et al., 2015). TLR2 and TLR3 respond to the mycobacteria-induced activation of PI3K-Akt signaling pathway in macrophages (Lasunskaia et al., 2006; Liu H. et al., 2013; Bai et al., 2014). In the Staphylococcus aureus infection rat model, RP105 activation in macrophages induces the accumulation of TLR2 and increased TLR2-associated inflammatory cytokines production via a MyD88 axis (Blumenthal et al., 2009). Some researchers conjectured that RP105-dependent activation of the PI3K-Akt signaling pathway might require TLR2 (Yu et al., 2015; Huang et al., 2020). But it worth noticing, the activation of PI3K via the TLR2-associated axis provides crosstalk with MAPKs and NF-κB pathway. Interestingly, the phosphorylation of p38, JNK, p65, and IκB is not altered in RP105 deficiency macrophages during mycobacterial infection (Blumenthal et al., 2009;

Yu et al., 2015). However, RP105 deficiency and RP105/TLR2 deficiency in macrophages directly reduced the production of TNF and IL-6 (Yu et al., 2015; Schultz et al., 2018). Based on the available literature, TLR2 is still considered as the most possible RP105 signaling partner in the activation of the PI3K-Akt signaling pathway in macrophages.

Pim-1L, another "signaling-competent" partner of RP105, contains an additional proline-rich motif at the N-terminus. Thus, it can interact with proteins and crosstalk with signaling cytokines other than Pim-1S (Tursynbay et al., 2016). Pim-1 positively regulates Akt phosphorylation and activates apoptosis in human and mouse hematopoietic malignancies and prostate cancer (Hu et al., 2009) (**Figure 5**). More importantly, Pim-1 regulates NFATc1 in osteoclastogenesis via the JAK/STAT pathway (Kim et al., 2010). However, whether Pim-1L exhibits a potential ability to link RP105 and the JAK/STAT pathway and directly regulate osteoclastogenesis remains to be elucidated.

TLR7 expression is upregulated in synovial tissues (Roelofs et al., 2005), fibroblasts (Carrión et al., 2011), macrophages (Alzabin et al., 2012), and DCs (Roelofs et al., 2005). Recently, TLR7 was determined to regulate osteoclastogenesis in rheumatoid arthritis via RANKL expression in synovial fibroblasts (Kim et al., 2019). At the same time, RP105 negatively regulates TLR7 and TLR9-mediated activation of macrophages and DCs via Lyn/SHP-1/2 signaling (Yang et al., 2018a), suggesting a possible mechanism of osteoclastogenesis in patients with rheumatoid arthritis.

B Cell-Derived Osteoclasts

A study showed that circulating myeloma B-lymphocytes have the potential to differentiate into osteoclast-like phenotype (Calvani et al., 2004). Researchers not only detected RANK on $CD19^+$ B lymphocytes (Atkins et al., 2006) but also observed that peripheral $CD19^+$ B lymphocytes isolated from patients with multiple myeloma exhibit phenotypic and functional properties of osteoclasts upon stimulation with RANKL (Calvani et al., 2004). Thus, $CD19^+$ B lymphocytes are RANKL-dependent osteoclast progenitors. As discussed above, CD19 is one of the most recognized accessory proteins of RP105. The frequency of $RP105^+$ cells is higher in the $CD19^+$ non-switched B cell subset, and these B cells show the strongest activation in response to anti-RP105 antibody treatment (Singh et al., 2014). Moreover, phosphorylation of CD19 is completely independent of TLR4 (Yazawa et al., 2003), which suggests that RP105 may directly drive B cells to differentiate into osteoclasts via the CD19 pathway. In B cells, the interaction between RP105 and CD19 forms a complex that directly recruits Lyn kinase (Yazawa et al., 2003). This RP105/CD19 complex is also required for optimal Lyn activation and phosphorylation (Yazawa et al., 2003) (**Table 1**). The interaction of RP105 and LPS induces Lyn activation and CD19 phosphorylation (Yazawa et al., 2003). Although Lyn inhibits osteoclast differentiation, survival, and function by interfering with PLCγ-mediated Ca^{2+} signaling, which leads to down-regulation of osteoclastogenesis (Yoon et al., 2009; Gavali et al., 2019), it also mediates the activation of Vav (Yazawa et al., 2003). Vav protein is required for RP105 function as it regulates LPS-mediated activation of Akt, ERK, phosphorylation of IκBα (Yazawa et al., 2003; Hebeis et al., 2005). Vav1/2-deficient B cells fail to respond to LPS or anti-RP105 antibodies *in vitro* (Yazawa et al., 2003; Hebeis et al., 2005). The CD19/Lyn/Vav signaling acts upstream of MAPKs to induce JNK and MEK/ERK axis activation (Chan et al., 1998; Yazawa et al., 2003; Hebeis et al., 2005) (**Figure 6**). In parallel, anti-RP105 cross-linking induces ERK as well as JNK phosphorylation within a short period (Chan et al., 1998). Phosphorylation of JNK by RP105 depends on CD19, however, phosphorylation of ERK is independent of CD19 (Yazawa et al., 2003).

Besides RP105/CD19/Lyn/Vav signaling axis, RP105/CD19/Lyn also acts upstream of Btk and links RP105-PI3K signaling (Yu et al., 2015) (**Figure 6**). RP105/CD19/Lyn signaling plays an important role in regulating IFN-α activation in B cells. You et al. observed that the RP105 ligation inhibits IFN-α-induced tyrosine phosphorylation of signal transducer and STAT2 via RP105/CD19/Lyn (You et al., 2017). Besides, Btk also acts as a downstream effector of RP105 in PI3K activation and promotes TNF-α release in BMMs in response to mycobacterial infection (Yu et al., 2015). At the same time, Btk directly participates in osteoclast formation. It has been demonstrated that Btk and Tec kinases form a complex with the BLNK adaptor and activate an essential calcium-signaling pathway with PLCγ (Shinohara et al., 2008; Choi et al., 2013). In summary, based on the aforementioned facts, RP105 seems to promote B cells' osteoclastic differentiation via MAPKs, PI3K-Akt, and Ca^{2+} signaling pathways (**Figure 6**).

Alternative Sources of Osteoclastogenesis-Regulation

RP105 not only influences the osteoclastogenic potential of monocytes, macrophages, and other cells, but also affects the microenvironment of osteoclast differentiation by regulating the secretion of various factors by surrounding cells. RP105 deficient mice have higher CCL2 secretion in vein graft lesions than WT mice, which increases the macrophage content in these lesions (Wezel et al., 2016). *In vitro* analysis also shown that $RP105^{-/-}$ smooth muscle cells produced a higher level of CCL2 than the control group (Wezel et al., 2016). CCL2 regulates hormonal and mechanical stimuli-induced physiological bone remodeling, as well as cancer-induced bone resorption (Siddiqui and Partridge, 2017). Besides, in a hind limb ischemia model, arteriogenesis is reduced in $RP105^{-/-}$ mice than WT mice (Bastiaansen et al., 2014). This effect might regulate bone healing, since angiogenesis is crucial for bone repair.

Activation of RP105 also stimulates Bax, caspase-3, and cytochrome c in myocardial cells during myocardial ischemia-reperfusion injury and upregulates Bc1-2 to restrain the apoptotic process (Yang et al., 2015). When challenged with an HFD, MD-1 expression is downregulated *in vivo* and *in vitro* (Shen et al., 2019). MD-1 deficiency causes cardiac hypertrophy and fibrosis via activation of MAPK and NF-κB that accelerates myocardial injury (Shen et al., 2019). Overexpression of MD-1 alleviates the effects of HFD-induced cardiac remodeling (Shen et al., 2019). Peng et al. reported that MD-1 deletion activates the TLR4/CaMKII signaling pathway and influences

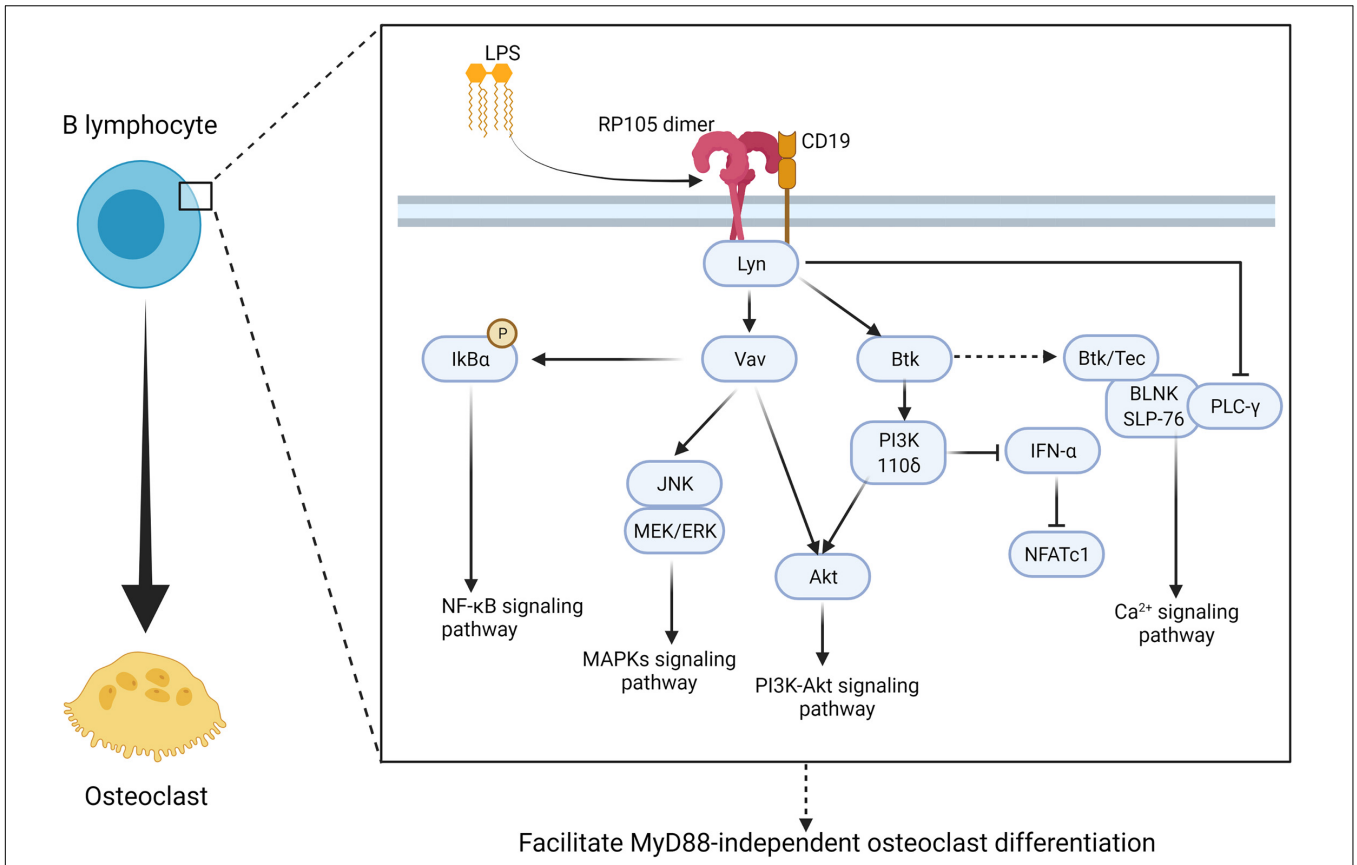

FIGURE 6 | RP105 activates MyD88-independent manner of CD19 + B lymphocyte and promote $CD19^+$ B lymphocyte to derive into osteoclast. RP105/CD19 initiates Lyn activation and phosphorylation then promotes MyD88-independent osteoclast different manner of $CD19^+$ B lymphocyte via two major pathways: (1) promote IκBα to promote NF-κB signaling (Yazawa et al., 2003; Hebeis et al., 2005), activate JNK, MEK/ERK to promote MAPKs signaling pathway (Chan et al., 1998; Yazawa et al., 2003; Hebeis et al., 2005), as well as activate Akt to promote PI3K-Akt signaling pathway though a Vav-associated manner (Yu et al., 2015); (2) activate PI3K 110δ to inhibit IFN-α and promote PI3K-Akt signaling pathway through Btk-associated manner (You et al., 2017). At the same time, Btk also directly promote osteoclastogenesis though Ca^{2+} signaling pathway, however, Lyn also inhibit PLCγ-mediated Ca^{2+} signaling (Shinohara et al., 2008; Choi et al., 2013). As a result, the regulate signaling axis of osteoclastogenesis in $CD19^+$ B lymphocyte remain to be further discussed. Figure was created using BioRender.com.

the expression of Ca^{2+} handling proteins, thereby increasing the vulnerability of HFD-fed mice to ventricular arrhythmia (Peng et al., 2017). The authors hypothesized that MD-1 deletion increases susceptibility to atrial fibrillation in heart failure with presented ejection fraction (HFpEJ) by enhancing the activation of TLR4/CaMKII signaling. Compared with wildtype mice, MD-1 knockout mice challenged with aldosterone infusion downregulate Ca^{2+}-ATPase 2a (SERCA2a) expression and phospholamban phosphorylation at Thr17 (Shuai et al., 2020). In the MD-1 knockout mice, sodium/calcium exchanger 1 and phosphorylation of ryanodine receptor 2 expression resulted in increased myocardial fibrosis and inflammation, proving that MD-1 regulates the activation of the TLR4/CaMKII signaling *in vivo* and *in vitro* (Shuai et al., 2020).

Qin et al. transfected mRNA-141-3p mimic to H9c2 rat cardiomyoblasts to analyze the role of miR-141-3p and RP105 in myocardial ischemia. The inhibition of miRNA-141-3p activates the RP105-dependent PI3K-Akt pathway in cardiomyocytes exposed to hypoxia. miRNA-141-3p inhibition reduces cell death, apoptosis, and generation of ROS in hypoxic H9c2 rat cardiomyocytes *in vitro*. miRNA-141-3p targets RP105 by directly binding to its 3'-UTR. Blocking RP105 reverses the effects of miRNA-141-3p inhibition in rat cardiomyoblast cells (Qin et al., 2019). The association between RP105 and miRNA-327 in myocardial ischemia has also been reported. miRNA-327 downregulates RP105 in a 3'-UTR-dependent manner. The reduction of miRNA-327 indirectly downregulates the TLR4 and TLR2 dependent-MyD88 and NF-κB signaling axis, whereas it upregulates RP105 (Yang et al., 2018b). This effect results in the reduction of myocardial infarct size, attenuates cardiomyocyte destruction, and alleviates inflammation.

CONCLUSION

Despite several years of research, the differentiation progress and induction mechanism of osteoclast received wide attention. Bone marrow-derived cells and immune cells activated by TLRs have the potential to generate osteoclast. Moreover, the pro-inflammatory cytokines produced by these cells create a suitable

microenvironment for osteoclastogenesis. Bone resorption and osteoporosis in cancer, diabetes mellitus, rheumatoid arthritis, and SLE are mainly caused by osteoclast overactivity. Patients with these diseases are in chronic inflammatory state or inflammatory stress state for a long time. In this state, patients have a high risk of orthopedic disease even without bacterial infection.

As a special cell member receptor, RP105 play a dual role in pro-inflammatory response. At one hand, RP105 serves as a low-affinity receptor of LPS but shares certain features with TLR4. With the simulation of LPS or other agonist, RP105 activates monocytes, macrophages, immune cells, and other peripheral tissue cells to produce pro-inflammatory cytokines, which facilitate the osteoclastogenesis. At the other hand, RP105 also negatively regulates other TLRs and reduces the production of pro-inflammatory cytokines, which seems to inhibit osteoclastogenesis to some extent. But the physiological function of RP105/MD-1 is not limited to inflammatory response. RP105 also regulates the multiple myeloma cells' growth and attachment to bone marrow stromal cells in the murine xenograft model (Kikuchi et al., 2018). Moreover, it has been verified *in vitro* and *in vivo*, that RP105/MD-1 plays important role in the regulation of monocytes migration, which influences early atherosclerotic plaque development (Wezel et al., 2015). RP105 and MD-1 directly influence the arteriogenesis after ischemia (Bastiaansen et al., 2014), aggravates vein graft disease (Wezel et al., 2016). These effects might regulate the bone niche or mechanical stimuli-induced physiological bone remodeling. Considered with the central role and high expression of RP105/MD-1 in adipose macrophages (Watanabe et al., 2012), myocardial cells (Shuai et al., 2020), cardiomyoblast cells (Qin et al., 2019), and smooth muscle cells (Wezel et al., 2016), this complex had been suggested as a possible therapeutic target in reducing chronic inflammatory of diabetes mellitus (Watanabe et al., 2012, 2013; Nagai et al., 2013), rheumatoid arthritis (Bruhl et al., 2015), and SLE (Yang et al., 2018a).

So far, several studies have focused on how RP105 negatively regulates other TLRs, however, its signaling pathways remain inadequately explored. Although "signaling-competent" partners and downstream signaling mechanisms of RP105 remain elusive, the available evidence allows us to hypothesize that the RP105/MD-1 complex activates Ca^{2+}, MAPK, NF-κB, and PI3K-Akt signaling to directly promote osteoclastogenesis of bone marrow-derived monocyte/macrophage precursor cells and a subset of B lymphocytes. Identification and characterization of RP105/MD-1 ligands will not only help in integrating the molecular mechanism of osteoclastogenesis derived from different cell sources but also help to delineate inflammation regulatory roles of RP105 under inflammatory conditions. Further insights into the biology of RP105 may inspire novel strategies to control and cure inflammation and inflammation-induced osteoclastogenesis.

AUTHOR CONTRIBUTIONS

JP and LG designed this study and edited the final draft. ZF wrote the manuscript. All authors approved the final version of the manuscript.

FUNDING

This study was supported by funding from the High-Level University Construction Talents of Guangzhou Medical University of China (B185006003014 and B195002003017). The funders had no role in the study design and collection, analysis, and interpretation of the results.

REFERENCES

Abou-Rjaily, G. A., Lee, S. J., May, D., Al-Share, Q. Y., Deangelis, A. M., Ruch, R. J., et al. (2004). CEACAM1 modulates epidermal growth factor receptor–mediated cell proliferation. *J. Clin. Invest.* 114, 944–952. doi: 10.1172/jci200421786

Aiba, Y., Kameyama, M., Yamazaki, T., Tedder, T. F., and Kurosaki, T. (2008). Regulation of B-cell development by BCAP and CD19 through their binding to phosphoinositide 3-kinase. *Blood* 111, 1497–1503. doi: 10.1182/blood-2007-08-109769

Akira, S., Takeda, K., and Kaisho, T. (2001). Toll-like receptors: critical proteins linking innate and acquired immunity. *Nat. Immunol.* 2, 675–680. doi: 10.1038/90609

Algate, K., Haynes, D. R., Bartold, P. M., Crotti, T. N., and Cantley, M. D. (2016). The effects of tumour necrosis factor-alpha on bone cells involved in periodontal alveolar bone loss; osteoclasts, osteoblasts and osteocytes. *J. Periodontal Res.* 51, 549–566. doi: 10.1111/jre.12339

Alnaeeli, M., Park, J., Mahamed, D., Penninger, J. M., and Teng, Y. T. A. (2007). Dendritic cells at the osteo-immune interface: implications for inflammation-induced bone loss. *J. Bone Miner. Res.* 22, 775–780. doi: 10.1359/jbmr.070314

AlQranei, M. S., and Chellaiah, M. A. (2020). Osteoclastogenesis in periodontal diseases: possible mediators and mechanisms. *J. Oral Biosci.* 62, 123–130. doi: 10.1016/j.job.2020.02.002

Alzabin, S., Kong, P., Medghalchi, M., Palfreeman, A., Williams, R., and Sacre, S. (2012). Investigation of the role of endosomal Toll-like receptors in murine collagen-induced arthritis reveals a potential role for TLR7 in disease maintenance. *Arthritis Res. Ther.* 14, R142.

Amarasekara, D. S., Yun, H., Kim, S., Lee, N., Kim, H., and Rho, J. (2018). Regulation of osteoclast differentiation by cytokine networks. *Immune Netw.* 18:e8.

Amcheslavsky, A., and Bar-Shavit, Z. (2007). Toll-like receptor 9 ligand blocks osteoclast differentiation through induction of phosphatase. *J. Bone Miner. Res.* 22, 1301–1310. doi: 10.1359/jbmr.070501

Andrade, I. Jr., Taddei, S. R., Garlet, G. P., Garlet, T. P., Teixeira, A. L., Silva, T. A., et al. (2009). CCR5 down-regulates osteoclast function in orthodontic tooth movement. *J. Dent. Res.* 88, 1037–1041. doi: 10.1177/0022034509346230

Atkins, G. J., Kostakis, P., Vincent, C., Farrugia, A. N., Houchins, J. P., Findlay, D. M., et al. (2006). RANK Expression as a cell surface marker of human osteoclast precursors in peripheral blood, bone marrow, and giant cell tumors of bone. *J. Bone Miner. Res.* 21, 1339–1349. doi: 10.1359/jbmr.060604

Bai, W., Liu, H., Ji, Q., Zhou, Y., Liang, L., Zheng, R., et al. (2014). TLR3 regulates mycobacterial RNA-induced IL-10 production through the PI3K/AKT signaling pathway. *Cell. Signal.* 26, 942–950. doi: 10.1016/j.cellsig.2014.01.015

Baliram, R., Sun, L., Cao, J., Li, J., Latif, R., Huber, A., et al. (2012). Hyperthyroid-associated osteoporosis is exacerbated by the loss of TSH signaling. *J. Clin. Invest.* 122, 3737–3741. doi: 10.1172/jci63948

Ban, T., Sato, G. R., Nishiyama, A., Akiyama, A., Takasuna, M., Umehara, M., et al. (2016). Lyn Kinase suppresses the transcriptional activity of IRF5 in the TLR-MyD88 pathway to restrain the development of autoimmunity. *Immunity* 45, 319–332. doi: 10.1016/j.immuni.2016.07.015

Bastiaansen, A., Karper, J., Wezel, A., de Boer, H., Welten, S., de Jong, R., et al. (2014). TLR4 accessory molecule RP105 (CD180) regulates monocyte-driven arteriogenesis in a murine hind limb ischemia model. *PLoS One* 9:e99882. doi: 10.1371/journal.pone.0099882

Batool, F., Stutz, C., Petit, C., Benkirane-Jessel, N., Delpy, E., Zal, F., et al. (2020). A therapeutic oxygen carrier isolated from Arenicola marina decreased *P. gingivalis* induced inflammation and tissue destruction. *Sci. Rep.* 10:14745.

Blasco-Baque, V., Garidou, L., Pomie, C., Escoula, Q., Loubieres, P., Le Gall-David, S., et al. (2017). Periodontitis induced by *Porphyromonas gingivalis* drives periodontal microbiota dysbiosis and insulin resistance via an impaired adaptive immune response. *Gut* 66, 872–885. doi: 10.1136/gutjnl-2015-309897

Blumenthal, A., Kobayashi, T., Pierini, L. M., Banaei, N., Ernst, J. D., Miyake, K., et al. (2009). RP105 facilitates macrophage activation by *Mycobacterium tuberculosis* lipoproteins. *Cell Host Microbe* 5, 35–46. doi: 10.1016/j.chom.2008.12.002

Bohnhorst, J., Rasmussen, T., Moen, S. H., Flottum, M., Knudsen, L., Borset, M., et al. (2006). Toll-like receptors mediate proliferation and survival of multiple myeloma cells. *Leukemia* 20, 1138–1144. doi: 10.1038/sj.leu.2404225

Boyle, W. J., Simonet, W. S., and Lacey, D. L. (2003). Osteoclast differentiation and activation. *Nature* 423, 337–342. doi: 10.1038/nature01658

Bruhl, H., Cihak, J., Talke, Y., Rodriguez Gomez, M., Hermann, F., Goebel, N., et al. (2015). B-cell inhibition by cross-linking CD79b is superior to B-cell depletion with anti-CD20 antibodies in treating murine collagen-induced arthritis. *Eur. J. Immunol.* 45, 705–715. doi: 10.1002/eji.201444971

Burns, E., Bachrach, G., Shapira, L., and Nussbaum, G. (2006). Cutting edge: TLR2 is required for the innate response to *Porphyromonas gingivalis*: activation leads to bacterial persistence and TLR2 deficiency attenuates induced alveolar bone resorption. *J. Immunol.* 177, 8296–8300. doi: 10.4049/jimmunol.177.12.8296

Calvani, N., Silvestris, F., Cafforio, P., and Dammacco, F. (2004). Osteoclast-like cell formation by circulating myeloma B lymphocytes: role of RANK-L. *Leuk. Lymphoma* 45, 377–380. doi: 10.1080/1042819031000159569 6

Carreras-Gonzalez, A., Navasa, N., Martin-Ruiz, I., Lavin, J. L., Azkargorta, M., Atondo, E., et al. (2018). A multi-omic analysis reveals the regulatory role of CD180 during the response of macrophages to *Borrelia burgdorferi*. *Emerg. Microbes Infect.* 7:19.

Carrión, M., Juarranz, Y., Pérez-García, S., Jimeno, R., Pablos, J., Gomariz, R., et al. (2011). RNA sensors in human osteoarthritis and rheumatoid arthritis synovial fibroblasts: immune regulation by vasoactive intestinal peptide. *Arthritis Rheum.* 63, 1626–1636. doi: 10.1002/art.30294

Chan, V., Mecklenbräuker, I., Su, I., Texido, G., Leitges, M., Carsetti, R., et al. (1998). The molecular mechanism of B cell activation by toll-like receptor protein RP-105. *J. Exp. Med.* 188, 93–101. doi: 10.1084/jem.188.1.93

Chang, M. K., Raggatt, L. J., Alexander, K. A., Kuliwaba, J. S., Fazzalari, N. L., Schroder, K., et al. (2008). Osteal tissue macrophages are intercalated throughout human and mouse bone lining tissues and regulate osteoblast function in vitro and *in vivo*. *J. Immunol.* 181, 1232–1244. doi: 10.4049/jimmunol.181.2.1232

Chaplin, J. W., Kasahara, S., Clark, E. A., and Ledbetter, J. A. (2011). Anti-CD180 (RP105) activates B cells to rapidly produce polyclonal Ig via a T cell and MyD88-independent pathway. *J. Immunol.* 187, 4199–4209. doi: 10.4049/jimmunol.1100198

Chen, J., Guo, X., Zeng, G., Liu, J., and Zhao, B. (2020). Transcriptome analysis identifies novel prognostic genes in osteosarcoma. *Comput. Math. Methods Med.* 2020:8081973.

Chen, X., Pan, H., Li, J., Zhang, G., Cheng, S., Zuo, N., et al. (2019). Inhibition of myeloid differentiation 1 specifically in colon with antisense oligonucleotide exacerbates dextran sodium sulfate-induced colitis. *J. Cell. Biochem.* 120, 16888–16899. doi: 10.1002/jcb.28947

Chen, Z. G., Chen, L. F., Baker, K., Olszak, T., Zeissig, S., Huang, Y. H., et al. (2011). CEACAM1 dampens antitumor immunity by down-regulating NKG2D ligand expression on tumor cells. *J. Exp. Med.* 208, 2633–2640. doi: 10.1084/jem.20102575

Chen, Z., Su, L., Xu, Q., Katz, J., Michalek, S., Fan, M., et al. (2015). IL-1R/TLR2 through MyD88 Divergently Modulates Osteoclastogenesis through Regulation of Nuclear Factor of Activated T Cells c1 (NFATc1) and B Lymphocyte-induced Maturation Protein-1 (Blimp1). *J. Biol. Chem.* 290, 30163–30174. doi: 10.1074/jbc.m115.663518

Choi, H. K., Kang, H. R., Jung, E., Kim, T. E., Lin, J. J., and Lee, S. Y. (2013). Early estrogen-induced gene 1, a novel RANK signaling component, is essential for osteoclastogenesis. *Cell Res.* 23, 524–536. doi: 10.1038/cr.2013.33

Coleman, R. E., Croucher, P. I., Padhani, A. R., Clezardin, P., Chow, E., Fallon, M., et al. (2020). Bone metastases. *Nat. Rev. Dis. Primers* 6:83.

Crotti, T. N., Flannery, M., Walsh, N. C., Fleming, J. D., Goldring, S. R., and McHugh, K. P. (2006). NFATc1 regulation of the human beta3 integrin promoter in osteoclast differentiation. *Gene* 372, 92–102. doi: 10.1016/j.gene.2005.12.012

Czimmerer, Z., Varga, T., Poliska, S., Nemet, I., Szanto, A., and Nagy, L. (2012). Identification of novel markers of alternative activation and potential endogenous PPARgamma ligand production mechanisms in human IL-4 stimulated differentiating macrophages. *Immunobiology* 217, 1301–1314. doi: 10.1016/j.imbio.2012.08.270

Ding, P. H., Darveau, R. P., Wang, C. Y., and Jin, L. (2017). 3LPS-binding protein and its interactions with P. *gingivalis* LPS modulate pro-inflammatory response and Toll-like receptor signaling in human oral keratinocytes. *PLoS One* 12:e0173223. doi: 10.1371/journal.pone.0173223

Divanovic, S., Trompette, A., Atabani, S. F., Madan, R., Golenbock, D. T., Visintin, A., et al. (2005). Negative regulation of Toll-like receptor 4 signaling by the Toll-like receptor homolog RP105. *Nat. Immunol.* 6, 571–578. doi: 10.1038/ni1198

Dong, G. J., Yao, X. Y., Yan, F. L., Zhang, H., Zhu, Y. Z., Yang, Y. H., et al. (2019). Ligation of CD180 contributes to endotoxic shock by regulating the accumulation and immunosuppressive activity of myeloid-derived suppressor cells through STAT3. *Biochim. Biophys. Acta* 1865, 535–546. doi: 10.1016/j.bbadis.2018.12.013

Egli, N., Zajonz, A., Burger, M. T., and Schweighoffer, T. (2015). Human CD180 transmits signals via the PIM-1L Kinase. *PLoS One* 10:e0142741. doi: 10.1371/journal.pone.0142741

Endo-Munoz, L., Cumming, A., Sommerville, S., Dickinson, I., and Saunders, N. A. (2010). Osteosarcoma is characterised by reduced expression of markers of osteoclastogenesis and antigen presentation compared with normal bone. *Br. J. Cancer* 103, 73–81. doi: 10.1038/sj.bjc.6605723

Engel, P., Zhou, L., Ord, D., Sato, S., Koller, B., and Tedder, T. (1995). Abnormal B lymphocyte development, activation, and differentiation in mice that lack or overexpress the CD19 signal transduction molecule. *Immunity* 3, 39–50. doi: 10.1016/1074-7613(95)90157-4

Flores-Borja, F., Kabouridis, P. S., Jury, E. C., Isenberg, D. A., and Mageed, R. A. (2005). Decreased Lyn expression and translocation to lipid raft signaling domains in B lymphocytes from patients with systemic lupus erythematosus. *Arthritis Rheum.* 52, 3955–3965. doi: 10.1002/art.21416

Fujii, T., Kitaura, H., Kimura, K., Hakami, Z. W., and Takano-Yamamoto, T. (2012). IL-4 inhibits TNF-alpha-mediated osteoclast formation by inhibition of RANKL expression in TNF-alpha-activated stromal cells and direct inhibition of TNF-alpha-activated osteoclast precursors via a T-cell-independent mechanism *in vivo*. *Bone* 51, 771–780. doi: 10.1016/j.bone.2012.06.024

Fuller, K., Murphy, C., Kirstein, B., Fox, S. W., and Chambers, T. J. (2002). TNFa potently activates osteoclasts, through a direct action independent of and strongly synergistic with RANKL. *Endocrinology* 143, 1108–1118. doi: 10.1210/endo.143.3.8701

Furukawa, Y., Kuroda, Y., and Kikuchi, J. (2018). [Involvement of innate immunity in the expansion of multiple myeloma cells and therapeutic intervention with lenalidomide]. *Rinsho ketsueki* 59, 1048–1057.

Gao, Y., Grassi, F., Ryan, M. R., Terauchi, M., Page, K., Yang, X., et al. (2007). IFN-gamma stimulates osteoclast formation and bone loss *in vivo* via antigen-driven T cell activation. *J. Clin. Invest.* 117, 122–132. doi: 10.1172/jci30074

Gavali, S., Gupta, M., Daswani, B., Wani, M., Sirdeshmukh, R., and Khatkhatay, M. (2019). LYN, a key mediator in estrogen-dependent suppression of osteoclast differentiation, survival, and function. *Biochim. Biophys. Acta* 1865, 547–557. doi: 10.1016/j.bbadis.2018.12.016

Gorczynski, R. M., Kai, Y., and Miyake, K. (2006). MD1 expression regulates development of regulatory T cells. *J. Immunol.* 177, 1078–1084. doi: 10.4049/jimmunol.177.2.1078

Gordiienko, I., Shlapatska, L., Kholodniuk, V., Sklyarenko, L., Gluzman, D. F., Clark, E. A., et al. (2017). The interplay of CD150 and CD180 receptor pathways contribute to the pathobiology of chronic lymphocytic leukemia B cells by selective inhibition of Akt and MAPK signaling. *PLoS One* 12:e0185940. doi: 10.1371/journal.pone.0185940

Grigoriadis, A. E., Wang, Z. Q., Cecchini, M. G., Hofstetter, W., Felix, R., Fleisch, H. A., et al. (1994). c-Fos: a key regulator of osteoclast-macrophage lineage determination and bone remodeling. *Science* 266, 443–448. doi: 10.1126/science.7939685

Gu, Y., and Han, X. (2020). Toll-like receptor signaling and immune regulatory lymphocytes in periodontal disease. *Int. J. Mol. Sci.* 21:3329. doi: 10.3390/ijms21093329

Guo, X., Hu, S., Liu, J. J., Huang, L., Zhong, P., Fan, Z. X., et al. (2021). Piperine protects against pyroptosis in myocardial ischaemia/reperfusion injury by regulating the miR-383/RP105/AKT signalling pathway. *J. Cell. Mol. Med.* 25, 244–258. doi: 10.1111/jcmm.15953

Gyori, D. S., and Mocsai, A. (2020). Osteoclast signal transduction during bone metastasis formation. *Front. Cell Dev. Biol.* 8:507. doi: 10.3389/fcell.2020.00507

Gyōri, D., and Mócsai, A. (2016). "Osteoclasts in inflammation," in *Compendium of Inflammatory Diseases*, ed. M. J. Parnham (Basel: Springer), 1047–1053. doi: 10.1007/978-3-7643-8550-7_155

Hebeis, B., Vigorito, E., Kovesdi, D., and Turner, M. (2005). Vav proteins are required for B-lymphocyte responses to LPS. *Blood* 106, 635–640. doi: 10.1182/blood-2004-10-3919

Herath, T. D., Darveau, R. P., Seneviratne, C. J., Wang, C. Y., Wang, Y., and Jin, L. (2013). Tetra- and penta-acylated lipid A structures of *Porphyromonas gingivalis* LPS differentially activate TLR4-mediated NF-kappaB signal transduction cascade and immuno-inflammatory response in human gingival fibroblasts. *PLoS One* 8:e58496. doi: 10.1371/journal.pone.0058496

Hienz, S. A., Paliwal, S., and Ivanovski, S. (2015). Mechanisms of Bone Resorption in Periodontitis. *J. Immunol. Res.* 2015:615486.

Hirose, J., Masuda, H., Tokuyama, N., Omata, Y., Matsumoto, T., Yasui, T., et al. (2014). Bone resorption is regulated by cell-autonomous negative feedback loop of Stat5-Dusp axis in the osteoclast. *J. Exp. Med.* 211, 153–163. doi: 10.1084/jem.20130538

Honda, Y., Yamagiwa, S., Matsuda, Y., Takamura, M., Ichida, T., and Aoyagi, Y. (2007). Altered expression of TLR homolog RP105 on monocytes hypersensitive to LPS in patients with primary biliary cirrhosis. *J. Hepatol.* 47, 404–411. doi: 10.1016/j.jhep.2007.03.012

Hu, X. F., Li, J., Vandervalk, S., Wang, Z., Magnuson, N. S., and Xing, P. X. (2009). PIM-1-specific mAb suppresses human and mouse tumor growth by decreasing PIM-1 levels, reducing Akt phosphorylation, and activating apoptosis. *J. Clin. Invest.* 119, 362–375.

Huang, W., Yang, J., He, C., and Yang, J. (2020). RP105 plays a cardioprotective role in myocardial ischemia reperfusion injury by regulating the Tolllike receptor 2/4 signaling pathways. *Mol. Med. Rep.* 22, 1373–1381. doi: 10.3892/mmr.2020.11242

Ishiura, N., Nakashima, H., Watanabe, R., Kuwano, Y., Adachi, T., Takahashi, Y., et al. (2010). Differential phosphorylation of functional tyrosines in CD19 modulates B-lymphocyte activation. *Eur. J. Immunol.* 40, 1192–1204. doi: 10.1002/eji.200939848

Jacome-Galarza, C. E., Percin, G. I., Muller, J. T., Mass, E., Lazarov, T., Eitler, J., et al. (2019). Developmental origin, functional maintenance and genetic rescue of osteoclasts. *Nature* 568, 541–545. doi: 10.1038/s41586-019-1105-7

Jeong, Y., Kim, G. B., Ji, Y., Kwak, G. J., Nam, G. H., Hong, Y., et al. (2020). Dendritic cell activation by an *E. coli*-derived monophosphoryl lipid A enhances the efficacy of PD-1 blockade. *Cancer Lett.* 472, 19–28. doi: 10.1016/j.canlet.2019.12.012

Ji, J. D., Park-Min, K. H., Shen, Z., Fajardo, R. J., Goldring, S. R., McHugh, K. P., et al. (2009). Inhibition of RANK expression and osteoclastogenesis by TLRs and IFN-gamma in human osteoclast precursors. *J. Immunol.* 183, 7223–7233. doi: 10.4049/jimmunol.0900072

Jin, M. S., Kim, S. E., Heo, J. Y., Lee, M. E., Kim, H. M., Paik, S. G., et al. (2007). Crystal structure of the TLR1-TLR2 heterodimer induced by binding of a tri-acylated lipopeptide. *Cell* 130, 1071–1082. doi: 10.1016/j.cell.2007.09.008

Kang, J. Y., Nan, X., Jin, M. S., Youn, S. J., Ryu, Y. H., Mah, S., et al. (2009). Recognition of lipopeptide patterns by Toll-like receptor 2-Toll-like receptor 6 heterodimer. *Immunity* 31, 873–884. doi: 10.1016/j.immuni.2009.09.018

Kanzaki, H., Shinohara, F., Kanako, I., Yamaguchi, Y., Fukaya, S., Miyamoto, Y., et al. (2016). Molecular regulatory mechanisms of osteoclastogenesis through cytoprotective enzymes. *Redox Biol.* 8, 186–191. doi: 10.1016/j.redox.2016.01.006

Kassem, A., Henning, P., Lundberg, P., Souza, P., Lindholm, C., and Lerner, U. (2015). *Porphyromonas gingivalis* stimulates bone resorption by enhancing RANKL (Receptor Activator of NF-κB Ligand) through activation of toll-like receptor 2 in Osteoblasts. *J. Biol. Chem.* 290, 20147–20158. doi: 10.1074/jbc.m115.655787

Kassem, A., Lindholm, C., and Lerner, U. (2016). Toll-Like Receptor 2 Stimulation of osteoblasts mediates *Staphylococcus aureus* induced bone resorption and osteoclastogenesis through enhanced RANKL. *PLoS One* 11:e0156708. doi: 10.1371/journal.pone.0156708

Kavanagh, N., Ryan, E., Widaa, A., Sexton, G., Fennell, J., O'Rourke, S., et al. (2018). Staphylococcal osteomyelitis: disease progression, treatment challenges, and future directions. *Clin. Microbiol. Rev.* 31:e00084-17.

Ketloy, C., Engering, A., Srichairatanakul, U., Limsalakpetch, A., Yongvanitchit, K., Pichyangkul, S., et al. (2008). Expression and function of Toll-like receptors on dendritic cells and other antigen presenting cells from non-human primates. *Vet. Immunol. Immunopathol.* 125, 18–30. doi: 10.1016/j.vetimm.2008.05.001

Kikuchi, J., and Furukawa, Y. (2020). [Toll-like receptor CD180 and the bone marrow microenvironment as therapeutic targets in multiple myeloma]. *Rinsho Ketsueki* 61, 832–841.

Kikuchi, J., Kuroda, Y., Koyama, D., Osada, N., Izumi, T., Yasui, H., et al. (2018). Myeloma cells are activated in bone marrow microenvironment by the CD180/MD-1 complex, which senses Lipopolysaccharide. *Cancer Res.* 78, 1766–1778. doi: 10.1158/0008-5472.can-17-2446

Kikuchi, T., Matsuguchi, T., Tsuboi, N., Mitani, A., Tanaka, S., Matsuoka, M., et al. (2001). Gene expression of osteoclast differentiation factor is induced by lipopolysaccharide in mouse osteoblasts via Toll-like receptors. *J. Immunol.* 166, 3574–3579. doi: 10.4049/jimmunol.166.5.3574

Kikuchi, T., Yoshikai, Y., Miyoshi, J., Katsuki, M., Musikacharoen, T., Mitani, A., et al. (2003). Cot/Tpl2 is essential for RANKL induction by lipid A in osteoblasts. *J. Dent. Res.* 82, 546–550. doi: 10.1177/154405910308200712

Kikuchi, Y., Koarada, S., Tada, Y., Ushiyama, O., Morito, F., Suzuki, N., et al. (2002). RP105-lacking B cells from lupus patients are responsible for the production of immunoglobulins and autoantibodies. *Arthritis Rheum.* 46, 3259–3265. doi: 10.1002/art.10672

Kim, H., Choi, H. K., Shin, J. H., Kim, K. H., Huh, J. Y., Lee, S. A., et al. (2009). Selective inhibition of RANK blocks osteoclast maturation and function and prevents bone loss in mice. *J. Clin. Invest.* 119, 813–825. doi: 10.1172/jci36809

Kim, K., Kim, B., Won, J., Lee, K., Kim, H., and Lee, S. (2019). Toll-like receptor 7 regulates osteoclastogenesis in rheumatoid arthritis. *J. Biochem.* 166, 259–270. doi: 10.1093/jb/mvz033

Kim, K., Kim, J. H., Lee, J., Jin, H. M., Lee, S. H., Fisher, D. E., et al. (2005). Nuclear factor of activated T cells c1 induces osteoclast-associated receptor gene expression during tumor necrosis factor-related activation-induced cytokine-mediated osteoclastogenesis. *J. Biol. Chem.* 280, 35209–35216. doi: 10.1074/jbc.m505815200

Kim, K., Kim, J., Youn, B., Jin, H., and Kim, N. (2010). Pim-1 regulates RANKL-induced osteoclastogenesis via NF-κB activation and NFATc1 induction. *J. Immunol.* 185, 7460–7466. doi: 10.4049/jimmunol.1000885

Kim, N., Saudemont, A., Webb, L., Camps, M., Ruckle, T., Hirsch, E., et al. (2007). The p110delta catalytic isoform of PI3K is a key player in NK-cell development and cytokine secretion. *Blood* 110, 3202–3208. doi: 10.1182/blood-2007-02-075366

Kim, Y., Sato, K., Asagiri, M., Morita, I., Soma, K., and Takayanagi, H. (2005). Contribution of nuclear factor of activated T cells c1 to the transcriptional control of immunoreceptor osteoclast-associated receptor but not triggering receptor expressed by myeloid cells-2 during osteoclastogenesis. *J. Biol. Chem.* 280, 32905–32913. doi: 10.1074/jbc.m505820200

Kimoto, M., Nagasawa, K., and Miyake, K. (2003). Role of TLR4/MD-2 and RP105/MD-1 in innate recognition of lipopolysaccharide. *Scand. J. Infect. Dis.* 35, 568–572. doi: 10.1080/00365540310015700

Koarada, S., and Tada, Y. (2012). RP105-negative B cells in systemic lupus erythematosus. *Clin. Dev. Immunol.* 2012:259186.

Koarada, S., Tada, Y., Ushiyama, O., Morito, F., Suzuki, N., Ohta, A., et al. (1999). B cells lacking RP105, a novel B cell antigen, in systemic lupus erythematosus. *Arthritis Rheum.* 42, 2593–2600. doi: 10.1002/1529-0131(199912)42:12<2593::aid-anr12>3.0.co;2-g

Kobayashi, N., Kadono, Y., Naito, A., Matsumoto, K., Yamamoto, T., Tanaka, S., et al. (2001). Segregation of TRAF6-mediated signaling pathways clarifies its role in osteoclastogenesis. *EMBO J.* 20, 1271–1280. doi: 10.1093/emboj/20.6.1271

Krzeszinski, J. Y., Wei, W., Huynh, H., Jin, Z. X., Wang, X. D., Chang, T. C., et al. (2014). miR-34a blocks osteoporosis and bone metastasis by inhibiting osteoclastogenesis and Tgif2. *Nature* 512, 431–U460.

Kwon, J. O., Jin, W. J., Kim, B., Ha, H., Kim, H. H., and Lee, Z. H. (2019). Haptoglobin Acts as a TLR4 Ligand to suppress Osteoclastogenesis via the TLR4-IFN-beta Axis. *J. Immunol.* 202, 3359–3369. doi: 10.4049/jimmunol.1800661

Laiño, J., Villena, J., Kanmani, P., and Kitazawa, H. (2016). Immunoregulatory effects triggered by lactic acid bacteria exopolysaccharides: new insights into molecular interactions with host cells. *Microorganisms* 4, 4030027–4030043.

Lam, J., Takeshita, S., Barker, J. E., Kanagawa, O., Ross, F. P., and Teitelbaum, S. L. (2000). TNF-alpha induces osteoclastogenesis by direct stimulation of macrophages exposed to permissive levels of RANK ligand. *J. Clin. Invest.* 106, 1481–1488. doi: 10.1172/jci11176

Lasunskaia, E. B., Campos, M. N., de Andrade, M. R., Damatta, R. A., Kipnis, T. L., Einicker-Lamas, M., et al. (2006). Mycobacteria directly induce cytoskeletal rearrangements for macrophage spreading and polarization through TLR2-dependent PI3K signaling. *J. Leukoc. Biol.* 80, 1480–1490. doi: 10.1189/jlb.0106066

Ledov, V., Golovina, M., Markina, A., Knirel, Y., L'vov, V., Kovalchuk, A., et al. (2019). Highly homogenous tri-acylated S-LPS acts as a novel clinically applicable vaccine against *Shigella flexneri* 2a infection. *Vaccine* 37, 1062–1072. doi: 10.1016/j.vaccine.2018.12.067

Lee, N. K., Choi, Y. G., Baik, J. Y., Han, S. Y., Jeong, D. W., Bae, Y. S., et al. (2005). A crucial role for reactive oxygen species in RANKL-induced osteoclast differentiation. *Blood* 106, 852–859. doi: 10.1182/blood-2004-09-3662

Lee, S. H., Rho, J., Jeong, D., Sul, J. Y., Kim, T., Kim, N., et al. (2006). v-ATPase V0 subunit d2-deficient mice exhibit impaired osteoclast fusion and increased bone formation. *Nat. Med.* 12, 1403–1409. doi: 10.1038/nm1514

Leite, F. R., de Aquino, S. G., Guimaraes, M. R., Cirelli, J. A., Zamboni, D. S., Silva, J. S., et al. (2015). Relevance of the myeloid differentiation factor 88 (MyD88) on RANKL, OPG, and nod expressions induced by TLR and IL-1R signaling in bone marrow stromal cells. *Inflammation* 38, 1–8. doi: 10.1007/s10753-014-0001-4

Levaot, N., Simoncic, P. D., Dimitriou, I. D., Scotter, A., La Rose, J., Ng, A. H. M., et al. (2011). 3BP2-deficient mice are osteoporotic with impaired osteoblast and osteoclast functions. *J. Clin. Invest.* 121, 3244–3257. doi: 10.1172/jci45843

Li, S. S., Miller, C. H., Giannopoulou, E., Hu, X. Y., Ivashkiv, L. B., and Zhao, B. H. (2014). RBP-J imposes a requirement for ITAM-mediated costimulation of osteoclastogenesis. *J. Clin. Invest.* 124, 5057–5073. doi: 10.1172/jci71882

Liang, H., Lum, H., Alvarez, A., Garduno-Garcia, J. J., Daniel, B. J., and Musi, N. (2018). A low dose lipid infusion is sufficient to induce insulin resistance and a pro-inflammatory response in human subjects. *PLoS One* 13:e0195810. doi: 10.1371/journal.pone.0195810

Lim, L., Benseler, S., Tyrrell, P., Harvey, E., Herbert, D., Charron, M., et al. (2012). Predicting longitudinal trajectory of bone mineral density in paediatric systemic lupus erythematosus patients. *Ann. Rheum. Dis.* 71, 1686–1691. doi: 10.1136/annrheumdis-2011-200805

Lim, S., Benseler, S., Tyrrell, P., Charron, M., Harvey, E., Hebert, D., et al. (2011). Low bone mineral density is present in newly diagnosed paediatric systemic lupus erythematosus patients. *Ann. Rheum. Dis.* 70, 1991–1994. doi: 10.1136/ard.2010.144311

Lin, J., Bi, L., Yu, X., Kawai, T., Taubman, M. A., Shen, B., et al. (2014). *Porphyromonas gingivalis* exacerbates ligature-induced, RANKL-dependent alveolar bone resorption via differential regulation of Toll-like receptor 2 (TLR2) and TLR4. *Infect. Immun.* 82, 4127–4134. doi: 10.1128/iai.02084-14

Liossis, S. N., Solomou, E. E., Dimopoulos, M. A., Panayiotidis, P., Mavrikakis, M. M., and Sfikakis, P. P. (2001). B-cell kinase lyn deficiency in patients with systemic lupus erythematosus. *J. Investig. Med.* 49, 157–165. doi: 10.2310/6650.2001.34042

Liu, B., Zhang, N., Liu, Z., Fu, Y., Feng, S., Wang, S., et al. (2013). RP105 involved in activation of mouse macrophages via TLR2 and TLR4 signaling. *Mol. Cell. Biochem.* 378, 183–193. doi: 10.1007/s11010-013-1609-7

Liu, G. Y. C., Lerner, U. H., and Teng, A. Y. T. (2010). Cytokine responses against periodontal infection: protective and destructive roles. *Periodontol 2000* 52, 163–206. doi: 10.1111/j.1600-0757.2009.00321.x

Liu, H., Liu, Z., Chen, J., Chen, L., He, X., Zheng, R., et al. (2013). Induction of CCL8/MCP-2 by mycobacteria through the activation of TLR2/PI3K/Akt signaling pathway. *PLoS One* 8:e56815. doi: 10.1371/journal.pone.0056815

Liu, J., Wang, S., Zhang, P., Said-Al-Naief, N., Michalek, S. M., and Feng, X. (2009). Molecular mechanism of the bifunctional role of lipopolysaccharide in osteoclastogenesis. *J. Biol. Chem.* 284, 12512–12523. doi: 10.1074/jbc.m809789200

Liu, Y. H., Huang, D., Li, Z. J., Li, X. H., Wang, X., Yang, H. P., et al. (2016). Toll-like receptor-4-dependence of the lipopolysaccharide-mediated inhibition of osteoblast differentiation. *Genet. Mol. Res.* 15:gmr7191.

Lobo, E. O., Zhang, Z. F., and Shively, J. E. (2009). CEACAM1 is a negative coreceptor for the B cell receptor and promotes CD19-mediated adhesion of B cells in a PI3K-dependent manner. *J. Leukoc. Biol.* 86, 205–218. doi: 10.1189/jlb.0109037

Louwe, M. C., Karper, J. C., de Vries, M. R., Nossent, A. Y., Bastiaansen, A. J., van der Hoorn, J. W., et al. (2014). RP105 deficiency aggravates cardiac dysfunction after myocardial infarction in mice. *Int. J. Cardiol.* 176, 788–793. doi: 10.1016/j.ijcard.2014.07.086

Low, P. C., Misaki, R., Schroder, K., Stanley, A. C., Sweet, M. J., Teasdale, R. D., et al. (2010). Phosphoinositide 3-kinase delta regulates membrane fission of Golgi carriers for selective cytokine secretion. *J. Cell Biol.* 190, 1053–1065. doi: 10.1083/jcb.201001028

Lu, R., Pan, H., and Shively, J. E. (2012). CEACAM1 negatively regulates IL-1beta production in LPS activated neutrophils by recruiting SHP-1 to a SYK-TLR4-CEACAM1 complex. *PLoS Pathog.* 8:e1002597. doi: 10.1371/journal.ppat.1002597

Maldonado, R. F., Sa-Correia, I., and Valvano, M. A. (2016). Lipopolysaccharide modification in Gram-negative bacteria during chronic infection. *FEMS Microbiol. Rev.* 40, 480–493. doi: 10.1093/femsre/fuw007

Mao, D., Epple, H., Uthgenannt, B., Novack, D. V., and Faccio, R. (2006). PLCgamma2 regulates osteoclastogenesis via its interaction with ITAM proteins and GAB2. *J. Clin. Invest.* 116, 2869–2879. doi: 10.1172/jci28775

Matsumoto, M., Kogawa, M., Wada, S., Takayanagi, H., Tsujimoto, M., Katayama, S., et al. (2004). Essential role of p38 mitogen-activated protein kinase in cathepsin K gene expression during osteoclastogenesis through association of NFATc1 and PU.1. *J. Biol. Chem.* 279, 45969–45979. doi: 10.1074/jbc.m408795200

Matsuo, K., Galson, D. L., Zhao, C., Peng, L., Laplace, C., Wang, K. Z., et al. (2004). Nuclear factor of activated T-cells (NFAT) rescues osteoclastogenesis in precursors lacking c-Fos. *J. Biol. Chem.* 279, 26475–26480. doi: 10.1074/jbc.m313973200

McGrath, K. E., Frame, J. M., Fegan, K. H., Bowen, J. R., Conway, S. J., Catherman, S. C., et al. (2015). Distinct sources of hematopoietic progenitors emerge before HSCs and provide functional blood cells in the mammalian embryo. *Cell Rep.* 11, 1892–1904. doi: 10.1016/j.celrep.2015.05.036

Miura, Y., Shimazu, R., Miyake, K., Akashi, S., Ogata, H., Yamashita, Y., et al. (1998). RP105 is associated with MD-1 and transmits an activation signal in human B cells. *Blood* 92, 2815–2822. doi: 10.1182/blood.v92.8.2815.420k09_2815_2822

Miyamoto, H., Suzuki, T., Miyauchi, Y., Iwasaki, R., Kobayashi, T., Sato, Y., et al. (2012). Osteoclast stimulatory transmembrane protein and dendritic cell-specific transmembrane protein cooperatively modulate cell-cell fusion to form osteoclasts and foreign body giant cells. *J. Bone Miner. Res.* 27, 1289–1297. doi: 10.1002/jbmr.1575

Miyauchi, Y., Ninomiya, K., Miyamoto, H., Sakamoto, A., Iwasaki, R., Hoshi, H., et al. (2010). The Blimp1-Bcl6 axis is critical to regulate osteoclast

differentiation and bone homeostasis. *J. Exp. Med.* 207, 751–762. doi: 10.1084/jem.20091957

Moon, J. B., Kim, J. H., Kim, K., Youn, B. U., Ko, A., Lee, S. Y., et al. (2012). Akt induces osteoclast differentiation through regulating the GSK3 beta/NFATc1 signaling cascade. *J. Immunol.* 188, 163–169. doi: 10.4049/jimmunol.1101254

Moresco, E. M., LaVine, D., and Beutler, B. (2011). Toll-like receptors. *Curr. Biol.* 21, R488–R493.

Murata, K., Fang, C., Terao, C., Giannopoulou, E., Lee, Y., Lee, M., et al. (2017). Hypoxia-Sensitive COMMD1 integrates signaling and cellular metabolism in human macrophages and suppresses osteoclastogenesis. *Immunity* 47, 66–79.e5.

Murofushi, Y., Villena, J., Morie, K., Kanmani, P., Tohno, M., Shimazu, T., et al. (2015). The toll-like receptor family protein RP105/MD1 complex is involved in the immunoregulatory effect of exopolysaccharides from *Lactobacillus plantarum* N14. *Mol. Immunol.* 64, 63–75. doi: 10.1016/j.molimm.2014.10.027

Nagai, Y., Kobayashi, T., Motoi, Y., Ishiguro, K., Akashi, S., Saitoh, S. I., et al. (2005). The Radioprotective 105/MD-1 complex links tlr2 and tlr4/md-2 in antibody response to microbial membranes. *J. Immunol.* 174, 7043–7049. doi: 10.4049/jimmunol.174.11.7043

Nagai, Y., Shimazu, R., Ogata, H., Akashi, S., Sudo, K., Yamasaki, H., et al. (2002). Requirement for MD-1 in cell surface expression of RP105/CD180 and B-cell responsiveness to lipopolysaccharide. *Blood* 99, 1699–1705. doi: 10.1182/blood.v99.5.1699

Nagai, Y., Watanabe, Y., and Takatsu, K. (2013). The TLR family protein RP105/MD-1 complex: a new player in obesity and adipose tissue inflammation. *Adipocyte* 2, 61–66. doi: 10.4161/adip.22929

Nagasawa, T., Kiji, M., Yashiro, R., Hormdee, D., He, L., Kunze, M., et al. (2007). Roles of receptor activator of nuclear factor-kappa B ligand (RANKL) and osteoprotegerin in periodontal health and disease. *Periodontol 2000* 43, 65–84. doi: 10.1111/j.1600-0757.2006.00185.x

Nason, R., Jung, J. Y., and Chole, R. A. (2009). Lipopolysaccharide-induced osteoclastogenesis from mononuclear precursors: a mechanism for osteolysis in chronic otitis. *J. Assoc. Res. Otolaryngol.* 10, 151–160. doi: 10.1007/s10162-008-0153-8

Negishi-Koga, T., and Takayanagi, H. (2009). Ca2+-NFATc1 signaling is an essential axis of osteoclast differentiation. *Immunol. Rev.* 231, 241–256. doi: 10.1111/j.1600-065x.2009.00821.x

Nemoto, E., Darveau, R., Foster, B., Nogueira-Filho, G., and Somerman, M. (2006). Regulation of cementoblast function by *P. gingivalis* lipopolysaccharide via TLR2. *J. Dent. Res.* 85, 733–738. doi: 10.1177/154405910608500809

Ogata, H., Su, I., Miyake, K., Nagai, Y., Akashi, S., Mecklenbräuker, I., et al. (2000). The toll-like receptor protein RP105 regulates lipopolysaccharide signaling in B cells. *J. Exp. Med.* 192, 23–29. doi: 10.1084/jem.192.1.23

Ohto, U., Miyake, K., and Shimizu, T. (2011). Crystal structures of mouse and human RP105/MD-1 complexes reveal unique dimer organization of the toll-like receptor family. *J. Mol. Biol.* 413, 815–825. doi: 10.1016/j.jmb.2011.09.020

Okamoto, K., Nakashima, T., Shinohara, M., Negishi-Koga, T., Komatsu, N., Terashima, A., et al. (2017). Osteoimmunology: the conceptual framework unifying the immune and skeletal systems. *Physiol. Rev.* 97, 1295–1349. doi: 10.1152/physrev.00036.2016

Okamoto, N., Mizote, K., Honda, H., Saeki, A., Watanabe, Y., Yamaguchi-Miyamoto, T., et al. (2017). Funiculosin variants and phosphorylated derivatives promote innate immune responses via the Toll-like receptor 4/myeloid differentiation factor-2 complex. *J. Biol. Chem.* 292, 15378–15394. doi: 10.1074/jbc.m117.791780

Ortiz-Suarez, M. L., and Bond, P. J. (2016). The structural basis for lipid and endotoxin binding in RP105-MD-1, and consequences for regulation of host lipopolysaccharide sensitivity. *Structure* 24, 200–211. doi: 10.1016/j.str.2015.10.021

Pan, H., and Shively, J. E. (2010). Carcinoembryonic antigen-related cell adhesion molecule-1 regulates granulopoiesis by inhibition of granulocyte colony-stimulating factor receptor. *Immunity* 33, 620–631. doi: 10.1016/j.immuni.2010.10.009

Park, J. H., Lee, N. K., and Lee, S. Y. (2017). Current understanding of RANK signaling in osteoclast differentiation and maturation. *Mol. Cells* 40, 706–713.

Peng, J. Y., Liu, Y., Xiong, X. J., Huang, C. X., Mei, Y., Wang, Z. Q., et al. (2017). Loss of MD1 exacerbates pressure overload-induced left ventricular structural and electrical remodelling. *Sci. Rep.* 7:5116.

Poy, M. N., Yang, Y., Rezaei, K., Fernstrom, M. A., Lee, A. D., Kido, Y., et al. (2002). CEACAM1 regulates insulin clearance in liver. *Nat. Genet.* 30, 270–276. doi: 10.1038/ng840

Puchner, A., Saferding, V., Bonelli, M., Mikami, Y., Hofmann, M., Brunner, J., et al. (2018). Non-classical monocytes as mediators of tissue destruction in arthritis. *Ann. Rheum. Dis.* 77, 1490–1497. doi: 10.1136/annrheumdis-2018-213250

Qiao, W., Ding, H., Zuo, Y., Jiang, L., Zhou, J., Han, X., et al. (2020). Lupus IgG deposition causes arthritis but inhibits bone destruction through competitive occupation of FcgammaRI and reduced RANKL signalling. *Clin. Transl. Immunol.* 9:e1174.

Qin, Q., Cui, L., Zhou, Z., Zhang, Z., Wang, Y., and Zhou, C. (2019). Inhibition of microRNA-141-3p reduces hypoxia-induced apoptosis in H9c2 rat cardiomyocytes by activating the RP105-dependent PI3K/AKT signaling pathway. *Med. Sci. Monit.* 25, 7016–7025. doi: 10.12659/msm.916361

Raetz, C. R., and Whitfield, C. (2002). Lipopolysaccharide endotoxins. *Annu. Rev. Biochem.* 71, 635–700.

Raetz, C. R., Reynolds, C. M., Trent, M. S., and Bishop, R. E. (2007). Lipid A modification systems in gram-negative bacteria. *Annu. Rev. Biochem.* 76, 295–329. doi: 10.1146/annurev.biochem.76.010307.145803

Rauber, S., Luber, M., Weber, S., Maul, L., Soare, A., Wohlfahrt, T., et al. (2017). Resolution of inflammation by interleukin-9-producing type 2 innate lymphoid cells. *Nat. Med.* 23, 938–944.

Roelofs, M., Joosten, L., Abdollahi-Roodsaz, S., van Lieshout, A., Sprong, T., van den Hoogen, F., et al. (2005). The expression of toll-like receptors 3 and 7 in rheumatoid arthritis synovium is increased and costimulation of toll-like receptors 3, 4, and 7/8 results in synergistic cytokine production by dendritic cells. *Arthritis Rheum.* 52, 2313–2322. doi: 10.1002/art.21278

Ru, J. Y., and Wang, Y. F. (2020). Osteocyte apoptosis: the roles and key molecular mechanisms in resorption-related bone diseases. *Cell Death Dis.* 11:846.

Sato, K., Suematsu, A., Okamoto, K., Yamaguchi, A., Morishita, Y., Kadono, Y., et al. (2006). Th17 functions as an osteoclastogenic helper T cell subset that links T cell activation and bone destruction. *J. Exp. Med.* 203, 2673–2682. doi: 10.1084/jem.20061775

Schultz, T. E., and Blumenthal, A. (2017). The RP105/MD-1 complex: molecular signaling mechanisms and pathophysiological implications. *J. Leukoc. Biol.* 101, 183–192. doi: 10.1189/jlb.2vmr1215-582r

Schultz, T. E., Wiesmuller, K. H., Lucas, M., Dobos, K. M., Baxter, A. G., and Blumenthal, A. (2018). The N-terminal peptide moiety of the *Mycobacterium tuberculosis* 19 kDa lipoprotein harbors RP105-agonistic properties. *J. Leukoc. Biol.* 103, 311–319. doi: 10.1002/jlb.2ma0517-190rr

Scott, A. J., Oyler, B. L., Goodlett, D. R., and Ernst, R. K. (2017). Lipid A structural modifications in extreme conditions and identification of unique modifying enzymes to define the Toll-like receptor 4 structure-activity relationship. *Biochim. Biophys. Acta* 1862, 1439–1450. doi: 10.1016/j.bbalip.2017.01.004

Shen, C. J., Kong, B., Shuai, W., Liu, Y., Wang, G. J., Xu, M., et al. (2019). Myeloid differentiation protein 1 protected myocardial function against high-fat stimulation induced pathological remodelling. *J. Cell. Mol. Med.* 23, 5303–5316. doi: 10.1111/jcmm.14407

Shen, Y., Kawamura, I., Nomura, T., Tsuchiya, K., Hara, H., Dewamitta, S. R., et al. (2010). Toll-like receptor 2- and MyD88-dependent phosphatidylinositol 3-kinase and Rac1 activation facilitates the phagocytosis of Listeria monocytogenes by murine macrophages. *Infect. Immun.* 78, 2857–2867. doi: 10.1128/iai.01138-09

Shin, J., Jang, H., Lin, J., and Lee, S. Y. (2014). PKC beta positively regulates RANKL-induced osteoclastogenesis by inactivating GSK-3 beta. *Mol. Cells* 37, 747–752. doi: 10.14348/molcells.2014.0220

Shinohara, M., Koga, T., Okamoto, K., Sakaguchi, S., Arai, K., Yasuda, H., et al. (2008). Tyrosine kinases Btk and Tec regulate osteoclast differentiation by linking RANK and ITAM signals. *Cell* 132, 794–806. doi: 10.1016/j.cell.2007.12.037

Shuai, W., Kong, B., Yang, H., Fu, H., and Huang, H. (2020). Loss of myeloid differentiation protein 1 promotes atrial fibrillation in heart failure with preserved ejection fraction. *ESC Heart Fail.* 7, 626–638. doi: 10.1002/ehf2.12620

Siddiqui, J. A., and Partridge, N. C. (2017). CCL2/Monocyte chemoattractant protein 1 and parathyroid hormone action on bone. *Front. Endocrinol.* 8:49. doi: 10.3389/fendo.2017.00049

Sinder, B. P., Pettit, A. R., and McCauley, L. K. (2015). Macrophages: their emerging roles in bone. *J. Bone Miner. Res.* 30, 2140–2149. doi: 10.1002/jbmr.2735

Singh, A. R., Peirce, S. K., Joshi, S., and Durden, D. L. (2014). PTEN and PI-3 kinase inhibitors control LPS signaling and the lymphoproliferative response in the CD19+ B cell compartment. *Exp. Cell Res.* 327, 78–90. doi: 10.1016/j.yexcr.2014.05.016

Souza, P. P. C., and Lerner, U. H. (2019). Finding a toll on the route: the fate of osteoclast progenitors after toll-like receptor activation. *Front. Immunol.* 10:1663. doi: 10.3389/fimmu.2019.01663

Staron, M., Yang, Y., Liu, B., Li, J., Shen, Y. K., Zuniga-Pflucker, J. C., et al. (2010). gp96, an endoplasmic reticulum master chaperone for integrins and Toll-like receptors, selectively regulates early T and B lymphopoiesis. *Blood* 115, 2380–2390. doi: 10.1182/blood-2009-07-233031

Sun, X., Zhang, J., Wang, Z., Liu, B., Zhu, S., Zhu, L., et al. (2019). Licorice isoliquiritigenin-encapsulated mesoporous silica nanoparticles for osteoclast inhibition and bone loss prevention. *Theranostics* 9, 5183–5199. doi: 10.7150/thno.33376

Tada, Y., Koarada, S., Morito, F., Mitamura, M., Inoue, H., Suematsu, R., et al. (2008). Toll-like receptor homolog RP105 modulates the antigen-presenting cell function and regulates the development of collagen-induced arthritis. *Arthritis Res. Ther.* 10:R121.

Takami, M., Kim, N., Rho, J., and Choi, Y. (2002). Stimulation by toll-like receptors inhibits osteoclast differentiation. *J. Immunol.* 169, 1516–1523. doi: 10.4049/jimmunol.169.3.1516

Takayanagi, H. (2007). Osteoimmunology: shared mechanisms and crosstalk between the immune and bone systems. *Nat. Rev. Immunol.* 7, 292–304. doi: 10.1038/nri2062

Takayanagi, H., Kim, S., Matsuo, K., Suzuki, H., Suzuki, T., Sato, K., et al. (2002). RANKL maintains bone homeostasis through c-Fos-dependent induction of interferon-β. *Nature* 416, 744–749. doi: 10.1038/416744a

Takayanagi, H., Ogasawara, K., Hida, S., Chiba, T., Murata, S., Sato, K., et al. (2000). T-cell-mediated regulation of osteoclastogenesis by signalling cross-talk between RANKL and IFN-γ. *Science* 30, 600–605. doi: 10.1038/35046102

Tang, Y., Sun, F., Li, X., Zhou, Y., Yin, S., and Zhou, X. (2011). Porphyromonas endodontalis lipopolysaccharides induce RANKL by mouse osteoblast in a way different from that of *Escherichia coli* lipopolysaccharide. *J. Endod.* 37, 1653–1658. doi: 10.1016/j.joen.2011.08.015

Taubman, M. A., Valverde, P., Han, X. Z., and Kawai, T. (2005). Immune response: the key to bone resorption in periodontal disease. *J. Periodontol.* 76, 2033–2041. doi: 10.1902/jop.2005.76.11-s.2033

Troutman, T. D., Hu, W., Fulenchek, S., Yamazaki, T., Kurosaki, T., Bazan, J. F., et al. (2012). Role for B-cell adapter for PI3K (BCAP) as a signaling adapter linking Toll-like receptors (TLRs) to serine/threonine kinases PI3K/Akt. *Proc. Natl. Acad. Sci. U.S.A.* 109, 273–278. doi: 10.1073/pnas.1118579109

Tursynbay, Y., Zhang, J., Li, Z., Tokay, T., Zhumadilov, Z., Wu, D., et al. (2016). Pim-1 kinase as cancer drug target: an update. *Biomed. Rep.* 4, 140–146. doi: 10.3892/br.2015.561

Udagawa, N., Takahashi, N., Akatsu, T., Tanaka, H., Sasaki, T., Nishihara, T., et al. (1990). Origin of osteoclasts: mature monocytes and macrophages are capable of differentiating into osteoclasts under a suitable microenvironment prepared by bone marrow-derived stromal cells. *Proc. Natl. Acad. Sci. U.S.A.* 87, 7260–7264. doi: 10.1073/pnas.87.18.7260

Ueki, Y., Lin, C. Y., Senoo, M., Ebihara, T., Agata, N., Onji, M., et al. (2007). Increased myeloid cell responses to M-CSF and RANKL cause bone loss and inflammation in SH3BP2 "cherubism" mice. *Cell* 128, 71–83. doi: 10.1016/j.cell.2006.10.047

Vaananen, K. (2005). Mechanism of osteoclast mediated bone resorption–rationale for the design of new therapeutics. *Adv. Drug Deliv. Rev.* 57, 959–971. doi: 10.1016/j.addr.2004.12.018

Vanhaesebroeck, B., Ali, K., Bilancio, A., Geering, B., and Foukas, L. C. (2005). Signalling by PI3K isoforms: insights from gene-targeted mice. *Trends Biochem. Sci.* 30, 194–204. doi: 10.1016/j.tibs.2005.02.008

Varol, C., Mildner, A., and Jung, S. (2015). Macrophages: development and tissue specialization. *Annu. Rev. Immunol.* 33, 643–675. doi: 10.1146/annurev-immunol-032414-112220

Wang, X., Quinn, P. J., and Yan, A. (2015). Kdo2-lipid A: structural diversity and impact on immunopharmacology. *Biol. Rev.* 90, 408–427. doi: 10.1111/brv.12114

Wang, Y., Brooks, S. R., Li, X., Anzelon, A. N., Rickert, R. C., and Carter, R. H. (2002). The physiologic role of CD19 cytoplasmic tyrosines. *Immunity* 17, 501–514. doi: 10.1016/s1074-7613(02)00426-0

Watanabe, Y., Nagai, Y., and Takatsu, K. (2013). Activation and regulation of the pattern recognition receptors in obesity-induced adipose tissue inflammation and insulin resistance. *Nutrients* 5, 3757–3778. doi: 10.3390/nu5093757

Watanabe, Y., Nakamura, T., Ishikawa, S., Fujisaka, S., Usui, I., Tsuneyama, K., et al. (2012). The Radioprotective 105/MD-1 complex contributes to diet-induced obesity and adipose tissue Inflammation. *Diabetes Metab. Res. Rev.* 615, 1199–1209. doi: 10.2337/db11-1182

Weekes, M. P., Antrobus, R., Talbot, S., Hör, S., Simecek, N., Smith, D., et al. (2012). Proteomic plasma membrane profiling reveals an essential role for gp96 in the cell surface expression of LDLR family members, including the LDL Receptor and LRP6. *J. Proteome Res.* 11, 1475–1484. doi: 10.1021/pr201135e

Werner, M., Hobeika, E., and Jumaa, H. (2010). Role of PI3K in the generation and survival of B cells. *Immunol. Rev.* 237, 55–71. doi: 10.1111/j.1600-065x.2010.00934.x

Westhrin, M., Kovcic, V., Zhang, Z., Moen, S., Nedal, T., Bondt, A., et al. (2020). Monoclonal immunoglobulins promote bone loss in multiple myeloma. *Blood* 136, 2656–2666. doi: 10.1182/blood.2020006045

Wezel, A., de Vries, M. R., Maassen, J. M., Kip, P., Peters, E. A., Karper, J. C., et al. (2016). Deficiency of the TLR4 analogue RP105 aggravates vein graft disease by inducing a pro-inflammatory response. *Sci. Rep.* 6:24248.

Wezel, A., van der Velden, D., Maassen, J. M., Lagraauw, H. M., de Vries, M. R., Karper, J. C., et al. (2015). RP105 deficiency attenuates early atherosclerosis via decreased monocyte influx in a CCR2 dependent manner. *Atherosclerosis* 238, 132–139. doi: 10.1016/j.atherosclerosis.2014.11.020

Xiong, Q., Zhang, L., Ge, W., and Tang, P. (2016). The roles of interferons in osteoclasts and osteoclastogenesis. *Joint Bone Spine* 83, 276–281. doi: 10.1016/j.jbspin.2015.07.010

Yagi, M., Miyamoto, T., Sawatani, Y., Iwamoto, K., Hosogane, N., Fujita, N., et al. (2005). DC-STAMP is essential for cell-cell fusion in osteoclasts and foreign body giant cells. *J. Exp. Med.* 202, 345–351. doi: 10.1084/jem.20050645

Yang, D., and Wan, Y. (2019). Molecular determinants for the polarization of macrophage and osteoclast. *Semin. Immunopathol.* 41, 551–563. doi: 10.1007/s00281-019-00754-3

Yang, J., Guo, X., Yang, J., Ding, J. W., Li, S., Yang, R., et al. (2015). RP105 protects against apoptosis in ischemia/reperfusion-induced myocardial damage in rats by suppressing TLR4-mediated signaling pathways. *Cell. Physiol. Biochem.* 36, 2137–2148. doi: 10.1159/000430180

Yang, Y., Wang, C., Cheng, P., Zhang, X., Li, X., Hu, Y., et al. (2018a). CD180 Ligation Inhibits TLR7- and TLR9-mediated activation of macrophages and dendritic cells through the Lyn-SHP-1/2 Axis in Murine Lupus. *Front. Immunol.* 9:2643. doi: 10.3389/fimmu.2018.02643

Yang, Y., Yang, J., Liu, X. W., Ding, J. W., Li, S., Guo, X., et al. (2018b). Down-Regulation of miR-327 alleviates ischemia/reperfusion-induced myocardial damage by targeting RP105. *Cell. Physiol. Biochem.* 49, 1049–1063.

Yazawa, N., Fujimoto, M., Sato, S., Miyake, K., Asano, N., Nagai, Y., et al. (2003). CD19 regulates innate immunity by the toll-like receptor RP105 signaling in B lymphocytes. *Blood* 102, 1374–1380. doi: 10.1182/blood-2002-11-3573

Yoon, S. I., Hong, M., and Wilson, I. A. (2011). An unusual dimeric structure and assembly for TLR4 regulator RP105-MD-1. *Nat. Struct. Mol. Biol.* 18, 1028–1035. doi: 10.1038/nsmb.2106

Yoon, S. I., Hong, M., Han, G. W., and Wilson, I. A. (2010). Crystal structure of soluble MD-1 and its interaction with lipid IVa. *Proc. Natl. Acad. Sci. U.S.A.* 107, 10990–10995. doi: 10.1073/pnas.1004153107

Yoon, S., Lee, Y., Kim, H., Lee, Z., Hyung, S., Lee, S., et al. (2009). Lyn inhibits osteoclast differentiation by interfering with PLCgamma1-mediated Ca2+ signaling. *FEBS Lett.* 583, 1164–1170. doi: 10.1016/j.febslet.2009.03.005

You, M., Dong, G., Li, F., Ma, F., Ren, J., Xu, Y., et al. (2017). Ligation of CD180 inhibits IFN-α signaling in a Lyn-PI3K-BTK-dependent manner in B cells. *Cell. Mol. Immunol.* 14, 192–202. doi: 10.1038/cmi.2015.61

Yu, C. H., Micaroni, M., Puyskens, A., Schultz, T. E., Yeo, J. C., Stanley, A. C., et al. (2015). RP105 engages phosphatidylinositol 3-kinase p110delta to facilitate

the trafficking and secretion of cytokines in macrophages during mycobacterial infection. *J. Immunol.* 195, 3890–3900. doi: 10.4049/jimmunol.1500017

Yu, X., Hu, Y., Freire, M., Yu, P., Kawai, T., and Han, X. (2018). Role of toll-like receptor 2 in inflammation and alveolar bone loss in experimental peri-implantitis versus periodontitis. *J. Periodontal Res.* 53, 98–106. doi: 10.1111/jre.12492

Zarember, K. A., and Godowski, P. J. (2002). Tissue expression of human Toll-like receptors and differential regulation of Toll-like receptor mRNAs in leukocytes in response to microbes, their products, and cytokines. *J. Immunol.* 168, 554–561. doi: 10.4049/jimmunol.168.2.554

Zhang, P., Liu, J. Z., Xu, Q. A., Harber, G., Feng, X., Michalek, S. M., et al. (2011). TLR2-dependent Modulation of Osteoclastogenesis by *Porphyromonas gingivalis* through Differential Induction of NFATc1 and NF-kappa B. *J. Biol. Chem.* 286, 24159–24169. doi: 10.1074/jbc.m110.198085

Zhang, Z., La Placa, D., Nguyen, T., Kujawski, M., Le, K., Li, L., et al. (2019). CEACAM1 regulates the IL-6 mediated fever response to LPS through the RP105 receptor in murine monocytes. *BMC Immunol.* 20:7. doi: 10.1186/s12865-019-0287-y

Zhao, B., Grimes, S. N., Li, S., Hu, X., and Ivashkiv, L. B. (2012). TNF-induced osteoclastogenesis and inflammatory bone resorption are inhibited by transcription factor RBP-J. *J. Exp. Med.* 209, 319–334. doi: 10.1084/jem.20111566

Zhao, B., Takami, M., Yamada, A., Wang, X., Koga, T., Hu, X., et al. (2009). Interferon regulatory factor-8 regulates bone metabolism by suppressing osteoclastogenesis. *Nat. Med.* 15, 1066–1071. doi: 10.1038/nm.2007

Conflict of Interest: The authors declare that the research was conducted in the absence of any commercial or financial relationships that could be construed as a potential conflict of interest.

Publisher's Note: All claims expressed in this article are solely those of the authors and do not necessarily represent those of their affiliated organizations, or those of the publisher, the editors and the reviewers. Any product that may be evaluated in this article, or claim that may be made by its manufacturer, is not guaranteed or endorsed by the publisher.

frontiers in Cell and Developmental Biology

ORIGINAL RESEARCH
published: 26 August 2021
doi: 10.3389/fcell.2021.705291

Autophagy-Related Genes and Long Noncoding RNAs Signatures as Predictive Biomarkers for Osteosarcoma Survival

*Jian Zhang[1,2], Rui Ding[1], Tianlong Wu[1,3], Jingyu Jia[1] and Xigao Cheng[1,2,3]**

[1] Department of Orthopedics, The Second Affiliated Hospital of Nanchang University, Nanchang, China, [2] Institute of Orthopedics of Jiangxi Province, Nanchang, China, [3] Institute of Minimally Invasive Orthopedics, Nanchang University, Nanchang, China

Osteosarcoma is a common malignant tumor that seriously threatens the lives of teenagers and children. Autophagy is an intracellular metabolic process mediated by autophagy-related genes (ARGs), which is known to be associated with the progression and drug resistance of osteosarcoma. In this study, RNA sequence data from TARGET and genotype-tissue expression (GTEx) databases were analyzed. A six autophagy-related long noncoding RNAs (ARLs) signature that accurately predicted the clinical outcomes of osteosarcoma patients was identified, and the relations between immune response and the ARLs prognostic signature were examined. In addition, we obtained 30 ARGs differentially expressed among osteosarcoma tissue and healthy tissue, and performed functional enrichment analysis on them. To screen for prognostic-related ARGs, univariate and LASSO Cox regression analyses were successively applied. Then, multivariate regression analysis was used to complete construction of the prognostic signature of ARGs. Based on the risk coefficient, we calculated the risk score and grouped the patients. Survival analysis showed that high-risk patients evolve with poor prognosis. And we verified the prognosis model in the GSE21257 cohort. Finally, verification was conducted by qRT-PCR and western blot to measure the expression of genes. The results show that autophagy-related marker models may provide a new therapeutic and diagnostic target for osteosarcoma.

Keywords: osteosarcoma, autophagy, lncRNA, prognostic signature, biomarkers

OPEN ACCESS

Edited by:
Amélie E. Coudert, Université Paris Diderot, France

Reviewed by:
Wenjie Zheng, Affiliated Hospital of Nantong University, China
Dominique Modrowski, Institut National de la Santé et de la Recherche Médicale (INSERM), France

***Correspondence:**
Xigao Cheng
228206846@qq.com

Specialty section:
This article was submitted to Molecular and Cellular Pathology, a section of the journal Frontiers in Cell and Developmental Biology

Received: *05 May 2021*
Accepted: *04 August 2021*
Published: *26 August 2021*

Citation:
Zhang J, Ding R, Wu T, Jia J and Cheng X (2021) Autophagy-Related Genes and Long Noncoding RNAs Signatures as Predictive Biomarkers for Osteosarcoma Survival. Front. Cell Dev. Biol. 9:705291. doi: 10.3389/fcell.2021.705291

INTRODUCTION

Osteosarcoma is a common and extremely threatening bone malignant tumor, occurs usually in adolescents, and children (Kansara et al., 2014). The current treatment methods include surgical resection and chemotherapy before and after surgery, for the patients with non-metastatic osteosarcoma, the 5-year survival rate of can reach 70% (Isakoff et al., 2015). However, about the patients with metastatic or recurrent osteosarcoma, the 5-year overall survival rate is only 20%, and has changed little over the past 30 years (Goorin et al., 2003; Kempf-Bielack et al., 2005; Meyers et al., 2011). In addition, osteosarcoma often develops resistance to standard chemotherapy regimens, which seriously impacts patient prognosis (Brown et al., 2017; Lilienthal and Herold, 2020). Therefore, seeking potential targets for effective osteosarcoma therapy is particularly important and necessary.

Autophagy is the main intracellular metabolic degradation process modulated by autophagy-related genes (ARGs), autophagosomes phagocytose cytoplasmic materials, then degradation, and recycling by lysosomes (Mizushima and Komatsu, 2011; Boya et al., 2013). In cancer, autophagy can exert two functions, either inhibitory and stimulatory actions, the specific role depends on the occurrence, progression, and type of cancer (Nazio et al., 2019; Mizushima and Levine, 2020). Deletion of the autophagy gene BECN1 is common in breast, ovarian, and prostate cancers (Kondo and Kondo, 2006). In various mouse models, the systemic or tissue-specific deletion of genes essential for autophagy can lead to defects in autophagy, and which accelerates the occurrence of tumors. For example, $becn1^{+/-}$ mice spontaneously develop malignant tumors, including lymphoma, lung cancer, and liver cancer (Liang et al., 1999; Qu et al., 2003). Autophagy also affects certain cellular processes, such as the epithelial to mesenchymal transition or migration, and therefore inhibits tumor progression and metastasis (White et al., 2015; Li et al., 2020). In short, autophagy can promote or inhibit cancer progression and metastasis at different stages of the disease. The link between cancer and autophagy is complex and requires further research.

Long noncoding RNAs (lncRNAs) have many functions (Ulitsky and Bartel, 2013). LncRNA is not only involved in the normal biological functions, but also participate in the process of a variety of diseases, including those related to tumor occurrence, development, and metastasis (Martens-Uzunova et al., 2014; Bartonicek et al., 2016). There is ample evidence that lncRNAs mediate the transcription and post-transcriptional levels of ARGs to regulate tumor development (Chen J.F. et al., 2018; Cai et al., 2019; Xu et al., 2019). However, there has been no systematic evaluation of the characteristics of ARGs in patients with osteosarcoma and their correlation with overall survival. Therefore, the purpose of our study was to identify new autophagy-related markers for the diagnosis and prognosis of osteosarcoma.

In this research, we identified a six autophagy-related lncRNAs (ARLs) signature has accurate predictive properties for the outcome of osteosarcoma patients. Then, we explored the role of the immune responses in the prognosis of autophagy. We also identified three ARGs that showed good performance for predicting the clinical outcomes of osteosarcoma patients. In a separate dataset (GSE21257), we evaluated their accurate prediction for the prognosis of patients with osteosarcoma. Our results show that autophagy-related marker models may provide potential prognostic and diagnostic targets for osteosarcoma therapy.

MATERIALS AND METHODS

Data Collection and Autophagy-Related Genes

The RNA expression data of healthy tissues were collected from the genotype-tissue expression database.[1] The fragments per kilobase of transcript per million mapped reads (FPKM) values in the expression data were converted using $\log2(x + 0.001)$. The RNA sequence data and osteosarcoma patient characteristics were collected from the TARGET database.[2] TARGET and GTEx data sets were merged and batch-to-batch variation was removed in the "sva" R package. The FPKM values were used to indicate gene expression levels.

A microarray data set, named the GSE21257 data set, was obtained by downloading the gene expression data of 53 patients with osteosarcoma and their corresponding clinical information from the gene expression omnibus database.[3] Gene expression levels are shown as normalized signal values. The Human Autophagy Database[4] was used to obtain ARGs.

Differentially Expressed ARGs and Functional Annotation

LogFC > 1 and $p < 0.05$ as the threshold, differentially expressed ARGs (DE-ARGs) and lncRNAs in osteosarcoma, and healthy tissues were identified using the limma package. gene ontology (GO) and kyoto encyclopedia of genes and genomes (KEGG) pathway analyses were performed for the DE-ARGs. The construction and visualization of the protein-protein interaction (PPI) network diagram are implemented by online tools STRING and Cytoscape software.

Identification and Construction of Prognostic Signatures

By univariate Cox regression analysis, we determined the ARGs that were associated to the survival in osteosarcoma patients from TARGET dataset ($p < 0.01$). Next, we used LASSO Cox regression analysis to filter the best prognostic genes. Finally, a prognostic signature was established by multivariate Cox regression analysis, which composed of three ARGs.

In order to obtain ARLs, in the TARGET database, we calculated the Pearson correlation coefficient to determine the correlation between the expression levels of lncRNAs, and ARGs. With the absolute value of the correlation coefficient greater than 0.4 ($|R| > 0.4$) and the P-value less than 0.05 ($P < 0.05$) as the standard, ARLs was screened out. Subsequently, to construct an ARLs prognosis model, we selected the differentially expressed ARLs, applied univariate Cox regression to screen for prognostic ARLs, and then constructed a ARLs prognostic signature including six ARLs by LASSO Cox analysis. The following formula was used to calculated risk score of each patient:

$$Risk\ score = \sum_{i=1}^{n} \left(Coef_i * x_i\right)$$

the $Coef_i$ means risk coefficients, x_i is the ARGs or ARLs expression value.

[1] https://gtexportal.org/

[2] https://portal.gdc.cancer.gov/

[3] https://www.ncbi.nlm.nih.gov/geo/

[4] http://www.autophagy.lu/

Evaluation and Verification of the Prognostic Signature

We rank the risk scores of all patients (calculated by the above formula), take the median value, and divide the patients based on this. Using Kaplan–Meier curve, we distinguished the survival of the two groups of patients. Based on the receiver operating characteristic (ROC) curve, we evaluated the prediction effectiveness of the signature. We also performed univariate and multivariate Cox regression analysis to assess whether the risk score was independent of other clinical variables, including age, sex, and metastasis. Subsequently, according to the clinical characteristics of patients, subgroup analyses were performed for individual genes in the autophagy-related prognostic models. Then, according to the patient's clinical information and risk, we used the "rms" package to establish a nomogram for clinical evaluation. A calibration curve was drawn to evaluate the agreement between the actual clinical outcome and the predicted clinical outcome, and the C index was calculated for the nomogram model. An independent dataset (GSE21257) was used to testify the reliability of the nomogram model and ARGs prognostic signature.

Gene Set Enrichment Analysis and Single Sample GSEA

Gene set enrichment analysis (GSEA) software (version 4.1.0) was used to evaluate the functional phenotype between the high-risk group and the low-risk group based on the ARLs prognostic signature. GO gene sets (go.bp.v7.4.symbols.gmt) were downloaded from Molecular Signatures Database as the reference gene set (Subramanian et al., 2005). Nominal p-value < 0.05 and NES (Normalized Enrichment Score) > 2 were set as the cut-off. ssGSEA was used to evaluate differential expression of immune cell infiltration and immune-related functions between the two groups of patients.

Cell Lines and Cell Cultures

The human osteoblast cell line hFOB1.19 and two human osteosarcoma cell lines (U2OS and 143B) were purchased from the National Collection of Authenticated Cell Cultures (Shanghai, China). The cells were cultured in Dulbecco's modified Eagle's medium (DMEM, Gibco) containing 10% fetal bovine serum (FBS, Gibco) and 1% penicillin/streptomycin (Thermo Fisher Scientific, United States). The human osteoblast cell line hFOB 1.19 was cultured at 34°C with 5% CO_2, and the osteosarcoma cell lines were cultured at 37°C with 5% CO_2 in a humid atmosphere.

RNA Extraction and Reverse-Transcription Quantitative PCR

Total RNA of cells was extracted with TRIzol reagent (Invitrogen, United States), and reverse transcribed into cDNA with PrimeScript^{TM} RT reagent Kit (Takara, Japan). Reverse-transcription quantitative PCR (RT-qPCR) was performed with SYBR Green qPCR Master Mixes (Thermo Fisher Scientific, United States). Glyceraldehyde 3-phosphate dehydrogenase (GAPDH) was used as the normalization control for lncRNA and mRNA. Primer information is provided in **Supplementary Table 1**.

Western Blot

To extract total protein from cells, RIPA lysis buffer (Beyotime, China) was used. To quantify proteins, a BCA protein quantification kit (Beyotime, China) was used. Proteins were separated on SDS-polyacrylamide gel and transferred to a PVDF membrane (Millipore, United States). The membrane was blocked with skim milk, incubated with the primary antibody overnight at 4°C, and incubated with the secondary antibody for 2 h at room temperature. The antibodies used in this study were AMBRA1 (1:500, Proteintech, China), MYC (1:1000, Abcam, United Kingdom), VEGFA (1:1000, Abcam, United Kingdom), GAPDH (1:5000, Abcam, United Kingdom), and goat anti-rabbit secondary antibody (1:5000; Abcam, United Kingdom). The protein bands were quantified using Image J software (version 1.8.0), and GADPH was used as the loading control.

Statistical Analysis

R v4.0.4 and GraphPad Prism v9.2 were used for the statistical analysis. Student's t-test was used to compare differences between two groups. Differences were considered to be significant at $p < 0.05$ if not specified.

RESULTS

Identification of Autophagy-Related lncRNAs and Signature Establishment

From the TARGET ($n = 84$) and GTEx ($n = 396$) RNA sequence data, 222 ARGs, and 994 lncRNAs were extracted. Based on the parameters $p < 0.05$ and logFC ≥ 1, we identified 252 different expressed lncRNAs (DELs). The heatmap and volcano plot showed DELs (**Figures 1A,B**). Then, by calculating the Pearson correlation coefficient between the expression of the ARGs and lncRNAs, using $|R| > 0.4$ and $p < 0.05$ as the selection criteria, and we obtained 552 ARLs. As shown in the Venn diagram demonstrated that there were 143 lncRNAs in the intersection of DELs and ARLs (**Figure 1C**). After univariate Cox regression analysis of the 143 lncRNAs, 13 prognostic ARLs were obtained (**Figure 1D**). Last, further LASSO Cox regression analysis determined the prognostic signature, which comprised six ARLs (**Figures 1E,F** and **Supplementary Table 2**).

Evaluation of the ARLs Prognostic Signature

Survival analysis showed that high-risk patients had the worse outcomes (**Figure 2A**). According to the ROC analysis, the predictive performance of the ARLs signature for 1-, 3-, and 5-year survival of osteosarcoma patients was excellent, with AUC values of 0.813, 0.814, and 0.802, respectively (**Figure 2B**). The PCA revealed different distribution patterns for the two groups of patients (**Figure 2C**). The risk score distribution, survival status, and six ARLs heat map were obtained (**Figures 2D–F**).

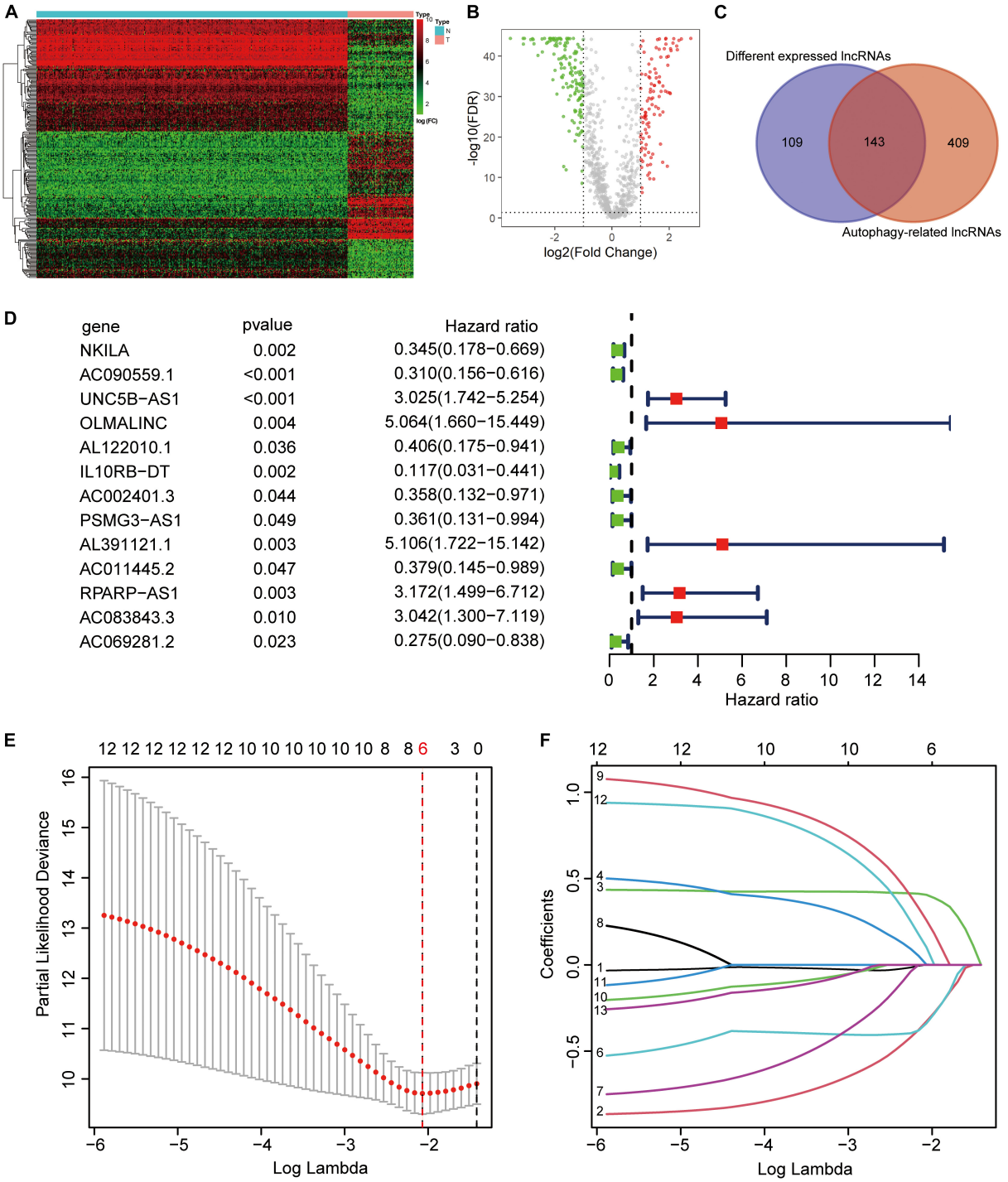

FIGURE 1 | Construction of autophagy-related lncRNA signature. **(A)** Heatmap of the differentially expression long noncoding RNAs (lncRNAs). **(B)** Volcano plot. **(C)** Venn diagram. **(D)** Univariate cox regression showed 13 lncRNAs related to osteosarcoma survival. **(E,F)** Lasso regression for lncRNAs in univariate cox regression. Coefficients refers to the risk coefficient corresponding to each gene.

The univariate Cox and multivariate Cox analyses showed that metastasis and risk score were significantly correlated with overall survival (**Figures 2G,H**). The risk score of patients with metastasis tended to be higher (**Supplementary Figure 1C**), although the difference was not significant (p = 0.071). In the Kaplan–Meier curves for single genes, the expression of AL391121.1 and UNC5B.AS1 was negatively correlated with prognosis of osteosarcoma patients, whereas the expression of AC090559.1, and IL10RB.DT was positively correlated (**Figures 2I–N**).

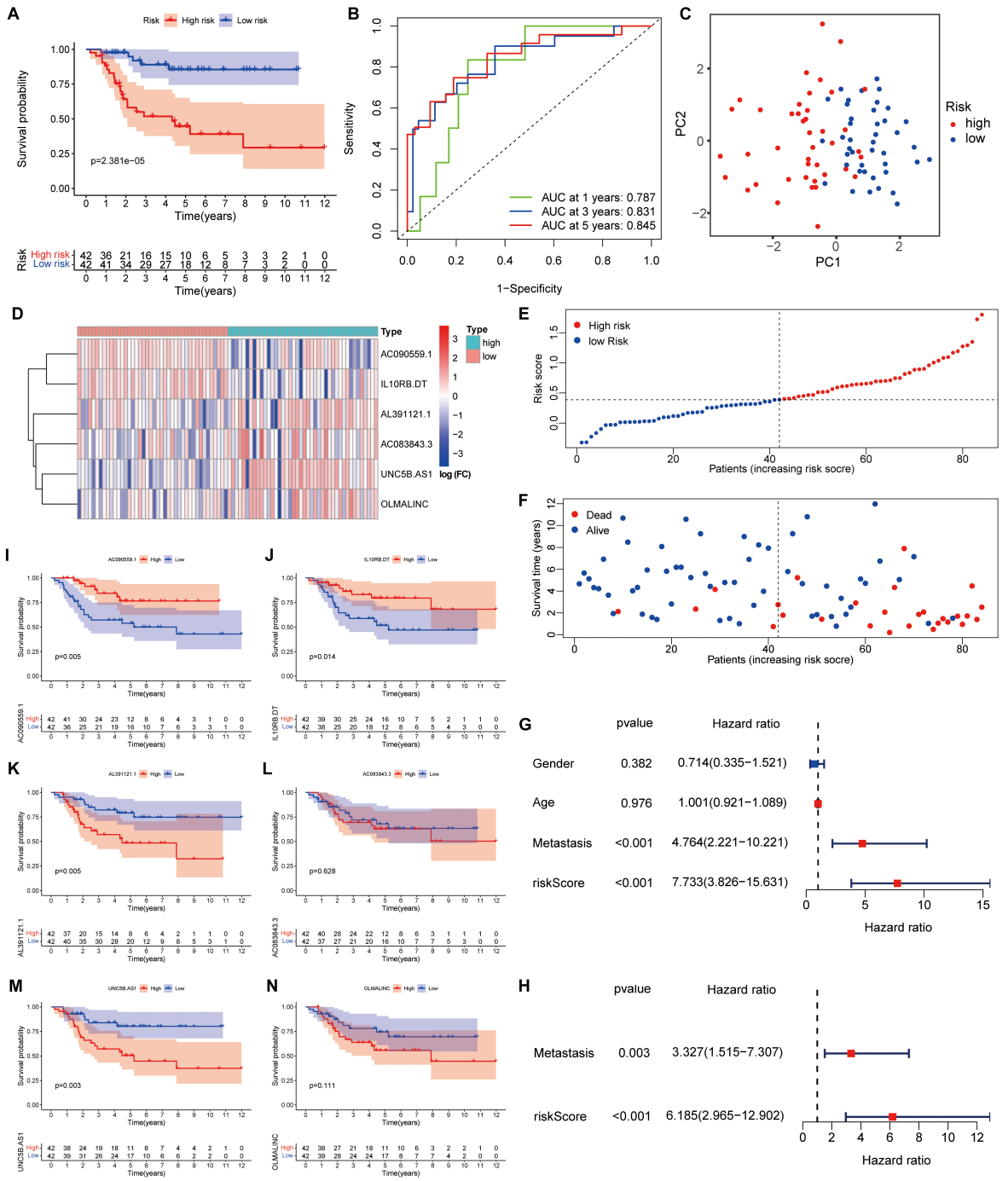

FIGURE 2 | A risk signature with the six autophagy-related lncRNA. **(A)** Kaplan–Meier survival curve analysis. **(B)** The AUC for the prediction of 1, 3, 5-year survival rate. **(C)** PCA based on the autophagy-related long noncoding RNAs (lncRNAs) signature. **(D)** Heatmap of the six key lncRNAs expressed between the high and low risk group. **(E,F)** Risk score analysis of the signature. **(G,H)** Univariate and multivariate cox analysis. **(I–N)** Kaplan–Meier survival curves for the six prognostic lncRNAs in TARGET dataset.

Gene Set Enrichment Analysis and Immune Score Analysis

The GSEA revealed that immune-related biological processes were significantly enriched in the low-risk group, including the T cell receptor-signaling pathway, integrin mediated-signaling pathway, and response to interferon gamma (**Figure 3A**). This result suggested that activation of immunomodulatory functions in the low-risk group led to a better prognosis. On the basis of ssGSEA, the correlations between the risk score and immune cells and immune-related functions were determined, and as shown in the boxplots in **Figures 3B,C**, there were significant differences

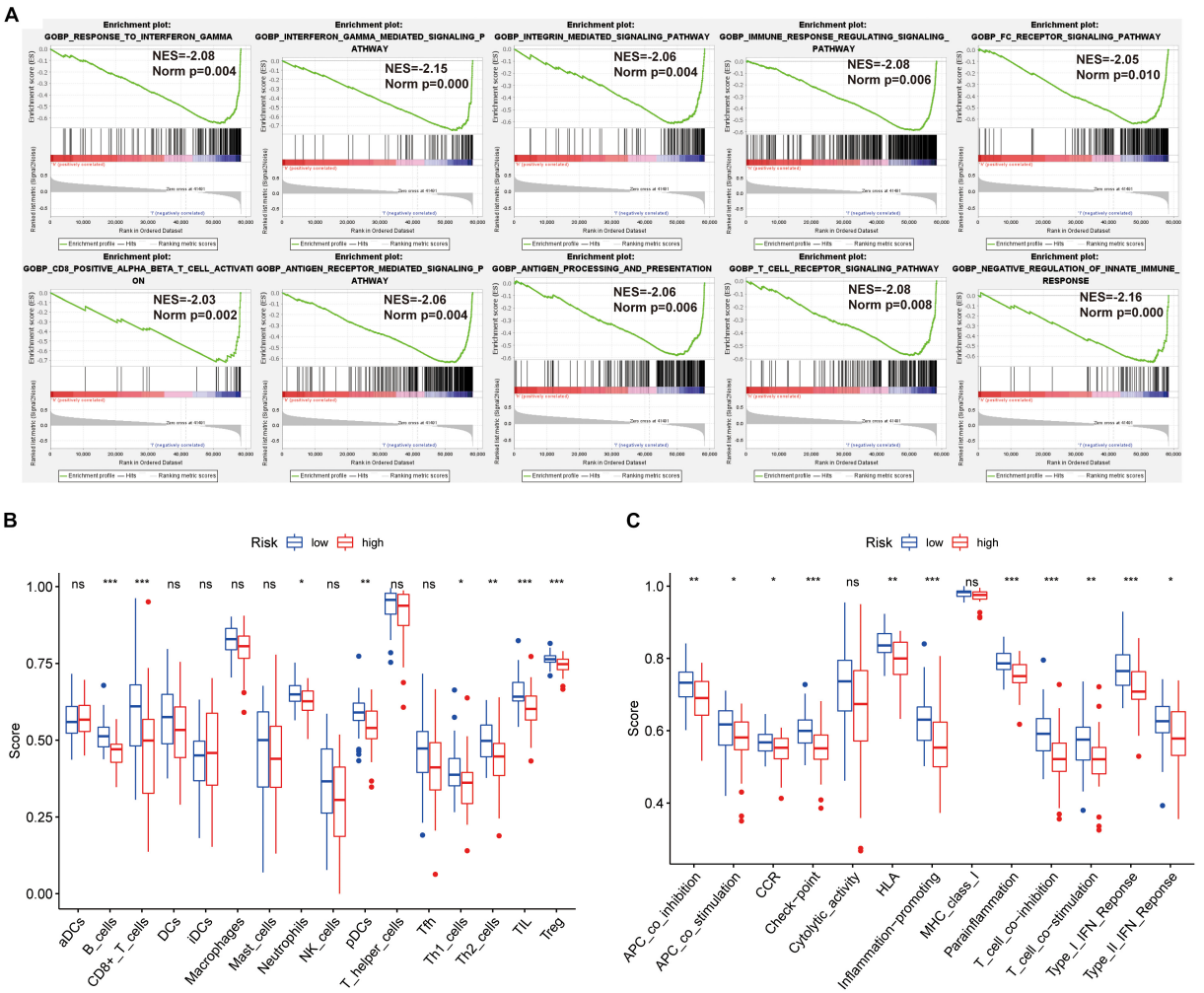

FIGURE 3 | GSEA of osteosarcoma patients based on the autophagy-related lncRNA prognostic signature. **(A)** GSEA results show significant enrichment of immune- and autophagy-related biological process in the low-risk patients. **(B,C)** Relationship between riskscore and immune cell infiltration and related functions *via* ssGSEA analysis. The score refers to the immune score, the higher the score, and the deeper the degree of immune cell infiltration. $^{*}P < 0.05$, $^{**}P < 0.01$, and $^{***}P < 0.001$.

between low-risk and high-risk groups for B cells, $CD8^{+}$ T cells, TIL, Treg, immune checkpoint, regulation of inflammation, and T cell co-inhibition.

Differentially Expression of ARGs and Functional Analysis

Thirty DE-ARGs were detected, of which 12 were up-regulated and 18 were down-regulated. The DE-ARGs between osteosarcoma and healthy tissues are shown in a heat map, and volcano plot in **Figures 4A,B**. The expression levels of the 30 DE-ARGs between the two groups were displayed with box plots (**Figure 4C**). The PPI network illustrated the relations between the DE-ARGs (**Figure 4D**).

To elucidate the underlying mechanisms of the DE-ARGs, functional and pathway enrichment analyses were used. In biological processes, the DE-ARGs primarily participated in macroautophagy and regulation of autophagy, and macroautophagy (**Figure 4E**). In molecular functions, enriched terms were primarily related to ubiquitin protein ligase binding, ionotropic glutamate receptor activity, and protein serine/threonine kinase activity (**Figure 4F**). In cellular components, enriched terms were primarily related to autophagosome, inclusion body, and vacuolar membrane (**Figure 4G**). KEGG analysis revealed that the DE-ARGs were mainly enriched in autophagy-animal pathways (**Figure 4H**).

Establishment of ARGs Prognostic Signature

Using univariate Cox regression analysis for the 222 ARGs, we identified 12 prognostic ARGs (**Figure 5A**). To construct the signature, LASSO Cox regression analysis was performed to these 12 ARGs, from which seven genes were selected (**Figures 5B,C**). At last, we used multivariate Cox regression analysis to build a ARGs prognostic signature, and three genes

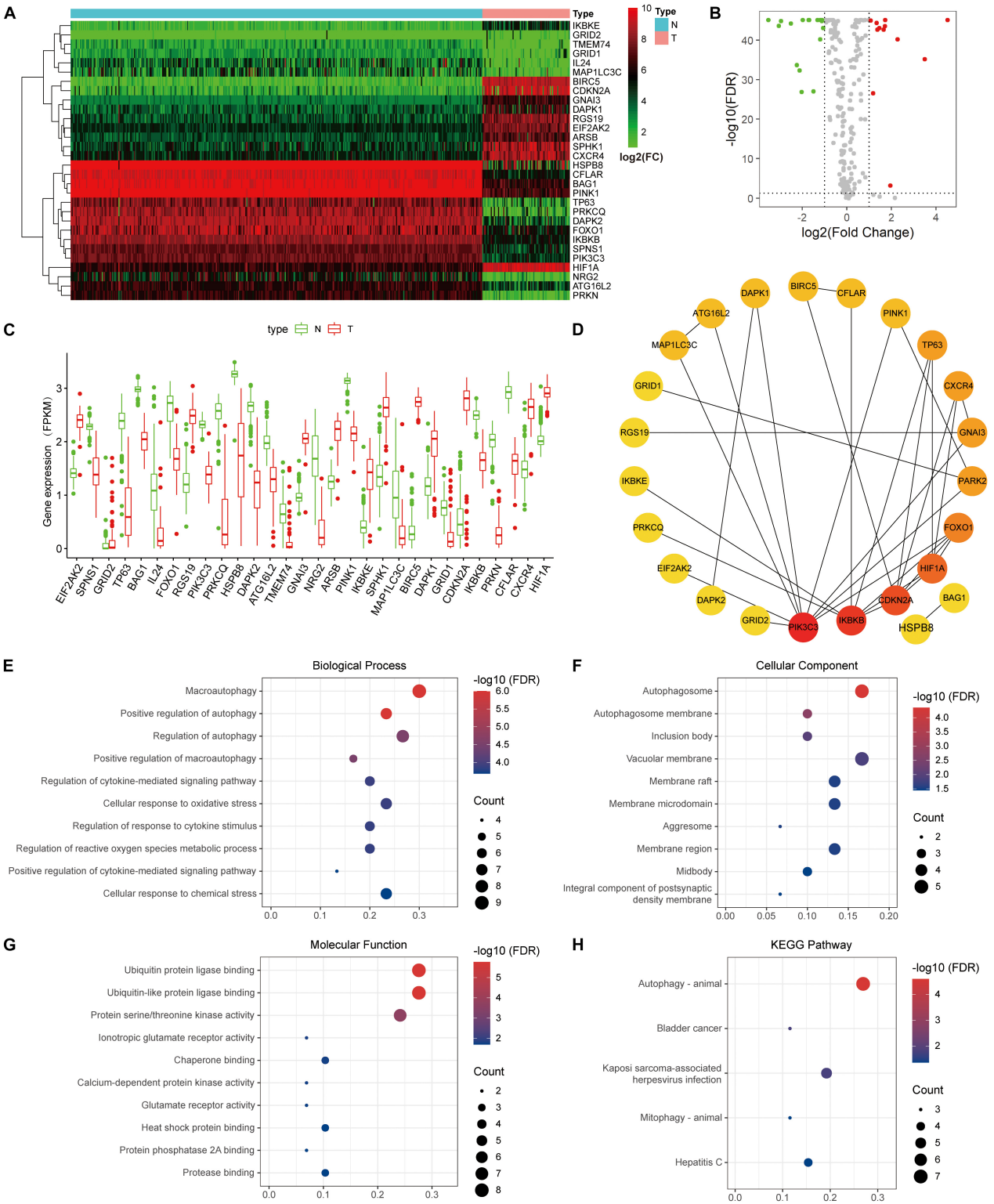

FIGURE 4 | Differentially expressed autophagy-related genes (ARGs) and functional enrichment. **(A)** Heatmap of the differentially expression ARGs. **(B)** Volcano plot. **(C)** The expression patterns of 30 ARGs in osteosarcoma and normal samples. The *X*-axis represents the differentially expressed ARGs and the *Y*-axis represents their gene expression levels (FPKM). **(D)** Protein-protein interaction network of the ARGs. **(E–G)** Functional enrichment of the 30 ARGs including biological process, cellular component and molecular function. **(H)** KEGG pathway analysis.

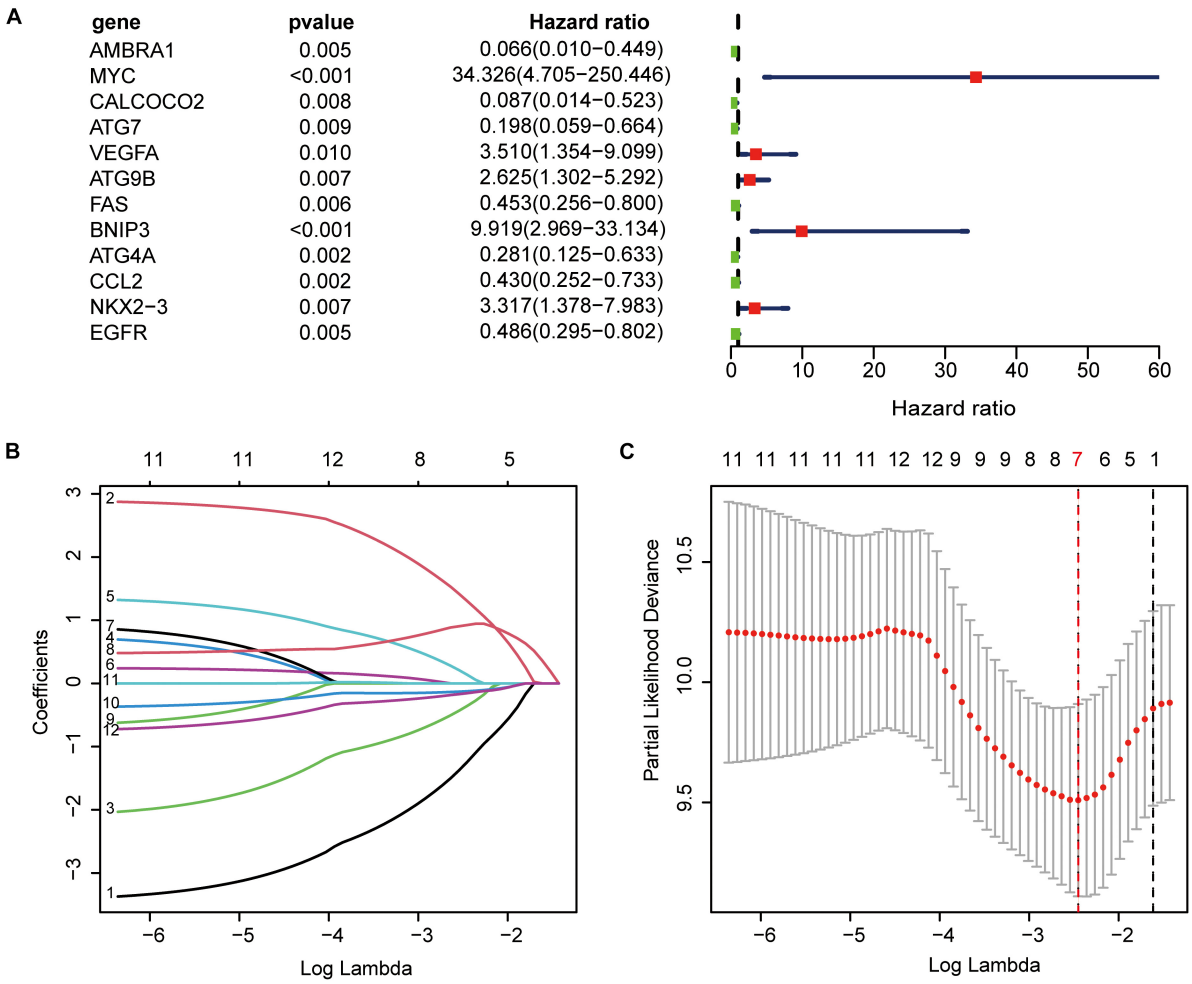

FIGURE 5 | Construction of the autophagy-related prognostic signature. **(A)** Univariate cox regression showed 12 ARGs related to osteosarcoma survival. **(B)** LASSO coefficient spectrum of the 12 genes. Coefficients refers to the risk coefficient corresponding to each gene. **(C)** Selection of the optimal λ value.

and their risk coefficients were identified: AMBRA1, MYC, and VEGFA (**Supplementary Table 3**).

Evaluation of the ARGs Prognostic Signature

We performed survival analysis to evaluate the signature. The Kaplan–Meier curve revealed that high-risk patients were accompanied by poor prognosis (**Figure 6A**). The ROC curve showed the prediction capability of the ARGs prognostic signature for 1-, 3- and 5-year survival rates in the TARGET cohort. The curve (AUC) was 0.791, 0.797, and 0.812, respectively (**Figure 6B**). Principal component analysis (PCA) showed the different distribution patterns for the two groups of patients (**Figure 6C**). The heatmap shows the expression profiles of these key genes (**Figure 6D**). The dot plot shows the distribution of individual patients (**Figures 6E,F**). In order to understand the role of these three prognostic genes in osteosarcoma, and Kaplan–Meier curve was drawn for them. AMBRA1 is significantly associated to the survival of osteosarcoma and plays a protective role (**Figures 6G–I**).

Clinical Relevance of the ARGs Prognostic Signature

The univariate and multivariate Cox regression analysis results revealed that the signature and tumor metastasis were two independent prognostic factors (**Figures 7A,B**). The relationship between the three key genes and clinical characteristics was displayed with box plot, it shows that in the low-risk patients, and the expression level of AMBRA1 is highly (**Figure 7C**). However, the opposite trend was found for the expression of MYC and VEGFR (**Figures 7D,E**). It is worth noting that only MYC was associated with metastasis, and that it was highly expressed in patients of the metastatic group (**Figure 7D**). And we attempted to determine whether the metastatic status was associated with the risk score, calculated based on the autophagy related genes prognostic signature (ARGs signature). The results revealed that osteosarcoma patients with metastasis

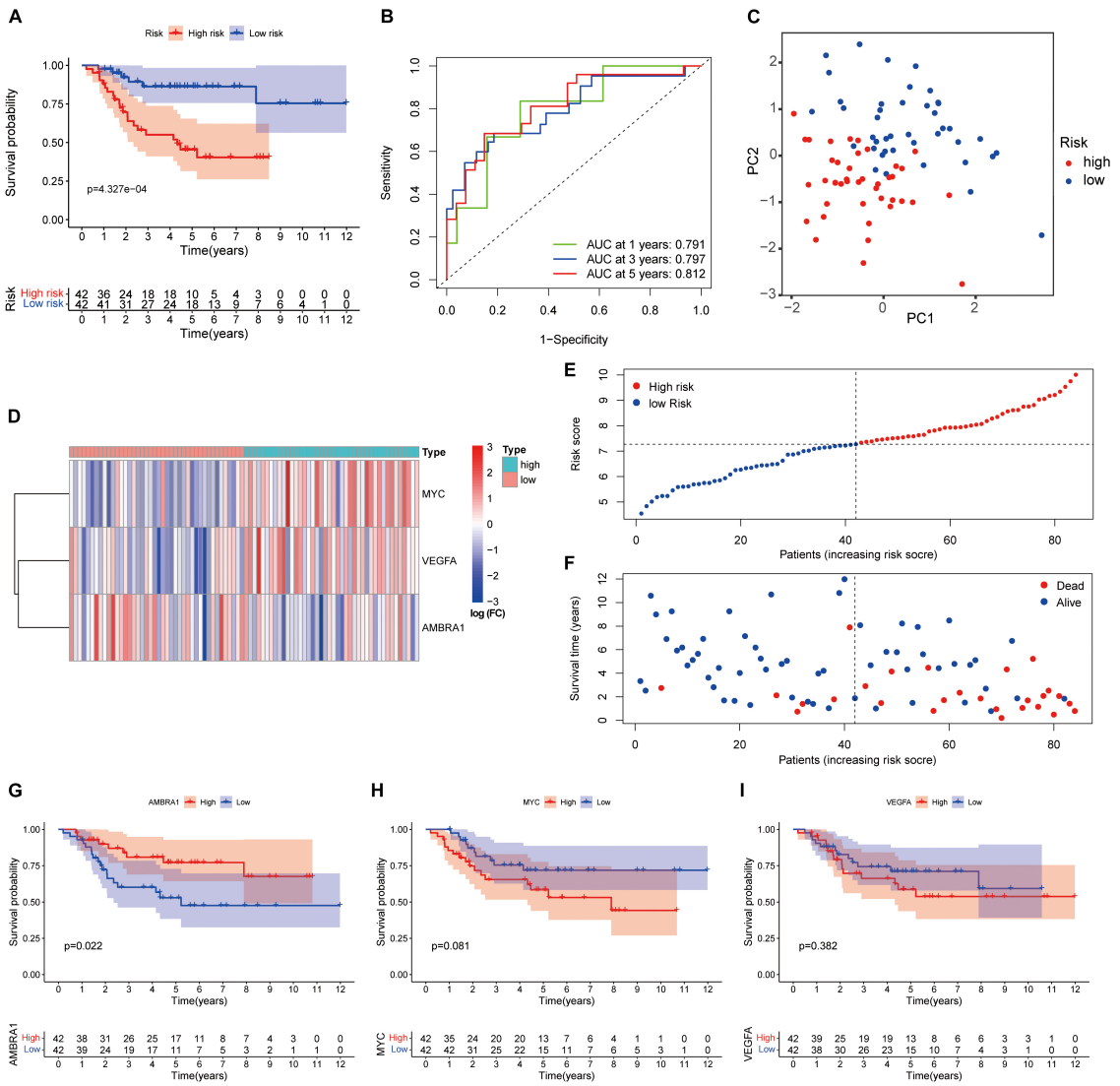

FIGURE 6 | Autophagy-related genes (ARGs) signature based on TARGET. **(A)** Kaplan–Meier curves result. **(B)** The AUC for the prediction of 1, 3, 5-year survival rate of osteosarcoma. **(C)** PCA based on the confirmed three ARGs signature. **(D)** Heatmap of the key genes expressed between the high and low risk group. **(E,F)** Risk score analysis of the signature. **(G–I)** Kaplan–Meier curves results of single gene.

(**Supplementary Figure 1A**) had higher risk scores, and it has been verified in the GSE21257 data set (**Supplementary Figure 1B**). By multivariate Cox regression, we built a nomogram model that contains indicators such as gender, age, metastasis, and risk (**Figure 7F**). The calibration curve shows that the nomogram has high prediction accuracy in the 3 and 5 years outcomes (**Figure 7G** and **Supplementary Figure 1C**), and it also shows good osteosarcoma prediction accuracy in the validation cohort (**Supplementary Figures 1D,E**).

Verification of the ARGs Signature in Dataset GSE21257

We verified the results in the GSE21257 dataset using the same risk coefficient. Consistent with the results from the TARGET database, in comparison between the two groups, and the high-risk patients tend to have poorer outcomes (**Figure 8A**). As shown by the ROC curve, the 1, 3, and 5-year AUC of the survival rate was 0.699, 0.741, and 0.714, respectively in the GSE21257 cohort (**Figure 8B**). Similarly, based on the risk coefficient of three key genes, we conducted PCA (**Figure 8C**). The heatmap shows the expression profile of ARGs in the GSE21257 dataset (**Figure 8D**), and the dot plot shows the distribution of prognostic indicators and the survival status of different groups of patients (**Figures 8E,F**). Based on these results, we confirmed that the prognosis of osteosarcoma patients can be reliable predicted by the ARGs signature. Moreover, the box plot shows that the relationship between the key genes and clinical information is consistent with the results obtained from the TARGET dataset (**Figures 8G–I**).

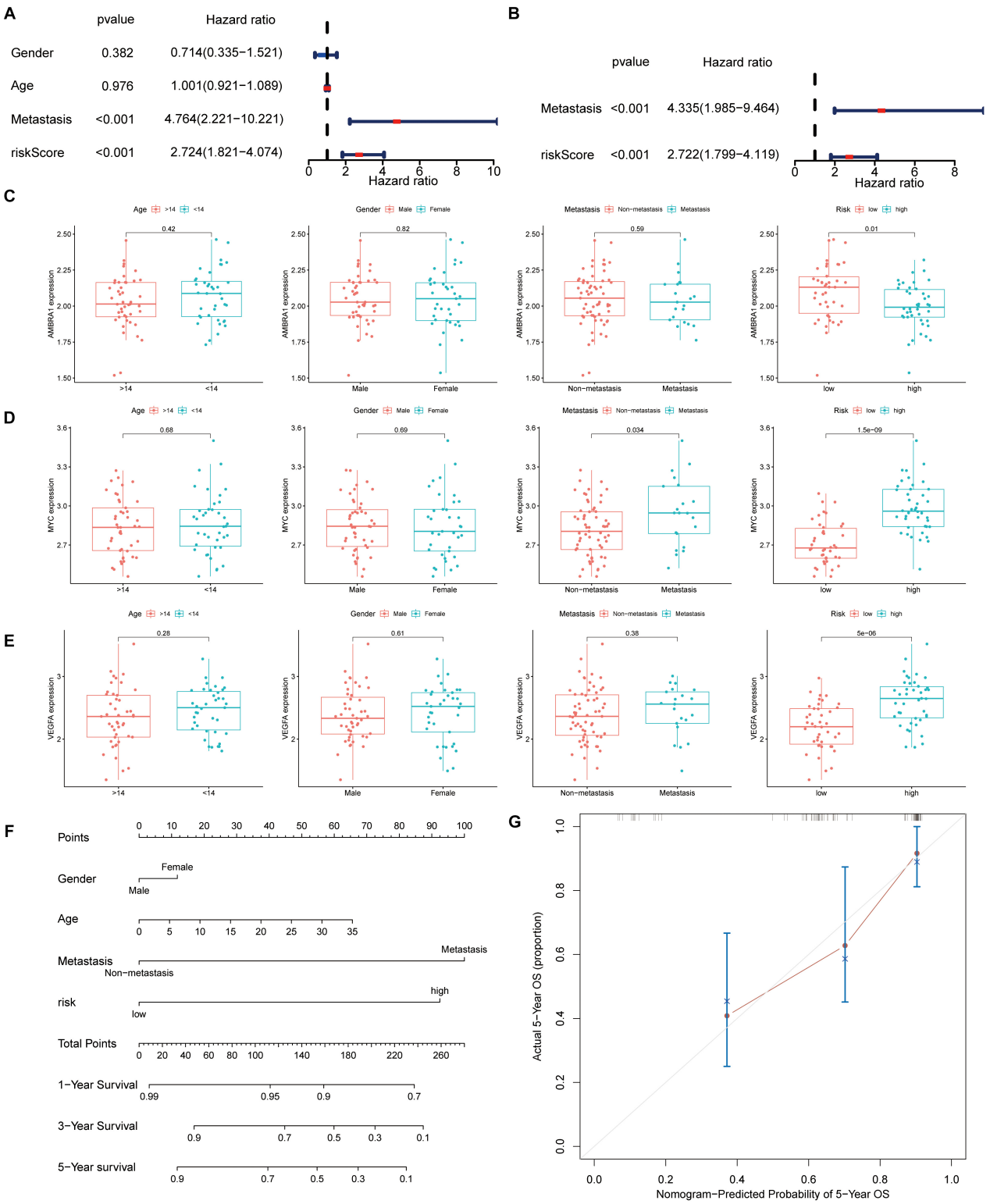

FIGURE 7 | Autophagy-associated gene signature was significantly related to survival in osteosarcoma and clinical correlation analyses. **(A,B)** Univariate and multivariate cox analysis showed the autophagy-related genes signature and metastasis were two independent predictor of prognosis in osteosarcoma. **(C–E)** The expression of the three key genes, the patients from the TARGET database were grouped according to age (< 14 y; ≥ 14 y), gender, metastasis, and riskscore. The *X*-axis represents the different groups and the *Y*-axis represents their gene expression levels (FPKM). **(F)** Nomogram based on gender, age, metastasis, and risk in the TARGET database. **(G)** Calibration plots of the nomogram for predicting the probability of OS at 5 years.

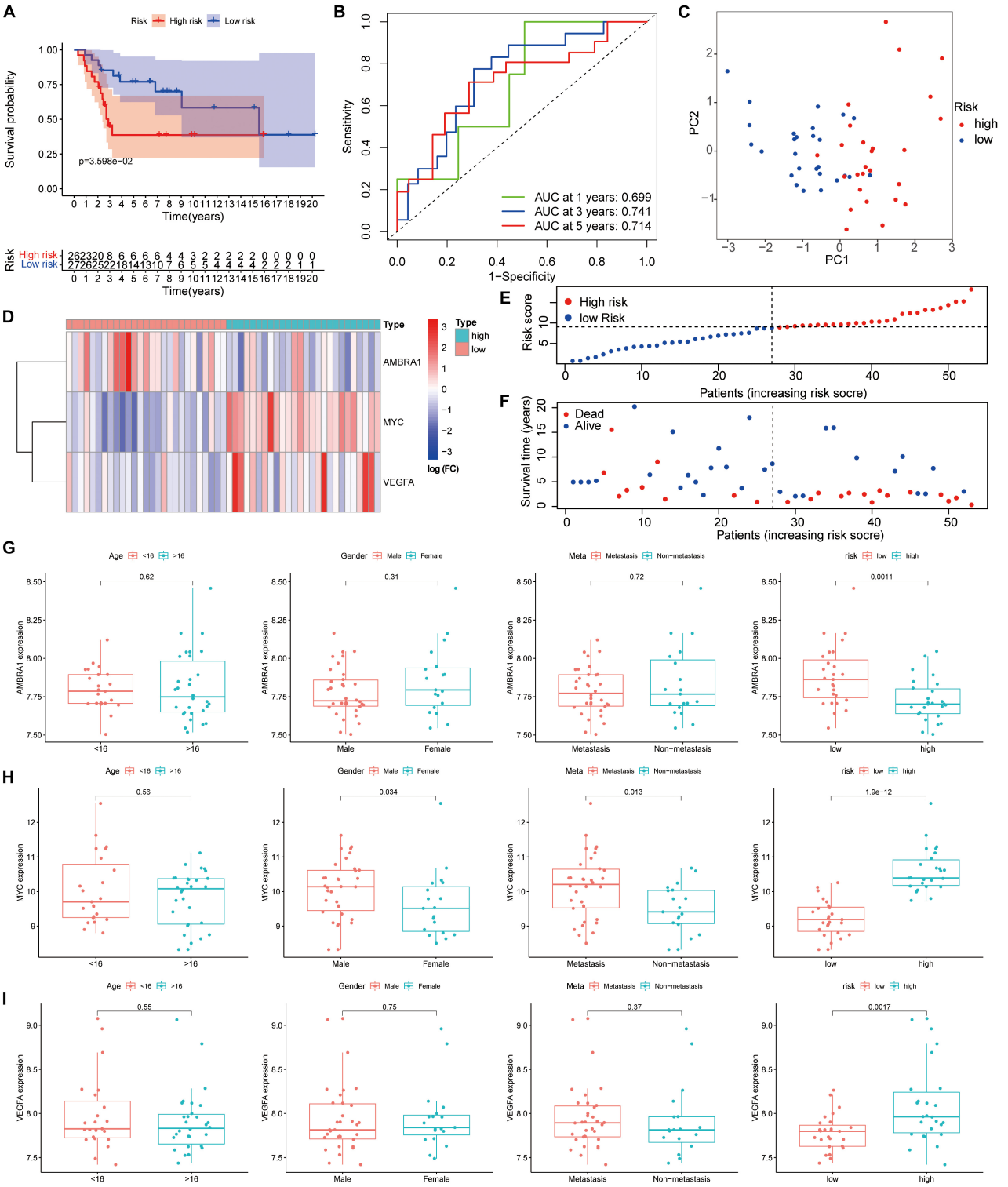

FIGURE 8 | Validation of the autophagy-associated gene signature in the testing group. **(A)** Kaplan–Meier curves result. **(B)** The AUC for the prediction of 1, 3, 5-year survival rate. **(C)** PCA based on the three autophagy-related genes signature. **(D)** Heatmap of the three genes expressed between the high and low risk group. **(E,F)** Risk score analysis of the signature. **(G–I)** The expression of the three key genes, the patients from the GSE21257 dataset were grouped according to age (< 16 y; ≥ 16 y), gender, metastasis, and riskscore. The *X*-axis represents the different groups and the *Y*-axis represents their gene expression levels (normalized signal values).

Correlation Between the Expression Levels of Autophagy-Related Prognostic Markers

To better understand the correlations among the ARLs and ARGs, we applied the Pearson correlation analysis. We found that the expression of lncRNA AC090559.1 is positively correlated with the expression of IL10RB.DT and negatively associated with MYC expression. The results shown in **Figure 9**.

Verification the Expression Level of Autophagy-Related Markers

In order to verify the expression levels of autophagy-related prognostic markers, we examined the expression levels of the three ARGs and the six ARLs in the osteoblast cell line hFOB and two osteosarcoma cell lines (U2OS and 143B) by using qRT-PCR and Western blotting analysis. Our results showed that compared with osteoblasts, AMBRA1 was down-regulated in U2OS and 143B, and while MYC and VEGFA were up-regulated in osteosarcoma cells (**Figures 10A,B**). For lncRNAs, AC090559.1, AL391121.1, UNC5B.AS1, and OLMALINC were significantly up-regulated in 143B and U2OS cell lines, while IL10RB.DT and AC083843.3 was down-regulated (**Figures 10C,D**).

DISCUSSION

Osteosarcoma is a common primary malignant bone tumor, and it remains a disease with high mortality rates in children and adolescents (Jo and Fletcher, 2014). Over the past 40 years, progress in the treatment of osteosarcoma has plateaued (Ballatori and Hinds, 2016), and innovative and effective strategies to overcome the current limitations are urgently needed. Autophagy is associated with the progression of osteosarcoma and may be related to the emergence of drug resistance during treatment (Niu et al., 2019). However, most studies examine the correlation between a single ARG and osteosarcoma (Liu et al., 2017; Livingston et al., 2018; Zhao et al., 2018), and the characteristics of ARGs in patients with osteosarcoma and their correlation with overall survival have not been systematically evaluated.

Because some lncRNAs can regulate tumor progression and metastasis by targeting ARGs, they can be used as prognostic biomarkers of cancer (Chen et al., 2017; Huang et al., 2018). In the analysis of public RNA sequence data in this study, 13 prognostic ARLs were identified. LASSO Cox regression analysis indicated that six ARLs (AC090559.1, IL10RB.DT, AL391121.1, AC083843.3, UNC5B.AS1, and OLMALINC) were good candidates to be prognostic markers. As shown in the autophagy-related lncRNA model, high-risk patients had significantly poorer outcomes than those of low-risk patients. The prognostic signature based on the six ARLs was also independent of other clinical characteristics. GSEA functional enrichment analysis showed that the low-risk group was enriched in some pathways related to autophagy and immune regulation, which indicated that immunomodulation was related to an improved prognosis. We also discussed the immune-related characteristics. In general, the degree of immune cell infiltration decreased significantly in the high-risk patients, and immune-related functions, including regulation of checkpoint, inflammation, and T cell co-inhibition, were also down-regulated significantly. These results indicate that high-risk patients have systemic immunosuppression, which may affect their prognosis. Thus, the six prognostic ARLs could accurately predict the overall survival in osteosarcoma. Notably, Wu et al. (2021) recently constructed an autophagy-related lncRNA signature, which also includes AC090559.1, that can predict the prognosis of lung adenocarcinoma. The ARLs IL10RB-DT and AL391121.1 are associated with the prognosis of clear cell renal cell carcinoma (Jiang et al., 2020; Yang et al., 2021), and compared with normal human renal cell lines, IL10RB-DT is highly expressed in renal cancer cell lines (Jiang et al., 2020). The ARL UNC5B.AS1 is highly expressed in a variety of tumors (Wang Y. et al., 2019; Tan J.J. et al., 2020; Tan S.F. et al., 2020; Wang et al., 2020), and is important in tumor proliferation and progression. In addition, In addition, Tan S.F. et al. (2020), showed that UNC5B-AS1 promotes the malignant progression of prostate cancer by competing with caspase-9, and caspase-9 is closely related to autophagy (An et al., 2020). In this study, UNC5B.AS1 was significantly up-regulated in osteosarcoma cell lines, compared with osteoblasts. Thus, UNC5B-AS1 also appears to be important in osteosarcoma, possibly *via* its association with autophagy. In this study, OLMALINC expression was also significantly higher in osteosarcoma cell lines. The role of OLMALINC in tumors has not been reported, but the results in this study indicate that further study of its functions is warranted.

Autophagy is an intracellular metabolic process that relies on the lysosomal degradation of cytoplasmic proteins, organelles, and pathogens (Kim and Lee, 2014). It is important to the dynamic balance of cells, tissues, and organisms, and is mediated by evolutionarily conserved ARGs (Levine and Kroemer, 2019). In cancer, autophagy may be inhibitory or stimulatory, depending on the type, stage, or genetic background of the disease. In this study, 30 DE-ARGs were identified between osteosarcoma and healthy tissues. Functional enrichment analysis of the DE-ARGs revealed that GO terms or signal pathways related to autophagy were enriched in osteosarcoma tissue. Univariate Cox regression analysis was used to identify 12 prognostic ARGs, and then, LASSO Cox regression analysis was used to identify the seven genes that were the best candidates. Last, multivariate regression analysis was used to complete the prognostic signature composed of three ARGs (AMBRA1, MYC, and VEGFA). Based on the risk coefficients, risk scores were obtained, and the patients were grouped. Survival analysis showed that high-risk patients evolved with poor prognosis. In addition, univariate and multivariate Cox regression analyses indicated that the signature and tumor metastasis were two independent prognostic factors. More importantly, the independent data set GSE21257 was used to validate the ARGs prognostic signature.

Currently, the most widely studied nuclear oncogene is MYC (Dang, 2012). Chen D. et al. (2018) revealed that MYC expression level increases significantly in samples of a metastatic group, compared with that in a non-metastatic group, and indicating that increased expression of MYC may be related to osteosarcoma

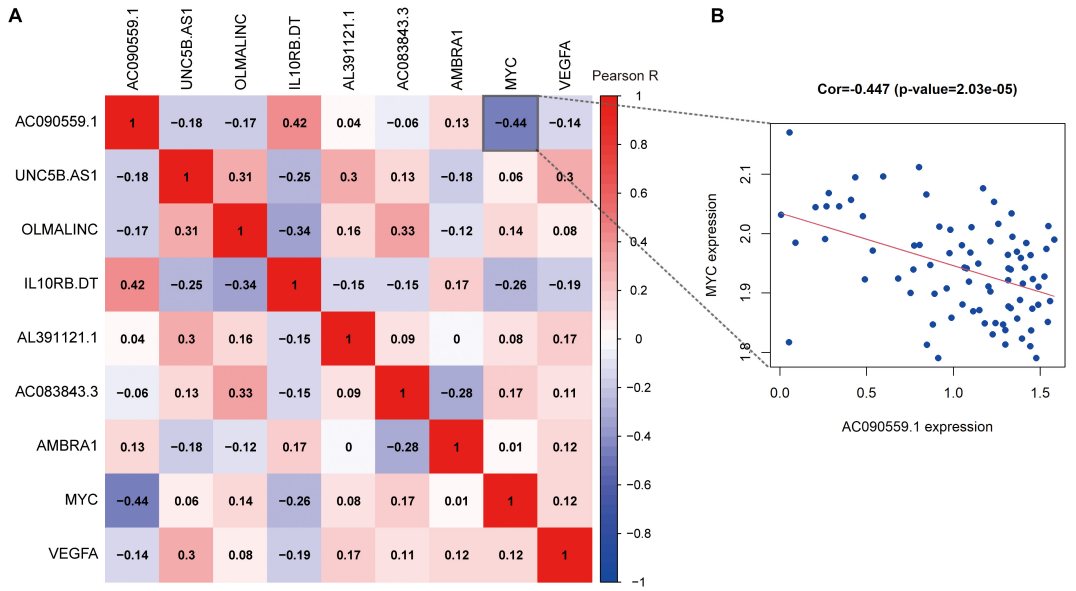

FIGURE 9 | The correlation analysis of prognostic autophagy-associated biomarkers. **(A)** The *x*-axis and *y*-axis represent genes. Red blocks represent positive correlation, and blue blocks represent negative correlation. And shade of color represents Pearson correlation index R. **(B)** Correlation between the expression of lncRNA AC090559.1 and MYC gene expression.

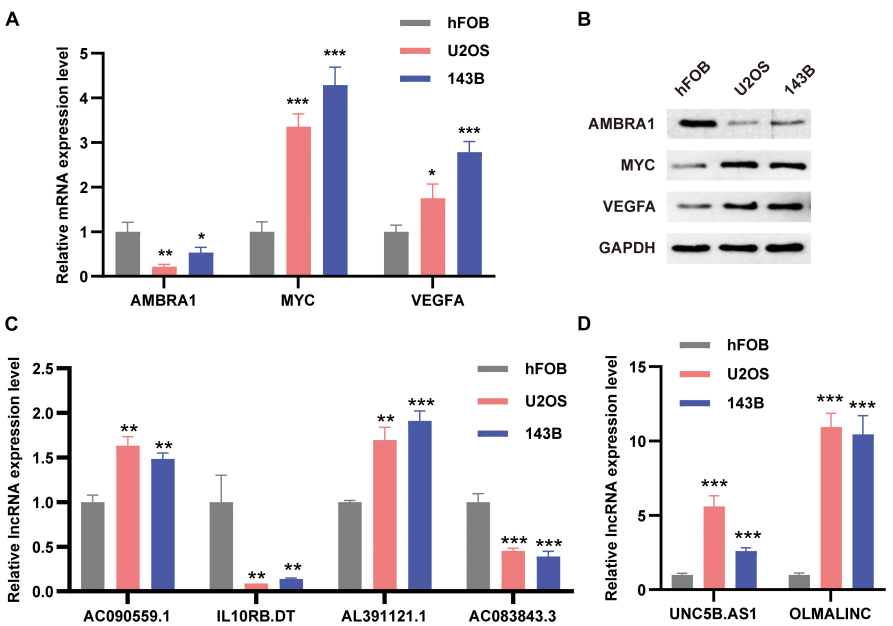

FIGURE 10 | The expression levels of ARGs and ARLs in osteosarcoma cell lines were compared with those of osteoblasts. **(A)** The qRT-PCR result of the three ARGs was evaluated by the 2−ΔΔCT method. **(B)** Western blotting results of AMBRA1, MYC, and VEGFA expression. **(C,D)** The qRT-PCR result of the six ARLs was evaluated by the 2-ΔΔCT method. The data are expressed as mean ± standard deviation. **P* < 0.05, ***P* < 0.01, and ****P* < 0.001.

metastasis. In addition, the expression of MYC in osteosarcoma samples is inversely proportional to survival time (Chen D. et al., 2018). These results are consistent with those in this study. Vascular endothelial growth factor-A (VEGFA, also known as VEGF) is a highly specific pro-vascular endothelial cell growth factor that is overexpressed in most human tumors, and its expression is related to tumor aggressiveness, increased blood vessel density, metastasis, tumor recurrence, and poor prognosis (Claesson-Welsh and Welsh, 2013; Ferrara and Adamis, 2016). Wu et al. (2019) found that VEGF is highly expressed in osteosarcoma tissues and that high VEGF expression is significantly correlated with low overall survival rate. AMBRA1 is an autophagy regulatory protein, and Cecconi et al. (Fimia et al., 2007; Nazio et al., 2013; Cianfanelli et al., 2015) showed that

it may be associated with cell proliferation, tumorigenesis, and neurodevelopment. In this study, AMBRA1 was closely related to the prognosis of osteosarcoma. However, its specific mechanism of action in osteosarcoma has not been reported. Therefore, how AMBRA1 may be involved in the pathology of osteosarcoma requires additional investigation.

A variety of autophagy-related prognostic models have been established. For example, Qiu et al. (2020) analyzed the RNA-seq data of 375 hepatocellular carcinoma patients from TCGA and obtained a four-gene signature that has predictive prognosis value. Wang S.S. et al. (2019) also proposed a four-gene prognostic marker as a potential survival prediction marker for bladder cancer patients. However, the results of those studies have not been verified in experiments. In this study, the TARGET tumor data set and the normal tissue GTEx data set were combined to establish a prognostic model of autophagy-related markers in osteosarcoma for the first time. The model was verified using an independent database, and its reliability was demonstrated in an experiment. Although a prognostic model was successfully developed with the approach used in this study, there were also some limitations. First, the number of healthy (n = 396) and osteosarcoma (n = 84) tissue samples was very different in the respective publicly available GTEx and TARGET databases, and which might distort the results. Thus, additional tumor samples need to be analyzed in the future. Second, because of the lack of lncRNA expression data, autophagy-related lncRNA models could not be verified in external data sets.

In summary, our research has shown that prognostic signatures comprising ARGs and ARLs can exactly predict the osteosarcoma overall survival. Moreover, our work highlights the importance of autophagy-related markers in osteosarcoma, and proposes the exploration of ARGs or ARLs as prospective biomarkers in osteosarcoma therapy.

DATA AVAILABILITY STATEMENT

The datasets presented in this study can be found in online repositories. The names of the repository/repositories and accession number(s) can be found below: The datasets analyzed for this study can be found in the TARGET (https://portal.gdc.cancer.gov/), Project ID: TARGET-OS, Gene Expression Omnibus (GEO) database (https://www.ncbi.nlm.nih.gov/geo/), accession number:GSE21257, Genotype-Tissue Expression (GTEx) database (https://gtexportal.org/).

AUTHOR CONTRIBUTIONS

JZ and XC designed the study. RD and TW searched the data from database. JZ and TW performed analysis of the data. JZ and RD carried out the experiments and analyzed the experimental results, and wrote the original draft of the manuscript. JJ and XC supervised this work revised the manuscript. All authors had read and approved the final manuscript.

FUNDING

This work was supported by the Natural Science Foundation of Jiangxi Province of China under Grant No. 20202ACBL206012.

SUPPLEMENTARY MATERIAL

The Supplementary Material for this article can be found online at: https://www.frontiersin.org/articles/10.3389/fcell.2021.705291/full#supplementary-material

Supplementary Figure 1 | (A–C) The relationship between autophagy-related markers and metastasis. **(D–F)** The calibration curve of the nomogram.

Supplementary Table 1 | Primers used in this study.

Supplementary Table 2 | Risk coefficients of six ARLs.

Supplementary Table 3 | Risk coefficients of three ARGs.

REFERENCES

An, H.-K., Chung, K. M., Park, H., Hong, J., Gim, J.-E., Choi, H., et al. (2020). CASP9 (caspase 9) is essential for autophagosome maturation through regulation of mitochondrial homeostasis. *Autophagy* 16, 1598–1617. doi: 10.1080/15548627.2019.1695398

Ballatori, S. E., and Hinds, P. W. (2016). Osteosarcoma: prognosis plateau warrants retinoblastoma pathway targeted therapy. *Signal Trans. Target. Therapy* 1:16001. doi: 10.1038/sigtrans.2016.1

Bartonicek, N., Maag, J. L. V., and Dinger, M. E. (2016). Long noncoding RNAs in cancer: mechanisms of action and technological advancements. *Mol. Cancer* 15:43. doi: 10.1186/s12943-016-0530-6

Boya, P., Reggiori, F., and Codogno, P. (2013). Emerging regulation and functions of autophagy. *Nat. Cell Biol.* 15, 713–720. doi: 10.1038/ncb2788

Brown, H. K., Tellez-Gabriel, M., and Heymann, D. (2017). Cancer stem cells in osteosarcoma. *Cancer Lett.* 386, 189–195. doi: 10.1016/j.canlet.2016.11.019

Cai, Q., Wang, S., Jin, L., Weng, M., Zhou, D., Wang, J., et al. (2019). Long non-coding RNA GBCDRlnc1 induces chemoresistance of gallbladder cancer cells by activating autophagy. *Mol. Cancer* 18:82. doi: 10.1186/s12943-019-1016-0

Chen, D., Zhao, Z., Huang, Z., Chen, D.-C., Zhu, X.-X., Wang, Y.-Z., et al. (2018). Super enhancer inhibitors suppress MYC driven transcriptional amplification and tumor progression in osteosarcoma. *Bone Res.* 6:11. doi: 10.1038/s41413-018-0009-8

Chen, J.-F., Wu, P., Xia, R., Yang, J., Huo, X.-Y., Gu, D.-Y., et al. (2018). STAT3-induced lncRNA HAGLROS overexpression contributes to the malignant progression of gastric cancer cells via mTOR signal-mediated inhibition of autophagy. *Mol. Cancer* 17:6. doi: 10.1186/s12943-017-0756-y

Chen, Z.-H., Wang, W.-T., Huang, W., Fang, K., Sun, Y.-M., Liu, S.-R., et al. (2017). The lncRNA HOTAIRM1 regulates the degradation of PML-RARA oncoprotein and myeloid cell differentiation by enhancing the autophagy pathway. *Cell Death And Different.* 24, 212–224. doi: 10.1038/cdd.2016.111

Cianfanelli, V., Fuoco, C., Lorente, M., Salazar, M., Quondamatteo, F., Gherardini, P. F., et al. (2015). AMBRA1 links autophagy to cell proliferation and tumorigenesis by promoting c-Myc dephosphorylation and degradation. *Nat. Cell Biol.* 17, 20–30. doi: 10.1038/ncb3072

Claesson-Welsh, L., and Welsh, M. (2013). VEGFA and tumour angiogenesis. *J. Int. Med.* 273, 114–127. doi: 10.1111/joim.12019

Dang, C. V. (2012). MYC on the path to cancer. *Cell* 149, 22–35. doi: 10.1016/j.cell.2012.03.003

Ferrara, N., and Adamis, A. P. (2016). Ten years of anti-vascular endothelial growth factor therapy. *Nat. Rev. Drug Discov.* 15, 385–403. doi: 10.1038/nrd.2015.17

Fimia, G. M., Stoykova, A., Romagnoli, A., Giunta, L., Di Bartolomeo, S., Nardacci, R., et al. (2007). Ambra1 regulates autophagy and development of the nervous system. *Nature* 447, 1121–1125. doi: 10.1038/nature05925

Goorin, A. M., Schwartzentruber, D. J., Devidas, M., Gebhardt, M. C., Ayala, A. G., Harris, M. B., et al. (2003). Presurgical chemotherapy compared with immediate surgery and adjuvant chemotherapy for nonmetastatic osteosarcoma: pediatric Oncology Group Study POG-8651. *J. Clin. Oncol. Off. J. Am. Soc. Clin. Oncol.* 21, 1574–1580. doi: 10.1200/jco.2003.08.165

Huang, F., Chen, W., Peng, J., Li, Y., Zhuang, Y., Zhu, Z., et al. (2018). LncRNA PVT1 triggers Cyto-protective autophagy and promotes pancreatic ductal adenocarcinoma development via the miR-20a-5p/ULK1 Axis. *Mol. Cancer* 17:98. doi: 10.1186/s12943-018-0845-6

Isakoff, M. S., Bielack, S. S., Meltzer, P., and Gorlick, R. (2015). Osteosarcoma: current treatment and a collaborative pathway to success. *J. Clin. Oncol. Off. J. Am. Soc. Clin. Oncol.* 33, 3029–3035. doi: 10.1200/JCO.2014.59.4895

Jiang, Y., Gou, X., Wei, Z., Tan, J., Yu, H., Zhou, X., et al. (2020). Bioinformatics profiling integrating a three immune-related long non-coding RNA signature as a prognostic model for clear cell renal cell carcinoma. *Cancer Cell Internatl.* 20:166. doi: 10.1186/s12935-020-01242-7

Jo, V. Y., and Fletcher, C. D. M. (2014). WHO classification of soft tissue tumours: an update based on the 2013. *Pathology* 46, 95–104. doi: 10.1097/PAT.0000000000000050

Kansara, M., Teng, M. W., Smyth, M. J., and Thomas, D. M. (2014). Translational biology of osteosarcoma. *Nat. Rev. Cancer* 14, 722–735. doi: 10.1038/nrc3838

Kempf-Bielack, B., Bielack, S. S., Jürgens, H., Branscheid, D., Berdel, W. E., Exner, G. U., et al. (2005). Osteosarcoma relapse after combined modality therapy: an analysis of unselected patients in the Cooperative Osteosarcoma Study Group (COSS). *J. Clin. Oncol. Off. J. Am. Soc. Clin. Oncol.*23, 559–568. doi: 10.1200/jco.2005.04.063

Kim, K. H., and Lee, M.-S. (2014). Autophagy–a key player in cellular and body metabolism. *Nat. Rev. Endocrinol.* 10, 322–337. doi: 10.1038/nrendo.2014.35

Kondo, Y., and Kondo, S. (2006). Autophagy and cancer therapy. *Autophagy* 2, 85–90. doi: 10.4161/auto.2.2.2463

Levine, B., and Kroemer, G. (2019). Biological functions of autophagy genes: a disease perspective. *Cell* 176, 11–42. doi: 10.1016/j.cell.2018.09.048

Li, X., He, S., and Ma, B. (2020). Autophagy and autophagy-related proteins in cancer. *Mol. Cancer* 19:12. doi: 10.1186/s12943-020-1138-4

Liang, X. H., Jackson, S., Seaman, M., Brown, K., Kempkes, B., Hibshoosh, H., et al. (1999). Induction of autophagy and inhibition of tumorigenesis by beclin 1. *Nature* 402, 672–676. doi: 10.1038/45257

Lilienthal, I., and Herold, N. (2020). Targeting molecular mechanisms underlying treatment efficacy and resistance in osteosarcoma: a review of current and future strategies. *Internatl. J. Mol. Sci.* 21:885. doi: 10.3390/ijms21186885

Liu, K., Ren, T., Huang, Y., Sun, K., Bao, X., Wang, S., et al. (2017). Apatinib promotes autophagy and apoptosis through VEGFR2/STAT3/BCL-2 signaling in osteosarcoma. *Cell Death Dis.* 8:e3015. doi: 10.1038/cddis.2017.422

Livingston, J. A., Wang, W.-L., Tsai, J.-W., Lazar, A. J., Leung, C. H., Lin, H., et al. (2018). Analysis of HSP27 and the autophagy marker LC3B Puncta following preoperative chemotherapy identifies high-risk osteosarcoma patients. *Mol. Cancer Therapeut.* 17, 1315–1323. doi: 10.1158/1535-7163.MCT-17-0901

Martens-Uzunova, E. S., Böttcher, R., Croce, C. M., Jenster, G., Visakorpi, T., and Calin, G. A. (2014). Long noncoding RNA in prostate, bladder, and kidney cancer. *Eur. Urol.* 65, 1140–1151. doi: 10.1016/j.eururo.2013.12.003

Meyers, P. A., Healey, J. H., Chou, A. J., Wexler, L. H., Merola, P. R., Morris, C. D., et al. (2011). Addition of pamidronate to chemotherapy for the treatment of osteosarcoma. *Cancer* 117, 1736–1744. doi: 10.1002/cncr.25744

Mizushima, N., and Komatsu, M. (2011). Autophagy: renovation of cells and tissues. *Cell* 147, 728–741. doi: 10.1016/j.cell.2011.10.026

Mizushima, N., and Levine, B. (2020). Autophagy in human diseases. *New Engl. J. Med.* 383, 1564–1576. doi: 10.1056/NEJMra2022774

Nazio, F., Bordi, M., Cianfanelli, V., Locatelli, F., and Cecconi, F. (2019). Autophagy and cancer stem cells: molecular mechanisms and therapeutic applications. *Cell Death Different.* 26, 690–702. doi: 10.1038/s41418-019-0292-y

Nazio, F., Strappazzon, F., Antonioli, M., Bielli, P., Cianfanelli, V., Bordi, M., et al. (2013). mTOR inhibits autophagy by controlling ULK1 ubiquitylation, self-association and function through AMBRA1 and TRAF6. *Nat. Cell Biol.* 15, 406–416. doi: 10.1038/ncb2708

Niu, J., Yan, T., Guo, W., Wang, W., and Zhao, Z. (2019). Insight into the role of autophagy in osteosarcoma and its therapeutic implication. *Front. Oncol.* 9:1232. doi: 10.3389/fonc.2019.01232

Qiu, J., Sun, M., Wang, Y., and Chen, B. (2020). Identification and validation of an individualized autophagy-clinical prognostic index in gastric cancer patients. *Cancer Cell Internatl.* 20:178. doi: 10.1186/s12935-020-01267-y

Qu, X., Yu, J., Bhagat, G., Furuya, N., Hibshoosh, H., Troxel, A., et al. (2003). Promotion of tumorigenesis by heterozygous disruption of the beclin 1 autophagy gene. *J. Clin. Investig.* 112, 1809–1820. doi: 10.1172/jci20039

Subramanian, A., Tamayo, P., Mootha, V. K., Mukherjee, S., Ebert, B. L., Gillette, M. A., et al. (2005). Gene set enrichment analysis: a knowledge-based approach for interpreting genome-wide expression profiles. *Proc. Natl. Acad. Sci. U.S.A.* 102, 15545–15550. doi: 10.1073/pnas.0506580102

Tan, J.-J., Long, S.-Z., and Zhang, T. (2020). Effects of LncRNA UNC5B-AS1 on adhesion, invasion and migration of lung cancer cells and its mechanism. *Chin. J. Appl. Physiol.* 36, 622–627. doi: 10.12047/j.cjap.5993.2020.130

Tan, S. F., Ni, J. X., and Xiong, H. (2020). LncRNA UNC5B-AS1 promotes malignant progression of prostate cancer by competitive binding to caspase-9. *Eur. Rev. Med. Pharmacol. Sci.* 24, 2271–2280. doi: 10.26355/eurrev_202003_20493

Ulitsky, I., and Bartel, D. P. (2013). lincRNAs: genomics, evolution, and mechanisms. *Cell* 154, 26–46. doi: 10.1016/j.cell.2013.06.020

Wang, H., Su, H., and Tan, Y. (2020). UNC5B-AS1 promoted ovarian cancer progression by regulating the H3K27me on NDRG2 via EZH2. *Cell Biol. Internatl.* 44, 1028–1036. doi: 10.1002/cbin.11300

Wang, S.-S., Chen, G., Li, S.-H., Pang, J.-S., Cai, K.-T., Yan, H.-B., et al. (2019). Identification and validation of an individualized autophagy-clinical prognostic index in bladder cancer patients. *Onco Targets Therapy* 12, 3695–3712. doi: 10.2147/OTT.S197676

Wang, Y., Bhandari, A., Niu, J., Yang, F., Xia, E., Yao, Z., et al. (2019). The lncRNA UNC5B-AS1 promotes proliferation, migration, and invasion in papillary thyroid cancer cell lines. *Human cell* 32, 334–342. doi: 10.1007/s13577-019-00242-8

White, E., Mehnert, J. M., and Chan, C. S. (2015). Autophagy, metabolism, and cancer. *Clin. Cancer Res. Off. J. Am. Associat. Cancer Res.* 21, 5037–5046. doi: 10.1158/1078-0432.CCR-15-0490

Wu, H., Zhang, J., Dai, R., Xu, J., and Feng, H. (2019). Transferrin receptor-1 and VEGF are prognostic factors for osteosarcoma. *J. Orthopaed. Surg. Res.* 14:296. doi: 10.1186/s13018-019-1301-z

Wu, L., Wen, Z., Song, Y., and Wang, L. (2021). A novel autophagy-related lncRNA survival model for lung adenocarcinoma. *J. Cell. Mol. Med.* 25, 5681–5690. doi: 10.1111/jcmm.16582

Xu, S., Wang, P., Zhang, J., Wu, H., Sui, S., Zhang, J., et al. (2019). Ai-lncRNA EGOT enhancing autophagy sensitizes paclitaxel cytotoxicity via upregulation of ITPR1 expression by RNA-RNA and RNA-protein interactions in human cancer. *Mol. Cancer* 18:89. doi: 10.1186/s12943-019-1017-z

Yang, W., Zhou, J., Zhang, K., Li, L., Xu, Y., Ma, K., et al. (2021). Identification and validation of the clinical roles of the VHL-related LncRNAs in clear cell renal cell carcinoma. *J. Cancer* 12, 2702–2714. doi: 10.7150/jca.55113

Zhao, G.-S., Gao, Z.-R., Zhang, Q., Tang, X.-F., Lv, Y.-F., Zhang, Z.-S., et al. (2018). TSSC3 promotes autophagy via inactivating the Src-mediated PI3K/Akt/mTOR pathway to suppress tumorigenesis and metastasis in osteosarcoma, and predicts a favorable prognosis. *J. Exp. Clin. Cancer Res.* 37:188. doi: 10.1186/s13046-018-0856-6

Conflict of Interest: The authors declare that the research was conducted in the absence of any commercial or financial relationships that could be construed as a potential conflict of interest.

Publisher's Note: All claims expressed in this article are solely those of the authors and do not necessarily represent those of their affiliated organizations, or those of the publisher, the editors and the reviewers. Any product that may be evaluated in this article, or claim that may be made by its manufacturer, is not guaranteed or endorsed by the publisher.

frontiers in Cell and Developmental Biology

ORIGINAL RESEARCH
published: 27 August 2021
doi: 10.3389/fcell.2021.706596

Stimulation of Treg Cells to Inhibit Osteoclastogenesis in Gorham-Stout Disease

*Michela Rossi[1], Ippolita Rana[2], Paola Sabrina Buonuomo[2], Giulia Battafarano[1], Viviana De Martino[3], Matteo D'Agostini[4], Ottavia Porzio[4,5], Cristiana Cipriani[3], Salvatore Minisola[3], Rita De Vito[6], Davide Vecchio[2], Michaela Veronika Gonfiantini[2], Alessandro Jenkner[7], Andrea Bartuli[2] and Andrea Del Fattore[1]**

[1] Bone Physiopathology Research Unit, Genetics and Rare Diseases Research Division, Bambino Gesù Children's Hospital, IRCCS, Rome, Italy, [2] Rare Diseases and Medical Genetic Unit, Bambino Gesù Children's Hospital, IRCCS, Rome, Italy, [3] Department of Clinical, Internal, Anaesthesiological and Cardiovascular Sciences, Sapienza University, Rome, Italy, [4] Clinical Laboratory, Bambino Gesù Children's Hospital, IRCCS, Rome, Italy, [5] Department of Experimental Medicine, University of Rome Tor Vergata, Rome, Italy, [6] Department of Histopathology, Bambino Gesù Children's Hospital, IRCCS, Rome, Italy, [7] Division of Immunology and Infectious Diseases, Department of Pediatrics, Bambino Gesù Children's Hospital, IRCCS, Rome, Italy

OPEN ACCESS

Edited by:
Rebecca Ann Wingert, University of Notre Dame, United States

Reviewed by:
Christina Møller Andreasen, University of Southern Denmark, Denmark
Sheik Pran Babu Sardar Pasha, University of California, Davis, United States

***Correspondence:**
Andrea Del Fattore
andrea.delfattore@opbg.net

Specialty section:
This article was submitted to Molecular and Cellular Pathology, a section of the journal Frontiers in Cell and Developmental Biology

Received: *07 May 2021*
Accepted: *10 August 2021*
Published: *27 August 2021*

Citation:
Rossi M, Rana I, Buonuomo PS, Battafarano G, De Martino V, D'Agostini M, Porzio O, Cipriani C, Minisola S, De Vito R, Vecchio D, Gonfiantini MV, Jenkner A, Bartuli A and Del Fattore A (2021) Stimulation of Treg Cells to Inhibit Osteoclastogenesis in Gorham-Stout Disease. Front. Cell Dev. Biol. 9:706596. doi: 10.3389/fcell.2021.706596

Gorham-Stout disease (GSD) is a very rare syndrome displaying excessive bone erosion and vascular lesion. Due to the rarity of the disease and to the limited studies, its etiopathogenesis is not entirely known. The involvement of immune system in the progressive osteolysis was recently suggested. Indeed, extensive reciprocal interactions between the immune and skeletal systems have been demonstrated. This study aimed to evaluate alterations of immune cells in GSD. An increase of CD8+ cells and reduction of CD4+ and CD4+CD25+CD127^{low} cells was revealed in patients. Interestingly, patients' regulatory T cells maintain the ability to respond to extracellular stimuli and to regulate osteoclastogenesis; GSD cells proliferate under aCD3/CD28 signal reaching similar levels to those observed in control culture and exert their immunomodulatory activity on effector T cells. GSD Treg cells preserved their inhibitory effects on the osteoclastogenesis. These results suggest that stimulation of Treg cells could open the way for the identification and testing of new therapeutic approaches for patients affected by GSD.

Keywords: diseases and disorders of/related to bone, osteoclasts, osteoimmunology, regulatory T cells, Gorham-Stout disease

INTRODUCTION

Gorham-Stout disease (GSD) or the so-called vanishing bone syndrome is a very rare disorder characterized by extensive bone resorption and vascular lesion. It was described for the first time in 1838 by Jackson who reported complete osteolysis of the humerus in a 12-year-old boy (Jackson, 1838). Fewer than 300 cases have been so far reported in the literature. GSD does not display a clear sex bias (1.6:1 male-to-female ratio) or inheritance pattern and can present at any age (age range is from 7 months to 80 years) (Patel, 2005; Dellinger et al., 2013, 2014; Hu et al., 2013; Nikolaou et al., 2014).

The disease may affect the appendicular or the axial skeleton (Patel, 2005; Dellinger et al., 2014). Nevertheless, Hu et al. (2013) recently reported a case series, in which the femur was the predominant affected bone. Radiologically, initial X-rays reveal changes resembling

patchy osteoporosis (Nikolaou et al., 2014). At later stage bone deformity is observed with bone mass loss and concentric shrinkage in the long bones of upper and lower extremities. Eventually, a complete resorption of the bone occurs, resulting in the appearance of the so-called "vanishing bone" disease (Nikolaou et al., 2014). The most common symptoms of GSD are pain, swelling, weakness and functional impairment of affected regions. Moreover, approximately 25% of GSD patients develop chylothorax, which can result in respiratory distress and failure. Additionally, involvement of the vertebrae can cause severe neurological defects, deformity, paralysis and death (Dellinger et al., 2014).

The diagnosis of GSD is challenging and it is usually performed by exclusion criteria (Dellinger et al., 2013, 2014; Nikolaou et al., 2014). For the diagnosis, several investigations are used (radiographs, bone scan, and computed tomography), but the diagnosis must histologically confirmed revealing local bone progressive resorption, angiomatous tissue and absence of cellular atypia (Patel, 2005; Tolis et al., 2016).

Due to the rarity of the disease and to the limited studies, the etiopathogenesis is not entirely known. Indeed, preliminary studies by Prof. Lorenzo's group suggested genetic imbalance in patients (Dellinger et al., 2013), but the pathways involved in the excessive bone erosion must be still identified. Nevertheless, the involvement of endothelial cells, osteoclasts, osteoblasts, and osteocytes has been suggested. Indeed, in GSD patients, increased serum levels of VEGF-A and -C have been found possibly stimulating lymphangiogenesis and osteoclastogenesis (Hagendoorn et al., 2014). Devlin et al. (1996) showed that patient serum can induce osteoclast formation in an IL-6-dependent manner. Recently, we demonstrated that Peripheral Blood Mononuclear Cells (PBMC) isolated from GSD patients showed increased ability to differentiate into osteoclasts with enhanced bone resorbing ability (Rossi et al., 2020). Moreover, we revealed defective osteoblast mineralization in patients (Rossi et al., 2020). Indeed, a remarkable aspect of GSD is the absence of bone formation activity by osteoblasts along surfaces of remaining bone fragments in sections of affected tissues (Dickson et al., 1990; Dellinger et al., 2014).

The involvement of immune system in the progressive osteolysis was recently suggested (Terashima and Takayanagi, 2018). It has been demonstrated that regulatory T cells ($CD4^+CD25^+CD127^{low}FoxP3^+$) are able to suppress the osteoclastogenesis while regulating osteoblast differentiation and activity (Zaiss et al., 2007; Del Fattore et al., 2010; Liu et al., 2011; Terashima and Takayanagi, 2018).

This study aimed to evaluate whether Treg could play an important role in the bone remodeling alterations leading to a complete bone loss in GSD patients.

MATERIALS AND METHODS

Patients

Ten patients were recruited by the Rare Diseases and Medical Genetics Unit of Bambino Gesù Children's Hospital (OPBG). The description of nine patients was previously reported (Rossi et al., 2021). A 12 years old female patient with swelling of the frontal bone, osteolysis of frontal and parietal bone, vertebrae and left scapula has been recently recruited for this study (**Supplementary Table 1**). Informed consent was obtained by parents/legal guardian. The study was approved by OPBG ethical committee (Protocol number: GR-2019-12370244, 01/02/2021). The diagnosis of GSD was based on radiological assessment and bone histology. Healthy Donor (HD) subjects were matched for age and gender and tested for C-Reactive Protein and Erythrocyte Sedimentation Rate to exclude inflammatory status.

ELISA Assay

Peripheral blood samples from 7 patients and 21 HD were centrifuged 1,000 g × 10 min at room temperature and serum was collected and stored at −80°C. Levels of TGFβ1 (Transforming Growth Factor-β1; R&D Systems, Minneapolis, United States), IL-4 (Interleukin 4; R&D Systems, Minneapolis, United States), IL-6 (R&D Systems, Minneapolis, United States), and IL-10 (R&D Systems, Minneapolis, United States) were measured by ELISA kits, according to the manufacturers' instructions.

Peripheral Blood Mononuclear Cells Isolation

Peripheral Blood Mononuclear Cells from 6 patients and 14 HD were prepared from peripheral blood layered over Ficoll 1.077 g/ml (PANCOLL, PAN Biotec, Germany) and centrifuged at 400 g for 30 min. "Buffy coat" was collected and washed twice with Phosphate Buffered Saline (PBS, Euroclone, Milano, Italy). Cells were resuspended in Dulbecco's Modified Essential Medium (DMEM, Euroclone, Milano, Italy) containing 50 U/ml penicillin, 50 mg/ml streptomycin, 2 mM L-glutamine, and 10% FBS (Fetal Bovine Serum).

Flow Cytometry Analysis

PBMC isolated from five patients and eight HD were incubated in the dark for 20 min at 4°C with directly conjugated monoclonal antibodies, purchased from BD Biosciences, directed against the following human surface molecules: CD3 (1:40 Alexa Fluor 700-conjugated; clone UCHT1), CD4 (1:5 PerCP-Cy 5.5 conjugated; clone L200), CD8 (1:90 APC-Cy7 conjugated; clone SK1), CD25 (1:5 PE-conjugated; clone 2A3) and CD127 (1:5 Alexa Fluor 647 conjugated; clone 40131.111). After labeling, cells were washed in PBS and analyzed with BD LSRFortessa^{TM} FACS. $CD4^+/CD25^-/CD127^{high}$ and $CD4^+/CD25^+/CD127^{low}$ cells were considered effector T (Teff) cells and Treg, respectively (Del Fattore et al., 2015). Flow cytometry profiles were analyzed using FlowJo software (BD, San Jose, CA, United States).

Histological/Histomorphometric Analysis of Bone Biopsies

Bone biopsies from lesions (L5 vertebral body, humerus, left ilium sacral region) of three pediatric patients and four HD were fixed in 10% formalin and processed for paraffin embedding with previous decalcification. For immunohistochemical analysis, sections were labeled with antibodies against human FoxP3

(Clone number 236A/E7) (Abcam, Cambridge, United Kingdom) at 4°C overnight, followed by secondary incubation for 1 h at room temperature with the corresponding secondary antibody (Agilent, Santa Clara, CA, United States). Histomorphometric measurements were carried out on 2–5 micron thick sections, with an interactive image analysis system (NIS-Elements BR 4.50.00). The Eroded Surface/Bone surface was evaluated according to the guidelines suggested by the Histomorphometry Nomenclature Committee of the American Society for Bone and Mineral Research (ASBMR) (Dempster et al., 2013). In $\sim$2.1 $\times$ 10^5 μm^2 of the ROI analyzed, $FoxP3^+$ cells in the bone marrow were counted and data were reported as positive cells per bone marrow area (mm^2).

Stimulation of Treg Cells

Peripheral Blood Mononuclear Cells (PBMC) were labeled with 0.5 μM Carboxyfluorescein Succinimidyl Ester (CFSE, Thermo Fischer Scientific, Waltham, MA, United States) according to manufacturer's instructions and cultured in RPMI-1640 medium (Euroclone, Milano, Italy) supplemented with 10% FBS with or without T-cell stimulation for 5 days. T stimulation was achieved adding Dynabeads Human T-activator CD3/CD28 beads (Thermo Fischer Scientific, Waltham, MA, United States) at a ratio of 1:50 (Del Fattore et al., 2015). Five-day non-adherent cells were resuspended, washed in PBS and analyzed by fluorescent-activated cell sorting (FACS) analysis.

Osteoclast and Treg Co-culture

Peripheral Blood Mononuclear Cells (PBMC) from three healthy donors were isolated as previously described and 1 $\times$ 10^6 cells/cm^2 were plated on 96-well plates. After 3 h, cell cultures were rinsed to remove non-adherent cells. Cells were cultured in DMEM with 10% of FBS and in the presence of 20 ng/ml human Macrophage Colony-Stimulating Factor (hM-CSF, PeproTech, United Kingdom) and 30 ng/ml human Receptor Activator of NF-κB Ligand (hRANKL, PeproTech, United Kingdom) for 3 days. In the next medium changes, in addition to 50 μl of DMEM supplemented with FBS and hM-CSF/hRANKL, 2 $\times$ 10^4 sorting-purified $CD4^+/CD25^+/CD127^{low}$ cells (from six HD and three patients) in 50 μl RPMI-1640 were added per well. As controls, cells were treated with 50 μl of DMEM supplemented with FBS and hM-CSF/hRANKL, added with 50 μl RPMI-1640. After 10 days, cells were fixed in 4% paraformaldehyde and stained for Tartrate Resistant Acid Phosphatase (TRAcP, Sigma-Aldrich, United States). Osteoclasts were identified as $TRAcP^+$ multinucleated ($\geq$3 nuclei) cells. Leica DMi8 microscope and LasX software were used for cell analysis.

Conditioned Medium Preparation

Peripheral Blood Mononuclear Cells (PBMC) (1 $\times$ 10^6 cells/ml) from patients and HD were maintained in culture with complete medium (RPMI-1640, 10% FBS, 50 U/ml penicillin, 50 mg/ml streptomycin) with or without aCD3/CD28 beads. After 5 days, medium was collected and beads were removed using a magnet; supernatants were centrifuged 500 g for 5 min to remove cell contamination and stored at –80°C.

Osteoclast Precursor Treatment With Conditioned Media

PBMC cultured for 3 days with 20 ng/ml hM-CSF and 30 ng/ml hRANKL were treated with (i) complete medium + 20 ng/ml hM-CSF + 30 ng/ml hRANKL, (ii) 100% Conditioned Medium (CM) from 5-day aCD3/CD28 stimulated PBMC of HD + 20 ng/ml hM-CSF + 30 ng/ml hRANKL, (iii) 100% CM from 5-day aCD3/CD28 stimulated PBMC of patients + 20 ng/ml hM-CSF + 30 ng/ml hRANKL. After 48 h total RNA was extracted from treated cells.

Osteoclastogenic Assay With CM

One million/cm^2 of HD PBMC were seeded in a 96-well culture plate. After 3 h non-adherent cells were removed and cultures were maintained under three different conditions: (i) complete medium + 20 ng/ml hM-CSF + 30 ng/ml hRANKL, (ii) 100% CM from 5-day aCD3/CD28 stimulated PBMC of healthy donors + 20 ng/ml hM-CSF + 30 ng/ml hRANKL, (iii) 100% CM from 5-day aCD3/CD28 stimulated PBMC of patients + 20 ng/ml hM-CSF + 30 ng/ml hRANKL. Medium was changed every 3 days. After 14 days, cells were stained for TRAcP and analyzed by microscopy.

Bone Resorption Assay With CM

Three HD-PBMC were differentiated on bovine bone slices (IDS, PANTEC) for 2 weeks and then treated for 4 days with (i) complete medium + 20 ng/ml M-CSF + 30 ng/ml RANKL, (ii) 100% CM from 5-day aCD3/CD28 stimulated PBMC of 3 HD + 20 ng/ml M-CSF + 30 ng/ml RANKL, (iii) 100% CM from 5-day aCD3/CD28 stimulated PBMC of 3 patients + 20 ng/ml M-CSF + 30 ng/ml RANKL. Then, cells were removed by prolonged sonication and section were stained with 1% toluidine blue. Resorption pits were observed by conventional light microscopy and area was measured by image analysis system (NIS Elements BR 4.50.00).

Real-Time RT-PCR

Total RNA was extracted using TRI Reagent (Sigma-Aldrich, United States); one microgram of RNA was reverse transcribed (SensiFAST cDNA synthesis kit, Bioline, United Kingdom) in a volume of 20 μl to produce complementary DNA (cDNA) and 25 ng of cDNA was used for Real-Time PCR reactions using SensiFAST SYBR Low-ROX kit (Bioline, United Kingdom). Primer sequences are listed in **Table 1**.

Statistics

Data were expressed as the mean ± SD of at least three independent experiments. Statistical analysis was performed by one-way analysis of variance, followed by the unpaired Student's *t*-test or the Mann-Whitney *U* test using GraphPad Prism 5. A p-value $\leq$ 0.05 was considered statistically significant.

TABLE 1 | List of primer pairs and sequence.

Gene	Forward primer	Reverse primer
DC-STAMP	5′-GGACATGGCTGGGACTGAAA-3′	5′-TGTTCTGCTGTGTTGCTCCA-3′
ATP6V0D2	5′- GGTCTCTCGGTCTTCTTTGC-3′	5′-CCTTGGGCCGTTTCACAGAA-3′
CLC7	5′-TGATCTCCACGTTCACCCTGA-3′	5′-TCTCCGAGTCAAACCTTCC-3′
TCRG1	5′-GGGATCCAGGGTAAGCATCG-3′	5′-CCGCTCCCTACACCATCATC-3′
MMP9	5′-TTGACAGCGACAAGAAGTGG-3′	5′-GCCATTCACGTCGTCCTTAT-3′
CATK	5′-TCGGGGATCTCTCTGTACCC-3′	5′-CCCGCAGTAATGACACCCTT-3′
GAPDH	5′-GACAAGCTTCCCGTTCTCAG-3′	5′-ACAGTCAGCCGCATCTTCTT-3′

RESULTS

Serum Analysis

Serum analysis of IL-4, IL-6, IL-10, and TGFβ1 was performed to evaluate alteration of cytokines involved in Treg regulation and activity. As shown in **Table 2**, high levels of IL-6 and reduction of TGFβ1 (Transforming Growth Factor-β) were revealed in GSD patients (**Table 2**). No detectable levels of IL-4 were measured (data not shown) and no differences of IL-10 values were observed between GSD patients and age- and sex-matched HD (**Table 2**).

Immunomodulatory Activity of GSD Treg

To evaluate alterations of T cells in GSD, PBMC were isolated from patients and HD and they were analyzed using flow cytometry. No alteration in CD3 population (**Figures 1A,B**) was identified in GSD patients, while an increase in $CD8^+$ subpopulation (**Figures 1C,D**) and a reduction of $CD4^+$ cells (**Figures 1E,F**) were disclosed. In $CD4^+$ cells gate, Treg were identified by expression of CD25 and low level of CD127. As shown in **Figures 1G,H** Treg were 2.2% of total $CD4^+$ T cells in peripheral blood of patients (range 0.6–4.2%) and 6.1% in HD (range 4.8–7.9%). Therefore, the percentage of Treg was significantly decreased compared to HD ($p = 0.0002$), without difference of Teff [% of $CD4^+CD25^-CD127^{high}$ in $CD4^+$ gate (mean ± SD): HD: 52.31 ± 11.17; GSD: 53.36 ± 19.67; $p = 0.90$].

The reduction of Treg was also confirmed in bone microenvironment by immunohistochemical analysis of bone biopsy. Indeed, besides the increased bone erosion (**Figure 2A**) histomorphometric measurement revealed about 50% reduction of $FoxP3^+$ cells in bone marrow of three patients compared to HD (**Figures 2B,C**).

Next, we evaluated the proliferation ability of $CD4^+CD25^+CD127^{low}$ Treg incubating PBMC with anti-CD3/anti-CD28-coated microbeads. This polyclonal expansion protocol greatly specifically increases Treg number while preserving their suppressive capacity (Del Fattore et al., 2015). Indeed, HD and patient $CD8^+$ cells and GSD $CD4^+$ were not affected by treatment (**Figures 3A,B**); the stimulation induced a slight decrease of HD $CD4^+$ subpopulation (**Figure 3B**). Anti-CD3/anti-CD28 (aCD3/CD28) beads induced the proliferation of Treg (**Figures 3C–E**); surprisingly, GSD cultures had a higher proliferation rate compared to HD as shown by FACS analysis revealing increased CFSE dilution for the multiple generations (**Figure 3D**). Moreover, a significant reduction of $CD4^+CD25^-CD127^{high}$ (Teff) number was revealed in stimulated cultures (**Figures 3C,F**), suggesting that GSD Treg maintain their immunomodulatory activity.

TABLE 2 | Serum cytokines involved in Treg regulation and activity.

	HD	GSD	p
IL-6 (pg/mL)	0.10 ± 0.05	1.89 ± 1.00*	0.001
IL-10 (pg/mL)	12.11 ± 4.77	4.51 ± 1.89	0.317
TGFβ1 (pg/mL)	27,680 ± 1,131	22,830 ± 2,509*	0.050

*Results are expressed as mean ± SD. *p ≤ 0.05.*

Inhibition of Osteoclasts by Interaction With GSD Treg

To evaluate the effects of Treg on osteoclast differentiation, we co-cultured hRANKL/hM-CSF-treated PBMC isolated from healthy donors with Treg cells of GSD patients and HD. A reduction of about 70–80% of TRAcP-positive multinucleated cells was observed in cultures of PBMC with Treg (**Figures 4A,B**); GSD cells retained their inhibitory activity on osteoclastogenesis (**Figures 4A,B**). No differences were revealed in the number of nuclei/osteoclast [N° nuclei/osteoclast (mean ± SD): PBS: 3.48 ± 0.46; HD Treg: 3.06 ± 0.11; GSD Treg: 3.00 ± 0.01]. To evaluate whether these effects were dependent on the direct cell-cell contact, we treated HD PBMC with conditioned medium isolated from aCD3/CD28-stimulated PBMC of healthy donors and patients. Real Time RT-PCR expression analysis revealed that the treatment for 48 h with GSD cell conditioned medium induced a downregulation of the osteoclast fusion gene *DC-STAMP* (Dendritic Cell-Specific TrAnsMembrane Protein) (**Figure 5A**) in osteoclast precursors, compared to cells treated with osteoclastogenic medium and with HD cells-derived conditioned medium, respectively. Conditioned medium from GSD cells induced a downregulation of *ATP6V0D2* (ATPase H + Transporting V0 Subunit A2) (**Figure 5B**) expression compared to cells treated with HD cells medium while no significant differences were observed between PBMC treated with osteoclastogenic medium and CM ($p = 0.08$).

No alterations were observed in the expression of genes involved in the acidification of resorption lacunae including *CLC7* (Chloride Channel Type 7) (**Figure 5C**) and *TCIRG1* (T Cell Immune Regulator 1, ATPase H+ Transporting V0 Subunit A3) (**Figure 5D**). The treatment with conditioned medium

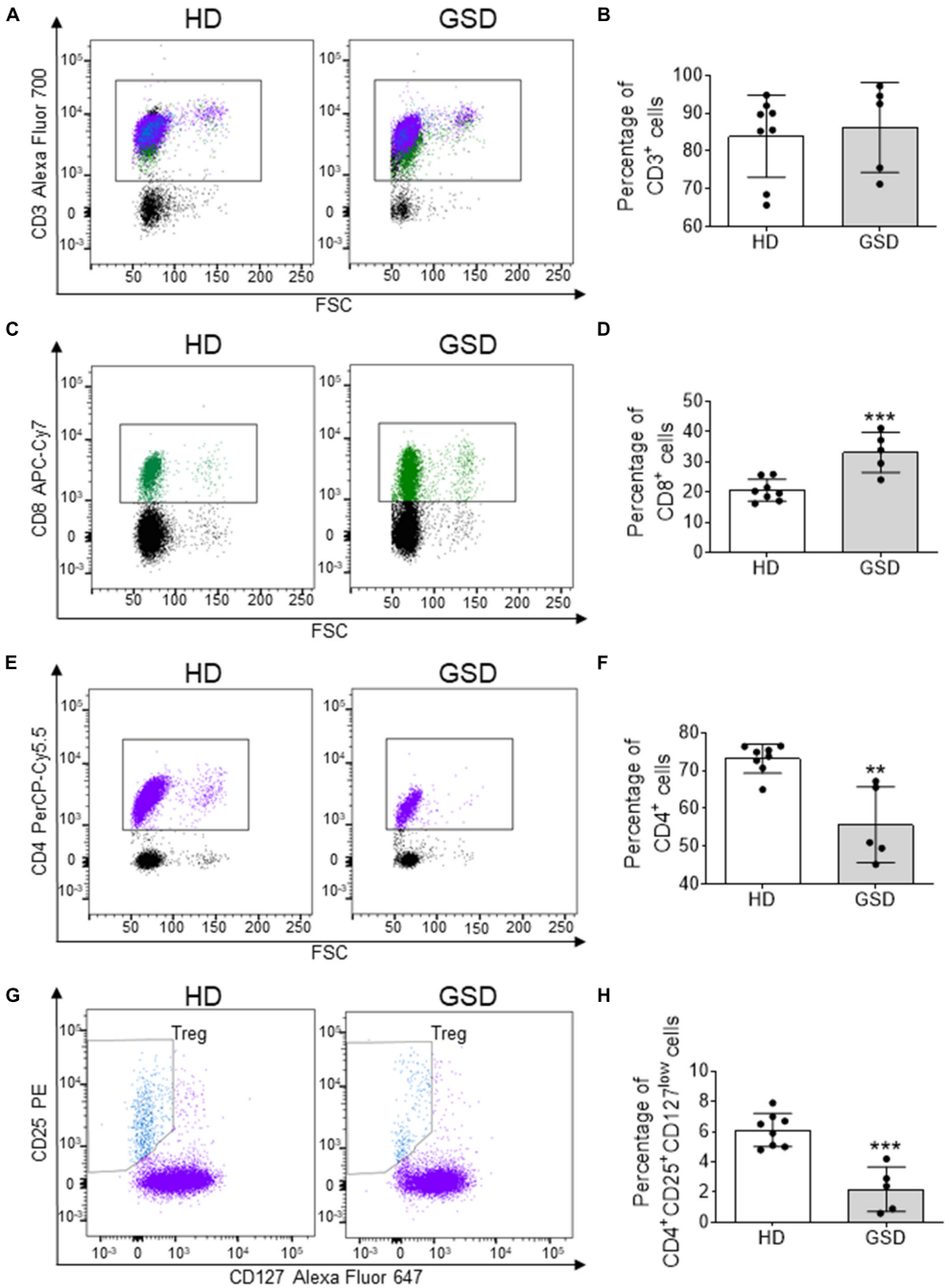

FIGURE 1 | Cytometric analysis performed on PBMC isolated from five patients and eight HD. **(A)** Representative FACS plot for $CD3^+$ cells; $CD8^+$ cells are in green, while $CD4^+$ and T reg are marked in purple and blue, respectively. **(B)** Percentage of $CD3^+$ cells. **(C)** Representative FACS analysis for $CD8^+$ cells in $CD3^+$ gate. **(D)** Percentage of $CD8^+$ cells in $CD3^+$ gate. **(E)** Representative FACS plot for $CD4^+$ cells. **(F)** Percentage of $CD4^+$ cells in $CD3^+$ gate. **(G)** Representative FACS analysis for $CD25^+CD127^{low}$ cells in $CD4^+$ gate. **(H)** Percentage of $CD25^+CD127^{low}$ Treg in $CD4^+$ gate. Results are expressed as mean ± SD. $^{**}p < 0.01$; $^{***}p < 0.001$.

downregulated the expression of *MMP*9 (Metalloprotease Type IX) and *CTSK* (Cathepsin K) important for the resorption of bone matrix; CM of cells isolated from patients induced a stronger ability to reduce the expression of these genes compared to that derived from HD cells (**Figures 5E,F**).

To investigate the mechanisms of inhibition, we evaluated the effects of conditioned medium on osteoclastogenesis and on bone resorption activity. As shown in **Figures 5G,H**, ∼75% reduction of osteoclast formation was observed in cultures treated with CM from HD' cells as revealed by TRAcP staining (**Figure 5G**)

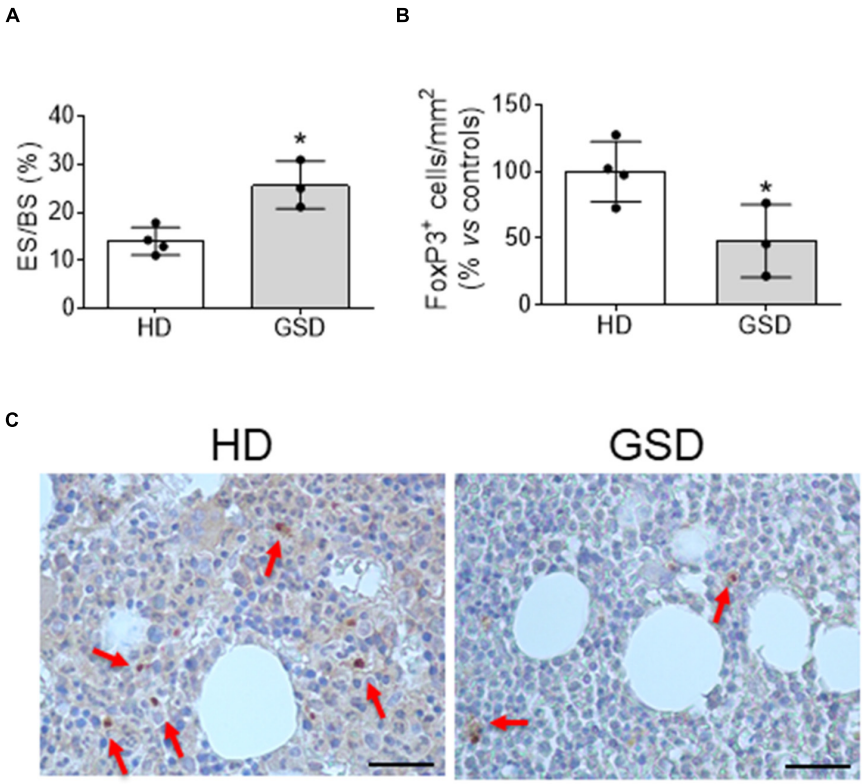

FIGURE 2 | Bone biopsy analysis of four HD and three patients. **(A)** Histomorphometric analysis of Eroded surface/Bone surface (%). **(B)** Histomorphometric analysis of FoxP3$^+$ cells/Total Bone marrow Area. **(C)** Representative pictures of immunohistochemical analysis of FoxP3. The arrows indicate FoxP3$^+$ cells. Scale bar: 25 μm. Results presented as percentage vs. aged-matched HD. Results are expressed as mean ± SD. *$p < 0.05$.

and the quantification of multinucleated (>3 nuclei) TRAcP positive cells (**Figure 5H**). The conditioned medium from GSD cultures was about 7.5-fold more effective than that from HD cells in inhibiting osteoclast differentiation (**Figures 5G,H**). No alteration was observed in the number of nuclei per cell (Number of nuclei/osteoclast; RPMI: 3.53 ± 0.39; HD CM: 3.07 ± 0.07; GSD CM: 3.00 ± 0.06) and in the resorption ability (Resorbed Area/Total Area, %; RPMI: 4.03 ± 1.02; HD CM: 4.19 ± 1.09; GSD CM: 3.70 ± 1.58).

DISCUSSION

Gorham Stout disease is a very rare disorder characterized by progressive bone erosion and vascular lesion. In this study we evaluated for the first time the role of immune cells in the progressive osteolysis. Indeed, the immune system and bone are tightly regulated and the term osteoimmunology was coined by Arron and Choi to describe the association between osteoclasts and T cells (Arron and Choi, 2000). These cells share the same hemopoietic origin and, as other hematopoietic cells, osteoclast precursors can be detected in the peripheral blood. Moreover, many inflammatory diseases are characterized by increased bone erosion including Rheumatoid Arthritis and Periodontal Disease (Sato et al., 2013). In GSD patients we observed an increase of bone resorbing activity as shown in **Figure 2A** and high levels of CD8$^+$ cells that could be related to the increase of osteoclastogenesis that we reported in our previous study (Rossi et al., 2020). Indeed, Kiesel et al. (2009) showed that murine osteoclasts are able to induce CD8$^+$ T cell proliferation and activation by antigen cross-presentation. Interestingly, a reduction of CD4$^+$ cells was observed in our patients. It was proved that osteoclasts are able to interact with naïve CD4$^+$ cells and to induce FoxP3$^+$ CD4$^+$ T cells in an antigen-specific manner (Ibanez et al., 2016). Interestingly, in the bone marrow Tregs localize within 15 μm of the endosteal surface (Fujisaki et al., 2011). Regulatory T cells can inhibit bone erosion by the release of inhibitor cytokines or by direct cell-cell contact (**Figure 6**). Zaiss et al. (2007) demonstrated that regulatory CD4$^+$CD25$^+$Foxp3$^+$ T cells suppress osteoclast formation in a cell contact-dependent manner, and that bone resorption serum markers inversely correlate with the amount of circulating Treg. The cell contact inhibition is mediated by T lymphocyte-associated antigen 4 (CTLA4) that directly binds to CD80/CD86 on osteoclast precursors' surface inducing cell apoptosis and inhibiting mature osteoclast formation (**Figure 6**; Bozec et al., 2014). Further studies showed that Treg cells protect from local and systemic bone destruction (Yuan et al., 2010; Zaiss et al., 2010). In our GSD patients we observed a reduction of CD4$^+$CD25$^+$CD127^{low} cells in peripheral

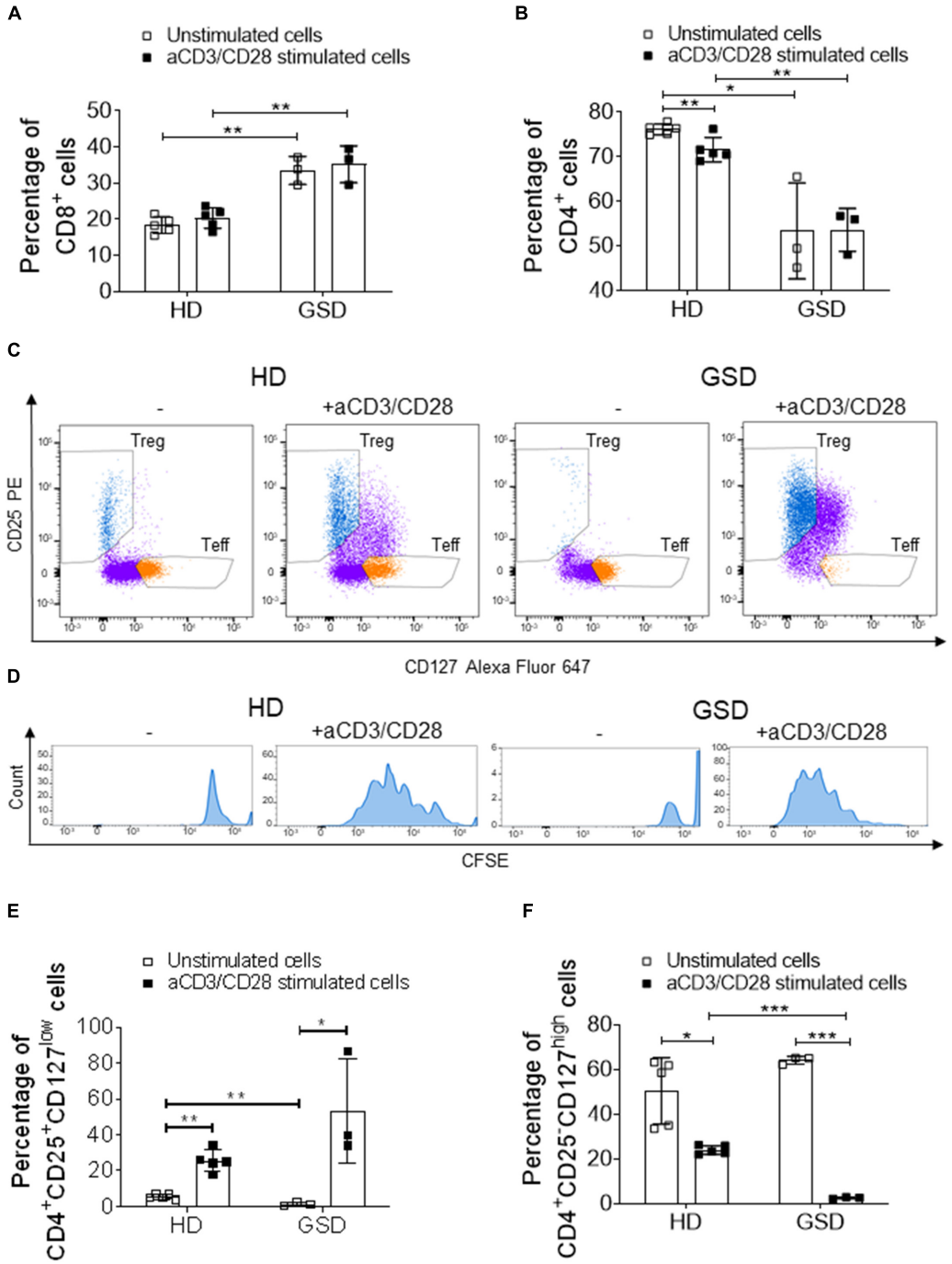

FIGURE 3 | Cytometric analysis performed on PBMC, isolated from three patients and five HD, stimulated or not with aCD3/CD28 beads for 5 days. **(A)** Percentage of $CD8^+$ cells and **(B)** $CD4^+$ cells in $CD3^+$ gate. **(C)** Representative FACS plots of HD and GSD $CD4^+$ cells with or without anti-CD3/CD28 ($CD4^+$ cells are marked in purple, while T reg and Teff are reported in blue and orange, respectively). **(D)** Representative plots of $CFSE^+$-labeled proliferative Treg (marked in blue) of HD and GSD patient stimulated or not with aCD3/CD28 beads. **(E)** Percentage of $CD25^+CD127^{low}$ Treg in $CD4^+$ gate. **(F)** Percentage of $CD25^-CD127^{high}$ Teff in $CD4^+$ gate. Results are expressed as mean ± SD. $^*p < 0.05$; $^{**}p < 0.01$; $^{***}p < 0.001$.

blood and of $FoxP3^+$ cells in the bone marrow. Furthermore, we demonstrated that GSD $CD4^+CD25^+CD127^{low}$ Treg maintain their immunomodulatory activity, as clarified by their ability to proliferate with aCD3/CD28 treatment and their immunosuppressive ability against Teff cells. For the isolation of Treg cells, we used surface markers CD4/CD25/CD127 since FoxP3 is an intracellular factor and its analysis requires permeabilization of the cells (Liu et al., 2006;

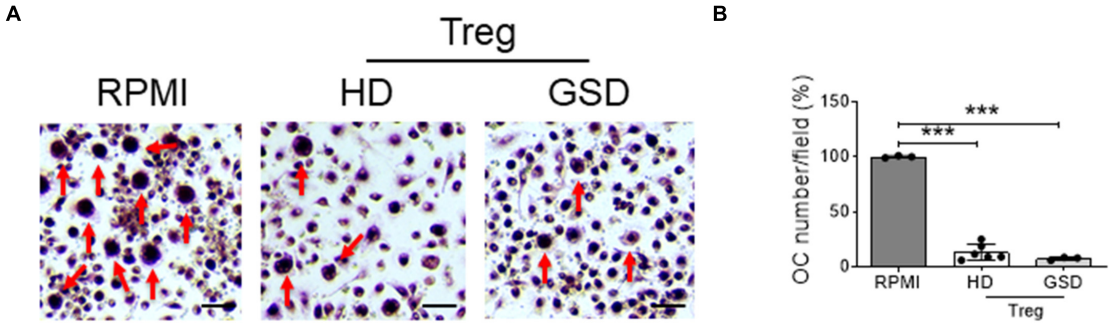

FIGURE 4 | Peripheral Blood Mononuclear Cells (PBMC) were isolated from three HD, treated with hRANKL/hM-CSF and co-cultured with six HD and three GSD aCD3/CD28-stimulated and sorted Treg. As control, cells were treated with hM-CSF/hRANKL and RPMI-1640. **(A)** Representative picture of TRAcP staining. Scale bar: 75 μm. **(B)** Percentage of TRAcP positive multinucleated (>3 nuclei) cells compared to RPMI treated culture. Results are expressed as mean ± SD. ***$p < 0.001$.

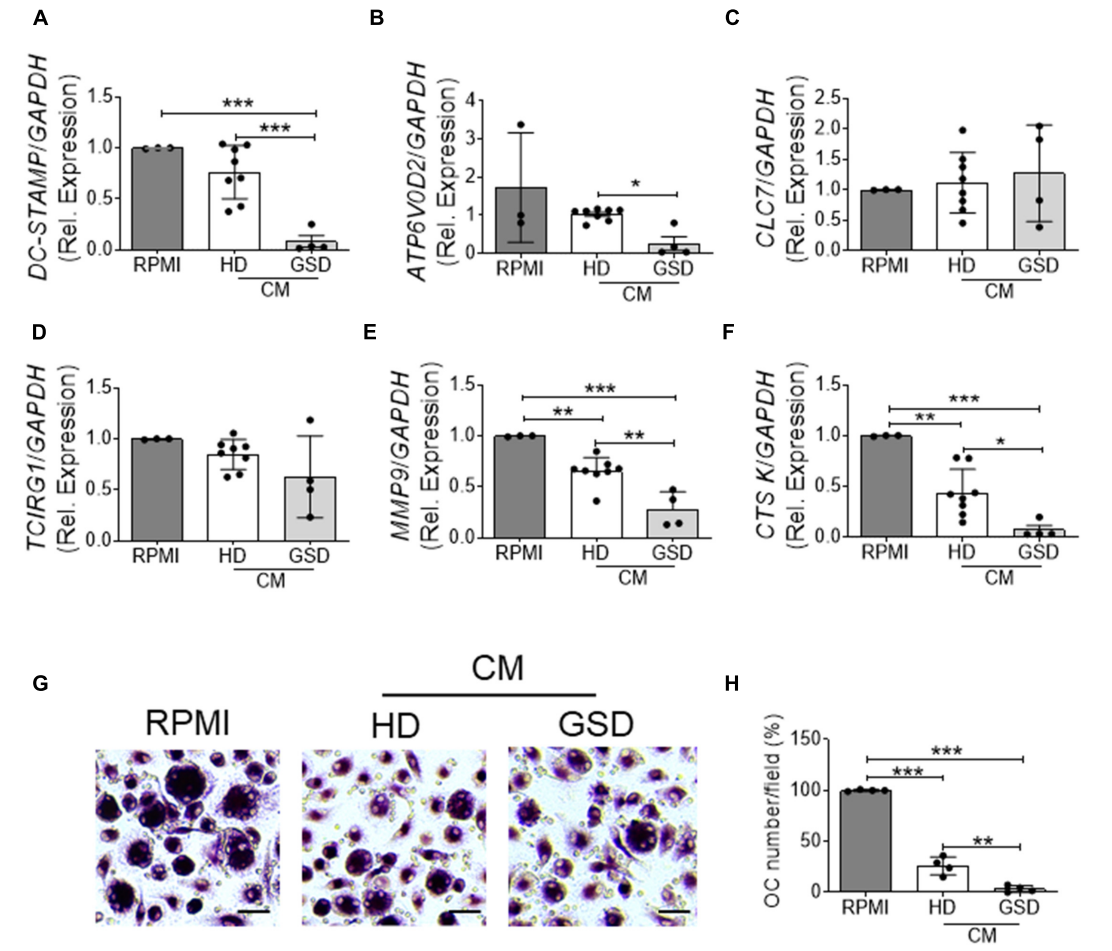

FIGURE 5 | (A–F) RNA was extracted from three HD-osteoclast precursors treated for 48 h with RPMI-1640 + M-CSF/RANKL as control (RPMI group) or 100% conditioned medium (CM) of aCD3/CD28 stimulated PBMC isolated from four patients and eight HD + hM-CSF/hRANKL and reverse transcribed; then cDNA was subjected to comparative Real-Time PCR using primer pairs and specific conditions for **(A)** *DC-STAMP*, **(B)** *ATP6V0D2*, **(C)** *CLC7*, **(D)** *TCIRG1*, **(E)** *MMP9*, and **(F)** *CTSK* genes. qRT-PCR Cycle threshold ranges are *DC-STAMP*: 19.5–28.2; *ATP6V0D2*: 22.6–29.9; *CLC7*: 23.0–27.0; *TCIRG1*: 21.8–26.6; *MMP9*: 18.0–22.6; *CTSK*: 20.9–28.6; *GAPDH*: 18.0–19.6. **(G,H)** PBMC were isolated from four HD and treated with RPMI-1640 + hM-CSF/hRANKL as control (RPMI group) or 100% conditioned medium (CM) of aCD3/CD28 stimulated PBMC isolated from four patients and four HD + hM-CSF/hRANKL. **(G)** Representative pictures of TRAcP staining. Scale bar: 30 μm. **(H)** Percentage of TRAcP positive multinucleated (>3 nuclei) cells. Results are expressed as mean ± SD. *$p < 0.05$; **$p < 0.01$; ***$p < 0.001$.

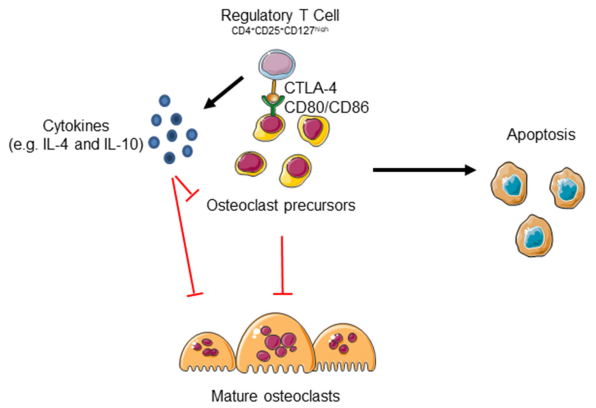

FIGURE 6 | Regulatory T cells could inhibit osteoclast formation by two mechanisms. Treg cells release several cytokines including IL-4 and IL-10 that inhibit osteoclast formation. Moreover, the binding of Cytotoxic T Lymphocyte-associated antigen 4 (CTLA-4) to CD80/CD86 receptor expressed on osteoclast precursors (pOC) induces pOC' apoptosis. The figure was produced using Servier Medical Art.

Del Fattore et al., 2015). We evaluated their interplay with osteoclast precursors and osteoclasts and we established that patient stimulated Treg are able to inhibit osteoclastogenesis by co-culture experiments and treatment with conditioned medium.

In the interplay between bone and immune system cytokines and secreted factors play a crucial role. Factors with regulatory properties in inflammatory responses, such as TGFβ1, IL-4 and IL-10, also negatively regulate osteoclast formation and bone resorption. Since it was demonstrated that interleukin-6 inhibits regulatory T cells (Lin et al., 2012) and TGFβ is essential for signals in safe-guarding specific Treg cell functions (Konkel et al., 2017), we performed serum analysis that revealed increase of IL-6, reduction of TGFβ1, and no significant alteration for IL-10. It was also evident that sclerostin promotes the production of IL-6 and transforming growth factor β in mesenchymal stem cells, reducing the differentiation of Treg (You et al., 2018). In our previous paper, we detected high levels of sclerostin in serum samples from GSD patients that could be correlated to defective bone formation and Treg alterations (You et al., 2018). Indeed, You et al. (2018) demonstrated that sclerostin promotes the differentiation of Th17 cells and reduces the differentiation of Treg. Concerning the interplay between Treg and osteoblast lineage, Liu et al. (2011) showed a positive effect on healing upon administration of combined Treg and bone marrow mesenchymal stem cells in a calvarial defect model in mice.

Due to rarity of the disease, limited published studies and incomplete knowledge of the etiology, the GSD lacks effective therapeutic approaches. Available therapeutic options (anti-VEGF-A antibody, bisphosphonates, radiation) are not curative and can be associated with severe side effects (Hagendoorn et al., 2014). The understanding of the impact of immune system on bone remodeling alterations observed in GSD patients could contribute to the identification of new therapeutic options for this rare disease. Recently, there has been an explosion in research investigating the potential to manipulate Treg for clinical purposes (Trzonkowski et al., 2009; Marek-Trzonkowska et al., 2012; von Boehmer and Daniel, 2013). There are several phase I clinical trials to test whether boosting Treg numbers and/or function is a feasible, safe, and potentially effective way to treat diseases such as graft vs. host disease, type 1 diabetes and to prevent the rejection of transplanted organs (Trzonkowski et al., 2009; Marek-Trzonkowska et al., 2012; von Boehmer and Daniel, 2013). An increase of the number of Treg is achievable by Treg transfer or treatment with mTOR (mammalian target of rapamycin) inhibitors (von Boehmer and Daniel, 2013). Recent studies (Ozeki and Fukao, 2019; Ricci et al., 2019; Liang et al., 2020) reported that effectiveness of mTOR inhibitor Sirolimus in the treatment of GSD patients; indeed Sirolimus is known to inhibit lymphangiogenesis and is thought to act on lymphatic tissue within lesions regulating production and leakage of lymph (Ozeki and Fukao, 2019). Sirolimus also stimulates Treg (Battaglia et al., 2006; Strauss et al., 2009), that according with our results, could inhibit bone erosion. Further studies are required to elucidate the effects of Sirolimus treatment on GSD immune and bone cells. However, these observations strengthen the concept that targeting the mechanisms involved in the immune system-bone crosstalk could represent a promising therapeutic approach for GSD patients.

DATA AVAILABILITY STATEMENT

The original contributions presented in the study are included in the article/**Supplementary Material**, further inquiries can be directed to the corresponding author/s.

ETHICS STATEMENT

The studies involving human participants were reviewed and approved by the OPBG Ethical Committee (Protocol Number: GR-2019-12370244, 01/02/2021). Written informed consent to participate in this study was provided by the participants' legal guardian/next of kin.

AUTHOR CONTRIBUTIONS

MR performed the osteoclast culture. GB and VD contributed to the gene expression analysis. IR, PSB, DV, MVG, and AJ recruited the patients and performed the ELISA assays. OP, MD'A, CC, and SM contributed to the hematologic tests and discussion of the results. RD performed the histological analysis. ADF and AB designed and supervised the work and wrote the manuscript. ADF was the guarantor of this work and, as such, had full access to all of the data in the study and takes responsibility for the integrity of the data and the accuracy of the data analysis. All authors reviewed the manuscript and approved the final version.

FUNDING

This work was supported by a research grant (#MDBR-19-116-LGDA/LMI) from the University of Pennsylvania Orphan

Disease Center in partnership with Lymphangiomatosis & Gorham's Disease Alliance and the Lymphatic Malformation Institute to ADF, the Ricerca Finalizzata Ministero della Salute GR-2019-12370244 to ADF, and the European Society for Paediatric Research (ESPR) Post-Doc Research grant to DV.

SUPPLEMENTARY MATERIAL

The Supplementary Material for this article can be found online at: https://www.frontiersin.org/articles/10.3389/fcell.2021.706596/full#supplementary-material

REFERENCES

Arron, J. R., and Choi, Y. (2000). Bone versus immune system. *Nature* 408, 535–536. doi: 10.1038/35046196

Battaglia, M., Stabilini, A., Migliavacca, B., Horejs-Hoeck, J., Kaupper, T., and Roncarolo, M. G. (2006). Rapamycin promotes expansion of functional CD4+CD25+FOXP3+ regulatory T cells of both healthy subjects and type 1 diabetic patients. *J. Immunol.* 177, 8338–8347. doi: 10.4049/jimmunol.177.12.8338

Bozec, A., Zaiss, M. M., Kagwiria, R., Voll, R., Rauh, M., Chen, Z., et al. (2014). T cell costimulation molecules CD80/86 inhibit osteoclast differentiation by inducing the IDO/tryptophan pathway. *Sci. Transl. Med.* 6:235ra60. doi: 10.1126/scitranslmed.3007764

Del Fattore, A., Capannolo, M., and Rucci, N. (2010). Bone and bone marrow: the same organ. *Arch. Biochem. Biophys.* 503, 28–34. doi: 10.1016/j.abb.2010.07.020

Del Fattore, A., Luciano, R., Pascucci, L., Goffredo, B. M., Giorda, E., Scapaticci, M., et al. (2015). Immunoregulatory effects of mesenchymal stem cell-derived extracellular vesicles on T lymphocytes. *Cell Transplant.* 24, 2615–2627. doi: 10.3727/096368915X687543

Dellinger, M. T., Garg, N., Ferry, T., Kelly, J., and Olsen, B. R. (2013). First international conference on generalized lymphatic anomaly and gorham-stout syndrome. *IBMS Bonekey* 10:476.

Dellinger, M. T., Garg, N., and Olsen, B. R. (2014). Viewpoints on vessels and vanishing bones in Gorham-Stout disease. *Bone* 63, 47–52. doi: 10.1016/j.bone.2014.02.011

Dempster, D. W., Compston, J. E., Drezner, M. K., Glorieux, F. H., Kanis, J. A., Malluche, H., et al. (2013). Standardized nomenclature, symbols, and units for bone histomorphometry: a 2012 update of the report of the ASBMR Histomorphometry Nomenclature Committee. *J. Bone Miner. Res.* 28, 2–17. doi: 10.1002/jbmr.1805

Devlin, R. D., Bone, H. G. III, and Roodman, G. D. (1996). Interleukin-6: a potential mediator of the massive osteolysis in patients with Gorham-Stout disease. *J. Clin. Endocrinol. Metab.* 81, 1893–1897. doi: 10.1210/jcem.81.5.8626854

Dickson, G. R., Hamilton, A., Hayes, D., Carr, K. E., Davis, R., and Mollan, R. A. (1990). An investigation of vanishing bone disease. *Bone* 11, 205–210. doi: 10.1016/8756-3282(90)90215-k

Fujisaki, J., Wu, J., Carlson, A. L., Silberstein, L., Putheti, P., Larocca, R., et al. (2011). In vivo imaging of Treg cells providing immune privilege to the haematopoietic stem-cell niche. *Nature* 474, 216–219. doi: 10.1038/nature10160

Hagendoorn, J., Yock, T. I., Borel Rinkes, I. H., Padera, T. P., and Ebb, D. H. (2014). Novel molecular pathways in Gorham disease: implications for treatment. *Pediatr. Blood Cancer* 61, 401–406. doi: 10.1002/pbc.24832

Hu, P., Yuan, X. G., Hu, X. Y., Shen, F. R., and Wang, J. A. (2013). Gorham-Stout syndrome in mainland China: a case series of 67 patients and review of the literature. *J. Zhejiang Univ. Sci. B* 14, 729–735. doi: 10.1631/jzus.B1200308

Ibanez, L., Abou-Ezzi, G., Ciucci, T., Amiot, V., Belaid, N., Obino, D., et al. (2016). Inflammatory osteoclasts prime TNFalpha-producing CD4(+) T cells and express CX3 CR1. *J. Bone Miner. Res.* 31, 1899–1908. doi: 10.1002/jbmr.2868

Jackson, J. (1838). A boneless arm. *Boston Med. Surg. J.* 18, 398–399.

Kiesel, J. R., Buchwald, Z. S., and Aurora, R. (2009). Cross-presentation by osteoclasts induces FoxP3 in CD8+ T cells. *J. Immunol.* 182, 5477–5487. doi: 10.4049/jimmunol.0803897

Konkel, J. E., Zhang, D., Zanvit, P., Chia, C., Zangarle-Murray, T., Jin, W., et al. (2017). Transforming growth factor-beta signaling in regulatory T cells controls T helper-17 cells and tissue-specific immune responses. *Immunity* 46, 660–674. doi: 10.1016/j.immuni.2017.03.015

Liang, Y., Tian, R., Wang, J., Shan, Y., Gao, H., Xie, C., et al. (2020). Gorham-Stout disease successfully treated with sirolimus (rapamycin): a case report and review of the literature. *BMC Musculoskelet. Disord.* 21:577. doi: 10.1186/s12891-020-03540-7

Lin, G., Wang, J., Lao, X., Wang, J., Li, L., Li, S., et al. (2012). Interleukin-6 inhibits regulatory T cells and improves the proliferation and cytotoxic activity of cytokine-induced killer cells. *J. Immunother.* 35, 337–343. doi: 10.1097/CJI.0b013e318255ada3

Liu, W., Putnam, A. L., Xu-Yu, Z., Szot, G. L., Lee, M. R., Zhu, S., et al. (2006). CD127 expression inversely correlates with FoxP3 and suppressive function of human CD4+ T reg cells. *J. Exp. Med.* 203, 1701–1711. doi: 10.1084/jem.20060772

Liu, Y., Wang, L., Kikuiri, T., Akiyama, K., Chen, C., Xu, X., et al. (2011). Mesenchymal stem cell-based tissue regeneration is governed by recipient T lymphocytes via IFN-gamma and TNF-alpha. *Nat. Med.* 17, 1594–1601. doi: 10.1038/nm.2542

Marek-Trzonkowska, N., Mysliwiec, M., Dobyszuk, A., Grabowska, M., Techmanska, I., Juscinska, J., et al. (2012). Administration of CD4+CD25highCD127- regulatory T cells preserves beta-cell function in type 1 diabetes in children. *Diabetes Care* 35, 1817–1820. doi: 10.2337/dc12-0038

Nikolaou, V. S., Chytas, D., Korres, D., and Efstathopoulos, N. (2014). Vanishing bone disease (Gorham-Stout syndrome): a review of a rare entity. *World J. Orthop.* 5, 694–698. doi: 10.5312/wjo.v5.i5.694

Ozeki, M., and Fukao, T. (2019). Generalized lymphatic anomaly and Gorham-Stout disease: overview and recent insights. *Adv. Wound Care (New Rochelle)* 8, 230–245. doi: 10.1089/wound.2018.0850

Patel, D. V. (2005). Gorham's disease or massive osteolysis. *Clin. Med. Res.* 3, 65–74. doi: 10.3121/cmr.3.2.65

Ricci, K. W., Hammill, A. M., Mobberley-Schuman, P., Nelson, S. C., Blatt, J., Bender, J. L. G., et al. (2019). Efficacy of systemic sirolimus in the treatment of generalized lymphatic anomaly and Gorham-Stout disease. *Pediatr. Blood Cancer* 66:e27614. doi: 10.1002/pbc.27614

Rossi, M., Buonuomo, P. S., Battafarano, G., Conforti, A., Mariani, E., Algeri, M., et al. (2020). Dissecting the mechanisms of bone loss in Gorham-Stout disease. *Bone* 130:115068. doi: 10.1016/j.bone.2019.115068

Rossi, M., Rana, I., Buonuomo, P. S., Battafarano, G., Mariani, E., D'Agostini, M., et al. (2021). Dysregulated miRNAs in bone cells of patients with Gorham-Stout disease. *FASEB J.* 35:e21424. doi: 10.1096/fj.202001904RR

Sato, M., Asada, N., Kawano, Y., Wakahashi, K., Minagawa, K., Kawano, H., et al. (2013). Osteocytes regulate primary lymphoid organs and fat metabolism. *Cell Metab.* 18, 749–758. doi: 10.1016/j.cmet.2013.09.014

Strauss, L., Czystowska, M., Szajnik, M., Mandapathil, M., and Whiteside, T. L. (2009). Differential responses of human regulatory T cells (Treg) and effector T cells to rapamycin. *PLoS One* 4:e5994. doi: 10.1371/journal.pone.0005994

Terashima, A., and Takayanagi, H. (2018). Overview of osteoimmunology. *Calcif. Tissue Int.* 102, 503–511. doi: 10.1007/s00223-018-0417-1

Tolis, K., Triantafyllopoulos, I. K., Tournis, S., and Papaioannou, N. A. (2016). Gorham-Stout disease of the pelvis: seven years follow up with complete radiological evaluation. *J. Musculoskelet. Neuronal. Interact.* 16, 79–82.

Trzonkowski, P., Bieniaszewska, M., Juscinska, J., Dobyszuk, A., Krzystyniak, A., Marek, N., et al. (2009). First-in-man clinical results of the treatment of patients with graft versus host disease with human ex vivo expanded CD4+CD25+CD127- T regulatory cells. *Clin. Immunol.* 133, 22–26. doi: 10.1016/j.clim.2009.06.001

von Boehmer, H., and Daniel, C. (2013). Therapeutic opportunities for manipulating T(Reg) cells in autoimmunity and cancer. *Nat. Rev. Drug Discov.* 12, 51–63. doi: 10.1038/nrd3683

You, L., Chen, L., Pan, L., Peng, Y., and Chen, J. (2018). SOST gene inhibits osteogenesis from adipose-derived mesenchymal stem cells by inducing Th17 cell differentiation. *Cell Physiol. Biochem.* 48, 1030–1040. doi: 10.1159/000491971

Yuan, F. L., Li, X., Lu, W. G., Xu, R. S., Zhao, Y. Q., Li, C. W., et al. (2010). Regulatory T cells as a potent target for controlling bone loss. *Biochem. Biophys. Res. Commun.* 402, 173–176. doi: 10.1016/j.bbrc.2010.09.120

Zaiss, M. M., Axmann, R., Zwerina, J., Polzer, K., Guckel, E., Skapenko, A., et al. (2007). Treg cells suppress osteoclast formation: a new link between the immune system and bone. *Arthritis Rheum.* 56, 4104–4112. doi: 10.1002/art.23138

Zaiss, M. M., Frey, B., Hess, A., Zwerina, J., Luther, J., Nimmerjahn, F., et al. (2010). Regulatory T cells protect from local and systemic bone destruction in arthritis. *J. Immunol.* 184, 7238–7246. doi: 10.4049/jimmunol.0903841

Conflict of Interest: The authors declare that the research was conducted in the absence of any commercial or financial relationships that could be construed as a potential conflict of interest.

Publisher's Note: All claims expressed in this article are solely those of the authors and do not necessarily represent those of their affiliated organizations, or those of the publisher, the editors and the reviewers. Any product that may be evaluated in this article, or claim that may be made by its manufacturer, is not guaranteed or endorsed by the publisher.

frontiers in Cell and Developmental Biology

ORIGINAL RESEARCH
published: 14 September 2021
doi: 10.3389/fcell.2021.720688

A Dominant Heterozygous Mutation in *COG4* Causes Saul–Wilson Syndrome, a Primordial Dwarfism, and Disrupts Zebrafish Development via Wnt Signaling

Zhi-Jie Xia[1], Xin-Xin I. Zeng[1,2], Mitali Tambe[1,3], Bobby G. Ng[1], P. Duc S. Dong[1,4] and Hudson H. Freeze[1]**

[1] Human Genetics Program, Sanford Burnham Prebys Medical Discovery Institute, La Jolla, CA, United States, [2] Development, Aging and Regeneration Program, Sanford Burnham Prebys Medical Discovery Institute, La Jolla, CA, United States, [3] National Centre for Advancing Translational Sciences, National Institutes of Health, Bethesda, MD, United States, [4] Graduate School of Biomedical Sciences, Sanford Burnham Prebys Medical Discovery Institute, La Jolla, CA, United States

OPEN ACCESS

Edited by:
Amélie E. Coudert, Université Paris Diderot, France

Reviewed by:
Ross F. Collery, Medical College of Wisconsin, United States
Tangliang Li, Shandong University, China

***Correspondence:**
Xin-Xin I. Zeng
szeng@sbpdiscovery.org
Hudson H. Freeze
hudson@sbpdiscovery.org

Specialty section:
This article was submitted to Molecular and Cellular Pathology, a section of the journal Frontiers in Cell and Developmental Biology

Received: *04 June 2021*
Accepted: *13 August 2021*
Published: *14 September 2021*

Citation:
Xia ZJ, Zeng XXI, Tambe M, Ng BG, Dong PDS and Freeze HH (2021) A Dominant Heterozygous Mutation in COG4 Causes Saul–Wilson Syndrome, a Primordial Dwarfism, and Disrupts Zebrafish Development via Wnt Signaling. Front. Cell Dev. Biol. 9:720688. doi: 10.3389/fcell.2021.720688

Saul–Wilson syndrome (SWS) is a rare, skeletal dysplasia with progeroid appearance and primordial dwarfism. It is caused by a heterozygous, dominant variant (p.G516R) in COG4, a subunit of the conserved oligomeric Golgi (COG) complex involved in intracellular vesicular transport. Our previous work has shown the intracellular disturbances caused by this mutation; however, the pathological mechanism of SWS needs further investigation. We sought to understand the molecular mechanism of specific aspects of the SWS phenotype by analyzing SWS-derived fibroblasts and zebrafish embryos expressing this dominant variant. SWS fibroblasts accumulate glypicans, a group of heparan sulfate proteoglycans (HSPGs) critical for growth and bone development through multiple signaling pathways. Consistently, we find that glypicans are increased in zebrafish embryos expressing the *COG4*$^{p.G516R}$ variant. These animals show phenotypes consistent with convergent extension (CE) defects during gastrulation, shortened body length, and malformed jaw cartilage chondrocyte intercalation at larval stages. Since non-canonical Wnt signaling was shown in zebrafish to be related to the regulation of these processes by glypican 4, we assessed *wnt* levels and found a selective increase of *wnt4* transcripts in the presence of *COG4*$^{p.G516R}$. Moreover, overexpression of *wnt4* mRNA phenocopies these developmental defects. LGK974, an inhibitor of Wnt signaling, corrects the shortened body length at low concentrations but amplifies it at slightly higher concentrations. WNT4 and the non-canonical Wnt signaling component phospho-JNK are also elevated in cultured SWS-derived fibroblasts. Similar results from SWS cell lines and zebrafish point to altered non-canonical Wnt signaling as one possible mechanism underlying SWS pathology.

Keywords: Saul–Wilson syndrome, COG4, glypican, WNT4, zebrafish, early development

INTRODUCTION

Saul–Wilson syndrome (SWS) is a rare skeletal dysplasia characterized by profound short stature and distinctive craniofacial features such as prominent forehead, prominent eyes, and micrognathia (Saul and Wilson, 1990; Ferreira et al., 2020). Recently, we defined a specific heterozygous COG4 substitution (p.G516R) as the molecular basis of this rare form of primordial dwarfism (Ferreira et al., 2018). COG4 is one of the eight subunits of the conserved oligomeric Golgi (COG) complex regulating protein trafficking and Golgi homeostasis (Ungar et al., 2002). Biallelic pathogenic variants in *COG4* and other COG subunits cause multiple human congenital disorders of glycosylation (CDGs) (D'Souza et al., 2020). COG4-CDG individuals have a very severe, usually lethal, phenotype with dysmorphia, neurological and intellectual disabilities, and altered N-glycosylation with an almost total loss of COG4 (Reynders et al., 2009; Ng et al., 2011). However, SWS subjects show very different features, since their N-glycans and their intellectual and neurological features appear normal (Ferreira et al., 2018). At the cellular level, the $COG4^{p.G516R}$ variant disrupted protein trafficking by accelerating brefeldin-A (BFA)-induced retrograde transport and delaying anterograde transport, causing the collapse of the Golgi stacks. This interrupted bidirectional trafficking between the ER and the Golgi and altered decorin, a proteoglycan (Ferreira et al., 2018), indicate that modified proteoglycans may be involved in the pathogenesis of SWS.

Proteoglycans play critical roles in multiple cell processes at the cellular, tissue, and organismal levels, and their deficiencies cause bone and connective tissue disorders (Iozzo and Schaefer, 2015; Paganini et al., 2019). Several proteoglycan deficiencies have been studied in zebrafish, a powerful vertebrate model for studying CDGs and skeletal disorders, with some showing a shortened body axis (Zoeller et al., 2009; Cline et al., 2012; Lee et al., 2020; Tonelli et al., 2020; Dietrich et al., 2021). Besides a body axis defect, morpholino-mediated knockdown of zebrafish decorin (*dcn*) displayed relatively severe defects in body curvature associated with a curved or not fully extended tail (Zoeller et al., 2009). Defects in glypicans, a group of heparan sulfate proteoglycans (HSPGs), can cause abnormal skull and skeletal dysplasia in both humans (Simpson–Golabi–Behmel syndrome: glypican 3, GPC3; Keipert syndrome: glypican 4, GPC4) and zebrafish (Knypek: Gpc4) (LeClair et al., 2009; Tenorio et al., 2014). Interestingly, studies of *knypek* (*kny*/*gpc4*) mutant zebrafish demonstrated that Gpc4 deficiency causes chondrocyte stacking and intercalation defects in Meckel's cartilage, which is not seen in *dcn* morphants or *chondroitin sulfate proteoglycan 4* (*cspg4*)-deficient zebrafish (Topczewski et al., 2001; Zoeller et al., 2009; Hu et al., 2012; Lee et al., 2020). *kny* adult zebrafish also show craniofacial defects including a smaller head, domed skull, and shorter jawbones, reminiscent of some of the clinical features of SWS individuals (Topczewski et al., 2001; LeClair et al., 2009). Studies also found that optimized expression of *gpc4* can suppress the defects caused by Wnt11f2 (formerly known as Wnt11/Silberblick; Postlethwait et al., 2019) deficiency, indicating the role of Gpc4 in the Wnt signaling pathway, probably as a Wnt coreceptor (LeClair et al., 2009). It is worth noting that both absence and high expression of *gpc4* lead to the loss of ability to suppress Wnt11f2 deficiency (Topczewski et al., 2001). Presumably, abnormalities arise when either these receptors or ligands are outside the optimal ratio. Taken together, the similarity between *kny* mutant zebrafish craniofacial defects and some of the SWS individuals' clinical features encouraged us to use zebrafish as a vertebrate model to explore the underlying pathological mechanism of SWS.

The zebrafish Cog4 is 72% identical to human COG4, and the amino acid corresponding to the SWS mutation site is conserved across multiple vertebrate species.[1] Zebrafish that lack the Cog4 protein show phenotypes consistent with the clinical features of COG4-CDG individuals, including defective synthesis of N- and O-linked glycans and decreased glycosphingolipid complexity (Clement et al., 2019). SWS individuals show very different features compared to COG4-CDG individuals, and SWS cells show accelerated BFA-induced retrograde trafficking in contrast to COG4-CDG cells. Considering these facts, a zebrafish model for the SWS-specific variant is highly desired to investigate phenotypic features and the possible pathogenesis of this heterozygous mutation in *COG4*.

In this study, we utilize SWS-derived fibroblasts and a zebrafish system to test a specific heterozygous COG4 substitution (p.G516R), which is causal for SWS. We assessed a broader category of proteoglycans and found a consistent increase of glypican level in SWS-derived fibroblasts and zebrafish expressing human $COG4^{p.G516R}$ variant. Further studies on non-canonical Wnts revealed that the presence of $COG4^{p.G516R}$ specifically elevated the *wnt4* transcript, but not *wnt5a*, *wnt5b*, or *wnt11f2*. Overexpression of *wnt4* phenocopies the $COG4^{p.G516R}$ zebrafish, and the Wnt inhibitor LGK974 suppresses the defects caused by the expression of $COG4^{p.G516R}$. These findings suggest that disrupted Wnt signaling is one possible mechanism underlying the pathogenesis of SWS.

RESULTS

Fibroblasts From SWS Individuals Accumulate Glypicans on the Cell Surface

As one of the major components of extracellular matrix (ECM) and cell membrane proteins, proteoglycans comprise a large, heterogeneous group including HSPGs and chondroitin sulfate proteoglycans (CSPGs). Decorin is a predominant proteoglycan in human skin, covalently linked with one glycosaminoglycan chain (GAG), which requires normal function of the Golgi for its posttranslational modification. Our results showing abnormal decorin modification encouraged us to study other proteoglycans in SWS cells. As a first step in determining which proteoglycan may change, we analyzed the core proteins of HSPGs using an antibody (3G10) against HS-stubs (a heparan sulfate neo-epitope) that appear only after heparinase III digestion. As shown in **Figure 1A**, glypicans, syndecan 1, and syndecan 2 were the most prevalent cell surface HSPGs in dermal fibroblasts.

[1] www.uniprot.org

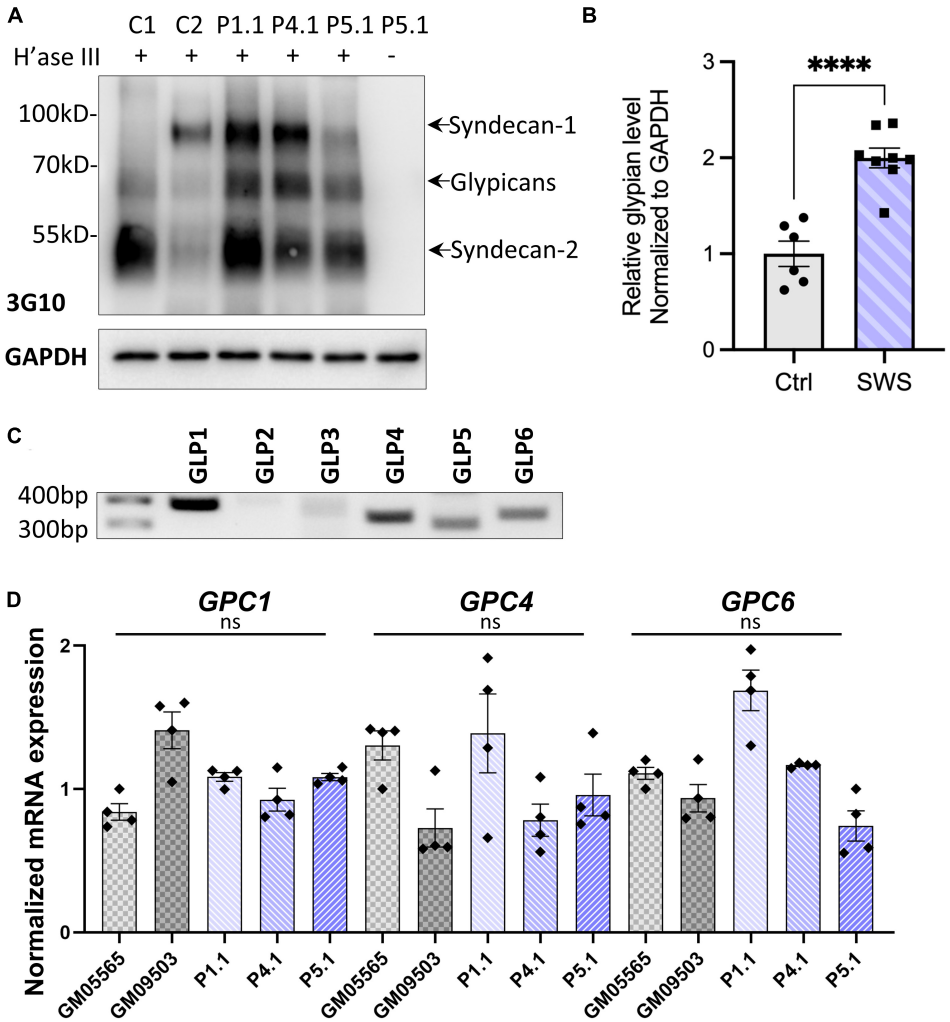

FIGURE 1 | SWS-derived fibroblasts show altered HSPGs and glypicans after heparinase III (H'ase III) digestion. **(A)** Western blotting of ΔHS-stub using 3G10 antibody following heparinase III digestion of three SWS-derived fibroblasts and two control fibroblasts. C1 and C2 are control fibroblasts. C1, GM08429; C2, GM08680. P1.1, P4.1, and P5.1 are SWS-derived fibroblasts. **(B)** Quantitation assay of glypican band density in **(A)** and two other replicates. The data are presented as mean ± SEM. An unpaired two-tailed *t*-test was used. ****$p < 0.0001$. **(C)** Agarose gel of six human glypicans after reverse-transcript PCR. **(D)** qPCR of three dominant glypicans in SWS-derived fibroblasts. The relative glypican level was normalized to GAPDH. The graphs represent the $2^{-\Delta\Delta Ct}$ values. Experiments were performed in triplicates with similar results.

Compared to syndecans, glypicans showed consistent increases in all three SWS cell lines with an average twofold elevation (**Figure 1B**). We performed qPCR to assess whether transcript abundance is also altered. There are six glypicans in humans, and among those, glypicans 1, 4, and 6 are present in multiple tissues, while glypicans 3 and 5 are restricted to the ovary and brain. Glypican 2 is specifically expressed in the nervous system during embryonic development (Thul and Lindskog, 2018; Guo et al., 2020). As seen in **Figure 1C**, glypicans 1, 4, 5, and 6 were detectable in dermal fibroblasts; however, we did not observe a significant change in any of their transcript abundance (**Figure 1D**). We hypothesize that this increase of glypicans results from SWS COG4-dependent abnormal trafficking or turnover, instead of transcriptional regulation. A similar strategy was applied to study CSPGs. Chondroitinase ABC was used to digest CSPGs followed by immunoblotting against the ΔDi-6S. There was a general decrease of CSPG core proteins in three out of four SWS-derived cell lines (**Supplementary Figure 1**). Considering that glypicans show the most prominent difference between controls and SWS-derived cells and the phenotypes of *gpc4* mutant zebrafish, we focused on glypicans in our study.

Expression of Human *COG4*$^{p.G516R}$ in Zebrafish Increases Glypican Proteins

To study the impact of the SWS variant on skeletal development, we used zebrafish as a vertebrate model. Since SWS is a dominant disorder, we overexpressed the human SWS allele in developing zebrafish embryos. Human *COG4*^{WT} and *COG4*$^{p.G516R}$ mRNAs

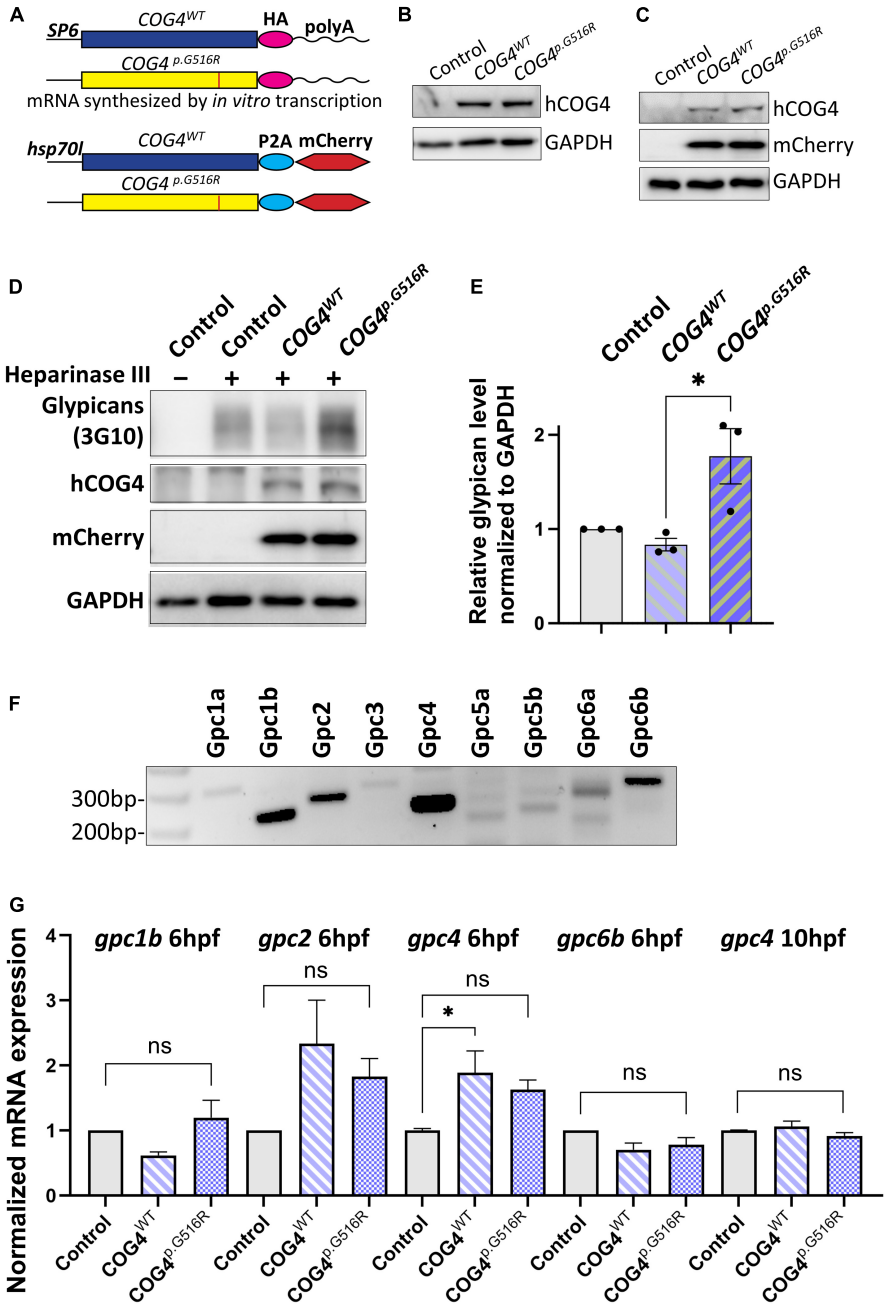

FIGURE 2 | Expression of human *COG4*$^{p.G516R}$ in zebrafish increases the protein level of glypicans. **(A–C)** Expression of human *COG4*^{WT} and *COG4*$^{p.G516R}$ in zebrafish after mRNA or DNA injection. **(A)** The scheme of *COG4* constructs for *in vitro* transcription (top) and DNA injection (bottom). **(B)** Western blot at 24 hpf to detect the presence of COG4 after mRNA injection. **(C)** Western blot at 48 hpf to detect COG4 after DNA injection; heat shock was performed at 24 hpf for 2 h at 38°C. **(D–G)** Glypican analysis in zebrafish. **(D)** Western blotting of ΔHS-stub using 3G10 antibody following heparinase III digestion of control and embryos injected with *COG4*^{WT} or *COG4*$^{p.G516R}$ mRNA at 3 dpf. **(E)** Quantitation assay of glypican band density in **(D)** and two more replicates. The data are presented as mean ± SEM. An unpaired two-tailed *t*-test was used. *$p < 0.05$. **(F)** mRNA expression of glypican genes by RT-PCR using cDNA from control embryos at 6 hpf. **(G)** qPCR analyses of highly expressed glypicans in control and zebrafish embryos injected with human *COG4*^{WT} or *COG4*$^{p.G516R}$ mRNA. The relative glypican level was normalized to β-*actin*. The graphs represent the $2^{-\Delta\Delta Ct}$ values. One-way ANOVA with Tukey's multiple comparison tests was applied. ns, not significant; *$p < 0.05$. Experiments were performed in triplicates with similar results.

or DNA constructs, as shown in **Figure 2A**, were injected into one-cell-stage embryos. The presence of human COG4 in zebrafish was confirmed by an antibody specifically recognizing human COG4 protein (**Figures 2B,C**). Lacking a zebrafish Cog4 antibody makes it impossible to determine the relative expression level of *COG4*$^{p.G516R}$; therefore, we include *COG4*^{WT} as an

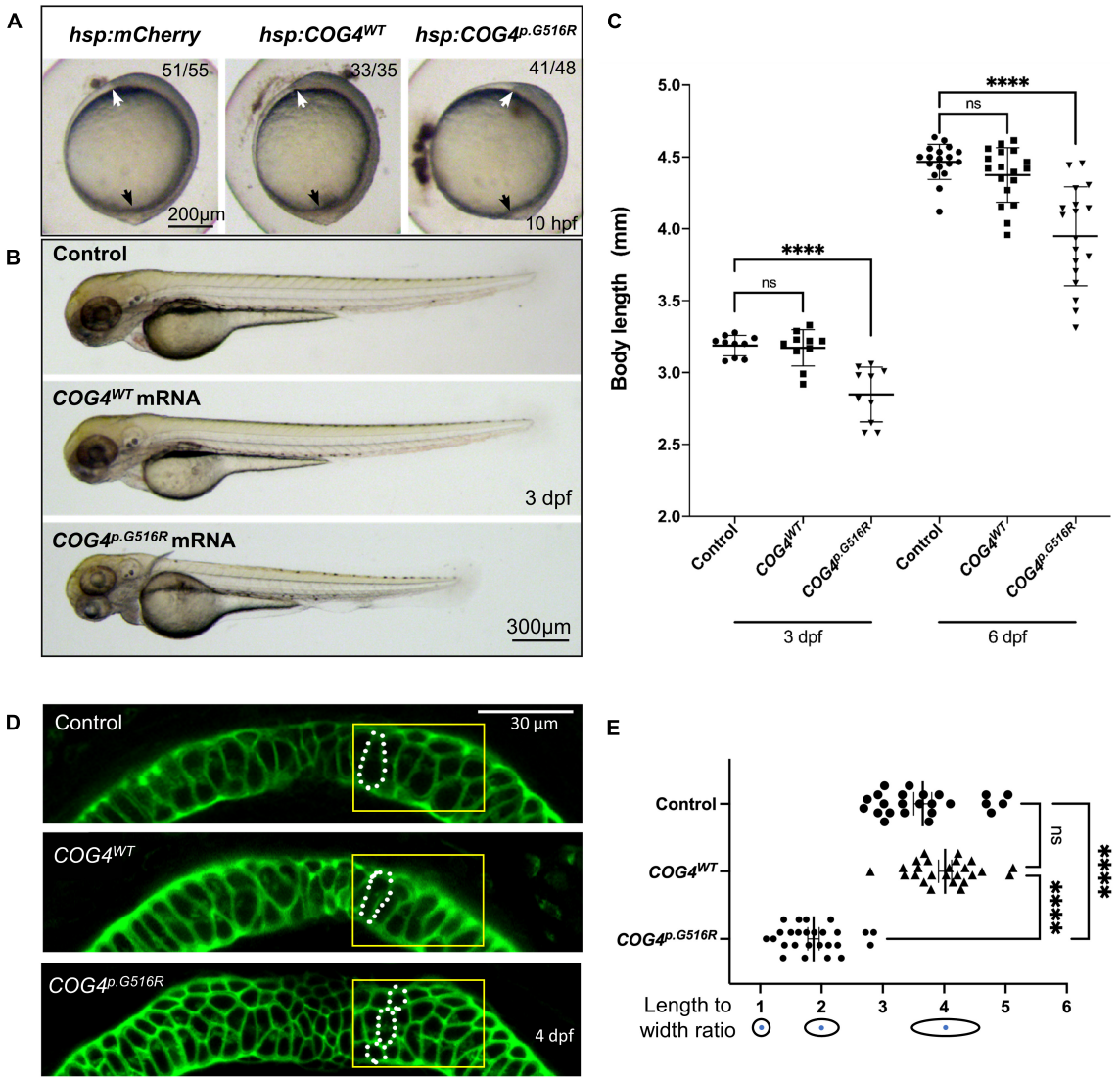

FIGURE 3 | Expression of human *COG4*$^{p.G516R}$ impairs zebrafish early development and chondrocyte intercalation. **(A,B)** Expression of *COG4*$^{p.G516R}$ in zebrafish causes gastrulation defects and shortened body axis. **(A)** Lateral view of representative embryos. Anterior to the top. Compared to the control construct *hsp70l:mCherry* and *COG4*^{WT}, embryos expressing *COG4*$^{p.G516R}$ show an axis extension defect at 10 hpf. White arrow points to the head region, and the black arrow points to the tailbud. Expression of *COG4*$^{p.G516R}$ mRNA causes similar results. **(C)** Graphs show the measured body length of each group at 3 and 6 dpf. The data are presented as mean ± SD. One-way ANOVA with Tukey's multiple comparison tests was applied. ****$p < 0.0001$; ns, not significant. **(D)** Expression of *COG4*$^{p.G516G}$ causes craniofacial abnormalities. Ventral view of representative Meckel's cartilage of zebrafish larvae at 4 dpf after WGA staining and imaged by a confocal microscope. Dotted circular lines highlight chondrocyte cell shape and their relative configuration with each other. **(E)** Graphical representation of the length-to-width ratio of chondrocytes in the region of interest, yellow box in **(D)**. Individual cell length-to-width ratio was measured in three representative Meckel's cartilage images of each group. The data are presented as mean ± SEM. One-way ANOVA with Tukey's multiple comparison tests was applied. ****$p < 0.0001$; ns, not significant. Experiments were performed in triplicates with similar results.

injected control to ensure comparable expression of *COG4*$^{p.G516R}$ in zebrafish. Both *COG4*^{WT} and *COG4*$^{p.G516R}$ were expressed at a very similar level (**Figures 2B,C**), and no adverse effects were seen in embryos expressing *COG4*^{WT} compared to uninjected siblings.

We first checked glypican proteins using the same strategy as in SWS-derived cells. Interestingly, we found increased glypicans in embryos expressing *COG4*$^{p.G516R}$ but not *COG4*^{WT} at 3 dpf (days post-fertilization) (**Figures 2D,E**), consistent with the observation in SWS-derived fibroblasts. Zebrafish have 10 glypicans expressed at different developmental stages (Gupta and Brand, 2013). At 6 hpf (hours post-fertilization), we detected five glypicans, namely, Gpc1b, Gpc2, Gpc4, Gpc6a, and Gpc6b, by RT-PCR (**Figure 2F**), followed by qPCR to compare their transcript levels. We found that the *gpc2* and *gpc4* transcript levels are elevated in both *COG4*^{WT} and *COG4*$^{p.G516R}$ embryos compared to the uninjected control, but there is no significant difference between *COG4*^{WT} and *COG4*$^{p.G516R}$ (**Figure 2G**). At 10 hpf, the transcript level of endogenous *gpc4* fell to a level comparable to

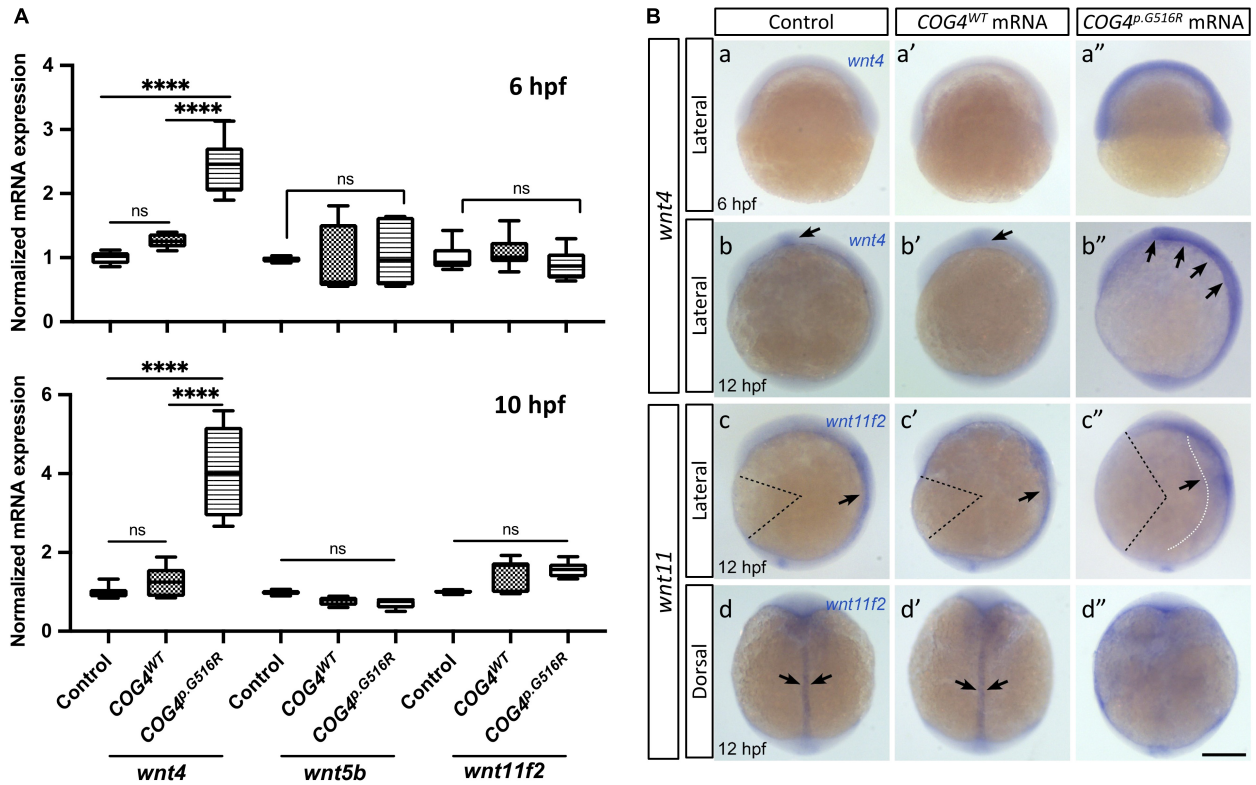

FIGURE 4 | Expression of human $COG4^{p.G516R}$ elevates the *wnt4* transcript in zebrafish embryos. **(A)** Quantitative PCR analyses of selective non-canonical Wnt pathway ligands in zebrafish embryos injected with human $COG4^{WT}$ or $COG4^{p.G516R}$ mRNA. At 6 hpf, *wnt4* expression is significantly upregulated in embryos injected with $COG4^{p.G516R}$ mRNA, but not in those injected with $COG4^{WT}$ mRNA. Similar upregulation of *wnt4* transcripts is observed at 10 hpf as well. Bar graphs represent average gene expression relative to the housekeeping gene β-*actin*. The data are presented as mean ± SD. One-way ANOVA with Tukey's multiple comparison tests was used. ****$p < 0.0001$; ns, not significant. **(B)** Representative images of whole-mount *in situ* hybridization from control and treated embryos. Whole-mount *in situ* hybridization analyses demonstrate that *wnt4* expression is elevated in embryos injected with $COG4^{p.G516R}$ mRNA (a″, at 6 hpf; b″ at 12 hpf), but there are no obvious changes in embryos injected with human $COG4^{WT}$ mRNA (a′ and b′). (b, b′) Arrows point to the restricted *wnt4* expression domain in the hindbrain of zebrafish embryos at 12 hpf; (b″) arrows point to expanded expression of *wnt4* in the hindbrain region. At 12 hpf, *wnt11f2* expression intensity is not significantly changed in embryos injected with $COG4^{p.G516R}$ mRNA (c″, d″), compared to either control siblings (c, d) or human $COG4^{WT}$ mRNA-injected embryos (c′, d′). The dotted black color lines landmark the degree of angle between the head and tail, which is much more increased in embryos injected with $COG4^{p.G516R}$ mRNA, suggesting defects in extension movement during gastrulation. Arrows in c, c′ and d, d″ indicate that *wnt11f2* is restricted to the dorsal midline; however, its expression pattern is dispersed in $COG4^{p.G516R}$ mRNA-injected embryos, suggesting that the convergence movement is impaired (c″, white dotted line and arrow; d″, there is no clear midline expression). Scale bars: 200 μm. Experiments were performed in triplicates with similar results.

that of the control, with no distinction between $COG4^{WT}$ and $COG4^{p.G516R}$ (**Figure 2G**). The *gpc2* mRNA level at 10 hpf was barely detectable.

Expression of Human $COG4^{p.G516R}$ in Zebrafish Shortens Body Length and Causes Abnormal Chondrocyte Stacking and Intercalation

We examined zebrafish body length at different stages to assess the developmental phenotypes caused by $COG4^{p.G516R}$ expression. At the end of gastrulation, embryos expressing the $COG4^{p.G516R}$ variant exhibit shorter axis extension (**Figure 3A**), suggesting an abnormal convergent extension (CE) movement (Topczewski et al., 2001). Embryos expressing $COG4^{WT}$ developed normally (**Figure 3A**). We tracked these injected embryos at later stages and found that expression of $COG4^{p.G516R}$ causes a shortened anterior–posterior (AP) body axis (**Figure 3B**) by an average of 18% at 3 dpf and 10% at 6 dpf (**Figure 3C**).

To investigate whether the presence of $COG4^{p.G516R}$ in zebrafish impacts chondrocyte development, zebrafish at 4 dpf were stained with wheat germ agglutinin (WGA), a lectin binding to glycoproteins in cartilage ECM to visualize chondrocyte morphology. In embryos expressing $COG4^{p.G516R}$, Meckel's cartilage was deformed, shown as defects in chondrocyte stacking and elongation (**Figure 3D**). Compared to $COG4^{WT}$ embryos, more rounded chondrocytes were present in Meckel's cartilage (**Figure 3E**). These defects can be observed as late as 7 dpf, as shown by Alcian blue staining (**Supplementary Figure 2**). Chondrocyte stacking and intercalation problems further confirmed that abnormal glypican levels could be one of the pathogenetic mechanisms involved in SWS. Other phenotypes seen in $COG4^{p.G516R}$-injected embryos also include abnormal, stunted fin, and cyclopia (**Supplementary Figures 3A,B**).

Expression of Human *COG4*$^{p.G516R}$ Elevates the *wnt4* Transcript in Zebrafish

Glypican 4 plays an essential role in gastrulation movements and contributes to craniofacial morphogenesis probably through planar cell polarity (PCP)/non-canonical Wnt signaling (Topczewski et al., 2001; Sisson et al., 2015). Therefore, we assessed the expression of non-canonical *wnt*s by qPCR and their spatial–temporal transcription pattern by whole-mount *in situ* hybridization. We found that *COG4*$^{p.G516R}$ mRNA-injected embryos contain more *wnt4* compared to controls (**Figure 4A**). In contrast, no significant changes were detected in a few other non-canonical *wnt*s, such as *wnt5b* and *wnt11f2*. Also, the upregulation of *wnt4* shows a dose-dependent response to the amount of *COG4*$^{p.G516R}$ mRNA injected (**Supplementary Figure 4**). This elevated transcript level of *wnt4* was further confirmed by whole-mount *in situ* hybridization (**Figure 4B**). At 6 hpf, *wnt4* was not detectable in either control or *COG4*^{WT} mRNA-injected embryos, but it was in *COG4*$^{p.G516R}$-mRNA injected embryos. At 10 hpf, *wnt4* is confined to the hindbrain in control and *COG4*^{WT} embryos, but *COG4*$^{p.G516R}$ embryos had both increased and spatially expanded expression of *wnt4*. The *wnt11f2* transcript level did not change, but the distribution pattern was significantly altered. In uninjected control and *COG4*^{WT} embryos, *wnt11f2* was restricted to the dorsal midline. However, its expression pattern is dispersed in *COG4*$^{p.G516R}$ embryos. No measurable difference was found for β-catenin protein, a marker of canonical Wnt signaling between *COG4*$^{p.G516R}$ and controls (**Supplementary Figure 6**).

Overexpression of Zebrafish *wnt4* Causes Shortened Body Length and Malformed Meckel's Cartilage

In zebrafish, *wnt4* overexpression has been studied at earlier embryonic stages and was found to inhibit cell movements without altering cell fates (Ungar et al., 1995; Topczewski et al., 2001). Thus, we evaluated the phenotypes of *wnt4* overexpression at a later embryonic stage. At 4 dpf, *wnt4* mRNA-injected embryos showed shortened body length in response to the dosage of *wnt4* injected (**Figure 5A**). Interestingly, we also found abnormal chondrocyte stacking in Meckel's cartilage (**Figure 5B**) and cyclopia (**Figure 5C**). These data show that overexpression of *wnt4* phenocopies shortened body length and malformed chondrocyte intercalation in *COG4*$^{p.G516R}$-injected zebrafish.

WNT Inhibitor LGK974 Suppresses the Defects Caused by *COG4*$^{p.G516R}$ Expression

We hypothesize that the increased abundance of *wnt4* contributes to the pathogenetic mechanism for SWS. Therefore, reducing Wnt4 activity may suppress the developmental defects caused by the presence of *COG4*$^{p.G516R}$. LGK974 is a pharmacological inhibitor of WNT porcupine *O*-acyltransferase (PORCN), which affects palmitoylation and secretion of Wnts. After optimizing the treatment procedure (**Figure 6A**), we found that 0.05–0.2 μM of LGK974 significantly shortened the body length of control siblings (**Supplementary Figure 5**) without causing optic cup morphogenesis and shorter tail induced by high concentrations of LGK974 (Eckert et al., 2019). A 24-h incubation with low concentrations (0.05 and 0.1 μM) of LGK974 restored the shortened body length caused by *COG4*$^{p.G516R}$ expression at 4 dpf (**Figure 6B**). Higher concentrations (0.15 and 0.2 μM) of LGK974 further shortened the body length in *COG4*$^{p.G516R}$ injected zebrafish, showing that there is a narrow optimal range for Wnt activity. These data suggest that the imbalance of Wnt signaling may contribute to SWS pathogenesis. We also examined the chondrocyte morphology in Meckel's cartilage and found that 0.05 and 0.1 μM of LGK974 are sufficient to suppress the deformed cartilage caused by *COG4*$^{p.G516R}$ expression. Up to 0.1 μM LGK974 does not cause significant defects in control chondrocytes (**Figures 6C,D**).

WNT4 Is Elevated at mRNA and Protein Levels in SWS-Derived Fibroblasts

To assess whether a similar mechanism was at play in human cells, we assayed the transcript abundance of *WNT4* and other non-canonical *WNT*s in SWS individuals' fibroblasts. Interestingly, both *WNT4* transcript and protein levels were increased in SWS individual fibroblasts (**Figures 7A–C**). Neither *WNT5a*, *WNT5b*, nor *WNT11* showed consistent significant differences in three SWS-derived cell lines (**Figure 7A**). We further detected downstream gene expression in the non-canonical pathway and found increased JNK phosphorylation (pJNK) in SWS cells compared to controls (**Figures 7B,C**), indicating an elevated non-canonical Wnt signaling. We further examined Wnt signaling markers in zebrafish and found that p-Rac1/cdc42, a marker for non-canonical Wnt pathway, was elevated in embryos expressing *COG4*$^{p.G516R}$, but not those of *COG4*^{WT}. A similar increase of p-Rac1/cdc42 was also seen in *wnt4* overexpression embryos (**Supplementary Figure 6**). β-Catenin, a marker for the canonical Wnt pathway, did not change (**Figure 7B**).

DISCUSSION

In this paper, we utilized SWS-derived fibroblasts and zebrafish, a vertebrate model to study SWS. In SWS-derived cells, the specific p.G516R amino acid substitution in COG4 selectively affected proteoglycans instead of global glycosylation. Increased glypicans were seen in both SWS-derived cells and *COG4*$^{p.G516R}$-injected zebrafish embryos. Glypicans are glycosylphosphatidylinositol-anchored proteins (GPI-APs) that consist of a conserved core glycan, phosphatidylinositol, glycan side chains, and a protein moiety (Kinoshita, 2020). A recent study found that subunits of the COG complex affect proteoglycan turnover and GAG chain polymerization (Adusumalli et al., 2021). Studies also found that glycosylation changes of a cell surface protein could affect the protein's half-life (Ohtsubo et al., 2005). Therefore, the increased glypicans are probably due to impaired protein trafficking or turnover caused by COG4$^{p.G516R}$ rather than changes in glypican transcript abundance. In previous *gpc4* zebrafish studies, Topczewski demonstrated that Gpc4 regulates cellular movements during gastrulation by potentiating Wnt11f2 signaling and chondrocyte behavior independent of core Wnt

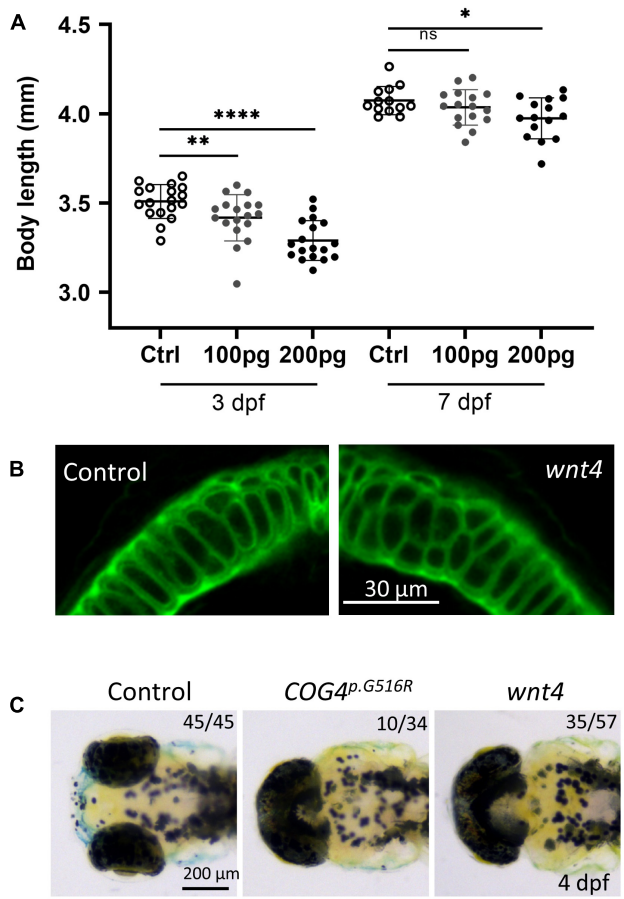

FIGURE 5 | Overexpression of *wnt4* phenocopies zebrafish embryos injected with the $COG4^{p.G516G}$ mRNA. **(A)** Graphs show the measured body length of each group after *wnt4* mRNA injection at 3 and 7 dpf. The data are presented as mean ± SD. An unpaired two-tailed *t*-test was used. $^{****}p < 0.0001$; $^{**}p < 0.01$; $^{*}p < 0.05$; ns, not significant. **(B)** Overexpression of *wnt4* causes abnormal chondrocyte stacking and intercalation at Meckel's cartilage. Ventral view of representative Meckel's cartilage of zebrafish larvae after *wnt4* injection at 4 dpf following WGA staining and imaged by a confocal microscope. **(C)** Overexpression of *wnt4* causes cyclopia as expression of the $COG4^{p.G516G}$ variant. Dorsal view of representative images of cyclopia compared to control. Two hundred picograms of *wnt4* or $COG4^{p.G516G}$ mRNA was used per embryo. Experiments were performed in triplicates with similar results.

pathway molecules (Topczewski et al., 2001; Sisson et al., 2015). Interestingly, low expression of *gpc4* suppressed Wnt11f2 defects, but high overexpression of *gpc4* inhibited the rescue, indicating a requirement for a fine balance between Gpc4 and Wnt11f2 to ensure normal development. This is also true for COG4 function, since more than twofold accumulation of COG4 leads to similar protein trafficking defects as seen in COG4-deficient cells (Reynders et al., 2009). Therefore, $COG4^{WT}$ is an essential control in this zebrafish study to confirm that the expression of *COG4* is not excessive to impair its normal function.

Multiple studies have shown the role of glypicans in regulating Wnt signaling. In zebrafish, Gpc4 has been reported as a positive modulator of non-canonical Wnt signaling during zebrafish gastrulation (Topczewski et al., 2001). Studies in both *Drosophila* and *Xenopus* found that glypicans can modulate the distribution of Wnt through binding the palmitoleate on Wnts and thus contribute to the release of signaling-competent Wnt (Franch-Marro et al., 2005; Yan et al., 2009; McGough et al., 2020). Among two groups of glypicans, Dally and Dally-like (Dlp) subfamilies, only Dlp has this palmitoleate-binding activity, which mainly includes Gpc4 and Gpc6 (McGough et al., 2020). Studies in chick embryos demonstrated that Gpc4 in the neural crest enhances Wnt1/Wnt3a signaling and *wnt11* expression on the dorsomedial lip (Serralbo and Marcelle, 2014). Our data also suggest the role of glypicans in regulating Wnt signaling. We hypothesize that the accumulation of glypican(s) could induce the transcriptional upregulation of *wnt4*. However, lacking a specific Gpc4 antibody in zebrafish makes it difficult to confirm whether Gpc4 is the major player in causing these phenotypes seen in $COG4^{p.G516R}$-injected embryos. Simply overexpressing *gpc4* in zebrafish seems to show no significant defects (LeClair et al., 2009). We speculate that the abnormalities seen in $COG4^{p.G516R}$-injected embryos are due to disrupted glypican trafficking or turnover rather than changes in glypican expression. Further studies on how glypican and Wnt4 crosstalk is yet to be demonstrated. More studies are ongoing in our lab to further address these questions. Whereas glypicans are the most impaired proteoglycans caused by the heterozygous variant in COG4 (p.G516R), we could not rule out that other proteoglycans may also contribute to the pathogenesis of SWS. Although knockdown of *dcn* and *cspg4* in zebrafish does not show chondrocyte intercalation problems, they may cause a shorter body axis or other types of cartilage malformations (Zoeller et al., 2009; Lee et al., 2020).

Besides increased glypicans, it is interesting that we also found an elevated *wnt4* transcript in SWS-derived cells and $COG4^{p.G516R}$-injected zebrafish embryos. Studies have shown that the cell surface receptor could directly regulate WNT4 expression in chondrocytes (Dennis et al., 2020). Therefore, we hypothesize that the increased WNT4 is probably a compensatory transcriptional response to increased glypicans. Wnts are a group of secreted glycoproteins involved in cell–cell signaling (Niehrs, 2012; Willert and Nusse, 2012). To date, 22 Wnts have been identified in vertebrates (the Wnt homepage: http://web.stanford.edu/group/nusselab/cgi-bin/wnt/). Among those, Wnt4 has shown important roles in embryonic development, skeletal/bone regeneration, and sex determination with additional developmental defects in a cell-specific and tissue-specific manner (Matsui et al., 2005; Bernard and Harley, 2007; Chang et al., 2007; Rao et al., 2019; Yang et al., 2020). Most importantly, Wnt4 plays a pivotal role in regulating chondrocyte differentiation. In chick limb studies, *Wnt4* expression is found in joint cells and cartilage, and its misexpression accelerates maturation of chondrocytes, causing shortened long bones (Kawakami et al., 1999; Hartmann and Tabin, 2000; Church et al., 2002). An *in vitro* study also found that Wnt4 blocks the initiation of chondrogenesis and accelerates terminal chondrocyte differentiation (Church et al., 2002). Misexpression of *Zwnt4* (zebrafish *wnt4*) and *Xwnt4* (*Xenopus wnt4*) in zebrafish causes shortened trunk and tail (Ungar et al., 1995) and abnormal chondrocyte intercalation in Meckel's cartilage (our

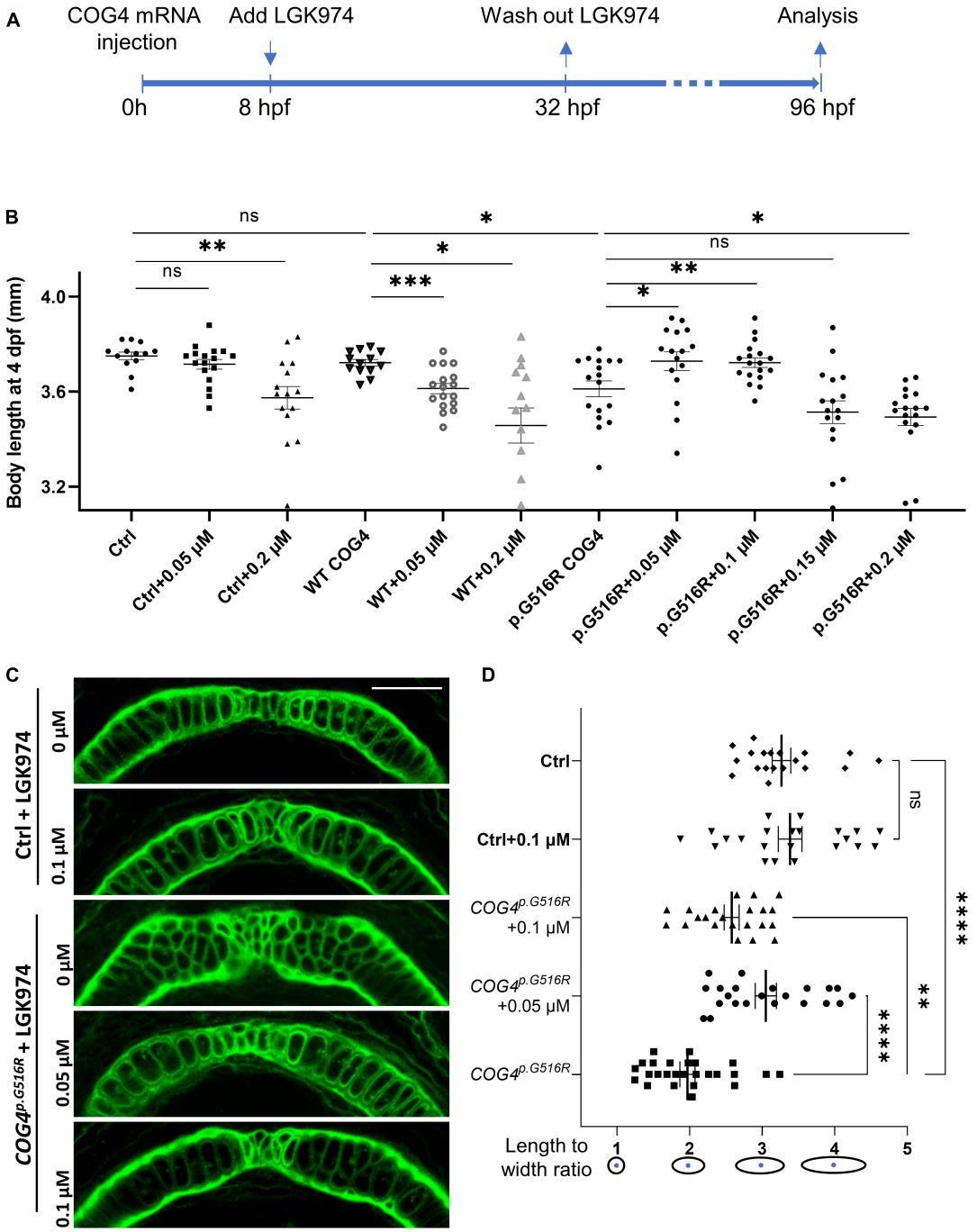

FIGURE 6 | LGK974 treatment suppresses shortened body length and chondrocyte defect caused by of *COG4*$^{p.G516G}$ expression in zebrafish. **(A)** Scheme of the LGK974 treatment procedure. **(B)** Graphs show the measured body length of each group at 4 dpf. The data are presented as mean ± SEM. An unpaired two-tailed *t*-test was used. ***$p < 0.001$; **$p < 0.01$; *$p < 0.05$; ns, not significant. **(C)** Ventral view of representative Meckel's cartilage of control and *COG4*$^{p.G516G}$-injected embryos with or without LGK974 treatment at 4 dpf following WGA staining and imaged by a confocal microscope. **(D)** Graphs show the length-to-width ratio of chondrocytes in Meckel's cartilage in **(C)** and two more representative Meckel's cartilage images of each group. The data are presented as mean ± SEM. One-way ANOVA with Tukey's multiple comparison tests was applied. ****$p < 0.0001$; **$p < 0.01$; ns, not significant. Experiments were performed in two biological replicates with similar results.

data), confirming Wnt4 is involved in regulation of chondrocyte behavior, like *gpc4* and *wnt5b* (Sisson et al., 2015). In mice, Wnt4 defects led to short-limb dwarfism (Dennis et al., 2020). Most relevant, conditional expression of *Wnt4* in mice also causes dwarfism with small skeletons, dome-shaped skulls, and small jaws (Lee and Behringer, 2007). Both *Wnt4* defects

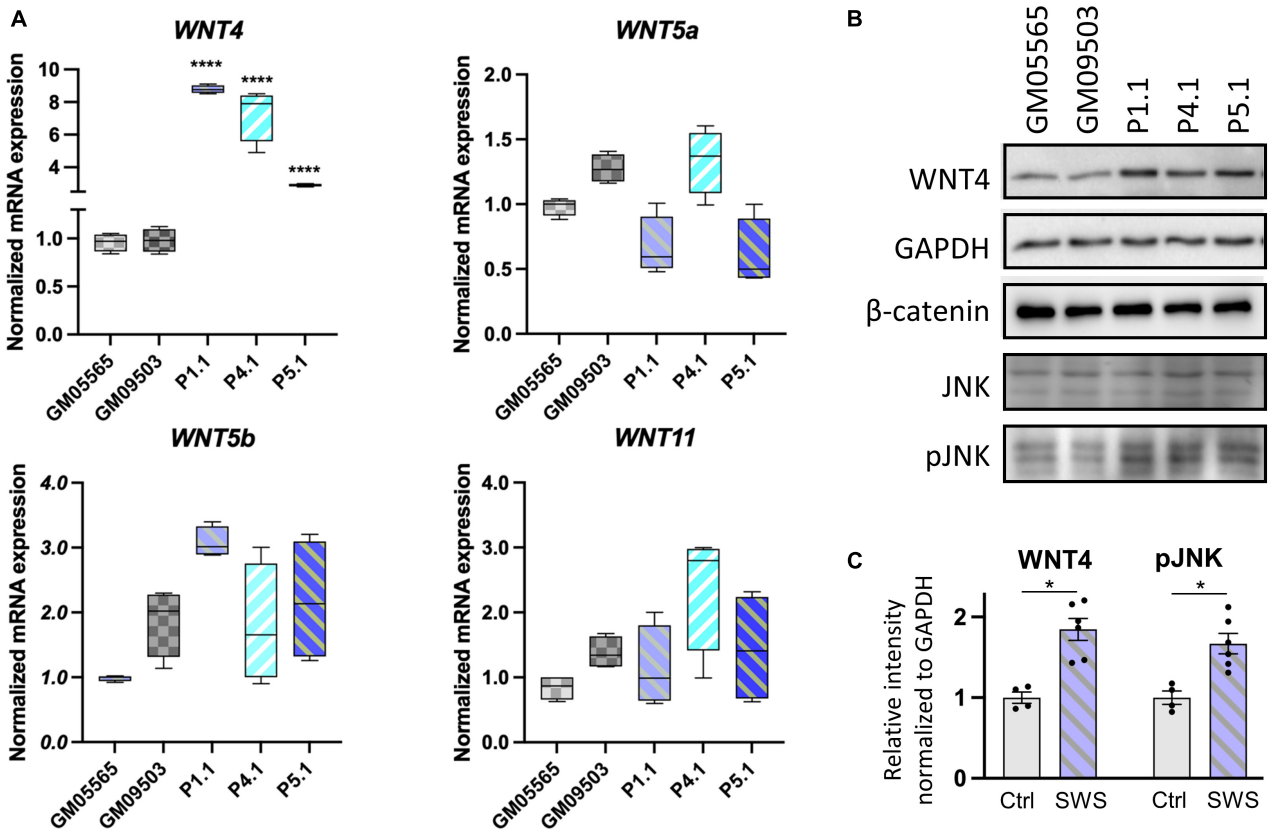

FIGURE 7 | Non-canonical WNTs and related component level in SWS-derived cells. **(A)** qPCR analyses of selective non-canonical Wnt pathway components in SWS-derived fibroblasts. GAPDH was used as an internal control. The graphs represent the $2^{-\Delta\Delta Ct}$ values. Unpaired two-tailed *t*-test was applied for comparison of each SWS fibroblast with two controls. ****$p < 0.0001$. Experiments were performed in triplicates with similar results. **(B)** Western blotting of a few Wnt pathway components. GM05565 and GM09503 are control fibroblasts. P1.1, P4.1, and P5.1 are SWS-derived fibroblasts. **(C)** Quantitation assay of WNT4 and pJNK band density in **(B)** and the other replicates. The data are presented as mean ± SEM. An unpaired two-tailed *t*-test was used. *$p < 0.05$.

and overexpression cause dwarfism, indicating Wnt4 functions within a narrow range for normal development, and bidirectional disturbance causes developmental abnormalities.

LGK974 is a PORCN inhibitor that blocks PORCN-dependent palmitoylation and secretion of WNT family ligands (Liu et al., 2013). Currently, it is being evaluated as an anticancer agent against a broad range of diseases associated with deviant Wnt signaling (Liu et al., 2013; Zhang and Lum, 2016). LGK974 has been used to inhibit canonical and non-canonical signaling in multiple studies as a WNT modifier (Han et al., 2017; Katoh, 2017; Lutze et al., 2019). In our study, titrating LGK974 allowed us to regulate the amount of Wnt during development. At low concentrations, it suppressed and nearly normalized the shortened body length caused by the presence of COG4$^{p.G516R}$, probably by inhibiting Wnt4 (or other Wnts) palmitoylation and secretion. This rescue experiment not only supports altered Wnt signaling as one of the possible pathogenesis mechanisms contributing to SWS but also suggests a potential therapeutic strategy for SWS individuals.

In our SWS zebrafish model, the specific heterozygous dominant variant in COG4 (p.G516R) shows elevated glypicans and *wnt4*, along with developmental defects. Compared to COG4-KO zebrafish (Ferreira et al., 2018; Clement et al., 2019), it is impressive that the single mutation in COG4 is sufficient for shortened body length and abnormal chondrocyte stacking. However, there are still some differences between COG4-KO and *COG4*$^{p.G516R}$ zebrafish; for example, the single variant in COG4 does not decrease the overall GAG amount shown in COG4-KO zebrafish by Alcian blue staining. *COG4*$^{p.G516R}$ larvae also show cyclopia and a distinct pectoral fin phenotype compared to COG4-KO zebrafish.

In summary, using SWS-derived fibroblasts and a zebrafish model, we demonstrated that the specific dominant variant COG4$^{p.G516R}$ causes the accumulation of GPI-anchored glypicans, which most likely involves COG4-dependent altered trafficking or turnover of these proteins. In zebrafish, the presence of COG4$^{p.G516R}$ also elevates *wnt4* transcript and causes chondrocyte morphogenesis defects, which might explain the short stature and distinctive craniofacial features in SWS individuals. WNT4 and non-canonical Wnt signaling component pJNK are also elevated in cultured SWS-derived fibroblasts. We further demonstrate that the Wnt inhibitor LGK974 could suppress the defects caused by *COG4*$^{p.G516R}$ in zebrafish. These results from SWS-derived cell lines and zebrafish point to

altered non-canonical Wnt signaling as one possible mechanism underlying SWS pathology. How increased $COG4^{p.G516R}$ leads to elevated *WNT4* in SWS cells and zebrafish is still unknown. Transgenic and CRISPR-knock-in SWS zebrafish lines are under development to address these issues.

MATERIALS AND METHODS

Cell Cultures

Dermal primary fibroblasts derived from healthy controls (GM08429, GM08680, GM03349, GM05565, and GM09503) were obtained from Coriell Institute for Medical Research (Camden, NJ). Each SWS-derived fibroblast line was obtained by the referring clinician and grown via a clinical laboratory service and then sent to us with consent through an approved IRB.

Fibroblasts were cultured in Dulbecco's Modified Eagle's medium (DMEM) containing 1 g/L glucose supplemented with 10% heat-inactivated fetal bovine serum (FBS) and 1% antibiotic–antimycotic (Life Technologies, Carlsbad, CA, United States).

Zebrafish Husbandry

All zebrafish experiments were performed in accordance with the protocols approved by SBP IACUC. Zebrafish were maintained under standard laboratory conditions at 28.5°C. Embryos were staged according to Kimmel et al. (1995).

Immunoblotting

For glypicans analysis, fibroblasts were treated with 5 mU/ml heparinase III in a serum-free medium for 1 h at 37°C. Zebrafish larvae were homogenized and treated with 25 mU heparinase III in H buffer (20 mM Tris-HCl, pH 7.0, 0.1 mg/ml BSA, and 4 mM $CaCl_2$) for 1.5 h at 37°C. Samples were harvested using SDS lysis buffer (62.5 mM Tris-HCl, pH 6.8, 2% SDS, and 10% glycerol) supplemented with protease and phosphatase inhibitors (Sigma-Aldrich) as previously described (Ferreira et al., 2018). For analysis of PCP pathway components, 2×10^4 fibroblast cells were seeded in six-well plates and harvested after 2 days using SDS lysis buffer. Equal amounts of denatured proteins were separated via SDS–polyacrylamide gel electrophoresis followed by transfer and antibody inoculation as described previously (Tambe et al., 2019). Antibodies used were Δ-heparan sulfate (AMSBIO, F69-3G10), chondroitin 6 sulfate (Millipore, MAB2035), GAPDH (Invitrogen, MA5-15738), WNT4 (R&D, MAB4751), mCherry (Rockland, 600-401-P16), COG4 (provided by Dr. Daniel Ungar, University of York, United Kingdom), β-catenin (Santa Cruz, sc-7963), JNK (sc-7345), pJNK (sc-293136), and p-Rac1/cdc42 (Cell Signaling, #2461).

mRNA Expression Analysis

Total RNA was extracted from cells or zebrafish embryos using TRIzol™ (Thermo Fisher, 15596081) reagent according to the manufacturer protocol. cDNA was synthesized using a QuantiTect Reverse Transcription Kit (QIAGEN, 205311). qPCR and data analysis were performed as described previously (Tambe et al., 2019). Briefly, primer pairs targeting genes of interest were designed using NCBI Primer-BLAST and available upon request. qPCRs were performed with the PowerUp SYBR®Green PCR Master Mix (Thermo Fisher, A25742). The standardized cycle conditions were applied in Applied Biosystems 7900HT Fast Real-Time PCR System. SDS2.3 software was used to analyze expression data of reference genes. The mRNA levels were normalized to the levels of housekeeping genes, *GAPDH* for fibroblasts and β-*actin* for zebrafish, and $2^{-\Delta\Delta Ct}$ values were calculated and compared.

Immunofluorescence

Whole-mount immunofluorescence was performed as previously described (Alexander et al., 1998), using lectin WGA (Vector Laboratories, FL1021) against the cell membrane. Fluorescence images were acquired using an LSM 510 confocal microscope (Zeiss, Germany) with a × 40 water objective. Digital images were processed with Adobe Creative Suites.

Cloning of Human *COG4* and *in vitro* mRNA Synthesis

Full-length human *COG4* was cloned into the pCS2 + vector from plasmid hCOG4-siR-3myc in AAZ6 (a gift from Professor Vladimir V. Lupashin) using an In-Fusion® HD Cloning Kit (TaKaRa Bio, 638909) with primers 5′-ATGGGAACCAAGATGGCGGA-3′, 5′-TTACAGGCGCAG CCTCTTGATAT-3′, 5′-ATCAAGAGGCTGCGCCTGTAATCA AGGCCTCTCGAGCCTCT-3′, and 5′-TCCGCCATCTTGGTT CCCATATTCGAATCGATGGGATCCT-3′. SWS point mutation of G to A was generated using Q5® Site-Directed Mutagenesis Kit (NEB, E0554S) with primers 5′-CATCCAGCGCa GGGTGACAAG-3′ and 5′-TCCTGGAAGGTGGTGGCA-3′. WT *COG4* and SWS *COG4* mRNAs ($COG4^{WT}$ and $COG4^{p.G516R}$) were synthesized using the Invitrogen mMESSAGE mMACHINE SP6 Transcription Kit (Thermo Fisher, AM1340) following restriction enzyme *Not*I digestion and purified using a MEGAclear™ Transcription Clean-Up Kit (Thermo Fisher, AM1908). One hundred picograms of mRNA was injected into each zebrafish embryo unless stated otherwise. As a complementing strategy, *Hsp70l:COG4-P2A-mCherry*, *cryaa:dsRED*, and SWS *COG4* were generated by cloning the coding sequence for WT *COG4* and SWS *COG4* downstream of the Hsp70l promoter in the parent vector *hsp70l:-LateSV40pA*, *cryaa:dsRED-RabBGpA*, and *I-Sce* vector (a gift from Dr. Joseph Lancman). I-*Sce*I meganuclease (NEB, R0694) was co-injected with 20 pg of the constructs per embryo.

Cloning of Full-Length Zebrafish *wnt4* and Synthesizing Antisense Probes

Full-length zebrafish *wnt4* was cloned from cDNA into the pCS2 + vector using an In-Fusion® HD Cloning Kit with the following primers: 5′-CCCATCGATTCGAATATGTCATCG GAGTATTTGATAAGGT-3′, 5′-CTCGAGAGGCCTTGATCA CCGACACGTGTGCAT-3′, 5′-TCAAGGCCTCTCGAGCCT CT-3′, and 5′-ATTCGAATCGATGGGATCCTGCA-3′. *wnt4* mRNA synthesis and purification were performed as described above. One hundred picograms of mRNA was injected into each

zebrafish embryo unless mentioned otherwise. For antisense RNA probe synthesis, the full length of *wnt4* including 3′-UTR was cloned into the pGEM-T easy vector (Promega, A1360) by primers 5′-ATGTCATCGGAGTATTTGATAAGG-3′ and 5′-AGTCTTTGACACAGCATATATTTC-3′ from cDNA. After verifying the insertion direction by sequencing, the antisense RNA probe was then synthesized with SP6 RNA polymerase following *Apa*I digestion.

Standard Whole-Mount *in situ* Hybridization

Standard whole-mount *in situ* hybridization was performed as described previously (Thisse and Thisse, 2008). INT/BCIP (175 μg/ml; Roche) was used as alkaline phosphatase substrates. The following molecular markers were used: *wnt4* and *wnt11f2* (a gift from Dr. Diane Sepich, previously used in Makita et al., 1998; Marlow et al., 2002).

Wnt Inhibition Assay

LGK974 (Cayman Chemical, No. 14072) was dissolved in DMSO to make a 10 μM stock. Different concentrations of LGK974 were added to the control or injected zebrafish groups at 8 hpf for 24 h. DMSO of 0.01% was used as a vehicle.

DATA AVAILABILITY STATEMENT

The datasets presented in this study can be found in online repositories. The names of the repository/repositories and accession number(s) can be found below: GenBank: NM_015386.3, NM_001040387.1 (https://www.ncbi.nlm.nih.gov/nuccore/NM_015386.3).

ETHICS STATEMENT

The animal study was reviewed and approved by the Institutional Animal Care and Use Committee (IACUC) protocols of Sanford Burnham Prebys Medical Discovery Institute.

AUTHOR CONTRIBUTIONS

Z-JX, X-XZ, PDSD, and HHF conceptualized the project, designed the experiments, and oversaw all studies. Z-JX, X-XZ, MT, and BGN performed the experiments and analyzed the data with HHF. Z-JX and X-XZ prepared the figures. HHF and PDSD contributed to research funding. Z-JX and X-XZ wrote the manuscript with coauthors. All authors reviewed and contributed to editing the manuscript.

FUNDING

This work was supported by the Rocket Fund (HHF), R01DK99551 (HHF), and R01DK124583 (PDSD). Z-JX was a Rocket Fund Fellow.

ACKNOWLEDGMENTS

We thank Heather Flanagan-Steet for providing reagents and guidance and for critical reading of the manuscript. We thank Yu Yamaguchi for critical discussion. We thank Diane Sepich for providing the *wnt11f2* DNA construct for *in situ* probe synthesis.

SUPPLEMENTARY MATERIAL

The Supplementary Material for this article can be found online at: https://www.frontiersin.org/articles/10.3389/fcell.2021.720688/full#supplementary-material

Supplementary Figure 1 | Western blots of CSPG following chondroitinase ABC digestion to generate CS-stubs. C1 and C2 are control fibroblasts. C1, GM0849; C2, GM0860. P1.1, P4.1, and P5.1 are SWS-derived fibroblasts.

Supplementary Figure 2 | Expression of $COG4^{p.G516R}$ in zebrafish shows abnormal chondrocyte intercalation of Meckel's cartilage at the late developmental stage. Ventral view of representative Meckel's cartilage of zebrafish larvae at 7 dpf after Alcian blue staining, imaged by a light dissecting microscope. Dotted circular lines highlight cell shape and their relative configuration with each other.

Supplementary Figure 3 | Expression of $COG4^{p.G516R}$ in zebrafish causes cyclopia, stunted fin, and abnormal ceratohyal cartilage in zebrafish. **(A)** Expression of $COG4^{p.G516G}$ causes cyclopia in zebrafish. Dorsal view of representative images of cyclopia compared to control and $COG4^{WT}$. Two hundred picograms of $COG4^{WT}$ or $COG4^{p.G516G}$ mRNA was injected into each embryo. **(B)** Ventral view of representative zebrafish larvae at 6 dpf after Alcian blue staining, imaged by a light dissecting microscope. Twenty picograms of DNA was injected into each embryo, and heat shock was performed at 24 and 46 hpf for 1 h each at 38°C.

Supplementary Figure 4 | *wnt4* upregulation shows a dose-dependent response to $COG4^{p.G516R}$ mRNA. Bar graphs represent quantitative PCR analyses of *wnt4* at 6 hpf after injection of different amounts of $COG4^{p.G516R}$ mRNA. *wnt4* expression was normalized to β-*actin*. $^{****}p < 0.0001$; $^{**}p < 0.01$; ns, not significant.

Supplementary Figure 5 | Dose-dependent response analysis of the Wnt inhibitor LGK974 in zebrafish. **(A)** Body length at 3 dpf after LGK974 treatment. **(B)** Representative images after LGK974 treatment at 3 dpf. The data are presented as mean. $^{****}p < 0.0001$.

Supplementary Figure 6 | Expression of $COG4^{p.G516R}$ and *wnt4* elevated non-canonical Wnt signaling in zebrafish. Samples for Western blots were collected at 6 hpf. The p-Rac1/cdc42 level increased in embryos injected with $COG4^{p.G516R}$ mRNA, but not with $COG4^{WT}$ mRNA. Similar elevation of p-Rac1/cdc42 was also seen in *wnt4* overexpression embryos. β-Catenin did not change.

REFERENCES

Adusumalli, R., Asheim, H. C., Lupashin, V., Blackburn, J. B., and Prydz, K. (2021). Proteoglycan synthesis in conserved oligomeric Golgi subunit deficient HEK293T cells is affected differently, depending on the lacking subunit. *Traffic* 22, 230–239. doi: 10.1111/tra.12804

Alexander, J., Stainier, D. Y., and Yelon, D. (1998). Screening mosaic F1 females for mutations affecting zebrafish heart induction and patterning. *Dev. Genet.* 22, 288–299. doi: 10.1002/(sici)1520-6408(1998)22:3<288::aid-dvg10>3.0.co;2-2

Bernard, P., and Harley, V. R. (2007). Wnt4 action in gonadal development and sex determination. *Int. J. Biochem. Cell Biol.* 39, 31–43. doi: 10.1016/j.biocel.2006.06.007

Chang, J., Sonoyama, W., Wang, Z., Jin, Q., Zhang, C., Krebsbach, P. H., et al. (2007). Noncanonical Wnt-4 signaling enhances bone regeneration of mesenchymal stem cells in craniofacial defects through activation of p38 MAPK. *J. Biol. Chem.* 282, 30938–30948. doi: 10.1074/jbc.m702391200

Church, V., Nohno, T., Linker, C., Marcelle, C., and Francis-West, P. (2002). Wnt regulation of chondrocyte differentiation. *J. Cell Sci.* 115, 4809–4818. doi: 10.1242/jcs.00152

Clement, A., Blanco-Sanchez, B., Peirce, J. L., and Westerfield, M. (2019). Cog4 is required for protrusion and extension of the epithelium in the developing semicircular canals. *Mech. Dev.* 155, 1–7. doi: 10.1016/j.mod.2018.09.003

Cline, A., Gao, N., Flanagan-Steet, H., Sharma, V., Rosa, S., Sonon, R., et al. (2012). A zebrafish model of PMM2-CDG reveals altered neurogenesis and a substrate-accumulation mechanism for N-linked glycosylation deficiency. *Mol. Biol. Cell* 23, 4175–4187. doi: 10.1091/mbc.e12-05-0411

Dennis, E. P., Edwards, S. M., Jackson, R. M., Hartley, C. L., Tsompani, D., Capulli, M., et al. (2020). CRELD2 is a novel LRP1 chaperone that regulates Noncanonical WNT signaling in skeletal development. *J. Bone Miner. Res.* 35, 1452–1469. doi: 10.1002/jbmr.4010

Dietrich, K., Fiedler, I. A., Kurzyukova, A., Lopez-Delgado, A. C., McGowan, L. M., Geurtzen, K., et al. (2021). Skeletal biology and disease modeling in Zebrafish. *J. Bone Miner. Res.* 36, 436–458.

D'Souza, Z., Taher, F. S., and Lupashin, V. V. (2020). Golgi inCOGnito: from vesicle tethering to human disease. *Biochim. Biophys. Acta Gen. Subj.* 1864:129694. doi: 10.1016/j.bbagen.2020.129694

Eckert, P., Knickmeyer, M. D., Schutz, L., Wittbrodt, J., and Heermann, S. (2019). Morphogenesis and axis specification occur in parallel during optic cup and optic fissure formation, differentially modulated by BMP and Wnt. *Open Biol.* 9:180179. doi: 10.1098/rsob.180179

Ferreira, C. R., Xia, Z. J., Clement, A., Parry, D. A., Davids, M., Taylan, F., et al. (2018). A recurrent *de novo* heterozygous COG4 substitution leads to saul-wilson syndrome, disrupted vesicular trafficking, and Altered Proteoglycan Glycosylation. *Am. J. Hum. Genet.* 103, 553–567. doi: 10.1016/j.ajhg.2018.09.003

Ferreira, C. R., Zein, W. M., Huryn, L. A., Merker, A., Berger, S. I., Wilson, W. G., et al. (2020). Defining the clinical phenotype of Saul-Wilson syndrome. *Genet. Med.* 22, 857–866.

Franch-Marro, X., Marchand, O., Piddini, E., Ricardo, S., Alexandre, C., and Vincent, J. P. (2005). Glypicans shunt the Wingless signal between local signalling and further transport. *Development* 132, 659–666. doi: 10.1242/dev.01639

Guo, M., Zhang, H., Zheng, J., and Liu, Y. (2020). Glypican-3: a new target for diagnosis and treatment of hepatocellular Carcinoma. *J. Cancer* 11, 2008–2021. doi: 10.7150/jca.39972

Gupta, M., and Brand, M. (2013). Identification and expression analysis of zebrafish glypicans during embryonic development. *PLoS One* 8:e80824. doi: 10.1371/journal.pone.0080824

Han, T., Schatoff, E. M., Murphy, C., Zafra, M. P., Wilkinson, J. E., Elemento, O., et al. (2017). R-Spondin chromosome rearrangements drive Wnt-dependent tumour initiation and maintenance in the intestine. *Nat. Commun.* 8:15945.

Hartmann, C., and Tabin, C. J. (2000). Dual roles of Wnt signaling during chondrogenesis in the chicken limb. *Development* 127, 3141–3159. doi: 10.1242/dev.127.14.3141

Hu, G., Codina, M., and Fisher, S. (2012). Multiple enhancers associated with ACAN suggest highly redundant transcriptional regulation in cartilage. *Matrix Biol.* 31, 328–337.

Iozzo, R. V., and Schaefer, L. (2015). Proteoglycan form and function: a comprehensive nomenclature of proteoglycans. *Matrix Biol.* 42, 11–55.

Katoh, M. (2017). Canonical and non-canonical WNT signaling in cancer stem cells and their niches: cellular heterogeneity, omics reprogramming, targeted therapy and tumor plasticity (Review). *Int. J. Oncol.* 51, 1357–1369. doi: 10.3892/ijo.2017.4129

Kawakami, Y., Wada, N., Nishimatsu, S. I., Ishikawa, T., Noji, S., and Nohno, T. (1999). Involvement of Wnt-5a in chondrogenic pattern formation in the chick limb bud. *Dev. Growth Differ.* 41, 29–40. doi: 10.1046/j.1440-169x.1999.00402.x

Kimmel, C. B., Ballard, W. W., Kimmel, S. R., Ullmann, B., and Schilling, T. F. (1995). Stages of embryonic development of the zebrafish. *Dev. Dyn.* 203, 253–310.

Kinoshita, T. (2020). Biosynthesis and biology of mammalian GPI-anchored proteins. *Open Biol.* 10:190290. doi: 10.1098/rsob.190290

LeClair, E. E., Mui, S. R., Huang, A., Topczewska, J. M., and Topczewski, J. (2009). Craniofacial skeletal defects of adult zebrafish Glypican 4 (knypek) mutants. *Dev. Dyn.* 238, 2550–2563. doi: 10.1002/dvdy.22086

Lee, H. H., and Behringer, R. R. (2007). Conditional expression of *Wnt4* during chondrogenesis leads to dwarfism in mice. *PLoS One* 2:e450. doi: 10.1371/journal.pone.0000450

Lee, Y. H., Kawakami, K., HuangFu, W. C., and Liu, I. H. (2020). Chondroitin sulfate proteoglycan 4 regulates zebrafish body axis organization via Wnt/planar cell polarity pathway. *PLoS One* 15:e0230943. doi: 10.1371/journal.pone.0230943

Liu, J., Pan, S., Hsieh, M. H., Ng, N., Sun, F., Wang, T., et al. (2013). Targeting Wnt-driven cancer through the inhibition of Porcupine by LGK974. *Proc. Natl. Acad. Sci. U.S.A.* 110, 20224–20229.

Lutze, G., Haarmann, A., Demanou Toukam, J. A., Buttler, K., Wilting, J., and Becker, J. (2019). Non-canonical WNT-signaling controls differentiation of lymphatics and extension lymphangiogenesis via RAC and JNK signaling. *Sci. Rep.* 9:4739.

Makita, R., Mizuno, T., Koshida, S., Kuroiwa, A., and Takeda, H. (1998). Zebrafish wnt11: pattern and regulation of the expression by the yolk cell and No tail activity. *Mech. Dev.* 71, 165–176. doi: 10.1016/s0925-4773(98)00013-6

Marlow, F., Topczewski, J., Sepich, D., and Solnica-Krezel, L. (2002). Zebrafish Rho kinase 2 acts downstream of Wnt11 to mediate cell polarity and effective convergence and extension movements. *Curr. Biol.* 12, 876–884. doi: 10.1016/s0960-9822(02)00864-3

Matsui, T., Raya, A., Kawakami, Y., Callol-Massot, C., Capdevila, J., Rodriguez-Esteban, C., et al. (2005). Noncanonical Wnt signaling regulates midline convergence of organ primordia during zebrafish development. *Genes Dev.* 19, 164–175. doi: 10.1101/gad.1253605

McGough, I. J., Vecchia, L., Bishop, B., Malinauskas, T., Beckett, K., Joshi, D., et al. (2020). Glypicans shield the Wnt lipid moiety to enable signalling at a distance. *Nature* 585, 85–90. doi: 10.1038/s41586-020-2498-z

Ng, B. G., Sharma, V., Sun, L., Loh, E., Hong, W., Tay, S. K., et al. (2011). Identification of the first COG-CDG patient of Indian origin. *Mol. Genet. Metab.* 102, 364–367. doi: 10.1016/j.ymgme.2010.11.161

Niehrs, C. (2012). The complex world of WNT receptor signalling. *Nat. Rev. Mol. Cell Biol.* 13, 767–779. doi: 10.1038/nrm3470

Ohtsubo, K., Takamatsu, S., Minowa, M. T., Yoshida, A., Takeuchi, M., and Marth, J. D. (2005). Dietary and genetic control of glucose transporter 2 glycosylation promotes insulin secretion in suppressing diabetes. *Cell* 123, 1307–1321. doi: 10.1016/j.cell.2005.09.041

Paganini, C., Costantini, R., Superti-Furga, A., and Rossi, A. (2019). Bone and connective tissue disorders caused by defects in glycosaminoglycan biosynthesis: a panoramic view. *FEBS J.* 286, 3008–3032. doi: 10.1111/febs.14984

Postlethwait, J. H., Navajas Acedo, J., and Piotrowski, T. (2019). Evolutionary origin and nomenclature of vertebrate Wnt11-Family Genes. *Zebrafish* 16, 469–476. doi: 10.1089/zeb.2019.1760

Rao, D. M., Shackleford, M. T., Bordeaux, E. K., Sottnik, J. L., Ferguson, R. L., Yamamoto, T. M., et al. (2019). Wnt family member 4 (WNT4) and WNT3A activate cell-autonomous Wnt signaling independent of porcupine O-acyltransferase or Wnt secretion. *J. Biol. Chem.* 294, 19950–19966. doi: 10.1074/jbc.ra119.009615

Reynders, E., Foulquier, F., Leao Teles, E., Quelhas, D., Morelle, W., Rabouille, C., et al. (2009). Golgi function and dysfunction in the first COG4-deficient CDG type II patient. *Hum. Mol. Genet.* 18, 3244–3256. doi: 10.1093/hmg/ddp262

Saul, R. A., and Wilson, W. G. (1990). A "new" skeletal dysplasia in two unrelated boys. *Am. J. Med. Genet.* 35, 388–393. doi: 10.1002/ajmg.1320350315

Serralbo, O., and Marcelle, C. (2014). Migrating cells mediate long-range WNT signaling. *Development* 141, 2057–2063. doi: 10.1242/dev.107656

Sisson, B. E., Dale, R. M., Mui, S. R., Topczewska, J. M., and Topczewski, J. (2015). A role of glypican4 and wnt5b in chondrocyte stacking underlying craniofacial cartilage morphogenesis. *Mech. Dev.* 138(Pt 3), 279–290. doi: 10.1016/j.mod.2015.10.001

Tambe, M. A., Ng, B. G., and Freeze, H. H. (2019). N-Glycanase 1 transcriptionally regulates aquaporins independent of its enzymatic activity. *Cell Rep.* 29, 4620–4631.e4.

Tenorio, J., Arias, P., Martinez-Glez, V., Santos, F., Garcia-Minaur, S., Nevado, J., et al. (2014). Simpson-Golabi-Behmel syndrome types I and II. *Orphanet. J. Rare Dis.* 9:138.

Thisse, C., and Thisse, B. (2008). High-resolution in situ hybridization to whole-mount zebrafish embryos. *Nat. Protoc.* 3, 59–69. doi: 10.1038/nprot.2007.514

Thul, P. J., and Lindskog, C. (2018). The human protein atlas: a spatial map of the human proteome. *Protein Sci.* 27, 233–244.

Tonelli, F., Bek, J. W., Besio, R., De Clercq, A., Leoni, L., Salmon, P., et al. (2020). Zebrafish: a resourceful vertebrate model to investigate skeletal disorders. *Front. Endocrinol.* 11:489.

Topczewski, J., Sepich, D. S., Myers, D. C., Walker, C., Amores, A., Lele, Z., et al. (2001). The zebrafish glypican knypek controls cell polarity during gastrulation movements of convergent extension. *Dev. Cell* 1, 251–264. doi: 10.1016/s1534-5807(01)00005-3

Ungar, A. R., Kelly, G. M., and Moon, R. T. (1995). Wnt4 affects morphogenesis when misexpressed in the zebrafish embryo. *Mech. Dev.* 52, 153–164. doi: 10.1016/0925-4773(95)00386-f

Ungar, D., Oka, T., Brittle, E. E., Vasile, E., Lupashin, V. V., Chatterton, J. E., et al. (2002). Characterization of a mammalian Golgi-localized protein complex, COG, that is required for normal Golgi morphology and function. *J. Cell Biol.* 157, 405–415. doi: 10.1083/jcb.200202016

Willert, K., and Nusse, R. (2012). Wnt proteins. *Cold Spring Harb. Perspect. Biol.* 4:a007864.

Yan, D., Wu, Y., Feng, Y., Lin, S. C., and Lin, X. (2009). The core protein of glypican Dally-like determines its biphasic activity in wingless morphogen signaling. *Dev. Cell* 17, 470–481. doi: 10.1016/j.devcel.2009.09.001

Yang, D., Li, Q., Shang, R., Yao, L., Wu, L., Zhang, M., et al. (2020). WNT4 secreted by tumor tissues promotes tumor progression in colorectal cancer by activation of the Wnt/beta-catenin signalling pathway. *J. Exp. Clin. Cancer Res.* 39, 251.

Zhang, L. S., and Lum, L. (2016). Delivery of the Porcupine Inhibitor WNT974 in Mice. *Methods Mol. Biol.* 1481, 111–117. doi: 10.1007/978-1-4939-6393-5_12

Zoeller, J. J., Pimtong, W., Corby, H., Goldoni, S., Iozzo, A. E., Owens, R. T., et al. (2009). A central role for decorin during vertebrate convergent extension. *J. Biol. Chem.* 284, 11728–11737. doi: 10.1074/jbc.m80899 1200

Conflict of Interest: The authors declare that the research was conducted in the absence of any commercial or financial relationships that could be construed as a potential conflict of interest.

Publisher's Note: All claims expressed in this article are solely those of the authors and do not necessarily represent those of their affiliated organizations, or those of the publisher, the editors and the reviewers. Any product that may be evaluated in this article, or claim that may be made by its manufacturer, is not guaranteed or endorsed by the publisher.

frontiers in Cell and Developmental Biology

ORIGINAL RESEARCH
published: 27 September 2021
doi: 10.3389/fcell.2021.722960

Sestrin2-Mediated Autophagy Contributes to Drug Resistance *via* Endoplasmic Reticulum Stress in Human Osteosarcoma

Zhen Tang[1†], Xinghui Wei[1†], Tian Li[2†], Wei Wang[3†], Hao Wu[1], Hui Dong[1], Yichao Liu[1], Feilong Wei[4], Lei Shi[1], Xiaokang Li[4], Zheng Guo[4*] and Xin Xiao[1*]*

[1] Department of Orthopaedics, Xijing Hospital, Fourth Military Medical University, Xi'an, China, [2] School of Basic Medicine, Fourth Military Medical University, Xi'an, China, [3] State Key Laboratory of Cancer Biology, Department of Immunology, Fourth Military Medical University, Xi'an, China, [4] Department of Orthopaedics, Tangdu Hospital, Fourth Military Medical University, Xi'an, China

OPEN ACCESS

Edited by:
Andrea Del Fattore, Bambino Gesù Children Hospital (IRCCS), Italy

Reviewed by:
Xisheng Weng, Peking Union Medical College Hospital (CAMS), China
Haitang Yang, Shanghai Jiao Tong University, China

***Correspondence:**
Xiaokang Li
lxkfmmu@163.com
Zheng Guo
guozheng@fmmu.edu.cn
Xin Xiao
xiao_xxtyfsxx@sina.com

[†] These authors have contributed equally to this work

Specialty section:
This article was submitted to Molecular and Cellular Pathology, a section of the journal Frontiers in Cell and Developmental Biology

Received: 09 June 2021
Accepted: 30 August 2021
Published: 27 September 2021

Citation:
Tang Z, Wei X, Li T, Wang W, Wu H, Dong H, Liu Y, Wei F, Shi L, Li X, Guo Z and Xiao X (2021) Sestrin2-Mediated Autophagy Contributes to Drug Resistance via Endoplasmic Reticulum Stress in Human Osteosarcoma. Front. Cell Dev. Biol. 9:722960. doi: 10.3389/fcell.2021.722960

One contributor to the high mortality of osteosarcoma is its reduced sensitivity to chemotherapy, but the mechanism involved is unclear. Improving the sensitivity of osteosarcoma to chemotherapy is urgently needed to improve patient survival. We found that chemotherapy triggered apoptosis of human osteosarcoma cells *in vitro* and *in vivo*; this was accompanied by increased Sestrin2 expression. Importantly, autophagy was also enhanced with increased Sestrin2 expression. Based on this observation, we explored the potential role of Sestrin2 in autophagy of osteosarcoma. We found that Sestrin2 inhibited osteosarcoma cell apoptosis by promoting autophagy via inhibition of endoplasmic reticulum stress, and this process is closely related to the PERK-eIF2α-CHOP pathway. In addition, our study showed that low Sestrin2 expression can effectively reduce autophagy of human osteosarcoma cells after chemotherapy, increase p-mTOR expression, decrease Bcl-2 expression, promote osteosarcoma cell apoptosis, and slow down tumour progression in NU/NU mice. Sestrin2 activates autophagy by inhibiting mTOR via the PERK-eIF2α-CHOP pathway and inhibits apoptosis via Bcl-2. Therefore, our results explain one underlying mechanism of increasing the sensitivity of osteosarcoma to chemotherapy and suggest that Sestrin2 is a promising gene target.

Keywords: Sestrin2, apoptosis, autophagy, drug resistance, endoplasmic reticulum stress

INTRODUCTION

Neoplasms remain the primary killer worldwide (Burns et al., 2020; Pantziarka et al., 2021). Osteosarcoma is a highly aggressive tumour occurring in long bones and is one of the most common primary malignancies in adolescents and young adults (Liu et al., 2020; Pan et al., 2021). Regardless of improvements in treatment options, including surgery with adjuvant chemotherapy, the recurrence rate of this malignant disease is still as high as 30–40%, and the 10-year survival

Abbreviations: SESN2, Sestrin2; ER, endoplasmic reticulum; ROS, reactive oxygen species; Cis, cisplatin; Dox, doxorubicin; Mtx, methotrexate; RIPA, radioimmunoprecipitation assay; TEM, Transmission electron microscopy; CCK8, Cell Counting Kit-8.

rate is as low as 20–30% due to drug-resistant metastasis (Yen et al., 2018; Chen J. et al., 2019). Therefore, to develop more effective and comprehensive treatments for clinical application, it is necessary to identify the underlying mechanisms relating to the proliferation, drug resistance and recurrence of osteosarcoma (Gu et al., 2018; Liu et al., 2021).

Autophagy plays a key role in numerous physiological and pathological processes, such as development and growth, as well as various diseases, including cancer (Dodson et al., 2013; Li et al., 2020a,b). Autophagy is considered an intracellular degradation process that is usually triggered by a variety of stress factors, such as nutrient deficiency, hypoxia, intracellular reactive oxygen species (ROS), oxidative stress and chemical drugs (Huang et al., 2018; Mrakovcic and Frohlich, 2019). In autophagy, abnormally expressed or folded cytoplasmic proteins and disrupted organelles are selectively transferred to lysosomes for degradation (Wang W. et al., 2018; Liu et al., 2019). Programmed cell death caused by autophagy plays an important role in various malignant tumours, but there is considerable controversy about the precise role of autophagy in tumour occurrence and progression, especially regarding the regulation of chemoresistance in malignant tumours. Some studies have suggested that autophagy can induce programmed death of tumour cells and thus inhibit tumorigenesis and metastasis (Mrakovcic and Frohlich, 2019). However, accumulating evidence has indicated that autophagy may protect cancer cells from further damage by removing damaged organelles, increasing their metabolism and recycling misfolded macromolecules. Autophagy is also believed to inhibit the exposure of cancer cells to accumulated damage and reduce apoptosis, and enhance the viability of cancer cells, thereby promoting tumour proliferation, drug resistance and metastasis (Wang et al., 2019). However, the relationship between autophagy and apoptosis, and the underlying mechanism of autophagy in drug resistance of osteosarcoma remains unclear (Hattori et al., 2021).

The acquisition of drug resistance is a very complex process mediated by gene mutations, changes in gene expression, selective splicing, post-translational protein modification, etc (Aleksakhina et al., 2019; Khan et al., 2021; Patra et al., 2021; Peixoto da Silva et al., 2021). Sestrins (SESNs) are highly conserved chaperones that play an important role in cell survival (Crisol et al., 2018). They are responsible for many cytoprotective mechanisms, especially under stress conditions (Dai et al., 2018). The expression of SESNs is upregulated in a wide range of tumours in response to cell stress and is closely associated with resistance to chemotherapy (Crisol et al., 2018; Sanchez-Alvarez et al., 2019). Previous studies have reported that the SESN family of proteins are considered as emerging targets for pharmacological intervention (Sanchez-Alvarez et al., 2019). Importantly, it has been reported that SESNs can regulate autophagy (Dai et al., 2018). There are correlations between the expression and activity of SESNs with unfolded protein responses from mitochondria and endoplasmic reticulum (ER), and eIF2AK2/PKR kinase centralised on the phosphorylation of the eIF2α translation initiation factor (Ye et al., 2015; Kimball et al., 2016). Endoplasmic reticulum stress-inducing drugs like bortezomib and nelfinavir resulted in the upregulation of Sestrin2 (SESN2) along with ER stress markers in breast, ovarian and cervical adenocarcinoma cancer cell lines (Bruning et al., 2013). Sestrin2, a member of the SESN family, was found to be one of the most important cellular stress proteins and to be involved in tumour progression and cancer cell invasion (Lear et al., 2019; Zhu et al., 2020). Jia-Hau Yen et al demonstrated that TIIA-mediated autophagy occurred in a SESN2-dependent but not Beclin-1-dependent manner in human osteosarcoma 143B cells, suggesting that SESN2 is a potential molecular target for cancer therapy (Yen et al., 2018; Jeong et al., 2019). However, little is known about the role of SESN2-dependent autophagy in drug resistance of human osteosarcoma. Studies should focus on determining the role of SESN2 in osteosarcoma cells with a particular focus on autophagy and its potential effects on drug resistance, and the underlying molecular mechanism of chemotherapy-driven SESN2-mediated autophagy in osteosarcoma also needs to be explored.

In this study, we found that SESN2 expression was upregulated in osteosarcoma cells during chemotherapy; thus, we further investigated the effects of SESN2 on the proliferation, apoptosis, drug resistance of osteosarcoma cells. In addition, we explored the potential mechanism by which SESN2 promotes drug resistance in osteosarcoma cells through increased autophagy. SESN2 activates autophagy and inhibits apoptosis through the PERK-eIF2α-CHOP pathway and Bcl-2. Our findings provide a novel therapeutic target for the treatment of osteosarcoma.

MATERIALS AND METHODS

Cell Culture and Reagents

The human osteosarcoma cell lines MG-63, HOS and 143B from the Cell Bank of Chinese Academy of Medical Sciences (Shanghai, China) were grown in Eagle's Minimum Essential medium (Gibco, Los Angeles, CA) containing 10% foetal bovine serum (Gibco) and antibiotics at 37°C under 5% CO_2. Cisplatin (Cis), doxorubicin (Dox), methotrexate (Mtx), ZVAD-FMK, rapamycin (Rap), and 3-methyladenine (3-MA), 4-Phenylbutyric acid (4-PBA) were purchased from Sigma Aldrich (St. Louis, Missouri, United States).

Cell Transfection

MG-63, HOS and 143B cells were seeded into 12-well plates and incubated at 37°C for 24 h until the cells reached approximately 50-60% confluence. A plasmid carrying the SESN2 gene and control/SESN2-specific shRNAs was purchased from Hanbio Co., Ltd. (Shanghai, China). Subsequently, the cells were transfected using a plasmid carrying the SESN2 gene according to the manufacturer's instructions. The sequence of shSESN2 was 5′-GGTCCACGTGAACTTGCTGC-3′. Western blot analysis was used to detect the protein expression level of SESN2 in osteosarcoma cell lines subjected to lentiviral transduction.

Cell Viability Assay

Osteosarcoma cells were seeded into 96-well plates. After incubation for 24 h, cells were treated with cisplatin (Cis,

20 μmol/L), doxorubicin (Dox, 0.2 μg/mL) or methotrexate (Mtx, 50 μmol/L) at the indicated concentrations for 24 h, 48 h, and 72 h. Cell viability was determined with a Cell Counting Kit-8 Assay Kit (Beyotime, Shanghai, China) and Caspase-3 colorimetric assay kit (Solarbio, Beijing, China) was used according to the manufacturer's instructions.

Colony Formation Assay

MG-63 and HOS cells in the logarithmic growth phase were seeded into a 10-cm dish at a density of 200 cells per millilitre. After treatment with Cis (20 μmol/L) and Dox (0.2 μg/mL) for 2 weeks, cell clones were fixed with 4% paraformaldehyde for 15 min. Subsequently, crystal violet solution was added to stain the cell clones for 20 min before they were photographed.

Apoptosis Analysis

After osteosarcoma cells were seeded into 6-well plates and incubated overnight, they were treated with Cis (20 μmol/L), Dox (0.2 μg/mL), or Mtx (50 μmol/L) for 24 h. Apoptotic cells were determined using an Annexin V-PE Apoptosis Detection kit (BD, Shanghai, China) by flow cytometry according to the manufacturer's instructions.

Western Blot Analysis

Cells were washed with PBS and lysed in radioimmunoprecipitation assay (RIPA) buffer, and then a BCA kit (Thermo Fisher Scientific, Shanghai, China) was used to determine the protein concentrations. Equal amounts of proteins were resolved by SDS-PAGE and transferred to activated PVDF membranes. The membranes were blocked with 5% non-fat dry milk and incubated with primary antibodies overnight at 4°C. The dilution ratio of primary antibodies against Sestrin2 (#8487, CST, United States), PARP (#9532, CST, United States), cleaved PARP (#5625, CST, United States), Beclin-1 (ab207612, Abcam, United States), LC3 (ab192890, Abcam, United States), P62 (ab109012, Abcam, United States), mTOR (ab2732, Abcam, United States), phospho-mTOR (ab131538, Abcam, United States), Bcl-2 (ab59348, Abcam, United States), PERK (ab65142, Abcam, United States), phospho-eIF2α (ab131505, Abcam, United States) and CHOP (ab11419, Abcam, United States) was 1:1000, and that of antibody against GAPDH (#5174, CST, United States) was 1:2000. After incubation with HRP-conjugated secondary antibodies (1:3000 dilution) for 40 min at room temperature, the protein bands were visualised with Amersham Imager 600.

Quantitative Real-Time Polymerase Chain Reaction

Total RNA was isolated from cells by using TRIzol (Sigma, Ventura, United States) according to a procedure modified from a previously described protocol. Quantitative real-time PCR (qRT-PCR) experiments were performed using SYBR Green reagents (Takara Bio Inc., Shiga, Japan) with specific primers. The cycle threshold (Ct) values were collected and normalised to the level of respective. The ΔΔ Ct method was adopted as our previous study. The primers were listed as follows: SESN2 (F) 5′- GACCATGGCTACTCGCTGAT -3′,(R) 5′- GCT GCC TGG AAC TTC TCA TC -3′; GAPDH (F) 5′-CCACAGTCCATGCCATCAC-3′, (R) 5′-TCCACCACCCTG TTGCTGTA-3′.

Immunofluorescence

To detect the formation of autolysosomes, cells were seeded into 24-well plates at 5×10^4 cells per well. After treatment with the indicated chemotherapeutic drugs for 24 h, cells were fixed in 4% paraformaldehyde for 20 min and incubated with a primary antibody against LC3 (ab192890, Abcam, United States) at 4°C overnight. The cells were washed with PBS three times for 3 min each time, followed by incubation with secondary antibodies for 1 h at room temperature. DAPI was incubated with cells for 3 min to stain nuclei. The samples were sealed in and photographed under a fluorescence microscope within 24 h of antibody treatment.

Measurement of Autophagic Flux

To analyse autophagic flux, HOS cells at a density of 50–70% were transiently transfected with GFP-RFP-LC3 (Hanbio Co. LTD) according to the manufacturer's instructions. They were divided into groups according to experimental requirements and treated with chemotherapy drugs or rapamycin (100 nmol/L) for the corresponding time. The expression levels of GFP and mRFP were observed by confocal fluorescence microscopy.

Transmission Electron Microscopy

Transmission electron microscopy (TEM) was performed to monitor autolysosome formation in cells treated with chemical drugs for 24 h. After the cells were centrifuged at 2000 × g for 15 min and the supernatant was removed, 1.5 mL of glutaraldehyde was added immediately and incubated overnight to fix cells in the pellet. Then, 1% osmium tetroxide was added and fixed at 4°C for 30 min. Next, a graded series of acetone was applied to the sample for 10 min per concentration before 1 mL of pure embedding agent was added and left overnight at room temperature. The cell mass was carefully inserted into the module at the bottom of the hole, and the embedding medium hole filling module was continued. When the sample hardened after 2 h at 60°C, the embedding blocks were sliced at a thickness of 50∼70 nm for follow-up observation.

Intracellular Ca^{2+} Measurement

The levels of cytosolic Ca^{2+} were detected using Fura-Red-AM (CAS 149732-62-7, AAT Bioquest, United States). After treatment with Cis (20 μmol/L) and Dox (0.2 μg/mL) for 24 h, HOS cells were treated and harvested according to the manufacturer's instructions. The fluorescence intensities of Fura Red alone and bound to Ca^{2+} were detected by flow cytometry.

In vivo Subcutaneous Tumour Model

All animal work was carried out following the guidelines of the Ethics Committee of the Fourth Military Medical University and was performed according to the institutional guidelines for the care and use of laboratory animals. NU/NU mice (the Fourth

Military Medical University, Shaanxi, China) were randomly assigned and used to investigate the effect of SESN2 on tumour formation *in vivo*. A total of 5×10^7 143B cells (sh-NC/sh-SESN2) suspended in serum-free medium were subcutaneously implanted into the flanks of mice. Tumour size was measured every 3 days from day 7 until day 28. The tumours were removed, weighed at day 28. NU/NU mice were intraperitoneally injected with chemotherapeutic drugs twice a week. The results were counted by three pathologists who were blind to the characteristics of each group. The tumour volume (mm^3) was calculated using the following formula: length $\times$ width^2/2.

RESULTS

Sestrin2 Expression Is Increased in Response to Chemotherapy Drugs

To analyse the expression of SESN2 in osteosarcoma cells after chemotherapy, we detected the expression of SESN2 in HOS, MG63 and 143B cells treated with Cis (20 μmol/L), Dox (0.2 μg/mL) or Mtx (50 μmol/L). These chemotherapeutic agents significantly increased the expression of SESN2 in all three cell lines (**Figure 1A**) at the mRNA and protein level (**Figure 1B**). More importantly, the increases in SESN2 expression were time dependent. We detected SESN2 expression at 24, 48, and 72 h after treatment and found that it was highest at 24 h, and there was no significant decrease at 48 and 72 h (**Figure 1C**). Therefore, we can conclude that SESN2 expression increases in a time-dependent manner after chemotherapeutic treatment.

Sestrin2 Reduces the Sensitivity of Osteosarcoma Cells to Chemotherapeutic Agents by Inhibiting Apoptosis to Confer Drug Resistance

To further explore the underlying role of SESN2 in the drug resistance of osteosarcoma cells, we reduced SESN2 expression via lentivirus transduction with a plasmid containing shRNA targeting SESN2. And we found that SESN2 expression was significantly reduced at the protein and mRNA level after lentivirus transfection (**Figures 2A,B**). The inhibition of osteosarcoma cell proliferation upon SESN2 knockdown in cells treated with chemotherapeutic drugs was measured by the CCK-8 kit and colony formation assay (**Figures 2C,E**). Flow cytometry confirmed that SESN2 knockdown increased the sensitivity of osteosarcoma cells to chemotherapeutic agents and increased their apoptosis rates compared with those of the control shRNA-treated group (**Figure 2D**). After chemotherapy, the apoptotic protein caspase 3 was significantly activated in the SESN2-knockdown group, which was reversed by treatment with the apoptotic inhibitor ZVAD-FMK (20 μmol/L) (**Figure 2F**).

Sestrin2-overexpressing osteosarcoma cells were constructed using a lentiviral plasmid, and the increased expression was

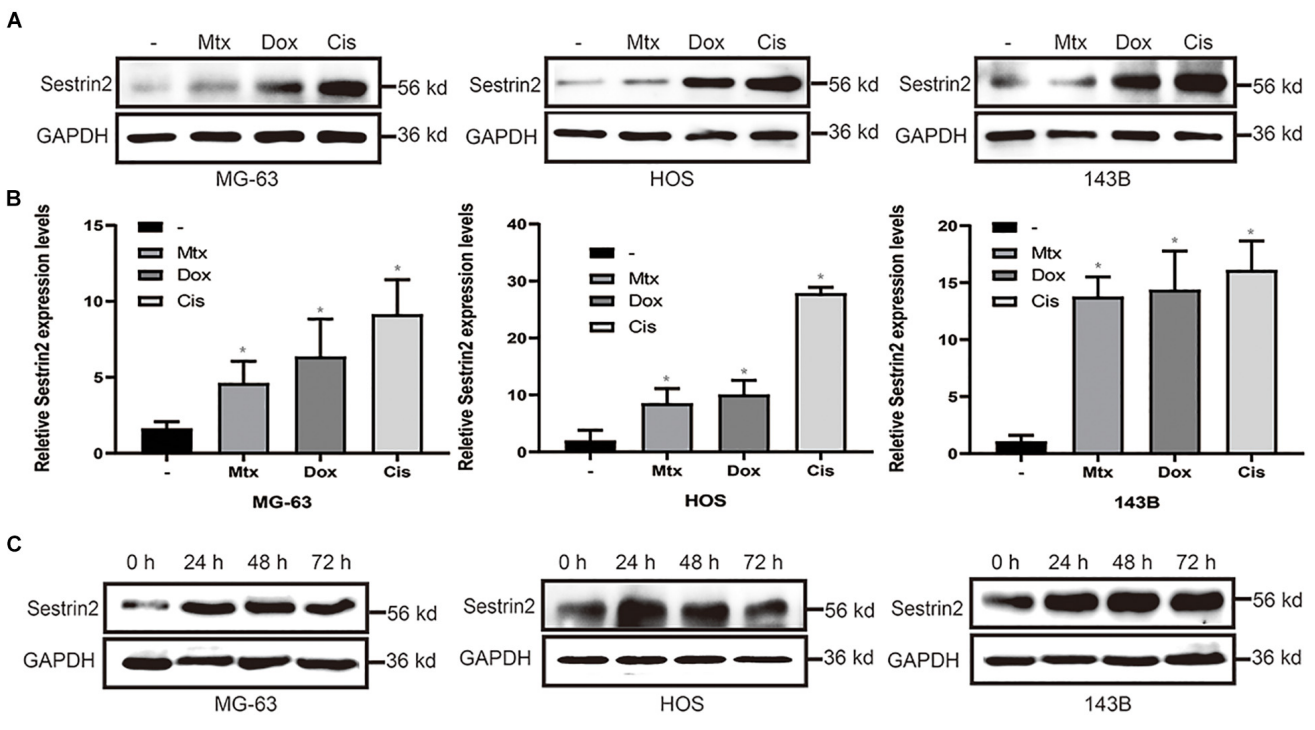

FIGURE 1 | Chemotherapeutic agents increased the expression of SESN2 in osteosarcoma cells **(A,B)**. After treatment with Cis (20 μmol/L), Dox (0.2 μg/mL) or Mtx (50 μmol/L), the expression level of SESN2 in osteosarcoma cells was detected by western blot **(A)** (n = 3), and the SESN2 mRNA level was detected by quantitative real-time PCR **(B)** (n = 3). Western blotting was used to detect SESN2 expression in MG-63, HOS, and 143B cells after Cis (20 μmol/L) treatment for 24 to 72 h **(C)** (n = 3). The data are presented as the mean ± SD. *$p < 0.05$ vs. the – group.

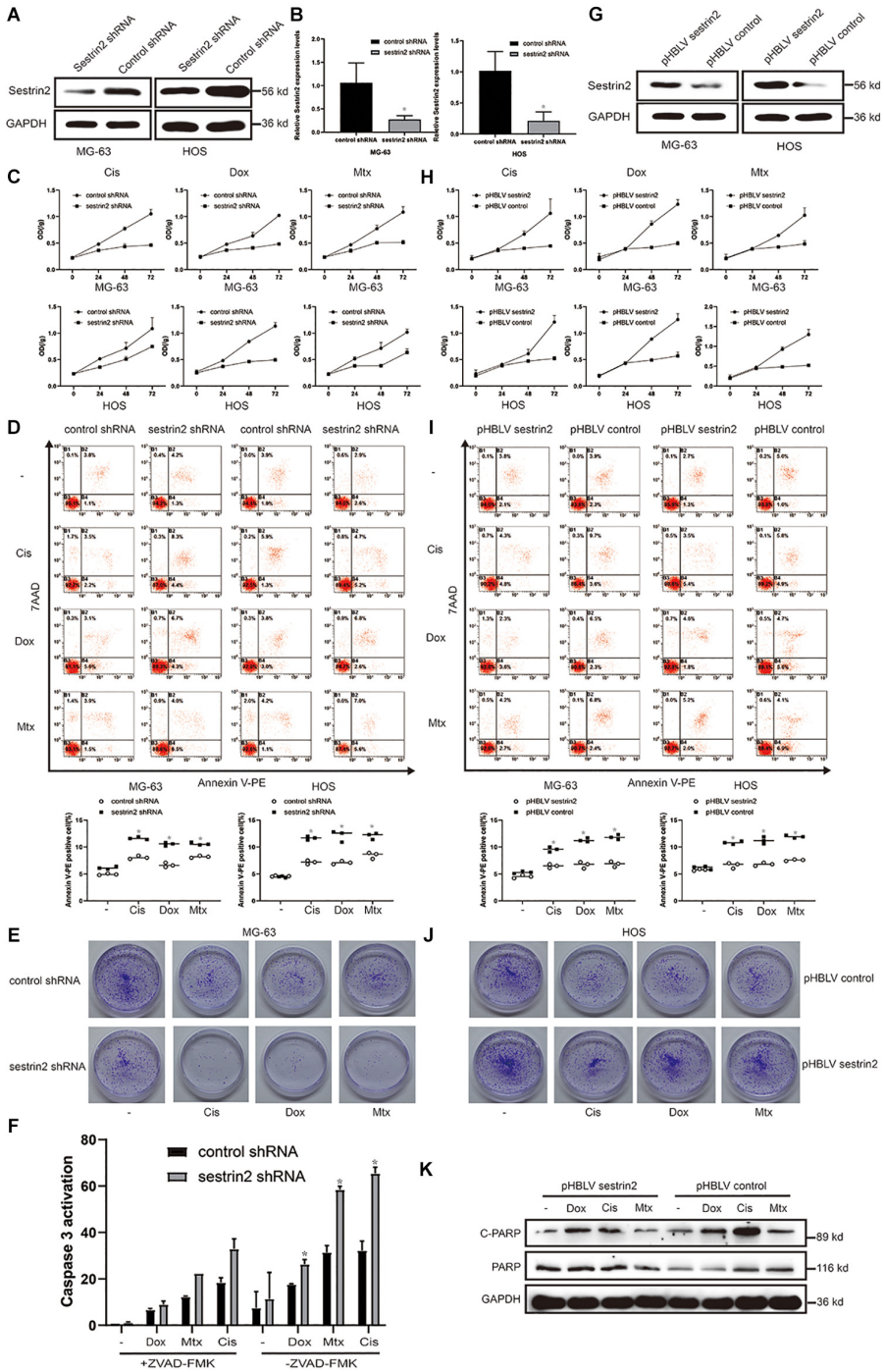

FIGURE 2 | SESN2 confers drug resistance to target cells by reducing their sensitivity to chemotherapeutic agents. MG-63 and HOS cells were transfected with control shRNA or SESN2 shRNA, and the knockdown effect was detected by western blot ($n = 3$) and quantitative real-time PCR ($n = 3$) **(A,B)**. MG-63 and HOS cells with SESN2 knockdown were treated with Cis (20 μmol/L), Dox (0.2 μg/mL), or Mtx (50 μmol/L) for 24, 48, and 72 h. Cell activity was detected by CCK-8 **(C)** ($n = 3$). After treatment for 24 h, apoptotic cells were detected by flow cytometry **(D)** ($n = 3$). SESN2 knockdown significantly reduced the number of colony-forming MG-63 cells **(E)** ($n = 3$). After MG-63 cells were treated with Cis (20 μmol/L), Dox (0.2 μg/mL) or Mtx (50 μmol/L) for 24 h, the apoptosis of cells transfected with control shRNA or SESN2 shRNA and cultured in the presence or absence of ZVAD-FMK (20 μmol/L) was detected using the Caspase 3 kit **(F)** ($n = 3$). The data are presented as the mean ± SD. $^*p < 0.05$ vs. the Control shRNA group. The expression of SESN2 after transfection of a plasmid carrying the SESN2 gene was evaluated by western blot **(G)** ($n = 3$). MG-63 and HOS cells overexpressing SESN2 as well as their corredsponding control cells were treated with Cis (20 μmol/L), Dox (0.2 μg/mL), or Mtx (50 μmol/L). Cell viability and apoptosis were detected by CCK-8 **(H)** ($n = 3$) and flow cytometry **(I)** ($n = 3$), respectively. SESN2 increases the number of colony-forming units of HOS cells **(J)** ($n = 3$). Cleaved and total PARP in SESN2-overexpressing and control HOS cells were analysed by western blot **(K)** ($n = 3$). The data are presented as the mean ± SD. $^*p < 0.05$ vs. the pHBLV control group.

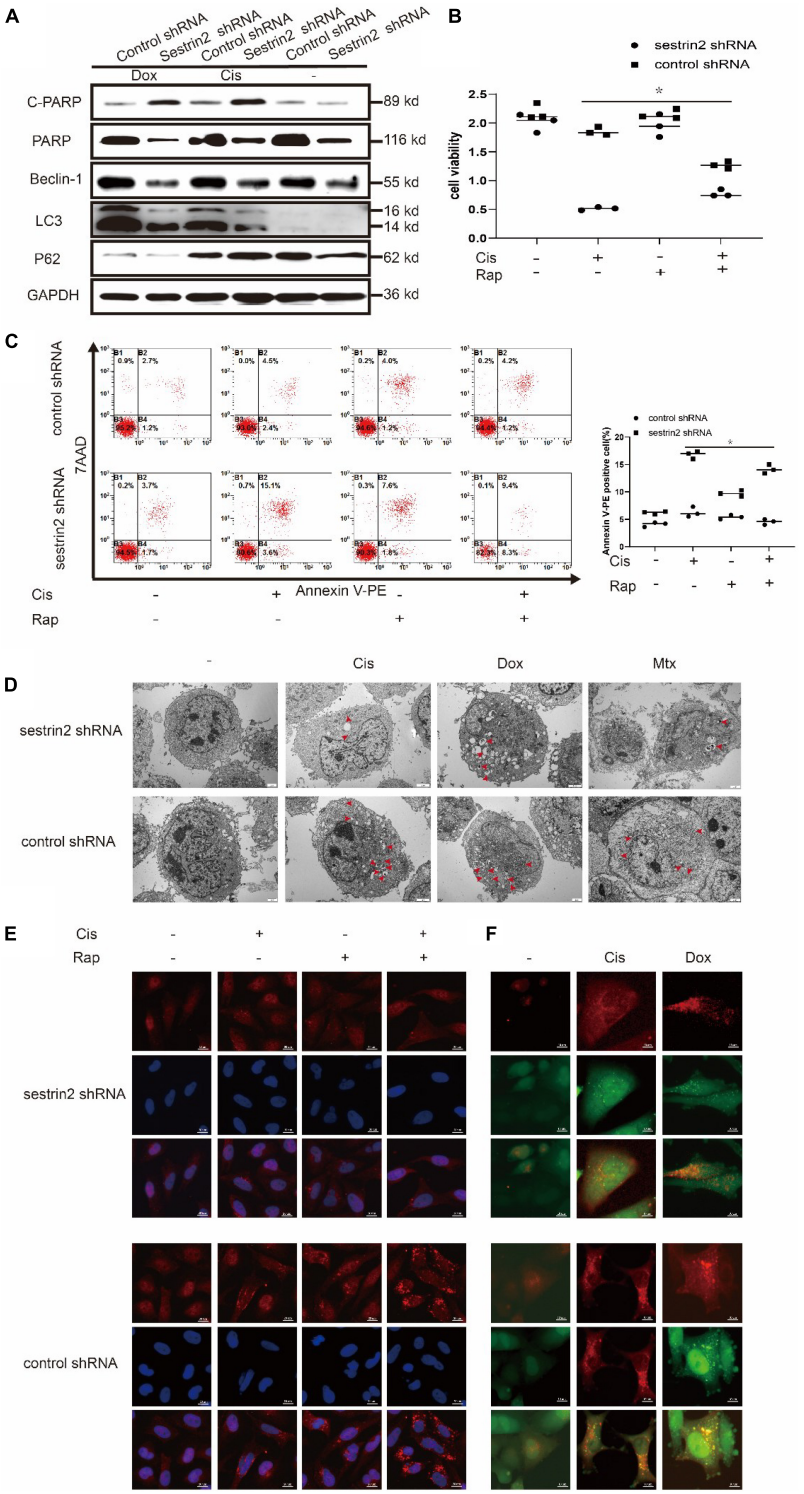

FIGURE 3 | Knockdown of SESN2 resulted in inhibited autophagy and increased apoptosis of osteosarcoma cells treated with chemotherapy. After treatment with Cis (20 μmol/L), Dox (0.2 μg/mL), or Mtx (50 μmol/L) for 24 h, SESN2-knockdown and control cells were subjected to western blot to detect the expression of cleaved and total PARP, LC3, and P62 expression levels **(A)** (n = 3). SESN2-knockdown HOS cells were treated with Cis (20 μmol/L) for 24 h with or without rapamycin (100 nmol/L) for 6 h. Proliferation was analysed by CCK-8 assay **(B)** (n = 3), apoptosis was assessed by Annexin V-PE/PI staining **(C)** (n = 3), and LC3 puncta formation was analysed by immunofluorescence **(E)** (n = 3, scale bar = 20 μm). Intracellular autophagosomes were observed by TEM **(D)** (n = 3, scale bar = 2 μm), and autophagic flux was monitored by fluorescence microscopy in HOS cells with transient expression of GFP-RFP-LC3 in HOS cells **(F)** (n = 3, scale bar = 10 μm). The data are presented as the mean ± SD. *$p < 0.05$ vs. the Control shRNA group.

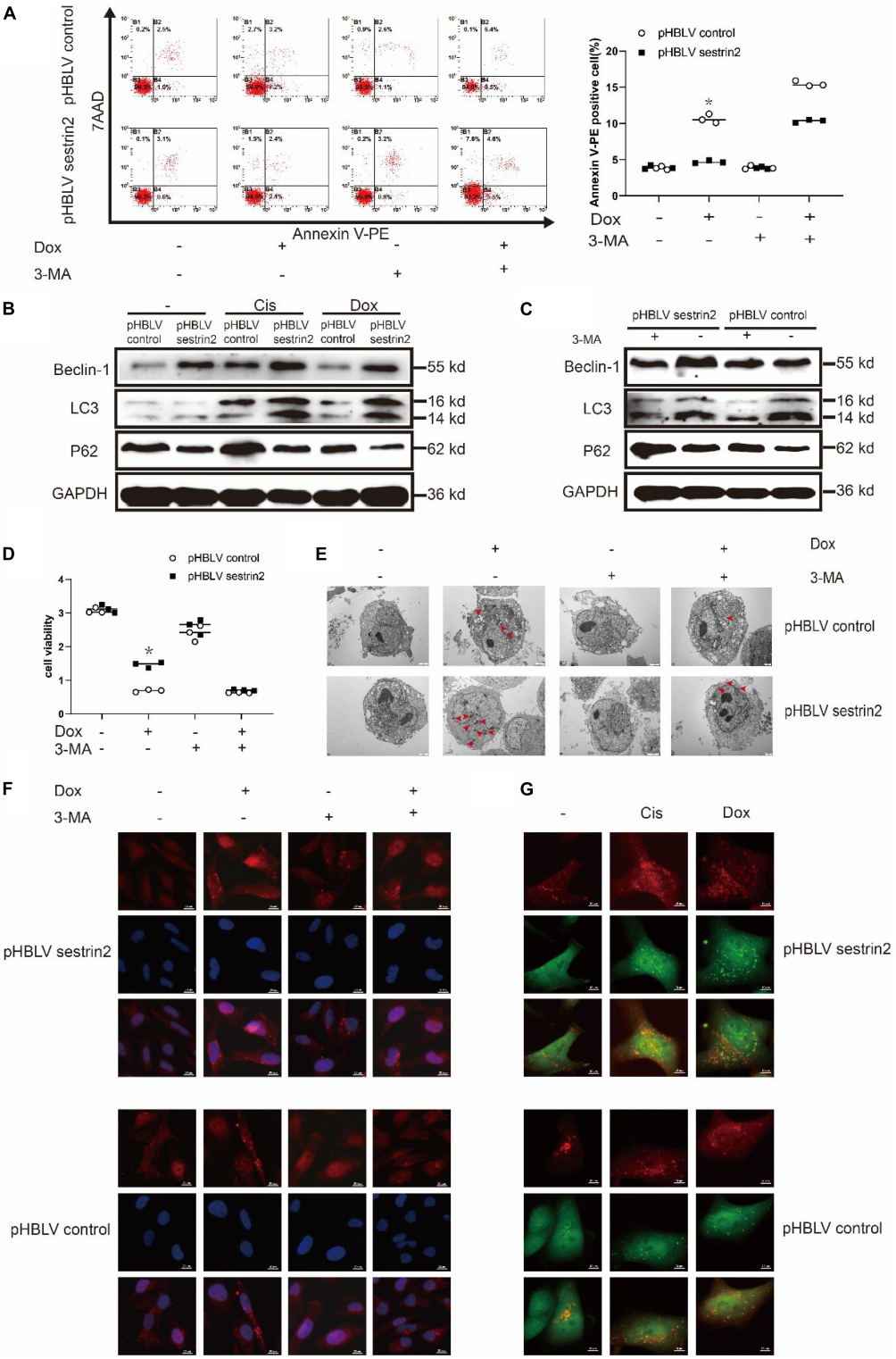

FIGURE 4 | SESN2 regulates autophagy and reduces the sensitivity of osteosarcoma cells to chemotherapy. In the presence or absence of 3-MA (5 mM), SESN2-overexpressing and control HOS cells were treated with Dox (0.2 μg/mL) for 24 h, and apoptosis was analysed by flow cytometry **(A)** (n = 3). After treatment with Cis (20 μmol/L) or Dox (0.2 μg/mL), the expression levels of LC3 and P62 in SESN2-overexpressing and control HOS cells were detected by western blot **(B)** (n = 3). The expression levels of LC3 and P62 in SESN2-overexpressing and control HOS cells treated with 3-MA (5 mM) were detected by western blot **(C)** (n = 3). In the presence or absence of 3-MA (5 mM), SESN2-overexpressing and control HOS cells were treated with Dox (0.2 μg/mL) for 24 h, cell activity was detected by

(Continued)

FIGURE 4 | (Continued)
CCK-8 **(D)** (n = 3), intracellular autophagosomes were observed by TEM **(E)** (n = 3, scale bar = 2 μm), and intracellular LC3 puncta formation was analysed by immunofluorescence **(F)** (n = 3, scale bar = 20 μm). After treatment with Cis (20 μmol/L) or Dox (0.2 μg/mL), autophagosome formation in HOS cells with ectopic SESN2 expression was monitored by immunofluorescence through transfection with RFP-GFP-LC3 lentivirus after upregulating SESN2 **(G)** (n = 3, scale bar = 10 μm). The data are presented as the mean ± SD. *$p < 0.05$ vs. the pHBLV control group.

detected by western blot (**Figure 2G**). Cell proliferation curves showed that after chemotherapy treatment, compared to the control cells, cells in the SESN2 overexpression group proliferated faster and showed reduced sensitivity to chemotherapy drugs (**Figures 2H,J**). Increased SESN2 expression reduced apoptosis in MG-63 cells and HOS cells, as indicated by the decrease in the number of Annexin V-PE-positive cells (**Figure 2I**). Similarly, western blot analysis showed that cleaved PARP expression was lower in the SESN2 overexpression group than in the control group, suggesting that SESN2 exerts an antiapoptotic effect (**Figure 2K**). These results indicate that SESN2 reduces the sensitivity of osteosarcoma cells to chemotherapeutic agents by reducing the apoptosis of osteosarcoma cells and thus leads to drug resistance.

Sestrin2 Reduces the Sensitivity of Osteosarcoma Cells to Chemotherapies by Promoting Autophagy

Previous reports have described the relationship between autophagy and apoptosis. Some studies have shown that autophagy protects cells under stress conditions, but others have proposed the opposite view: that autophagy can promote apoptosis. After treatment with Cis (20 μmol/L) and Dox (0.2 μg/mL), LC3 expression was significantly decreased in the SESN2 knockdown group compared to the control group, whereas P62 expression showed an upward trend. Cleaved PARP expression, which reflects the level of apoptosis, was increased upon knockdown of SESN2 (**Figure 3A**). Cell viability assays showed that the decrease in the cell proliferation rate induced by SESN2 knockdown after Cis (20 μmol/L) and Dox (0.2 μg/mL) treatment was reversed by treatment with the autophagy inducer rapamycin (100 nmol/L) (**Figure 3B**). The flow cytometry results showed that the number of Annexin V-PE-positive cells was increased by SESN2 knockdown after treatment with Cis (20 μmol/L) and Dox (0.2 μg/mL); this effect was reversed by rapamycin (100 nmol/L) (**Figure 3C**). Ultrastructural analysis of autophagosomes using TEM also showed that the number of intracellular autophagosomes increased significantly after SESN2 knockdown (**Figure 3D**). Similarly, autophagy flow was blocked in shRNA-transfected cells after chemotherapeutic drug treatment compared with control cells treated with the same drug (**Figure 3F**). As the immunofluorescence results show in **Figure 3E**, we observed that after chemotherapy treatment, knocking down SESN2 significantly reduced the recruitment of LC3 to the autophagy membrane even after treatment with rapamycin (100 nmol/L). These results suggest that SESN2 plays an important role in the inhibition of apoptosis by regulating autophagy after chemotherapeutic treatment.

Annexin V-PE staining revealed that the apoptosis of SESN2-overexpressing osteosarcoma cells treated with Dox (0.2 μg/mL) and 3-MA (3-methyladenine, 5 mM) was significantly higher than that in cells treated with Dox (0.2 μg/mL) alone and was close to the apoptosis of the control cells (**Figure 4A**). Western blot analysis showed that LC3 accumulation was significantly increased in SESN2-overexpressing cells treated with Cis (20 μmol/L) and Dox (0.2 μg/mL) (**Figure 4B**). In addition, we treated HOS cells transduced with control or SESN2-overexpressing pHBLV with 3-MA (5 mM) and found that autophagy enhancement due to SESN2 overexpression was inhibited by 3-MA (5 mM) (**Figure 4C**). To investigate the role of SESN2 in autophagy-mediated apoptosis, we treated SESN2-overexpressing and control cells with 3-MA (5 mM) and chemotherapeutic agents and observed that apoptosis of the SESN2-overexpressing HOS cells was increased and that the protective effect of SESN2 on osteosarcoma cells was decreased after 3-MA (5 mM) treatment (**Figure 4D**). The submicroscopic structure of autophagosomes was observed by TEM. The results indicated that the number and size of autophagosomes in the SESN2 overexpression group were significantly increased after Dox (0.2 μg/mL) treatment, but this chemotherapy-induced autophagy was inhibited by 3-MA (5 mM) (**Figure 4E**). The same results were confirmed by immunofluorescence, which showed that the accumulation of LC3 in HOS cells induced by chemotherapeutic drugs in the SESN2 overexpression group was inhibited by 3-MA (5 mM) (**Figure 4F**). In addition, we observed autophagic flux through mRFP-GFP-LC3 adenovirus transfection and found that the SESN2-mediated autophagic flux of HOS cells was significantly enhanced after treatment with Cis (20 μmol/L) and Dox (0.2 μg/mL) (**Figure 4G**). These experimental results indicate that SESN2-mediated autophagy reduces the sensitivity of osteosarcoma cells to chemotherapy drugs, leading to the occurrence of drug resistance.

Sestrin2 Promotes Autophagy and Inhibits Apoptosis of Osteosarcoma Cells Through Endoplasmic Reticulum Stress

We have previously shown that Cis (20 μmol/L), Dox (0.2 μg/mL), and Mtx (50 μmol/L) inhibit the growth of human osteosarcoma cells, but the underlying mechanisms have not been investigated. In addition, electron microscopy revealed that these three chemotherapeutic agents induced osteosarcoma cell vacuolation (**Figure 5A**). Compared with cells in the control group, HOS cells in the SESN2 knockdown group were more exposed to expanded cytoplasmic

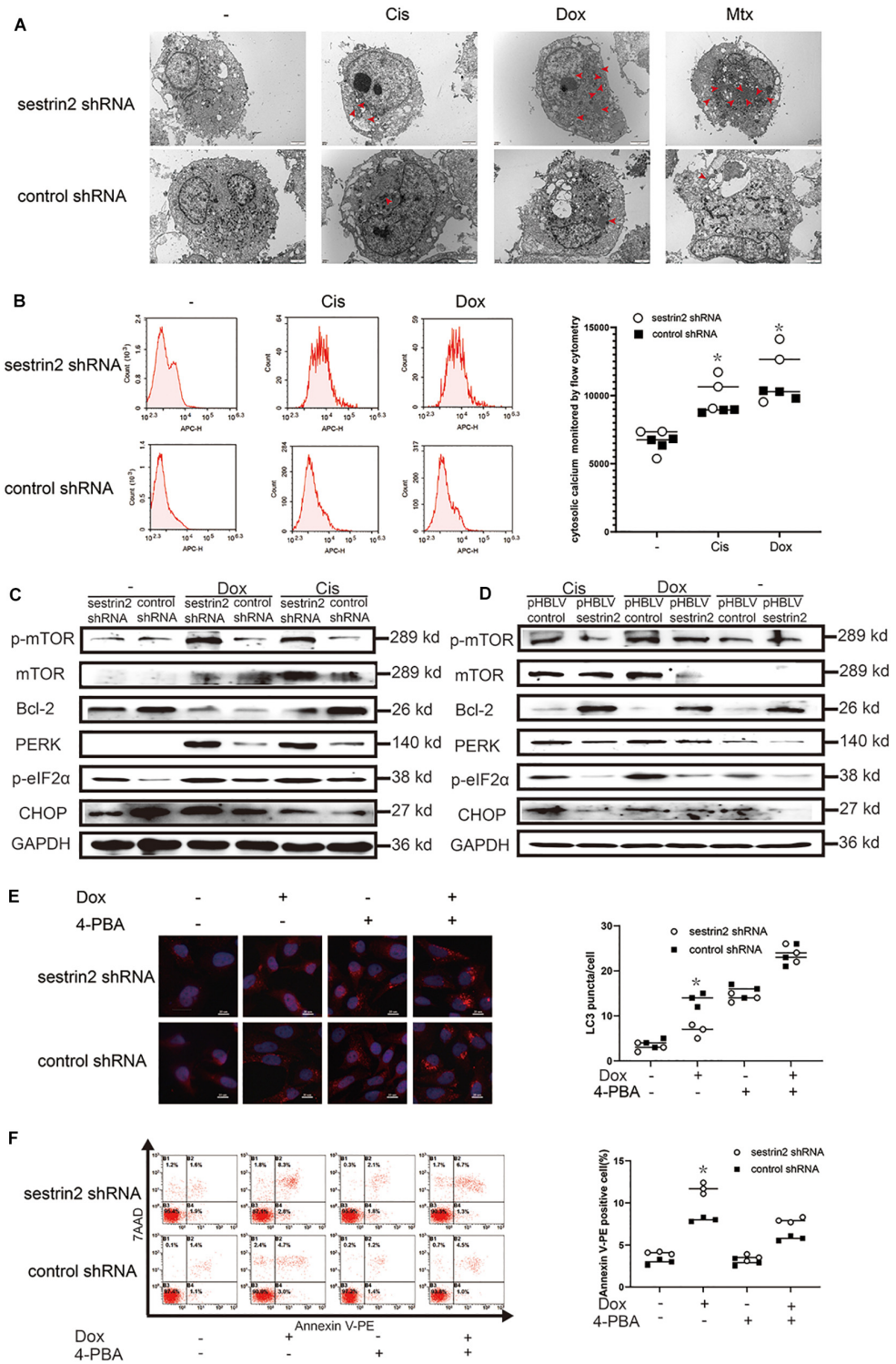

FIGURE 5 | SESN2 promotes autophagy and inhibits apoptosis through endoplasmic reticulum (ER) stress. After cells were treated with Cis (20 μmol/L), Dox (0.2 μg/mL), or Mtx (50 μmol/L) for 24 h, ER stress in SESN2-knockdown HOS cells was observed by TEM **(A)** (n = 3, scale bar = 2 μm). After cells were treated with Cis (20 μmol/L) and Dox (0.2 μg/mL) for 24 h, intracellular calcium in SESN2-knockdown and control HOS cells was monitored by flow cytometry **(B)** (n = 3). The protein expression levels of genes involved in apoptosis-, autophagy- and ER stress-related pathways in HOS cells with upregulated and downregulated SESN2 expression were detected by western blot **(C,D)** (n = 3). Twenty-four hours after Dox (0.2 μg/mL) treatment, the LC3 puncta in HOS cells from the SESN2-knockdown group and the control group were detected by immunofluorescence, and apoptosis was analysed by flow cytometry in the presence and absence of 4-PBA (5 mM) **(E,F)** (n = 3, scale bar = 20 μm). The data are presented as the mean ± SD. *$p < 0.05$ vs. the Control shRNA group.

vacuolation groups after chemotherapeutic treatment. The expansion of cytoplasmic vacuolation is considered to be an expanded endoplasmic cavity, indicating increased endoplasmic stress. To further explain this phenomenon, we evaluated chemotherapy-treated HOS cells using flow cytometry. Calcium homeostasis is an important function of the ER, and calcium dysregulation leads to ER stress. In this study, Fura-Red-AM was used to indicate cytoplasmic calcium. The results showed that the cytoplasmic calcium level was significantly increased in the chemotherapy-treated HOS cells, and the Ca^{2+} content in the SESN2-knockdown group was significantly higher than that in the control group (**Figure 5B**). We further demonstrated that the ER stress pathway PERK-eIF2α-CHOP was significantly activated by chemotherapy treatment, and western blot results also demonstrated that low SESN2 expression led to activation of PERK-eIF2α-CHOP. Moreover, upregulated SESN2 expression decreased the expression of ER stress-related proteins in osteosarcoma cells treated with chemotherapy drugs (**Figures 5C,D**). These interesting findings strongly suggest that chemotherapeutic agents can induce ER stress in human osteosarcoma cell lines. To investigate whether osteosarcoma cells inhibit apoptosis by regulating ER stress to promote autophagy, we treated osteosarcoma cells with chemotherapeutic agents and showed that these treated cells had significant LC3 accumulation compared with that in cells with SESN2 knockdown, and this gap was reduced by 5mM of 4-phenylbutyric acid (4-PBA) (Sigma Aldrich, St. Louis, Missouri, United States) (**Figure 5E**). We then used flow cytometry to investigate the relationship between ER stress and apoptosis and found that 4-PBA (5 mM) reduced chemotherapy-induced apoptosis in osteosarcoma cells with SESN2 knockdown (**Figure 5F**).

Mouse Xenograft Models Demonstrate That Inhibition of Sestrin2 Reduces Autophagy to Increase Apoptosis and Thus Increases the Sensitivity of Osteosarcoma to Chemotherapeutic Agents

To investigate the relationship between SESN2 and chemotherapeutic sensitivity and the potential mechanism *in vivo*, 143B cells transfected with SESN2 shRNA or control shRNA were subcutaneously injected into NU/NU nude mice, and tumour growth was observed periodically. The nude mice were intraperitoneally injected with chemotherapeutic agents twice every seven days, starting from day 8 until day 28. And tumour size was measured every 3 days until day 28. We found that SESN2 knockdown significantly slowed tumour growth in response to chemotherapeutic agents (**Figure 6A**); the tumour volume and weight are significantly decreased in the SESN2 shRNA + Cis group compared with those in the control shRNA + Cis group (**Figures 6B,C**). TUNEL staining showed that SESN2 knockdown induced more apoptosis in osteosarcoma cells after chemotherapy treatment compared to that in control cells subjected to chemotherapy treatment (**Figure 6D**). We also found that compared to control cells, SESN2-knockdown cells exhibited decreased autophagy and activated ER stress in the presence of chemotherapeutic agents (**Figure 6D**). These results also confirm that SESN2 regulates osteosarcoma cell apoptosis through autophagy, thereby mediating their drug resistance.

DISCUSSION

Osteosarcoma is a malignant tumour with a very high mortality rate in adolescents, and available effective treatments are very limited. Neoadjuvant chemotherapy can prolong the survival of patients, but the resistance of osteosarcoma to chemotherapy drugs is still a major problem today (Li and Ma, 2021; Su et al., 2021). Cis, Dox, and Mtx are the current routine chemotherapy drugs for osteosarcoma in clinical practice, and the decreased sensitivity of osteosarcoma to these drugs leads to the occurrence of drug resistance, which is the main challenge to improve the overall survival of patients (Wang Y. et al., 2018; Xiao et al., 2018; Chen R. et al., 2019). In this paper, the occurrence of drug resistance in osteosarcoma treated with Cis, Dox, and Mtx aroused our interest in the potential molecular mechanism. Autophagy is one of many mechanisms involved in the development of drug resistance in tumours and is widely considered a cellular response under stress conditions. However, it has two sides—autophagy can protect cells from apoptosis caused by external stress conditions, but excessive autophagy can induce cell death. In a study of the mechanism of drug resistance in osteosarcoma, we found that chemotherapy drug treatment stimulated autophagy to protect cells and reduce apoptosis, thus leading to drug resistance (Niu et al., 2019).

Sestrin2 has been identified as a protein that induces DNA damage and oxidative stress by inhibiting mammalian targets of rapamycin complex 1 while accelerating autophagy (Wang et al., 2017; Jeong et al., 2019). It has been reported that SESN2 can cooperate with P62 to promote autophagy-driven degradation (Hua et al., 2018). We found an association between SESN2 and autophagy pathways and observed that SESN2 inhibited the ER stress signalling pathway PERK-eIF2α-CHOP following treatment with chemotherapy, thereby upregulating autophagy in osteosarcoma cells, which was accompanied by a slight decrease in P62. Consistent with these findings, we provided a schematic diagram of signalling axis regulation that plays a role in chemotherapy drugs-induced SESN2-dependent apoptosis in osteosarcoma cells.

It has been reported that many antineoplastic drugs activate various mechanisms of cell death and regulate ER homeostasis by inducing undeveloped protein response (UPR)-mediated ER stress in cancer cells (Chiu et al., 2015; Cheng et al., 2018). Endoplasmic reticulum homeostasis is regulated by the maintenance of intracellular calcium

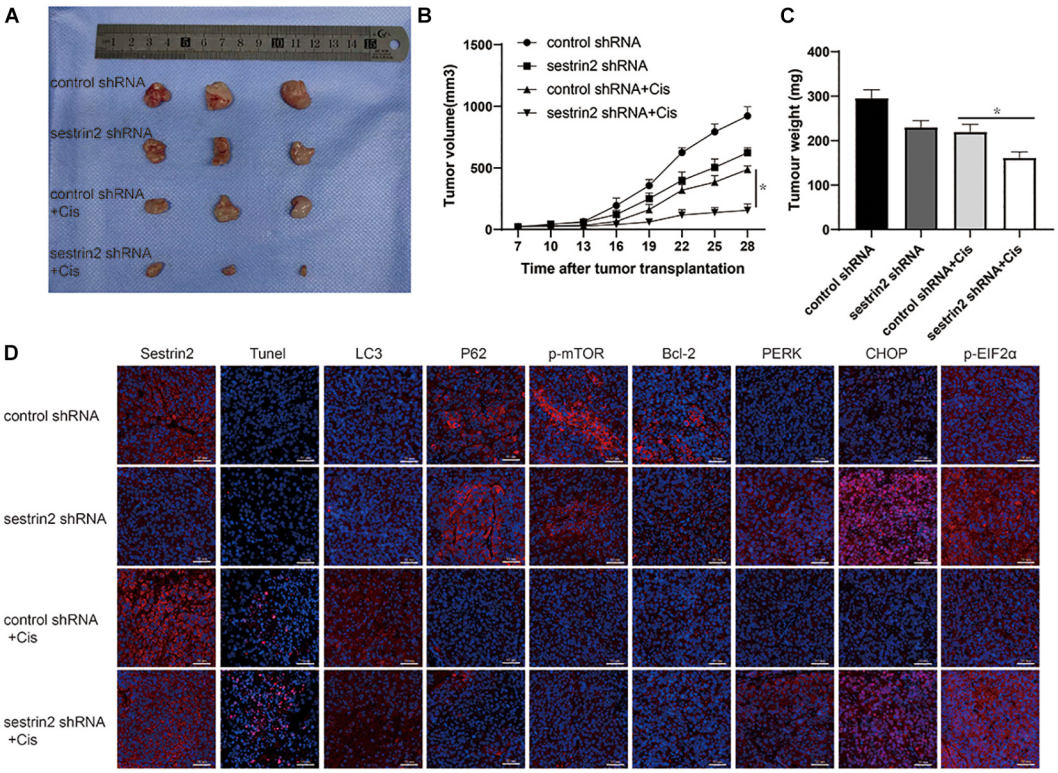

FIGURE 6 | Suppression of SESN2 increases sensitivity to chemotherapy *in vivo*. NU/NU nude mice were subcutaneously injected with SESN2-knockdown or control 143B cells. After 7 days, the mice were intraperitoneally injected with Cis (20 μmol/L) until they were killed on day 28. Tumour volume was measured on day 28 **(A)** (n = 3). Tumour growth curves were measured from days 7 to 28 **(B)** (n = 3). Tumour weight was measured on day 28 **(C)** (n = 3). Immunofluorescence staining of TUNEL, SESN2 expression, LC3 expression, P62 expression, p-mTOR expression, Bcl-2 expression, PERK expression, CHOP expression and p-eIF2α expression after tumour sample injection **(D)** (n = 3, scale bar = 50 μm). The data are presented as the mean ± SD. *$p < 0.05$ vs. the Control shRNA + Cis group.

balance (Cheng et al., 2018). Depending on the severity of stress, cancer cells decide to resume protein unfolding or activate the cell death mechanism through autophagy or apoptosis. ER stress is a double-edged sword that plays an important role in regulating the pro-death or pro-survival signals of solid tumour cells (White-Gilbertson et al., 2013). In this paper, we found that failure to resolve ER stress activates two interrelated biological processes: autophagy and apoptosis. Inhibition of endoplasmic reticulum stress in the presence of chemotherapeutic agents reduced PERK-mediated phosphorylation of eIF2α, thus further inhibiting the activation of CHOP related transcription factors. On the one hand, this leaded to the occurrence of autophagy, which degraded the accumulation of misfolded proteins, played a protective role in osteosarcoma cells and reduced the apoptosis of osteosarcoma cells. This process is accompanied by an increase in mTOR phosphorylation. On the other hand, the inhibition of endoplasmic reticulum stress accompanied by the increase of Bcl-2 lead to the inhibition of osteosarcoma cell apoptosis. Therefore, we found that the mechanism of drug resistance in osteosarcoma cells is bidirectional.

Consistent with recent data, the present study exerts synergistic antitumour effects by activating ER stress-mediated autophagy and apoptosis. Subsequent analysis showed that chemotherapy treatment of SESN2-knockdown osteosarcoma cells not only caused intracytoplasmic calcium accumulation and ER swelling and vacuolisation but also enhanced PERK-mediated phosphorylation of eIF2α (Liu et al., 2019). Through observation, we found that SESN2 leads to a decrease in p-mTOR protein levels by reducing CHOP expression, which may be related to chemotherapy-mediated autophagy. This suggestion was further substantiated by the data, revealing that autophagy is associated with dysregulated response to ER stress. The correlation between the expression of mTOR and SESN2 was determined by SESN2 knockout. We found that low SESN2 expression led to upregulation of p-mTOR expression, autophagy inactivation and downregulation of Bcl-2. We suggest that chemotherapeutic agents induce autophagy in a SESN2-dependent manner by downregulating mTOR phosphorylation, which further promotes the inhibition of chemotherapeutic drug-induced apoptosis of osteosarcoma cells. The ER stress inhibitor 4-PBA reduced the apoptosis of osteosarcoma cells after chemotherapeutic treatment to reduce the sensitivity of osteosarcoma cells to chemotherapy drugs. In addition, treatment with 4-PBA showed that chemotherapy-induced autophagy and apoptosis operated via the PERK-eIF2α-CHOP axis of the ER stress response.

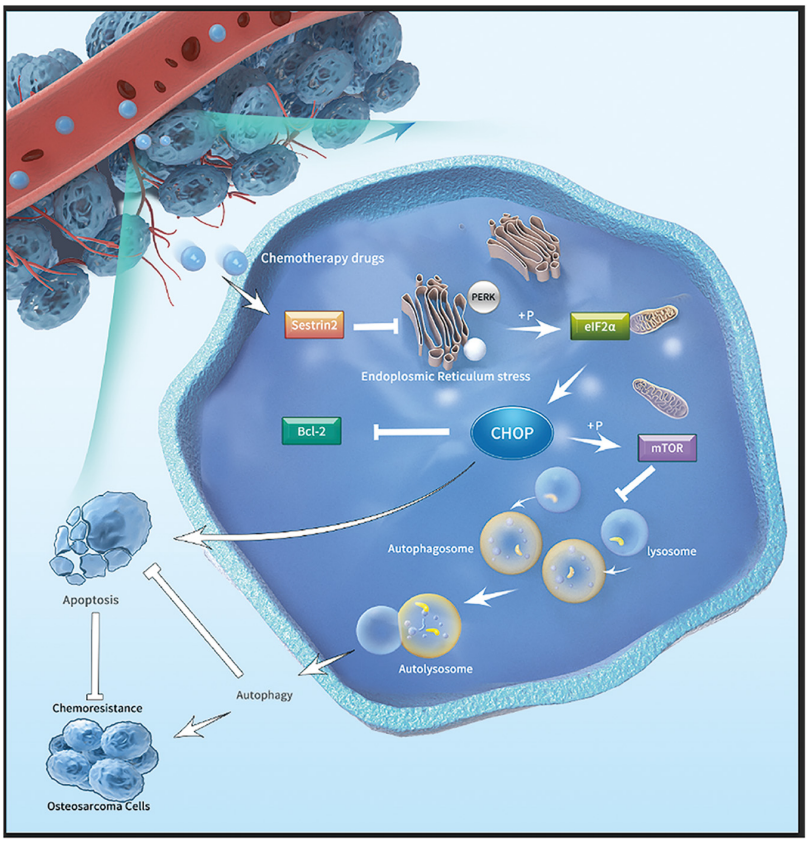

FIGURE 7 | Mechanistic model depicting the effects of SESN2 on the drug resistance of osteosarcoma. After chemotherapy drugs are applied to osteosarcoma cells, SESN2 expression is increased, and the phosphorylation of eIF2α by PERK during ER stress is inhibited. Finally, the expression of CHOP is suppressed, and apoptosis and autophagy are regulated by Bcl-2 and mTOR, respectively, thus causing drug resistance in osteosarcoma cells.

CONCLUSION

In summary, our data show that SESN2 expression in osteosarcoma cell lines is increased in response to chemotherapeutic agents. SESN2 regulated autophagy and reduced apoptosis via the PERK-eIF2α-CHOP signalling pathway of ER stress and eventually led to drug resistance. In addition, knockdown of SESN2 decreased autophagy and increased apoptosis, which corresponds to increased sensitivity of osteosarcoma cells to chemotherapeutic agents (**Figure 7**). Therefore, our results suggest that SESN2 is a novel therapeutic target for drug resistance in osteosarcoma.

DATA AVAILABILITY STATEMENT

The raw data supporting the conclusions of this article will be made available by the authors, without undue reservation.

ETHICS STATEMENT

The animal study was reviewed and approved by Ethics Committee of the Fourth Military Medical University.

AUTHOR CONTRIBUTIONS

ZT, XX, and ZG studied concept and design. ZT, XW, HW, HD, YL, WW, XX, XL, and LS acquired data. ZT and XW analyzed data. ZT and XX drafted the manuscript. ZT, XW, HW, HD, and YL provided acquisition, analysis and interpretation of data, and statistical analysis. ZT and FW made substantial revision to this manuscript. All authors read and approved the final manuscript.

FUNDING

This work was supported by grants from Key R&D Programme of Shaanxi Province (2020SF-075), National Natural Science Foundation of China (No. 81902897), the Independent Program of the State Key Laboratory of Cancer Biology, China (CBSKL2019ZZ21), and the Natural Science Foundation of Shaanxi Province, China (2020JQ-448).

ACKNOWLEDGMENTS

We thank all researchers involved in this study for their constructive comments.

SUPPLEMENTARY MATERIAL

The Supplementary Material for this article can be found online at: https://www.frontiersin.org/articles/10.3389/fcell.2021.722960/full#supplementary-material

Supplementary Figure 1 | After MG-63 cells were treated with Cis (20 μmol/L), Dox (0.2 μg/mL) or Mtx (50 μmol/L) for 24 h, the apoptosis of cells transfected with pHBLV control or pHBLV sestrin2 and cultured in the presence or absence of ZVAD-FMK (20 μmol/L) was detected using the Caspase 3 kit (F) (*n* = 3).

Supplementary Figure 2 | After MG-63 cells were treated with Cis (20 μmol/L), Dox (0.2 μg/mL) or Mtx (50 μmol/L) for 24 h, the expression of Cleaved-Caspase 3 transfected with pHBLV control or pHBLV sestrin2 and sestrin2 shRNA or control shRNA, and cultured in the presence or absence of ZVAD-FMK (20 μmol/L) was detected by western blot (F) (*n* = 3).

Supplementary Figure 3 | MG-63 and HOS cells were transfected with pHBLV control or pHBLV sestrin2, and the transfection effect was detected by quantitative real-time PCR (*n* = 3).

Supplementary Figure 4 | SESN2-knockdown HOS cells were treated with Cis (20 μmol/L) for 24 h with or without rapamycin (100 nmol/L) for 6 h. Proliferation was analysed by CCK-8 assay (*n* = 3).

Supplementary Figure 5 | The red arrows are autophagosomes in **Figures 3D**, **4E**, **5A**.

REFERENCES

Aleksakhina, S. N., Kashyap, A., and Imyanitov, E. N. (2019). Mechanisms of acquired tumor drug resistance. *Biochim. Biophys. Acta Rev. Cancer* 1872:188310. doi: 10.1016/j.bbcan.2019.188310

Bruning, A., Rahmeh, M., and Friese, K. (2013). Nelfinavir and bortezomib inhibit mTOR activity via ATF4-mediated sestrin-2 regulation. *Mol. Oncol.* 7, 1012–1018. doi: 10.1016/j.molonc.2013.07.010

Burns, J., Wilding, C. P., Jones, R. L., and Huang, P. H. (2020). Proteomic research in sarcomas–current status and future opportunities. *Semin Cancer Biol.* 61, 56–70. doi: 10.1016/j.semcancer.2019.11.003

Chen, J., Liu, G., Wu, Y., Ma, J., Wu, H., Xie, Z., et al. (2019). CircMYO10 promotes osteosarcoma progression by regulating miR-370-3p/RUVBL1 axis to enhance the transcriptional activity of beta-catenin/LEF1 complex via effects on chromatin remodeling. *Mol. Cancer* 18:150. doi: 10.1186/s12943-019-1076-1

Chen, R., Wang, G., Zheng, Y., Hua, Y., and Cai, Z. (2019). Drug resistance-related microRNAs in osteosarcoma: translating basic evidence into therapeutic strategies. *J. Cell. Mol. Med.* 23, 2280–2292. doi: 10.1111/jcmm.14064

Cheng, X., Feng, H., Wu, H., Jin, Z., Shen, X., Kuang, J., et al. (2018). Targeting autophagy enhances apatinib-induced apoptosis via endoplasmic reticulum stress for human colorectal cancer. *Cancer Lett.* 431, 105–114. doi: 10.1016/j.canlet.2018.05.046

Chiu, H. W., Tseng, Y. C., Hsu, Y. H., Lin, Y. F., Foo, N. P., Guo, H. R., et al. (2015). Arsenic trioxide induces programmed cell death through stimulation of ER stress and inhibition of the ubiquitin-proteasome system in human sarcoma cells. *Cancer Lett.* 356(2 Pt B), 762–772. doi: 10.1016/j.canlet.2014.10.025

Crisol, B. M., Lenhare, L., Gaspar, R. S., Gaspar, R. C., Munoz, V. R., da Silva, A. S. R., et al. (2018). The role of physical exercise on Sestrin1 and 2 accumulations in the skeletal muscle of mice. *Life Sci.* 194, 98–103. doi: 10.1016/j.lfs.2017.12.023

Dai, J., Huang, Q., Niu, K., Wang, B., Li, Y., Dai, C., et al. (2018). Sestrin 2 confers primary resistance to sorafenib by simultaneously activating AKT and AMPK in hepatocellular carcinoma. *Cancer Med.* 7, 5691–5703. doi: 10.1002/cam4.1826

Dodson, M., Darley-Usmar, V., and Zhang, J. (2013). Cellular metabolic and autophagic pathways: traffic control by redox signaling. *Free Radic. Biol. Med.* 63, 207–221. doi: 10.1016/j.freeradbiomed.2013.05.014

Gu, Z., Hou, Z., Zheng, L., Wang, X., Wu, L., and Zhang, C. (2018). LncRNA DICER1-AS1 promotes the proliferation, invasion and autophagy of osteosarcoma cells via miR-30b/ATG5. *Biomed. Pharmacother.* 104, 110–118. doi: 10.1016/j.biopha.2018.04.193

Hattori, T., Takahashi, Y., Chen, L., Tang, Z., Wills, C. A., Liang, X., et al. (2021). Targeting the ESCRT-III component CHMP2A for noncanonical Caspase-8 activation on autophagosomal membranes. *Cell Death Differ.* 28, 657–670. doi: 10.1038/s41418-020-00610-0

Hua, X., Xu, J., Deng, X., Xu, J., Li, J., Zhu, D. Q., et al. (2018). New compound ChlA-F induces autophagy-dependent anti-cancer effect via upregulating Sestrin-2 in human bladder cancer. *Cancer Lett.* 436, 38–51. doi: 10.1016/j.canlet.2018.08.013

Huang, K., Chen, Y., Zhang, R., Wu, Y., Ma, Y., Fang, X., et al. (2018). Honokiol induces apoptosis and autophagy via the ROS/ERK1/2 signaling pathway in human osteosarcoma cells in vitro and in vivo. *Cell Death Dis.* 9:157. doi: 10.1038/s41419-017-0166-5

Jeong, S., Kim, D. Y., Kang, S. H., Yun, H. K., Kim, J. L., Kim, B. R., et al. (2019). Docosahexaenoic acid enhances oxaliplatin-induced autophagic cell death via the ER Stress/Sesn2 pathway in colorectal cancer. *Cancers (Basel)* 11:982. doi: 10.3390/cancers11070982

Khan, M. A., Vikramdeo, K. S., Sudan, S. K., Singh, S., Wilhite, A., Dasgupta, S., et al. (2021). Platinum-resistant ovarian cancer: from drug resistance mechanisms to liquid biopsy-based biomarkers for disease management. *Semin Cancer Biol.* doi: 10.1016/j.semcancer.2021.08.005

Kimball, S. R., Gordon, B. S., Moyer, J. E., Dennis, M. D., and Jefferson, L. S. (2016). Leucine induced dephosphorylation of Sestrin2 promotes mTORC1 activation. *Cell Signal.* 28, 896–906. doi: 10.1016/j.cellsig.2016.03.008

Lear, T. B., Lockwood, K. C., Ouyang, Y., Evankovich, J. W., Larsen, M. B., Lin, B., et al. (2019). The ring-type E3 ligase RNF186 ubiquitinates Sestrin-2 and thereby controls nutrient sensing. *J. Biol. Chem.* 294, 16527–16534. doi: 10.1074/jbc.AC119.010671

Li, M., and Ma, W. (2021). miR-26a reverses multidrug resistance in osteosarcoma by targeting MCL1. *Front. Cell. Dev. Biol.* 9:645381. doi: 10.3389/fcell.2021.645381

Li, T., Mu, N., Yin, Y., Yu, L., and Ma, H. (2020a). Targeting AMP-activated protein kinase in aging-related cardiovascular diseases. *Aging Dis.* 11, 967–977. doi: 10.14336/AD.2019.0901

Li, T., Yin, Y., Mu, N., Wang, Y., Liu, M., Chen, M., et al. (2020b). Metformin-enhanced cardiac AMP-activated protein kinase/atrogin-1 pathways inhibit charged multivesicular body protein 2B accumulation in ischemia-reperfusion injury. *Front. Cell. Dev. Biol.* 8:621509. doi: 10.3389/fcell.2020.621509

Liu, S., Lin, H., Wang, D., Li, Q., Luo, H., Li, G., et al. (2019). PCDH17 increases the sensitivity of colorectal cancer to 5-fluorouracil treatment by inducing apoptosis and autophagic cell death. *Signal. Transduct. Target Ther.* 4:53. doi: 10.1038/s41392-019-0087-0

Liu, W., Jiang, D., Gong, F., Huang, Y., Luo, Y., Rong, Y., et al. (2020). miR-210-5p promotes epithelial-mesenchymal transition by inhibiting PIK3R5 thereby activating oncogenic autophagy in osteosarcoma cells. *Cell Death Dis.* 11:93. doi: 10.1038/s41419-020-2270-1

Liu, Z., Wang, H., Hu, C., Wu, C., Wang, J., Hu, F., et al. (2021). Targeting autophagy enhances atezolizumab-induced mitochondria-related apoptosis in osteosarcoma. *Cell Death Dis.* 12:164. doi: 10.1038/s41419-021-03449-6

Mrakovcic, M., and Frohlich, L. F. (2019). Molecular determinants of cancer therapy resistance to HDAC inhibitor-induced autophagy. *Cancers (Basel)* 12:109. doi: 10.3390/cancers12010109

Niu, J., Yan, T., Guo, W., Wang, W., and Zhao, Z. (2019). Insight into the role of autophagy in osteosarcoma and its therapeutic implication. *Front. Oncol.* 9:1232. doi: 10.3389/fonc.2019.01232

Pan, Z., Cheng, D. D., Wei, X. J., Li, S. J., Guo, H., and Yang, Q. C. (2021). Chitooligosaccharides inhibit tumor progression and induce autophagy through the activation of the p53/mTOR pathway in osteosarcoma. *Carbohydr. Polym.* 258:117596. doi: 10.1016/j.carbpol.2020.117596

Pantziarka, P., Verbaanderd, C., Huys, I., Bouche, G., and Meheus, L. (2021). Repurposing drugs in oncology: from candidate selection to clinical adoption. *Semin Cancer Biol.* 68, 186–191. doi: 10.1016/j.semcancer.2020.01.008

Patra, S., Pradhan, B., Nayak, R., Behera, C., Rout, L., Jena, M., et al. (2021). Chemotherapeutic efficacy of curcumin and resveratrol against cancer: chemoprevention, chemoprotection, drug synergism and clinical pharmacokinetics. *Semin Cancer Biol.* 73, 310–320. doi: 10.1016/j.semcancer.2020.10.010

Peixoto da Silva, S., Caires, H. R., Bergantim, R., Guimaraes, J. E., and Vasconcelos, M. H. (2021). miRNAs mediated drug resistance in hematological malignancies. *Semin Cancer Biol.* doi: 10.1016/j.semcancer.2021.03.014

Sanchez-Alvarez, M., Strippoli, R., Donadelli, M., Bazhin, A. V., and Cordani, M. (2019). Sestrins as a therapeutic bridge between ROS and autophagy in cancer. *Cancers (Basel)* 11:1415. doi: 10.3390/cancers11101415

Su, X., Zhang, X., Liu, W., Yang, X., An, N., Yang, F., et al. (2021). Advances in the application of nanotechnology in reducing cardiotoxicity induced by cancer chemotherapy. *Semin Cancer Biol.* doi: 10.1016/j.semcancer.2021.08.003

Wang, M., Xu, Y., Liu, J., Ye, J., Yuan, W., Jiang, H., et al. (2017). Recent insights into the biological functions of sestrins in health and disease. *Cell Physiol. Biochem.* 43, 1731–1741. doi: 10.1159/000484060

Wang, W., Chen, D., and Zhu, K. (2018). SOX2OT variant 7 contributes to the synergistic interaction between EGCG and Doxorubicin to kill osteosarcoma via autophagy and stemness inhibition. *J. Exp. Clin. Cancer Res.* 37:37. doi: 10.1186/s13046-018-0689-3

Wang, Y., Deng, X., Yu, C., Zhao, G., Zhou, J., Zhang, G., et al. (2018). Synergistic inhibitory effects of capsaicin combined with cisplatin on human osteosarcoma in culture and in xenografts. *J. Exp. Clin. Cancer Res.* 37:251. doi: 10.1186/s13046-018-0922-0

Wang, Z., Yin, F., Xu, J., Zhang, T., Wang, G., Mao, M., et al. (2019). CYT997(Lexibulin) induces apoptosis and autophagy through the activation of mutually reinforced ER stress and ROS in osteosarcoma. *J. Exp. Clin. Cancer Res.* 38:44. doi: 10.1186/s13046-019-1047-9

White-Gilbertson, S., Hua, Y., and Liu, B. (2013). The role of endoplasmic reticulum stress in maintaining and targeting multiple myeloma: a double-edged sword of adaptation and apoptosis. *Front. Genet.* 4:109. doi: 10.3389/fgene.2013.00109

Xiao, X., Wang, W., Li, Y., Yang, D., Li, X., Shen, C., et al. (2018). HSP90AA1-mediated autophagy promotes drug resistance in osteosarcoma. *J. Exp. Clin. Cancer Res.* 37:201. doi: 10.1186/s13046-018-0880-6

Ye, J., Palm, W., Peng, M., King, B., Lindsten, T., Li, M. O., et al. (2015). GCN2 sustains mTORC1 suppression upon amino acid deprivation by inducing Sestrin2. *Genes Dev.* 29, 2331–2336. doi: 10.1101/gad.269324.115

Yen, J. H., Huang, S. T., Huang, H. S., Fong, Y. C., Wu, Y. Y., Chiang, J. H., et al. (2018). HGK-sestrin 2 signaling-mediated autophagy contributes to antitumor efficacy of Tanshinone IIA in human osteosarcoma cells. *Cell Death Dis.* 9:1003. doi: 10.1038/s41419-018-1016-9

Zhu, G., Xu, P., Guo, S., Yi, X., Wang, H., Yang, Y., et al. (2020). Metastatic melanoma cells rely on Sestrin2 to acquire anoikis resistance via detoxifying intracellular ROS. *J. Investig. Dermatol.* 140, 666–675.e2. doi: 10.1016/j.jid.2019.07.720

Conflict of Interest: The authors declare that the research was conducted in the absence of any commercial or financial relationships that could be construed as a potential conflict of interest.

Publisher's Note: All claims expressed in this article are solely those of the authors and do not necessarily represent those of their affiliated organizations, or those of the publisher, the editors and the reviewers. Any product that may be evaluated in this article, or claim that may be made by its manufacturer, is not guaranteed or endorsed by the publisher.

frontiers | Frontiers in Cell and Developmental Biology

TYPE Correction
PUBLISHED 11 October 2022
DOI 10.3389/fcell.2022.882270

OPEN ACCESS

EDITED AND REVIEWED BY
Andrea Del Fattore,
Bambino Gesù Children's Hospital (IRCCS), Italy

*CORRESPONDENCE
Xiaokang Li,
lxkfmmu@163.com
Zheng Guo,
guozheng@fmmu.edu.cn
Xin Xiao,
xiao_xxtyfsxx@sina.com

†These authors have contributed equally to this work

SPECIALTY SECTION
This article was submitted to Molecular and Cellular Pathology, a section of the journal Frontiers in Cell and Developmental Biology

RECEIVED 23 February 2022
ACCEPTED 05 September 2022
PUBLISHED 11 October 2022

CITATION
Tang Z, Wei X, Li T, Wang W, Wu H, Dong H, Liu Y, Wei F, Shi L, Li X, Guo Z and Xiao X (2022), Corrigendum: Sestrin2-mediated autophagy contributes to drug resistance via endoplasmic reticulum stress in human osteosarcoma.
Front. Cell Dev. Biol. 10:882270.
doi: 10.3389/fcell.2022.882270

Corrigendum: Sestrin2-mediated autophagy contributes to drug resistance *via* endoplasmic reticulum stress in human osteosarcoma

Zhen Tang[1†], Xinghui Wei[1†], Tian Li[2†], Wei Wang[3†], Hao Wu[1], Hui Dong[1], Yichao Liu[1], Feilong Wei[4], Lei Shi[1], Xiaokang Li[4*], Zheng Guo[4*] and Xin Xiao[1*]

[1]Department of Orthopaedics, Xijing Hospital, Fourth Military Medical University, Xi'an, China, [2]School of Basic Medicine, Fourth Military Medical University, Xi'an, China, [3]State Key Laboratory of Cancer Biology, Department of Immunology, Fourth Military Medical University, Xi'an, China, [4]Department of Orthopaedics, Tangdu Hospital, Fourth Military Medical University, Xi'an, China

KEYWORDS

Sestrin2, apoptosis, autophagy, drug resistance, endoplasmic reticulum stress

A Corrigendum on
Sestrin2-mediated autophagy contributes to drug resistance *via* endoplasmic reticulum stress in human osteosarcoma

by Tang Z, Wei X, Li T, Wang W, Wu H, Dong H, Liu Y, Wei F, Shi L, Li X, Guo Z and Xiao X (2021). Front. Cell Dev. Biol. 9:722960. doi: 10.3389/fcell.2021.722960

In the original article, there was a mistake in Figures 3D,E, 4E as published. The transmission electron microscopy shown in Figures 3D, 4E, and immunofluorescence in Figure 3E were mistakenly used.

The red arrows in the figure legends of Figures 3, 4 are autophagosomes.

The authors apologize for this error and state that this does not change the scientific conclusions of the article in any way. The original article has been updated.

10.3389/fcell.2022.882270

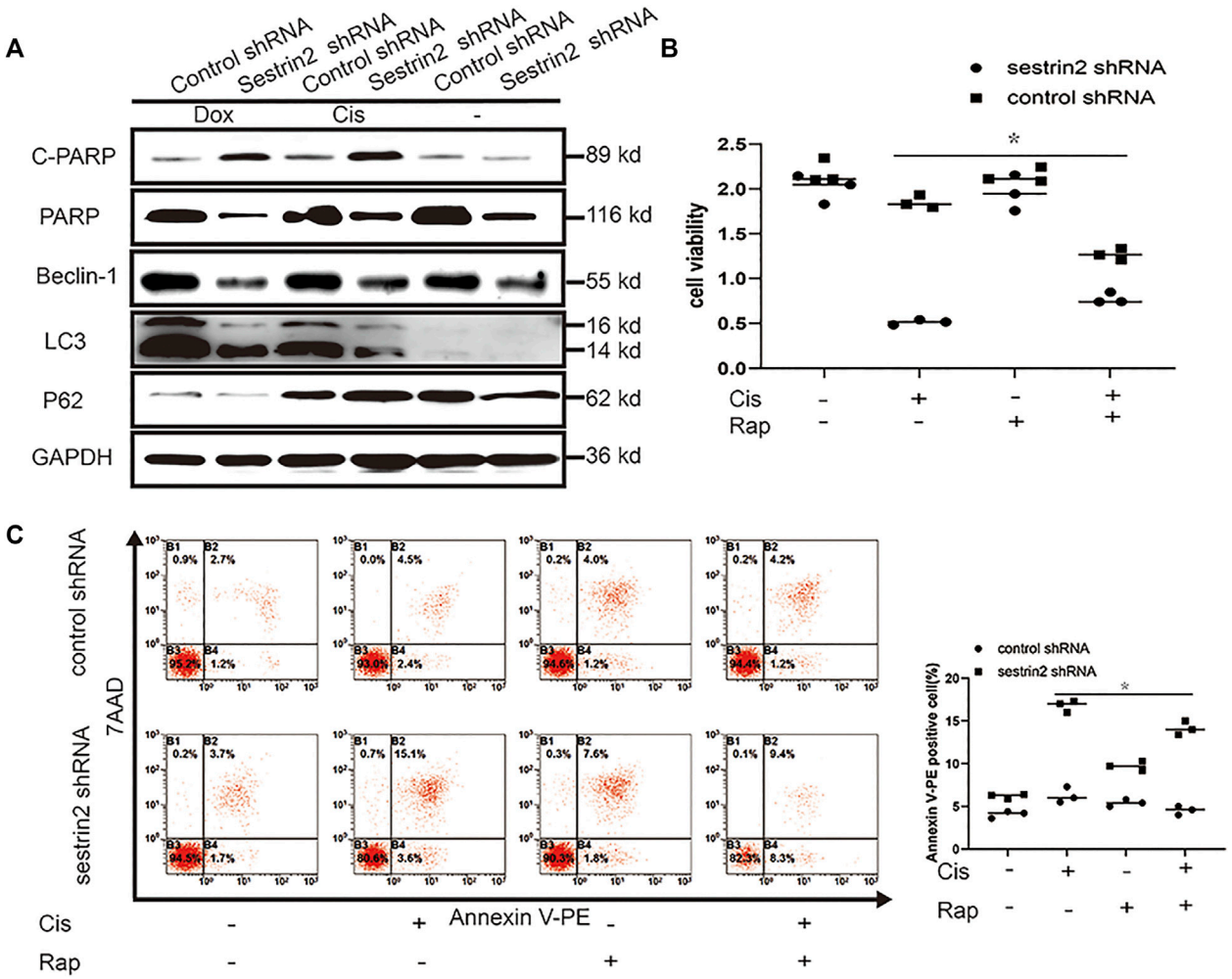

FIGURE 3
(Continued)

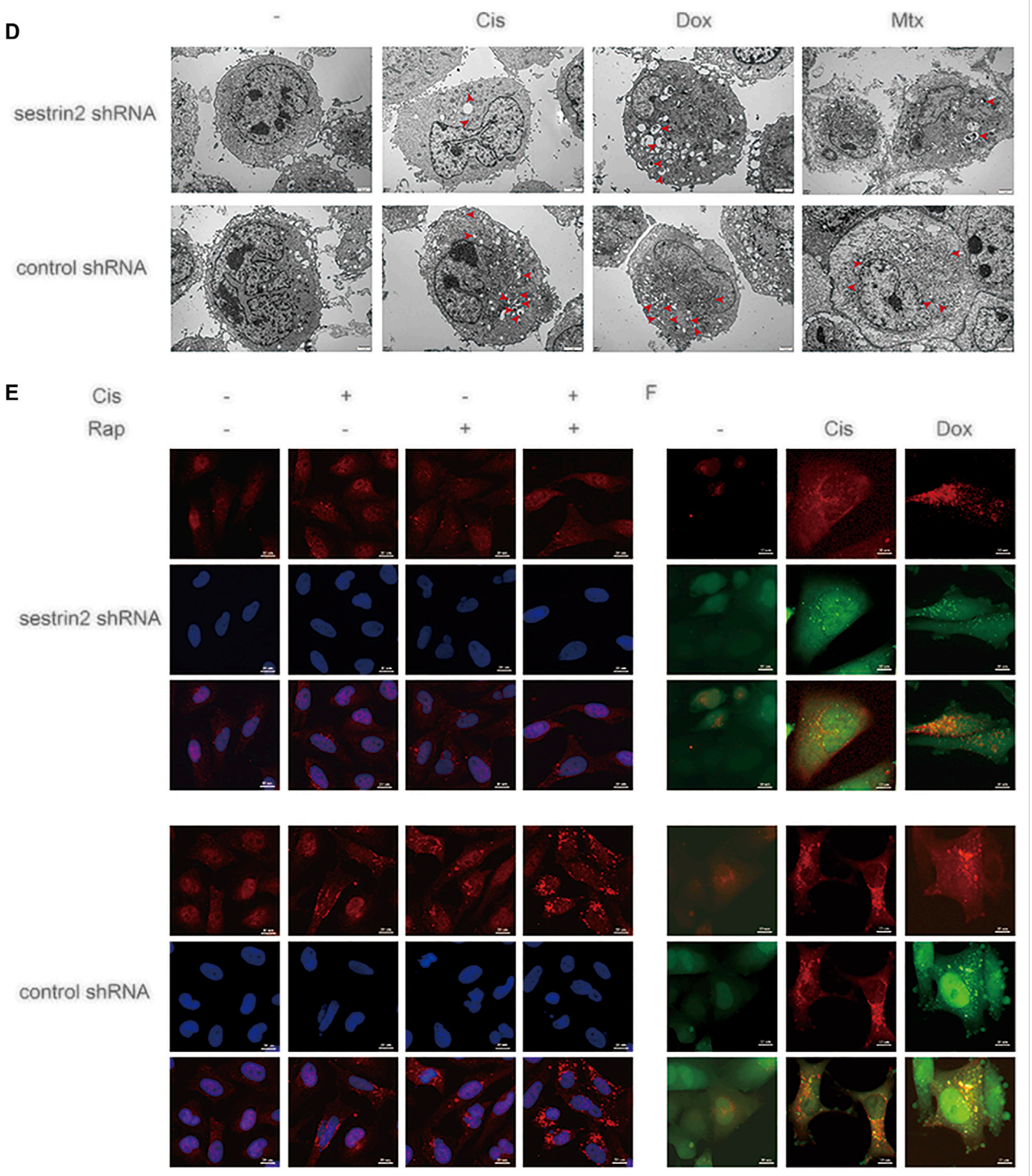

FIGURE 3
(Continued). Knockdown of SESN2 resulted in inhibited autophagy and increased apoptosis of osteosarcoma cells treated with chemotherapy. After treatment with Cis (20 μmol/L), Dox (0.2 μg/ml), or Mtx (50 μmol/L) for 24 h, SESN2-knockdown and control cells were subjected to western blot to detect the expression of cleaved and total PARP, LC3, and P62 expression levels **(A)** (n = 3). SESN2-knockdown HOS cells were treated with Cis (20 μmol/L) for 24 h with or without rapamycin (100 nmol/L) for 6 h. Proliferation was analysed by CCK-8 assay **(B)** (n = 3), apoptosis was assessed by Annexin V-PE/PI staining **(C)** (n = 3), and LC3 puncta formation was analysed by immunofluorescence **(E)** (n = 3, scale bar = 20 μm). Intracellular autophagosomes were observed by TEM **(D)** (n = 3, scale bar = 2 μm), and autophagic flux was monitored by fluorescence microscopy in HOS cells with transient expression of GFP-RFP-LC3 in HOS cells **(F)** (n = 3, scale bar = 10 μm). The data are presented as the mean ± SD. *p < 0.05 vs. the Control shRNA group.

10.3389/fcell.2022.882270

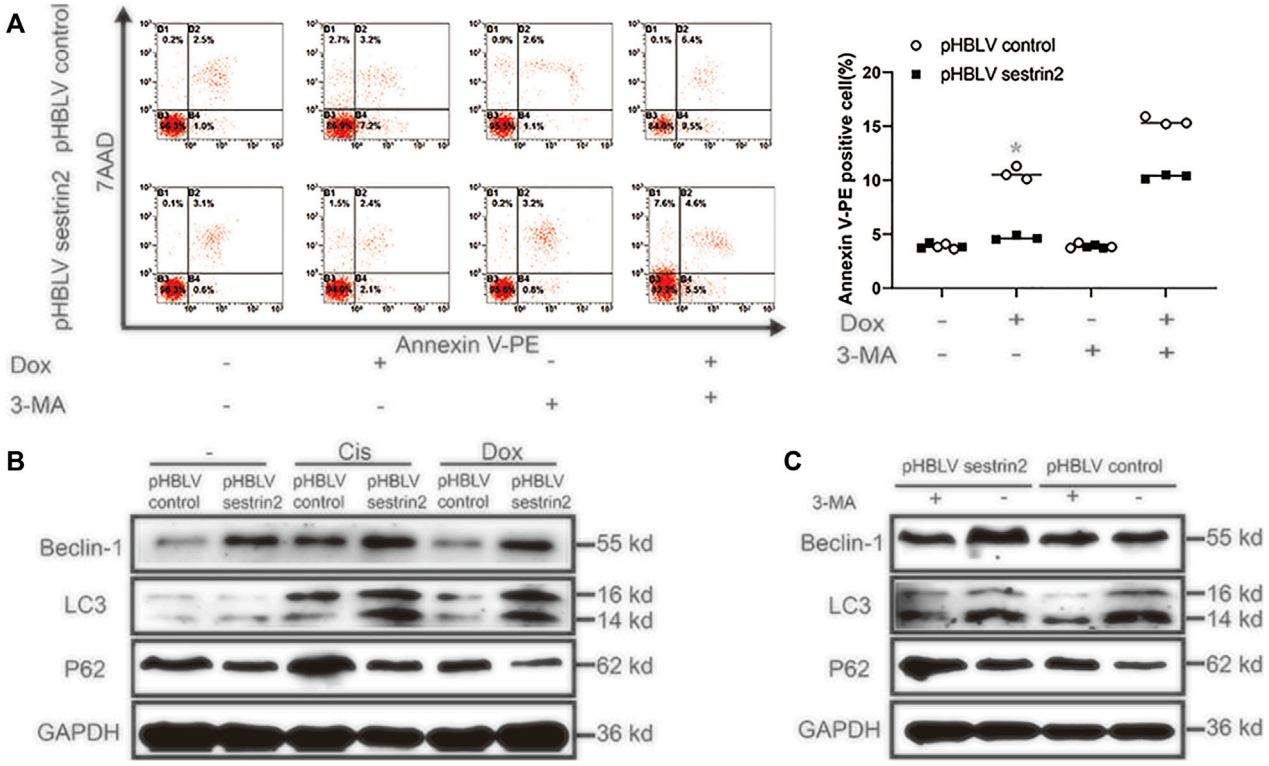

FIGURE 4
(Continued)

10.3389/fcell.2022.882270

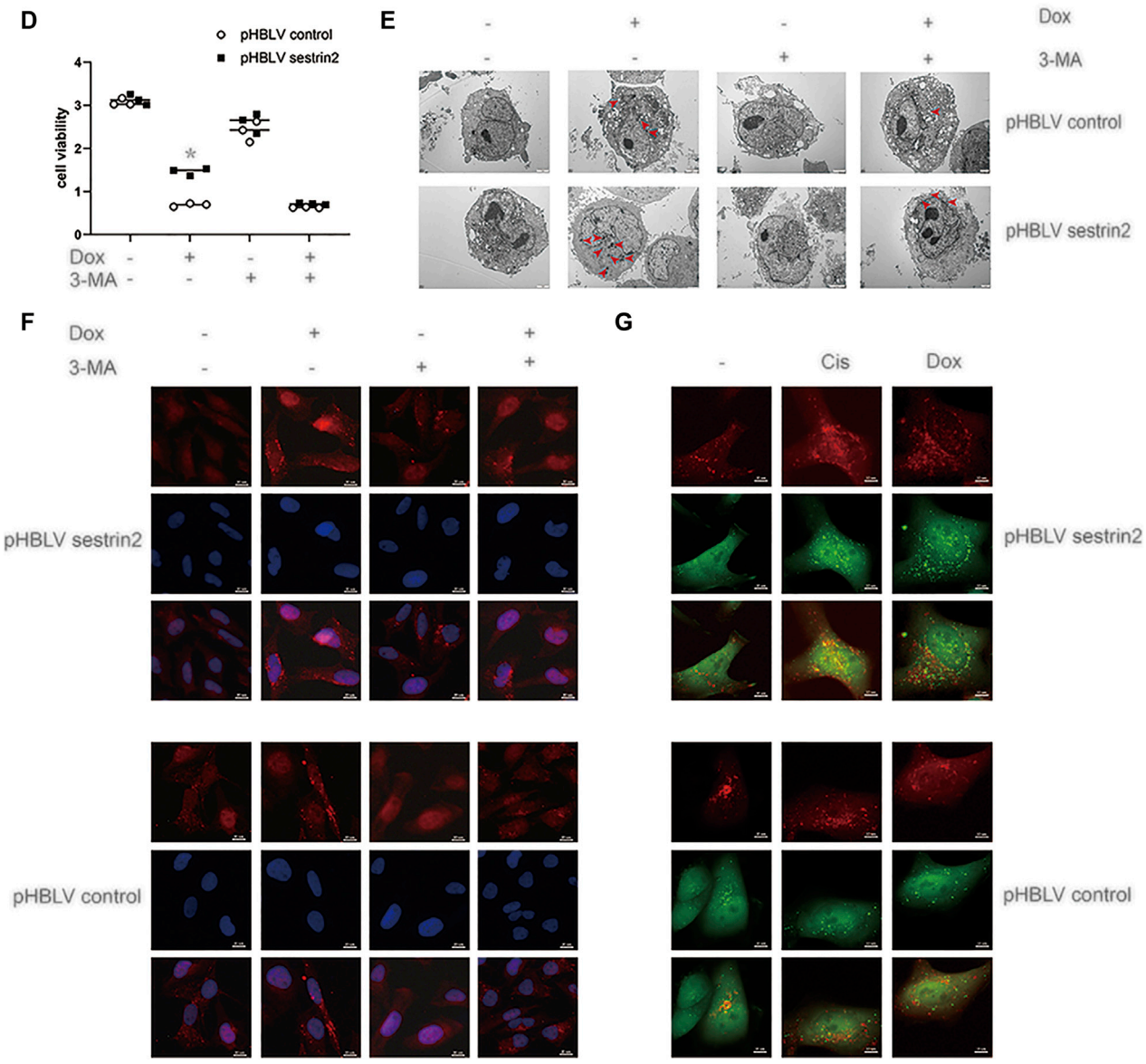

FIGURE 4
(Continued). SESN2 regulates autophagy and reduces the sensitivity of osteosarcoma cells to chemotherapy. In the presence or absence of 3-MA (5 mM), SESN2-overexpressing and control HOS cells were treated with Dox (0.2 μg/ml) for 24 h, and apoptosis was analysed by flow cytometry **(A)** (n = 3). After treatment with Cis (20 μmol/L) or Dox (0.2 μg/ml), the expression levels of LC3 and P62 in SESN2-overexpressing and control HOS cells were detected by western blot **(B)** (n = 3). The expression levels of LC3 and P62 in SESN2-overexpressing and control HOS cells treated with 3-MA (5 mM) were detected by western blot **(C)** (n = 3). In the presence or absence of 3-MA (5 mM), SESN2-overexpressing and control HOS cells were treated with Dox (0.2 μg/ml) for 24 h, cell activity was detected by CCK-8 **(D)** (n = 3), intracellular autophagosomes were observed by TEM **(E)** (n = 3, scale bar = 2 μm), and intracellular LC3 puncta formation was analysed by immunofluorescence **(F)** (n = 3, scale bar = 20 μm). After treatment with Cis (20 μmol/L) or Dox (0.2 μg/ml), autophagosome formation in HOS cells with ectopic SESN2 expression was monitored by immunofluorescence through transfection with RFP-GFP-LC3 lentivirus after upregulating SESN2 **(G)** (n = 3, scale bar = 10 μm). The data are presented as the mean ± SD. *p < 0.05 vs. the pHBLV control group.

Publisher's note

frontiers in Cell and Developmental Biology

ORIGINAL RESEARCH
published: 26 November 2021
doi: 10.3389/fcell.2021.753194

PPARβ/δ Agonist Alleviates Diabetic Osteoporosis *via* Regulating M1/M2 Macrophage Polarization

Miao Chen[1,2], *Weimin Lin*[1], *Rui Ye*[1,2], *Jianru Yi*[1,2]* *and Zhihe Zhao*[1,2]*

[1]State Key Laboratory of Oral Diseases and National Clinical Research Center for Oral Diseases, West China Hospital of Stomatology, Sichuan University, Chengdu, China, [2]Department of Orthodontics, West China Hospital of Stomatology, Sichuan University, Chengdu, China

Diabetic osteoporosis is a common complication in diabetic patients, leading to increased fracture risk and impaired bone healing. As a member of the peroxisome proliferator-activated receptor (PPAR) family, PPARβ/δ agonist is suggested as a therapeutic target for the treatment of metabolic syndrome, and has been reported to positively regulate bone turnover by improving osteogenesis. However, its regulatory role in diabetic osteoporosis has not been reported yet. Here, we explored the therapeutic effects and potential mechanisms of PPARβ/δ agonist to the osteoporotic phenotypes of diabetic mice. Our results indicated that the osteoporotic phenotypes could be significantly ameliorated in diabetic mice by the administration of PPARβ/δ agonists. *In vitro* experiments suggested that PPARβ/δ agonist treatment could alleviate the abnormal increase of osteoclast activity in diabetic mice by rectifying high glucose-mediated macrophage dysfunction instead of directly inhibiting osteoclast differentiation. Mechanistically, *Angptl4* may act as a downstream target of PPARβ/δ to regulate macrophage polarization. In conclusion, our study demonstrates the potential of PPARβ/δ agonist as a therapeutic target for the treatment of osteoporosis and immune homeostasis disorder in diabetic patients.

Keywords: PPARβ/δ, diabetes mellitus, diabetic osteoporosis, macrophage polarization, inflammation

OPEN ACCESS

Edited by:
Andrea Del Fattore,
Bambino Gesù Children Hospital (IRCCS), Italy

Reviewed by:
Makoto Makishima,
Nihon University, Japan
Elisabetta Benedetti,
University of L'Aquila, Italy
Ciro Menale,
University of Naples Federico II, Italy

***Correspondence:**
Jianru Yi
jianruyi@scu.edu.cn
Zhihe Zhao
zhzhao@scu.edu.cn

Specialty section:
This article was submitted to Molecular and Cellular Pathology, a section of the journal Frontiers in Cell and Developmental Biology

Received: *04 August 2021*
Accepted: *05 November 2021*
Published: *26 November 2021*

Citation:
Chen M, Lin W, Ye R, Yi J and Zhao Z (2021) PPARβ/δ Agonist Alleviates Diabetic Osteoporosis via Regulating M1/M2 Macrophage Polarization. Front. Cell Dev. Biol. 9:753194. doi: 10.3389/fcell.2021.753194

INTRODUCTION

Diabetes mellitus, a systemic metabolic disorder syndrome, is usually accompanied by hyperglycemia and chronic tissue and organ damage. In the last decade, the incidence of diabetes mellitus has increased rapidly worldwide with changes in diet and lifestyle (Unnikrishnan et al., 2016). The imbalance of immune homeostasis is one of the main characteristics of diabetic complications. Diabetes mellitus can lead to increased inflammatory infiltration, pro-inflammatory mediators including TNF-α, IL-1β, IL-6 and IL-18, resulting in aggravated inflammatory response (Graves and Kayal, 2008). ROS production in macrophages also increases under high glucose culture, resulting in abnormal macrophage polarization and disordered immune response (Rendra et al., 2019). Skeletal syndrome is an important complication of diabetic patients, including osteoporosis, increased fracture risk, and impaired bone healing properties. The inflammatory environment in diabetes mellitus suppressed the osteogenic differentiation and led to osteoblast apoptosis (Eller-Vainicher et al., 2020). Current evidence also suggested that diabetic status could stimulate osteoclast differentiation and bone resorption (Jiao et al., 2015). In diabetic patients, the circulating levels of tartrate-resistant acid phosphatase (TRAP) increased, which indicated the enhanced osteoclast activity (Suzuki et al., 2005). During the fracture healing process, diabetic rats showed increased

number of osteoclasts and the up-regulated expression of inflammatory factors compared with healthy control (Kayal et al., 2007). Our previous study also found that hyperglycemia increased M1 macrophage polarization and osteoclast differentiation in diabetic rats, leading to the accelerated progression of periodontitis (Zhang et al., 2021).

Peroxisome proliferators-activated receptors (PPARs) belong to ligand-activated receptors in the nuclear hormone receptor family, which can bind to the PPAR response element (PPRE) of the target gene to regulate various intracellular processes (Khoo et al., 2013). As a member of PPARs, PPARβ/δ activation could alleviate osteoporosis by up-regulating Wnt signal pathway in osteoblasts (Scholtysek et al., 2013). PPARβ/δ knockout-mice were found to exhibit glucose intolerance and impaired bone formation (Fu et al., 2014). In addition, the activation of PPARβ/δ accelerated osteoblast differentiation and increased peroxisome number, which had the potential to improve oxidative stress overload (Qian et al., 2015). PPARβ/δ agonist could effectively reduce tissue damage caused by oxidative stress and promote wound repair (Barlaka et al., 2015; Jimenez et al., 2018). Loss of PPARβ/δ led to the failure of macrophages M2 polarization under IL-4 induction (Odegaard et al., 2008). However, its effects on diabetic osteoporosis and osteoclast differentiation have not been reported yet.

Therefore, we speculate that PPARβ/δ activation may be a possible therapeutic target for improving immune homeostasis imbalance and osteoporosis under diabetic condition. In this study, we explored the therapeutic effect of PPARβ/δ agonist GW501516 on osteoporotic phenotype in diabetic mice, and investigated the regulation effect of PPARβ/δ agonist on the oxidative stress and macrophages polarization in high glucose environment, as well as its regulatory effect on osteoclast differentiation.

MATERIALS AND METHODS

Animal Model

The mice were purchased from Dashuo Company (Chengdu, China). Mice were housed in box cages, maintained on a 12 h light/12 h dark cycle, and fed a chow diet ad libitum (Sakai et al., 2019). The diabetes mellitus model of mice was constructed as described previously (Zhou X. et al., 2019). In brief, male C57BL/6J mice aged 8 weeks were fasted for 12 h and then injected intraperitoneally of 1% streptozotocin dissolved in saline solution with a dose of 50 mg/kg for 4 consecutive days. Tail vein blood was taken to test the fasting blood glucose level on the 1st and 2nd week post-injection. The mice with a fasting blood glucose higher than 16.7 mmol/L were regarded as successful diabetes model (Jiang et al., 2021). The mice were randomly divided into following three groups of eight mice each: 1) normal mice (Control); 2) normal mice treated with PPARβ/δ agonist GW501516 (Control + GW); 3) diabetes mellitus group (DM) and 4) diabetes mellitus group treated with PPARβ/δ agonist GW501516 (DM + GW).

Control + GW and DM + GW groups were injected with GW501516 (5 mg/kg/d, Sigma-Aldrich) dissolved in 0.1 ml dimethyl sulfoxide (DMSO) every other day (Mosti et al., 2014). Control group and DM group were injected with 0.1 ml DMSO every other day. The mice were sacrificed after 4 and 8 weeks of injection. The femurs were collected for subsequent histomorphological analysis.

Micro–Computed Tomography Analysis

The femurs were dissected and fixed in 4% paraformaldehyde for 2 days and then stored in 70% ethanol at 4°C. Micro-computed tomography (μCT) analysis was performed (μCT50, SCANCO Medical) with a spatial resolution of 10 μm (55 kV, 114 mA, 500 ms integration time). The regions of interest (ROI) were defined as the trabecular bone and cortical bone at the distal femur (Bouxsein et al., 2010). Bone mineral density (BMD), bone volume/total volume (BV/TV), trabecular number (Tb.N), trabecular separation (Tb.Sp), trabecular thickness (Tb.Th), cortical bone thickness (Ct.Th), and cortical bone porosity (Ct.Po) were evaluated within the delimited ROI (Wang et al., 2020).

Histomorphological Analysis

The mouse femurs were fixed and decalcified, and then embedded in paraffin. Sections of 4.5 μm were prepared. H&E staining (Solarbio, Beijing, China) was performed as the manufacturer's instruction. The stained sections were observed using an inverted microscope (IX81, Olympus).

TRAP staining was performed according to the procedure described previously (Liu et al., 2016). TRAP staining solution (Sigma) was added to cover the tissue sections. After incubating at 37°C for 40 min, the sections were stained with 0.1% methyl green solution (Sigma) for 10 s. The stained sections were observed using an inverted microscope (IX81, Olympus).

Bone Marrow-Derived Macrophage Culture

Eight-week-old C57BL/6J mice were sacrificed to separate the femur and tibia. The bone marrow was flashed into a petri dish and centrifuged. The supernatant was discarded, and the red blood cell lysate was added. The cells were seeded in a 10 cm diameter petri dish, cultured in DMEM medium with 10% fetal bovine serum (FBS), and supplied with 50 ng/ml m-CSF (R&D). After 4 days, the suspension cells were discarded and bone marrow-derived macrophages (BMDMs) were obtained for subsequent experiment.

DEME medium with 5.6 or 30 mM glucose were used for normal glucose (NG) or high glucose (HG) culture, and 5 μM GW501516 was added to HG + GW group. After 3 days of culture, different macrophage culture supernatants were obtained. To avoid the inhibition of osteoclast differentiation by high glucose concentration, DMEM medium without glucose was used to mix with the culture supernatant. Osteoclast-induced BMDMs are divided into three groups: NG Supernatant group, HG Supernatant group, and HG + GW Supernatant group.

Osteoclast Induction

For osteoclast induction, BMDMs (4×10^4 cells/well) were seeded in 24-well plates. 50 ng/ml RANKL (R&D) was added to the BMDM culture medium, and the medium was changed every 2 days. After 3 days of culture, mature osteoclasts could be observed and subsequent experiments were performed.

TRAP staining (Sigma-Aldrich) was performed according to the previously described procedure (Liu et al., 2016). The cells were fixed with 4% paraformaldehyde for 10 min, added with TRAP staining solution, and incubated at 37°C for 40 min. TRAP-positive cells containing three or more nuclei were considered osteoclasts.

Reverse Transcription Polymerase Chain Reaction

The total RNA of BMDMs and osteoclasts was extracted using Trizol reagent (Invitrogen, Carlsbad, CA, United States), and then reversely transcribed to obtain stable cDNA using PrimeScript™ RT reagent Kit with gDNA Eraser (TaKaRa Bio, Otsu, Japan). The RT-PCR was performed using SYBR Premix Ex Taq II (TaKaRa Bio) in Quant Studio™ three real-time fluorescent PCR instrument (ThermoFisher Scientific, China). Glyceraldehyde 3-phosphate dehydrogenase (*Gapdh*) was used as an internal reference to normalize the gene expression (Wang et al., 2020). The result was calculated using the $2^{-\Delta\Delta Ct}$ method and expressed as a multiple change relative to *Gapdh*. The primer sequences are summarized in **Supplementary Table S1**.

ROS Detection

The detection of ROS levels in BMDMs was carried out in accordance with the recommended protocol (Pang et al., 2019). In brief, BMDMs (2×10^5 cells/well) were seeded in 6-well plates under NG, HG, or HG + GW culture. Then, the ROS fluorescent probe DCFH-DA (Beyotime Biotechnology) was diluted with serum-free DMEM medium at a ratio of 1:1,000. After culturing for 72 h, the culture medium was removed and then DMEM medium containing DCFH-DA was added. After incubation at 37°C for 20 min, the cells were washed three times with serum-free DMEM medium without phenol red and digested by trypsin. The fluorescence intensity was analyzed on a flow cytometer (ThermoFisher).

Flow Cytometry

For flow cytometry analysis, the mouse femur was cut into pieces, digested in 1 mg/ml collagenase I, 1 mg/ml dispase II at 37°C for 30 min, centrifuged. After lysis of red blood cells on ice, the samples were passed through a 70-μm filter, centrifuged, and ready for staining. Anti-mouse CD45, anti-mouse CD11b, anti-mouse CD86, and anti-mouse CD206 were purchased from BD Biosciences, and the permeabilization/fixation kit was purchased from eBioscience. All staining processes were performed in 100 μl PBS. The cells were stained on ice for 30 min and then analyzed by flow cytometry (BD Biosciences).

ELISA

The expression levels of TNF-α and IL-1β were measured by mouse ELISA kits (Cusabio) according to the recommended protocol. Briefly, 100 μl of culture supernatant was added to a 96-well plate with high binding capacity and incubated for 2 h, and the absorbance was measured with a microplate reader. Serum concentration of PINP, CTX and ANGPTL4 were measured using ELISA kits (CUSABIO). Mice were fasted for 4 h and then we collected the blood samples by puncturing the cheek pouch and allowed the blood to coagulate on ice for 1 h before centrifugation to obtain the serum.

Gene Knockdown

siRNA sequence for *Angptl4* and *Ppard* were designed and synthesized by Sangon Biotech (Shanghai, China). BMDMs were transfected with Lipofectamine® RNAimax (Invitrogen) in serum-free DMEM medium followed by the manufacturer's instructions. In all experiments using siRNA, control siRNA and Lipofectamine® RNAimax were added to other group to eliminate other potential influence.

Immunofluorescence Staining

For immunofluorescence staining, sodium citrate solution was used for antigen retrieval. After blocking by 5% BSA at 37°C for 1 h, primary antibodies (anti-CD86, anti-CD206, Abcam) were incubated overnight at 4°C. Then the fluorescent secondary antibodies (Abcam) were incubated for 1 h at room temperature. DAPI was used to mark the nucleus with 15 min of staining. The stained sections were observed under a fluorescent microscope (Olympus BX53).

Chromatin Immunoprecipitation

Chromatin immunoprecipitation (ChIP) assay was performed according to the manufacturer's instructions with EZ-Zyme Chromatin Preparation Kit (Millipore) and Magna Chip HiSens (Millipore). Rabbit IgG (Sigma) was used as the control, and antibody against PPARβ/δ (Santa Cruz) was set as the experimental group. The DNA-protein complex was dissociated, PCR primers were designed to detect the target area, and then the pull-down DNA and input DNA were tested by PCR analysis with the primers flanking the PPRE region of *Angptl4*.

For ChIP-seq analysis, we downloaded the ChIP-seq data of PPARβ/δ in GEO database, with the accession number GSE50144 (Inoue et al., 2014). The binding peak of PPARβ/δ in *ANGPTL4* gene segment was visualized *via* integrative genomics viewer (IGV) software.

Statistical Analysis

All quantified data were expressed as mean ± standard deviation (SD). Statistical differences were performed *via* unpaired two-tailed Student's *t* test for comparison between two groups and by one-way or two-way analysis of variance (ANOVA) followed by the Tukey's post hoc test for multiple comparisons. p values < 0.05 were considered to be statistically significant.

RESULTS

PPARβ/δ Agonist Alleviates the Osteoporotic Phenotypes of Diabetic Mice *in Vivo*

First, we explored the effect of PPARβ/δ agonist on the osteoporotic phenotypes of diabetic mice (**Figure 1A**).

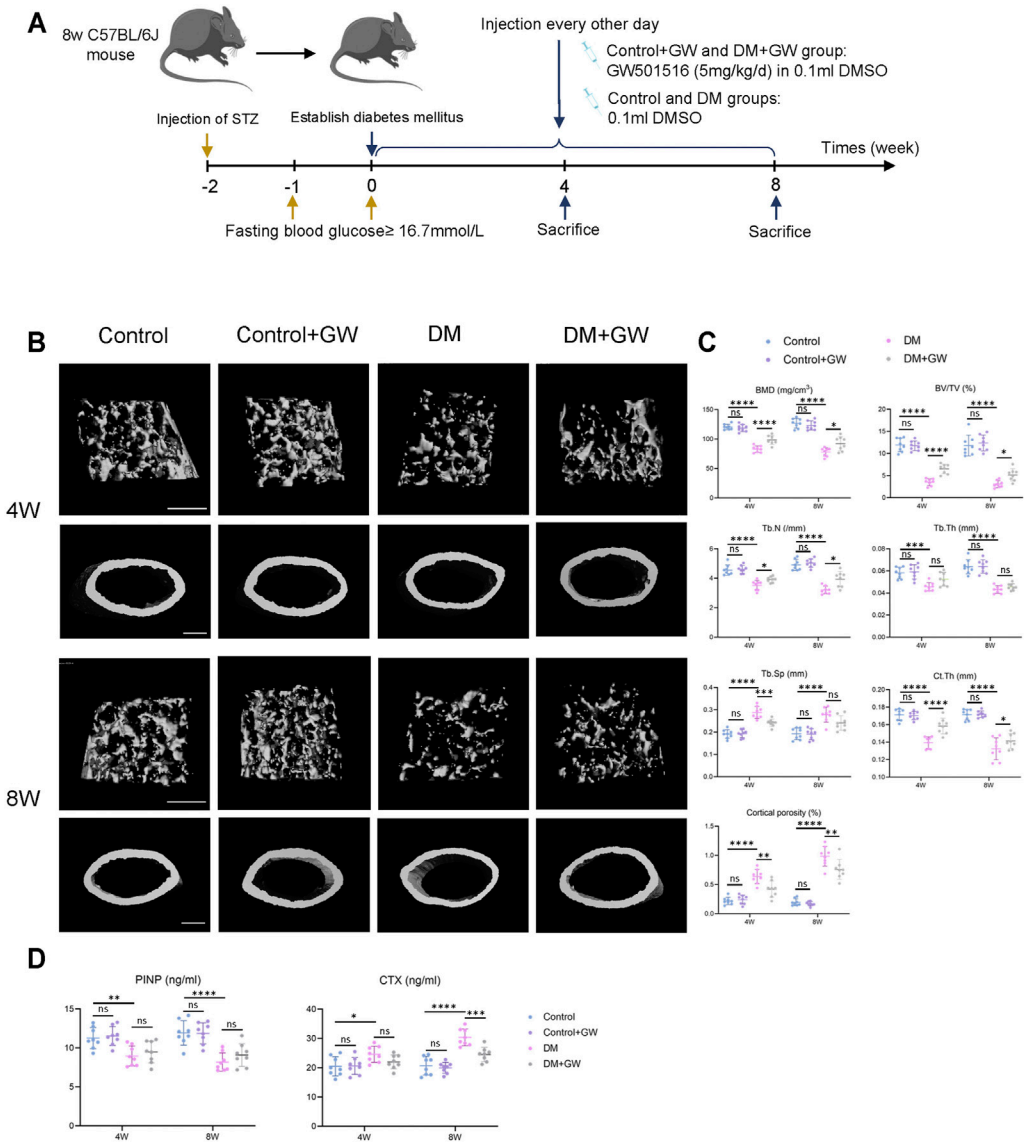

FIGURE 1 | PPARβ/δ agonist alleviates the osteoporosis phenotype in diabetic mice. **(A)** Schematic illustration of experimental design for PPARβ/δ agonist treatment. **(B)** Representative images of μCT of distal femoral tissue at the 4th and 8th week. Scale bar = 500 μm. **(C)** Quantitative μCT analyses of bone mineral density (BMD), bone volume/total volume (BV/TV), trabecular number (Tb.N), trabecular separation (Tb.Sp), trabecular thickness (Tb.Th), cortical bone thickness (Ct.Th), and cortical bone porosity (Ct.Po) of distal femoral tissue (n = 8). **(D)** Serum levels of PINP and CTX in each group. Data were expressed as mean ± SD. The p values were calculated by two-way ANOVA. (ns, not statistically significant, $^{*}p < 0.05$, $^{**}p < 0.01$, $^{***}p < 0.001$, $^{****}p < 0.0001$).

Through μCT analysis of the distal femur, we found that both trabecular bone and cortical bone were affected by the diabetic condition and manifested as bone loss. PPARβ/δ agonist could partially relieve the diabetic osteoporosis. In addition, PPARβ/δ agonist treatment had no significant influence on bone phenotype in healthy control mice (**Figures 1B,C**). H&E staining results showed the number and thickness of trabecular bone and the thickness of cortical bone decreased in DM group, while in the DM + GW group, the osteoporotic phenotype was restored (**Figure 2A**). Through TRAP staining, we found that osteoclast activity in DM group was significantly increased, and PPARβ/δ agonist treatment could reduce the activation of osteoclasts under diabetic condition (**Figures 2B,C**). Also, bone resorption marker CTX decreased after PPARβ/δ agonist treatment (**Figure 1D**). Overall, we found that at the 4th week and 8th week, the bone mass of the DM group was significantly lower than that of the control group, and PPARβ/δ agonist alleviated the diabetic bone loss.

PPARβ/δ Agonist has no Direct Effect on Osteoclast Differentiation *in Vitro*

Seizing the evidence that PPARβ/δ agonist alleviated the diabetic osteoporosis phenotypes and reduced osteoclast activity *in vivo*,

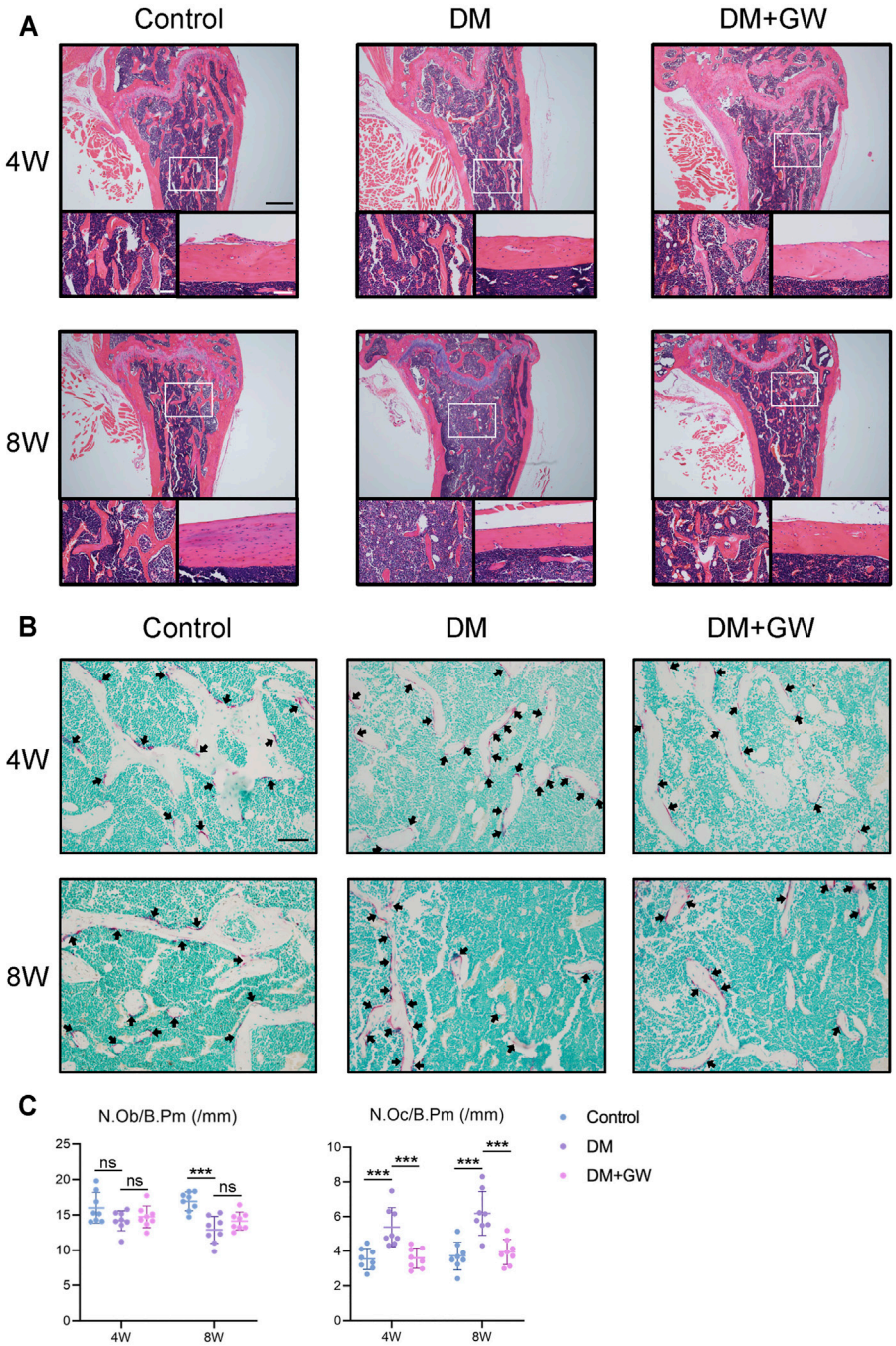

FIGURE 2 | PPARβ/δ agonist reduces the bone loss and osteoclast activation in diabetic mice. **(A)** Representative images of H&E staining of distal femoral tissue sections. Scale bar = 500 μm (top), scale bar = 100 μm (bottom). **(B)** Representative images of TRAP staining of distal femoral tissue sections. TRAP positive cells were indicated by arrows. Scale bar = 100 μm. **(C)** Statistics for the number of osteoblasts and osteoclasts. Data were expressed as mean ± SD. The *p* values were calculated by one-way ANOVA. (ns, not statistically significant, ***$p < 0.001$). N. Ob/B.Pm = osteoblast number/bone perimeter, N. Oc/B.Pm = osteoclast number/bone perimeter.

we speculated that PPARβ/δ might directly inhibit osteoclast differentiation. Considering that high glucose environment inhibited osteoclast differentiation *in vitro* (Wittrant et al., 2008), we explored the regulatory effect of PPARβ/δ agonist on osteoclast differentiation under normal glucose culture. However, PPARβ/δ agonist exhibited no effect on osteoclast differentiation *in vitro* (**Figures 3A,B**). RT-PCR results showed there is no significant difference in osteoclastogenesis-related genes before and after PPARβ/δ agonist treatment (**Figure 3C**).

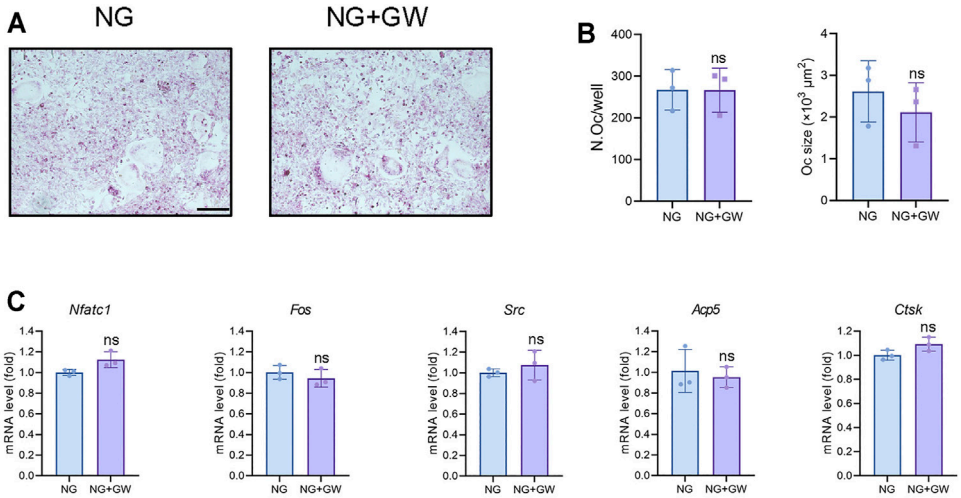

FIGURE 3 | PPARβ/δ agonist cannot directly regulate osteoclast differentiation *in vitro*. **(A)** TRAP staining for osteoclast differentiation before and after PPARβ/δ agonist treatment. Scale bar = 100 μm. **(B)** Statistics on the number and size of osteoclasts. **(C)** RT-PCR results of the expressions of the osteoclastogenesis-related genes before and after PPARβ/δ agonist treatment. Data were expressed as mean ± SD. The *p* values were calculatedby two-tailed Student's t test. (ns, not statistically significant). N. Oc = number of osteoclasts.

PPARβ/δ Agonist Improves High Glucose-Mediated Macrophage Inflammation

Given that immune homeostasis imbalance was an important factor leading to diabetic complications, we explored the effect of PPARβ/δ agonist one the ROS level and pro-inflammatory polarization of macrophages induced by high glucose. The results showed that PPARβ/δ agonist effectively reduced the high glucose-induced ROS production (**Figures 4A,B**) and the expression of M1 signature genes (iNOS, IL-1β, and TNF-α), while improved the expression of M2 signature genes (CD206, Arg-1, and IL-10) (**Figure 4C**).

Our previous studies proved that the macrophage polarization could affect osteoclast differentiation (Zhang et al., 2021). Therefore, we supposed that the reduced inflammatory phenotypes of macrophage might be the key mechanism for PPARβ/δ agonist to alleviate diabetic osteoclast activity. After adding macrophage culture supernatant of NG, HG, and HG + GW groups, the differentiation levels of osteoclasts were different (**Figure 4E**). The macrophage culture supernatant from HG group could significantly increase both the number and size of osteoclasts, while supernatant from HG + GW group reversed the stimulating effect on osteoclast differentiation (**Figures 4F,G**). The results of RT-PCR showed that the macrophage culture supernatant from HG group could significantly increase the expression of osteoclastogenesis-related genes, which were partially reduced by HG + GW Supernatant group (**Figure 4H**). To clarify which factor in the culture supernatant affected the osteoclast differentiation, we extracted the macrophage culture supernatant and measured the protein levels of IL-1β and TNF-α by ELISA. We found that high-glucose culture increased the expression level of IL-1β and TNF-α, and PPARβ/δ agonist treatment significantly decreased IL-1β and TNF-α level, and the reduction of TNF-α was the most significant (**Figure 4D**). In addition, after neutralizing antibodies treatment, we found that TNF-α blockade had the most obvious effect on inhibiting osteoclast differentiation, and IL-1β blockade also inhibited the osteoclast differentiation (**Supplementary Figure S1**). We speculate that TNF-α is the most important inflammatory factor that stimulates osteoclast differentiation under high glucose, and PPARβ/δ agonist treatment can reduce osteoclast differentiation by reducing the level of TNF-α.

Abnormal M1/M2 Polarization is Restored by PPARβ/δ Agonist in Diabetic Mice

To validate that PPARβ/δ agonist could reduce the inflammatory phenotypes of macrophage *in vivo*, immunofluorescence staining (**Figures 5A–C**) and flow cytometry analysis (**Figures 5D,E**) of bone marrow tissue were performed to detect the expression of CD86 (M1 marker) and CD206 (M2 marker). The $CD86^+$ cells in the DM group significantly increased compared to control group, while the number of $CD206^+$ cells decreased, indicating that M1 polarization of macrophages increased while the M2 polarization decreased in DM group. PPARβ/δ agonist reduced the proportion of $CD86^+$ cells and enhanced the proportion of $CD206^+$ cells, indicating that PPARβ/δ agonist treatment *in vivo* could effectively rectify the macrophage dysfunction in skeletal system under diabetic condition.

PPARβ/δ Agonist Treatment Restored the M1/M2 Polarization *via* Up-Regulating *Angptl4*

After determining the regulatory effect of PPARβ/δ agonists on macrophage polarization *in vivo* and *in vitro*, we hope to explore the regulatory mechanism and downstream signaling pathways of PPARβ/δ agonist. As an important transcription factor, PPARβ/δ had been reported to bind to the PPRE region of genes and activate

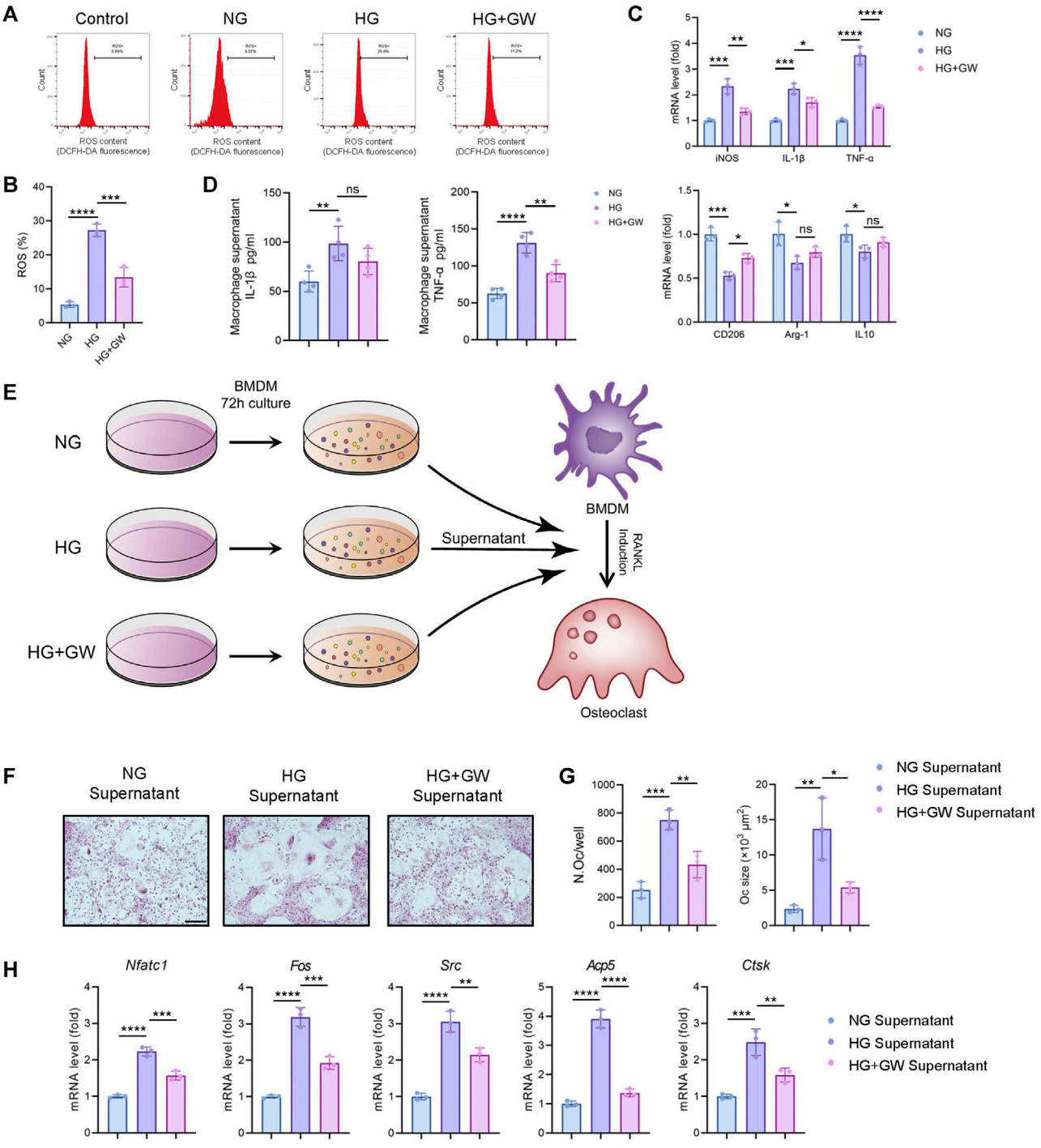

FIGURE 4 | PPARβ/δ agonist alleviates high glucose-induced macrophage inflammation and supernatant-mediated osteoclast differentiation. **(A)** Flow cytometry analysis of ROS levels detected by fluorescent probe in different groups. **(B)** Statistics for the ROS levels. **(C)** RT-PCR results regarding the expression levels of macrophage polarization-related genes in different groups. **(D)** Expression level of IL-1β and TNF-α detected by ELISA. **(E)** Schematic illustration of experimental design for regulating osteoclast differentiation through macrophage culture supernatant. **(F)** Representative images of TRAP staining for osteoclast differentiation in different groups. Scale bar = 100 μm. **(G)** Statistics for the number and size of osteoclasts. **(H)** RT-PCR results of the expressions of the osteoclastogenesis-related genes in different groups. Data were expressed as mean ± SD. The *p* values were calculated by one-way ANOVA. (ns, not statistically significant, *$p < 0.05$, **$p < 0.01$, ***$p < 0.001$, ****$p < 0.0001$).

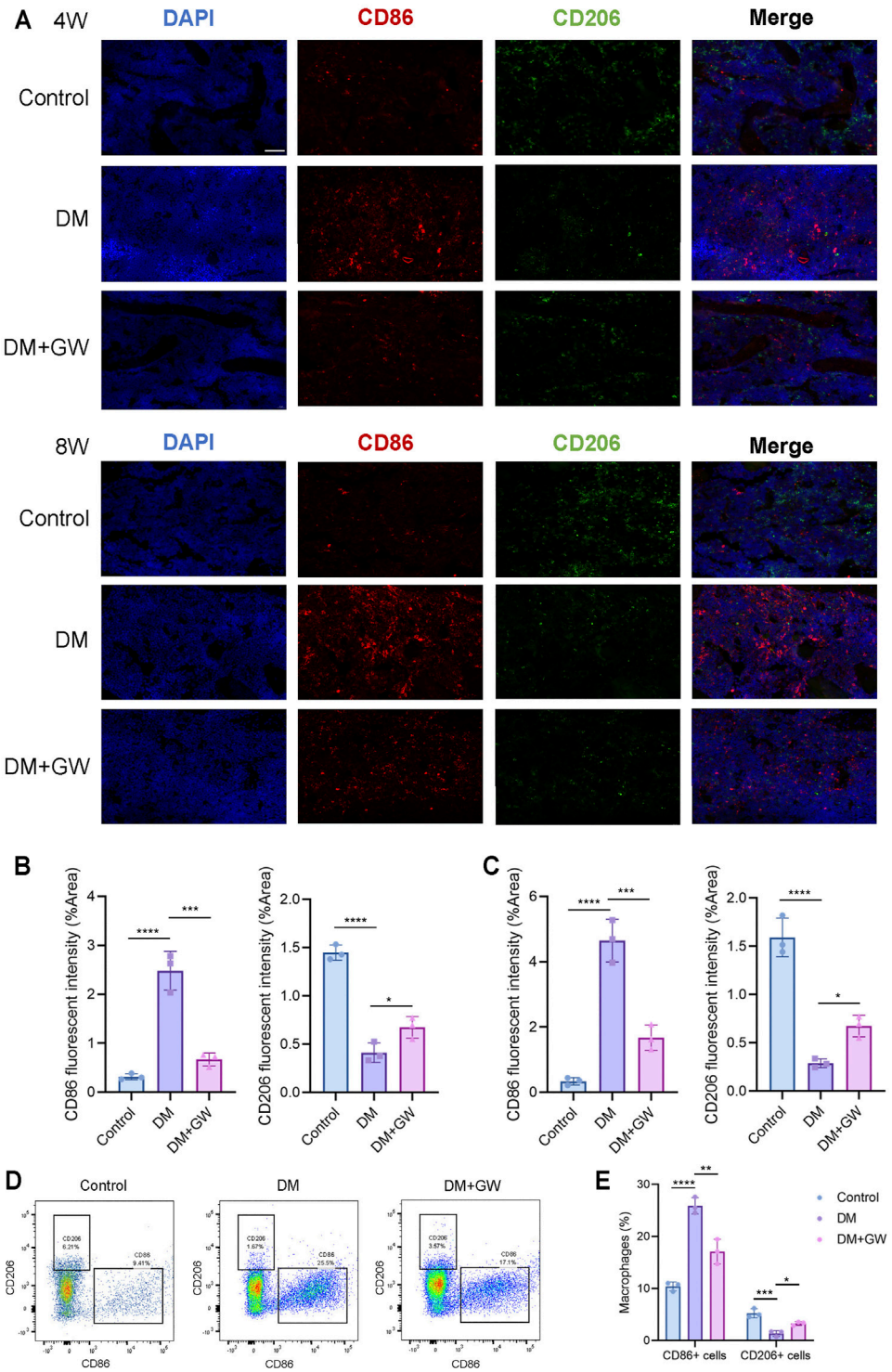

FIGURE 5 | PPARβ/δ agonist improves the abnormal macrophage polarization in skeletal system of diabetic mice. **(A)** Representative images of immunofluorescence staining of the M1/M2 macrophage polarization at the 4th and 8th week is in control, DM and DM + GW group. Red-CD86, Green-CD206, Blue-DAPI. Scale bar = 50 μm. **(B)** Quantitative analysis of CD86 and CD206 fluorescence intensity at the 4th week. **(C)** Quantitative analysis of CD86 and CD206 fluorescence intensity at the 8th week. **(D)** Flow cytometry analysis of CD86^{+} and CD206^{+} macrophage proportion in each group. **(E)** Statistics for CD86^{+} and CD206^{+} macrophage proportion. Data were expressed as mean ± SD. The *p* values were calculated by one-way ANOVA. (*$p < 0.05$, **$p < 0.01$, ***$p < 0.001$, ****$p < 0.0001$).

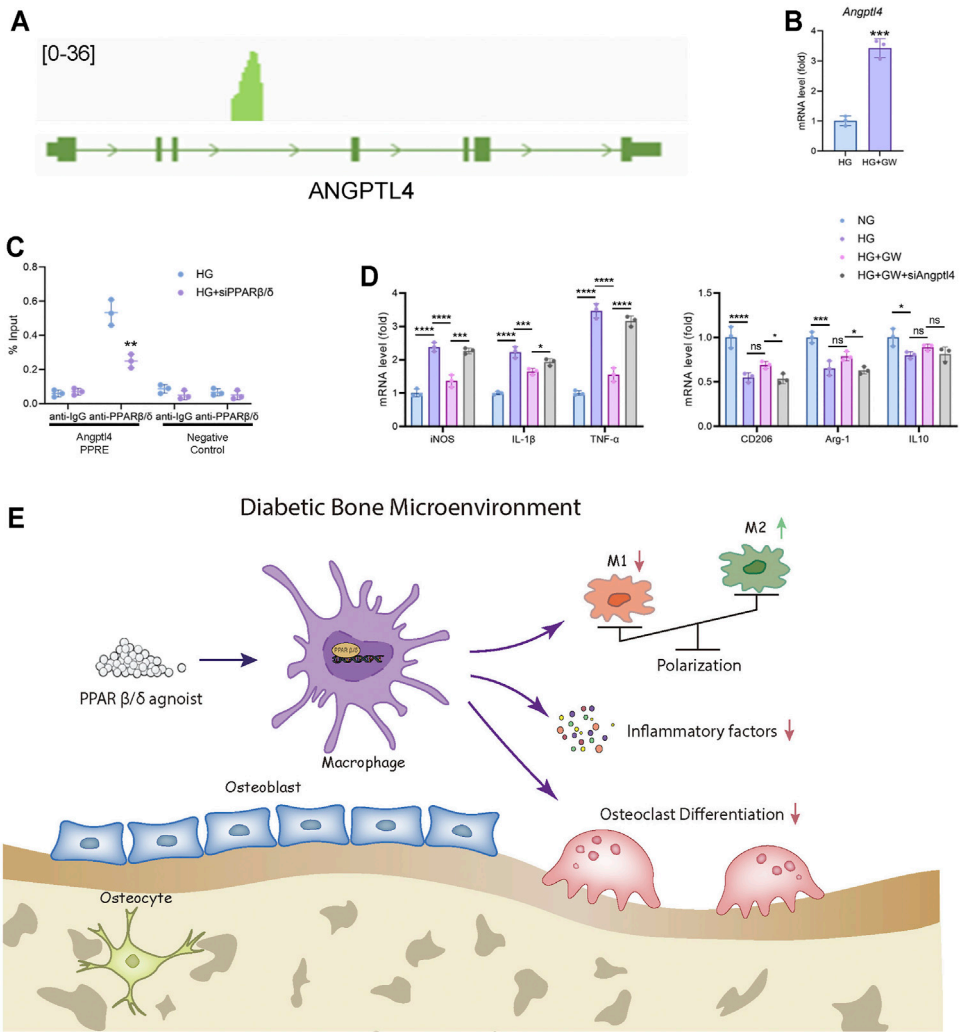

FIGURE 6 | *Angptl4* is a downstream target of PPARβ/δ agonist to exert an anti-inflammatory effect in macrophage. **(A)** ChIP-seq analysis of the binding peak of PPARβ/δ in *Angptl4* gene segment. **(B)** RT-PCR result of the expression level of *Angptl4* after PPARβ/δ agonist treatment in macrophage. **(C)** ChIP-PCR validation of the binding of PPARβ/δ to the PPRE region of *Angptl4*. **(D)** RT-PCR results of PPARβ/δ knockdown on the expression of macrophage polarization-related genes. **(E)** The mechanism diagram of PPARβ/δ agonist alleviating diabetic osteoporosis. Data were expressed as mean ± SD. The *p* values were calculated by two-tailed Student's t test or one-way ANOVA. (ns, not statistically significant, $*p < 0.05$, $**p < 0.01$, $***p < 0.001$, $****p < 0.0001$).

gene transcription. By analyzing ChIP-seq data in GEO database, we found that there is a binding peak at the intronic region of *Angptl4*, which is reported to coincide with the PPRE region (Inoue et al., 2014) (**Figure 6A**). Based on the above evidence, we speculated that *Angptl4* could serve as a potential downstream gene of PPARβ/δ.

In mice BMDM, PPARβ/δ agonist treatment also up-regulated the expression level of *Angptl4* (**Figure 6B**). Through ChIP assay, we proved that PPARβ/δ had a binding site in the gene segment of *Angptl4* in BMDM (**Figure 6C**). Knockdown of *Angptl4* by siRNA in BMDM eliminated the protective effect of PPARβ/δ agonist on the inflammatory phenotypes of macrophages under high-glucose culture (**Figure 6D**). We evaluated the expression level of ANGPTL4 in serum of diabetic mice by ELISA test and verified ANGPTL4 expression in bone marrow tissue through immunohistochemical staining. We found that after PPARβ/δ agonist treatment, ANGPTL4 was significantly up-regulated (**Supplementary Figure S2**). However, as for the effect of secreted ANGPTL4, blockade of ANGPTL4 by neutralizing antibody in culture supernatant did not significantly affect osteoclast differentiation, which suggested that the regulation of osteoclast differentiation by PPARβ/δ agonist seemed to be independent of secreted ANGPTL4 (**Supplementary Figure S3**). Therefore, we believed that *Angptl4* could serve as an important downstream gene of PPARβ/δ to regulate macrophage polarization (**Figure 6E**).

DISCUSSION

Diabetes mellitus disturbs bone metabolism, leading to diabetic osteoporosis and increased fracture risk (Schwartz, 2017).

Successful glycemic control can reduce the incidence of diabetes osteoporosis (Paschou et al., 2017). Agonists of the PPAR family were developed to treat metabolic syndrome. However, for the skeletal system, PPAR α and PPAR γ agonists had been shown to exert a negative impact on osteoblast differentiation and promote adipogenesis (Hauner, 2002; Patel et al., 2014). Different from the other two members, PPARβ/δ agonist was believed to be beneficial to the skeletal system and could promote osteogenic differentiation (Scholtysek et al., 2013). Therefore, PPARβ/δ agonist seemed to be a promising target for protecting skeletal health.

Abnormal activation of the immune system is one of the main manifestations of diabetes mellitus, leading to the inflammatory damage. Increased polarization of M1 macrophages under diabetic status enhanced the secretion of inflammatory factors such as TNF-α, which further promoted the differentiation of osteoclasts (Jiao et al., 2015). Treatment with LPS-induced M1 macrophage culture supernatant stimulated the osteoclastogenesis (Zhang et al., 2021). PPARβ/δ agonist has been found to reduce the expression of inflammatory factors such as IL-1β and IL-6 by inhibiting NF-κB signaling (Rival et al., 2002; Bishop-Bailey and Bystrom, 2009; Coll et al., 2010), and promote the recruitment of M2 macrophages to accelerate the injury repair process (Tobita et al., 2020). However, its role in diabetic osteoporosis has not been reported yet. In the current study, we proved that PPARβ/δ agonist could alleviate the oxidative stress response and inflammatory products of macrophages induced by high glucose *in vitro*. Moreover, PPARβ/δ agonist could also reduce the stimulating effect of high glucose-induced macrophage culture supernatant on osteoclast differentiation. Through immunofluorescence staining and flow cytometry, we confirmed that PPARβ/δ agonist could improve the diabetes-mediated imbalance of macrophage polarization *in vivo*. Based on the above evidence, we believe that PPARβ/δ agonist can alleviate osteoclast differentiation and bone loss by reducing the M1 macrophage polarization under diabetic condition. In addition to inhibiting osteoclast differentiation, PPARβ/δ agonists could also promote bone formation (Scholtysek et al., 2013), but the bone resorption markers decreased more obviously after PPARβ/δ agonist treatment. Therefore, the inhibition of bone resorption and osteoclast differentiation might play a major role in PPARβ/δ agonist-mediated bone loss protection.

PPARβ/δ, a transcription factor, could regulate the transcription of downstream genes *via* a ligand-activated manner (Liu et al., 2018). Among them, *Angptl4* was considered to be an important downstream target of PPARβ/δ transcriptional regulation (Legrand et al., 2019). *Angptl4* had been reported to affect immune response and macrophage polarization (Cho et al., 2019). *Angptl4* knockout mice showed a large number of macrophage infiltration and high expression of TNF-α, IL-1β and other inflammatory factors (Oteng et al., 2019). During *in vitro* culture, the level of TNF-α in the supernatant of *Angptl4* −/− macrophages was higher than that of wild-type macrophages (Ding et al., 2020). By administering recombinant human ANGPTL4 protein *in vitro*, Zhou et al. proved that ANGPTL4 could promote the M2 macrophage polarization and facilitate cardiac repair (Zhou et al., 2020). Hence, we supposed that *Angptl4* could act as a downstream gene of PPARβ/δ in macrophages to exert an anti-inflammatory effect. PPARβ/δ agonist increased the expression of *Angptl4* and ChIP assay proved that PPARβ/δ could bind to the *Angptl4* gene segment. Knockdown of *Angptl4* could eliminate the improvement to abnormal polarization of macrophages by PPARβ/δ agonist. Therefore, activating the transcription of *Angptl4* might be a downstream target for PPARβ/δ agonist to regulate macrophage polarization.

In conclusion, our study proves that PPARβ/δ agonist can effectively reduce the osteoporotic phenotype of diabetic mice. PPARβ/δ agonist ameliorates macrophage polarization imbalance and osteoclast abnormal activation under diabetic condition. *Angptl4* is considered as a key downstream factor for the biological effects of PPARβ/δ to regulate macrophage polarization. However, it should be noted that GW501516 has been reported to have potential pro-oncogenic effect, which affected its clinical application (Zhou D. et al., 2019; Liu et al., 2019). We believe that PPARβ/δ agonists without pro-oncogenic effect could be developed, and PPAR agonist treatment may serve as a promising therapeutic target for diabetic osteoporosis.

DATA AVAILABILITY STATEMENT

The original contributions presented in the study are included in the article/**Supplementary Material**, further inquiries can be directed to the corresponding authors.

ETHICS STATEMENT

The animal study was reviewed and approved by the Animal Care and Ethics Committee of West China Hospital of Stomatology, Sichuan University.

AUTHOR CONTRIBUTIONS

JY and ZZ designed the study. MC, WL, and RY performed the experiments and were involved in data analyses and interpretation. MC, JY, and ZZ wrote and revised the manuscript. All authors read and approved the final manuscript.

FUNDING

This work was supported by the grants from National Natural Science Foundation of China (Grant no. 81801018, 81771048 and 81400522), Research and Development Program, West China Hospital of Stomatology Sichuan University (RD-03-202012), and Sichuan Science and Technology Program (Grant no. 2020YFS0170).

SUPPLEMENTARY MATERIAL

The Supplementary Material for this article can be found online at: https://www.frontiersin.org/articles/10.3389/fcell.2021.753194/full#supplementary-material

REFERENCES

Barlaka, E., Görbe, A., Gáspár, R., Pálóczi, J., Ferdinandy, P., and Lazou, A. (2015). Activation of PPARβ/δ Protects Cardiac Myocytes from Oxidative Stress-Induced Apoptosis by Suppressing Generation of Reactive Oxygen/nitrogen Species and Expression of Matrix Metalloproteinases. *Pharmacol. Res.* 95-96, 102–110. doi:10.1016/j.phrs.2015.03.008

Bishop-Bailey, D., and Bystrom, J. (2009). Emerging Roles of Peroxisome Proliferator-Activated Receptor-β/δ in Inflammation. *Pharmacol. Ther.* 124, 141–150. doi:10.1016/j.pharmthera.2009.06.011

Bouxsein, M. L., Boyd, S. K., Christiansen, B. A., Guldberg, R. E., Jepsen, K. J., and Müller, R. (2010). Guidelines for Assessment of Bone Microstructure in Rodents Using Micro-Computed Tomography. *J. Bone Miner Res.* 25, 1468–1486. doi:10.1002/jbmr.141

Cho, D. I., Kang, H. J., Jeon, J. H., Eom, G. H., Cho, H. H., Kim, M. R., et al. (2019). Antiinflammatory Activity of ANGPTL4 Facilitates Macrophage Polarization to Induce Cardiac Repair. *JCI Insight* 4, e125437. doi:10.1172/jci.insight.125437

Coll, T., Barroso, E., Alvarez-Guardia, D., Serrano, L., Salvadó, L., Merlos, M., et al. (2010). The Role of Peroxisome Proliferator-Activated Receptor Beta/delta on the Inflammatory Basis of Metabolic Disease. *PPAR Res.* 2010, 368467. doi:10.1155/2010/368467

Ding, S., Wu, D., Lu, Q., Qian, L., Ding, Y., Liu, G., et al. (2020). Angiopoietin-Like 4 Deficiency Upregulates Macrophage Function Through the Dysregulation of Cell-Intrinsic Fatty Acid Metabolism. *Am. J. Cancer Res.* 10, 595–609.

Eller-Vainicher, C., Cairoli, E., Grassi, G., Grassi, F., Catalano, A., Merlotti, D., et al. (2020). Pathophysiology and Management of Type 2 Diabetes Mellitus Bone Fragility. *J. Diabetes Res.* 2020, 7608964. doi:10.1155/2020/7608964

Fu, H., Desvergne, B., Ferrari, S., and Bonnet, N. (2014). Impaired Musculoskeletal Response to Age and Exercise in PPARβ−/− Diabetic Mice. *Endocrinology* 155, 4686–4696. doi:10.1210/en.2014-1585

Graves, D. T., and Kayal, R. A. (2008). Diabetic Complications and Dysregulated Innate Immunity. *Front. Biosci.* 13, 1227–1239. doi:10.2741/2757

Hauner, H. (2002). The Mode of Action of Thiazolidinediones. *Diabetes Metab. Res. Rev.* 18 Suppl 2, S10–S15. doi:10.1002/dmrr.249

Inoue, T., Kohro, T., Tanaka, T., Kanki, Y., Li, G., Poh, H.-M., et al. (2014). Cross-enhancement of ANGPTL4 Transcription by HIF1 Alpha and PPAR Beta/delta Is the Result of the Conformational Proximity of Two Response Elements. *Genome Biol.* 15, R63. doi:10.1186/gb-2014-15-4-r63

Jiang, Y., Xie, F., Lv, X., Wang, S., Liao, X., Yu, Y., et al. (2021). Mefunidone Ameliorates Diabetic Kidney Disease in STZ and Db/db Mice. *Faseb j* 35, e21198. doi:10.1096/fj.202001138rr

Jiao, H., Xiao, E., and Graves, D. T. (2015). Diabetes and its Effect on Bone and Fracture Healing. *Curr. Osteoporos. Rep.* 13, 327–335. doi:10.1007/s11914-015-0286-8

Jimenez, R., Toral, M., Gómez-Guzmán, M., Romero, M., Sanchez, M., Mahmoud, A. M., et al. (2018). The Role of Nrf2 Signaling in PPARβ/δ-Mediated Vascular Protection against Hyperglycemia-Induced Oxidative Stress. *Oxid. Med. Cel. Longev.* 2018, 5852706. doi:10.1155/2018/5852706

Kayal, R. A., Tsatsas, D., Bauer, M. A., Allen, B., Al-Sebaei, M. O., Kakar, S., et al. (2007). Diminished Bone Formation during Diabetic Fracture Healing Is Related to the Premature Resorption of Cartilage Associated with Increased Osteoclast Activity. *J. Bone Miner Res.* 22, 560–568. doi:10.1359/jbmr.070115

Khoo, N. K. H., Hebbar, S., Zhao, W., Moore, S. A., Domann, F. E., and Robbins, M. E. (2013). Differential Activation of Catalase Expression and Activity by PPAR Agonists: Implications for Astrocyte protection in Anti-glioma Therapy. *Redox Biol.* 1, 70–79. doi:10.1016/j.redox.2012.12.006

Legrand, N., Bretscher, C. L., Zielke, S., Wilke, B., Daude, M., Fritz, B., et al. (2019). PPARβ/δ Recruits NCOR and Regulates Transcription Reinitiation of ANGPTL4. *Nucleic Acids Res.* 47, 9573–9591. doi:10.1093/nar/gkz685

Liu, W., Zhou, L., Zhou, C., Zhang, S., Jing, J., Xie, L., et al. (2016). GDF11 Decreases Bone Mass by Stimulating Osteoclastogenesis and Inhibiting Osteoblast Differentiation. *Nat. Commun.* 7, 12794. doi:10.1038/ncomms12794

Liu, Y., Colby, J. K., Zuo, X., Jaoude, J., Wei, D., and Shureiqi, I. (2018). The Role of PPAR-δ in Metabolism, Inflammation, and Cancer: Many Characters of a Critical Transcription Factor. *Int. J. Mol. Sci.* 19, 3339. doi:10.3390/ijms19113339

Liu, Y., Deguchi, Y., Tian, R., Wei, D., Wu, L., Chen, W., et al. (2019). Pleiotropic Effects of PPARD Accelerate Colorectal Tumorigenesis, Progression, and Invasion. *Cancer Res.* 79, 954–969. doi:10.1158/0008-5472.can-18-1790

Mosti, M. P., Stunes, A. K., Ericsson, M., Pullisaar, H., Reseland, J. E., Shabestari, M., et al. (2014). Effects of the Peroxisome Proliferator-Activated Receptor (PPAR)-δ Agonist GW501516 on Bone and Muscle in Ovariectomized Rats. *Endocrinology* 155, 2178–2189. doi:10.1210/en.2013-1166

Odegaard, J. I., Ricardo-Gonzalez, R. R., Red Eagle, A., Vats, D., Morel, C. R., Goforth, M. H., et al. (2008). Alternative M2 Activation of Kupffer Cells by PPARδ Ameliorates Obesity-Induced Insulin Resistance. *Cel Metab.* 7, 496–507. doi:10.1016/j.cmet.2008.04.003

Oteng, A.-B., Ruppert, P. M., Boutens, L., Dijk, W., Van Dierendonck, X. M. H., Olivecrona, G., et al. (2019). Characterization of ANGPTL4 Function in Macrophages and Adipocytes Using Angptl4-Knockout and Angptl4-Hypomorphic Mice. *J. Lipid Res.* 60, 1741–1754. doi:10.1194/jlr.m094128

Pang, D., Li, C., Yang, C., Zou, Y., Feng, B., Li, L., et al. (2019). Polyphyllin VII Promotes Apoptosis and Autophagic Cell Death via ROS-Inhibited AKT Activity, and Sensitizes Glioma Cells to Temozolomide. *Oxid. Med. Cel. Longev.* 2019, 1805635. doi:10.1155/2019/1805635

Paschou, S. A., Dede, A. D., Anagnostis, P. G., Vryonidou, A., Morganstein, D., and Goulis, D. G. (2017). Type 2 Diabetes and Osteoporosis: A Guide to Optimal Management. *J. Clin. Endocrinol. Metab.* 102, 3621–3634. doi:10.1210/jc.2017-00042

Patel, J. J., Butters, O. R., and Arnett, T. R. (2014). PPAR Agonists Stimulate Adipogenesis at the Expense of Osteoblast Differentiation while Inhibiting Osteoclast Formation and Activity. *Cell Biochem Funct* 32, 368–377. doi:10.1002/cbf.3025

Qian, G., Fan, W., Ahlemeyer, B., Karnati, S., and Baumgart-Vogt, E. (2015). Peroxisomes in Different Skeletal Cell Types during Intramembranous and Endochondral Ossification and Their Regulation during Osteoblast Differentiation by Distinct Peroxisome Proliferator-Activated Receptors. *PLoS One* 10, e0143439. doi:10.1371/journal.pone.0143439

Rendra, E., Riabov, V., Mossel, D. M., Sevastyanova, T., Harmsen, M. C., and Kzhyshkowska, J. (2019). Reactive Oxygen Species (ROS) in Macrophage Activation and Function in Diabetes. *Immunobiology* 224, 242–253. doi:10.1016/j.imbio.2018.11.010

Rival, Y., Benéteau, N., Taillandier, T., Pezet, M., Dupont-Passelaigue, E., Patoiseau, J.-F., et al. (2002). PPARα and PPARδ Activators Inhibit Cytokine-Induced Nuclear Translocation of NF-κB and Expression of VCAM-1 in EAhy926 Endothelial Cells. *Eur. J. Pharmacol.* 435, 143–151. doi:10.1016/s0014-2999(01)01589-8

Sakai, S., Yamamoto, T., Takabatake, Y., Takahashi, A., Namba-Hamano, T., Minami, S., et al. (2019). Proximal Tubule Autophagy Differs in Type 1 and 2 Diabetes. *J. Am. Soc. Nephrol.* 30, 929–945. doi:10.1681/asn.2018100983

Scholtysek, C., Katzenbeisser, J., Fu, H., Uderhardt, S., Ipseiz, N., Stoll, C., et al. (2013). PPARβ/δ Governs Wnt Signaling and Bone Turnover. *Nat. Med.* 19, 608–613. doi:10.1038/nm.3146

Schwartz, A. V. (2017). Efficacy of Osteoporosis Therapies in Diabetic Patients. *Calcif Tissue Int.* 100, 165–173. doi:10.1007/s00223-016-0177-8

Suzuki, K., Kurose, T., Takizawa, M., Maruyama, M., Ushikawa, K., Kikuyama, M., et al. (2005). Osteoclastic Function Is Accelerated in Male Patients with Type 2 Diabetes Mellitus: the Preventive Role of Osteoclastogenesis Inhibitory Factor/osteoprotegerin (OCIF/OPG) on the Decrease of Bone mineral Density. *Diabetes Res. Clin. Pract.* 68, 117–125. doi:10.1016/j.diabres.2004.08.006

Tobita, Y., Arima, T., Nakano, Y., Uchiyama, M., Shimizu, A., and Takahashi, H. (2020). Peroxisome Proliferator-Activated Receptor Beta/Delta Agonist Suppresses Inflammation and Promotes Neovascularization. *Int. J. Mol. Sci.* 21, 5296. doi:10.3390/ijms21155296

Unnikrishnan, R., Anjana, R. M., and Mohan, V. (2016). Diabetes Mellitus and its Complications in India. *Nat. Rev. Endocrinol.* 12, 357–370. doi:10.1038/nrendo.2016.53

Wang, Y., Deng, P., Liu, Y., Wu, Y., Chen, Y., Guo, Y., et al. (2020). Alpha-ketoglutarate Ameliorates Age-Related Osteoporosis via Regulating Histone Methylations. *Nat. Commun.* 11, 5596. doi:10.1038/s41467-020-19360-1

Wittrant, Y., Gorin, Y., Woodruff, K., Horn, D., Abboud, H. E., Mohan, S., et al. (2008). High D(+)glucose Concentration Inhibits RANKL-Induced Osteoclastogenesis. *Bone* 42, 1122–1130. doi:10.1016/j.bone.2008.02.006

Zhang, B., Yang, Y., Yi, J., Zhao, Z., and Ye, R. (2021). Hyperglycemia Modulates M1/M2 Macrophage Polarization via Reactive Oxygen Species Overproduction in Ligature-Induced Periodontitis. *J. Periodontal Res.* 56, 991–1005. doi:10.1016/j.bone.2008.02.006

Zhou, D., Jin, J., Liu, Q., Shi, J., and Hou, Y. (2019a). PPARδ Agonist Enhances Colitis-Associated Colorectal Cancer. *Eur. J. Pharmacol.* 842, 248–254. doi:10.1016/j.ejphar.2018.10.050

Zhou, X., Zhang, P., Wang, Q., Ji, N., Xia, S., Ding, Y., et al. (2019b). Metformin Ameliorates Experimental Diabetic Periodontitis Independently of Mammalian Target of Rapamycin (mTOR) Inhibition by Reducing NIMA-Related Kinase 7(Nek7) Expression. *J. Periodontol.* 90 (9), 1032–1042. doi:10.1002/JPER.18-0528

Zhou, S., Tu, J., Ding, S., Lu, G., Lin, Z., Ding, Y., et al. (2020). High Expression of Angiopoietin-like Protein 4 in Advanced Colorectal Cancer and its Association with Regulatory T Cells and M2 Macrophages. *Pathol. Oncol. Res.* 26, 1269–1278. doi:10.1007/s12253-019-00695-0

Conflict of Interest: The authors declare that the research was conducted in the absence of any commercial or financial relationships that could be construed as a potential conflict of interest.

Publisher's Note: All claims expressed in this article are solely those of the authors and do not necessarily represent those of their affiliated organizations, or those of the publisher, the editors and the reviewers. Any product that may be evaluated in this article, or claim that may be made by its manufacturer, is not guaranteed or endorsed by the publisher.

frontiers in Cell and Developmental Biology

REVIEW
published: 04 January 2022
doi: 10.3389/fcell.2021.788773

YAP/TAZ in Bone and Cartilage Biology

Mylène Zarka[1,2], *Eric Haÿ*[1,2] *and Martine Cohen-Solal*[1,2]*

[1]INSERM UMR 1132 BIOSCAR, Hôpital Lariboisière, Paris, France, [2]Faculté de Santé, Université de Paris, Paris, France

YAP and TAZ were initially described as the main regulators of organ growth during development and more recently implicated in bone biology. YAP and TAZ are regulated by mechanical and cytoskeletal cues that lead to the control of cell fate in response to the cellular microenvironment. The mechanical component represents a major signal for bone tissue adaptation and remodelling, so YAP/TAZ contributes significantly in bone and cartilage homeostasis. Recently, mice and cellular models have been developed to investigate the precise roles of YAP/TAZ in bone and cartilage cells, and which appear to be crucial. This review provides an overview of YAP/TAZ regulation and function, notably providing new insights into the role of YAP/TAZ in bone biology.

Keywords: osteocyte, bone, cartilage, YAP, TAZ, hippo signaling, biomechanic, mechanotransduction

OPEN ACCESS

Edited by:
Andrea Del Fattore, Bambino Gesù Children Hospital (IRCCS), Italy

Reviewed by:
Jormay Lim, National Taiwan University, Taiwan
Hiroshi Nishina, Tokyo Medical and Dental University, Japan

***Correspondence:**
Martine Cohen-Solal
martine.cohen-solal@inserm.fr

Specialty section:
This article was submitted to Molecular and Cellular Pathology, a section of the journal Frontiers in Cell and Developmental Biology

Received: *03 October 2021*
Accepted: *23 November 2021*
Published: *04 January 2022*

Citation:
Zarka M, Haÿ E and Cohen-Solal M (2022) YAP/TAZ in Bone and Cartilage Biology. Front. Cell Dev. Biol. 9:788773. doi: 10.3389/fcell.2021.788773

1 INTRODUCTION

YAP (*yes associated protein*) and TAZ (*transcriptional coactivator with PDZ-binding motif*) were identified in mammals in 1995, and 2000, respectively (Sudol et al., 1995; Kanai et al., 2000). YAP/TAZ are transcriptional cofactors considered important cellular mediators that define the cell fate, such as differentiation, proliferation or apoptosis. Because of this central role, YAP/TAZ regulate numerous physiological cellular processes and thereby act as major protagonists in the maintenance of tissue homeostasis but also represent a target in different pathological contexts.

Bone and cartilage are two tissues particularly regulated by mechanical cues because tissue adaptation and remodelling in response to loading are essential to maintain their integrity. Dysregulation of this mechanoadaptive mechanism leads to osteoarticular pathogenesis such as osteoporosis or osteoarthritis. Hence, YAP/TAZ signaling may represent a central mediator that maintains constant adaptation of bone and cartilage tissues in response to modification of the mechanical environment. For this reason, numerous recent studies have aimed to improve our knowledge of YAP/TAZ regulation in bone and cartilage.

2 BONE AND CARTILAGE

2.1 Bone Biology

Bone is a dynamic tissue characterized by a permanent remodeling allowing adaptation to mechanical environment. Bone integrity is maintained by its composition, its quality and its quantity. These characteristics are tightly regulated by different soluble factors whose actions is finely coordinated spatially and temporally by bone cells (osteoblasts, osteoclasts, and osteocytes). The major component of bone is the extracellular matrix that is composed principally by the collagen type I. This matrix was synthetised by osteoblasts that come from the differentiation of mesenchymal stem cells that expressed Prx1 (**Figure 1A**). Young osteoblasts are characterised by the expression of early markers such as the transcription factors Osterix (Osx), while more matures osteoblasts

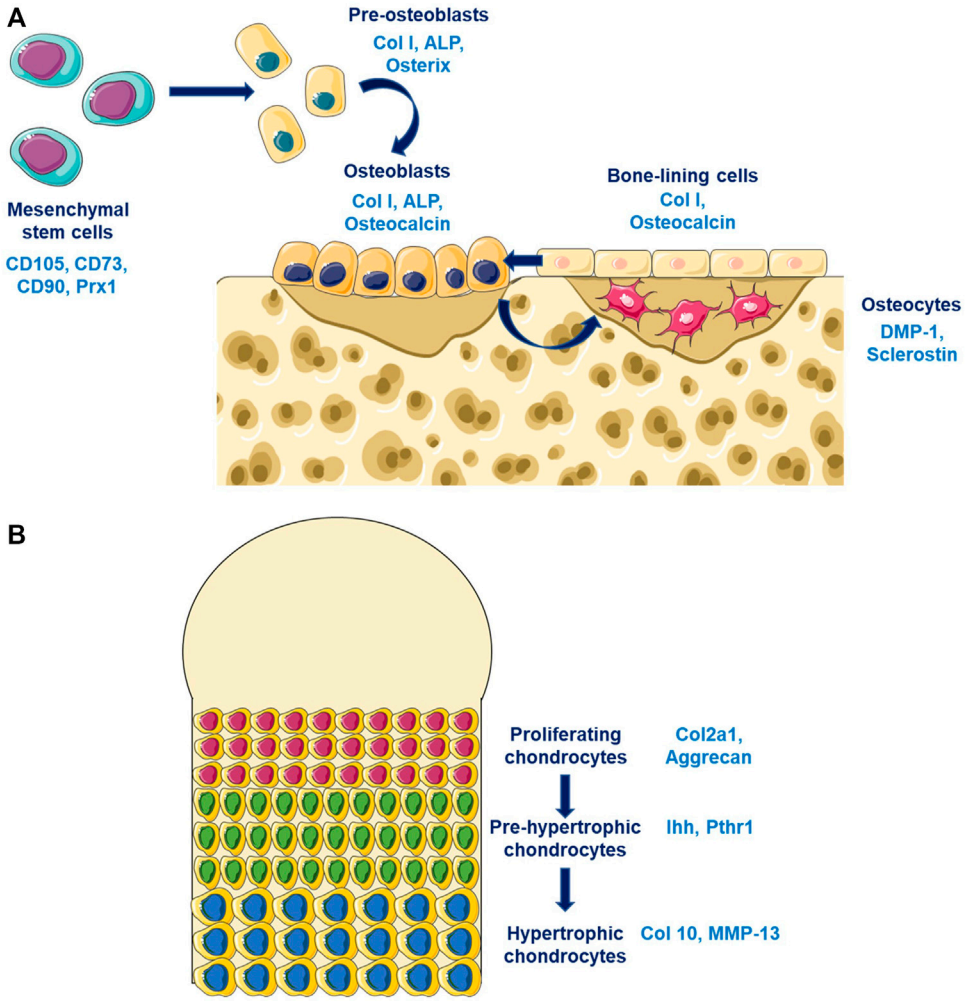

FIGURE 1 | Bone and cartilage cells differentiation **(A)** Osteoblasts differentiation are characterized by the expression of different markers according to the stage of differentiation. Pre-osteoblasts expressed early osteoblastic genes such as Osterix while old osteoblasts/osteocytes expressed late osteoblastic genes such as DMP-1. **(B)** Chondrocytes differentiates from proliferating chondrocytes expressing Col2a1 in the surface layer through an hypertrophic phenotype characterized by the expression of late markers such as Col10.

expressed the Osteocalcin (Ocn). The osteoblasts differentiation is regulated by different factors notably Runx2 and principally by the Wnt/β-catenin pathway. Osteocytes represents the ultimate stage of differentiation for osteoblasts that have been included in the bone matrix during the process of bone mineralization. Late osteoblasts/osteocytes expressed late markers such as the Dentin Matrix Protein 1 (DMP1). The third bone cell types are the osteoclasts that was originated from the hematopoietic stem cells lineage and that is responsible for bone degradation. Three mains soluble factors are essential for osteoclastogenesis, the RANK-L, the M-CSF, and Osteoprotegerin (OPG). These factors are particularly important for the coupling of osteoblasts and osteoclasts during the bone remodeling process. The renewal of bone matrix is allowed by bone remodeling which is divided in different phases: 1) the initiation of bone remodeling; 2) the bone resorption; 3) the bone formation; and 4) the matrix mineralisation. The coordinated action of osteoblasts and osteoclasts in time and space are partly regulated by the RANK-L/OPG. RANK-L, and its antagonists OPG, are two ligands synthetised by osteoblasts, and whose expression is modulated by the Wnt/β-catenin pathway in order to maintain a balanced between formation and resorption.

The bone remodeling is regulated by systemic factors principally hormones such as oestrogen and parathormone, but also by growth factors that are included in the bone matrix or by cytokines synthetized locally. TGF-β and BMPs are released by bone matrix during resorption and allow the regulation of osteoblastogenesis and osteoclastogenesis. TGF-β are able to induced the recruitment and the proliferation of osteoclasts and osteoblasts precursors. It also regulates the expression of RANK-L/OPG by osteoblasts and inhibits terminal differentiation of osteoblasts. BMPs could also regulates osteoblastogenesis by inducing the expression of Osx and Runx2, or two

antagonists of the Wnt/β-catenin pathway, Dkk1, and sclerostin.

2.2 Cartilage Homeostasis

Cartilage is an avascular tissue composed by chondrocytes and extracellular matrix. Cartilage matrix is composed mostly by the collagen type II and by proteoglycans which allow their mechanical properties. The extracellular matrix protects chondrocytes from mechanical loading, represents a storage area for cytokines and growth factors, and controls nutriments diffusion and contribute to the transmission of extracellular signals to chondrocytes. Chondrocytes at the cartilage surfaces are characterized by a strong expression of the collagene type II, while hypertrophic chondrocytes in the mineralized compartment are expressing the collagen type X (**Figure 1B**). The early stage of chondrocytes differentiation is mainly modulated by the Sox9 transcription factors that regulates the collagen type II expression, while the late stage of hypertrophic chondrocytes is mostly controls by Runx2. Different signaling pathway are essential for chondrogenesis such as the Wnt/β-catenin pathway, the TGF-β/BMPs pathway, and the sonic hedgehog pathway (Shh). TGF-β stimulates the chondrocytes at early stage of differentiation while it inhibits terminal differentiation. The role of the canonical Wnt/β-catenin pathway in chondrocytes is complex since it could inhibit chondrogenesis and stimulates chondrocytes hypertrophy.

3 YAP AND TAZ BIOLOGY

The YAP/TAZ complex is a downstream effector of the Hippo signaling pathway, discovered in *Drosophila* and described as a main regulator of organ growth during development (Dong et al., 2007; Pan, 2007). Several studies identified the main actors of Hippo signaling in *Drosophila*: Warts (Justice et al., 1995; Xu et al., 1995), Salvador (Kango-Singh et al., 2002; Tapon et al., 2002), Hippo (Harvey et al., 2003; Jia et al., 2003; Pantalacci et al., 2003; Udan et al., 2003; Wu et al., 2003), and Mats (Lai et al., 2005). The mutation of each of these proteins leads to a hyper-proliferative phenotype that allowed for identifying Hippo signaling as a regulator of tissue homeostasis. Yorki, the YAP/TAZ ortholog, identified in 2005 as a downstream effector of this pathway and can negatively regulate apoptosis, and induce cellular proliferation (Huang et al., 2005). The discovery and functional description of Hippo signaling in *Drosophila* allowed for considerable progress in understanding the mechanisms in mammals.

3.1 YAP/TAZ Functions

YAP/TAZ functions are numerous and are coordinately fine-tuned at the cellular and nuclear level. Mostly, YAP/TAZ are transcriptional co-factors acting directly on their target genes via their co-factors, and notably TEAD family members. YAP/TAZ are also signaling molecules implicated in the communication between Hippo signaling and other signaling pathways.

3.1.1 Transcriptional Co-activation

YAP/TAZ are transcriptional co-activators without a DNA binding domain and therefore require interaction with molecular partners. This interaction allows for the expression of target genes that control proliferation, growth, and cell survival. Among those genes, the most described are CYR61, CTGF, ANKRD1, REG, AXL, and MYC. Several transcription factors have been described to interact with YAP/TAZ, mostly members of the TEAD family. This family consists of four homologous transcription factors, TEAD1-4, and which share the same structural domain (Kaneko and DePamphilis, 1998). The TEAD family facilitates the tumorigenic effect induced by YAP *in vivo* and induces gene expression required for proliferation and cellular growth (Zhao et al., 2008; Zhao et al., 2009; Liu-chittenden et al., 2012). The expression of some TEAD family members is strongly increased in a large number of cancer types and so could be used as prognosis markers of disease progression (Zhou et al., 2016). Finally, YAP/TAZ can interact with other transcriptional cofactors such as p73, the RUNX family and SMAD to induce apoptosis, and differentiation or proliferation (Kim et al., 2018).

3.1.2 Interaction of YAP/TAZ With Others Signaling Pathways

YAP/TAZ interacts with different signaling pathways such as the Notch, Wnt/β-catenin, TGF-β, and BMP pathways. The Wnt/β-catenin pathway, which is crucial for osteoblastogenesis, is closely related to YAP/TAZ, and Hippo signaling (**Figure 2**). Therefore, inhibiting YAP/TAZ via Hippo signaling could represent a negative regulation of the Wnt canonical pathway. Indeed, the phosphorylation of YAP/TAZ inhibits the phosphorylation of Dvl by CK1δ/ε and subsequently the binding between Dvl, and LRP5/6-Frizzled induced by Wnt (Varelas et al., 2010a). Also, the Wnt ligand could activate YAP/TAZ via the non-canonical Wnt pathway by the FZD/$G_{\alpha 12/13}$/Rho axis to induce target genes such as DKK1, BMP4, and IGFBP4 (Park et al., 2015). Different studies demonstrated a direct interaction between β-catenin and YAP in the transcriptional complex β-catenin/TCF4/YAP (Heallen et al., 2011; Konsavage et al., 2012; Deng F. et al., 2018). Finally, YAP/TAZ could be degraded into the cytoplasm by the proteasome whereby YAP/TAZ interacts with β-catenin to allow for binding to the ubiquitin ligase β-TrCP (Imajo et al., 2012; Azzolin et al., 2014).

Many studies also demonstrated that YAP/TAZ could interact with Smads signaling, mainly TGF-β and BMP signaling, and implicated in osteoblastogenesis (Chen et al., 2012; Moon et al., 2016). Indeed, YAP/TAZ are required for the TGF-β response by interacting with phospho-Smad2/3 to translocate into the nucleus (Hiemer et al., 2014; Mahoney et al., 2014). In response to high cellular density, phosphorylated YAP/TAZ could be retained in cytoplasm with Smad 2/3, and which inhibits the TGF-β response (Varelas et al., 2010b). Finally, YAP and TAZ act in synergy after BMP stimulation because YAP interacts with Smad1/5 to induce target genes, and whereas TAZ induces BMP4 expression (Alarcón et al., 2009; Lai and Yang, 2013).

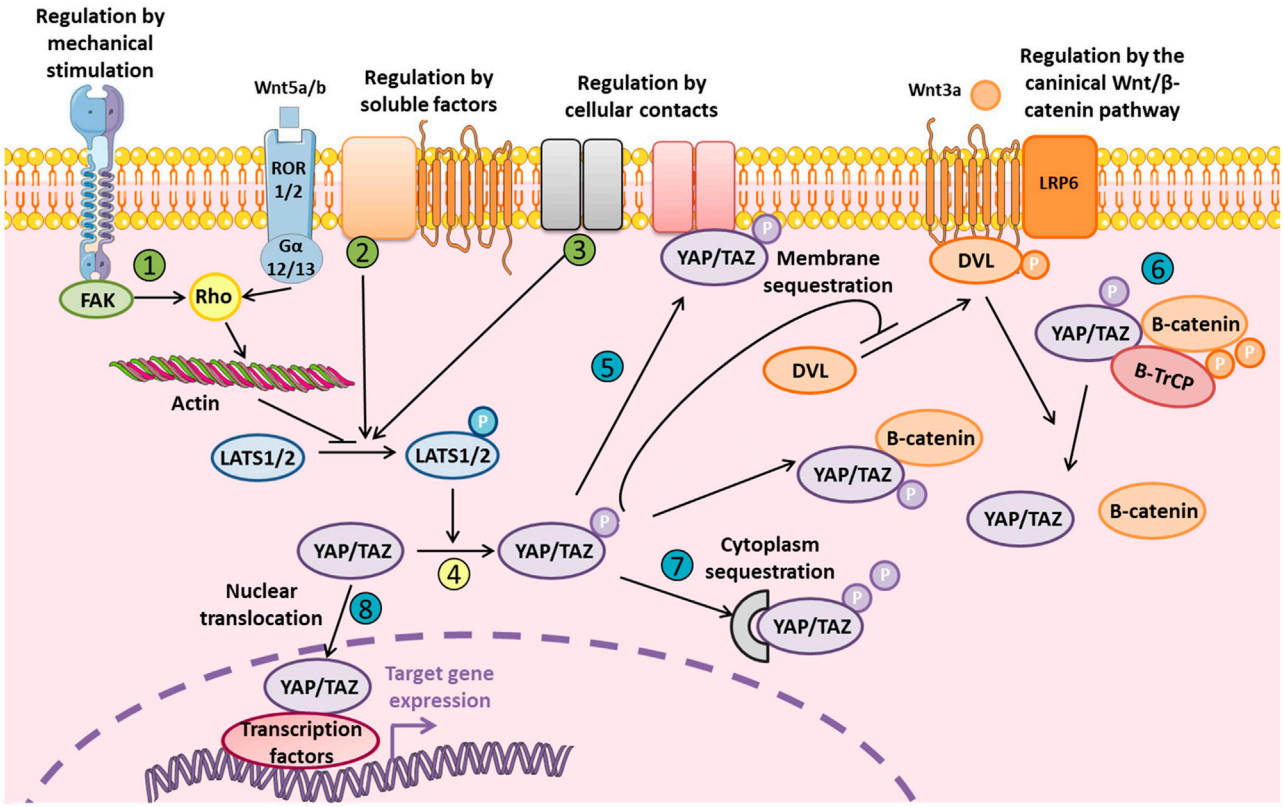

FIGURE 2 | Levels of regulation of YAP and TAZ YAP/TAZ regulation is fine-tuned and mediated by external stimuli or soluble factors via LATS1/2 (in green: 1, 2, and 3) that phosphorylates YAP/TAZ (in yellow: 4). YAP/TAZ localization and degradation could be also modulated at different levels (in blue: 5, 6, 7, and 8). Phosphorylated inactive YAP/TAZ can induce cytoplasmic sequestration of β-catenin and inhibit Wnt/β-catenin signaling by inhibiting Dvl translocation to LRP5/6-Frizzled complex. Phosphorylated YAP/TAZ are also present in the β-catenin proteosomal degradation complex. YAP/TAZ could also be a transcriptional co-factor for β-catenin and its interaction with TCF/LEF. Finally, non-canonical Wnt/β-catenin signaling inhibits YAP/TAZ phosphorylation via LATS1/2.

3.2 YAP/TAZ Regulation

YAP/TAZ regulation is tightly modulated and occurs at multiple levels, notably by YAP/TAZ inactivation via phosphorylation leading to their degradation and/or cytoplasmic sequestration to avoid YAP/TAZ nuclear translocation (**Figure 2**). YAP/TAZ regulation could depend on Hippo signaling or be independent, via direct modulation of YAP/TAZ cellular localization. The cellular microenvironment is really important to take in consideration since it could restrain YAP/TAZ to nucleus or the cytoplasm, which can totally modify the modality of YAP/TAZ molecular regulation. In fact, for example, large surface area, and stiff matrix or the presence of mechanical forces lead to the nuclear translocation of YAP/TAZ. *In vitro* study which are performed on stiff plastic support, is associated with a basal activation state of YAP/TAZ due to the stiff properties of the matrix.

3.2.1 YAP/TAZ Regulation via Hippo signaling

Hippo signaling pathway regulates a number of biological processes such as cellular proliferation, cell fate, cellular differentiation, organ size, and tissue homeostasis. The pathway is composed of a complex cascade of serine/threonine-protein kinase including the Hippo kinase core that consists of two enzymatic complexes, LATS1/2-MOB1A/B and MST1/2-SAV1. The kinase MST1/2, associated with its regulatory protein SAV, activates LATS1/2-MOB1A/B via phosphorylation (Chan et al., 2005; Praskova et al., 2008). This active complex can phosphorylate YAP/TAZ, with effects depending on the targeted serine (Zhao et al., 2010). YAP/TAZ phosphorylation induces the cytoplasmic sequestration, nuclear exclusion, and/or proteasomal degradation (Zhao et al., 2007, 2010; Lei et al., 2008; Liu et al., 2010). Among the different sites of phosphorylation, Ser127 (Ser89 for TAZ), and Ser381 (Ser311 for TAZ) are the most decisive for protein inactivation. In fact, the phosphorylation of Ser381 by LATS1/2 allowed for recruitment of the ubiquitin complex $SCF^{\beta-TRCP}$E3 leading to YAP/TAZ degradation by the proteasome (Liu et al., 2010; Zhao et al., 2010). Moreover, Ser127 phosphorylation induced YAP/TAZ recognition by 14-3-3 protein and their cytoplasmic sequestration (Lei et al., 2008).

Regulation of LATS1/2 phosphorylation is an indirect regulation of YAP/TAZ activity and could be modulated by both soluble factors and/or cellular contact. Many soluble extracellular factors can regulate YAP/TAZ via Hippo signaling to promote cellular migration and proliferation. Members of the epidermal growth factor family,

lysophosphatidic acid or sphingosine-1-phosphate, can inhibit LATS1/2, and subsequent YAP/TAZ nuclear translocation (Komuro et al., 2003; Omerovic et al., 2004; Fan et al., 2013; Reddy and Irvine, 2013; Haskins et al., 2014). G protein-coupled receptors can also modulate YAP/TAZ differentially depending on the subunit and ligand. Indeed, RCPGα12/13 are mostly activated by ligands such as LPA, and S1P or thrombin to activate YAP/TAZ dependent on Rho GTPase (Miller et al., 2012; Mo et al., 2012; Yu et al., 2012). However, G protein-coupled receptors associated with the Gα/s subunit can activate Hippo signaling via cAMP/protein kinase A signaling (Kim et al., 2013; Yu et al., 2013).

Cellular contacts can also facilitate the YAP/TAZ axis activation indirectly by modulating LATS1/2 activation. This activation involves three major complexes associated with the cellular membrane: NF2/KIBRA, SCRIB, and α-catenin/AMOT/AJUBA/NF2 (see **Figure 2** from Totaro et al., 2018 and Meng et al., 2016 for review). KIBRA protein was identified upstream of Hippo signaling and can activate LATS1/2 (Baumgartner et al., 2010; Genevet et al., 2010; Yu et al., 2010). KIBRA can restrain proliferation notably on polarized cells because it negatively regulates YAP/TAZ via LATS1/2 phosphorylation (Xiao et al., 2011). Also in response to cellular polarity, SCRIB protein, described as a scaffold protein involved in this process, regulates Hippo signaling (Doggett et al., 2011; Verghese et al., 2012). For example, the SCRIB membrane delocalization observed during the epithelial–mesenchymal transition of cancer stem cells leads to YAP/TAZ activation by inhibiting Hippo signaling (Cordenonsi et al., 2011). The third major complex, α-catenin/AJUBA/NF2/AMOT, regulates cellular proliferation following adhesion, and cellular contacts. This situation may restrain YAP/TAZ activation via LATS1/2 phosphorylation in response to adherents junctions and cytoskeletal tension (Das Thakur et al., 2010; Kim et al., 2011; Rauskolb et al., 2014).

3.2.2 Direct Regulation of YAP/TAZ Cellular Localization

YAP/TAZ regulation via membrane or cytoplasmic sequestration may occur by a distinct mechanism. YAP/TAZ sequestration at the cellular membrane that abolishes any transcriptional activity could be regulated by AMOT (Wang et al., 2011; Zhao et al., 2011). AMOT can also modulate YAP nuclear localization to facilitate its interaction with the transcriptional co-factor TEAD and promote YAP-dependant proliferation (Moleirinho et al., 2017). At adherents junctions, α-catenin interacts with YAP/TAZ/14-3-3 complexes to inhibit epidermal stem cell proliferation induced by nuclear translocation of YAP (Schlegelmilch et al., 2011). The WW domain of YAP/TAZ allows for direct interaction with PTPN14, which leads to YAP/TAZ cytoplasmic sequestration, and prevents their nuclear translocation (Liu et al., 2013; Michaloglou et al., 2013).

Cytoplasmic sequestration is not the only mechanism of YAP/TAZ inhibition independent of Hippo signaling because YAP/TAZ can also be inhibited at the nuclear level. This mechanism involves direct competition between YAP/TAZ and VGGL4 protein for fixation on the transcriptional cofactor TEAD (Jiao et al., 2014; Zhang et al., 2014).

3.3 Effect of the Cellular Microenvironment on YAP/TAZ

YAP/TAZ localization and activity are also regulated by different physical constraints that occur at the cellular level. These environmental constraints depend on matrix properties, the presence of a cellular contact or tension forces such as shear stress.

3.3.1 YAP/TAZ Regulation via Cellular Junctions and Adhesion

Matrix rigidity and adhesion surfaces regulate YAP/TAZ localization and allow for modulation of cellular behaviours to adapt to the cellular microenvironment. Indeed, a stiff matrix or large adhesive area is associated with YAP/TAZ nuclear translocation (Dupont et al., 2011; Aragona et al., 2013; Totaro et al., 2017). Conversely, high cellular density inhibits YAP/TAZ translocation (Zhao et al., 2007; Wada et al., 2011; Hsiao et al., 2016). Therefore, YAP/TAZ are regulated by both the presence of a matrix contact that promotes their nuclear translocation and by the presence of a cellular contact that inhibits this process. In this context, integrin signaling is crucial for YAP/TAZ regulation by the organization of actin filaments and PI3K/PDK1 signaling, and which inhibits Hippo signaling. Indeed, the structural organization of the actin network and the formation of stress fibres are required to activate YAP/TAZ, independent of the ratio of G to F actin (Connelly et al., 2010; Dupont et al., 2011; Aragona et al., 2013). Hence, the inhibitors of actin polymerization and inhibitors of the actomyosin network reduce YAP/TAZ activity. This regulatory mechanism is independent of the Hippo pathway because LATS1/2 inhibition is not sufficient to restore YAP/TAZ activity in the presence of actin polymerization inhibitors (Dupont et al., 2011). In recent years, different studies have highlighted the integrin/FAK/CFC42/PP1A axis as a regulator of YAP/TAZ nuclear translocation (Elbediwy et al., 2016; Hu et al., 2017; Xiang et al., 2018). Notably, integrins β1 and α3 are upstream of YAP/TAZ activation in epithelial cells and transit-amplifying cells (Elbediwy et al., 2016; Hu et al., 2017). Also, integrin α5 controls osteoblast mechano-sensing and is required to induce YAP/TAZ nuclear translocation in osteoblasts under shear stress (Kaneko et al., 2014).

The activation of integrin and focal adhesion kinase by fibronectin stimulates PDK1 via PI3K to inhibit LATS1/2 and promote YAP/TAZ nuclear translocation (Kim and Gumbiner, 2015). All of these studies demonstrate that integrins are part of the cellular perception of the microenvironment and are thus capable of regulating YAP/TAZ.

3.3.2 YAP/TAZ and Mechanical Forces

The YAP/TAZ regulatory mechanisms described above allow for the modulation of cellular responses to the different forces applied from the environment, notably shear stress. For example, mechanical stress regulates cellular proliferation, and as shown in quiescent epithelial cells. In these cells, stress activates the expression of anti-apoptotic genes (Birc5, AREG) as well as proliferative genes (c-Myc, Cyclin D1) via YAP and β-catenin

nuclear translocation (Benham-pyle et al., 2015). Shear stress also regulates YAP/TAZ cellular localization, mainly described during atherosclerosis, and in which the hemodynamic environment regulates endothelial cells. Hence, the modification of shear stress induces an inflammatory response and the emergence of YAP/TAZ-dependant lesions, and homogenous shear stress inhibits this process (Wang K.-C. et al., 2016; Wang et al., 2016 L.). In zebrafish, YAP/TAZ activation resulted from actin filament reorganization in response to shear stress, and YAP/TAZ consecutive interaction with AMOT protein (Nakajima et al., 2017). Shear stress facilitates osteoblastogenesis from mesenchymal stem cells (MSCs) via RhoA activation and YAP/TAZ nuclear translocation (Kim et al., 2014).

It was also demonstrated *in vitro* that increasing the stiffness of a mineralized collagen glycosaminoglycan matrix allow osteoblastogenesis from bone marrow-derrived hMSCs through YAP/TAZ activation (Zhou et al., 2021). This result was elegantly confirmed during *in situ* bone regeneration in a bone defect model with a self-mineralizable matrix inducing osteoblastogenesis from MSC across time according to the level of mineralization (Li J. et al., 2021). It was demonstrated that stiffness could modulate YAP/TAZ through RAP2 downstream of the phospholipase Cγ1 (Meng et al., 2018). Indeed, at low stiffness, active RAP2 could act on LATS1/2 activation which lead to YAP/TAZ inhibition.

Interestingly, Major and its collaborators demonstrated that cellular volume should be more relevant than just stiffness of the matrix. Indeed, they shown opposite effect of stiffness in 2D vs 3D since 3D soft matrix favours osteoblastogenesis from adipose-derived stem cells (Major et al., 2019).

All of these results highlight the fact that all of forces emanating from the microenvironment are integrated at cellular level and affect YAP/TAZ activation states. In the context of bone, osteoblast lining cells and osteocyte matrix-embedded cells have different 3-dimensional mechanical environment which necessarily lead to a different regulation of YAP/TAZ.

In degenerative diseases, modifications of the matrix properties could also lead to the modification of YAP/TAZ activation that could contributes to the pathogenesis (Fearing et al., 2019). For example, in the adult nucleus pulposus (NP), cells are embedded in a soft matrix that becomes fibrotic and stiffness with age. Modifications of mechanical cues emanating from this altered matrix modify the cell shape and activate YAP that is normally sequestered in the cytoplasm.

4 YAP/TAZ AND BONE BIOLOGY

Bone is a dynamic tissue associated with permanent remodelling that is required to adapt the bone structure and density to maintain physical integrity upon mechanical loading. Different studies have highlighted a role for YAP/TAZ in this process. Hence, YAP/TAZ regulates chondrogenesis and osteoblast differentiation from MSCs to late osteoblast stage/osteocytes. Recently, our lab and others have characterised the role of YAP/TAZ in osteocyte perilacunar/canalicular remodeling and in mechanotransduction.

4.1 Role of YAP/TAZ in Craniofacial and Dental Development

YAP/TAZ and the Hippo pathway are known to be implicated in development especially in organ size. Different works aims to elucidated their roles on craniofacial and dental development such as the work of Wang and its collaborators that demonstrates the role of YAP/TAZ in neural crest-derived craniofacial development (Wang et al., 2016a). Deletion of YAP/TAZ in cranial neural crest using $Wnt1^{Cre}$ and $Wnt1^{Cre2SOR}$ lead to embryonic lethality with vascular defect probably causing haemorrhage. This work indicates that YAP/TAZ regulate vascular development that is known to be essential for bone development. It was also demonstrated that YAP/TAZ modulates the secondary palate development notably by regulating genes involved in mineralization such as Phex, which could lead to the regulation of collagen cross-linking in the palate shelf mesenchyme (Goodwin et al., 2020). This suggest that YAP/TAZ could themselves influence their matrix stiffness by modulating gene implicated in bone mineralization.

YAP/TAZ was also study in the context of the generation of transit-amplifying cell (TAC) populations during growth of mouse incisor (Hu et al., 2017). It was shown *in vivo* that this process is modulated by the ITGA3-FAK-CDC42 signaling axis in order to activate YAP in a LATS-independent manner. This regulation led to nuclear accumulation of YAP and the maintenance of a high proliferation rate necessary to maintain organ renewal. Interestingly, Li and its collaborators demonstrates that the α-E catenin are able to inhibit YAP in the mouse incisor (Li et al., 2016). This regulation allows the establishment of non-dividing cells for dental mesenchymal condensation and epithelial invagination.

4.2 Role of YAP/TAZ in Bone and Cartilage Stem Cells Differentiation

YAP/TAZ allow for the MSC commitment toward an osteoblastic lineage while inhibiting adipogenesis and chondrogenesis (**Figure 3**) (Hong et al., 2005; Lorthongpanich et al., 2019). This differentiation process is regulated by different mechanisms such as matrix metalloproteinase (MMP) synthesis, cellular contact and shear stress. MSCs produce MT1-MMP (MMP-14) to induce matrix remodelling responsible for nuclear translocation of YAP/TAZ via the activation of integrin β1/RhoA axis *in vivo* (Tang et al., 2013). Thus, the matrix remodelling triggers the differentiation of MSCs toward an osteoblastic lineage rather than chondrogenesis or adipogenesis. In addition, the absence of cellular contact induces morphological changes in MSCs such as a large adhesion surface, thereby promoting osteoblastogenesis, and inhibiting adipogenesis (McBeath et al., 2004). Snail/Slug signaling also participates *in vivo* in the differentiation process via YAP/TAZ activation and subsequent expression of osteoblastic genes such as Runx2 (Tang and Weiss, 2017).

Dupont and collaborators demonstrated that the osteogenic differentiation normally induced in MSCs on stiff matrix was

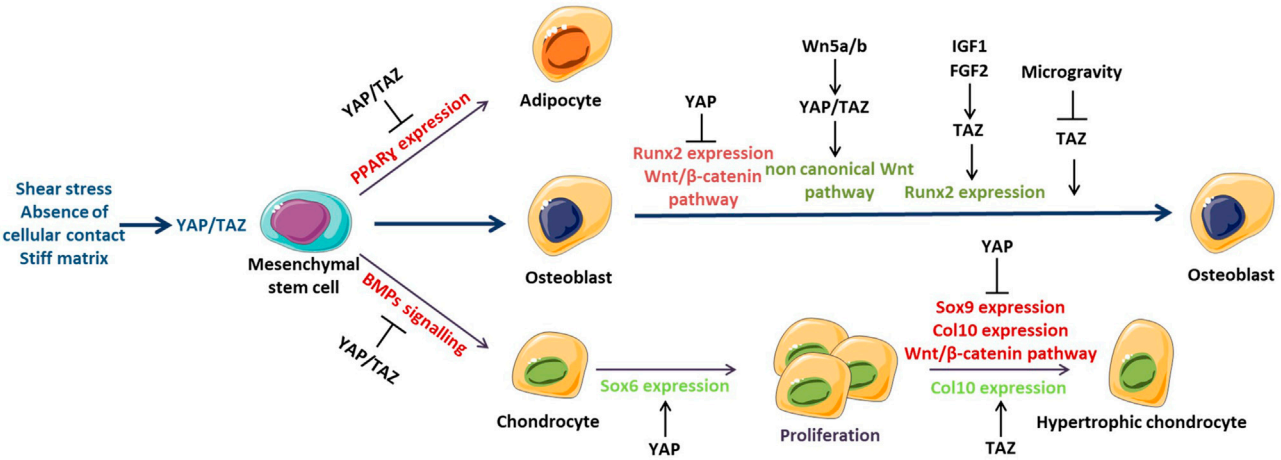

FIGURE 3 | YAP/TAZ in bone and cartilage biology YAP/TAZ regulates mesenchymal stem cell commitment toward an osteoblastic lineage and inhibits adipogenesis and chondrogenesis by inhibiting PPARγ, and BMP, respectively. This process allows for osteoblast differentiation in relation to microenvironment modifications such as shear stress, absence of cellular contact, and/or a stiff matrix that promotes YAP/TAZ activation. YAP/TAZ regulate osteoblastogenesis by modulating Runx2 and the Wnt/β-catenin pathway.

TABLE 1 | Partners of YAP/TAZ in bone and cartilage.

Bone partners	Cellular consequences	References
α-catenin	Cytoplamic retention of YAP to establish a group of non-dividing and specialized cells for formation of the tooth signalling centre, the enamel knot (EK)	Li et al. (2016)
Snail/Slug	Interaction inside the complex Snail/Slug-YAP/TAZ-Runx2 to stimulate MSC differentiation	Tang et al. (2016)
Runx2	Stimulate Osteocalcin gene expression and osteoblastogenesis	Cui et al. (2003), Hong et al. (2005)
PPARγ	Inhibit adipogenesis	Hong et al. (2005)
β-catenin	Stimulate osteoblastogenesis	Pan et al. (2018)
Smad1/5/8	Stimulate osteoblastogenesis in response to BMP-2	Wei et al. (2020)

YAP/TAZ, interacts in protein complex with different signaling pathway such as TGFβ/BMPs, and the Wnt/β-catenin pathway. YAP/TAZ, also interacts as DNA, and binding partners with Runx2.

inhibited *in vitro* by YAP/TAZ small interfering RNA (siRNA) (Dupont et al., 2011). YAP/TAZ silencing enabled adipogenic differentiation even on a stiff matrix that inhibited this process, thus imitating a soft environment. Moreover, shear stress induced the nuclear translocation of YAP/TAZ and the differentiation of MSCs *in vitro* via the osteoblastic lineage associated with the increased expression of Runx2, Dlx5, and Msx2 (Zhong et al., 2013; Kim et al., 2014). This mechanism involves RhoA because RhoA inhibition abolished the nuclear translocation of YAP/TAZ and the concomitant to activate target genes.

Recently, a role of YAP/TAZ in subchondral bone stem/progenitor cells (SCP-SPC) was described *ex vivo* in the context of the radial extracorporeal shockwave (Zhao et al., 2021). They demonstrated that radial shockwave influences the self-renewal of SCB-SPC through modulation of YAP.

4.3 Role of YAP/TAZ in Osteoblastogenesis

Several studies have highlighted the role of YAP and TAZ in regulating osteoblastogenesis and their proteins partners (**Table 1**). Mostly, TAZ was described as a transcriptional co-activator interacting with Runx2, and the master regulator gene of osteoblastogenesis (Cui et al., 2003; Byun et al., 2014). The growth factors FGF-2 and IGF-1 were described *in vitro* as inducers of osteoblast differentiation by increasing TAZ expression and its nuclear translocation involving ERK signaling (Xue et al., 2013; Byun et al., 2014). Hence, the inhibition of TAZ by siRNA abolished osteogenic differentiation induced by FGF-2 and IGF-1 *in vitro* in cultures of rat bone marrow and C3H10 cell lines. In contrast to TAZ, YAP inhibited Runx2 activity in the osteoblast-like cells ROS 17/2.8 (Zaidi et al., 2004). Pan and collaborators demonstrated that YAP regulates osteoblastogenesis via Wnt/β-catenin signaling *in vitro* and *in vivo* (Pan et al., 2018). Finally, microgravity decreased the osteogenic differentiation induced by downregulation of TAZ activity on MSCs isolated from rat long bones (Chen et al., 2015). TAZ activation by lipophosphatidic acid blocked the inhibitory effect of gravity on osteoblast differentiation by inducing ROCK signaling.

Recently, mouse models were used to explore the role of YAP/TAZ in bone (**Table 2**). These works highlighted the differential role of YAP/TAZ according to stage of osteoblast differentiation. YAP/TAZ double knockout in the osteoprogenitors Osx+ or

TABLE 2 | Bone phenotype induced by YAP and TAZ modulation.

Genotype	Stage of differentiation	Bone structure	Histo-morphometric parameters	Age	References
$YAP^{fl/fl}$; $TAZ^{fl/fl}$; $Prx1^{Cre}$	Mesenchymal stem cells	Lethality (severe hemorrhage and edema)	—	Embryonic lethality	Xiong et al. (2018)
$YAP^{fl/fl}$; $TAZ^{fl/fl}$; Osx^{Cre}	Young osteoblasts	Lethality (neonatal asphyxiation due to ribcage malformation, fracture)	—	Neonatal lethality	Kegelman et al. (2018)
$YAP^{fl/+}$; $TAZ^{fl/fl}$; $Prx1^{Cre}$	Mesenchymal stem cells	BV/TV + Ct. Th +	Ob. N/BS + Oc. N/BS = MS/BS + MAR = BFR/BS +	12-week-old-female	Xiong et al. (2018)
$YAP^{fl/+}$; $TAZ^{fl/+}$; $Osx^{Cre}YAP^{fl/fl}$; $TAZ^{fl/+}$; Osx^{Cre} $TAZ^{fl/fl}$; $YAP^{fl/+}$; Osx^{Cre}	Young osteoblasts	BV/TV– Ct. Th –	Ob. N/BS – Oc. N/BS + MS/BS = MAR – BFR/BS =	8-week-old male	Kegelman et al. (2018)
$YAP^{fl/fl}$; Ocn^{Cre}	Osteoblasts	BV/TV – Ct. Th =	Ob. N/BS – MAR – BFR/BS –	3-month-old male	Pan et al. (2018)
$YAP^{fl/fl}$; $TAZ^{fl/fl}$; $DMP1^{Cre}$	Mature osteoblasts/ osteocytes	BV/TV – Ct. Th –	Ob. N/BS – Oc. N/BS + MS/BS – MAR – BFR/BS –	12-week-old-male	Xiong et al. (2018)
$YAP^{fl/fl}$; $TAZ^{fl/fl}$; $DMP1(8\ kb)^{Cre}$	Mature osteoblasts/ osteocytes	BV/TV – Ct. Th –	Ob. N/BS – Oc. N/BS + MS/BS – MAR – BFR/BS –	Post-natal-day 84	Kegelman et al. (2020)

Synthesis of the bone phenotype observed in different mouse models invalidated for YAP, and/or TAZ, at different stages of differentiation. YAP/TAZ, deletion in osteoprogenitors results in lethality, and later invalidation using Osx, and Ocn or DMP1-Cre decreases bone volume. Obl.S/BS, osteoblast surface, Oc.S/BS, osteoclast surface, MS/BS, mineralized surface/bone surface, MAR, mineral apposition rate, and BFR/BS, bone formation rate/bone surface.

Prx1+ led to a lethality induced by ribcage malformation and the occurrence of haemorrhage, respectively, and during embryonic development (Kegelman et al., 2018; Xiong et al., 2018). The inducible double deletion of YAP/TAZ in Osx+ osteoprogenitors promoted osteoblastogenesis and bone formation in compact bone of 12-week-old mouse vertebrae. In parallel, a reduced mineral apposition rate resulted in the absence of any modified bone formation rate. Of note, $YAP^{fl/+}$, and $TAZ^{fl/fl}$; $Prx1^{Cre}$ mice featured a bone mass owing to increased bone formation, and which suggests that YAP/TAZ have distinct roles depending on the stage of differentiation (Xiong et al., 2018). Thus, conditional deletion of YAP in fully differentiated osteoblasts from $YAP^{fl/fl}$; Ocn^{Cre} mice resulted in bone loss associated with decreased osteoblast proliferation and differentiation. Moreover, bone marrow from $YAP^{fl/+}$, $TAZ^{fl/fl}$; $Prx1^{Cre}$ and $YAP^{fl/fl}$, $TAZ^{fl/fl}$; Osx^{Cre} mice showed increased osteogenic differentiation, notably with increased levels of bone formation markers such as Osx, osteocalcin, and collagen I (Xiong et al., 2018). This double deletion in osteoprogenitors was associated with increased Wnt/β-catenin signaling and Runx2 expression. Hence, single deletion of YAP or TAZ in Osx + cells ($YAP^{fl/fl}$; Osx^{Cre}, and $TAZ^{fl/fl}$; Osx^{Cre}) or double deletion of YAP/TAZ at the mature osteoblast/osteocyte stage ($YAP^{fl/fl}$, $TAZ^{fl/fl}$; $DMP1^{Cre}$) decreased bone mass, which was associated with increased osteoclast activity, and decreased osteoblastogenesis (Kegelman et al., 2018; Xiong et al., 2018). $YAP^{fl/fl}$, $TAZ^{fl/fl}$; $DMP1^{Cre}$ mice showed decreased osteoblast number and bone formation rate resulting from decreased mineralized surface and apposition mineral rate. Together, these data show that YAP/TAZ could promote the commitment toward an osteoblastic lineage but inhibit the activity of fully differentiated osteoblasts/osteocytes.

The role of each co-factor was also assessed. TAZ overexpression in osteoblasts or the administration of TAZ lentivirus in a model of bone loss promoted the increase in bone mass and density associated with increased levels of osteoblast markers such as Runx2 and osteocalcin (Yang et al., 2013; Zhang et al., 2016). Overexpression of TAZ in the osteoblast cell line C3H10 upregulated Runx2 transcriptional activity associated with increased TGF-β response and decreased Wnt-β-catenin signaling (Yang et al., 2013).

Finally, YAP/TAZ could contribute to bone fracture healing because YAP/TAZ deletion in adult mice impaired bone formation in the callus (Kegelman et al., 2021). Thus, YAP/TAZ accelerated bone fracture healing via the expansion and differentiation of periosteal osteoblast precursors.

4.4 YAP/TAZ and Osteocytes

Recent studies highlighted the implication of YAP/TAZ in osteocytes with a role in bone quality and adaptative

TABLE 3 | Cartilage phenotype induced by YAP and TAZ modulation.

Genotype or model	YAP/TAZ status	Effect on cartilage and OA	References
$Mob1a^{fl/fl}$; $Mob1b^{-/-}$; $Col2a1^{CreERT}$	YAP/TAZ overexpression from P0	Chondrodysplasia phenotype	Goto et al. (2018)
nls-$YAP5SA^{KI/+}$; $Col2a1^{Cre}$	YAP overexpression	Chondrodysplasia phenotype	Vanyai et al. (2020)
Tg-Col2a1-YAP	YAP overexpression	Protects from OA	Deng et al. (2018a)
$Mst1^{fl/fl}$; $Mst2^{fl/fl}Col2a1^{Cre}$	YAP/TAZ overexpression	Protects from OA	Deng et al. (2018b)
Intra-articular injection of YAP siRNA	YAP silencing	Protects from OA	Gong et al. (2019)
Intra-articular injection of YAP inhibitor, Verteporfin	YAP/TAZ silencing	Protects from OA	Zhang et al. (2020)
$YAP^{fl/fl}$; $Col2a1^{CreERT}$	YAP silencing from 8 week-old	Protects from OA	Zhang et al. (2020)
$Yap^{fl/fl}$; $Taz^{fl/fl}$; $Col2a1^{Cre}$	YAP/TAZ silencing	Neonatal lethality	Vanyai et al. (2020)

Synthesis of cartilage phenotypes induced by YAP, or YAP/TAZ, silencing, and upregulation in vivo *found in the literature. OA, osteoarthritis.*

mechanical features. Two roles of YAP/TAZ were described in osteocytes with specific functions in perilacunar/canalicular remodeling and in mechanotransduction. Kegelman and collaborators investigated the role of YAP/TAZ in osteocyte-mediated bone remodeling by the conditional deletion of YAP and TAZ in $DMP1^{Cre}$ mice (Kegelman et al., 2020). The invalidation of YAP/TAZ in osteocytes resulted in lower bone mass and dysregulated matrix collagen content and organization, thereby reducing bone mechanical properties. The authors also showed that YAP/TAZ is crucial for TGF-β-induced matrix protease gene expression and osteocyte perilacunar/canalicular remodeling. In line with these findings, we assessed the implication of YAP/TAZ in osteocyte mechanotransduction and showed that YAP/TAZ translocated to the nucleus and activated their target genes in a 3D *in vitro* culture model of the MLO-Y4 osteocyte-like cell line under mechanical compression (Zarka et al., 2021). YAP/TAZ silencing by short hairpin RNA partially blocked the increased M-csf and Cxcl3 gene expression induced by osteocyte loading, which suggests their role as mediators of mechanically induced chemokine expression in MLO-Y4 osteocytes. Moreover, transcriptomic analysis of YAP/TAZ-deleted osteocytes under compression strain revealed the regulation of several factors that initiate the formation of dendrites. This observation suggests the central role of YAP/TAZ in the formation of a perilacunar/canalicular network and in osteocyte-mediated bone remodeling.

4.5 Role of YAP/TAZ in Chondrocyte Function

The involvement of YAP was mostly analysed in chondrogenesis given that YAP induces chondrocyte proliferation and inhibits their differentiation (Karystinou et al., 2015; Yang et al., 2017). Chondrocyte proliferation is controlled by YAP, which induces the expression of Sox6 required for the proliferation while inhibiting the expression of collagen type X, a marker of hypertrophic chondrocytes *in vitro* and *in vivo* (Deng et al., 2016). Hence, inhibition of YAP activity is necessary to allow chondrocyte differentiation because YAP inhibits the BMP response that is essential for chondrocyte differentiation *in vitro* (Karystinou et al., 2015). Also, YAP inhibits chondrocyte differentiation *in vitro* by reducing Wnt/β-catenin signaling, whereas chondrocyte de-differentiation was found associated with increased YAP/TAZ level induced by RhoA signaling (Yang et al., 2017). Consistently, YAP is mostly localised in the nucleus of pre-hypertrophic chondrocytes, and hypertrophic chondrocytes show decreased YAP nuclear localization during embryogenesis (Goto et al., 2018).

These data suggest that YAP/TAZ promote the commitment of chondrocyte differentiation while blocking the final hypertrophic differentiation as a compensatory mechanism. These was confirmed by a recent study demonstrating the role of TAZ during chondrogenesis *in vivo* (Li Y. et al., 2021). They show that TAZ expression increased during chondrogenic differentiation and that TAZ deletion using $Col2a1^{Cre}$ mice inhibits growth plate and articular cartilage development. TAZ was found to promote chondroprogenitors cell proliferation while inhibiting chondrocyte maturation.

Overexpression of YAP/TAZ in chondrocytes induced by MOB1A/B and constitutive activation of YAP in cartilage resulted in a phenotype of chondrodysplasia (**Table 3**) (Goto et al., 2018; Vanyai et al., 2020). MOB1A/B deletion in mice revealed a low growth plate length and long bones, associated with altered proliferation, differentiation, and endochondral ossification. Primary chondrocytes isolated from these mice showed decreased proliferation related to decreased Sox9 expression induced by YAP/TAZ overexpression. In addition, Deng and collaborators demonstrated that YAP-specific overexpression in chondrocytes, in transgenic Col2a1-YAP mice or by Mst1/2 deletion under Cre-recombinase Col2a1, protected articular cartilage against osteoarthritis (Deng Y. et al., 2018). YAP overexpression attenuated NF-κB signaling and protected against extracellular matrix degradation by inhibiting matrix-degrading enzymes.

Recently, Vanyai and collaborators demonstrated that YAP/TAZ conditional deletion in chondrocytes from Col2a1 Cre mice ($Yap^{fl/fl}$; $Tazfl^{/fl}$; $Col2a1^{Cre+}$) resulted in neonatal lethality due in part to a cleft palate (Vanyai et al., 2020). The authors highlighted the phenotype inconsistency between *in vitro* and *in vivo* because YAP/TAZ are not required for cell proliferation in the cartilage growth plate *in vivo*. However, this study showed that modulating YAP/TAZ levels does not impair cell proliferation but rather induces skeletal deformities *in vivo* probably via the expression of matrix remodelling genes.

The ubiquitous expression of YAP/TAZ and the tissue-specific regulation of the complex are clues for interactions with several other

cell signaling pathways. The Hippo pathway interacts with NF-κB signaling to regulate protease expression and cartilage degradation during osteoarthritis. Conversely, the related effect was investigated by the use of intra-articular injection of YAP siRNA or the YAP inhibitor verteporfin: YAP inhibition protected against osteoarthritis (Gong et al., 2019; Zhang et al., 2020). Indeed, intra-articular injection of verteporfin or deletion of YAP by using $YAP^{fl/fl}$; $Col2a1^{CreERT}$ maintained cartilage homeostasis in osteoarthritic mice (Zhang et al., 2020). Silencing YAP by siRNA inhibited interleukin-1β–induced chondrocyte apoptosis and catabolic gene expression (Gong et al., 2019). Of note, osteoarthritic mice treated with YAP siRNA showed reduced subchondral bone attrition. More studies are needed to fully elucidate and clarify the role of YAP/TAZ in chondrocytes and environmental cells within the joints.

5 CONCLUSION

YAP and TAZ are regulators of bone and cartilage homeostasis that allows for structural and cellular adaptation in response to the microenvironment. YAP/TAZ contribute significantly in bone and cartilage by feeding into the regulation of master orchestrators such as Runx2, Osx, and Sox9. Biomechanical components have a crucial impact on the development of bone and cartilage diseases, so YAP/TAZ are central players for the initiation and progression of the diseases. Therefore, members of YAP/TAZ signaling are potential targets in treating bone and cartilage disorders.

AUTHOR CONTRIBUTIONS

All authors listed have made a substantial, direct, and intellectual contribution to the work and approved it for publication.

FUNDING

This work was funded by Inserm.

REFERENCES

Alarcón, C., Zaromytidou, A., Xi, Q., Gao, S., Fujisawa, S., Barlas, A., et al. (2009). CDK8/9 Drive Smad Transcriptional Action, Turnover and YAP Interactions in BMP and TGFβ Pathways. *Cell.* 139, 757–769. doi:10.1016/j.cell.2009.09.035.CDK8/9

Aragona, M., Panciera, T., Manfrin, A., Giulitti, S., Michielin, F., Elvassore, N., et al. (2013). A Mechanical Checkpoint Controls Multicellular Growth Through YAP/TAZ Regulation by Actin-Processing Factors. *Cell.* 154, 1047–1059. doi:10.1016/j.cell.2013.07.042

Azzolin, L., Panciera, T., Soligo, S., Enzo, E., Bicciato, S., Dupont, S., et al. (2014). YAP/TAZ Incorporation in the β-Catenin Destruction Complex Orchestrates the Wnt Response. *Cell.* 158, 157–170. doi:10.1016/j.cell.2014.06.013

Baumgartner, R., Poernbacher, I., Buser, N., Hafen, E., and Stocker, H. (2010). The WW Domain Protein Kibra Acts Upstream of Hippo in Drosophila. *Developmental Cell.* 18, 309–316. doi:10.1016/j.devcel.2009.12.013

Benham-pyle, B. W., Pruitt, B. L., and Nelson, W. J. (2015). Mechanical Strain Induces E-Cadherin-Dependent Yap1 and β-Catenin Activation to Drive Cell Cycle Entry. *Science.* 348, 1024–1027. doi:10.1126/science.aaa4559.Mechanical

Byun, M. R., Kim, A. R., Hwang, J.-H., Kim, K. M., Hwang, E. S., and Hong, J.-H. (2014). FGF2 Stimulates Osteogenic Differentiation Through ERK Induced TAZ Expression. *Bone.* 58, 72–80. doi:10.1016/j.bone.2013.09.024

Chan, E. H. Y., Nousiainen, M., Chalamalasetty, R. B., Schäfer, A., Nigg, E. A., and Silljé, H. H. W. (2005). The Ste20-Like Kinase Mst2 Activates the Human Large Tumor Suppressor Kinase Lats1. *Oncogene.* 24, 2076–2086. doi:10.1038/sj.onc.1208445

Chen, G., Deng, C., and Li, Y.-P. (2012). TGF-β and BMP Signaling in Osteoblast Differentiation and Bone Formation. *Int. J. Biol. Sci.* 8, 272–288. doi:10.7150/ijbs.2929

Chen, Z., Luo, Q., Lin, C., and Song, G. (2015). Simulated Microgravity Inhibits Osteogenic Differentiation of Mesenchymal Stem Cells Through Down Regulating the Transcriptional Co-Activator TAZ. *Biochem. Biophysical Res. Commun.* 468, 21–26. doi:10.1016/j.bbrc.2015.11.006

Connelly, J. T., Gautrot, J. E., Trappmann, B., Tan, D. W.-M., Donati, G., Huck, W. T. S., et al. (2010). Actin and Serum Response Factor Transduce Physical Cues From the Microenvironment to Regulate Epidermal Stem Cell Fate Decisions. *Nat. Cell Biol.* 12, 711–718. doi:10.1038/ncb2074

Cordenonsi, M., Zanconato, F., Azzolin, L., Forcato, M., Rosato, A., Frasson, C., et al. (2011). The Hippo Transducer TAZ Confers Cancer Stem Cell-Related Traits on Breast Cancer Cells. *Cell.* 147, 759–772. doi:10.1016/j.cell.2011.09.048

Cui, C. B., Cooper, L. F., Yang, X., Karsenty, G., and Aukhil, I. (2003). Transcriptional Coactivation of Bone-Specific Transcription Factor Cbfa1 by TAZ. *Mol. Cell. Biol.* 23, 1004–1013. doi:10.1128/MCB.23.3.1004-1013.2003

Das Thakur, M., Feng, Y., Jagannathan, R., Seppa, M. J., Skeath, J. B., and Longmore, G. D. (2010). Ajuba LIM Proteins Are Negative Regulators of the Hippo Signaling Pathway. *Curr. Biol.* 20, 657–662. doi:10.1016/j.cub.2010.02.035.Ajuba

Deng, F., Peng, L., Li, Z., Tan, G., Liang, E., Chen, S., et al. (2018a). YAP Triggers the Wnt/β-Catenin Signalling Pathway and Promotes Enterocyte Self-Renewal, Regeneration and Tumorigenesis After DSS-Induced Injury. *Cell Death Dis.* 9, 153. doi:10.1038/s41419-017-0244-8

Deng, Y., Lu, J., Li, W., Wu, A., Zhang, X., Tong, W., et al. (2018b). Reciprocal Inhibition of YAP/TAZ and NF-Kb Regulates Osteoarthritic Cartilage Degradation. *Nat. Commun.* 9, 4564. doi:10.1038/s41467-018-07022-2

Deng, Y., Wu, A., Li, P., Li, G., Qin, L., Song, H., et al. (2016). Yap1 Regulates Multiple Steps of Chondrocyte Differentiation During Skeletal Development and Bone Repair. *Cell Rep.* 14, 2224–2237. doi:10.1016/j.celrep.2016.02.021

Doggett, K., Grusche, F. A., Richardson, H. E., and Brumby, A. M. (2011). Loss of the Drosophila Cell Polarity Regulator Scribbled Promotes Epithelial Tissue Overgrowth and Cooperation with Oncogenic Ras-Raf through Impaired Hippo Pathway Signaling. *BMC Dev. Biol.* 11, 57. doi:10.1186/1471-213X-11-57

Dong, J., Feldmann, G., Huang, J., Wu, S., Zhang, N., Comerford, S. A., et al. (2007). Elucidation of a Universal Size-Control Mechanism in Drosophila and Mammals. *Cell.* 130, 1120–1133. doi:10.1016/j.cell.2007.07.019

Dupont, S., Morsut, L., Aragona, M., Enzo, E., Giulitti, S., Cordenonsi, M., et al. (2011). Role of YAP/TAZ in Mechanotransduction. *Nature.* 474, 179–183. doi:10.1038/nature10137

Elbediwy, A., Vincent-Mistiaen, Z. I., Spencer-Dene, B., Stone, R. K., Boeing, S., Wculek, S. K., et al. (2016). Integrin Signalling Regulates YAP/TAZ to Control Skin Homeostasis. *Development.* 143, 1674–1687. doi:10.1242/dev.133728

Fan, R., Kim, N.-G., and Gumbiner, B. M. (2013). Regulation of Hippo Pathway by Mitogenic Growth Factors via Phosphoinositide 3-Kinase and Phosphoinositide-Dependent Kinase-1. *Proc. Natl. Acad. Sci.* 110, 2569–2574. doi:10.1073/pnas.1216462110

Fearing, B. V., Jing, L., Barcellona, M. N., Witte, S. E., Buchowski, J. M., Zebala, L. P., et al. (2019). Mechanosensitive Transcriptional Coactivators MRTF-A and YAP/TAZ Regulate Nucleus Pulposus Cell Phenotype through Cell Shape. *FASEB j.* 33, 14022–14035. doi:10.1096/fj.201802725RRR

Genevet, A., Wehr, M. C., Brain, R., Thompson, B. J., and Tapon, N. (2010). Kibra Is a Regulator of the Salvador/Warts/Hippo Signaling Network. *Developmental Cell.* 18, 300–308. doi:10.1016/j.devcel.2009.12.011

Gong, Y., Li, S.-J., Liu, R., Zhan, J.-F., Tan, C., Fang, Y.-F., et al. (2019). Inhibition of YAP With siRNA Prevents Cartilage Degradation and Ameliorates Osteoarthritis Development. *J. Mol. Med.* 97, 103–114. doi:10.1007/s00109-018-1705-y

Goodwin, A. F., Chen, C. P., Vo, N. T., Bush, J. O., and Klein, O. D. (2020). YAP/TAZ Regulate Elevation and Bone Formation of the Mouse Secondary Palate. *J. Dent. Res.* 99, 1387–1396. doi:10.1177/0022034520935372

Goto, H., Nishio, M., To, Y., Oishi, T., Miyachi, Y., Maehama, T., et al. (2018). Loss of Mob1a/b in Mice Results in Chondrodysplasia Due to YAP1/TAZ-TEAD-Dependent Repression of SOX9. *Development.* 145(6), dev159244. doi:10.1242/dev.159244

Harvey, K. F., Pfleger, C. M., and Hariharan, I. K. (2003). The Drosophila Mst Ortholog, Hippo, Restricts Growth and Cell Proliferation and Promotes Apoptosis. *Cell.* 114, 457–467. doi:10.1016/S0092-8674(03)00557-9

Haskins, J. W., Nguyen, D. X., and Stern, D. F. (2014). Neuregulin 1-Activated ERBB4 Interacts With YAP to Induce Hippo Pathway Target Genes and Promote Cell Migration. *Sci. Signal.* 7, ra116–207. doi:10.1126/scisignal.2005770

Heallen, T., Zhang, M., Wang, J., Bonilla-claudio, M., Klysik, E., Johnson, R. L., et al. (2011). Hippo Pathway Inhibits Wnt Signaling to Restrain Cardiomyocyte Proliferation and Heart Size. *Science.* 332, 458–461. doi:10.1126/science.1199010.Hippo

Hiemer, S. E., Szymaniak, A. D., and Varelas, X. (2014). The Transcriptional Regulators TAZ and YAP Direct Transforming Growth Factor β-Induced Tumorigenic Phenotypes in Breast Cancer Cells. *J. Biol. Chem.* 289, 13461–13474. doi:10.1074/jbc.M113.529115

Hong, J.-H., Hwang, E. S., McManus, M. T., Amsterdam, A., Tian, Y., Kalmukova, R., et al. (2005). TAZ, a Transcriptional Modulator of Mesenchymal Stem Cell Differentiation. *Science.* 309, 1074–1078. doi:10.1126/science.1110955

Hsiao, C., Lampe, M., Nillasithanukroh, S., Han, W., Lian, X., and Palecek, S. P. (2016). Human Pluripotent Stem Cell Culture Density Modulates YAP Signaling. *Biotechnol. J.* 11, 662–675. doi:10.1002/biot.201500374

Hu, J. K.-H., Du, W., Shelton, S. J., Oldham, M. C., Dipersio, C. M., and Klein, O. D. (2017). An FAK-YAP-mTOR Signaling Axis Regulates Stem Cell-Based Tissue Renewal in Mice. *Cell Stem Cell.* 21, 91–106. doi:10.1016/j.stem.2017.03.023.A

Huang, J., Wu, S., Barrera, J., Matthews, K., and Pan, D. (2005). The Hippo Signaling Pathway Coordinately Regulates Cell Proliferation and Apoptosis by Inactivating Yorkie, the Drosophila Homolog of YAP. *Cell.* 122, 421–434. doi:10.1016/j.cell.2005.06.007

Imajo, M., Miyatake, K., Iimura, A., Miyamoto, A., and Nishida, E. (2012). A Molecular Mechanism that Links Hippo Signalling to the Inhibition of Wnt/β-Catenin Signalling. *EMBO J.* 31, 1109–1122. doi:10.1038/emboj.2011.487

Jia, J., Zhang, W., Wang, B., Trinko, R., and Jiang, J. (2003). The Drosophila Ste20 Family Kinase dMST Functions as a Tumor Suppressor by Restricting Cell Proliferation and Promoting Apoptosis. *Genes Dev.* 17, 2514–2519. doi:10.1101/gad.1134003

Jiao, S., Wang, H., Shi, Z., Dong, A., Zhang, W., Song, X., et al. (2014). A Peptide Mimicking VGLL4 Function Acts as a YAP Antagonist Therapy Against Gastric Cancer. *Cancer Cell.* 25, 166–180. doi:10.1016/j.ccr.2014.01.010

Justice, R. W., Zilian, O., Woods, D. F., Noll, M., and Bryant, P. J. (1995). The Drosophila Tumor Suppressor Gene Warts Encodes a Homolog of Human Myotonic Dystrophy Kinase and Is Required for the Control of Cell Shape and Proliferation. *Genes Dev.* 9, 534–546. doi:10.1101/Gad.9.5.534

Kanai, F., Marignani, P. A., Sarbassova, D., Yagi, R., Hall, R. A., Donowitz, M., et al. (2000). TAZ: A Novel Transcriptional Co-activator Regulated by Interactions With 14-3-3 and PDZ Domain Proteins. *EMBO J.* 19, 6778–6791. doi:10.1093/emboj/19.24.6778

Kaneko, K., Ito, M., Naoe, Y., Lacy-Hulbert, A., and Ikeda, K. (2014). Integrin αv in the Mechanical Response of Osteoblast Lineage Cells. *Biochem. Biophysical Res. Commun.* 447, 352–357. doi:10.1016/j.bbrc.2014.04.006.Integrin

Kaneko, K. J., and DePamphilis, M. L. (1998). Regulation of Gene Expression at the Beginning of Mammalian Development and the TEAD Family of Transcription Factors. *Dev. Genet.* 22, 43–55. doi:10.1002/(sici)1520-6408(1998)22:1<43:aid-dvg5>3.0.co;2-7

Kango-Singh, M., Nolo, R., Tao, C., Verstreken, P., Hiesinger, P. R., Bellen, H. J., et al. (2002). Shar-pei Mediates Cell Proliferation Arrest During Imaginal Disc Growth inDrosophila. *Development.* 129, 5719–5730. doi:10.1242/dev.00168

Karystinou, A., Roelofs, A. J., Neve, A., Cantatore, F. P., Wackerhage, H., and De Bari, C. (2015). Yes-Associated Protein (YAP) Is a Negative Regulator of Chondrogenesis in Mesenchymal Stem Cells. *Arthritis Res. Ther.* 17, 147. doi:10.1186/s13075-015-0639-9

Kegelman, C. D., Coulombe, J. C., Jordan, K. M., Horan, D. J., Qin, L., Robling, A. G., et al. (2020). YAP and TAZ Mediate Osteocyte Perilacunar/Canalicular Remodeling. *J. Bone Miner Res.* 35, 196–210. doi:10.1002/jbmr.3876

Kegelman, C. D., Mason, D. E., Dawahare, J. H., Horan, D. J., Vigil, G. D., Howard, S. S., et al. (2018). Skeletal Cell YAP and TAZ Combinatorially Promote Bone Development. *FASEB j.* 32, 2706–2721. doi:10.1096/fj.201700872R

Kegelman, C. D., Nijsure, M. P., Moharrer, Y., Pearson, H. B., Dawahare, J. H., Jordan, K. M., et al. (2021). YAP and TAZ Promote Periosteal Osteoblast Precursor Expansion and Differentiation for Fracture Repair. *J. Bone Miner Res.* 36, 143–157. doi:10.1002/jbmr.4166.YAP

Kim, K. M., Choi, Y. J., Hwang, J.-H., Kim, A. R., Cho, H. J., Hwang, E. S., et al. (2014). Shear Stress Induced by an Interstitial Level of Slow Flow Increases the Osteogenic Differentiation of Mesenchymal Stem Cells Through TAZ Activation. *PLoS One.* 9, e92427. doi:10.1371/journal.pone.0092427

Kim, M.-K., Jang, J.-W., and Bae, S.-C. (2018). DNA Binding Partners of YAP/TAZ. *BMB Rep.* 51, 126–133. doi:10.5483/bmbrep.2018.51.3.015

Kim, M., Kim, M., Lee, S., Kuninaka, S., Saya, H., Lee, H., et al. (2013). CAMP/PKA Signalling Reinforces the LATS-YAP Pathway to Fully Suppress YAP in Response to Actin Cytoskeletal Changes. *EMBO J.* 32, 1543–1555. doi:10.1038/emboj.2013.102

Kim, N.-G., and Gumbiner, B. M. (2015). Adhesion to Fibronectin Regulates Hippo Signaling via the FAK-Src-Pi3k Pathway. *J. Cell Biol.* 210, 503–515. doi:10.1083/jcb.201501025

Kim, N.-G., Koh, E., Chen, X., and Gumbiner, B. M. (2011). E-cadherin Mediates Contact Inhibition of Proliferation Through Hippo Signaling-Pathway Components. *Proc. Natl. Acad. Sci.* 108, 11930–11935. doi:10.1073/pnas.1103345108

Komuro, A., Nagai, M., Navin, N. E., and Sudol, M. (2003). WW Domain-Containing Protein YAP Associates With ErbB-4 and Acts as a Co-Transcriptional Activator for the Carboxyl-Terminal Fragment of ErbB-4 that Translocates to the Nucleus. *J. Biol. Chem.* 278, 33334–33341. doi:10.1074/jbc.M305597200

Konsavage, W. M., Kyler, S. L., Rennoll, S. A., Jin, G., and Yochum, G. S. (2012). Wnt/β-Catenin Signaling Regulates Yes-Associated Protein (YAP) Gene Expression in Colorectal Carcinoma Cells. *J. Biol. Chem.* 287, 11730–11739. doi:10.1074/jbc.M111.327767

Lai, D., and Yang, X. (2013). BMP4 Is a Novel Transcriptional Target and Mediator of Mammary Cell Migration Downstream of the Hippo Pathway Component TAZ. *Cell Signal.* 25, 1720–1728. doi:10.1016/j.cellsig.2013.05.002

Lai, Z.-C., Wei, X., Shimizu, T., Ramos, E., Rohrbaugh, M., Nikolaidis, N., et al. (2005). Control of Cell Proliferation and Apoptosis by Mob as Tumor Suppressor, Mats. *Cell.* 120, 675–685. doi:10.1016/j.cell.2004.12.036

Lei, Q.-Y., Zhang, H., Zhao, B., Zha, Z.-Y., Bai, F., Pei, X.-H., et al. (2008). TAZ Promotes Cell Proliferation and Epithelial-Mesenchymal Transition and Is Inhibited by the Hippo Pathway. *Mol. Cell. Biol.* 28, 2426–2436. doi:10.1128/MCB.01874-07

Li, C.-Y., Hu, J., Lu, H., Lan, J., Du, W., Galicia, N., et al. (2016). Ae-catenin Inhibits YAP/TAZ Activity to Regulate Signalling Centre Formation During Tooth Development. *Nat. Commun.* 7, 12133. doi:10.1038/ncomms12133

Li, J., Yan, J.-F., Wan, Q.-Q., Shen, M.-J., Ma, Y.-X., Gu, J.-T., et al. (2021a). Matrix Stiffening by Self-Mineralizable Guided Bone Regeneration. *Acta Biomater.* 125, 112–125. doi:10.1016/j.actbio.2021.02.012

Li, Y., Yang, S., Qin, L., and Yang, S. (2021b). TAZ Is Required for Chondrogenesis and Skeletal Development. *Cell Discov.* 7, 26. doi:10.1038/s41421-021-00254-5

Liu, C.-Y., Zha, Z.-Y., Zhou, X., Zhang, H., Huang, W., Zhao, D., et al. (2010). The Hippo Tumor Pathway Promotes TAZ Degradation by Phosphorylating a Phosphodegron and Recruiting the SCFβ-TrCP E3 Ligase. *J. Biol. Chem.* 285, 37159–37169. doi:10.1074/jbc.M110.152942

Liu, X., Yang, N., Figel, S. A., Wilson, K. E., Morrison, C. D., Gelman, I. H., et al. (2013). PTPN14 Interacts With and Negatively Regulates the Oncogenic Function of YAP. *Oncogene.* 32, 1266–1273. doi:10.1038/onc.2012.147.PTPN14

Liu-chittenden, Y., Huang, B., Shim, J. S., Chen, Q., Lee, S.-J., Anders, R. A., et al. (2012). Genetic and Pharmacological Disruption of the TEAD-YAP Complex

Suppresses the Oncogenic Activity of YAP. *Genes Dev.* 26, 1300–1305. doi:10.1101/gad.192856.112.1300

Lorthongpanich, C., Thumanu, K., Tangkiettrakul, K., Jiamvoraphong, N., Laowtammathron, C., Damkham, N., et al. (2019). YAP as a Key Regulator of Adipo-Osteogenic Differentiation in Human MSCs. *Stem Cell Res. Ther.* 10, 402. doi:10.1186/s13287-019-1494-4

Mahoney, J. E., Mori, M., Szymaniak, A. D., Varelas, X., and Cardoso, W. V. (2014). The Hippo Pathway Effector Yap Controls Patterning and Differentiation of Airway Epithelial Progenitors. *Developmental Cell.* 30, 137–150. doi:10.1016/j.devcel.2014.06.003

Major, L. G., Holle, A. W., Young, J. L., Hepburn, M. S., Jeong, K., Chin, I. L., et al. (2019). Volume Adaptation Controls Stem Cell Mechanotransduction. *ACS Appl. Mater. Inter.* 11, 45520–45530. doi:10.1021/acsami.9b19770

McBeath, R., Pirone, D. M., Nelson, C. M., Bhadriraju, K., and Chen, C. S. (2004). Cell Shape, Cytoskeletal Tension, and RhoA Regulate Stem Cell Lineage Commitment. *Developmental Cell.* 6, 483–495. doi:10.1016/S1534-5807(04)00075-9

Meng, Z., Moroishi, T., and Guan, K.-L. (2016). Mechanisms of Hippo Pathway Regulation. *Genes Dev.* 30, 1–17. doi:10.1101/gad.274027.115

Meng, Z., Qiu, Y., Lin, K. C., Kumar, A., Placone, J. K., Fang, C., et al. (2018). RAP2 Mediates Mechanoresponses of the Hippo Pathway. *Nature.* 560, 655–660. doi:10.1038/s41586-018-0444-0.RAP2

Michaloglou, C., Lehmann, W., Martin, T., Delaunay, C., Hueber, A., Barys, L., et al. (2013). The Tyrosine Phosphatase PTPN14 Is a Negative Regulator of YAP Activity. *PLoS One.* 8, e61916. doi:10.1371/journal.pone.0061916

Miller, E., Yang, J., Deran, M., Wu, C., Su, A. I., Bonamy, G. M. C., et al. (2012). Identification of Serum-Derived Sphingosine-1-Phosphate as a Small Molecule Regulator of YAP. *Chem. Biol.* 19, 955–962. doi:10.1016/j.chembiol.2012.07.005

Mo, J.-S., Yu, F.-X., Gong, R., Brown, J. H., and Guan, K.-L. (2012). Regulation of the Hippo-YAP Pathway by Protease-Activated Receptors (PARs). *Genes Dev.* 26, 2138–2143. doi:10.1101/gad.197582.112

Moleirinho, S., Hoxha, S., Mandati, V., Curtale, G., Troutman, S., Ehmer, U., et al. (2017). Regulation of Localization and Function of the Transcriptional Co-Activator YAP by Angiomotin. *Elife.* 6, e23966. doi:10.7554/eLife.23966.001

Moon, Y. J., Yun, C.-Y., Choi, H., Ka, S.-O., Kim, J. R., Park, B.-H., et al. (2016). Smad4 Controls Bone Homeostasis Through Regulation of Osteoblast/Osteocyte Viability. *Exp. Mol. Med.* 48, e256. doi:10.1038/emm.2016.75

Nakajima, H., Yamamoto, K., Agarwala, S., Terai, K., Fukui, H., Fukuhara, S., et al. (2017). Flow-Dependent Endothelial YAP Regulation Contributes to Vessel Maintenance. *Developmental Cell.* 40, 523–536. doi:10.1016/j.devcel.2017.02.019

Omerovic, J., Puggioni, E. M. R., Napoletano, S., Visco, V., Fraioli, R., Frati, L., et al. (2004). Ligand-Regulated Association of ErbB-4 to the Transcriptional Co-Activator YAP65 Controls Transcription at the Nuclear Level. *Exp. Cell Res.* 294, 469–479. doi:10.1016/j.yexcr.2003.12.002

Pan, D. (2007). Hippo Signaling in Organ Size Control. *Genes Dev.* 21, 886–897. doi:10.1101/gad.1536007

Pan, J.-X., Xiong, L., Zhao, K., Zeng, P., Wang, B., Tang, F.-L., et al. (2018). YAP Promotes Osteogenesis and Suppresses Adipogenic Differentiation by Regulating β-catenin Signaling. *Bone Res.* 6, 18. doi:10.1038/s41413-018-0018-7

Pantalacci, S., Tapon, N., and Léopold, P. (2003). The Salvador Partner Hippo Promotes Apoptosis and Cell-Cycle Exit in Drosophila. *Nat. Cell Biol.* 5, 921–927. doi:10.1038/ncb1051

Park, H. W., Kim, Y. C., Yu, B., Moroishi, T., Mo, J.-S., Plouffe, S. W., et al. (2015). Alternative Wnt Signaling Activates YAP/TAZ. *Cell.* 162, 780–794. doi:10.1016/j.cell.2015.07.013

Praskova, M., Xia, F., and Avruch, J. (2008). MOBKL1A/MOBKL1B Phosphorylation by MST1 and MST2 Inhibits Cell Proliferation. *Curr. Biol.* 18, 311–321. doi:10.1038/ncomms5234.SUMO1

Rauskolb, C., Sun, S., Sun, G., Pan, Y., and Irvine, K. D. (2014). Cytoskeletal Tension Inhibits Hippo Signaling Through an Ajuba-Warts Complex. *Cell.* 158, 143–156. doi:10.1016/j.cell.2014.05.035.Cytoskeletal

Reddy, B. V. V. G., and Irvine, K. D. (2013). Regulation of Hippo Signaling by EGFR-MAPK Signaling Through Ajuba Family Proteins. *Developmental Cell.* 24, 459–471. doi:10.1016/j.neuron.2009.10.017.A

Schlegelmilch, K., Mohseni, M., Kirak, O., Pruszak, J., Rodriguez, J. R., Zhou, D., et al. (2011). Yap1 Acts Downstream of α-Catenin to Control Epidermal Proliferation. *Cell.* 144, 782–795. doi:10.1016/j.neuron.2009.10.017.A

Sudol, M., Bork, P., Einbond, A., Kastury, K., Druck, T., Negrini, M., et al. (1995). Characterization of the Mammalian YAP (Yes-Associated Protein) Gene and its Role in Defining a Novel Protein Module, the WW Domain. *J. Biol. Chem.* 270, 14733–14741. doi:10.1074/jbc.270.24.14733

Tang, Y., Feinberg, T., Keller, E. T., Li, X. -Y., and Weiss, S. J. (2016). Snail/Slug Binding Interactions with YAP/TAZ Control Skeletal Stem Cell Self-Renewal and Differentiation. *Nat. Cell. Biol.* 18(9), 917–929. doi:10.1038/ncb3394

Tang, Y., Rowe, R. G., Botvinick, E. L., Kurup, A., Putnam, A. J., Seiki, M., et al. (2013). MT1-MMP-Dependent Control of Skeletal Stem Cell Commitment via a β1-Integrin/YAP/TAZ Signaling Axis. *Developmental Cell.* 25, 402–416. doi:10.1016/j.devcel.2013.04.011.MT1-MMP-Dependent

Tang, Y., and Weiss, S. J. (2017). Snail/Slug-YAP/TAZ Complexes Cooperatively Regulate Mesenchymal Stem Cell Function and Bone Formation. *Cell Cycle.* 16, 399–405. doi:10.1080/15384101.2017.1280643

Tapon, N., Harvey, K. F., Bell, D. W., Wahrer, D. C. R., Schiripo, T. A., Haber, D. A., et al. (2002). Salvador Promotes Both Cell Cycle Exit and Apoptosis in Drosophila and Is Mutated in Human Cancer Cell Lines. *Cell.* 110, 467–478. doi:10.1016/S0092-8674(02)00824-3

Totaro, A., Castellan, M., Battilana, G., Zanconato, F., Azzolin, L., Giulitti, S., et al. (2017). YAP/TAZ Link Cell Mechanics to Notch Signalling to Control Epidermal Stem Cell Fate. *Nat. Commun.* 8, 15206. doi:10.1038/ncomms15206

Totaro, A., Panciera, T., and Piccolo, S. (2018). YAP/TAZ Upstream Signals and Downstream Responses. *Nat. Cell Biol.* 20, 888–899. doi:10.1038/s41556-018-0142-z

Udan, R. S., Kango-Singh, M., Nolo, R., Tao, C., and Halder, G. (2003). Hippo Promotes Proliferation Arrest and Apoptosis in the Salvador/Warts Pathway. *Nat. Cell Biol.* 5, 914–920. doi:10.1038/ncb1050

Vanyai, H. K., Prin, F., Guillermin, O., Marzook, B., Boeing, S., Howson, A., et al. (2020). Control of Skeletal Morphogenesis by the Hippo-YAP/TAZ Pathway. *Development.* 147, dev187187. doi:10.1242/dev.187187

Varelas, X., Miller, B. W., Sopko, R., Song, S., Gregorieff, A., Fellouse, F. A., et al. (2010a). The Hippo Pathway Regulates Wnt/β-Catenin Signaling. *Developmental Cell.* 18, 579–591. doi:10.1016/j.devcel.2010.03.007

Varelas, X., Samavarchi-Tehrani, P., Narimatsu, M., Weiss, A., Cockburn, K., Larsen, B. G., et al. (2010b). The Crumbs Complex Couples Cell Density Sensing to Hippo-Dependent Control of the TGF-β-SMAD Pathway. *Developmental Cell.* 19, 831–844. doi:10.1016/j.devcel.2010.11.012

Verghese, S., Waghmare, I., Kwon, H., Hanes, K., and Kango-Singh, M. (2012). Scribble Acts in the Drosophila Fat-Hippo Pathway to Regulate Warts Activity. *PLoS One.* 7, e47173. doi:10.1371/journal.pone.0047173

Wada, K.-I., Itoga, K., Okano, T., Yonemura, S., and Sasaki, H. (2011). Hippo Pathway Regulation by Cell Morphology and Stress Fibers. *Development.* 138, 3907–3914. doi:10.1242/dev.070987

Wang, J., Xiao, Y., Hsu, C.-W., Martinez-Traverso, I. M., Zhang, M., Bai, Y., et al. (2015a). Yap and Taz Play a Crucial Role in Neural Crest-Derived Craniofacial Development. *Development.* 143, 504–515. doi:10.1242/dev.126920

Wang, K.-C., Yeh, Y.-T., Nguyen, P., Limqueco, E., Lopez, J., Thorossian, S., et al. (2016b). Flow-dependent YAP/TAZ Activities Regulate Endothelial Phenotypes and Atherosclerosis. *Proc. Natl. Acad. Sci. USA.* 113, 11525–11530. doi:10.1073/pnas.1613121113

Wang, L., Luo, J.-Y., Li, B., Tian, X. Y., Chen, L.-J., Huang, Y., et al. (2016c). Integrin-YAP/TAZ-JNK Cascade Mediates Atheroprotective Effect of Unidirectional Shear Flow. *Nature.* 540, 579–582. doi:10.1038/nature20602

Wang, W., Huang, J., and Chen, J. (2011). Angiomotin-Like Proteins Associate With and Negatively Regulate YAP1. *J. Biol. Chem.* 286, 4364–4370. doi:10.1074/jbc.C110.205401

Wei, Q., Holle, A., Li, J., Posa, F., Biagioni, F., Croci, C., et al. (2020). BMP-2 Signaling and Mechanotransduction Synergize to Drive Osteogenic Differentiation via YAP/TAZ. *Adv. Sci. (Weinh).* 7(15), 1902931. doi:10.1002/advs.201902931

Wu, S., Huang, J., Dong, J., and Pan, D. (2003). Hippo Encodes a Ste-20 Family Protein Kinase that Restricts Cell Proliferation and Promotes Apoptosis in Conjunction With Salvador and Warts. *Cell.* 114, 445–456. doi:10.1016/S0092-8674(03)00549-X

Xiang, X., Wang, Y., Zhang, H., Piao, J., Muthusamy, S., Wang, L., et al. (2018). Vasodilator-Stimulated Phosphoprotein Promotes Liver Metastasis of Gastrointestinal Cancer by Activating a β1-Integrin-FAK-YAP1/TAZ Signaling Pathway. *npj Precision Onc.* 2, 2. doi:10.1038/s41698-017-0045-7

Xiao, L., Chen, Y., Ji, M., and Dong, J. (2011). KIBRA Regulates Hippo Signaling Activity via Interactions With Large Tumor Suppressor Kinases. *J. Biol. Chem.* 286, 7788–7796. doi:10.1074/jbc.M110.173468

Xiong, J., Almeida, M., and O'Brien, C. A. (2018). The YAP/TAZ Transcriptional Co-Activators Have Opposing Effects at Different Stages of Osteoblast Differentiation. *Bone.* 112, 1–9. doi:10.1016/j.bone.2018.04.001

Xu, T., Wang, W., Zhang, S., Stewart, R. A., and Yu, W. (1995). Identifying Tumor Suppressors in Genetic Mosaics: the Drosophila Lats Gene Encodes a Putative Protein Kinase. *Development.* 121, 1053–1063. doi:10.1242/dev.121.4.1053

Xue, P., Wu, X., Zhou, L., Ma, H., Wang, Y., Liu, Y., et al. (2013). IGF1 Promotes Osteogenic Differentiation of Mesenchymal Stem Cells Derived From Rat Bone Marrow by Increasing TAZ Expression. *Biochem. Biophysical Res. Commun.* 433, 226–231. doi:10.1016/j.bbrc.2013.02.088

Yang, B., Sun, H., Song, F., Yu, M., Wu, Y., and Wang, J. (2017). YAP1 Negatively Regulates Chondrocyte Differentiation Partly by Activating the β-catenin Signaling Pathway. *Int. J. Biochem. Cell Biol.* 87, 104–113. doi:10.1016/j.biocel.2017.04.007

Yang, J.-Y., Cho, S. W., An, J. H., Jung, J. Y., Kim, S. W., Kim, S. Y., et al. (2013). Osteoblast-Targeted Overexpression of TAZ Increases Bone Mass *In Vivo*. *PLoS One.* 8, e56585. doi:10.1371/journal.pone.0056585

Yin, Z., Zhang, Y., Wang, Z., Ding, L., Damaolar, A., Li, Z., et al. (2016). Lentivirus-TAZ Administration Alleviates Osteoporotic Phenotypes in the Femoral Neck of Ovariectomized Rats. *Cell. Physiol. Biochem.* 38, 283–294. doi:10.1159/000438629

Yu, F.-X., Zhang, Y., Park, H. W., Jewell, J. L., Chen, Q., Deng, Y., et al. (2013). Protein Kinase A Activates the Hippo Pathway to Modulate Cell Proliferation and Differentiation. *Genes Dev.* 27, 1223–1232. doi:10.1101/gad.219402.113

Yu, F.-X., Zhao, B., Panupinthu, N., Jewell, J. L., Lian, I., Wang, L. H., et al. (2012). Regulation of the Hippo-YAP Pathway by G-Protein-Coupled Receptor Signaling. *Cell.* 150, 780–791. doi:10.1016/j.cell.2012.06.037

Yu, J., Zheng, Y., Dong, J., KluszaDeng, S., Deng, W.-M., and Pan, D. (2010). Kibra Functions as a Tumor Suppressor Protein that Regulates Hippo Signaling in Conjunction With Merlin and Expanded. *Developmental Cell.* 18, 288–299. doi:10.1016/j.neuron.2009.10.017.A10.1016/j.devcel.2009.12.012

Zaidi, S. K., Sullivan, A. J., Medina, R., Ito, Y., Van Wijnen, A. J., Stein, J. L., et al. (2004). Tyrosine Phosphorylation Controls Runx2-Mediated Subnuclear Targeting of YAP to Repress Transcription. *EMBO J.* 23, 790–799. doi:10.1038/sj.emboj.7600073

Zarka, M., Etienne, F., Bourmaud, M., Szondi, D., Schwartz, J.-M., Kampmann, K., et al. (2021). Mechanical Loading Activates the YAP/TAZ Pathway and Chemokine Expression in the MLO-Y4 Osteocyte-Like Cell Line. *Lab. Invest.* 101, 1597–1604. doi:10.1038/s41374-021-00668-5

Zhang, W., Gao, Y., Li, P., Shi, Z., Guo, T., Li, F., et al. (2014). VGLL4 Functions as a New Tumor Suppressor in Lung Cancer by Negatively Regulating the YAP-TEAD Transcriptional Complex. *Cell Res.* 24, 331–343. doi:10.1038/cr.2014.10

Zhang, X., Cai, D., Zhou, F., Yu, J., Wu, X., Yu, D., et al. (2020). Targeting Downstream Subcellular YAP Activity as a Function of Matrix Stiffness with Verteporfin-Encapsulated Chitosan Microsphere Attenuates Osteoarthritis. *Biomaterials.* 232, 119724. doi:10.1016/j.biomaterials.2019.119724

Zhao, B., Kim, J., Ye, X., Lai, Z.-C., and Guan, K.-L. (2009). Both TEAD-Binding and WW Domains Are Required for the Growth Stimulation and Oncogenic Transformation Activity of Yes-Associated Protein. *Cancer Res.* 69, 1089–1098. doi:10.1158/0008-5472.CAN-08-2997

Zhao, B., Li, L., Lu, Q., Wang, L. H., Liu, C.-Y., Lei, Q., et al. (2011). Angiomotin Is a Novel Hippo Pathway Component that Inhibits YAP Oncoprotein. *Genes Dev.* 25, 51–63. doi:10.1101/gad.2000111

Zhao, B., Li, L., Tumaneng, K., Wang, C.-Y., and Guan, K.-L. (2010). A Coordinated Phosphorylation by Lats and CK1 Regulates YAP Stability Through SCFβ-TRCP. *Genes Dev.* 24, 72–85. doi:10.1101/gad.1843810

Zhao, B., Wei, X., Li, W., Udan, R. S., Yang, Q., Kim, J., et al. (2007). Inactivation of YAP Oncoprotein by the Hippo Pathway Is Involved in Cell Contact Inhibition and Tissue Growth Control. *Genes Dev.* 21, 2747–2761. doi:10.1101/gad.1602907.Hpo/Sav

Zhao, B., Ye, X., Yu, J., Li, L., Li, W., Li, S., et al. (2008). TEAD Mediates YAP-Dependent Gene Induction and Growth Control. *Genes Dev.* 22, 1962–1971. doi:10.1101/gad.1664408.2007

Zhao, Z., Wang, Y., Wang, Q., Liang, J., Hu, W., Zhao, S., et al. (2021). Radial Extracorporeal Shockwave Promotes Subchondral Bone Stem/Progenitor Cell Self-Renewal by Activating YAP/TAZ and Facilitates Cartilage Repair *In Vivo*. *Stem Cell Res. Ther.* 12, 19. doi:10.1186/s13287-020-02076-w

Zhong, W., Tian, K., Zheng, X., Li, L., Zhang, W., Wang, S., et al. (2013). Mesenchymal Stem Cell and Chondrocyte Fates in a Multishear Microdevice Are Regulated by Yes-Associated Protein. *Stem Cell Development.* 22, 2083–2093. doi:10.1089/scd.2012.0685

Zhou, Q., Lyu, S., Bertrand, A. A., Hu, A. C., Chan, C. H., Ren, X., et al. (2021). Stiffness of Nanoparticulate Mineralized Collagen Scaffolds Triggers Osteogenesis via Mechanotransduction and Canonical Wnt Signaling. *Macromol. Biosci.* 21, 2000370. doi:10.1002/mabi.202000370

Zhou, Y., Huang, T., Cheng, A., Yu, J., Kang, W., and To, K. (2016). The TEAD Family and its Oncogenic Role in Promoting Tumorigenesis. *Int. J. Mol. Sci.* 17, 138. doi:10.3390/ijms17010138

Conflict of Interest: The authors declare that the research was conducted in the absence of any commercial or financial relationships that could be construed as a potential conflict of interest.

Publisher's Note: All claims expressed in this article are solely those of the authors and do not necessarily represent those of their affiliated organizations, or those of the publisher, the editors and the reviewers. Any product that may be evaluated in this article, or claim that may be made by its manufacturer, is not guaranteed or endorsed by the publisher.

frontiers in Cell and Developmental Biology

ORIGINAL RESEARCH
published: 11 January 2022
doi: 10.3389/fcell.2021.781388

GLIS Family Zinc Finger 1 was First Linked With Preaxial Polydactyly I in Humans by Stepwise Genetic Analysis

Jie-Yuan Jin[1], Pan-Feng Wu[2,3], Fang-Mei Luo[1], Bing-Bing Guo[1], Lei Zeng[2,3], Liang-Liang Fan[1,3,4], Ju-Yu Tang[2,3]* and Rong Xiang[1,2,3,4]**

[1]School of Life Sciences, Central South University, Changsha, China, [2]Department of Orthopaedics, Xiangya Hospital of Central South University, Changsha, China, [3]Hunan Key Laboratory of Animal Models for Human Diseases, School of Life Sciences, Central South University, Changsha, China, [4]Hunan Key Laboratory of Medical Genetics, School of Life Sciences, Central South University, Changsha, China

Background: Preaxial polydactyly (PPD) is one of the most common developmental malformations, with a prevalence of 0.8–1.4% in Asians. PPD is divided into four types, PPD I–IV, and PPD I is the most frequent type. Only six loci (*GLI1*, *GLI3*, *STKLD1*, ZRS, pre-ZRS, and a deletion located 240 kb from *SHH*) have been identified in non-syndromic PPD cases. However, pathogenesis of most PPD patients has never been investigated. This study aimed to understand the genetic mechanisms involved in the etiology of PPD I in a family with multiple affected members.

Methods: We recruited a PPD I family (PPD001) and used stepwise genetic analysis to determine the genetic etiology. In addition, for functional validation of the identified *GLIS1* variant, *in vitro* studies were conducted. *GLIS1* variants were further screened in additional 155 PPD cases.

Results: We identified a *GLIS1* variant (NM_147193: c.1061G > A, p.R354H) in the PPD001 family. *In vitro* studies showed that this variant decreased the nuclear translocation of GLIS1 and resulted in increased cell viability and migration. RNA sequencing revealed abnormal *TBX4* and *SFRP2* expression in 293T cells transfected with mutant GLIS1. Additionally, we identified a *GLIS1* variant (c.664G > A, p.D222N) in another PPD case.

Conclusion: We identified two *GLIS1* variants in PPD I patients and first linked *GLIS1* with PPD I. Our findings contributed to future molecular and clinical diagnosis of PPD and deepened our knowledge of this disease.

Keywords: Glis1, PPD I, SFPR2, stepwise genetic analysis, nuclear localization signal, preaxial polydactyly

OPEN ACCESS

Edited by:
Andrea Del Fattore, Bambino Gesù Children Hospital (IRCCS), Italy

Reviewed by:
Jianquan Chen, Soochow University, China
Anne-Gaelle Borycki, The University of Sheffield, United Kingdom

****Correspondence:***
Liang-Liang Fan
swfanliangliang@csu.edu.cn
Ju-Yu Tang
tangjuyu7749@163.com
Rong Xiang
shirlesmile@csu.edu.cn

Specialty section:
This article was submitted to Molecular and Cellular Pathology, a section of the journal Frontiers in Cell and Developmental Biology

Received: *22 September 2021*
Accepted: *02 December 2021*
Published: *11 January 2022*

Citation:
Jin J-Y, Wu P-F, Luo F-M, Guo B-B, Zeng L, Fan L-L, Tang J-Y and Xiang R (2022) GLIS Family Zinc Finger 1 was First Linked With Preaxial Polydactyly I in Humans by Stepwise Genetic Analysis. Front. Cell Dev. Biol. 9:781388. doi: 10.3389/fcell.2021.781388

INTRODUCTION

Preaxial polydactyly (PPD) is one of the most common developmental malformations, occurring in 0.8–1.4% of Asians (Evanson et al., 2016). PPD is phenotypically divided into four types: PPD I–IV, and PPD I (OMIM_174400) is the most common type in many populations (Handforth, 1950). PPD I is characterized by the duplication of one or more of the skeletal components of biphalangeal thumbs. The severity varies from a mere broadening of the distal phalanx with a slight bifurcation at

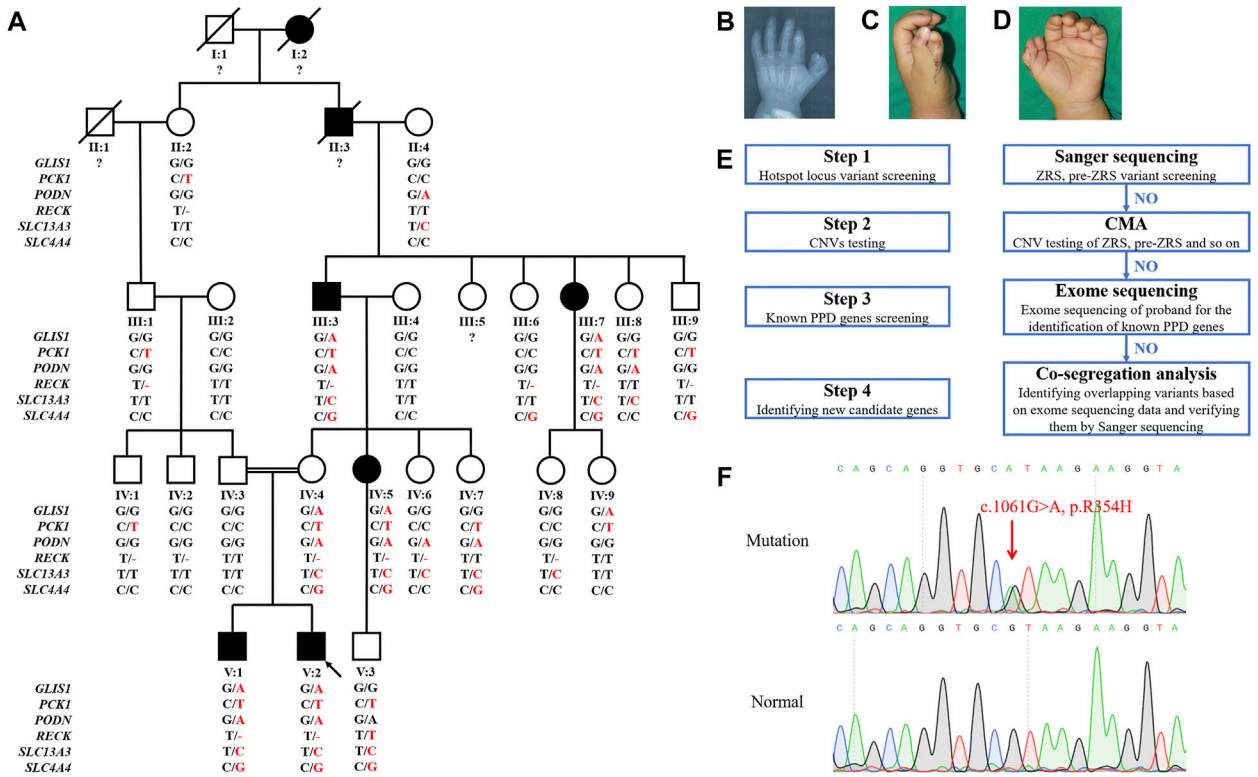

FIGURE 1 | Pedigree, symptoms, and stepwise genetic analysis of the PPD001 family. **(A)** Pedigree of PPD001 family with seven patients. The black symbols represent the affected members, and the arrow indicates the proband. Genotypes are identified by letters and a slash, with red letters representing variants. Question marks represent unknown data or symptoms. **(B–D)** The proband was affected by PPD I. **(E)** The stepwise genetic analysis strategy. **(F)** Sanger sequencing results of the *GLIS1* variant (c.1061G > A, p.R354H).

the tip to a full duplication of the thumb, including the metacarpals (Lange and Muller, 2017). Currently, six loci have been identified in nonsyndromic PPD cases, including *GLI1*, *GLI3*, *STKLD1*, the zone of polarizing activity (ZPA) regulatory region (ZRS), which is a limb-specific enhancer of *SHH* that is located within intron five of *LMBR1*, the pre-ZRS region (a noncoding evolutionary conserved sequence 500 bp upstream of the ZRS), and a deletion located 240 kb from the *SHH* promotor. Genetic etiologies in most PPD patients have never been evaluated (Petit et al., 2016; Potuijt et al., 2018; Ullah et al., 2019; Umair et al., 2019; Xu et al., 2020; Baas et al., 2021).

GLIS1 encodes GLIS family zinc finger protein 1, a transcriptional activator and repressor, though it primarily functions as a transcriptional activator. GLISs, together with GLIs and ZICs, constitute the Krüppel-like zinc finger family, which is characterized by classical Cys2-His2 zinc fingers (Lee et al., 2017). *In situ* hybridization of mouse embryos showed that Glis1 is expressed primarily in tissues with mesodermal lineages, including limb buds. Glis1 was first observed in the anterior-proximal mesenchyme during early limb bud development in mice (E9.5) and then extends along the entire apical ectodermal ridge (AER) at E11.5 (Kim et al., 2002). The expression pattern is similar to Gli3 expression, suggesting that Glis1 may play an important role in mouse limb patterning. However, Glis1 function in limb development remains ambiguous. In addition, GLIS1 is commonly used to generate human induced pluripotent stem cells (iPSCs), where GLIS1 can replace c-MYC and interact with OCT3/4, SOX2, and KLF4 to markedly enhance iPSC generation and promote multiple pro-reprogramming pathways, including NANOG, WNT, and the mesenchymal–epithelial transition (Maekawa et al., 2011). In breast cancers, GLIS1 and CUX1 cooperate to stimulate the WNT signaling pathway (Vadnais et al., 2014). *GLIS1* confers susceptibility to mitral valve prolapse (MVP). The single nucleotide polymorphism (SNP), rs1879734, which is located in the first intron of *GLIS1*, is specifically associated with MVP (Yu et al., 2019).

Thus far, no study has reported a correlation between *GLIS1* and PPD in humans. In this study, we identified a heterozygous missense variant in *GLIS1* (NM_147,193: c.1061G > A, p.R354H) responsible for PPD I in a large Chinese family by stepwise genetic analysis and functional verification. This correlation was verified in other PPD cases. In summary, our study was the first to link *GLIS1* variants with PPD and contributed to genetic

screening for PPD patients, thereby deepening our knowledge of PPD.

MATERIALS AND METHODS

Patients and Subjects

This research was approved by the Review Board of Xiangya Hospital of Central South University. We recruited a five-generation Chinese family (PPD001) with PPD I (**Figure 1A**). Additional 155 PPD families or sporadic cases were recruited to screen the candidate gene. Written informed consent was obtained from the patients and their guardians. Blood was collected from the probands and blood relations. Genomic DNA (gDNA) was extracted using DNeasy Blood & Tissue Kit (Qiagen).

Polymerase Chain Reaction and Sanger Sequencing

The sequences of ZRS regulatory region and pre-ZRS region were obtained from NCBI (https://www.ncbi.nlm.nih.gov/gene/105804841). Primers were designed by IDT (http://sg.idtdna.com/Primerquest/Home/Index) (**Supplementary Table S1**). Target sequences were amplified using polymerase chain reaction (PCR) and detected by Biosune Company Limited (Shanghai China).

Chromosomal Microarray Analysis

Chromosomal microarray analysis (CMA) was conducted in two affected individuals (V:1 and V:2 of the PPD001 family) as described by Jin et al. (2019), with slight modifications where necessary (Jin et al., 2019).

Exome Sequencing and Co-Segregated Analysis

Berry Genomics Company Limited (Chengdu, China) performed exome capture, high-throughput sequencing, and common filtering, as described previously (Jin et al., 2020). After filtering common variants (allele frequency >0.05) from the 1000G (https://www.genome.gov/27528684/1000-genomes-project/) and GnomAD (http://gnomad.broadinstitute.org), unique SNPs and insertions/deletions (indels) were identified. MutationTaster (http://www.mutationtaster.org/), PolyPhen-2 (http://genetics.bwh.harvard.edu/pph2/), and SIFT (http://provean.jcvi.org/index.php) were used to predict variant pathogenicity. Gene function, inheritance pattern, and clinical phenotype were annotated according to OMIM (https://www.omim.org). Pathogenicity was classified according to the American College of Medical Genetics classification (Richards et al., 2015).

Eight subjects of the PPD001 family (III:3–4, III:7, IV:3-5, and V:1–2) were subjected to exome sequencing. First, we screened unique SNPs that were predicted to be disease-causing. Then, we selected variants in patients (III:3, III:7, IV:5, V:1, and V:2) and IV:4, which were absent in III:4 and IV:3. We determined whether these overlapping variants were PPD causative or candidate genes (classical limb bud pattern-related genes). Finally, we selected variants that may be associated with PPD and conducted PCR and Sanger sequencing in all family members for co-segregation analysis.

Mutagenesis of GLIS1-1061G > A

pcDNA3.1-flag-GLIS1 plasmids were obtained from WZ Biosciences Inc. (Jinan, China). Mutagenesis of GLIS1-1061G > A (pcDNA3.1-flag-mGLIS1) was performed using Fast Mutagenesis Kit V2 (Vazyme). GLIS1 mutant and wild-type plasmids were validated using Sanger sequencing.

Cell Culture, Transfection, Transwell, and CCK8 Test

293T cells were obtained from the National Collection of Authenticated Cell Cultures. Cells were seeded in 6-well plates (5×10^5 cells per well) and transfected with pcDNA3.1-flag-GLIS1 vectors or pcDNA3.1-flag-mGLIS1 vectors (2 μg per well) using Lipofectamine 3,000 (Invitrogen) for 24 h, or seeded in 24-well plates (1×10^5 cells per well) with 0.4 μg vectors per well. Transwell assays using 3,000 cells were performed 24 h after transfection using transwell chambers (Costar). Five thousand transfected cells were seeded into a 96-well plate and cultured for 24 h. Then, CCK8 assays were performed using CCK-8 Cell Proliferation and Cytotoxicity Assay Kit (Solarbio).

Protein Extraction and Western Blot

Nuclear and cytosolic proteins from 293T cells were extracted using Nuclear Protein Extraction Kit (Solarbio). SDS-PAGE was performed using a 12.5% PAGE Gel Rapid Preparation Kit (Yeasen). Lysates were mixed with SDS-gel sample buffer and heated at 90°C for 10 min. Then, the protein samples were loaded onto the PAGE gels. After electrophoresis, the bands were electrophoretically transferred onto a nitrocellulose membrane. After blocking with 1% bovine serum albumin (BSA) in Tris-buffered saline, the membranes were incubated with anti-FLAG primary antibody (Proteintech, 20543-1-AP, 1:5,000), anti-GAPDH primary antibody (Proteintech, 10494-1-AP, 1:5,000), and anti-Histone-H3 polyclonal antibody (Proteintech, 17168-1-AP, 1:1,000). Chemiluminescent signals were scanned, and integrated density values were calculated with a chemiluminescent imaging system (Alpha Innotech).

Immunofluorescence

Immunofluorescence was performed on cells 48 h after transfection. Cells were fixed with 4% paraformaldehyde for 15 min and blocked in 5% BSA in PBS for 30 min at room temperature. The samples were permeabilized with Triton X-100 (0.15%) and incubated overnight at 4°C with anti-FLAG primary antibody (Proteintech, 20543-1-AP, 1:1,000) in PBS containing 5% BSA. The cells were then incubated with mouse Alexa 488-conjugated secondary antibody (Invitrogen, A-11094, 1:400) for 1 h at room temperature. Nuclei were stained with

TABLE 1 | Phenotypes of parts family members in PPD001 family.

Family member	I:2	II:3	III:3	III:7	IV:5	V:1	V:2	IV:4	IV:9
Gender	F	M	M	F	F	M	M	F	F
Age (years)	Unknown	73	57	51	28	8	3	32	23
Preaxial polydactyly	+	Left hand	Left hand	Left hand	Left hand	Left hand	Left hand	-	-
Triphalangeal thumb	Unknown	Unknown	-	-	-	-	-	-	-
Other phenotypes of upper lambs	Unknown	-	-	-	-	-	-	-	-
Lower limbs	-	-	-	-	-	-	-	-	-
Other	Unknown	Unknown	Hypertension	Diabetes	-	-	-	-	Arrhythmia

F, female; M, male; +, observed phenotype; -, no symptoms.

DAPI (Solarbio), and the cells were examined using Leica SP5 confocal microscope (Leica).

Total RNA Extraction, Transcriptome Sequencing, and Real-Time PCR

Total RNA was extracted from cells 24 h after transfection using RNA Extraction Kit (Qiagen) and stored at −80°C. Transcriptome sequencing was performed by Berry Genomics Company Limited using Illumina HiSeq 4,000 sequencing platform (Illumina). Genes with $p < 0.05$ and -1 < log2 fold change >1 were considered differentially expressed genes.

Total RNA was reverse transcribed using RevertAid First Strand cDNA Synthesis Kit (Thermo) and then subjected to real-time PCR by 2xSYBR Green qPCR Mix (Thermo).

Mutant Modeling

The GLIS1 protein structure (Q8NBF1) was downloaded from SWISS-MODEL database (https://swissmodel.expasy.org/). PyMol was used to build mutant models according to the wide-type structure.

Statistical Analysis

Statistical analyses were conducted using SPSS (version 18.0; IBM, Inc.). The data were first tested for normal distribution using the Kolmogorov-Smirnov test. Differences between groups were identified using Student's *t*-test or analysis of variance (ANOVA) if the data were normally distributed, and the Mann-Whitney *U* test or Kruskal-Wallis test was used for non-normally distributed data. Categorical data were compared using the chi-squared test.

RESULTS

Clinical Features of the Five-Generation PPD I Family

We identified a five-generation Chinese family with PPD I (PPD001, **Figure 1A**). The proband (V:2) was a 3-year-old boy, who was diagnosed with PPD I (**Figures 1B–D**). Tracing his family history, we found seven PPD I patients (including two deceased individuals) across five generations. All affected members (III:3, III:7, IV:5, V:1, and V:2) had PPD I (**Table 1**). No conspicuous phenotypes were observed in the fingers or toes of other subjects.

Genetic Analysis of the PPD001 Family

Stepwise strategies were used to identify the genetic etiology of the PPD001 family (**Figure 1E**). We screened variants in ZRS and pre-ZRS regions by Sanger sequencing, but did not detect variants in the proband. CMA results of the proband and his brother (V:1) showed an unfavorable copy number variation (CNV; **Supplementary Table S2**). Then, we conducted exome sequencing to detect known PPD-related genes in the proband, but did not identify variants in these genes, indicating that there was a novel gene variant causing PPD in this family.

To further identify pathogenic variants, we selected five affected (III:3, III:7, IV:5, V:1, and V:2) and three normal family members (III:4, IV:3, and IV:4) for exome sequencing. Based on the family pedigree, we hypothesized that PPD in this family was transmitted via autosomal dominant inheritance and that IV:4 was a carrier. Thus, we screened overlapping variants in several patients and IV:4. Finally, variants in six genes were identified (**Table 2**). After co-segregation of all subjects, a *GLIS1* variant (NM_147193: c.1061G > A, p.R354H) was retained (**Figures 1A,F**). Thus, we reasoned that the *GLIS1* variant could be the major etiological factor in this family.

Functional Analysis of the GLIS1 p.R354H Variant

Amino acid sequence alignment analysis showed that p.R354 in GLIS1 was highly conserved throughout evolution (**Figure 2A**). We used UniProtKB database (https://www.uniprot.org/uniprot/Q8NBF1) to predict that the variant p.R354H occurred in a bilateral nuclear localization signal (BNLS, **Figure 2B**). We hypothesized that the mutant BNLS hampered GLIS1 transportation to the nucleus and damaged GLIS1 function as a transcription factor. Wild-type GLIS1 plasmids (pcDNA-flag-GLIS1) were mutated into GLIS1-1061G > A plasmids (pcDNA-flag-mGLIS1, **Figure 2C**). Both wild-type and mutant plasmids were transfected into 293T cells. Subsequent immunofluorescence and Western blot analysis demonstrated that compared with wild-type, the mutant GLIS1 had increased cytoplasmic retention, which reduced its proportion in the

TABLE 2 | Overlapping variants identified in PPD001 family by WES.

Gene	Variant	Mutation taster	PolyPhen-2	SIFT	MUpro	GnomAD	OMIM clinical phenotype	American College of medical genetics classification
GLIS1	NM_147193: c.1061G > A, p.R354H	D	D/B	D	Decrease stability	0.00009	-	Likely pathogenic (PS3, PP1, PP3, PP5)
PCK1	NM_002591: c. 1576C > T, p.L526F	D	D/D	D	Decrease stability	0.00005	AR, Phosphoenolpyruvate carboxykinase deficiency, cytosolic	Uncertain significance (PP3, PP5, BS4)
PODN	NM_001199080: c.781G > A, p.V261M	D	D/D	T	Decrease stability	0.00001	-	Uncertain significance (PP3, PP5, BS4)
RECK	NM_021111: c.789delT, p.C263fs	D	–/–	-	-	-	-	Uncertain significance (PM2, PP3, PP5, BS4)
SLC13A3	NM_022829: c.857T > C, p.M286T	D	D/D	D	Decrease stability	0.00011	AR, Leukoencephalopathy, acute reversible, with increased urinary alpha-ketoglutarate	Uncertain significance (PP3, PP5, BS4)
SLC4A4	NM_003759: c.1435C > G, p.L479V	D	D/D	D	Mildly decrease stability	-	AR, Renal tubular acidosis, proximal, with ocular abnormalities	Uncertain significance (PM2, PP3, PP5)

D, disease causing; T, tolerated; B, benign; AR, autosomal recessive.
PolyPhen-2, results showed the prediction of HumDiv and HumVar in turn.

nucleus (**Figures 2D,E**). CCK8 and transwell assays showed that mutant GLIS1 promoted cell viability and migration (**Figures 2F,G**). Transcriptome sequencing data showed abnormal *TBX4* and *SFRP2* expression in 293T cells expressing mutant GLIS1, and these results were verified by real-time PCR (**Figures 2I,J**). TBX4 and SFRP2 play important roles in limb development(Ikegawa et al., 2008; Jain et al., 2018). Furthermore, p.R354H also led to alterations in the expression of other 237 genes, including *BMP3*, *BMPER*, *PCDHB15*, *WISP1*, *HOXD1*, and *FGF3* (**Figures 2I,K**). Thus, we confirmed that the *GLIS1* variant decreased nuclear translocation, resulting in an increase in cell viability and migration.

Screening GLIS1 Variants in Sporadic or Familial Cases

We recruited additional 155 sporadic or familial cases with PPD to further verify the correlation between *GLIS1* variants and PPD. Two *GLIS1* variants (c.449C > T, p.A150V and c.664G > A, p.D222N) were identified in two PPD families (PPD087 and PPD141; **Figures 3A–D**; **Table 3**). The variant (c.449C > T, p.A150V) was identified in two patients of the PPD087 family, with a minor allele frequency (MAF) of 0.00043. p.A150 was highly conserved and located in zinc finger domains (ZFDs), but bioinformatics analysis predicted that p.A150V was benign (**Figures 3E,F**; **Table 3**). Thus, it was considered a polymorphism. The variant (c.664G > A, p.D222N) arose *de novo* and was detected in a baby with PPD I that was conceived *in vitro*. The variant was predicted to be disease-causing (**Table 3**). p.D222 was located in ZFDs with high evolutionary conservation (**Figures 3E,F**). According to three-dimensional modeling of GLIS1 protein, p.D222N caused surface charge modifications that may impact the ability to bind target DNA sequences (**Figure 3G**). We reasoned that the *GLIS1* variant (c.664G > A, p.D222N) may be the genetic etiology in the PPD141 family, and *GLIS1* may be a novel causative gene of PPD I.

DISCUSSION

PPD I is a frequent developmental defect worldwide, while disease-causing variants have only been identified in a few patients (Ullah et al., 2019; Umair et al., 2019; Xu et al., 2020). Genetic etiologies of most cases remain to be studied. In this study, we aimed to understand the genetic mechanisms involved in the etiology of PPD I in the PPD001 family through stepwise genetic analysis, a classic variant screening strategy. Six variants in six genes were detected, including *GLIS1*, *PCK1*, *PODN*, *RECK*, *SLC13A3*, and *SLC4A4*. The *PODN* and *SLC13A3* variants were derived from II:4. II:2 and her normal descendants (III:1, IV:1, and IV:2) harbored the *PCK1* and *RECK* variants, but these individuals did not have limb malformations. Thus, we excluded these four candidate genes from the analysis. Moreover, five members (III:6, III:9, IV:4, IV:7, and V:3) presented with a heterozygous variant of *SLC4A4*, which is responsible for isolated proximal renal tubular acidosis, an autosomal recessive disease (Igarashi et al., 1999). In contrast, only two normal members carried the *GLIS1* variant (c.1061G > A, p.R354H). Given that PPD is associated with environmental effects, gender differences, and genetic factors, we speculated that the *GLIS1* variant carriers without PPD (IV:4 and IV:9) may be due to individual differences, the lower possibility of PPD in females, and the variant being the main cause of PPD rather than the only cause. Hence, we determined that the *GLIS1* variant was more likely to cause PPD in this family. Subsequent genetic screening in 155 cases further verified that *GLIS1* was associated with PPD.

GLIS1 contains a DNA-binding domain (DBD) consisting of five Cys2-His2 ZFDs, a BNLS, and a transcription activation

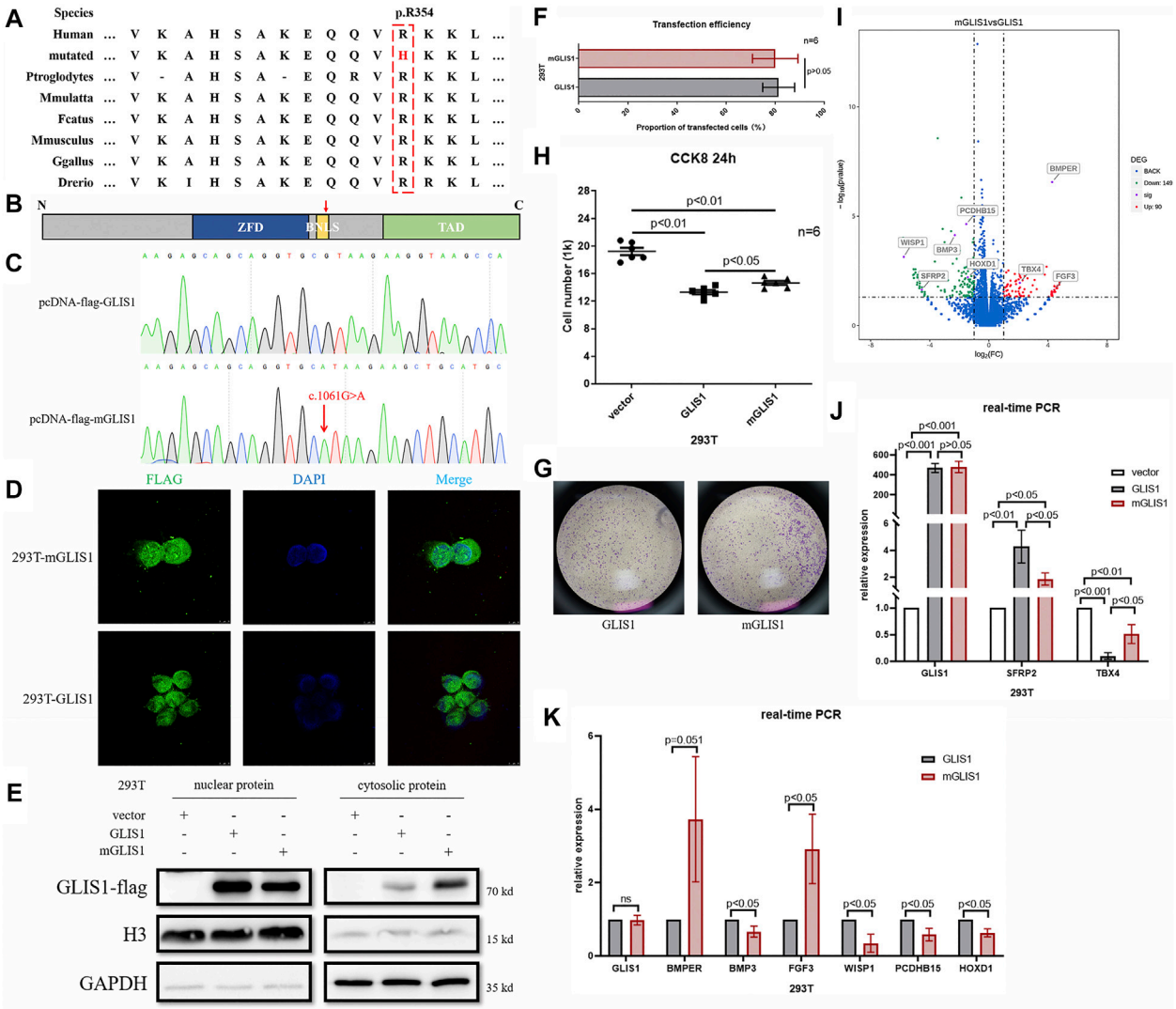

FIGURE 2 | Functional analysis of variant p.R354H *in vitro*. **(A)** Species conservation analysis of the mutant amino acid of GLIS1. **(B)** Schematic diagram of GLIS1 structure. Red arrow indicates variant p.R354H. **(C)** Sequencing results of GLIS1-1061G > A mutagenesis plasmids. **(D)** Immunofluorescence results demonstrating that mutant GLIS1 had increased cytoplasmic retention and reduced the proportion of nuclear protein. **(E)** Western blot showed that compared with wild-type, nuclear protein of the mutant GLIS1 was reduced, and cytosolic protein was increased. **(F)** The transfection efficiency of GLIS1/mGLIS1 plasmids in 293T cells. **(G, H)** CCK8 and transwell results showing that mutant GLIS1 promoted cell viability and migration. "$p < 0.05$" presents data with statistical significance, "$p > 0.05$" presents data without statistical significance, and "n" represents the number of cell samples. **(I)** A volcano plot based on RNA sequencing data. **(J, K)** Validation of RNA sequencing data by the real-time PCR. "$p < 0.05$" presents data with statistical significance, and "$p > 0.05$" presents data without statistical significance.

domain (TAD) (Jetten, 2018). Variant p.R354H was located in the BNLS and affected GLIS1 translocation to nucleus, causing cytoplasmic retention. We speculated that p.R354H may decrease GLIS1 nuclear translocation efficiency and may impede GLIS1 function as a transcription factor. Variant p.D222N occurred in ZFDs and caused the substitution of an acidic amino acid with a basic residue. Based on the three-dimensional modeling results, the variant would change surface charge, which may affect the capacity of DNA binding.

GLIS1 is a regulator of mesenchymal multipotency *in vitro* and plays a crucial role in cell reprogramming (Scoville et al., 2017; Gerard et al., 2019). Several studies showed that GLIS1 acted on multipotent stem cells. In mouse embryos, GLIS1 is expressed primarily in the mesodermal lineages, including craniofacial regions, branchial arches, myotomes, and limb buds (Kim et al., 2002). We hypothesized that GLIS1 participated in the development of mesoblast-derived embryonic structures. PPD occurrence is accompanied by an increase in cell proliferation and migration in the anterior-proximal region of limb buds (Crick et al., 2003). Variants in *GLI3* and ZRS cause PPD by inducing the anterior ectopic expression of SHH (Deng et al., 2015; Xu et al., 2020). SHH promotes cell proliferation and migration *in vivo* and *in vitro* (Hayes et al., 2001; Wang et al., 2019). We confirmed increased 293T cell viability and migration after transfection with

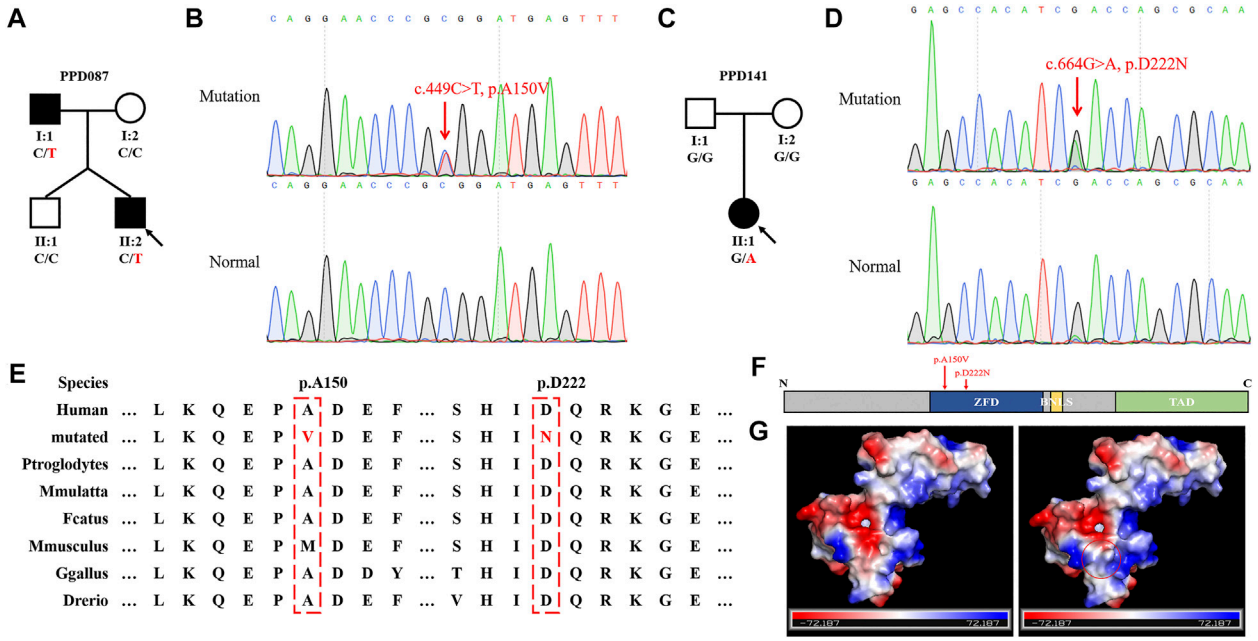

FIGURE 3 | *GLIS1* variants identified in PPD I cases. **(A, C)** Pedigrees of PPD I families. The black symbols represent affected members, and the arrow indicates the proband. Genotypes are identified by letters and a slash, with red representing variants. **(B, D)** Sanger sequencing results of *GLIS1* variants. **(E)** Species conservation analysis of mutant amino acid sites of GLIS1. **(F)** Schematic diagram of GLIS1 structure. The red arrows indicate variants. **(G)** Protein models of GLIS1 with or without the variant (p.D222N). The red circle indicates the variant site.

TABLE 3 | Phenotypes and genotypes of PPD patients with *GLIS1* (NM_147193) variants.

Patient	Phenotype	*GLIS1* variant	MutationTaster	PolyPhen-2	SIFT	MUpro	GnomAD	American college of medical genetics classification
PPD087-I:1 PPD087-II:2	PPD I on the right hand Bilateral PPD I	c.449C > T, p.A150V	P	B/B	T	Decrease stability	0.00043	Uncertain significance (PP1, BP4)
PPD141-II:1	PPD I on the right hand	c.664G > A, p.D222N	D	D/B	D	Decrease stability	0.00000	Likely pathogenic (PS2, PM2, PP3)

PPD I, preaxial polydactyly type I; D, disease causing; T, tolerated; P, polymorphism; B, benign.
PolyPhen-2, results showed the prediction of HumDiv and HumVar in turn.

the variant p.R354H. However, we did not observe SHH overexpression. Additionally, there is no report on the correlation between GLIS1 and SHH. We speculated that GLIS1 may be downstream of SHH, analogous to GLI1 and SFRP2; however, this hypothesis should be further validated (Ikegawa et al., 2008; Jeon and Seong, 2016). Sfrp2 inactivation can inhibit apoptosis in the central interdigital spaces of mice (Ikegawa et al., 2008). Decreased SFRP2 expression induced by mutant GLIS1 may better protect cells from apoptosis and may be responsible for increased cell viability in mGLIS1 293T cells.

GLIS1, GLIS2, and GLIS3 constitute a subfamily of Krüppel-like zinc finger proteins (Kang et al., 2010). As transcription factors, GLISs interact with target genes with GLIS-binding sites (GLISBS). GLISBS is a G-rich DNA sequence, (G/C)TGGGGG(A/C). The GLI and ZIC binding sites are G-rich DNA response elements similar to GLISBS (Jetten, 2018). In fact, ZFDs are highly homologous among GLISs and GLIs (Kang et al., 2010). Therefore, GLISs, GLIs, and ZICs might compete for these binding sites. For example, GLIS2 can compete with GLI1 for the same binding site as *WNT4*, making antagonistic action against GLI1 (Vasanth et al., 2011). Moreover, these Krüppel-like zinc finger proteins might interact and form heterodimers, such as the GLI and ZIC subfamilies (Koyabu et al., 2001). We speculated that GLIS1 can interact with GLIs or act on genes activated by GLIs during limb development. GLIs are downstream proteins of SHH in SHH signaling pathway and deeply involve in finger developments.

SFRP2, a known SHH/GLIs target gene, was downregulated in 293T cells with mutant GLIS1 (p.R354H), hinting at the effect of GLIS1 on the SHH/GLIs signaling pathway (Milla et al., 2012). A single *Sfrp2* deletion triggered syndactyly and preaxial synpolydactyly in mice, and a loss of Sfrp2 function resulted in brachy-syndactyly in mice through the Wnt signaling pathway (Ikegawa et al., 2008; Morello et al., 2008). The *GLIS1* variants (c.1061G > A, p.R354H; c.664G > A, p.D222N) identified in the present study may lead to PPD by downregulating SFRP2, although there is no report about GLIS1 regulating SFPR2.

In cancers and during cellular reprogramming, GLIS1 activates the WNT signaling pathway, especially several WNTs (Maekawa et al., 2011). In this study, mutant GLIS1 upregulated BMPER, TBX4, and FGF3, while downregulating PCDHB15, BMP3, WISP1, and HOXD1. Tbx4 triggers the initiation of vertebrate limb development through activation of the Wnt/Fgf signaling cascade (Takeuchi et al., 2003). PCDHB15, WISP1, and FGF3 are involved in the WNT or FGF signaling pathways (Wong et al., 2020). BMPER regulates BMP2/4, and BMP3 antagonizes BMP2 to induce osteoprogenitor differentiation and ossification (Daluiski et al., 2001; Moser et al., 2003). BMP2 is crucial for finger outgrowth, and its variants lead to finger deformities (Dathe et al., 2009). Although WNTs did not show prominent differences in our RNA sequencing data, the expression of many WNT signaling pathway-related genes was altered in 293T cells with mutant GLIS1. This may be because different cell lines have distinct expression profiles and GLIS1 target genes may be variable in different cell lines.

In this study, we detected *GLIS1* variants only in two PPD I families (PPD001 family and PPD141 family). There was no evidence of a correlation between *GLIS1* and other PPD types, though this conclusion required further study. The PPD001 family followed an incomplete autosomal dominant inheritance pattern, in which two *GLIS1* variant carriers (IV:4 and IV:9) had no apparent limb malformations. These findings suggested that genetic factors acted in concert with environmental effects. Genome-wide association studies (GWAS) had identified *GLIS1* as a susceptibility gene for MVP, but none of carriers with GLIS1 variants in this study had MVP (Yu et al., 2019).

CONCLUSION

In summary, we first associated *GLIS1* with PPD I in humans by stepwise genetic analysis and examined the pathogenic potential of *GLIS1* variants (c.1061G > A, p.R354H; c.664G > A, p.D222N) *in vitro* or by three-dimensional modeling. There are only a few known causative genes or enhancers of PPD in humans, and our research further helped us understand this disease and contributed to future molecular and clinical diagnosis of PPD. Further study should be performed to determine the potential mechanism by which GLIS1 defects cause PPD, which will be beneficial for future treatments. Given that Sfrp2 deletion is associated with limb defects in mice, and that our *in vitro* experiments suggested that GLIS1 can mediate SFRP2, we hypothesized that GLIS1 upregulated SFRP2 expression. Our findings hinted that GLIS1 defects may trigger reduction in SFRP2 levels to lead to PPD.

DATA AVAILABILITY STATEMENT

The original contributions presented in the study are included in the article/**Supplementary Material**. Further inquiries can be directed to the corresponding authors.

ETHICS STATEMENT

The studies involving human participants were reviewed and approved by the Review Board of Xiangya Hospital of the Central South University. Written informed consent to participate in this study was provided by the participants' legal guardian/next of kin.

AUTHOR CONTRIBUTIONS

JY contributed to sequencing analysis and functional verification. PW contributed to recruiting samples and collecting clinical phenotypes. LF contributed to sequencing analysis. BG contributed to variant interpretation and analysis. ZL contributed to recruiting samples and collecting clinical phenotypes. FL contributed to designing experiments and writing original draft. JT contributed to designing experiments, raising the idea of the project, and reviewing and editing the draft. RX contributed to supervision, project administration, and reviewing and editing the draft.

FUNDING

This work was supported by the National Science and Technology Major Project of the Ministry of Science and Technology of China (2017ZX10103005-006), The National Natural Science Foundation of China (81970403, 82000427, 82170598,and 82102527), Natural Science Foundation of Hunan province (2020JJ5785), The Fundamental Research Funds for the Central Universities of Hunan Province (CX20190104), and The Emergency Project of Prevention and Control for COVID-19 of Central South University (160260003).

ACKNOWLEDGMENTS

We thank the patients and their family members for their participation in this study and all patient advisers for their assistance in clinical examination and blood specimen collection.

SUPPLEMENTARY MATERIAL

The Supplementary Material for this article can be found online at: https://www.frontiersin.org/articles/10.3389/fcell.2021.781388/full#supplementary-material

REFERENCES

Baas, M., Burger, E. B., van den Ouweland, A. M., Hovius, S. E., de Klein, A., van Nieuwenhoven, C. A., et al. (2021). Variant Type and Position Predict Two Distinct Limb Phenotypes in Patients with GLI3-Mediated Polydactyly Syndromes. *J. Med. Genet.* 58 (6), 362–368. doi:10.1136/jmedgenet-2020-106948

Crick, A. P., Babbs, C., Brown, J. M., and Morriss-Kay, G. M. (2003). Developmental Mechanisms Underlying Polydactyly in the Mouse Mutant Doublefoot. *J. Anat.* 202 (1), 21–26. doi:10.1046/j.1469-7580.2003.00132.x

Daluiski, A., Engstrand, T., Bahamonde, M. E., Gamer, L. W., Agius, E., Stevenson, S. L., et al. (2001). Bone Morphogenetic Protein-3 Is a Negative Regulator of Bone Density. *Nat. Genet.* 27 (1), 84–88. doi:10.1038/83810

Dathe, K., Kjaer, K. W., Brehm, A., Meinecke, P., Nürnberg, P., Neto, J. C., et al. (2009). Duplications Involving a Conserved Regulatory Element Downstream of BMP2 Are Associated with Brachydactyly Type A2. *Am. J. Hum. Genet.* 84 (4), 483–492. doi:10.1016/j.ajhg.2009.03.001

Deng, H., Tan, T., and Yuan, L. (2015). Advances in the Molecular Genetics of Non-syndromic Polydactyly. *Expert Rev. Mol. Med.* 17, e18. doi:10.1017/erm.2015.18

Evanson, B. J., Hosseinzadeh, P., Riley, S. A., and Burgess, R. C. (2016). Radial Polydactyly and the Incidence of Reoperation Using A New Classification System. *J. Pediatr. Orthop.* 36 (2), 158–160. doi:10.1097/BPO.0000000000000395

Gérard, D., Schmidt, F., Ginolhac, A., Schmitz, M., Halder, R., Ebert, P., et al. (2019). Temporal Enhancer Profiling of Parallel Lineages Identifies AHR and GLIS1 as Regulators of Mesenchymal Multipotency. *Nucleic Acids Res.* 47 (3), 1141–1163. doi:10.1093/nar/gky1240

Handforth, J. R. (1950). Polydactylism of the Hand in Southern Chinese. *Anat. Rec.* 106 (2), 119–125. doi:10.1002/ar.1091060202

Hayes, C., Rump, A., Cadman, M. R., Harrison, M., Evans, E. P., Lyon, M. F., et al. (2001). A High-Resolution Genetic, Physical, and Comparative Gene Map of the Doublefoot (Dbf) Region of Mouse Chromosome 1 and the Region of Conserved Synteny on Human Chromosome 2q35. *Genomics* 78 (3), 197–205. doi:10.1006/geno.2001.6657

Igarashi, T., Inatomi, J., Sekine, T., Cha, S. H., Kanai, Y., Kunimi, M., et al. (1999). Mutations in SLC4A4 Cause Permanent Isolated Proximal Renal Tubular Acidosis with Ocular Abnormalities. *Nat. Genet.* 23 (3), 264–266. doi:10.1038/15440

Ikegawa, M., Han, H., Okamoto, A., Matsui, R., Tanaka, M., Omi, N., et al. (2008). Syndactyly and Preaxial Synpolydactyly in the singleSfrp2deleted Mutant Mice. *Dev. Dyn.* 237 (9), 2506–2517. doi:10.1002/dvdy.21655

Jain, D., Nemec, S., Luxey, M., Gauthier, Y., Bemmo, A., Balsalobre, A., et al. (2018). Regulatory Integration of Hox Factor Activity with Tbox Factors in Limb Development. *Development* 145 (6). doi:10.1242/dev.159830

Jeon, S., and Seong, R. H. (2016). Anteroposterior Limb Skeletal Patterning Requires the Bifunctional Action of SWI/SNF Chromatin Remodeling Complex in Hedgehog Pathway. *Plos Genet.* 12 (3), e1005915. doi:10.1371/journal.pgen.1005915

Jetten, A. M. (2018). GLIS1-3 Transcription Factors: Critical Roles in the Regulation of Multiple Physiological Processes and Diseases. *Cell. Mol. Life Sci.* 75 (19), 3473–3494. doi:10.1007/s00018-018-2841-9

Jin, J.-Y., Wu, P.-F., He, J.-Q., Fan, L.-L., Yuan, Z.-Z., Pang, X.-Y., et al. (2020). Novel Compound Heterozygous DST Variants Causing Hereditary Sensory and Autonomic Neuropathies VI in Twins of a Chinese Family. *Front. Genet.* 11, 492. doi:10.3389/fgene.2020.00492

Jin, J. Y., Zeng, L., Li, K., He, J. Q., Pang, X., Huang, H., et al. (2019). A Novel Mutation (c.1010G>T; p.R337L) in TP63 as a Cause of Split-hand/foot Malformation with Hypodontia. *J. Gene Med.* 21 (10), e3122. doi:10.1002/jgm.3122

Kang, H. S., ZeRuth, G., Lichti-Kaiser, K., Vasanth, S., Yin, Z., Kim, Y. S., et al. (2010). Gli-similar (Glis) Krüppel-like Zinc finger Proteins: Insights into Their Physiological Functions and Critical Roles in Neonatal Diabetes and Cystic Renal Disease. *Histol. Histopathol* 25 (11), 1481–1496. doi:10.14670/HH-25.1481

Kim, Y.-S., Lewandoski, M., Perantoni, A. O., Kurebayashi, S., Nakanishi, G., and Jetten, A. M. (2002). Identification of Glis1, a Novel Gli-Related, Krüppel-like Zinc Finger Protein Containing Transactivation and Repressor Functions. *J. Biol. Chem.* 277 (34), 30901–30913. doi:10.1074/jbc.M203563200

Koyabu, Y., Nakata, K., Mizugishi, K., Aruga, J., and Mikoshiba, K. (2001). Physical and Functional Interactions between Zic and Gli Proteins. *J. Biol. Chem.* 276 (10), 6889–6892. doi:10.1074/jbc.C000773200

Lange, A., and Müller, G. B. (2017). Polydactyly in Development, Inheritance, and Evolution. *Q. Rev. Biol.* 92 (1), 1–38. doi:10.1086/690841

Lee, S.-Y., Noh, H. B., Kim, H.-T., Lee, K.-I., and Hwang, D.-Y. (2017). Glis Family Proteins Are Differentially Implicated in the Cellular Reprogramming of Human Somatic Cells. *Oncotarget* 8 (44), 77041–77049. doi:10.18632/oncotarget.20334

Maekawa, M., Yamaguchi, K., Nakamura, T., Shibukawa, R., Kodanaka, I., Ichisaka, T., et al. (2011). Direct Reprogramming of Somatic Cells Is Promoted by Maternal Transcription Factor Glis1. *Nature* 474 (7350), 225–229. doi:10.1038/nature10106

Milla, L. A., Cortés, C. R., Hodar Q, C., Oñate, M. G., Cambiazo, V., Burgess, S. M., et al. (2012). Yeast-based Assay Identifies Novel Shh/Gli Target Genes in Vertebrate Development. *BMC Genomics* 13, 2. doi:10.1186/1471-2164-13-2

Morello, R., Bertin, T. K., Schlaubitz, S., Shaw, C. A., Kakuru, S., Munivez, E., et al. (2008). Brachy-syndactyly Caused by Loss ofSfrp2function. *J. Cel. Physiol.* 217 (1), 127–137. doi:10.1002/jcp.21483

Moser, M., Binder, O., Wu, Y., Aitsebaomo, J., Ren, R., Bode, C., et al. (2003). BMPER, a Novel Endothelial Cell Precursor-Derived Protein, Antagonizes Bone Morphogenetic Protein Signaling and Endothelial Cell Differentiation. *Mol. Cel Biol* 23 (16), 5664–5679. doi:10.1128/MCB.23.16.5664-5679.2003

Petit, F., Jourdain, A.-S., Holder-Espinasse, M., Keren, B., Andrieux, J., Duterque-Coquillaud, M., et al. (2016). The Disruption of a Novel Limb Cis-Regulatory Element of SHH Is Associated with Autosomal Dominant Preaxial Polydactyly-Hypertrichosis. *Eur. J. Hum. Genet.* 24 (1), 37–43. doi:10.1038/ejhg.2015.53

Potuijt, J. W. P., Baas, M., Sukenik-Halevy, R., Douben, H., Nguyen, P., Venter, D. J., et al. (2018). A point Mutation in the Pre-ZRS Disrupts Sonic Hedgehog Expression in the Limb Bud and Results in Triphalangeal Thumb-Polysyndactyly Syndrome. *Genet. Med.* 20 (11), 1405–1413. doi:10.1038/gim.2018.18

Richards, S., Aziz, N., Bale, S., Bick, D., Das, S., Gastier-Foster, J., et al. (2015). Standards and Guidelines for the Interpretation of Sequence Variants: a Joint Consensus Recommendation of the American College of Medical Genetics and Genomics and the Association for Molecular Pathology. *Genet. Med.* 17 (5), 405–424. doi:10.1038/gim.2015.30

Scoville, D. W., Kang, H. S., and Jetten, A. M. (2017). GLIS1-3: Emerging Roles in Reprogramming, Stem and Progenitor Cell Differentiation and Maintenance. *Stem Cel Investig.* 4, 80. doi:10.21037/sci.2017.09.01

Takeuchi, J. K., Koshiba-Takeuchi, K., Suzuki, T., Kamimura, M., Ogura, K., and Ogura, T. (2003). Tbx5 and Tbx4 Trigger Limb Initiation through Activation of the Wnt/Fgf Signaling cascade. *Development* 130 (12), 2729–2739. doi:10.1242/dev.00474

Ullah, A., Umair, M., Majeed, A. I., AbdullahJan, A., Jan, A., and Ahmad, W. (2019). A Novel Homozygous Sequence Variant in GLI1 Underlies First Case of Autosomal Recessive Pre-axial Polydactyly. *Clin. Genet.* 95 (4), 540–541. doi:10.1111/cge.13495

Umair, M., Bilal, M., Ali, R. H., Alhaddad, B., Ahmad, F., Abdullah, et al. (2019). Whole-exome Sequencing Revealed a Nonsense Mutation in STKLD1 Causing Non-syndromic Pre-axial Polydactyly Type A Affecting Only Upper Limb. *Clin. Genet.* 96 (2), 134–139. doi:10.1111/cge.13547

Vadnais, C., Shooshtarizadeh, P., Rajadurai, C. V., Lesurf, R., Hulea, L., Davoudi, S., et al. (2014). Autocrine Activation of the Wnt/β-Catenin Pathway by CUX1 and GLIS1 in Breast Cancers. *Biol. Open* 3 (10), 937–946. doi:10.1242/bio.20148193

Vasanth, S., ZeRuth, G., Kang, H. S., and Jetten, A. M. (2011). Identification of Nuclear Localization, DNA Binding, and Transactivating Mechanisms of Krüppel-like Zinc Finger Protein Gli-Similar 2 (Glis2). *J. Biol. Chem.* 286 (6), 4749–4759. doi:10.1074/jbc.M110.165951

Wang, X.-Z., Zhang, H.-H., Qian, Y.-L., and Tang, L.-F. (2019). Sonic Hedgehog (Shh) and CC Chemokine Ligand 2 Signaling Pathways in Asthma. *J. Chin. Med. Assoc.* 82 (5), 343–350. doi:10.1097/JCMA.0000000000000094

Wong, C. C., Xu, J., Bian, X., Wu, J.-L., Kang, W., Qian, Y., et al. (2020). In Colorectal Cancer Cells with Mutant KRAS, SLC25A22-Mediated Glutaminolysis Reduces DNA Demethylation to Increase WNT Signaling, Stemness, and Drug Resistance. *Gastroenterology* 159 (6), 2163–2180. doi:10.1053/j.gastro.2020.08.016

Xu, C., Yang, X., Zhou, H., Li, Y., Xing, C., Zhou, T., et al. (2020). A Novel ZRS Variant Causes Preaxial Polydactyly Type I by Increased Sonic Hedgehog Expression in the Developing Limb Bud. *Genet. Med.* 22 (1), 189–198. doi:10.1038/s41436-019-0626-7

Yu, M., Georges, A., Tucker, N. R., Kyryachenko, S., Toomer, K., Schott, J.-J., et al. (2019). Genome-Wide Association Study-Driven Gene-Set Analyses, Genetic, and Functional Follow-Up Suggest GLIS1 as a Susceptibility Gene for Mitral Valve Prolapse. *Circ. Genomic Precision Med.* 12 (5), e002497. doi:10.1161/CIRCGEN.119.002497

Conflict of Interest: The authors declare that the research was conducted in the absence of any commercial or financial relationships that could be construed as a potential conflict of interest.

frontiers in Cell and Developmental Biology

ORIGINAL RESEARCH
published: 16 March 2022
doi: 10.3389/fcell.2022.802635

Whole-Exome Sequencing Identifies a Novel *CPT2* Mutation in a Pedigree With Gout

Yong Guo[1†], Jing Jin[2†], Zhenni Zhou[3], Yihui Chen[4], Li Sun[5†], Chunwu Zhang[6†] and Xiaoru Xia[5]*

[1]Department of Urology, The First Affiliated Hospital of Wenzhou Medical University, Wenzhou, China, [2]Zhejiang Center for Clinical Laboratory, Zhejiang Provincial People's Hospital, Affiliated People's Hospital, Hangzhou Medical College, Hangzhou, China, [3]Department of Internal Medicine, Yueqing People's Hospital, Yueqing, Wenzhou, China, [4]Wenzhou Medical University, Wenzhou, China, [5]Department of Rheumatology, The First Affiliated Hospital of Wenzhou Medical University, Wenzhou, China, [6]Department of Injury Orthopaedics, The First Affiliated Hospital of Wenzhou Medical University, Wenzhou, China

Background: Gout is a common inflammatory arthritis, and its exact pathogenesis remains unclear. Multiple studies have demonstrated that genetic factors play important roles in the development of gout. This study aims to investigate the genetic basis of gout in a three-generation pedigree of affected individuals.

Methods: Whole-exome sequencing (WES), comprehensive variant analyses, and co-segregation testing were performed. The effects of candidate variants on protein localization and cellular expression were analyzed, as were interactions with gout-related genes.

Results: After comprehensive bioinformatic analysis, Sanger sequencing validation, and pedigree co-segregation analysis, we identified a rare heterozygous missense variant (c.1891C > T, p.R631C) in *CPT2*. Although no associated changes in localization were observed, the fluorescence intensity of p.R631C mutants was obviously reduced in comparison to the wild-type protein, suggesting that protein degradation is induced by the mutant. Furthermore, our results also indicate that the c.1891C > T variant influences the ability of CPT2 to bind UCP2.

Conclusion: This study identified a rare *CPT2* mutation in a large Chinese pedigree with gout. Functional studies were used to define the effect of this mutant. This study provides novel insight into the genetic etiology of gout.

Keywords: whole-exome sequencing, novel mutation, gout, CPT2 gene, pedigree

OPEN ACCESS

Edited by:
Amélie E. Coudert, Université Paris Diderot, France

Reviewed by:
Hae Jeong Park, Kyung Hee University, South Korea
Miles Douglas Thompson, University of California, San Diego, United States

***Correspondence:**
Xiaoru Xia
xxr7799@163.com

[†]*These authors have contributed equally to this work*

Specialty section:
This article was submitted to Molecular and Cellular Pathology, a section of the journal Frontiers in Cell and Developmental Biology

Received: *27 October 2021*
Accepted: *31 January 2022*
Published: *16 March 2022*

Citation:
Guo Y, Jin J, Zhou Z, Chen Y, Sun L, Zhang C and Xia X (2022) Whole-Exome Sequencing Identifies a Novel CPT2 Mutation in a Pedigree With Gout. Front. Cell Dev. Biol. 10:802635. doi: 10.3389/fcell.2022.802635

INTRODUCTION

Gout is a common inflammatory arthritis caused by the deposition of monosodium urate crystals in and around the joints following longstanding hyperuricaemia (Richette and Bardin, 2010). As the aging population grows, the global burden of gout continues to rise. Although the exact pathogenesis of gout remains unclear, rapid expansion in our knowledge of genetic factors over recent years has expanded our understanding of its etiology (Major et al., 2018). Evidence from genome-wide association studies (GWAS) has demonstrated important roles for a genetic basis of gout. Multiple genetic loci have been reported to be associated with gout, including *ABCG2*, *ALDH16A1*, *ATXN2*,

TABLE 1 | Clinical information and genotypes

Individual ID	Gender	Age	Genotypes	Uric acid (mg/L)	Hyperuricemia (+/–)	Arthritis	Tophi	Comorbidity				
								Hyper tension	Hyper lipermia	Hyper glycemia	Obesity (BMI)	Hyper bilirubinaemia
II:1	M	67	+/–	617	+	+	+	+	-	-	+	+
II:2	F	62	–/–	347	-	-	-	+	+	+	+	N/A
II:3	M	64	+/–	474	+	+	-	+	-	-	+	-
II:4	F	60	–/–	N/A	-	-	-	-	N/A	N/A	-	N/A
II:5	M	57	+/–	472	+/–	-	-	+	-	+	+	-
II:7	M	51	+/–	580	+	+	+	+	-	-	+	+
II:8	F	47	–/–	350	-	-	-	-	N/A	-	+	N/A
II:11	F	68	–/–	364	-	-	-	-	-	-	+	-
III:3	F	36	+/–	451	+	+	-	-	-	-	-	-
III:5	M	25	–/–	378	-	-	-	-	-	-	-	-
III:6	M	34	+/–	610	+	+	-	-	-	-	+	-
III:9	M	33	–/–	325	-	-	-	-	-	-	-	-
III:11	M	45	–/–	249	-	-	-	-	-	-	-	+

BCAS3, *CUX2*, *GCKR*, *KCNQ1*, *PDZK1*, *RFX3*, and *SLC2A9* (Sulem et al., 2011; Köttgen et al., 2013; Li et al., 2015a; Matsuo et al., 2016; Phipps-Green et al., 2016; Nakayama et al., 2017). Of note, previous GWAS studies were insufficient to report associations between rare variants and gout, due to methodological limitations.

Whole-exome sequencing (WES) has proven to be a powerful tool for discovering rare mutations, and this approach has been successfully applied to a wide range of disorders (Huang et al., 2018; Huang et al., 2019). However, only a few reports have been made concerning patients with gout. Recently, our group performed WES in a pedigree with early-onset gout (Huang et al., 2020). After comprehensive variant analyses and co-segregation testing, a novel missense variant (c.277C > A, p.L93M) in *SLC16A9* was identified (Huang et al., 2020). This study indicates that WES can be used to provide new insight into the genetic etiology of gout.

The *CPT2* gene encodes carnitine palmitoyltransferase II, an enzyme that participates in fatty acid oxidation. Together with carnitine palmitoyltransferase I, the encoded protein oxidizes long-chain fatty acids in the mitochondria. Defects in this gene are associated with mitochondrial long-chain fatty-acid (LCFA) oxidation disorders, known as CPT II deficiency (Bonnefont et al., 1996). However, the association between *CPT2* gene and gout has never been reported.

In this study, we aimed to investigate the genetic basis of gout in a three-generation affected pedigree. Ultimately, we identified a rare missense variant in the *CPT2* gene (c.1891C > T, p.R631C). Evidence from further functional experiments supports a role for this mutation in the pathogenesis of gout.

MATERIALS AND METHODS

Participant Recruitment

This study was approved by the Ethics Committee of the First Affiliated Hospital of Wenzhou Medical University (Wenzhou, China; approval no. 2018-020). All participants were administered according to the principles of the Declaration of Helsinki. All subjects provided informed consent. Diagnosis of gout was performed by physicians in accordance with the 2015 gout classification criteria defined by the American College of Rheumatology/European League Against Rheumatism Collaborative Initiative (Neogi et al., 20152015). Patients with inherited metabolic disorders, including glycogen storage diseases and Lesch-Nyhan syndrome, were excluded in this study. Patient information is provided in **Table 1**. Patients reported suffering monoarthritis in the first metatarsophalangeal joint (MTP1), ankles, or knees, which was relieved within 1 week.

Whole Exome Sequencing and Variant Calling

Genomic DNA was isolated from peripheral blood according to standard procedures using a Qiamp Blood DNA mini Kit (Qiagen, Hilden, Germany). About 2 μg of genomic DNA sample was randomly sheared to 200–250 bp in size using a Covaris S220 System, after which the fragments of DNA were ligated to attach A-tails and adapters to both ends. After amplification, purification, and hybridization of adapter-ligated DNA, as well as the removal of nonhybridized fragments, capture and enrichment of exome regions were conducted using an Agilent SureSelect Human All Exon V6 kit (Agilent Technologies, Palo Alto, CA, United States) according to the manufacturer's protocol. High-throughput library sequencing was performed on an Illumina HiSeq4000 Analyzer (Illumina, San Diego, CA, United States).

Raw sequencing data obtained from the sequencer was processed according to a customized bioinformatics pipeline as previously described (Liu et al., 2018). Briefly, raw reads were filtered to remove sequence adapters and low-quality reads based on Phred-scaled quality scores <30 and read lengths <80 bp using FastQC software (version 1.11.4). After quality control testing, remaining reads were aligned to the human reference genome (GRCh37/hg19) using the Burrows-Wheeler alignment tool (Li and Durbin, 2010) and further visualized using the

SplicingViewer software (Liu et al., 2012). The Genome Analysis ToolKit (GATK; version 4.0.10.0) was used to remove duplicated reads, perform local realignment, and recalibrate map quality scores. SNV and Indel variant calling were performed using GATK Unified Genotype (version 4.0.10.0).

Variant Annotation and Prioritization

All variants were functionally annotated as previously described (Li et al., 2015b) using mirTrios with integrated ANNOVAR. Variants were then prioritized by allele frequency, evolutionary conservation, and predicted effect on protein function, as well as based on segregation testing for disease phenotype. Variants were discarded if the base on allele frequency was present at more than 0.01% in any publicly available databases (Chen et al., 2019), including Genome Aggregation Database (http://gnomad.broadinstitute.org/), Exome Aggregation Consortium (ExAC, http://exac.broadinstitute.org/), 1,000 Genome (http://www.1000genomes.org), and NHLBI Exome Sequencing Project (ESP, http://evs.gs.washington.edu/EVS/). The effects of detected variants were assessed by four *in silico* prediction programs: SIFT, Polyphen-2, CADD, and MutationTaster. Variants were considered pathogenic if they were predicted to be deleterious or damaging by all prediction tools. Sanger sequencing (primers: CPT2-5F, GCTTTGACCGACACTTGT TTG; CPT2-5R, TGGTCTCAAACTCCTGACCT) was used to confirm family screening of identified candidates and segregation testing.

Expression Vector Construction and Mutagenesis

The full-length coding sequences of wild-type CPT2 and UCP2 were synthesized *in vitro* by Jiangxi Zhonghong Boyuan Biological Technology Company and cloned into the pcDNA3.1 vector. Site-directed mutagenesis was performed on wild-type *CPT2* to create the c.1891C > T variant in the pcDNA3.1 vector using specific primers according to the standard procedures of the KOD-Plus-Mutagenesis Kit (Toyobo Life Science). Green fluorescent protein (GFP) and a His tag were then fused to the N terminus of wild-type *CPT2* in the pcDNA3.1 vector, via dual-enzyme digestion with HindIII and NotI (New England Biolabs). Similarly, red fluorescent protein (RFP) and a His tag were fused to the N terminus of mutant *CPT2* mutant in the pcDNA3.1 vector using the same dual-enzyme digestion approach. In addition, a Flag tag was fused to the N terminus of *UCP2* in the pcDNA3.1 vector using the same dual-enzyme digestion approach.

Cell Culture and Transfection

Human embryonic kidney (HEK)-derived 293T cells were purchased from ATCC (ATCC; Manassas, VA, United States) and grown in Dulbecco's modified Eagle medium/GlutaMaxTM medium (GIBCO, 15140–122) supplemented with 10% fetal bovine serum, 2 mM L-glutamine, and 10 U/ml Penicillin-Streptomycin at 37°C in a 5% CO_2 incubator. The HEK cells were transiently transfected with 2 μg of plasmid DNA of wild-type or mutant CPT2 constructs using Lipofectamine 2000 according to the standard protocol from the manufacturer (Invitrogen, Grand Island, NY, United States).

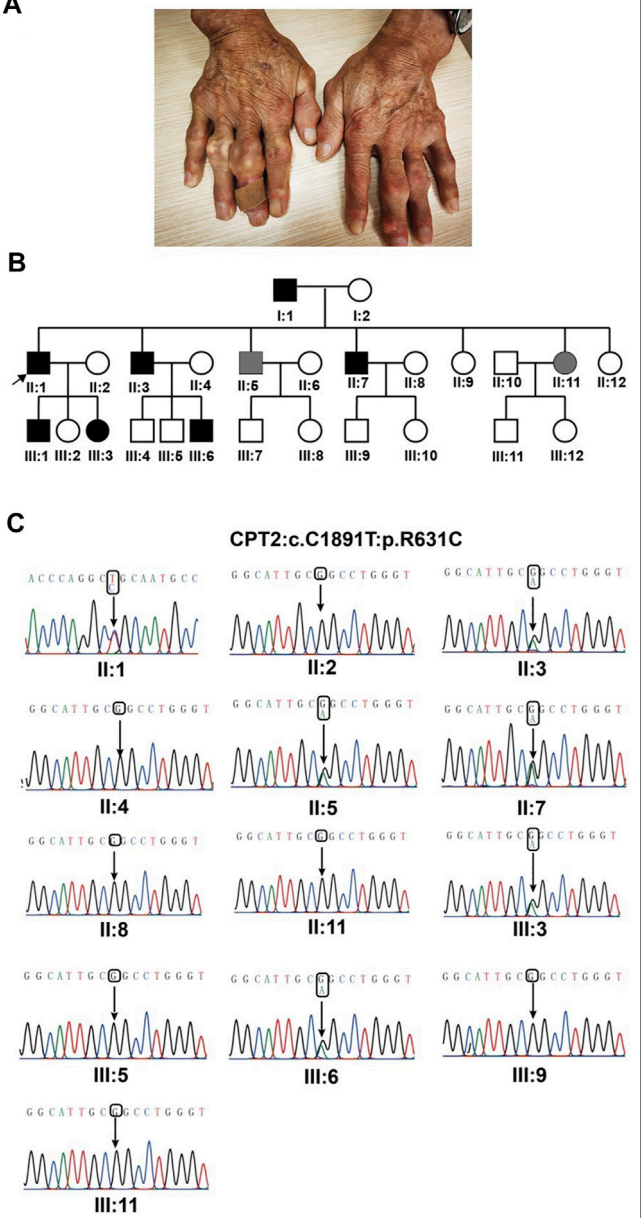

FIGURE 1 | Identification of *CPT2* missense in the gout family. **(A)**. Representative photographs of the proband in gout family reveal multiple tophi, indicating long disease duration and a severe disease burden. **(B)**. Pedigree and co-segregation results. Affected individual is represented as a filled square. Normal individuals are shown as empty symbols. **(C)**. Sanger sequencing confirmed the segregation of the rare missense variant, c.1891C > T, (p.R631C).

Fluorescence Microscopy

24 h after transfection, transfected HEK cells were washed three times with PBS for 3 min per wash, then fixed for 15 min in PBS containing 4% paraformaldehyde. For nuclear DNA

visualization, cell samples were mounted with ProLong Gold antifade reagent containing 1:600 DAPI for 5 min while being sheltered from light. Samples were then blocked with 50% normal glycerinum for microscopic observation. All confocal images were captured using a laser scanning confocal microscope (LSM710, Zeiss). Subcellular localization of wild-type or mutant CPT2, as well as quantitation of fluorescence signal intensity, was assessed using ImageJ software.

Immunoprecipitation Assays

To validate the interaction between UCP2 and CPT2, we performed an immunoprecipitation assay using SureBeads Protein A/G (Bio-Rad). HEK cells were transfected with wild-type or mutant CPT2 constructs as well as the UCP2 construct in different combinations. According to the standard protocols provided by the manufacturer, cells were harvested 24 h after transfection and lysed for 30 min at 4°C in lysis buffer containing 20 mM HEPES (pH 7.4), 100 mM KCl, 2 mM MgCl2, 1 mM PMSF, 1% Triton X-100, and supplemental protease inhibitors. Lysates were then centrifuged at 14,000×*g* for 10 min at 4°C, after which the supernatants were mixed with antibody (anti-flag)-conjugated magnetic beads and incubated overnight at 4°C on a rotating wheel with end-over-end mixing. Next, beads were collected from the supernatants by centrifugation and washed four times in lysis buffer. Finally, bound protein was eluted in SDS loading buffer onto a 10% acrylamide gel, resolved by SDS-PAGE, and analyzed by Western blot with the following primary antibodies: anti-flag at 1:1,000 dilution and anti-his at 1:1,000 dilution.

RESULTS

Characteristics of the Patient Cohort

All patients suffered acute monoarticular arthritis in the MTP1 and/or knee. Acute gouty arthritis is painful and unbearable, even occasionally accompanied by fever. All symptoms could be completely relieved within 1 week of treatment with a nonsteroidal anti-inflammatory drug and colchicines. Palpable tophi were observed in some of the patients (**Figure 1A**). The metabolic conditions of all patients were evaluated, and clinical data are presented in **Table I**. All patients have normal intelligence, and antinuclear antibody, rheumatoid factor, and HLA-B27 tests were negative for all patients.

Detection of Rare Deleterious Variants From Proband Whole-Exome Sequencing Data

To determine the genetic etiology of gout, we performed WES on the proband (family member II:1) from a three-generation pedigree with early-onset gout. After the removal of low-quality and duplicated reads from the raw sequencing data, we identified a total of 541,954 single nucleotide variations (SNVs) and 84,415 indels using the GATK tool, of which 67,707 coding SNVs and 2,200 indels were located within splicing regions. Further application of variant filtration against variants found that at a frequency <0.001% in multiple public databases, the numbers of novel SNVs and indels potentially associated with gout were reduced to 228 and 29, respectively. To further prioritize these SNVs, we subjected the variants to functional assessment by multiple prediction tools, including SIFT, Polyphen2, MutationTaster and CADD, and retained variants predicted as deleterious by all prediction tools. Following these analyses, two SNVs in the coding regions of two gout-associated genes (*CPT2* and *ABCC4*) were retained.

These candidate variants were submitted for Sanger sequencing validation and co-segregation analysis in the pedigree. Following this analysis, one variant remained promising: a rare heterozygous missense variant (c.1891C > T, p.R631C) in *CPT2*. Segregation analysis confirmed that the presence of this heterozygous variant was shared by all patients, while unaffected individuals did not exhibit the nucleotide change; in other words, R631C co-segregates with the disease phenotype in this pedigree (**Figures 1B,C**). Additionally, *in silico* predictive algorithms for nonsynonymous variation in all prediction tools suggested strong pathogenicity for this variant based on effects on protein function. By querying against multiple public databases, we found that this variant is extremely rare (rs74315293) in gnomAD and ExAC databases, with respective allele frequencies of 0.002475% (7 in 282,810) and 0.002471% (3 in 121,398), but is not present in 1,000 genomes or ESP6500 (**Table 2**). The heterozygous missense variant causes an arginine (Arg) to cysteine (Cys) substitution at amino acid 631, adjacent to the C terminus. Meanwhile, multiple orthologous sequence alignment revealed that the arginine at position 631 is highly conserved among different vertebrate and invertebrate species (**Figure 2**). According to the standards and guidelines of ACMG, the missense variants were classified as likely pathogenic. Specifically, the interpretation for pathogenesis of variant c.1891C > T is rated as pathogenic by the ClinVar database.

Effects of CPT2 Variants on Protein Localization and Expression in Cells

To assess the effects of missense variant p.R631C on the subcellular localization of CPT2 protein in affected individuals, we constructed vectors driving expression of the wild-type protein in association with a GFP protein tag (WT-CPT2-GFP), as well fusions of the mutant variant with RFP for identification (Mut-CPT2-GFP). After transfection of wild-type and mutant CPT2 constructs into HEK293 cells, cell morphology did not differ noticeably between cells overexpressing the wild-type protein or p.R631C mutant and those transfected only with GFP, RFP, or an empty vector (**Figure 3A**). In addition, we found that the CPT2 protein is mainly localized to the nucleus but is partially distributed in the cytoplasm. Further analysis of fluorescence signal indicated that there was no overt subcellular mislocalization of the p.R631C mutant compared to wild-type CPT2 (**Figure 3A**). However, the fluorescence intensity of p.R631C mutants was obviously compared to that of the wild-type protein, which could be the result of protein degradation caused by the mutations (**Figure 3B**).

TABLE 2 | In silico analysis of the missense variant in *CPT2*

Variants	AA conservation	gnomAD (%)	ExAC (%)	1,000 genomes	ESP6500	SIFT	PolyPhen-2	CADD	Mutation Taster
p.(R631C)	Highly conserved	0.002475	0.002471	_	_	Damaging (0.004)	probably damaging (1.0)	Damaging (28.4)	Disease-causing (1.0)

Abbreviations: AA, amino acid; CADD, combined annotation dependent depletion; ExAC, exome aggregation consortium; gnomAD, genome aggregation database; PolyPhen-2, polymorphism phenotyping v2; SIFT, sorting intolerant from tolerant.

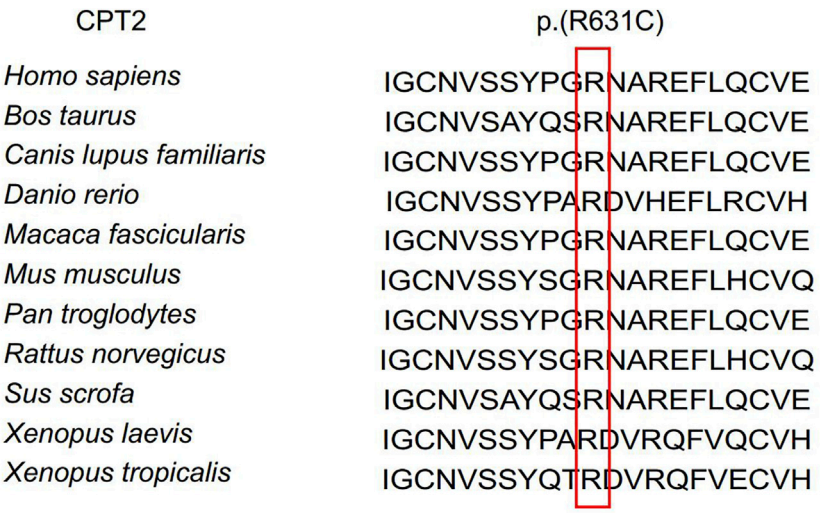

FIGURE 2 | Conservation analyses. Conservation analyses of the mutated residues 631 in *CPT2* across different species.

Functional Analyses of CPT2

It has been previously suggested that the interaction between CPT2 and UCP2 is associated with gout or hyperuricemia. To further evaluate the possible role of CPT2 in gout, we first assessed the interaction between UCP2 and wild-type CPT2, then determined the effect of the p.R631C mutation on this interaction. Therefore, we performed an *in vitro* immunoprecipitation assay by constructing expression vectors with His tags fused to the N termini of CPT2 (His-WT-CPT2) and c.1891C > T mutants (His-mu-CPT2) and FLAG tags fused to the N terminus of UCP (Flag-UCP). These constructs were transfected into HEK293 cells alone or in combination. Immunoprecipitation with anti-FLAG beads coupled with Western blot analysis with histone antibodies showed a strong physical interaction between CPT2 and UCP2 (**Figure 4**). Of note, no obvious interaction signal was observed between the CPT2 mutant and UCP2, indicating that the c.1891C > T variant influences the ability of CPT2 and UCP2 to bind (**Figure 4**).

DISCUSSION

In the present study, we recruited a multi-generational pedigree with gout and comprehensively performed WES and co-segregation testing to investigate the genetic basis of gout in this family. Ultimately, this study identified a rare mutation (c.1891C > T, p.R631C) in the *CPT2* gene.

The CPT2 gene encodes carnitine palmitoyltransferase II, an enzyme that participates in fatty acid oxidation. Britton et al. distinguished CPT I and CPT II (Britton et al., 1995). Mutations in the CPT2 gene can cause Carnitine Palmitoyltransferase II Deficiency (Demaugre et al., 1991; Taroni et al., 1992; Bonnefont et al., 1996). Of note, the R631C mutation was previously reported in a patient with infantile carnitine palmitoyltransferase II deficiency (Taroni et al., 1992). Taken together, these findings highlight the genetic and clinical heterogeneity of defects in *CPT2*.

In addition to the evidence from WES and genetic analyses, this study also provides evidence from functional experiments. We constructed vectors driving expression of the wild-type protein in association with a GFP protein tag (WT-CPT2-GFP), as well as of the mutant variant fused to RFP for identification (Mut-CPT2-GFP). Although no change in localization was observed, the results showed that the fluorescence intensity of p.R631C mutants was obviously reduced compared to the wild-type protein, suggesting that the mutation leads to protein degradation.

The effect of the CPT2 mutant was further defined by studying the interaction between UCP2 and CPT2. UCP2 has been reported to be associated with serum urate concentrations, as well as with hyperuricemia (Yang et al., 2016). To assess the

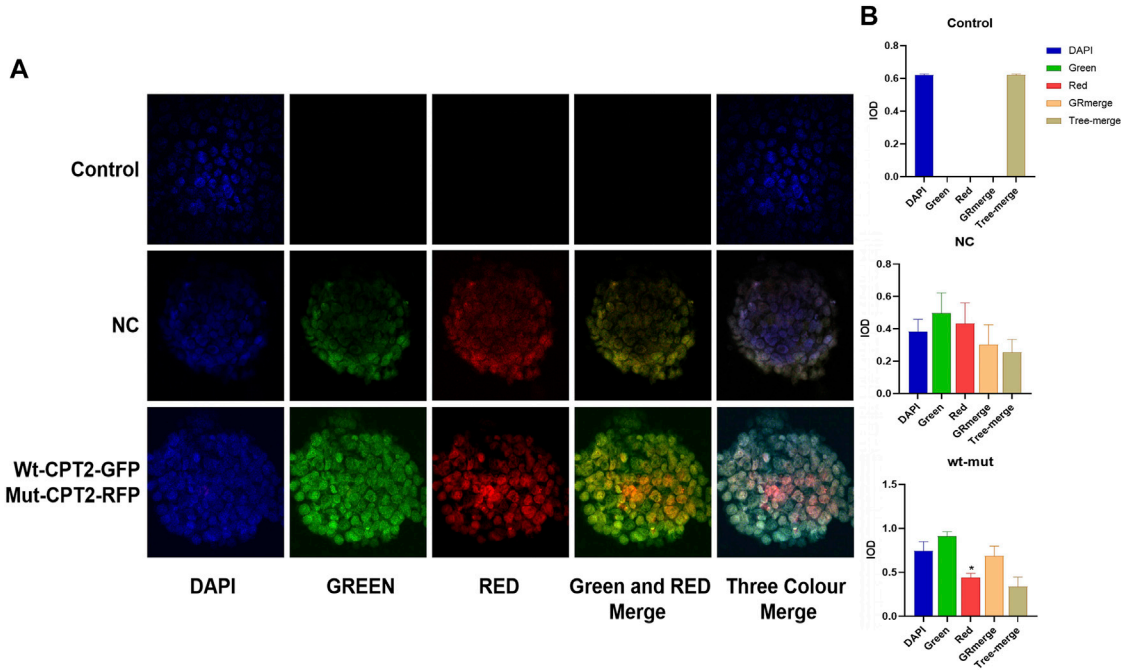

FIGURE 3 | Missense variant p.R631C on the subcellular localization of CPT2 protein under confocal microscopy. **(A)**. The vectors drove the expression of the wild-type protein in association with GFP protein tag (WT-CPT2-GFP) as well as the mutant variants fusion with RFP fusion protein for identification (Mut-CPT2-GFP). The CPT2 protein was mainly localized in the nucleus, partly distributed in the cytoplasm. The fluorescence signal showed that there was no overt subcellular mislocalization of the p.R631C mutant with respect to wild-type CPT2. **(B)**. The fluorescence intensity of p.R631C mutants was obviously reduced than wild-type protein.

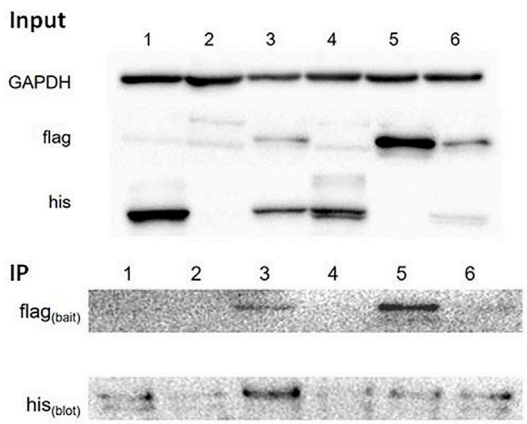

1:his-wt-CPT2;2:control;3:his-wt-CPT2+flag-UCP2;4:his-mu-CPT2;5:flag-UCP2;6:his-mu-CPT2+flag-UCP2

FIGURE 4 | Immunoprecipitation assay of the interaction between CPT2 protein with UCP2 protein. Results of a co-immunoprecipitation assay between the CPT2-his and UCP2-flag proteins. Immunoprecipitation with anti-FLAG beads coupled with Western blot analysis by histone antibody showed a strong physical interaction between CPT2 and UCP2. No obvious interacted signal was observed between mutant CPT2 and UCP2.

effects of the R631C mutation, we performed an *in vitro* immunoprecipitation assay by constructing expression vectors with His tags fused to the N termini of CPT2 (His-WT-CPT2) and c.1891C > T mutants (His-mu-CPT2) and FLAG tags fused to the N terminus of UCP (Flag-UCP). Interestingly, while our results showed a strong physical interaction between wild-type CPT2 and UCP2, no obvious interaction signal was observed between the CPT2 mutant and UCP2. These results indicate that the c.1891C > T variant influences the ability of CPT2 to bind UCP2. Taken as a whole, evidence from functional experiments further supports the pathogenicity of the R631C mutation.

Interestingly, our previous study reported an association between *SLC16A9* and gout, and *SLC16A9* is known to be associated with carnitine levels (Demirkan et al., 2015). Thus, it is reasonable to speculate that the carnitine-related pathway may play an important role in gout development.

In conclusion, this study identifies a rare *CPT2* mutation in a large Chinese pedigree with gout. Functional studies were used to determine the effect of this mutant. This study provides novel insight into the genetic etiology of gout.

DATA AVAILABILITY STATEMENT

The data presented in the study are deposited in the SRA Bioproject repository, accession number PRJNA 776345.

ETHICS STATEMENT

The studies involving human participants were reviewed and approved by the Ethics Committee of the First Affiliated Hospital of Wenzhou Medical University (Wenzhou, China; approval no. 2018 020). The patients/participants provided their written informed consent to participate in this study.

AUTHOR CONTRIBUTIONS

YG and JJ conceived and designed the study. ZZ, YC, and LS performed experiment and analyzed experimental data. CZ wrote the article. XX collected the data and revised the article. All authors approved the final submission.

FUNDING

This study is supported by Zhejiang Provincial Natural Science Foundation of China (LY20H100001) and Wenzhou Science and technology Bureau (Y20180129).

ACKNOWLEDGMENTS

We gratefully acknowledge all the participants in this study.

REFERENCES

Bonnefont, J. P., Taroni, F., Cavadini, P., Cepanec, C., Brivet, M., Saudubray, J. M., et al. (1996). Molecular Analysis of Carnitine Palmitoyltransferase II Deficiency with Hepatocardiomuscular Expression. *Am. J. Hum. Genet.* 58 (5), 971–978.

Britton, C. H., Schultz, R. A., Zhang, B., Esser, V., Foster, D. W., and McGarry, J. D. (1995). Human Liver Mitochondrial Carnitine Palmitoyltransferase I: Characterization of its cDNA and Chromosomal Localization and Partial Analysis of the Gene. *Proc. Natl. Acad. Sci.* 92 (6), 1984–1988. doi:10.1073/pnas.92.6.1984

Chen, X., Jin, J., Wang, Q., Xue, H., Zhang, N., Du, Y., et al. (2019). A De Novo Pathogenic CSNK1E Mutation Identified by Exome Sequencing in Family Trios with Epileptic Encephalopathy. *Hum. Mutat.* 40 (3), 281–287. doi:10.1002/humu.23690

Demaugre, F., Bonnefont, J. P., Colonna, M., Cepanec, C., Leroux, J. P., and Saudubray, J. M. (1991). Infantile Form of Carnitine Palmitoyltransferase II Deficiency with Hepatomuscular Symptoms and Sudden Death. Physiopathological Approach to Carnitine Palmitoyltransferase II Deficiencies. *J. Clin. Invest.* 87 (3), 859–864. doi:10.1172/jci115090

Demirkan, A., Henneman, P., Verhoeven, A., Dharuri, H., Amin, N., van Klinken, J. B., et al. (2015). Insight in Genome-wide Association of Metabolite Quantitative Traits by Exome Sequence Analyses. *Plos Genet.* 11 (1), e1004835. doi:10.1371/journal.pgen.1004835

Huang, X. F., Sun, L., Zhang, C., Zhou, Z., Chen, H., Zhang, L., et al. (2020). Whole-Exome Sequencing Reveals a Rare Missense Variant in SLC16A9 in a Pedigree with Early-Onset Gout. *Biomed. Res. Int.* 2020, 4321419. doi:10.1155/2020/4321419

Huang, X. F., Xiang, L., Cheng, W., Cheng, F. F., He, K. W., Zhang, B. W., et al. (2018). Mutation of IPO13 Causes Recessive Ocular Coloboma, Microphthalmia, and Cataract. *Exp. Mol. Med.* 50 (4), 53. doi:10.1038/s12276-018-0079-0

Huang, X. F., Xiang, L., Fang, X. L., Liu, W. Q., Zhuang, Y. Y., Chen, Z. J., et al. (2019). Functional Characterization of CEP250 Variant Identified in Nonsyndromic Retinitis Pigmentosa. *Hum. Mutat.* 40 (8), 1039–1045. doi:10.1002/humu.23759

Köttgen, A., Albrecht, E., Teumer, A., Vitart, V., Krumsiek, J., Hundertmark, C., et al. (2013). Genome-wide Association Analyses Identify 18 New Loci Associated with Serum Urate Concentrations. *Nat. Genet.* 45 (2), 145–154. doi:10.1038/ng.2500

Li, C., Li, Z., Liu, S., Wang, C., Han, L., Cui, L., et al. (2015). Genome-wide Association Analysis Identifies Three New Risk Loci for Gout Arthritis in Han Chinese. *Nat. Commun.* 6, 7041. doi:10.1038/ncomms8041

Li, H., and Durbin, R. (2010). Fast and Accurate Long-Read Alignment with Burrows-Wheeler Transform. *Bioinformatics* 26 (5), 589–595. doi:10.1093/bioinformatics/btp698

Li, J., Jiang, Y., Wang, T., Chen, H., Xie, Q., Shao, Q., et al. (2015). mirTrios: an Integrated Pipeline for Detection of De Novo and Rare Inherited Mutations from Trios-Based Next-Generation Sequencing. *J. Med. Genet.* 52 (4), 275–281. doi:10.1136/jmedgenet-2014-102656

Liu, Q., Chen, C., Shen, E., Zhao, F., Sun, Z., and Wu, J. (2012). Detection, Annotation and Visualization of Alternative Splicing from RNA-Seq Data with SplicingViewer. *Genomics* 99 (3), 178–182. doi:10.1016/j.ygeno.2011.12.003

Liu, Z., Li, Z., Zhi, X., Du, Y., Lin, Z., and Wu, J. (2018). Identification of De Novo DNMT3A Mutations that Cause West Syndrome by Using Whole-Exome Sequencing. *Mol. Neurobiol.* 55 (3), 2483–2493. doi:10.1007/s12035-017-0483-9

Major, T. J., Dalbeth, N., Stahl, E. A., and Merriman, T. R. (2018). An Update on the Genetics of Hyperuricaemia and Gout. *Nat. Rev. Rheumatol.* 14 (6), 341–353. doi:10.1038/s41584-018-0004-x

Matsuo, H., Yamamoto, K., Nakaoka, H., Nakayama, A., Sakiyama, M., Chiba, T., et al. (2016). Genome-wide Association Study of Clinically Defined Gout Identifies Multiple Risk Loci and its Association with Clinical Subtypes. *Ann. Rheum. Dis.* 75 (4), 652–659. doi:10.1136/annrheumdis-2014-206191

Nakayama, A., Nakaoka, H., Yamamoto, K., Sakiyama, M., Shaukat, A., Toyoda, Y., et al. (2017). GWAS of Clinically Defined Gout and Subtypes Identifies Multiple Susceptibility Loci that Include Urate Transporter Genes. *Ann. Rheum. Dis.* 76 (5), 869–877. doi:10.1136/annrheumdis-2016-209632

Neogi, T., Jansen, T. L. T. A., Dalbeth, N., Fransen, J., Schumacher, H. R., Berendsen, D., et al. (20152015). 2015 Gout Classification Criteria: An American College of

Rheumatology/European League against Rheumatism Collaborative Initiative. *Arthritis Rheumatol.* 67 (10), 2557–2568. doi:10.1002/art.39254

Phipps-Green, A. J., Merriman, M. E., Topless, R., Altaf, S., Montgomery, G. W., Franklin, C., et al. (2016). Twenty-eight Loci that Influence Serum Urate Levels: Analysis of Association with Gout. *Ann. Rheum. Dis.* 75 (1), 124–130. doi:10.1136/annrheumdis-2014-205877

Richette, P., and Bardin, T. (2010). Gout. *The Lancet* 375 (9711), 318–328. doi:10.1016/s0140-6736(09)60883-7

Sulem, P., Gudbjartsson, D. F., Walters, G. B., Helgadottir, H. T., Helgason, A., Gudjonsson, S. A., et al. (2011). Identification of Low-Frequency Variants Associated with Gout and Serum Uric Acid Levels. *Nat. Genet.* 43 (11), 1127–1130. doi:10.1038/ng.972

Taroni, F., Verderio, E., Fiorucci, S., Cavadini, P., Finocchiaro, G., Uziel, G., et al. (1992). Molecular Characterization of Inherited Carnitine Palmitoyltransferase II Deficiency. *Proc. Natl. Acad. Sci.* 89 (18), 8429–8433. doi:10.1073/pnas.89.18.8429

Yang, L., Dong, Z., Zhou, J., Ma, Y., Pu, W., Zhao, D., et al. (2016). Common UCP2 Variants Contribute to Serum Urate Concentrations and the Risk of Hyperuricemia. *Sci. Rep.* 6, 27279. doi:10.1038/srep27279

Conflict of Interest: The authors declare that the research was conducted in the absence of any commercial or financial relationships that could be construed as a potential conflict of interest.

Publisher's Note: All claims expressed in this article are solely those of the authors and do not necessarily represent those of their affiliated organizations, or those of the publisher, the editors, and the reviewers. Any product that may be evaluated in this article, or claim that may be made by its manufacturer, is not guaranteed or endorsed by the publisher.

frontiers | Frontiers in Cell and Developmental Biology

TYPE Correction
PUBLISHED 04 August 2022
DOI 10.3389/fcell.2022.988348

OPEN ACCESS

APPROVED BY
Frontiers in Editorial Office,
Frontiers Media SA, Switzerland

*CORRESPONDENCE
Xiaoru Xia,
xxr7799@163.com

†These authors have contributed equally to this work

SPECIALTY SECTION
This article was submitted to Molecular and Cellular Pathology, a section of the journal Frontiers in Cell and Developmental Biology

RECEIVED 08 July 2022
ACCEPTED 08 July 2022
PUBLISHED 04 August 2022

CITATION
Guo Y, Jin J, Zhou Z, Chen Y, Sun L, Zhang C and Xia X (2022), Corrigendum: Whole-exome sequencing identifies a novel CPT2 mutation in a pedigree with gout.
Front. Cell Dev. Biol. 10:988348.
doi: 10.3389/fcell.2022.988348

Corrigendum: Whole-exome sequencing identifies a novel CPT2 mutation in a pedigree with gout

Yong Guo[1†], Jing Jin[2†], Zhenni Zhou[3], Yihui Chen[4], Li Sun[5†], Chunwu Zhang[6†] and Xiaoru Xia[5*]

[1]Department of Urology, The First Affiliated Hospital of Wenzhou Medical University, Wenzhou, China, [2]Zhejiang Center for Clinical Laboratory, Zhejiang Provincial People's Hospital, Affiliated People's Hospital, Hangzhou Medical College, Hangzhou, China, [3]Department of Internal Medicine, Yueqing People's Hospital, Yueqing, China, [4]Wenzhou Medical University, Wenzhou, China, [5]Department of Rheumatology, The First Affiliated Hospital of Wenzhou Medical University, Wenzhou, China, [6]Department of Injury Orthopaedics, The First Affiliated Hospital of Wenzhou Medical University, Wenzhou, China

KEYWORDS

whole-exome sequencing, novel mutation, gout, CPT2 gene, pedigree

A Corrigendum on
Whole-exome sequencing identifies a novel CPT2 mutation in a pedigree with gout

by Guo, Y., Jin, J., Zhou, Z., Chen, Y., Sun, L., Zhang, C., and Xia, X. (2022). Front. Cell Dev. Biol. 10:802635. doi: 10.3389/fcell. 2022.802635

In the published article, there was an error in affiliations 1 and 6. Instead of "The First Affiliated Hospital of Wenzhou University", it should be "The First Affiliated Hospital of Wenzhou Medical University".

The authors apologize for this error and state that this does not change the scientific conclusions of the article in any way. The original article has been updated.

Publisher's note

All claims expressed in this article are solely those of the authors and do not necessarily represent those of their affiliated organizations, or those of the publisher, the editors and the reviewers. Any product that may be evaluated in this article, or claim that may be made by its manufacturer, is not guaranteed or endorsed by the publisher.

frontiers | Frontiers in Cell and Developmental Biology

ORIGINAL RESEARCH
published: 20 June 2022
doi: 10.3389/fcell.2022.698282

Self-Assembling Imageable Silk Hydrogels for the Focal Treatment of Osteosarcoma

*Zhibin Peng[1,2†], Ming Li[3†], Yuan Wang[4], Hongbo Yang[5], Wei Wei[6], Min Liang[1], Jianhui Shi[7], Ruixuan Liu[1], Rui Li[1], Yubo Zhang[1], Jingsong Liu[1], Xu Shi[6], Ran Wan[1], Yao Fu[1], Rui Xie[8] and Yansong Wang[1]**

[1]Department of Orthopedic Surgery, The First Affiliated Hospital of Harbin Medical University, Harbin Medical University, Harbin, China, [2]The Key Laboratory of Myocardial Ischemia, Ministry of Education, Harbin Medical University, Harbin, China, [3]Department of Critical Care Medicine, The Second Affiliated Hospital of Harbin Medical University, Harbin Medical University, Harbin, China, [4]Innovation and Entrepreneurship Square, Science and Technology Innovation City, Hi-Tech Zone, Harbin, China, [5]Department of Orthopedic Surgery, Affiliated Hospital of Chifeng University, Chifeng University, Chifeng, China, [6]Department of Orthopedic Surgery, Harbin 242 Hospital, Harbin, China, [7]Department of Orthopedic Surgery, Heilongjiang Provincial Hospital, Harbin, China, [8]Department of Digestive Internal Medicine and Photodynamic Therapy Center, Harbin Medical University Cancer Hospital, Harbin Medical University, Harbin, China

OPEN ACCESS

Edited by:
Andrea Del Fattore,
Bambino Gesù Children's Hospital (IRCCS), Italy

Reviewed by:
Michael Todhunter,
City of Hope National Medical Center, United States
Jing Gao,
Karolinska Institutet (KI), Sweden
Zi-Chun Hua,
Nanjing University, China

***Correspondence:**
Yansong Wang
wyshmu1975@163.com

†These authors have contributed equally to this work

Specialty section:
This article was submitted to Molecular and Cellular Pathology, a section of the journal Frontiers in Cell and Developmental Biology

Received: 21 April 2021
Accepted: 02 May 2022
Published: 20 June 2022

Citation:
Peng Z, Li M, Wang Y, Yang H, Wei W, Liang M, Shi J, Liu R, Li R, Zhang Y, Liu J, Shi X, Wan R, Fu Y, Xie R and Wang Y (2022) Self-Assembling Imageable Silk Hydrogels for the Focal Treatment of Osteosarcoma. Front. Cell Dev. Biol. 10:698282. doi: 10.3389/fcell.2022.698282

Background: The standard treatment for osteosarcoma comprises complete surgical resection and neoadjuvant chemotherapy, which may cause serious side effects and partial or total limb loss. Therefore, to avoid the disadvantages of traditional treatment, we developed self-assembling imageable silk hydrogels for osteosarcoma.

Methods: We analysed whether iodine induced apoptosis in MG-63 and Saos-2 cells by using CCK-8 and flow cytometry assays and transmission electron microscopy. Western blotting was used to analyse the pathway of iodine-induced apoptosis in osteosarcoma cells. PEG400, silk fibroin solution, polyvinylpyrrolidone iodine (PVP-I), and meglumine diatrizoate (MD) were mixed to produce an imageable hydrogel. A nude mouse model of osteosarcoma was established, and the hydrogel was injected locally into the interior of the osteosarcoma with X-ray guidance. The therapeutic effect and biosafety of the hydrogel were evaluated.

Results: Iodine treatment at 18 and 20 μM for 12 h resulted in cell survival rate reduced to 50 ± 2.1% and 50.5 ± 2.7% for MG-63 and Sao-2 cells, respectively ($p < 0.01$). The proportion of apoptotic cells was significantly higher in the iodine-treatment group than in the control group ($p < 0.05$), and apoptotic bodies were observed by transmission electron microscopy. Iodine could regulate the death receptor pathway and induce MG-63 and Saos-2 cell apoptosis. The hydrogels were simple to assemble, and gels could be formed within 38 min. A force of less than 50 N was required to inject the gels with a syringe. The hydrogels were readily loaded and led to sustained iodine release over 1 week. The osteosarcoma volume in the PEG-iodine-silk/MD hydrogel group was significantly smaller than that in the other three groups ($p < 0.001$). Caspase-3 and poly (ADP-ribose) polymerase (PARP) expression levels were significantly higher in the PEG-iodine-silk/MD hydrogel group than in the other three groups ($p < 0.001$). Haematoxylin and eosin

(H&E) staining showed no abnormalities in the heart, liver, spleen, lung, kidney, pancreas or thyroid in any group.

Conclusions: Self-assembling imageable silk hydrogels could be injected locally into osteosarcoma tissues with X-ray assistance. With the advantages of good biosafety, low systemic toxicity and minimal invasiveness, self-assembling imageable silk hydrogels provide a promising approach for improving the locoregional control of osteosarcoma.

Keywords: iodine, minimally invasive, osteosarcoma, imageable hydrogel, silk fibroin

INTRODUCTION

Osteosarcoma (OS), a malignant and highly metastatic cancer, is the most common type of primary malignant bone tumour in children and adolescents (Ottaviani and Jaffe, 2009; Arndt et al., 2012; Whelan et al., 2012; Cersosimo et al., 2020; Yang et al., 2020; Jiang et al., 2021). Conventional treatments for OS include neoadjuvant chemotherapy and a combination of complete surgical resection and adjuvant chemotherapy with drugs such as doxorubicin, cisplatin, methotrexate or ifosfamide (Muscolo, Ayerza, Aponte-Tinao, & Ranalletta, 2005; Anninga et al., 2011; Marec-Berard et al., 2020; Chen et al., 2021; Lin et al., 2021). However, chemotherapy often causes severe adverse systemic reactions and drug resistance. In addition, although limb salvage surgery is often performed, the resection surgery can still result in partial or total limb loss (Simon, Aschliman, Thomas, & Mankin, 1986; Rhodes, 1987; Bacci et al., 2002; Muscolo et al., 2005; Takeuchi et al., 2019). Therefore, the development of a new treatment for OS is critical.

Polyvinylpyrrolidone iodine (PVP-I) can effectively kill bacteria, viruses, fungi, and protozoa (Cunliffe and Fawcett, 2002; Lepelletier et al., 2020; Stathis et al., 2021). As a broad-spectrum antibacterial agent, it is routinely used to disinfect the skin and clean wounds. PVP-I can release free iodine, which has a strong antimicrobial effect. Similarly, free iodine is an effective tumoricidal agent and is becoming increasingly popular as an antitumour treatment in clinical practice. PVP-I has been widely used as an irrigation fluid during percutaneous endoscopic gastrostomy and in head, neck, and colorectal cancer surgery to eliminate free cancer cells to prevent implantation, metastasis and recurrence (Wu et al., 1998; Basha et al., 2000; Pattana-arun and Wolff, 2008; Hah et al., 2012; Chang et al., 2014). Furthermore, in a rat model study, researchers found that tumour formation can be impeded by the presence of iodine. These results indicate that iodine can prevent early cancer progression by exerting an inhibitory effect on cancer-initiating cells (Ghent et al., 1993; Funahashi et al., 1996; Kessler, 2004; Garcia-Solis et al., 2005). However, few studies have been conducted on the use of iodine as a treatment for OS, and the mechanism underlying the anti-OS effect of iodine is still unclear.

Cell death is divided into four types according to the appearance of the dead cells: type I cell death (apoptosis), type II cell death (autophagy), type III cell death (necrosis) and type IV cell death (pyroptosis) (Arndt et al., 2012). Apoptotic cell death is triggered by two main signalling pathways: the extrinsic pathway (the death receptor pathway) and the intrinsic pathway (the mitochondrial pathway) (Green and Llambi, 2015; Yuan et al., 2018). The death receptor pathway involves classical ligand-cell surface receptor interactions. Apoptotic cell death is mainly caused by either death receptors (DRs) or the mitochondrial pathway, although additional pathways exist. DRs, such as factor-associated suicide (Fas), cluster of differentiation 95 (CD95), trail receptor (TRAIL-R), and TNFR1, induce apoptosis by directly recruiting a caspase-activation platform upon binding to their respective ligand (Green and Llambi, 2015; Krishnan et al., 2019). The association of the receptor Fas with its ligand FasL triggers the DR pathway, which plays an important role in the immune regulation, development, and progression of cancers (Suda et al., 1993; Lee and Ferguson, 2003). Receptor clustering upon stimulation induces FADD and caspase-8 oligomerization, activating the caspase signalling pathway. Cleaved caspase-3 is a critical executioner of apoptosis, as it is either partially or totally responsible for the proteolytic cleavage of many key proteins, such as the nuclear enzyme Poly (ADP-ribose) polymerase (PARP) (Fernandes-Alnemri, Litwack, & Alnemri, 1994). PARP and cleaved PARP ultimately trigger apoptosis.

Meglumine diatrizoate (MD) is a water-soluble contrast agent, it is a colourless or faint yellow liquid. MD has a short half-life and is rapidly metabolized in the kidneys, and it has been widely used for imaging the digestive system, cardiovascular system, urinary system, and female reproductive system as well as for myelography but is mainly used for auxiliary diagnosis(White et al., 1993; Mercadante et al., 2004; Arndt et al., 2012; Khasawneh et al., 2013; Khaleel et al., 2019; Barret et al., 2020; Wu et al., 2020).

Silk fibroin is the major structural protein in silkworm cocoons. Due to their hypoimmunogenicity, biocompatibility and biodegradability, silk biomaterials have been widely used in tissue engineering and for drug delivery. A silk fibroin solution can form hydrogels after physical and chemical treatment, for example, treatment by sonication, vortexing, electrical fields, inorganic ions and macromolecular compounds (Wang et al., 2008; Yucel et al.,n, 2009; Leisk et al., 2010; Wang et al., 2015; Ma et al., 2016; Gholipourmalekabadi et al., 2020). Polyethylene glycol (PEG) is an organic compound that can be mixed with silk fibroin to form silk hydrogels. The gel formed by PEG and silk fibroin can be used as a sustained-release system to deliver biological factors and drugs (Seib et al., 2013; Wang et al., 2015; Ma et al., 2016; Turkkan et al., 2017; Boni et al., 2020). In addition, silk fibroin hydrogels can be delivered through

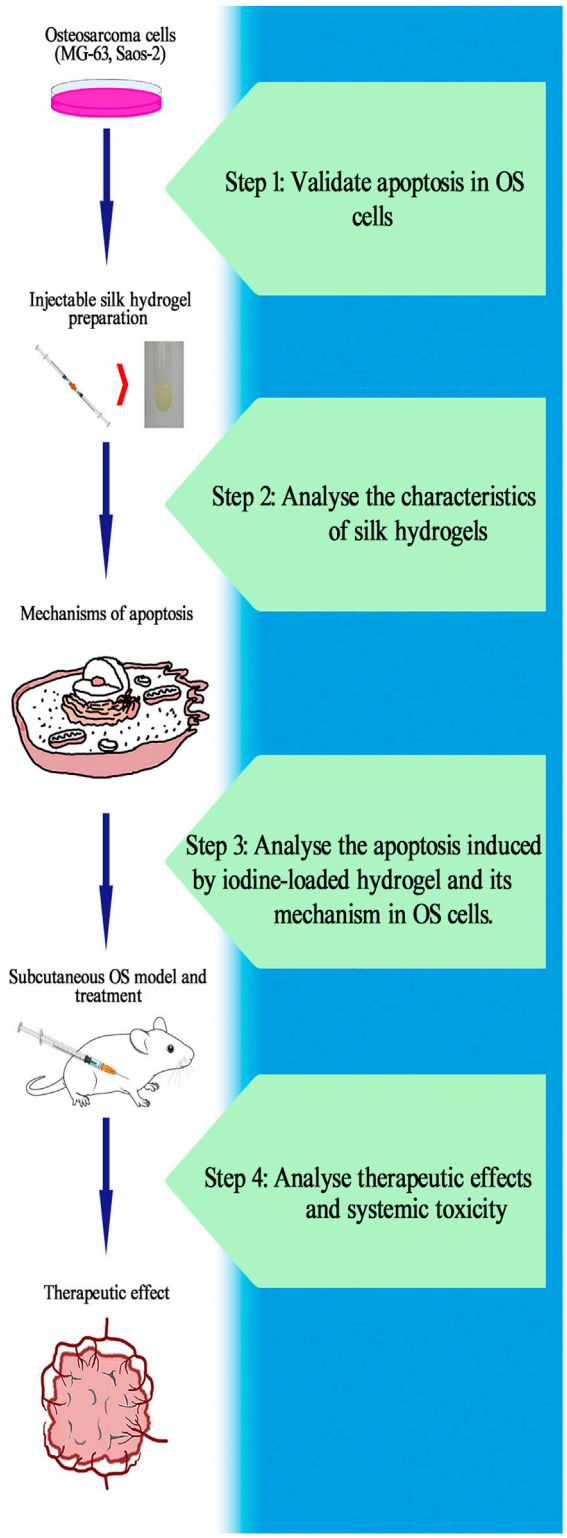

FIGURE 1 | Ideal workflow for the research of self-assembling imageable silk hydrogels. Step 1: Verify the apoptosis induced by iodine in OS cells and calculate the IC_{50}. Step 2: Prepare hydrogels and analyse its characteristics. Ensure that the hydrogels can be used as a controlled-release platform for iodine in the treatment of OS. Step 3: After treatment with released iodine solution, analyse the proportion of OS cells that undergo apoptosis, observe the apoptotic bodies and investigate the mechanism of apoptosis. Step 4: Construct a subcutaneous OS model and inject hydrogel into the OS to analyse the therapeutic effect and systemic toxicity of self-assembling imageable silk hydrogels on OS. (OS: osteosarcoma. IC_{50}: the median inhibitory concentration).

(*Continued*)

syringes, allowing silk hydrogels to be delivered to the required site in a minimally invasive manner to deliver drugs or biological factors to the target area (Seib et al., 2013; Wang et al., 2015; Ma et al., 2016; Liang et al., 2019; Farokhi et al., 2020). Many researchers have used silk fibroin for sustained-release drug delivery to tumours. Silk fibroin was used in several forms in these studies, including nanoparticles (Kim et al., 2015; Yang et al., 2015; Li et al., 2016; Xie et al., 2017), films (Seib and Kaplan, 2012; Zhang et al., 2019), and hydrogels (Seib et al., 2013; Hong et al., 2020). Therefore, silk fibroin products (including hydrogels) can play an important role in inhibiting tumour growth by stably releasing drugs during tumour treatment. However, few studies have been conducted on the use of silk fibroin products for the treatment of OS.

Therefore, we developed a local drug delivery system for OS. An ideal workflow in this study is shown in **Figure 1**. We conducted *in vivo* experiments with subcutaneous OS models in nude mice. The subcutaneous OS model allows for the easy observation of OS growth and improves the feasibility of experimental surgery. The self-assembling imageable silk hydrogels can be radiologically imaged because they are mixed with MD. Hence, the hydrogel can be injected into the local OS site with X-ray guidance. Hydrogels can locally release iodine, which plays a role in OS therapy. Self-assembling imageable silk hydrogels allowed drug loading under general ambient conditions and led to sustained iodine delivery, suggesting that this approach is a promising avenue for focal OS therapy.

MATERIALS AND METHODS

Cell Culture and Lentiviral Transduction

The human OS cell lines Saos-2 and MG-63 were purchased from the Shanghai Institute of Cell Biology, China. All cell lines were cultured in McCoy's 5A (Sigma, United States) and MEM (Gibco, United States) supplemented with 10% foetal bovine serum (Gibco, United States) and 100 μg/ml normocin (InvivoGen, United States) at 37°C in 5% CO_2. This study specifically used cells that were received less than 6 months prior to the beginning of the study. MG-63 cells were engineered with luciferase (LUC)-td tomato lentiviruses (GENE, China). Lentiviral production and concentration were performed according to standard procedures. MG-63 cells were transduced for 12 h at 37°C in 5% CO_2. After 12 h, the cells were washed repeatedly to remove extracellular lentiviral particles, and the cells were cultured with 2 μg/ml puromycin to screen for luciferase-positive cells until all the cells in the control group had died. After screening with puromycin, MG-63 + LUC cells were harvested by using 0.25% trypsin containing 0.02% EDTA. A 100-μL cell

suspension was seeded in a 96-well plate (8×10^3 cells/well) and cultured for 24 h at 37°C in 5% CO_2. After 24 h, the medium was removed, and 200 μL of fluorescein sodium solution (150 μg/ml) was added. The luciferase content in MG-63 cells (MG-63 + LUC) was measured with a Leica SP8 *in vivo* imaging system.

Iodine Solution, Cell Counting Kit-8 (CCK-8) Assays, Flow Cytometry, and Transmission Electron Microscopy

An iodine solution containing 5 g/L I_2 was prepared using polyvinyl pyrrolidone (PVP) (Sigma, United States), I_2 (Sigma, United States) and deionized water. MG-63 and Saos-2 cells were washed three times with PBS and harvested by using 0.25% trypsin supplemented with 0.02% ethylenediaminetetraacetic acid (EDTA). A total of 100 μL of the cell suspension was seeded in a 96-well plate (5×10^3 cells/well) and cultured for 24 h at 37°C in 5% CO_2. After 24 h, the cells were divided into 11 groups (8 replicate wells/group). Different concentrations of iodine (0, 6, 8, 12, 14, 18, 20, 24 and 26 μM) and iodine solution released by self-assembling imageable silk hydrogels were added, and cell viability was measured at 3, 6, 12 and 24 h with Cell Counting Kit-8 solution (Dojindo, Japan). The optical density (OD) was measured at a wavelength of 540 nm using an Infinite 200Pro UV–visible spectrophotometer (Tecan, Austria). The differences in cell survival rates between the test group and the control group were compared. The median inhibitory concentration (IC_{50}) was calculated. The cells were treated with iodine at the IC_{50} level in subsequent experiments. The following formula was used for calculations:

$$Cell\ survival\ rate\,(\%) = \frac{OD_{(treatment\ group)} - OD_{(blank\ group)}}{OD_{(control\ group)} - OD_{(blank\ group)}} \times 100\%$$

Apoptosis was assessed using the Annexin V-FITC/PI Apoptosis Detection Kit (BD, United States) according to the manufacturer's specifications. After 12 h of treatment, MG-63 and Saos-2 cells were immediately collected and analysed using a fluorescence-activated cell sorting (FACS) flow cytometer (FACSCalibur, BD Biosciences, Heidelberg, Germany) for annexin V and PI staining. Annexin V+/PI + cells were considered the apoptotic cells.

For ultrastructural analyses to observe apoptotic corpuscles, after being washed with PBS, cells were fixed with 2% glutaraldehyde for 30 min and then further fixed with 1% (vol. ratio) osmium tetroxide for 2 h. Subsequently, the samples were dehydrated in an ethanol gradient and embedded in Spurr's resin. The resin blocks were then cut into ultrathin sections (8 nm), and the sections were stained with uranyl acetate and lead citrate and examined using an electron microscope (Hitachi, Tokyo, Japan) operated at an accelerating voltage of 80 kV.

Western Bloting

After the iodine solution released by the self-assembling imageable silk hydrogel and iodine treatment, human OS cells (Saos-2 and MG-63) were collected and the total protein was extracted and quantified using radioimmunoprecipitation assay (RIPA) buffer and a BCA protein assay kit (Beyotime, China). Total protein was boiled in buffer for 10 min, and equal amounts (30 μg) were resolved *via* 10 and 15% sodium dodecyl sulfate–polyacrylamide gel electrophoresis (SDS–PAGE) and transferred to polyvinylidene fluoride (PVDF) membranes (Bio–Rad). The membranes were blocked with skim milk dissolved in Tris-buffered saline (TBS) supplemented with 0.1% Tween-20, followed by incubation for 12 h at 4°C with the following primary rabbit polyclonal anti-human antibodies: GAPDH (1:1000, CST/5174, United States), Fas (1:1000, Proteintech/13098-1-AP, United States), FADD (1:1000, CST/2782, United States), FasL (1:1000, CST/68405, United States), caspase-3 (1:1000, Proteintech/19677-1-AP, United States), cleaved caspase-3 (1:1000, CST/9664, United States), PARP (1:1000, CST/9532, United States) and mouse monoclonal caspase-8 (1:1000, CST/9746, United States) antibodies. After three washes with TBS containing 0.1% Tween-20, the membranes were incubated with the appropriate secondary antibody for 1 h, washed three times, and visualized using enhanced chemiluminescence (ECL kit, Beyotime, China).

Preparation of Injectable Silk Hydrogels

PEG 400 (MW 400 g mol^{-1}), 60% silk fibroin solution, PVP-I (I_2: 5 g/L) and MD (Sigma, United States) were prepared. To make PEG-iodine-silk hydrogels, PEG was mixed with silk and PVP-I in 2.5 ml or 1 ml injectors. The total volume was 1 ml, and the percentage of each component in the PEG-silk hydrogel was as follows: 40% PEG 400 (V/V) and 13.5% (W/V) silk fibroin. The volume was adjusted to 1 ml with ultrapure water. The components of the PEG-silk/MD hydrogel were as follows: 40% PEG 400 (V/V), 13.5% silk fibroin (W/V), and 18% MD (V/V). The volume was adjusted to 1 ml with ultrapure water. The components of the PEG-iodine-silk/MD hydrogel were as follows: 40% PEG 400 (V/V), 13.5% silk fibroin (W/V), 18% MD (V/V), and 19.5% PVP-I (V/V). The volume was adjusted to 1 ml with ultrapure water.

Characterization of the Silk Hydrogels

Gelation Time

After several solutions were mixed, the OD value also changed due to the change in structure. The gelation kinetics were recorded as a function of OD changes over time as reported previously (Matsumoto et al., 2006; Wang et al., 2015; Ma et al., 2016). The mixture was injected into a 96-well plate at 200 μL per well, and then, the plate was subjected to OD measurements at 550 nm in kinetics mode on an Infinite 200Pro UV–visible spectrophotometer (Tecan, Austria) set at 37°C. The OD change was monitored for more than 60 min at 1-min intervals. Each testing group contained 6 samples (n = 6) to obtain average OD values and standard deviations.

Scanning Electron Microscopy

PEG can complicate the freeze-drying process; thus, the hydrogels were rinsed to remove PEG 400 and then lyophilized. PEG can be removed when hydrogels are

immersed in water. After the hydrogels were rinsed three times, they were frozen at −80°C overnight and lyophilized in a vacuum freeze drier (LICHEN LC-10N-50A, China) for 48 h. These freeze-dried gels were mounted on sample stubs and coated with Au, and images were captured using a scanning electron microscope (JEOL JSM-6300 SEM, Japan) at 12.5 kV (n = 3).

X-Ray Diffraction

A piece of hydrogel was evaluated by XRD (D/MAX-2500, Rigaku Co., Tokyo, Japan) to evaluate the degree of crystallinity. The samples were powdered and analysed with a 40-kV tube voltage, a 40-mA tube current, a 2θ = 5°–45° diffraction angle and a 4°/min scanning rate (n = 3).

Fourier Transform Infrared Spectroscopy

To determine whether the residual solvent and the addition of MD and PVP-I influence the conformational transformation, after removing PEG 400 and performing lyophilization, samples (n = 3) were powdered and placed on a zinc selenide (ZnSe) crystal cell, and the spectra were recorded in the reflection mode of the FTIR instrument (Thermo Fisher Scientific, Nicolet 6700 FT-IR,United States) in the spectral region of 550–4000 cm^{-1}; background measurements were performed with an empty cell and subtracted from the sample reading. Deconvolution of the amide I spectra was performed using the Gaussian-Lorentzian function in Opus 4.2 software. (Bruker, United States).

Injectability

The injection performance of the hydrogel was evaluated by measuring the force required to inject a 200-μL sample from a 1-ml syringe through a 25-G 7/800 long needle with a crosshead speed of 114 mm min^{-1} corresponding to a 2 ml min^{-1} injection rate (Wang et al., 2015). PEG 400, silk solution, PVP-I solution and MD were mixed, and samples from each group were loaded into separate syringes and tested over 70 min. At the designated time, a syringe was selected and loaded into a custom fixture mounted on an Instron 3366 load frame (Instron, United States), and the entire sample was extruded. The data are presented as the average injection force (n = 3).

Mechanical Properties

Hydrogels (silk fibroin protein concentration of 13.5%) were prepared for mechanical tests, with an 8 mm final diameter and 10 mm height (n = 3). Samples were loaded in an Instron 5848 Microtester (Instron, United States) between stainless steel parallel plates, and the upper plate was lowered continuously at a rate of 1 mm/min until the compressive force did not increase due to gel fracture. The compressive stress and strain were determined by normalization against the sample geometries, and the elastic modulus was calculated as reported previously (Ma et al., 2016).

Iodine Release *in vitro*

The hydrogel samples (1 cm^3) (n = 3) from each group were immersed in 4 ml of ultrapure water. The ultrapure water exposed to the hydrogel was collected, and the concentration of iodine released by each hydrogel was determined by the ICP–MS method. For the ICP–MS measurement of I, a matrix adjustment was necessary. For the measurements, the samples were diluted, and tetramethylammonium hydroxide was added, which caused hydrolysis of the organic compounds and decreased the redox potential. The liquid was then transferred into a corresponding centrifuge tube, and the samples were measured at 0, 3, 6, 9, 12, 24, 48, 72, 96, 120, 144 and 168 h. The release curve was generated according to the iodine release concentration measured by ICP–MS (Agilent 7700, United States).

Osteosarcoma Xenografts in Nude Mice and Hydrogel Treatment

All animal experiments complied with animal research guidelines; the manuscript was written in accordance with the ARRIVE reporting guidelines, and the experiments were carried out according to the National Institutes of Health Guide for the Care and Use of Laboratory Animals (NIH Publications No. 8023, revised 1978). This study was performed in accordance with China's national legislation and approved by the Ethics Committee of the First Affiliated Hospital of Harbin Medical University (ID:2021062), and the methods were conducted in accordance with the approved guidelines. Twenty 4-week-old female BALB/c athymic nude mice (14–15 g) were obtained from Beijing Vital River Laboratory Animal Technology Co., Ltd. According to the guidelines of the laboratory animal centre, the experimental animals were bred in a specific pathogen-free (SPF) environment in the experimental animal centre of Harbin Medical University with a constant temperature and humidity (22–24°C, 50–70% humidity) in a living environment under 12:12 h light:dark conditions. All animals were housed in pathogen-free conditions for an additional 7 days before OS inoculation. For the *in vivo* study, 100 μL of a suspension of 3×10^6 MG-63 + LUC cells was subcutaneously injected into the right axilla of the mice. The OS volume was evaluated every 3 days using a vernier caliper, and the OS volume was calculated with the following formula: $1/6\pi ab^2$ (a: long axis of the OS; b: short axis of the OS). When the OS volume was close to 0.5 cm^3, the mice were randomly divided into four groups (5 mice per group). The control group was injected with normal saline, the PEG-silk/MD hydrogel group was injected with PEG-silk/MD hydrogels, the iodine group was injected with PVP-I and the PEG-iodine-silk/MD hydrogel group was injected with PEG-iodine-silk/MD hydrogels. The experimental group received an intratumoural injection of 50 μL of hydrogel and PVP-I, and the control group received an injection of 50 μL of saline. All operations were performed with X-ray guidance, and the mice were anaesthetized *via* intraperitoneal injection of 1% pentobarbital sodium (45 mg/kg) during the entire process. Then, 42 days after the injection, the animals were sacrificed by spinal dislocation under anaesthetization with intraperitoneal injection of 1% pentobarbital sodium (45 mg/kg), and the OSs and organs were harvested and fixed in 4% formalin.

Live Bioluminescence Imaging

Forty-two days after the injection, the mice were anaesthetized *via* intraperitoneal injection of 1% pentobarbital sodium (45 mg/kg), and 200 μL of sodium fluorescein (Sigma,

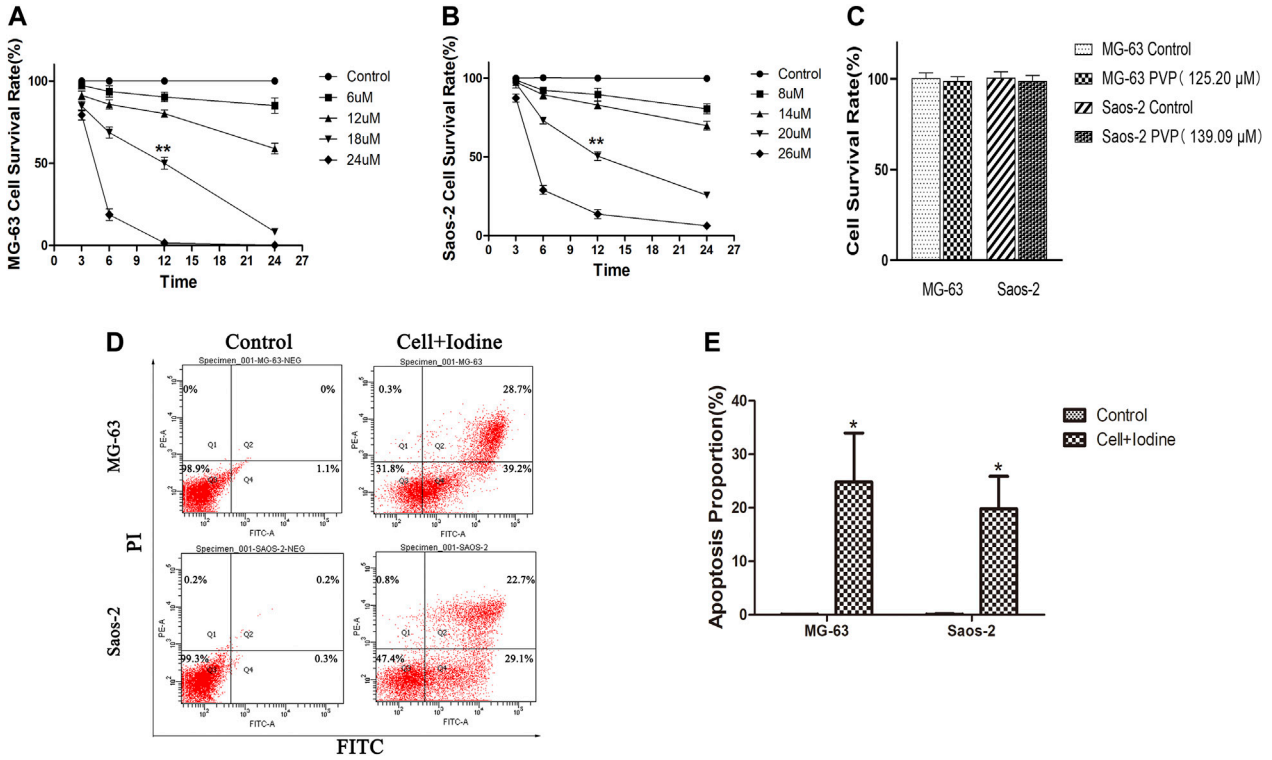

FIGURE 2 | Iodine induced apoptosis in OS cells. **(A,B)** After 3, 6, 12 and 24 h of treatment with iodine, the cell survival rate was assessed using a CCK-8 assay. The IC_{50} values of MG-63 and Saos-2 at 12 h were 18 and 20 μM, respectively (**$p < 0.01$). **(C)** The cell survival rate of MG-63 and Saos-2 cells after treatment with PVP solution (125.20 and 139.09 μM) for 12 h, which corresponded to the iodine (18 and 20 μM) concentration used. **(D)** After 12 h of treatment with iodine, the proportions of cells (MG-63 and Saos-2) undergoing apoptosis were analysed by flow cytometry after staining with Annexin V-FITC/PI. **(E)** The proportion of apoptotic OS cells after treatment with iodine (*$p < 0.05$). The mean percentages of cells undergoing apoptosis (±SD) are shown. (OS, osteosarcoma; CCK-8, Cell Counting Kit-8; IC_{50}, the median inhibitory concentration; PVP, polyvinylpyrrolidone; Annexin V-FITC/PI, Annexin V-FITC/PI Apoptosis Detection Kit; SD, standard deviation).

United States) (15 mg/ml) was injected intraperitoneally. After 10 min, *in vivo* imaging was performed with a Leica SP8 *in vivo* imaging system (Leica, GER).

Histopathological Analysis

For the histopathological analysis, the collected OS samples and organs were fixed in 4% paraformaldehyde for 48 h at room temperature (RT) and then dehydrated using an alcohol gradient. The tissues were embedded in paraffin and cut into 4-μm sections. Sections were stained with haematoxylin and eosin (H&E) and analysed by immunohistochemistry (IHC). The paraffin-embedded tissue sections were mounted onto microscope slides, dewaxed and rehydrated. After hematoxylin and eosin (H&E) staining, images were taken under an optical microscope. For IHC staining, antigen retrieval was performed by microwave heating for 2 min in 0.1 mol/L citrate buffer (pH 6.0) followed by blocking with endogenous peroxide with 3% H_2O_2 in methanol for 5 min. After cooling, the slides were washed with distilled water and blocked with 10% goat serum for 30 min. The slides were then washed with distilled water and incubated with the primary antibodies anti-caspase-3 (1:200, Proteintech/19677-1-AP, United States) and anti-PARP(1:200, CST/9532, United States) at 4°C for 12 h and then rinsed with running water and PBST. The slides were then stained with the secondary antibody goat anti-rabbit IgG H&L (Abcam, United States) for 60 min, washed in running tap water, stained with diaminobenzidine (DAB), and counterstained with haematoxylin. Finally, the slides were dehydrated and visualized using a microscope. The results were analysed with Image-Pro Plus (IPP) 6.0 software (Media Cybernetics, United States).

Statistical Analysis

All statistical analyses were performed using SPSS 19.0 (SPSS, Inc., Chicago, IL, United States). When the data were normally distributed, two samples were analysed using Student's t test to determine significant differences ($p \leq 0.05$), and multiple comparisons were evaluated by one-way analysis of variance (ANOVA) followed by Dunnet's test to determine whether there were significant differences (*$p \leq 0.05$, **$p \leq 0.01$, ***$p \leq 0.001$). Continuous variables are expressed as the mean ± standard deviation. During data analysis, the analysts were unaware of the groups and treatments.

RESULTS

Iodine Induces the Apoptosis of OS Cells

We analysed the effect of iodine on the survival rates and apoptosis of MG-63 and Saos-2 OS cells. As shown in **Figures 2A,B**, treatment of MG-63 and Saos-2 cells with PVP-I stimulated cell

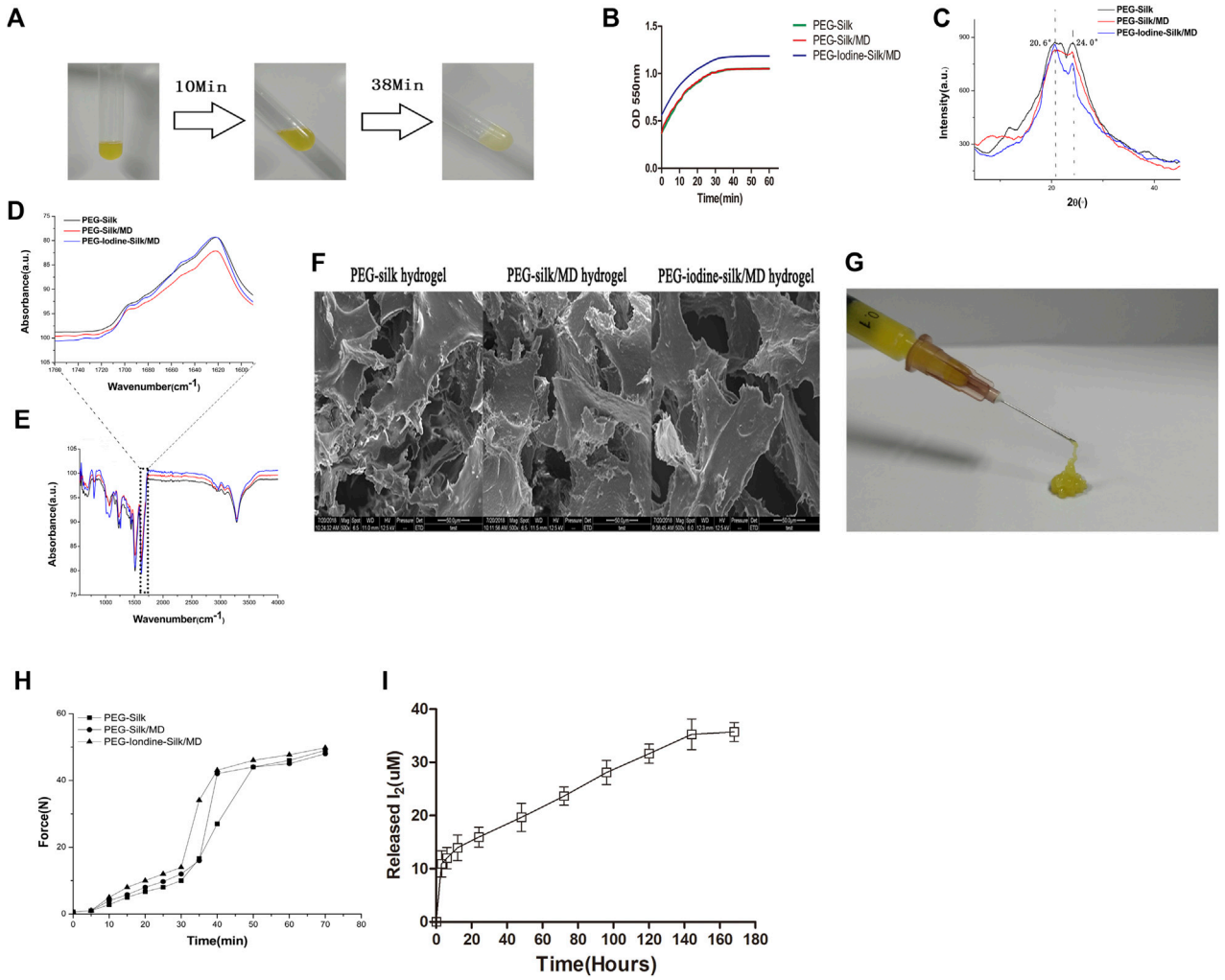

FIGURE 3 | Characterization of the silk hydrogels. **(A)** Gelation process after mixing silk fibroin, PEG 400, MD and PVP-I solution at room temperature. **(B)** Time-dependent OD measurement after mixing silk fibroin, PEG 400, MD and PVP-I solution. **(C)** XRD measurement of the silk hydrogels. **(D,E)** FTIR spectra of the PEG-silk hydrogel, PEG-silk/MD hydrogel and PEG-iodine-silk/MD hydrogel. **(F)** Silk hydrogel morphologies determined by SEM (scale bars = 50 μm). **(G,H)** Injectability measurement. **(I)** I_2 released from the PEG-iodine-silk/MD hydrogel. (PEG 400, polyethylene glycol 400; MD, meglumine diatrizoate; PVP-I, polyvinylpyrrolidone iodine; OD, optical density; XRD, X-ray diffraction; FTIR, Fourier transform infrared spectroscopy; PEG, polyethylene glycol; SEM, scanning electron microscopy).

death with time- and concentration-dependent effects, respectively. When the iodine concentrations were 18 and 20 μM, the cell survival rates were 50 ± 2.1% and 50.5 ± 2.7% for MG-63 and Saos-2 cells at 12 h, respectively ($p < 0.01$). We identified the I_2 concentration at 12 h as the IC_{50} value. The PVP concentrations corresponding to iodine concentrations of 18 and 20 μM were 125.20 and 139.09 μM, respectively. PVP solution was also used to stimulate the two types of cells for 12 h and did not affect cell survival (**Figure 2C**), which suggested that iodine causes cell death.

As the flow cytometry results showed, after 12 h of treatment with 18 and 20 μM iodine, the proportions of MG-63 and Saos-2 undergoing apoptosis were 24.8 ± 9.2% and 19.8 ± 6.1%, respectively, which were significantly higher than those of the control cells ($p < 0.05$) (**Figures 2D,E**).

Characterization of the Silk Hydrogels

Gelation Time

The solutions were fluids when the ingredients were mixed and became more viscous and opaquer over time (**Figure 3A**). The gelation time was defined as the time from the beginning of mixing to the time when the plateau was reached. As shown in **Figure 3B** and **Table 1**, the gelation times of the three groups ranged from 36.7 min to 37.7 min. The gelation time depended on the concentrations of silk and PEG used. The similarity of the gelation time between the three groups was due to the use of the same concentrations of silk and PEG 400 in all of the gels.

Crystallinity Analysis by XRD

XRD was performed to study the crystallinity of the silk hydrogels. The XRD results revealed analogous

TABLE 1 | Silk gelation time.

Concentrations of silk (W/V, %) and PEG 400 (V/V, %)	PEG-silk hydrogel (min)	PEG-silk/MD hydrogel (min)	PEG-Iodine-silk/MD hydrogel (min)
13.5/40	36.7 ± 0.58	37.3 ± 0.58	37.7 ± 1.15

The gelation time was defined as the time when the optical density plateaued (n = 6). There was no significant difference in gelation time among the three groups (p > 0.05) (PEG: polyethylene glycol, MD: meglumine diatrizoate).

TABLE 2 | Unconfined compression data for silk hydrogel.

Group	PEG-silk hydrogel	PEG-silk/MD hydrogel	PEG-Iodine-silk/MD hydrogel
Compressive strength (kPa)	15.7 ± 0.8	16.1 ± 0.9	16.5 ± 0.8
Elastic modulus (kPa)	146.5 ± 1.5	150.0 ± 2.0	151.67 ± 2.46
Strain-to-failure (%)	14.17 ± 0.35	14.9 ± 0.4	14.97 ± 0.35

The concentrations of silk (w/v, %) and PEG, 400 (w/w, %) were 13.5 and 40%, respectively (n = 3). The results showed that there was no significant difference in unconfined compression among the three groups (p > 0.05) (PEG, polyethylene glycol; MD, meglumine diatrizoate).

crystallization in all three types of hydrogels. A strong peak at 20.6° implied that the silk existed mainly in the silk II form (**Figure 3C**), further confirming the FTIR results. The results indicated that PVP-I and MD had a negligible influence on the silk crystallinity analysis.

Structural Analysis by FTIR

Silk gelation was accompanied by β-sheet structure formation, as shown by the major peak at 1622 cm^{-1} in the amide I region of the FTIR spectrum (**Figure 3D**). The strong peak at wavelengths lower than 1218–1262 cm^{-1} and the peak centred at 2934–2952 cm^{-1} resulted from residual PEG (**Figure 3E**), as reported in the literature (Nguyen and Janik, 1987). PEG did not show peaks in the amide I and II band regions and thus had a negligible influence on the silk structural analysis. As shown in **Figures 3D,E**, PVP-I and MD did not affect the silk structure.

Microstructure of Lyophilized Silk Hydrogels

The porous morphology of 13.5% silk hydrogels after extraction and lyophilization was examined by SEM. The overall gel morphology showed small pores, an elongated shape and randomly orientated silk laminar layers, indicating high porosity and interconnectivity. The diameter of the pores, whose walls were extraordinarily thin, varied from 20 to 100 μm (**Figure 3F**, **Supplementary Figure S1**). The presence of PEG might have changed the freezing rate and the pore structure of the silk gels during lyophilization. Since the concentrations of silk and PEG were the same in all three groups, all of the hydrogels had similar pore diameters.

Mechanical Properties and Injectability of Silk Fibroin Hydrogels

The hydrogels were subjected to an unconfined compressive strain to the point of failure to assess their mechanical properties. The compressive strengths, elastic moduli, and strains-to-failure of the hydrogels were similar (**Table 2**) because the concentrations of silk fibroin and PEG were the same in all three groups. The gels were easily injected with a syringe (**Figure 3G**). The supervised injection force started to significantly increase 30–40 min after mixing the solutions. The injection forces reached 50 N by the end of the measurement period (60–70 min) and continued to slowly increase afterwards (**Figure 3H**). These properties contributed to the ease of hydrogel injection.

Iodine Release

Figure 3I shows the quantity of iodine released into the medium at different time points. The quantity of iodine released increased over time. The results showed a burst release in the first 12 h; then, the release of iodine slowed and sustained release occurred over the following 6 days. The concentration of released iodine reached its highest level of 35.3 μM on day 7. Furthermore, when the concentration of released iodine was highest, the cumulative release amount following 7 days of release was approximately 36.3% of the initial iodine content.

Iodine Solution Released by Self-Assembling Imageable Silk Hydrogels Induces the Apoptosis of OS Cells

The anti-OS ability of the self-assembling imageable silk hydrogels was verified *in vitro*. The hydrogel (1 cm^3) was immersed in 4 ml of OS cell culture medium, and the cells were cultured in medium for 12 h. We analysed the effect of released iodine solution on the survival rates of OS cells. To verify the effects of both types of OS cells on apoptosis at the same time, with reference to the iodine release results (**Figure 3I**), we chose the iodine solution released by the hydrogel for 72 h. As shown in **Figures 4A,B**, the anti-OS effect of the self-assembling imageable silk hydrogels was excellent. The cell survival rates were 2.0 ± 0.4% and 20.3 ± 3.5% for MG-63 and Saos-2 cells at 12 h, respectively, which were significantly lower than those of the

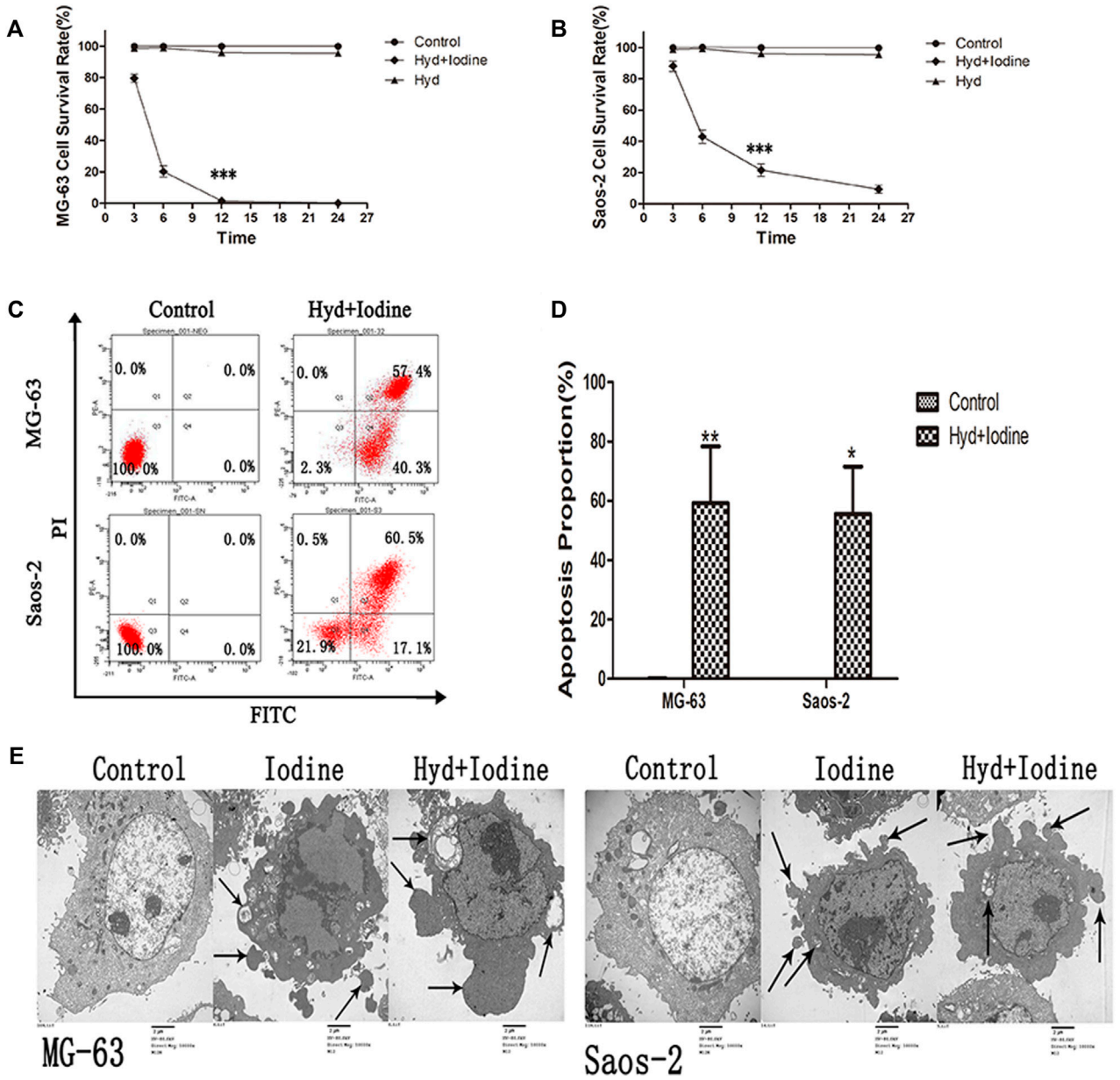

FIGURE 4 | Iodine released by the self-assembling imageable silk hydrogel induced apoptosis in OS cells. **(A,B)** After 3, 6, 12 and 24 h of treatment with released iodine solution, the cell survival rate was assessed by a CCK-8 assay (***$p < 0.001$). **(C)** After 12 h of treatment with released iodine solution, the proportions of cells (MG-63 and Saos-2) undergoing apoptosis were analysed by flow cytometry after staining with Annexin V-FITC/PI. **(D)** The proportion of apoptotic OS cells after treatment with released iodine solution (*$p < 0.05$, **$p < 0.01$). The mean percentages of cells undergoing apoptosis (±SD) are shown. **(E)** The apoptotic ultrastructure of OS cells treated with iodine and released iodine solution. The arrows indicate apoptotic bodies. The cells were examined under a transmission electron microscope. Control: untreated OS cells, Iodine: treated with PVP-I, Hyd + Iodine: treated with iodine solution released by hydrogel (Magnification, 10000X; Scale bar = 2 μm) (OS, osteosarcoma; CCK-8, Cell Counting Kit-8; Annexin V-FITC/PI, Annexin V-FITC/PI Apoptosis Detection Kit; SD, standard deviation; PVP-I, polyvinylpyrrolidone iodine).

control group and the hydrogel group without iodine loading ($p < 0.001$).

To further verify the occurrence of apoptosis, we observed the morphology of dead cells by flow cytometry and TEM. After 12 h of released iodine solution and iodine treatment, the proportions of cells undergoing apoptosis were 59.3 ± 19.1% and 55.6 ± 15.9% (**Figures 4C,D**), respectively. The apoptosis rates of the MG-63 and Saos-2 cells were significantly higher than those of the control cells ($p < 0.05$) (**Figure 4D**). Typical morphological features of apoptosis were observed by TEM, including the following: condensation of nuclear chromatin, denser cytoplasm, and the formation of dense round apoptotic bodies (**Figure 4E**). Plasma membrane blebbing and shedding of apoptotic bodies indicated apoptotic cell death. These data demonstrated that iodine

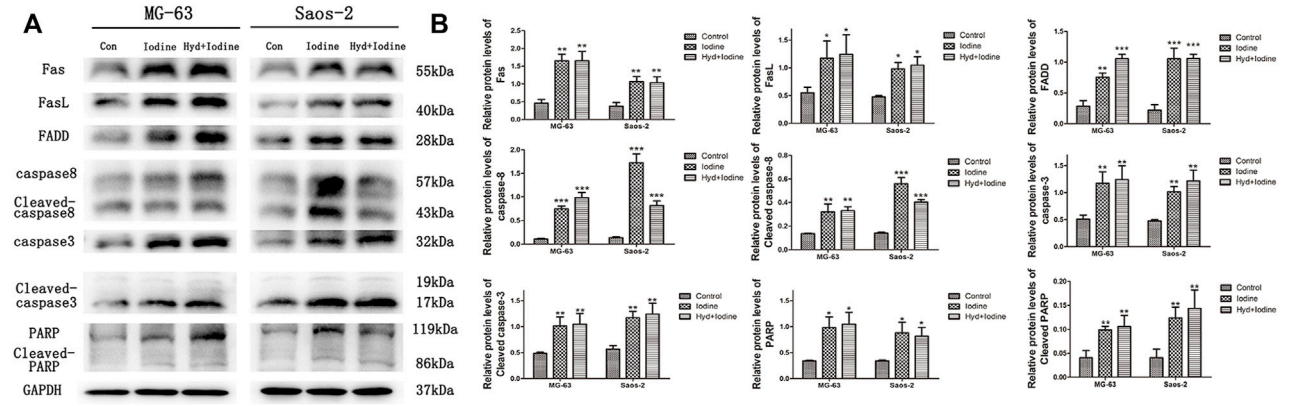

FIGURE 5 | Iodine induces apoptosis through the death receptor pathway. **(A)** A representative Western blot of Fas, FasL, FADD, caspase-8, cleaved caspase-8, caspase-3, cleaved caspase-3, PARP and cleaved PARP in protein extracts of MG-63 and Saos-2 cells pretreated with iodine and released iodine solution for 12 h. **(B)** Densitometric analysis of Fas, FasL, FADD, caspase-8, cleaved caspase-8, caspase-3, cleaved caspase-3, PARP and cleaved PARP levels. The results are presented as the mean ± SD (n = 3) (*p < 0 0.05, **p < 0 0.01, ***p < 0 0.001) (SD: standard deviation).

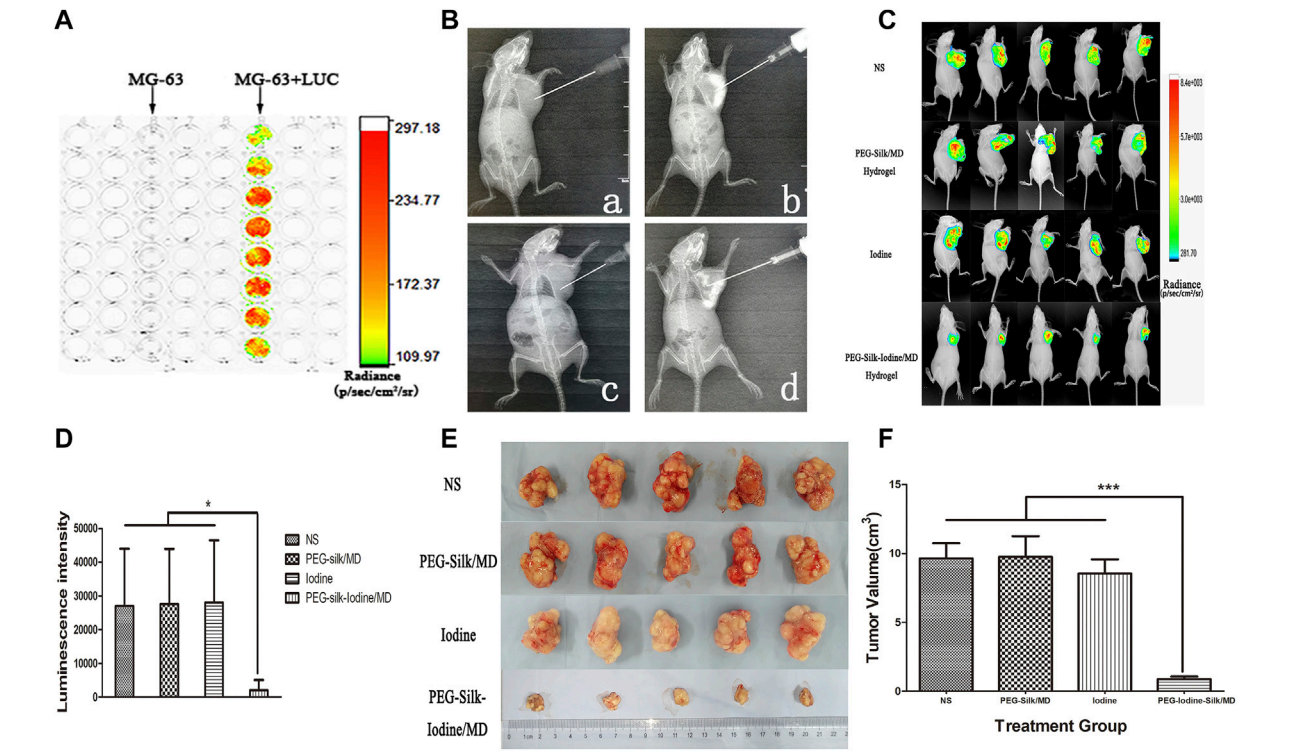

FIGURE 6 | Iodine-loaded hydrogels inhibit OS growth *in vivo*. **(A)** The bioluminescence of MG-63 cells after transfection with luciferase. **(B)** A representative image of the injectable hydrogels in the X-ray field. The image shows the distribution of the imageable hydrogels in the OS. a, Control group mice were inoculated with normal saline. b, PEG-silk/MD hydrogel group mice were inoculated with PEG-silk/MD hydrogel. c, Iodine group mice were inoculated with PVP-I. d, PEG-iodine-silk/MD hydrogel group mice were inoculated with PEG-iodine-silk/MD hydrogel. **(C)** The bioluminescence imaging of OS *in vivo*. **(D)** Quantification of bioluminescence signals from OS-bearing mice. **(E)** A representative image of xenograft OSs in the four groups. **(F)** Volume of xenograft OSs in nude mice after 42 days of hydrogel and saline injection. The data are presented as the mean ± SD. (*p < 0.05, ***p < 0.001.) (OS, osteosarcoma; PEG, polyethylene glycol; MD, meglumine diatrizoate; PVP-I, polyvinylpyrrolidone iodine;SD, standard deviation).

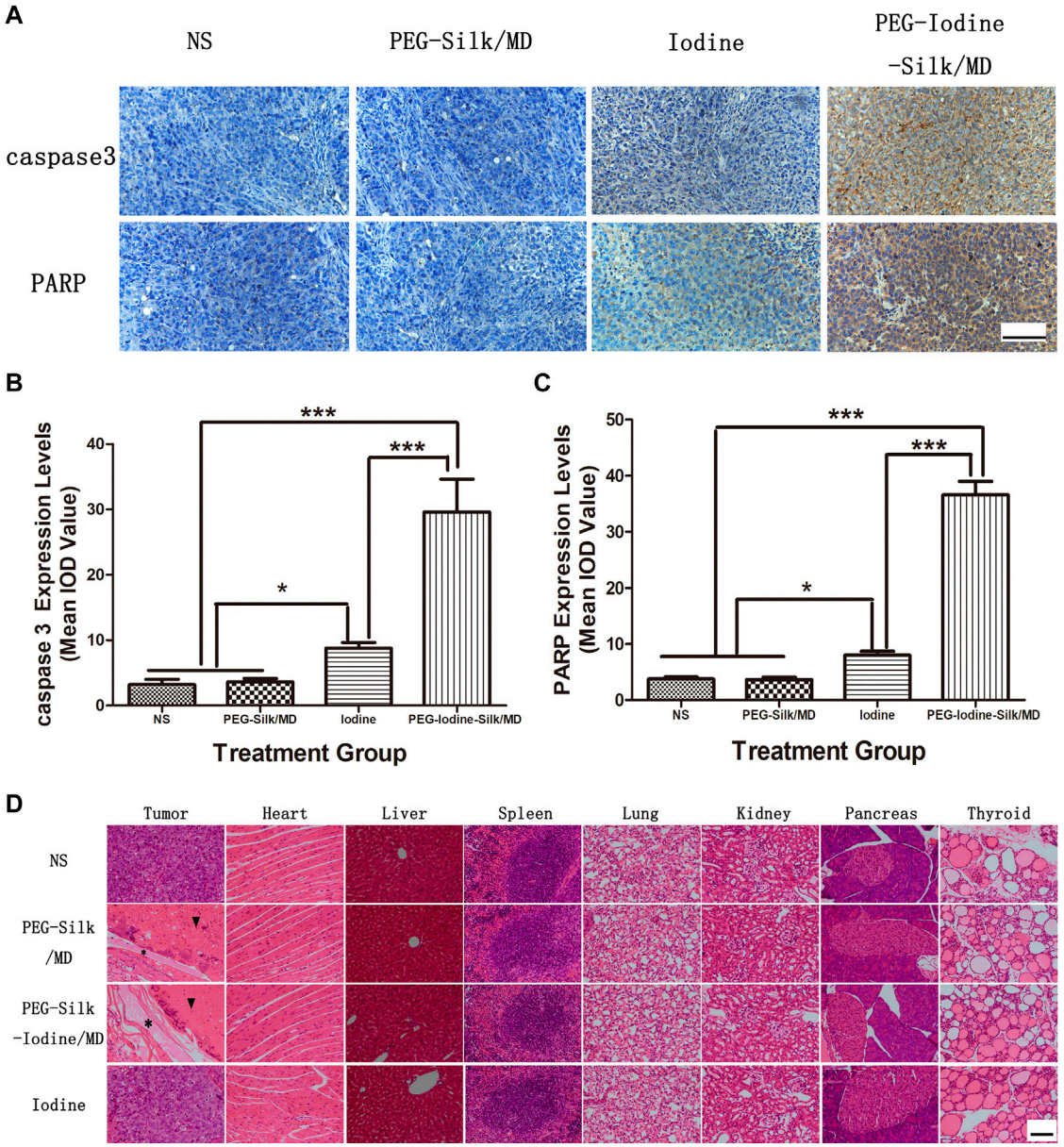

FIGURE 7 | Immunohistochemical and H&E staining. **(A)** Caspase-3 and PARP expression in OS sections from the different groups was characterized by immunohistochemistry. The data are representative images (scale bars = 100 μm). **(B)** Quantification of the caspase-3 staining densities. The data expressed as the mean ± SD of in individual groups of OSs ($n = 5$) (*$p < 0.05$, ***$p < 0.001$). **(C)** Quantification of the PARP staining densities. The data are expressed as the mean ± SD of individual groups of OSs ($n = 5$) (*$p < 0.05$, ***$p < 0.001$). **(D)** OSs and main organs (heart, liver, spleen, lung, kidney, pancreas and thyroid) were dissected for H&E staining on the 42nd day after injection. No significant abnormal damage was observed in the organs. * indicates silk hydrogel. ▼ indicates necrotic OS tissue (scale bars = 100 μm). (OS, osteosarcoma; PEG, polyethylene glycol; MD, meglumine diatrizoate; SD, standard deviation; H&E, haematoxylin and eosin; IOD, integrated optical density).

solution released by the hydrogel and iodine alone enhanced MG-63 and Saos-2 cell apoptosis *in vitro*.

Iodine Induces Saos-2 and MG-63 Cell Apoptosis by Regulating the Fas/FasL Signalling Pathway

To further elucidate how iodine causes apoptosis, we performed Western blot analysis. The Western blot results showed that the levels of Fas, FasL and FADD were significantly increased in MG-63 and Saos-2 cells after incubation with iodine and released iodine solution compared with those of the control group. Similarly, the levels of caspase-8, caspase-3, PARP and their cleaved forms were also increased in both MG-63 and Saos-2 cells after treatment with iodine and released iodine solution compared with those of the control group (**Figure 5A**). In the quantitative analysis, the expression levels of Fas (40–55 kDa), FasL (40 kDa), FADD (28 kDa), caspase-8 (57 kDa), cleaved

caspase-8 (43 kDa), caspase-3 (32 kDa), cleaved caspase-3 (17/19 kDa), PARP (116 kDa) and cleaved PARP (89 kDa) were significantly higher in iodine-treated cells than in control cells (**Figure 5B**) ($p < 0.05$).

Iodine Inhibition of OS Growth *In Vivo* in a Nude Mouse Model

The effect of iodine on OS was explored *in vivo*. Fluorescence was observed after the successful transfection of MG-63 cells with luciferase (LUC)-td tomato lentiviruses (**Figure 6A**). Silk hydrogels contain MD; therefore, the injection, distribution and dispersion of the silk hydrogel can be visualized by X-ray analysis (**Figure 6B**). For *in vivo* bioluminescence imaging, the bioluminescence levels in the PEG-silk-iodine/MD hydrogel-treated mice decreased significantly compared with those in the control, iodine and PEG-silk/MD hydrogel mice ($p < 0.05$) (**Figures 6C,D**), whereas the bioluminescence levels in the mice that were treated with PVP-I and PEG-silk/MD hydrogel were not decreased compared with those in the control mice. As shown in **Figures 6E,F**, the OS volume in the group of mice injected with PEG-iodine-silk/MD hydrogel was significantly smaller than that in the other three groups of mice ($p < 0.001$). These results indicated that OS growth was significantly inhibited in the mice that received iodine released from the hydrogel. In the pre-experiments we constructed animal models using both MG-63 + LUC and Saos-2+LUC cells, but we found that Saos-2 cells could not form subcutaneous tumours (**Supplementary Figure S2**).

Immunohistochemical Staining and Systemic Toxicity

The levels of caspase-3 and PARP expression are associated with the apoptosis in OS. We used IHC to measure the expression levels of caspase-3 and PARP in different OS groups (**Figure 7A**). Quantitative analysis of the intensity of anti-caspase-3 and anti-PARP staining indicated that there were no significant differences in OS between the control and PEG-silk/MD hydrogel groups (**Figure 7A**). The levels of caspase-3 and PARP expression in the PEG-iodine-silk/MD hydrogel group were significantly higher than those in the control, iodine and PEG-silk/MD hydrogel groups ($p < 0.001$), whereas the levels of caspase-3 and PARP expression in the mice that were treated with PVP-I were increased compared with those in the control and PEG-silk/MD hydrogel mice ($p < 0.05$) (**Figures 7B,C**). Collectively, these data indicated that treatment with the implanted PEG-iodine-silk/MD hydrogel increased the expression levels of caspase-3 and PARP in the OS model in nude mice. Furthermore, we examined the biocompatibility and systemic toxicity of the silk hydrogels. At day 42 after injection, the mice were sacrificed, and important organs in each group were collected, including the heart, liver, spleen, lungs, kidneys, pancreas and thyroid. No cells with tumour cell characteristics were observed in the organs; in particular, the thyroid, which is sensitive to iodine, was unaffected, which is critical, as changes in iodine levels often cause pathological changes in the thyroid (**Figure 7D**). This result indicated that the PEG-iodine-silk/MD hydrogel exhibited good biocompatibility and biosafety *in vivo*. In addition, as shown in **Figure 7D**, incompletely degraded hydrogel and a large amount of necrotic OS tissue appeared around the PEG-iodine-silk hydrogel (* indicates silk hydrogel; ▼ indicates necrotic OS tissue).

DISCUSSION

In this study, we showed that iodine significantly inhibited proliferation and induced apoptosis in OS cell lines. The inhibitory effect of iodine on cell proliferation was time- and concentration-dependent ($p < 0.01$). In the flow cytometric analysis, the rates of MG-63 and Saos-2 cells undergoing apoptosis were approximately 24.8 ± 9.2% and 19.8 ± 6.1% after 12 h of iodine stimulation at 18 and 20 μM, respectively, and the apoptosis rates were significantly higher in the OS cells than in the control cells ($p < 0.05$). We also used TEM to observe typical apoptotic morphological features, including the condensation of nuclear chromatin, denser cytoplasm, and the formation of dense round apoptotic bodies (Li et al., 2015; Antunovic et al., 2019). These results indicated that iodine induced apoptosis in MG-63 and Saos-2 cells.

Although iodine has been widely used in antitumour studies, its antitumour mechanism is still unclear. In this study, we elucidated the mechanism by which iodine activates the death receptor pathway, leading to apoptosis in OS cells. We found that apoptotic cell death in OS cells (MG-63 and Saos-2) was predominantly initiated by the death receptor Fas (40–55 kDa), which bound to FasL (40 kDa) to activate the death domain FADD (28 kDa); subsequently, caspase-8 (57 kDa) was activated (Nagata, 1997; Ashkenazi and Dixit, 1998; Kuang, et al., 2000). The first cleavage stabilizes the active dimer, and the second cleavage releases it from the death-induced signalling complex (DISC) (Dickens et al., 2012; Yin et al., 2018; Wu et al., 2019). In our study, cleaved caspase-8 (43 kDa) activated caspase-3 (32 kDa), which further activated PARP to promote apoptosis (Green and Llambi, 2015). PARP is a 116 kDa nuclear poly(ADP-ribose) polymerase, and cleaved PARP contains the carboxy-terminal catalytic domain (89 kDa) (Lazebnik et al., 1994; Nicholson et al., 1995). The cleavage of PARP facilitates DNA fragmentation and cell disintegration and disassembly, thus serving as a marker of cells undergoing apoptosis (Oliver et al., 1998).

Silk fibroin is known to be degraded *in vivo* and has a robust safety record in humans (Leisk et al., 2010; Omenetto and Kaplan, 2010; Diab et al., 2012; Ma et al., 2016; Leng et al., 2017). The degradation profile of silk hydrogels can be controlled and can last from weeks to months depending on the crystallinity level (Vepari and Kaplan, 2007). Additionally, different forms of silk fibroin products, such as microparticles, films and hydrogels, can allow stabilization of the drug load and control of drug release using endogenous parameters such as the crystallinity and molecular weight of the silk fibroin (Pritchard and Kaplan, 2011; Wenk et al., 2011; Li et al., 2016). Although numerous silk formulations have been used in previous studies, no study has examined the therapeutic potential of silk hydrogels for human OS therapy *in vitro* or *in vivo*. In this study, we developed a local delivery system that was injectable, imageable, biodegradable and safe and was capable of delivering anti-OS drugs that target OS cells *in vitro* and *in vivo*. In previous studies,

high silk fibroin concentrations (>8%) were suggested to be desirable to avoid rapid *in vivo* degradation of the gel (Wang et al., 2015). In our study, silk fibroin concentrations reached 13.5%, which ensured slow *in vivo* degradation of the gel. Only low-molecular weight PEG (<1500 Da) can force the hydrophobic domains on the silk molecules to form crystalline β-sheets and a gel network; in contrast, higher-molecular weight PEG induces silk to form fibres and particles (Wang et al., 2015). Regarding the use of PEG, as a pharmaceutical ingredient, the highest concentration of PEG 400 used in medicinal formulations for injection approaches 50% (Strickley, 2004). In our study, the concentration of PEG 400 in the silk hydrogels was 40% (<50%); thus, toxicity was not a concern.

This study aimed to explore the feasibility of using imageable hydrogels to deliver anti-OS drugs for the treatment of OS. We analysed the hydrogel characteristics. During the gelation of silk fibroin, nanospheres, nanofilaments and microfibres formed, which affected the clarity of the solution. Therefore, the change in the OD could be measured to monitor the molecular hierarchical self-assembly process during silk gelation. In our study, the gelation time was 36.7–37.7 min. The change in the injection force was also determined. The retardation times measured by the change in the injection force (40 and 50 min) were longer than those measured by the change in the OD (37 min). This difference may be due to the difference in the testing temperature, as the injection experimental temperature (RT) was lower than that used in the gelation time experiment (37°C). Another possible reason is that the molecular entanglements of silk such that these structural changes preceded the formation of nano- and microstructural features, resulting in a time discrepancy between force and OD measurements. In addition, the injection of a mixed solution required less than a 10 N compression force to pass through a thin needle (27 G). At the end of the measurement, the force was 40–50 N, but the hydrogel was still injectable despite requiring more force. A relatively slow increase in injection force and smaller compression force could also be observed for silk hydrogels, which could be beneficial for clinical application. As shown by scanning electron microscopy, the internal network of the gel was small and compact. In addition, the mechanical properties of the three hydrogels were stable and homoplastic. The process of hydrogel formation is also a process of β-sheet and gel network formation. The main diffraction peaks found at 12.3°, 19.7°, 24.7°, 28.5° and 33.3° represented silk I, while those at 9.1°, 18.8° and 20.5° represented silk β-sheet structures.The curves that had absorption bands in the frequency range of 1620–1630 cm^{-1} and 1695–1700 cm^{-1} represented an enriched β-sheet structure in the silk II form (Wang et al., 2015). The contribution of these curves (β-sheet structural content) to the amide I band was assessed by integrating the area under the curve and then normalizing it to the total area under the amide I band region (1600–1700 cm^{-1}), as described previously. Although mixed with PVP-I and MD, based on XRD and FTIR, PVP-I and MD had no obvious impact on the conformation transition because they did not interact with silk or PEG; only phase separation was observed. Silk hydrogels are a mature and stable drug release system; nevertheless, we tested silk hydrogels for their ability to release iodine. As the results showed, in the first 12 h, iodine was released quickly. The release of iodine subsequently slowed and was sustained over 6 days, maintaining a maximum concentration of 35.3 μM. Furthermore, the cumulative released amount following 7 days of release was approximately 36.3% of the initial iodine content. We chose the iodine solution released by the hydrogel for 72 h, and treated MG-63 and Saos-2 for 12 h, the proportions of cells undergoing apoptosis were 59.3 ± 19.1% and 55.6 ± 15.9%, respectively. The apoptosis rates of the MG-63 and Saos-2 cells were significantly higher than those of the control cells ($p < 0.05$). This indicate that the iodine released from self-assembled hydrogels can effectively promote MG-63 and Saos-2 apoptosis *in vitro*.

With X-rays, the imageable hydrogels were observed as a high-density image, and X-rays could be used to guide the localization of the hydrogels injected into the OS. As the X-ray image shows, the hydrogels remained inside the OS and dispersed. With the introduction of MD and imaging in the X-ray field, the injection was less invasive, which was beneficial for injecting hydrogels and delivering anti-OS drugs to local lesions.

We then determined whether our *in vitro* observations would translate into *in vivo* OS therapy. Therefore, we used a humanized subcutaneous OS nude mouse model. In the *in vivo* study, the local treatment of mice with PEG-iodine-silk/MD hydrogels suppressed OS growth. Compared with the other three groups, the group treated with PEG-iodine-silk/MD hydrogels showed not only a significantly decreased OS volume but also a significant decrease in luminescence intensity. Immunohistochemical tests were performed to determine whether iodine transferred by hydrogels *in vivo* could induce apoptosis as it did *in vitro*. We found that the expression levels of caspase-3 and PARP in the PEG-iodine-silk/MD hydrogel treatment group were significantly higher than those in the other three groups ($p < 0.001$). These results indicated that iodine can induce the apoptosis of OS *in vivo* and *in vitro*. The local injection of PVP-I into the OS did not achieve ideal results. We suspected that the injection of PVP-I alone, without hydrogel to control its release, could cause iodine to enter the circulation system quickly and be metabolized without long-term effects on OS. The systemic damage caused by iodine was far less severe than that caused by chemotherapeutic drugs. The results show that the iodine-loaded hydrogels had high biological safety and no systemic toxicity and induced no damage to the main organs, such as the heart, liver, spleen, lung, kidneys, pancreas and thyroid. In particular, thyroid tissue is sensitive to iodine, and changes in iodine can cause thyroid tissue lesions. However, in this study, iodine-loaded hydrogels did not damage the thyroid. Therefore, iodine-loaded hydrogels not only inhibited OS *in vivo* growth but also exhibited good biosafety.

In this study, we constructed self-assembled imageable silk hydrogels as a controlled release system for the local release of iodine for OS treatment, a novel attempt to avoid multiorgan damage caused by conventional chemotherapeutic drugs and major surgical trauma. Self-assembling imageable silk hydrogels could be injected *via* syringe, which mad transdermal injection to

the interior of the OS possible, as the injection was far less invasive than surgery. MD allowed the hydrogel to be imageable with X-rays; thus, the hydrogel could be injected inside the OS with X-ray guidance, which was beneficial for injecting hydrogels and delivering anti-OS drugs to local lesions. Moreover, the systemic damage caused by iodine was far less severe than that caused by chemotherapeutic drugs. No abnormalities were found in any of the seven types of organs we collected, and the iodine-loaded hydrogel achieved excellent results in the treatment of OS, which few chemotherapeutic drugs can achieve. Of course, hydrogels also have some limitations such as low mechanical strength and limited support, which might increase their risk of fracture. To address the limitations of hydrogels that may be encountered in future applications, it is possible to combine the application of hydrogels with external fixation and use the supportive properties of external fixation to compensate for the lack of mechanical strength and support of hydrogels. With regard to the risk of metastasis, we were also concerned at the beginning of the study that injecting a volume of hydrogel solution into an OS might lead to an increase in local pressure, thus increasing the risk of OS metastasis. However, bioluminescence was not observed at sites other than OS by *in vivo* bioluminescence imaging at the end of the *in vivo* trial. No cells with tumour cell characteristics were observed in the organs. In this study, hydrogel injections were not found to increase the risk of OS metastasis.

We conducted only a short-term assessment of systemic injury; we will evaluate the long-term systemic damage, therapeutic effect and metastasis in the *in situ* OS model in subsequent experimental studies. There are various death receptors, such as Fas, tumour necrosis factor receptor 1, tumour necrosis factor-related apoptosis-inducing ligand receptor 1, tumour necrosis factor-related apoptosis-inducing ligand receptor 2, activation of death receptor-4 and activation of death receptor-5. Fas/FasL is the classic receptor and ligand of the death receptor pathway, and although some studies have reported the role of Fas in osteosarcoma, there are few studies on the tumour-inhibiting effect of iodine. Therefore, we chose the receptor-ligand pair Fas and FasL to investigate whether iodine can induce apoptosis in osteosarcoma cells by activating the death receptor pathway. In our subsequent studies, we will examine other receptors and ligands in the death receptor family. In addition, no chemotherapeutic drugs were used in this study, which reduced the emission of pollutants. During the experiment, all invasive operations were carried out under anaesthesia. The experimental animals felt minor pain or no pain during and after the operation. With these measures, the expected experimental results were obtained, and the welfare of the experimental animals was ensured.

CONCLUSION

We demonstrated that iodine induced apoptosis in MG-63 and Saos-2 cells by regulating the death receptor pathway. Imageable hydrogels could be appropriately injected and localized with X-ray imaging. The operation was simple and minimally invasive. Moreover, iodine-loaded hydrogels were safe, had good biosafety and could control the release of iodine, which minimized systemic side effects and maximized the therapeutic impact. Our results suggested that self-assembling imageable silk hydrogels had good biosafety, were easy to operate, were minimally invasive and had substantial anti-OS effects. Our study promises efficient, systemic and locally less invasive treatment of OS in the future, which might replace the current treatment strategies used for OS.

DATA AVAILABILITY STATEMENT

The raw data supporting the conclusion of this article will be made available by the authors, without undue reservation.

ETHICS STATEMENT

The animal study was reviewed and approved by the First Affiliated Hospital of Harbin Medical University Ethics Clerical Association.

AUTHOR CONTRIBUTIONS

YaW lead this study. Binzhi Peng and MLi carried out the *in vitro* and *in vivo* experiments. JS, RLiu, RLi, YZ, JL, XS and RW carried out the histopathological analysis. Data analyses were performed by HY, WW, MLia, YF and RX. Funding was obtained from YaW, Binzhi Peng and YuW. The manuscript was written by ZP, commented and revised by YaW. All authors listed have made a substantial, direct, and intellectual contribution to the work and approved it for publication.

FUNDING

The study was financially supported by the Natural Science Foundation of China Grant (Project No. 81871781), the Graduate Student Innovation Research Project of Harbin Medical University (Project No. YJSCX 2017-35HYD), and the Key Laboratory of My-ocardial Ischemia, Ministry of Education, Harbin Medical University (Project No. KF201702).

SUPPLEMENTARY MATERIAL

The Supplementary Material for this article can be found online at: https://www.frontiersin.org/articles/10.3389/fcell.2022.698282/full#supplementary-material

REFERENCES

Anninga, J. K., Gelderblom, H., Fiocco, M., Kroep, J. R., Taminiau, A. H. M., Hogendoorn, P. C. W., et al. (2011). Chemotherapeutic Adjuvant Treatment for Osteosarcoma: Where Do We Stand? *Eur. J. Cancer* 47 (16), 2431–2445. doi:10.1016/j.ejca.2011.05.030

Antunovic, M., Matic, I., Nagy, B., Caput Mihalic, K., Skelin, J., Stambuk, J., et al. (2019). FADD-Deficient Mouse Embryonic Fibroblasts Undergo RIPK1-Dependent Apoptosis and Autophagy After NB-UVB Irradiation. *J. Photochem. Photobiol. B Biol.* 194, 32–45. doi:10.1016/j.jphotobiol.2019.03.007

Arndt, C. A. S., Rose, P. S., Folpe, A. L., and Laack, N. N. (2012). Common Musculoskeletal Tumors of Childhood and Adolescence. *Mayo Clin. Proc.* 87 (5), 475–487. doi:10.1016/j.mayocp.2012.01.015

Ashkenazi, A., and Dixit, V. M. (1998). Death Receptors: Signaling and Modulation. *Science* 281 (5381), 1305–1308. doi:10.1126/science.281.5381.1305

Bacci, G., Ferrari, S., Lari, S., Mercuri, M., Donati, D., Longhi, A., et al. (2002). Osteosarcoma of the Limb. *J. Bone Jt. Surg. Br. volume* 84-B (1), 88–92. doi:10.1302/0301-620x.84b1.0840088

Barret, M., Dohan, A., Oudjit, A., Leblanc, S., Belle, A., Abouali, E., et al. (2020). Meglumine Diatrizoate Esophagogram After Peroral Endoscopic Myotomy (POEM): Identification of Imaging Findings Associated with Clinical Complications and Longer Hospital Stay. *Eur. Radiol.* 30 (8), 4175–4181. doi:10.1007/s00330-020-06758-0

Basha, G., Ghirardi, M., Geboes, K., Yap, S. H., and Penninckx, F. (2000). Limitations of Peritoneal Lavage with Antiseptics in Prevention of Recurrent Colorectal Cancer Caused by Tumor-Cell Seeding: Experimental Study in Rats. *Dis. Colon Rectum* 43 (12), 1713–1718. doi:10.1007/bf02236856

Boni, R., Ali, A., Giteru, S. G., Shavandi, A., and Clarkson, A. N. (2020). Silk Fibroin Nanoscaffolds for Neural Tissue Engineering. *J. Mater Sci. Mater Med.* 31 (9), 81. doi:10.1007/s10856-020-06422-5

Cersosimo, F., Lonardi, S., Bernardini, G., Telfer, B., Mandelli, G. E., Santucci, A., et al. (2020). Tumor-Associated Macrophages in Osteosarcoma: From Mechanisms to Therapy. *Int. J. Mol. Sci.* 21 (15), 207. doi:10.3390/ijms21155207

Chang, W.-K., Lin, H.-H., Hsieh, T.-Y., Ou, T.-M., and Chen, H.-W. (2014). Benefits of the Povidone-Iodine: Simultaneously Decrease Risk of Infection and Tumor Seeding After Percutaneous Endoscopic Gastrostomy. *Med. Hypotheses* 82 (6), 678–680. doi:10.1016/j.mehy.2014.03.002

Chen, C., Xie, L., Ren, T., Huang, Y., Xu, J., and Guo, W. (2021). Immunotherapy for Osteosarcoma: Fundamental Mechanism, Rationale, and Recent Breakthroughs. *Cancer Lett.* 500, 1–10. doi:10.1016/j.canlet.2020.12.024

Cunliffe, P. J., and Fawcett, T. N. (2002). Wound Cleansing: The Evidence for the Techniques and Solutions Used. *Prof. Nurse* 18 (2), 95

Diab, T., Pritchard, E. M., Uhrig, B. A., Boerckel, J. D., Kaplan, D. L., and Guldberg, R. E. (2012). A Silk Hydrogel-Based Delivery System of Bone Morphogenetic Protein for the Treatment of Large Bone Defects. *J. Mech. Behav. Biomed. Mater.* 11, 123–131. doi:10.1016/j.jmbbm.2011.11.007

Dickens, L. S., Powley, I. R., Hughes, M. A., and MacFarlane, M. (2012). The 'complexities' of Life and Death: Death Receptor Signalling Platforms. *Exp. Cell. Res.* 318 (11), 1269–1277. doi:10.1016/j.yexcr.2012.04.005

Farokhi, M., Mottaghitalab, F., Reis, R. L., Ramakrishna, S., and Kundu, S. C. (2020). Functionalized Silk Fibroin Nanofibers as Drug Carriers: Advantages and Challenges. *J. Control. Release* 321, 324–347. doi:10.1016/j.jconrel.2020.02.022

Funahashi, H., Imai, T., Tanaka, Y., Tobinaga, J., Wada, M., Morita, T., et al. (1996). Suppressive Effect of Iodine on DMBA-Induced Breast Tumor Growth in the Rat. *J. Surg. Oncol.* 61 (3), 209–213. doi:10.1002/(sici)1096-9098(199603)61:3<209::aid-jso9>3.0.co;2-f

García-Solís, P., Alfaro, Y., Anguiano, B., Delgado, G., Guzman, R. C., Nandi, S., et al. (2005). Inhibition of N-Methyl-N-Nitrosourea-Induced Mammary Carcinogenesis by Molecular Iodine (I2) but Not by Iodide (I-) Treatment Evidence That I2 Prevents Cancer Promotion. *Mol. Cell. Endocrinol.* 236 (1-2), 49–57. doi:10.1016/j.mce.2005.03.001

Ghent, W. R., Eskin, B. A., Low, D. A., and Hill, L. P. (1993). Iodine Replacement in Fibrocystic Disease of the Breast. *Can. J. Surg.* 36 (5), 453

Gholipourmalekabadi, M., Sapru, S., Samadikuchaksaraei, A., Reis, R. L., Kaplan, D. L., and Kundu, S. C. (2020). Silk Fibroin for Skin Injury Repair: Where Do Things Stand? *Adv. Drug Deliv. Rev.* 153, 28–53. doi:10.1016/j.addr.2019.09.003

Green, D. R., and Llambi, F. (2015). Cell Death Signaling. *Cold Spring Harb. Perspect. Biol.* 7 (12), 6080. doi:10.1101/cshperspect.a006080

Hah, J. H., Roh, D. H., Jung, Y. H., Kim, K. H., and Sung, M.-W. (2012). Selection of Irrigation Fluid to Eradicate Free Cancer Cells during Head and Neck Cancer Surgery. *Head. Neck* 34 (4), 546–550. doi:10.1002/hed.21773

Hong, H., Seo, Y. B., Kim, D. Y., Lee, J. S., Lee, Y. J., Lee, H., et al. (2020). Digital Light Processing 3D Printed Silk Fibroin Hydrogel for Cartilage Tissue Engineering. *Biomaterials* 232, 119679. doi:10.1016/j.biomaterials.2019.119679

Jiang, Y., Wang, G., Mu, H., Ma, X., Wang, Z., Lv, Y., et al. (2021). Bromodomain Inhibition Attenuates the Progression and Sensitizes the Chemosensitivity of Osteosarcoma by Repressing GP130/STAT3 Signaling. *Front. Oncol.* 11, 642134. doi:10.3389/fonc.2021.642134

Kessler, J. H. (2004). The Effect of Supraphysiologic Levels of Iodine on Patients with Cyclic Mastalgia. *Breast J.* 10 (4), 328–336. doi:10.1111/j.1075-122x.2004.21341.x

Khaleel, S. A., Raslan, N. A., Alzokaky, A. A., Ewees, M. G., Ashour, A. A., Abdel-Hamied, H. E., et al. (2019). Contrast Media (Meglumine Diatrizoate) Aggravates Renal Inflammation, Oxidative DNA Damage and Apoptosis in Diabetic Rats Which Is Restored by Sulforaphane Through Nrf2/HO-1 Reactivation. *Chemico-Biological Interact.* 309, 108689. doi:10.1016/j.cbi.2019.06.002

Khasawneh, M. A., Eiken, P. W., Srvantstyan, B., Bannon, M. P., and Zielinski, M. D. (2013). Use of the Gastrografin Challenge in Patients with a History of Abdominal or Pelvic Malignancy. *Surgery* 154 (4), 769–776. Discussion 775-766. doi:10.1016/j.surg.2013.07.002

Kim, S. Y., Naskar, D., Kundu, S. C., Bishop, D. P., Doble, P. A., Boddy, A. V., et al. (2015). Formulation of Biologically-Inspired Silk-Based Drug Carriers for Pulmonary Delivery Targeted for Lung Cancer. *Sci. Rep.* 5, 11878. doi:10.1038/srep11878

Krishnan, A., Kocab, A. J., Zacks, D. N., Marshak-Rothstein, A., and Gregory-Ksander, M. (2019). A Small Peptide Antagonist of the Fas Receptor Inhibits Neuroinflammation and Prevents Axon Degeneration and Retinal Ganglion Cell Death in an Inducible Mouse Model of Glaucoma. *J. Neuroinflammation* 16 (1), 184. doi:10.1186/s12974-019-1576-3

Kuang, A. A., Diehl, G. E., Zhang, J., and Winoto, A. (2000). FADD Is Required for DR4- and DR5-Mediated Apoptosis. *J. Biol. Chem.* 275 (33), 25065–25068. doi:10.1074/jbc.c000284200

Lazebnik, Y. A., Kaufmann, S. H., Desnoyers, S., Poirier, G. G., and Earnshaw, W. C. (1994). Cleavage of Poly(ADP-Ribose) Polymerase by a Proteinase with Properties Like ICE. *Nature* 371 (6495), 346–347. doi:10.1038/371346a0

Lee, H. O., and Ferguson, T. A. (2003). Biology of FasL. *Cytokine Growth Factor Rev.* 14 (3-4), 325–335. doi:10.1016/s1359-6101(03)00028-5

Leisk, G. G., Lo, T. J., Yucel, T., Lu, Q., and Kaplan, D. L. (2010). Electrogelation for Protein Adhesives. *Adv. Mat.* 22 (6), 711–715. doi:10.1002/adma.200902643

Leng, X., Liu, B., Su, B., Liang, M., Shi, L., Li, S., et al. (2017). *In Situ* Ultrasound Imaging of Silk Hydrogel Degradation and Neovascularization. *J. Tissue Eng. Regen. Med.* 11 (3), 822–830. doi:10.1002/term.1981

Lepelletier, D., Maillard, J. Y., Pozzetto, B., and Simon, A. (2020). Povidone Iodine: Properties, Mechanisms of Action, and Role in Infection Control and *Staphylococcus aureus* Decolonization. *Antimicrob. Agents Chemother.* 64 (9), 20. doi:10.1128/AAC.00682-20

Li, H., Tian, J., Wu, A., Wang, J., Ge, C., and Sun, Z. (2016). Self-Assembled Silk Fibroin Nanoparticles Loaded with Binary Drugs in the Treatment of Breast Carcinoma. *Int. J. Nanomedicine* 11, 4373–4380. doi:10.2147/IJN.S108633

Li, Y., Zhou, Q., Hu, Z., Yang, B., Li, Q., Wang, J., et al. (2015). 5-Aminolevulinic Acid-Based Sonodynamic Therapy Induces the Apoptosis of Osteosarcoma in Mice. *PLoS One* 10 (7), e0132074. doi:10.1371/journal.pone.0132074

Liang, M., Liu, W., Peng, Z., Lv, S., Guan, Y., An, G., et al. (2019). The Therapeutic Effect of Secretome from Human Umbilical Cord-Derived Mesenchymal Stem Cells in Age-Related Osteoporosis. *Artif. Cells, Nanomedicine, Biotechnol.* 47 (1), 1357–1366. doi:10.1080/21691401.2019.1596945

Lin, H., Chen, X., Zhang, C., Yang, T., Deng, Z., Song, Y., et al. (2021). EF24 Induces Ferroptosis in Osteosarcoma Cells Through HMOX1. *Biomed. Pharmacother.* 136, 111202. doi:10.1016/j.biopha.2020.111202

Ma, D., An, G., Liang, M., Liu, Y., Zhang, B., and Wang, Y. (2016). A Composited PEG-Silk Hydrogel Combining with Polymeric Particles Delivering rhBMP-2 for Bone Regeneration. *Mater. Sci. Eng. C* 65, 221–231. doi:10.1016/j.msec.2016.04.043

Marec-Berard, P., Dalban, C., Gaspar, N., Brugieres, L., Gentet, J.-C., Lervat, C., et al. (2020). Multicentric Randomized Phase II Clinical Trial Evaluating High-Dose Thiotepa as Adjuvant Treatment to Standard Chemotherapy in Patients with Resectable Relapsed Osteosarcoma. *Eur. J. Cancer* 125, 58–68. doi:10.1016/j.ejca.2019.11.007

Matsumoto, A., Chen, J., Collette, A. L., Kim, U.-J., Altman, G. H., Cebe, P., et al. (2006). Mechanisms of Silk Fibroin Sol–Gel Transitions. *J. Phys. Chem. B* 110 (43), 21630–21638. doi:10.1021/jp056350v

Mercadante, S., Ferrera, P., Villari, P., and Marrazzo, A. (2004). Aggressive Pharmacological Treatment for Reversing Malignant Bowel Obstruction. *J. Pain Symptom Manag.* 28 (4), 412–416. doi:10.1016/j.jpainsymman.2004.01.007

Muscolo, D. L., Ayerza, M. A., Aponte-Tinao, L. A., and Ranalletta, M. (2005). Partial Epiphyseal Preservation and Intercalary Allograft Reconstruction in High-Grade Metaphyseal Osteosarcoma of the Knee. *J. Bone Jt. Surgery-American Volume* 87 (Suppl. 1Pt 2), 226–236. doi:10.2106/00004623-200509001-00006

Nagata, S. (1997). Apoptosis by Death Factor. *Cell.* 88 (3), 355–365. doi:10.1016/s0092-8674(00)81874-7

Nguyen, T. T., and Janik, L. J. (1987). Fourier-Transform Infrared Study of Ethylene Glycol Monoethyl Ether Adsorbed on Montmorillonite: Implications for Surface Area Measurements of Clays. *Clays Clay Minerals* 35, 60–67. doi:10.1346/ccmn.1987.0350108

Nicholson, D. W., Ali, A., Thornberry, N. A., Vaillancourt, J. P., Ding, C. K., Gallant, M., et al. (1995). Identification and Inhibition of the ICE/CED-3 Protease Necessary for Mammalian Apoptosis. *Nature* 376 (6535), 37–43. doi:10.1038/376037a0

Oliver, F. J., de la Rubia, G., Rolli, V., Ruiz-Ruiz, M. C., de Murcia, G., and Murcia, J. M.-d. (1998). Importance of Poly(ADP-Ribose) Polymerase and its Cleavage in Apoptosis. Lesson from an Uncleavable Mutant. *J. Biol. Chem.* 273 (50), 33533–33539. doi:10.1074/jbc.273.50.33533

Omenetto, F. G., and Kaplan, D. L. (2010). New Opportunities for an Ancient Material. *Science* 329 (5991), 528–531. doi:10.1126/science.1188936

Ottaviani, G., and Jaffe, N. (2009). The Epidemiology of Osteosarcoma. *Cancer Treat. Res.* 152, 3–13. doi:10.1007/978-1-4419-0284-9_1

Pattana-arun, J., and Wolff, B. G. (2008). Benefits of Povidone-Iodine Solution in Colorectal Operations: Science or Legend. *Dis. Colon Rectum* 51 (6), 966–971. doi:10.1007/s10350-008-9213-8

Pritchard, E. M., and Kaplan, D. L. (2011). Silk Fibroin Biomaterials for Controlled Release Drug Delivery. *Expert Opin. Drug Deliv.* 8 (6), 797–811. doi:10.1517/17425247.2011.568936

Rhodes, M. A. (1987). Limb-Salvage Treatment versus Amputation for Osteosarcoma of the Distal End of the Femur. *J. Bone & Jt. Surg.* 69 (5), 792–793. doi:10.2106/00004623-198769050-00029

Seib, F. P., and Kaplan, D. L. (2012). Doxorubicin-Loaded Silk Films: Drug-Silk Interactions and *In Vivo* Performance in Human Orthotopic Breast Cancer. *Biomaterials* 33 (33), 8442–8450. doi:10.1016/j.biomaterials.2012.08.004

Seib, F. P., Pritchard, E. M., and Kaplan, D. L. (2013). Self-Assembling Doxorubicin Silk Hydrogels for the Focal Treatment of Primary Breast Cancer. *Adv. Funct. Mat.* 23 (1), 58–65. doi:10.1002/adfm.201201238

Simon, M. A., Aschliman, M. A., Thomas, N., and Mankin, H. J. (1986). Limb-Salvage Treatment versus Amputation for Osteosarcoma of the Distal End of the Femur. *J. Bone & Jt. Surg.* 68 (9), 1331–1337. doi:10.2106/00004623-198668090-00005

Stathis, C., Victoria, N., Loomis, K., Nguyen, S. A., Eggers, M., Septimus, E., et al. (2021). Review of the Use of Nasal and Oral Antiseptics During a Global Pandemic. *Future Microbiol.* 16, 119–130. doi:10.2217/fmb-2020-0286

Strickley, R. G. (2004). Solubilizing Excipients in Oral and Injectable Formulations. *Pharm. Res.* 21 (2), 201–230. doi:10.1023/b:pham.0000016235.32639.23

Suda, T., Takahashi, T., Golstein, P., and Nagata, S. (1993). Molecular Cloning and Expression of the Fas Ligand, a Novel Member of the Tumor Necrosis Factor Family. *Cell.* 75 (6), 1169–1178. doi:10.1016/0092-8674(93)90326-l

Takeuchi, A., Yamamoto, N., Hayashi, K., Matsubara, H., Miwa, S., Igarashi, K., et al. (2019). Joint-Preservation Surgery for Pediatric Osteosarcoma of the Knee Joint. *Cancer Metastasis Rev.* 38 (4), 709–722. doi:10.1007/s10555-019-09835-z

Türkkan, S., Pazarçeviren, A. E., Keskin, D., Machin, N. E., Duygulu, Ö., and Tezcaner, A. (2017). Nanosized CaP-Silk Fibroin-PCL-PEG-PCL/PCL Based Bilayer Membranes for Guided Bone Regeneration. *Mater. Sci. Eng. C* 80, 484–493. doi:10.1016/j.msec.2017.06.016

Vepari, C., and Kaplan, D. L. (2007). Silk as a Biomaterial. *Prog. Polym. Sci.* 32 (8-9), 991–1007. doi:10.1016/j.progpolymsci.2007.05.013

Wang, X., Kluge, J. A., Leisk, G. G., and Kaplan, D. L. (2008). Sonication-Induced Gelation of Silk Fibroin for Cell Encapsulation. *Biomaterials* 29 (8), 1054–1064. doi:10.1016/j.biomaterials.2007.11.003

Wang, X., Partlow, B., Liu, J., Zheng, Z., Su, B., Wang, Y., et al. (2015). Injectable Silk-Polyethylene Glycol Hydrogels. *Acta Biomater.* 12, 51–61. doi:10.1016/j.actbio.2014.10.027

Wenk, E., Merkle, H. P., and Meinel, L. (2011). Silk Fibroin as a Vehicle for Drug Delivery Applications. *J. Control. Release* 150 (2), 128–141. doi:10.1016/j.jconrel.2010.11.007

Whelan, J., McTiernan, A., Cooper, N., Wong, Y. K., Francis, M., Vernon, S., et al. (2012). Incidence and Survival of Malignant Bone Sarcomas in England 1979-2007. *Int. J. Cancer* 131 (4), E508–E517. doi:10.1002/ijc.26426

White, C. S., Templeton, P. A., and Attar, S. (1993). Esophageal Perforation: CT Findings. *Am. J. Roentgenol.* 160 (4), 767–770. doi:10.2214/ajr.160.4.8456662

Wu, J. S., Pfister, S. M., Ruiz, M. B., Connett, J. M., and Fleshman, J. W. (1998). Local Treatment of Abdominal Wound Reduces Tumor Implantation. *J. Surg. Oncol.* 69 (1), 9–14. Discussion 14. doi:10.1002/(sici)1096-9098(199809)69:1<9::aid-jso3>3.0.co;2-7

Wu, R., Geng, L., Zhao, Z., Liao, D., He, B., Hu, H., et al. (2020). Clinical Application of Oral Meglumine Diatrizoate Esophagogram in Screening for Esophageal Fistula During Radiotherapy or Chemoradiotherapy for Esophageal Cancer. *Front. Oncol.* 10, 562147. doi:10.3389/fonc.2020.562147

Wu, X., Liao, Z., Wang, K., Hua, W., Liu, X., Song, Y., et al. (2019). Targeting the IL-1β/IL-1Ra Pathways for the Aggregation of Human Islet Amyloid Polypeptide in an *Ex Vivo* Organ Culture System of the Intervertebral Disc. *Exp. Mol. Med.* 51 (9), 1–16. doi:10.1038/s12276-019-0310-7

Xie, M., Fan, D., Li, Y., He, X., Chen, X., Chen, Y., et al. (2017). Supercritical Carbon Dioxide-Developed Silk Fibroin Nanoplatform for Smart Colon Cancer Therapy. *Ijn* Vol. 12, 7751–7761. doi:10.2147/ijn.s145012

Yang, C., Tian, Y., Zhao, F., Chen, Z., Su, P., Li, Y., et al. (2020). Bone Microenvironment and Osteosarcoma Metastasis. *Int. J. Mol. Sci.* 21 (19). doi:10.3390/ijms21196985

Yang, M.-H., Chung, T.-W., Lu, Y.-S., Chen, Y.-L., Tsai, W.-C., Jong, S.-B., et al. (2015). Activation of the Ubiquitin Proteasome Pathway by Silk Fibroin Modified Chitosan Nanoparticles in Hepatic Cancer Cells. *Ijms* 16 (1), 1657–1676. doi:10.3390/ijms16011657

Yin, L. L., Wen, X. M., Li, M., Xu, Y. M., Zhao, X. F., Li, J., et al. (2018). A Gene Mutation in RNA-Binding Protein 10 Is Associated with Lung Adenocarcinoma Progression and Poor Prognosis. *Oncol. Lett.* 16 (5), 6283–6292. doi:10.3892/ol.2018.9496

Yuan, X., Gajan, A., Chu, Q., Xiong, H., Wu, K., and Wu, G. S. (2018). Developing TRAIL/TRAIL Death Receptor-Based Cancer Therapies. *Cancer Metastasis Rev.* 37 (4), 733–748. doi:10.1007/s10555-018-9728-y

Yucel, T., Cebe, P., and Kaplan, D. L. (2009). Vortex-Induced Injectable Silk Fibroin Hydrogels. *Biophysical J.* 97 (7), 2044–2050. doi:10.1016/j.bpj.2009.07.028

Zhang, X., Chen, Z., Bao, H., Liang, J., Xu, S., Cheng, G., et al. (2019). Fabrication and Characterization of Silk Fibroin/Curcumin Sustained-Release Film. *Mater. (Basel)* 12 (20), 340. doi:10.3390/ma12203340

Conflict of Interest: The authors declare that the research was conducted in the absence of any commercial or financial relationships that could be construed as a potential conflict of interest.

Publisher's Note: All claims expressed in this article are solely those of the authors and do not necessarily represent those of their affiliated organizations, or those of the publisher, the editors and the reviewers. Any product that may be evaluated in this article, or claim that may be made by its manufacturer, is not guaranteed or endorsed by the publisher.

Advantages of publishing in Frontiers

OPEN ACCESS
Articles are free to read for greatest visibility and readership

FAST PUBLICATION
Around 90 days from submission to decision

HIGH QUALITY PEER-REVIEW
Rigorous, collaborative, and constructive peer-review

TRANSPARENT PEER-REVIEW
Editors and reviewers acknowledged by name on published articles

Frontiers
Avenue du Tribunal-Fédéral 34
1005 Lausanne | Switzerland

Visit us: www.frontiersin.org
Contact us: frontiersin.org/about/contact

REPRODUCIBILITY OF RESEARCH
Support open data and methods to enhance research reproducibility

DIGITAL PUBLISHING
Articles designed for optimal readership across devices

FOLLOW US
@frontiersin

IMPACT METRICS
Advanced article metrics track visibility across digital media

EXTENSIVE PROMOTION
Marketing and promotion of impactful research

LOOP RESEARCH NETWORK
Our network increases your article's readership